Journal of Turbomachinery

Published Quarterly by The American Society of Mechanical Engineers

VOLUME 121 • NUMBER 4 • OCTOBER 1999

TECHNICAL PAPERS

(Contents continued)

ANNOUNCEMENTS

1997 John P. Davis Award

The Impact of Machining Techniques on Centrifugal Compressor Impeller Performance

P. R. N. Childs

Thermo-Fluid Mechanics Research Centre,
University of Sussex,
Sussex, United Kingdom

M. B. Noronha

Turbocam, Inc.,
Dover, NH

A large proportion of modern centrifugal impellers are machined from solid forgings rather than made from cast metal. The CNC milling process offers options to manufacturers to minimize manufacturing costs while also enhancing the performance of the impeller. Efficient manufacturing can result in cutter tool marks and paths and associated roughness remaining on the hub and blade surfaces of impellers as a result of minimizing passes and maximizing the cut. The goal of manufacturers is to allow these marks to be as deep as possible to minimize machining costs, but without any negative effects on performance, and possibly even enhancing it. There are existing modeling methods that predict the influence of roughness on compressor performance using the definition of an equivalent sand grain roughness. The purpose of this study is to relate the performance directly to the tool mark characteristics that are by-products of machining, namely cusp height, cutter path roughness, and orientation of the cutter path relative to the local flow velocity, to review the current modeling techniques for predicting the influence of surface condition on compressor performance and to show the scope for optimization of manufacturing and performance considerations.

1 Introduction

CNC milling of centrifugal compressor impellers is a mature technology that is ideal for rapid prototyping and low-quantity pre-production, and may sometimes be economical for large production runs. Casting, the alternative process, is cheaper for larger quantities, but inferior in accuracy, consistency, and structural integrity. For example, automotive turbocharger impellers have traditionally been cast due to economies of scale. The cost ratio of cast to milled impellers would be at least 1:20. For production runs of a few hundred, the cost ratio falls between 1:1 and 1:2. For runs of fewer than 50 parts, the ratio could be 2:1, and when delivery is taken into account, casting may not be a viable option. For large, high-performance centrifugal compressors, structural integrity (stress, fatigue, and frequency response) demands the use of forged billets, and therefore milling. With CNC manufacture, accuracy and consistency can be achieved in all directions, irrespective of the size or location.

The manufacture of compressor impellers, whether by casting or machining, results in an inherent surface roughness (see Figs. 1 and 2). The form of roughness depends on the manufacture process. For casting, a sand-grain-type roughness results, while for machining, the surface roughness is composed of two elements: the cusp height and the cutter path roughness (see Fig. 2). The centerline average roughness is defined, with reference to Fig. 1, by Eqs. (1) and (2): (1) (2)

$$R_a = \frac{\sum\limits_{n=1}^{n} r_n + \sum\limits_{n=1}^{n} s_n}{L} \qquad (1)$$

$$H_m = \frac{\text{Area } P}{L} \qquad (2)$$

Numerous investigations have been undertaken on the effect of Reynolds number on centrifugal compressor performance. Several of the resulting methods relate the frictional losses in the impeller directly to the friction factor for internal flows. As the friction factor is dependent on both the Reynolds number and the relative surface roughness ratio, the influence of surface roughness can be quantified, albeit not entirely reliably. A complication in using these methods is that the definition of sand grain roughness does not relate to CNC machined impellers due to the formation of cusps in machining and the variation in surface finish across the geometry of the impeller from say a "smooth" finish on the suction blade to the deliberately "cuspy" hub profile. CNC software typically calculates the roughness based entirely on cusp geometry (see Fig. 2). An additional parameter is the orientation of the cusps or machine cutter path relative to the local flow velocity (as illustrated in Figs. 3 and 4). Optimization of the tool path only may result in the cusp orientation actually increasing the level of over-tip leakage to the detriment of the overall performance. Opportunity exists, given understanding of surface condition effects, to specify the surface finish of each region of the impeller for optimum performance and manufacture costs.

2 CNC Impeller Manufacture

CNC milling can be undertaken using a range of three and a half to five axis machines, varying from under $100,000 to over $2,000,000 in cost (1996 prices), the choice being dependent on the complexity of the impeller geometry and the resources and know-how of the manufacturing company.

In addition to the impeller blade coordinates (the impeller geometry must be clearly specified to the manufacturer (Turbocam, 1996)), several critical features must be specified by the customer or negotiated between the manufacturer and the customer. Chief
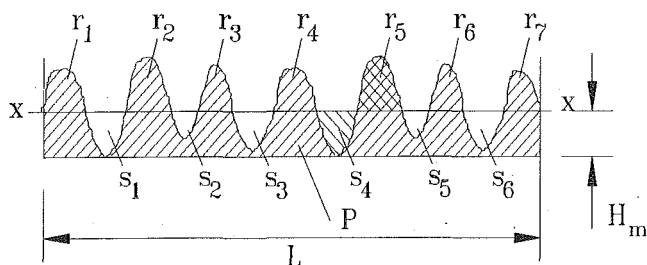
Fig. 1 Centerline average roughness definition

Fig. 2 Application of the centerline average roughness definition to CNC bull nose cutter machining

among these are the blade-to-hub fillet radius, the smallest passage in the impeller, and the blade and hub surface finishes. While it is typical for manufacturers to estimate the cost of a part based on its outside diameter, wise choices of these features can make a huge difference in manufacturing time and cost.

2.1 The Blade-to-Hub Fillet. The designer has to choose a convenient balance between the needs of aerodynamic performance and stress and vibration resistance. A fixed radius fillet is usually the easiest to machine, especially when the radius is the same as that of the tool ideally suited to machining the blade. Variable fillet radii, Fig. 5, increase programming time, but minimally affect machining time for parts in production.

2.2 The Smallest Passage. The length of a splitter blade is often based on flow considerations. It is common for the fillet radius between the splitter and the adjacent full blade to become the real defining limit for the location of the splitter leading edge. If this fillet radius is not kept to a reasonable size, it may have a major impact on the engineering costs and the production cost of the impeller. It should be no lower than the general fillet radius around the rest of the blades. The smallest distance between consecutive blades is the normal distance from one blade to another, and this is usually not in the circumferential direction, Fig. 6.

It is common machining practice to leave 0.25 to 1.25 mm (0.010 to 0.050 in.) on a surface during the rough milling operation, depending on the size of the part. This is removed during the final finishing operations. Although it is possible to machine a part while allowing considerably less than ideal finishing stock, this may lead to damaged parts, gouged surfaces, roughness, and severe increase in manufacturing costs. Fillet radii should be specified that allow for some finishing stock in addition to the diameter of the tool that is expected to pass through a passage (the narrowest throat distance between blades).

The fillet radius and the smallest passage width determine the size of tools that have to be used on the part. Very small tools require high spindle speeds, which may dictate the use of a specific milling machine, raise manufacturing costs, and restrict manufacturing options.

2.3 Surface Finish. Typical blade surface finishes are in the range of 1.6 μm. Hub surfaces may vary from 0.8 to 12.5 μm, though some go to 50 μm or more. Blades may be flank milled (machined with the side of a cutter), or point milled (machined with the tip of a cutter), or milled by some combination of these methods. It is evident that flank milling takes less time than point milling, as the latter requires far more machine time. Flank-milled blades are less accurate, but may produce very satisfactory surfaces that are smoother than 1.6 μm. Typical point-milled surfaces, which are more accurate, have uniform roughness, which may slightly exceed 1.6 μm. This can be reduced through increasing machining time or by light polishing by hand, with a corresponding rise in manufacturing cost.
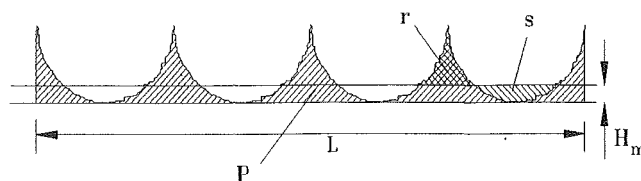
When a hub is machined leaving high ridges (cusps) between machining passes, a significant amount of time is saved in machining. When a hub is machined to a smooth surface, there may be much additional time spent in machining; however, this time is relatively low in cost, because hub machining is simple and low risk, and can run in a "lights out," unmanned mode. Thus, smooth hubs cost extra, but the difference in cost may be affordable.

2.3.1 Limitations of Flank Milling. The vast majority of centrifugal compressor impellers are designed with straight line elements defining the hub and tip locations, creating ruled surfaces. The tool vectors required to follow these rulings must be mapped to the motion of the five axes of a milling machine. While many representations of the rulings and the tool motion to achieve them can be expressed mathematically on a CAD model, the ability for the milling machine to map the CAD model accurately may be limited.

Flank milling requires the tool to follow the blade rulings, or a slight modification thereof, accurately. This limits the ability of the programmer to fit the program within a smaller machine envelope. The larger machine needed is slower, and the dynamics that it introduces may translate into what looks like chatter on the blade surfaces. This "chatter" may appear along the line of contact of the tool with the blade, and it may appear along the blade-to-hub fillet. It can be reduced by careful programming, but in the end it is often a unique signature of a given machine tool and its control system. The worst aspect of this "chatter" is that it may leave ridges that go from hub to blade tip, in a direction that may affect flow adversely. The solution often chosen to combat this problem is "benching," or polishing by hand. Flank milling also requires very accurate tools to be used. It is common to see striations on flank milled impeller blades, that are caused by tool inaccuracies, deflections, and machine dynamics. These striations may or may not be large enough

---

Nomenclature

a = empirical constant	
b_2 = exducer width, m	
c = semi-empirical constant	
D_2 = exducer diameter, m	
f = friction factor	
f_t = friction factor at known test conditions	
f_∞ = Reynolds number independent friction factor	
H_m = centerline height, m	

k_s = sand grain roughness, m
m = empirical constant
r_2 = exducer radius, m
r_n = element area, m^2
R_a = centerline average (CLA) roughness or arithmetic average (AA) roughness
Re = Reynolds number
Re$_t$ = Reynolds number at known test conditions
s_n = element area, m^2

U_2 = exducer tangential velocity, m/s
Δf = change in friction factor
$\Delta \eta$ = change in efficiency
η = efficiency
η_{is} = isentropic efficiency
η_t = efficiency at known test conditions
ν = kinematic viscosity, m^2/s
ν_1 = kinematic viscosity at inlet, m^2/s
μ_0 = work done factor
ω = angular velocity, rad/s
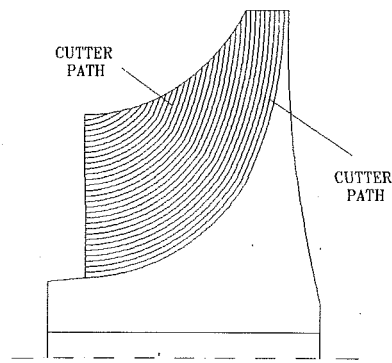
Fig. 3 Cutter path offset from hub

to affect flow. They are typically not in the direction of flow, but may be on curves parallel to the hub line.

Flank milling is also unable to machine a ruled surface blade accurately. This is because a straight line element is being used to machine what is actually a curved surface. The error is significant on larger impellers and impellers with much twist on the blades. On smaller impellers it may be negligible. There are many software techniques that are used to minimize the error, but with highly twisted blades the error will continue to exist. Whether this error is of serious significance to the performance of the impeller is not well known and will vary with the application.

It should be noted that flank milling cannot be used to machine nonruled surfaces except with special techniques using specially ground cutters. The vast majority of compressor impellers seen in industry have ruled blades. This is mainly due to the lack of design codes for development of nonruled surfaces, rather than unfavorable economics of manufacturing.

2.3.2 Limitations and Opportunities in Point Milling. The evident disadvantage of point milling is the relatively large amount of time taken to contour a blade surface compared to flank milling. The typical flank milled blade has a 1.6 μm finish on most parts of the surface, with the exceptions of "chatter" referred to earlier. This has become the *de facto* industry standard for smoothness. Thus point-milled blades are usually expected to meet this standard, as designers rarely specify that a blade is to be milled in a particular way.

Point-milled blades have several advantages: Smaller machines may be used, with lower horsepower requirements, and the cutting force applied on the blade is a small fraction of what is being applied during flank milling. Deflections are smaller, and accuracy higher. With such positives going for it, the bad news about cutting times deserves to be challenged.

- Is 1.6 μm necessary, or is it based on a subjective touch and feel?
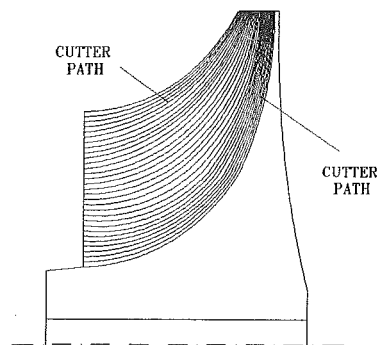
Fig. 4 Cutter path orientation assumed relative to an arbitrary meridional velocity

Table 1 Times in minutes per blade

SIZE (mm)	150	300	450	600
0.8μm	32.5	124.5	-	-
1.6μm	25.9	99.1	193.8	-
3.2μm	20.9	80.3	157.4	308.5
6.4μm	17.1	66.0	129.7	254.7
12.5μm	14.4	55.4	108.7	213.1
25μm	12.4	48.2	95.0	187.4
50μm	11.5	43.3	84.0	163.0

- If point milling is to be used, what machining patterns could help or hinder flow?
- What is the threshold of roughness at which flow gets affected at all?

Consider the machining patterns used to finish blades. The standard approach would be to have all passes match the presumed flow. This is wasteful in machining terms, as more passes are required near the inducer, and fewer passes are needed near the impeller exit. The most economical method of machining is to make all passes parallel to the hub surface, so that all parts of the blade have the same density of cuts. Now the passes no longer match the presumed flow. The passes actually may direct flow from the inducer toward the blade tip. If they do this, they may increase tip losses, and adversely affect secondary flow. It will be necessary to get test data to establish the threshold of roughness where flow actually is being redirected by the cutter marks.

Cutter marks may affect fatigue life of the blades. In some process compressors, flow passages with cutter marks may tend to attract and retain deposits, reducing the flow area and accelerating stress corrosion on the substrate metal. These effects are beyond the scope of this study.

Table 1 lists the estimated cutting times that would result from using different kinds of finishes on point milled blades. These estimates are based on cutting four scaled centrifugal impellers made from 17-4 PH stainless steel.

Cutting times do not increase directly with lengths of cutting programs, as cutting feed-rates also increase as the cuts get smaller. The limiting factors in cutting speed are the dynamics of the milling machine and its control system. This estimation uses a feed-rate of 250 mm/min for 50 μm cuts and 625 mm/min for 0.8 μm cuts. Cutter paths optimized as shown in Fig. 3 are assumed. The next estimation (Table 2) is made by applying a market price of $100 per hour for 50 μm cuts and $70 per hour for 0.8 μm cuts to an impeller with 16 blades. The range of prices reflects the relative ease and risk of high and low depths of cuts in finishing.

The costs shown in Table 2 present the case for rougher machining finishes. The $300 change in price for a 150 mm impeller can make all the difference in taking a product to market with a cast or machined impeller. If the cutter marks can be "tuned" to

Table 2 Estimated cost for finish machining a 16 blade impeller (1996 costings)

	SIZE (mm) $ per hour	150	300	450	600
0.8μm	70	606	2324	-	-
1.6μm	75	518	1982	3617	-
3.2μm	80	446	1713	3148	6581
6.4μm	85	388	1496	2940	5773
12.5μm	90	345	1330	2609	5114
25μm	95	314	1221	2407	4747
50μm	100	307	1155	2240	4346

R .094 PRESSURE SIDE   R .375 SUCTION SIDE

Fig. 5   Variable fillet radii

Fig. 7   Flow over sand grain roughness
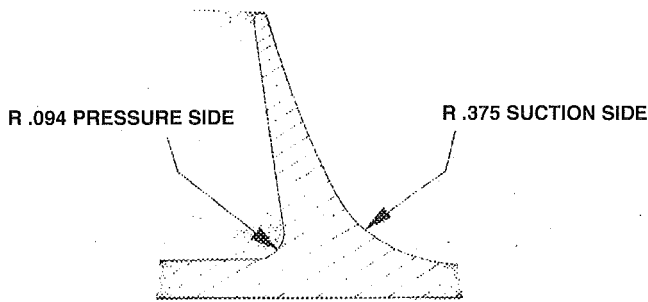
bring out a performance increase, then there may be a winner out there somewhere!

3   Prediction of Impeller Performance Variation With Surface Finish

Most of the existing methods for predicting the variation of compressor performance or efficiency with relative surface roughness are based on relating the frictional losses in the impeller channel to the friction factor for internal flows.

Wiesner (1979) proposed a relationship of the form (3)

$$\frac{1 - \eta}{1 - \eta_t} = a + (1 - a)\left(\frac{\mathrm{Re}_t}{\mathrm{Re}}\right)^m \tag{3}$$

where η is the efficiency to be determined at Reynolds number Re, η_t is a measured efficiency at a test Reynolds number Re_t, a is a constant accounting for the nonfrictional losses, and m is an empirical constant. Problems arise in the use of this method due to difficulties in establishing reliable values for the constants a and m.

Simon and Bulskamper (1984) and Strub et al. (1987) proposed the following form of equation for predicting the influence of Reynolds number and relative surface roughness: (4)

$$\frac{1 - \eta}{1 - \eta_t} = \frac{a + (1 - a)(f/f_\infty)}{a + (1 - a)(f_t/f_\infty)} \tag{4}$$

where η is the efficiency to be determined for flow conditions with a friction factor f, η_t is a measured efficiency at test flow conditions with a friction factor of f_t, f_∞ is the friction factor for fully turbulent conditions, and a is an empirical constant. These methods have been further developed by Wright (1989).

The friction factor can be calculated from the Colebrook–White formula: (5)

$$\frac{1}{\sqrt{f}} = 1.74 - 2 \log_{10}\left(\frac{2R_a}{b_2} + \frac{18.7}{\mathrm{Re}\sqrt{f}}\right) \tag{5}$$

where f is the friction factor, R_a is the surface roughness ($R_a \approx k_s/2$), b_2 is the impeller exit width, and $\mathrm{Re} = \omega b_2 D_2/\nu$ is the impeller Reynolds number. This equation requires iteration or successive substitution to calculate the friction factor for a given Reynolds number and friction factor and is best achieved by use of a spreadsheet or computer program.

Casey (1985) proposed a technique for determining the influence of Reynolds number effects that avoids the necessity to determine the empirical constant a: (6)

$$\Delta\eta = -\frac{c}{\mu_o} \Delta f \tag{6}$$

where $\Delta\eta$ is the change in efficiency resulting from a change in the flow or surface conditions, c is a semi-empirical constant related to the compressor width ratio b_2/D, μ_0 is the work coefficient, and Δf is the change in the friction factor resulting from the change in

CIRCUMFERENTIAL DISTANCE

THROAT DISTANCE BETWEEN BLADE AND SPLITTER
MAY LIMIT LOCATION OF SPLITTER LEADING EDGE.

Fig. 6   Circumferential distances between blades for an impeller with splitters
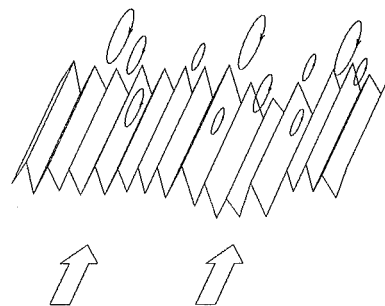
Fig. 8   Flow over roughness elements parallel to lay lines
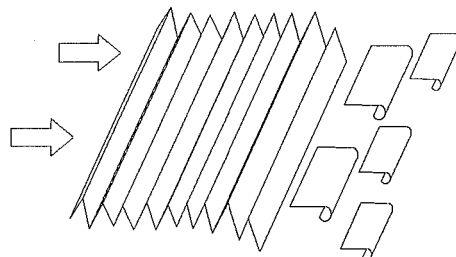
Fig. 9   Flow over roughness elements normal to lay lines
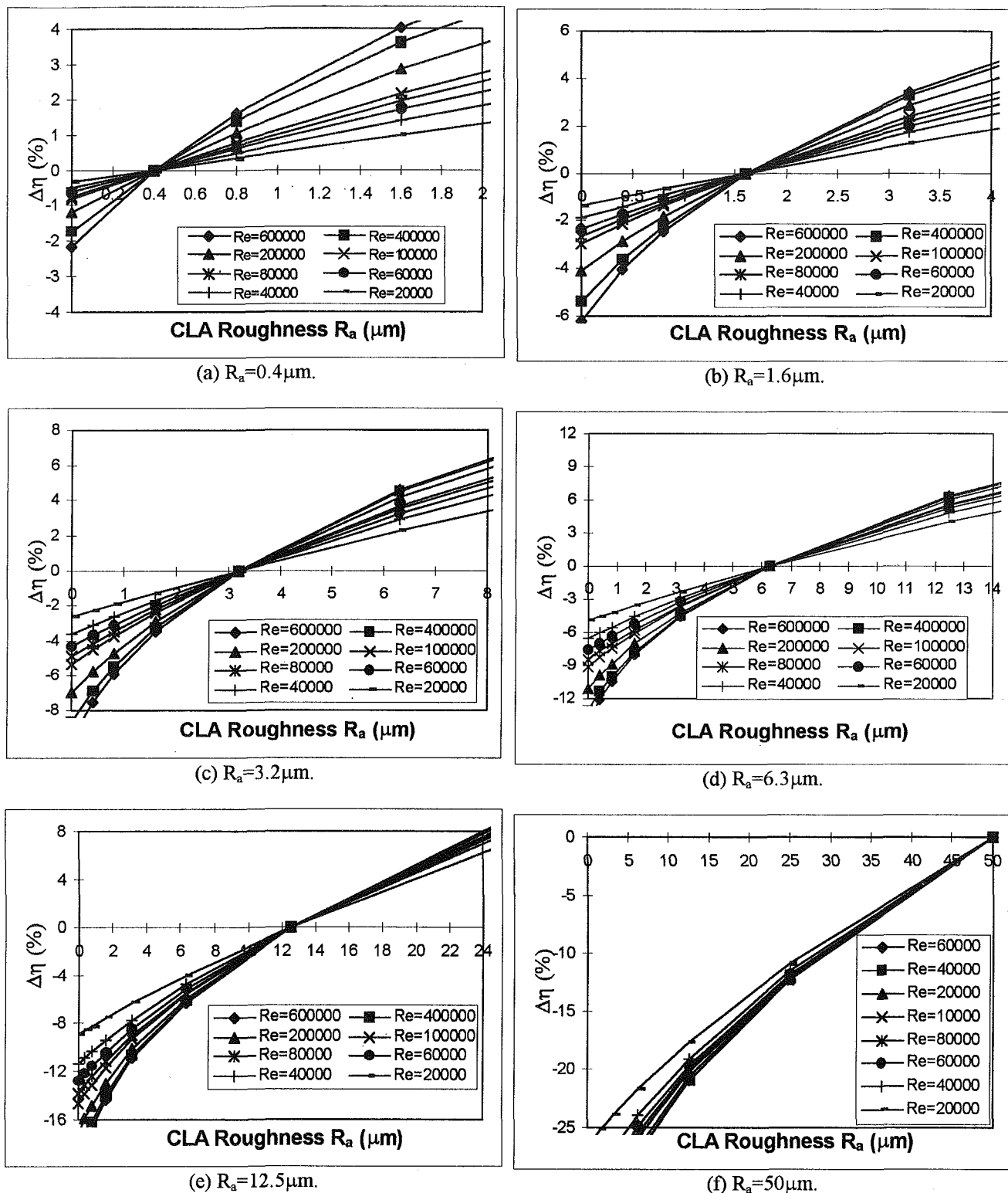
Fig. 10 Charts showing deviation in compressor efficiency with variation of surface roughness from baseline values of R_a = 0.4, 1.6, 3.2, 6.3, 12.5, and 50 μm (a) R_a = 0.4 μm (c) R_a = 3.2 μm (e) R_a = 12.5 μm (b) R_a = 1.6 μm (d) R_a = 6.3 μm (f) R_a = 50 μm

flow and surface conditions. Equation (6) can be used to determine the change in efficiency resulting from variation of the impeller surface roughness for a given Reynolds number.

It should be noted that use of Eq. (6) to model surface roughness effects requires some justification. As discussed in Section 1, the roughness criteria for CNC-machined impellers differ from the simple sand grain roughness defined in determining friction fac-

tors. Figure 7 shows a schematic of the flow and resultant vortex shedding over reasonably regularly spaced elements representative of sand grain roughness. Point milling results in roughness with lay lines, as illustrated in Fig. 8. The resultant eddy motion and vortex shedding over lay roughness depends on the orientation of the flow and is shown schematically in Figs. 8 and 9. The friction factor for flow parallel to the machined paths is likely to be lower than that
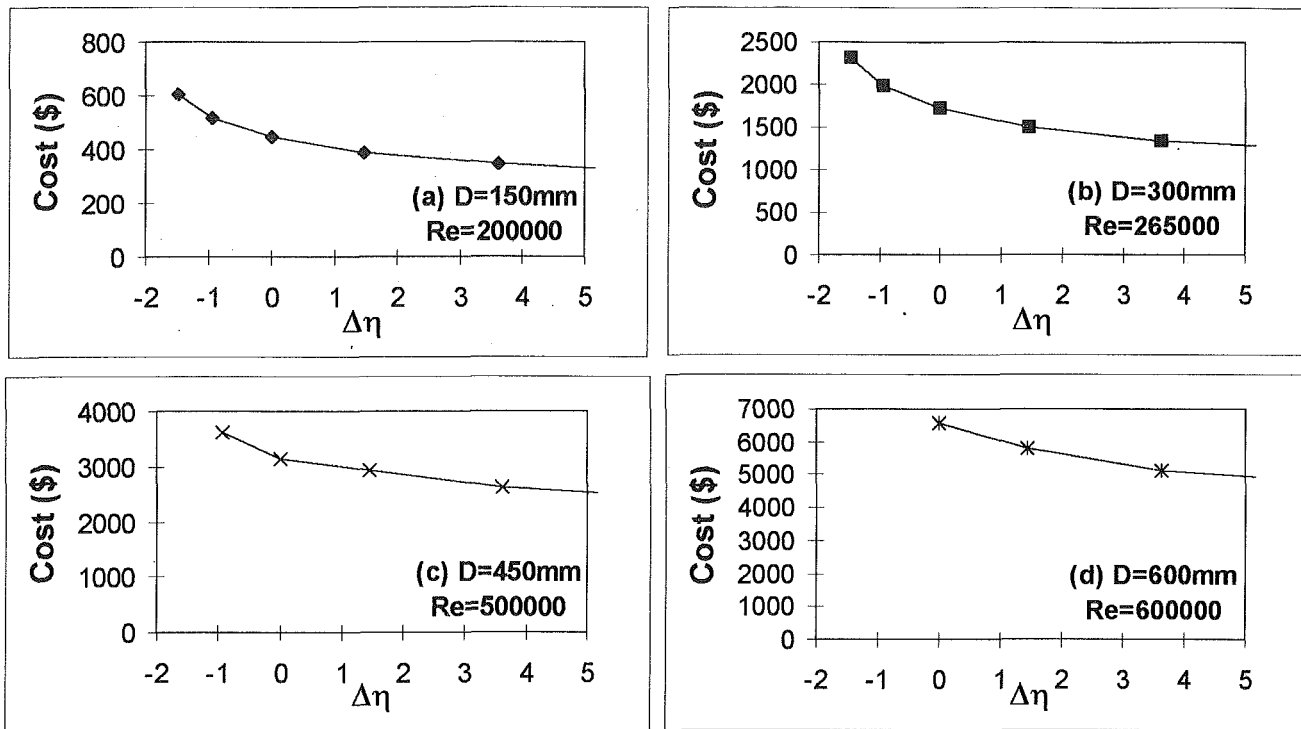
Fig. 11 Charts to determine the impact of efficiency variation on cost. The efficiency is given relative to a known efficiency for an impeller with roughness equal to 3.2 μm. A negative value of $\Delta\eta$ denotes an improvement in efficiency.

for the equivalent sand grain roughness due to the lower surface area and weaker vortex shedding. In addition, the wide range of centrifugal machines from low mass flow and high pressure ratio, where surface roughness would be expected to be significant due to the proximity of surfaces to the bulk flow, to high mass flow, low pressure machines where roughness effects are likely less significant, means that a single empirical equation would have to cover an extensive range of physical conditions. Equation (6) has been used here as it provides results not inconsistent with the data of Simon and Bulskamper (1984) who obtained the variation of impeller performance with Reynolds number for a range of surface roughness from 0.8 μm to 6.4 μm for a 350 mm diameter impeller. While Eq. (6) is not able to model the detailed physics of the flows for the wide range of impellers and flow conditions experienced accurately, within limited ranges of application it allows quantification of the effect of impeller surface roughness on performance. This is a necessary requirement if management/design decisions are to be taken concerning the trade between impeller performance and impeller first cost. In addition the simplicity of Casey's equation allows for modification according to proprietary know-how.

Charts for the practical use of this method are presented in Fig. 10. The method requires that a baseline efficiency for an impeller of a specified roughness be known. Using this roughness value, the corresponding roughness chart should be selected. The operating Reynolds number should be determined and the corresponding Reynolds number line on the chart identified. The change in efficiency resulting from a change in the roughness can then be determined by following this line and reading values from the chart. Note that in the charts presented a positive value of the efficiency change, $\Delta\eta$, corresponds to a reduction in the overall efficiency and a negative value corresponds to an improvement.

An alternative method is actually to model the effect of surface roughness in a full CFD solution of the impeller channel. Various codes have been developed using empirical models for representing surface roughness effects (e.g., Tarada, 1987, 1990). However, problems with the accuracy of viscous modeling and general validation of such codes still exist and they cannot yet be used with confidence at the design stage.

4 Optimization of Impeller Manufacture and Performance

Given the existing techniques available for quantification of the effect of surface roughness, experience from previous designs, and proprietary test data, combined with a knowledge of the process of manufacture as detailed in Section 2, scope exists to undertake an optimization of impeller performance and manufacture costs. This could be achieved by consideration of the cost implication of increased efficiency and life-time cycle costs as a function of performance and manufacture costs.

In addition, new concepts could be considered, such as purposefully defining the cusp orientation in an impeller channel to minimize over-tip leakage, and specifying variable surface roughness over a region to modify local flow conditions. For example, roughness elements, i.e., the cutter path, could be deliberately specified normal to the local flow velocity on the suction surface at say 70 percent along the meridional, to elevate local turbulence and encourage the delay of separation or partial flow reattachment. The effects of using local surface patches to influence local flow conditions can be predicted using CFD packages with surface roughness modeling capability. This technique, however, does not yield results quickly and is awkward to use as a design optimization tool.

The strategy proposed here is to utilize the methods proposed by Casey to quantify the effect of variation of Reynolds numbers on compressor efficiency to model the effect of surface roughness and combine this with the information concerning manufacture costings outlined here. Decisions concerning the trade of performance efficiency and manufacture costs, combined with the desirability for low lifetime cost, can then be quantified. Charts illustrating the variation of manufacture costs as a function of compressor performance are illustrated in Fig. 11. These charts have been produced using the data from Table 2 and Eq. (6) to evaluate performance

for a range of impeller diameters with an assumed baseline performance with a roughness value of 3.2 μm. These charts show that once running costs are considered, skimping on manufacture costs is rarely justifiable even for the smallest impellers. The economy gained by specifying a roughly finished large impeller would be lost in a matter of days as a result of increased operating costs.

5 Conclusions

Machining of compressor impellers impacts on compressor performance. For instance, surface roughness is known to influence compressor performance and generally rougher impellers result in poorer compressor efficiency. Additional machining factors include fillet radii, passage size, and the type of milling. Classically machining costs rise as the time to program and time of machining increases. In order to optimize both compressor performance and machining costs, methods must be available to quantify both. By utilizing an empirical relationship for the effect of variation of Reynolds numbers on compressor efficiency and proprietary company costings, these have been developed. The challenge facing the compressor manufacturer is to use this information to optimize choice of surface finish against compressor performance, keeping total life-time costs in mind.

The methods used for quantifying impeller performance variation with surface roughness will be supplanted, in time, by viscous flow CFD solvers capable of modeling surface roughness. Using this form of research tool, the effect of variable surface roughness, or using roughness patches, can be quantified and even used to control the local flow to minimize over tip leakage and interact with separated flow regions.

References

British Standards Institute, 1984, *Manual of British Standards in Engineering Metrology*, BSI/Hutchinson.

Casey, M. V., 1985, "The effects of Reynolds number on the efficiency of centrifugal compressor stages," ASME *Journal of Engineering for Power*, Vol. 107, pp. 541–548.

Simon, H., and Bulskamper, A., 1984, "On the evaluation of Reynolds number and relative surface roughness effects on centrifugal compressor performance based in systematic experimental investigations," ASME *Journal of Engineering for Power*, Vol. 106, pp. 489–498.

Strub, R. A., Bonciani, L., Borer, C. J., Casey, M. V., Cole, S. L., Cook, B. B., Kotzur, J., Simon, H., and Strite, M. A., 1987, "Influence of the Reynolds number on the performance of centrifugal compressors," ASME JOURNAL OF TURBOMACHINERY, Vol. 109, pp. 541–544.

Tarada, F. H. A., 1987, "Heat transfer to rough turbine blading," D Phil Thesis, University of Sussex, United Kingdom.

Tarada, F. H. A., 1990, "Prediction of rough wall boundary layers using a low Reynolds number k–ϵ model," *International Journal of Heat and Fluid Flow*, No. 4, pp. 331–345.

Turbocam, 1996, "Describing impellers for easy manufacture," available at http://www.turbocam.com/biz/turbocam.

White, F. M., 1994, *Fluid Mechanics*, McGraw-Hill.

Wiesner, F. J., 1979. "A new appraisal of Reynolds number effects on centrifugal compressor performance," ASME *Journal of Engineering for Power*, Vol. 101, pp. 384–396.

Wright, T., 1989, "Comments on compressor efficiency scaling with Reynolds number and relative roughness," ASME Paper No. 89-GT-31.

—

1998 Turbomachinery Committee Best Paper Award

An Experimental Study of Tip Clearance Flow in a Radial Inflow Turbine

R. Dambach

H. P. Hodson

Whittle Laboratory,
University of Cambridge,
Cambridge, United Kingdom

I. Huntsman
Dept. of Mech. Engineering,
University of Canterbury,
Christchurch, New Zealand

This paper describes an experimental investigation of tip clearance flow in a radial inflow turbine. Flow visualization and static pressure measurements were performed. These were combined with hot-wire traverses into the tip gap. The experimental data indicate that the tip clearance flow in a radial turbine can be divided into three regions. The first region is located at the rotor inlet, where the influence of relative casing motion dominates the flow over the tip. The second region is located toward midchord, where the effect of relative casing motion is weakened. Finally, a third region exists in the exducer, where the effect of relative casing motion becomes small and the leakage flow resembles the tip flow behavior in an axial turbine. Integration of the velocity profiles showed that there is little tip leakage in the first part of the rotor because of the effect of scraping. It was found that the bulk of tip leakage flow in a radial turbine passes through the exducer. The mass flow rate, measured at four chordwise positions, was compared with a standard axial turbine tip leakage model. The result revealed the need for a model suited to radial turbines. The hot-wire measurements also indicated a higher tip gap loss in the exducer of the radial turbine. This explains why the stage efficiency of a radial inflow turbine is more affected by increasing the radial clearance than by increasing the axial clearance.

Introduction

The behavior of tip clearance flow in axial turbines has been investigated in detail. A number of tip gap mass flow models and tip clearance loss models for axial turbines have been developed as a result of the better understanding of the tip gap flow. The most important omission for these models, with the exception of Rains (1954) and Yaras and Sjolander (1992a), is the effect of relative wall motion. According to Yaras and Sjolander (1992b) and in light of the present investigation, more data are needed to clarify the effect of relative casing motion on tip clearance flow.

Very little is known about tip clearance flow in radial turbines. This is partly because a radial turbine blade row cannot be investigated in a linear cascade environment and detailed measurements in small radial machines are very difficult. The best-known investigation of clearance effects on the overall performance of a radial turbine was undertaken by Futral and Holeski (1970). Tests investigated clearance effects at the rotor inlet and exit. They concluded that radial clearance increases at the rotor exit have about 10 times the effect on the overall efficiency as axial clearance increases at the rotor inlet. Reasons for this have never been put forward.

During the present investigation it has become apparent that the relative casing motion cannot be neglected in the study of tip clearance flow in radial turbines. The objectives of this paper are to understand the flow structure over the tip of a radial inflow turbine, to quantify the mass flow rate over the tip, and to establish a qualitative estimate of tip gap loss in a radial turbine. The results will then be used to explain why the overall performance of a radial inflow turbine suffers less from an increase in axial clearance than from the same increase in radial clearance as a percentage of local span.

Experimental Apparatus

The radial inflow turbine has been described by Huntsman et al. (1992), Huntsman and Hodson (1993, 1994) in detail. The working section is shown schematically in Fig. 1.

All measurements were performed at the design condition as described by Huntsman and Hodson (1993). Table 1 summarizes the most important parameters for this particular study in the tip gap region.

The tip gap height of the present radial inflow turbine can be approximated by a third-order polynomial. The inlet and exit clearance and clearances of 1 mm at $S_m = 21$ percent and 1.35 mm at $S_m = 63$ percent are needed to describe the polynomial. The tip gap height corresponds to about 0.6 percent of the local blade height.

Experimental Techniques

Flow Visualization in the Tip Gap Region. The flow features of the rotor tip region were visualized by using Ammonia gas and "Ozalid" paper. This technique was previously used by Huntsman et al. (1992) in the same rig. The diazo paper was stuck onto the flat surface of the blade tip, using double-sided adhesive tape. The angle of the flow trace was read with a vernier protractor (± 1 deg). Two different flow visualization experiments were conducted.

1 The ammonia gas was ejected through a vinyl tube (outer diameter 1.27 mm). The end of the vinyl tube was set flush with the blade tip surface in the pressure side corner of the tip gap. Nineteen flow traces between 5 and 96 percent meridional length were obtained.

2 The end of the vinyl tube was set flush with the blade tip surface in the suction side corner of the tip gap. Seven flow traces between 2.5 and 38 percent meridional length were obtained.

Static Pressure Measurements on the Blade Tip Surface. A high-resolution measurement technique (Bindon, 1987) was used to measure the pressure on the blade surface in the gap region. As
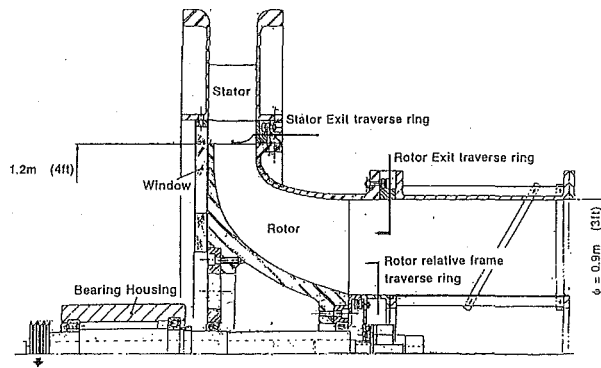
Fig. 1 Schematic of the radial inflow turbine test facility

Table 1 Leading parameters for the test section at the design point.

Rotational speed	450 rpm
Mass flow rate	5.4 kg/s
No. of rotor blades	14
Average blade normal thickness at the tip	8 mm
Axial clearance at rotor inlet	1.2 mm
Radial clearance at rotor exit	1.8 mm
Meridional chord at the casing	460 mm
Rotor inlet radius	609 mm
Rotor exit radius at the tip	445 mm
Rotor inlet angle (mean flow)	-18.4°
Rotor exit angle at the tip (mean flow)	-72°
Pressure side tip corner radius	0.25 mm

shown in Fig. 2, a 16 mm deep and 2 mm wide slot was cut across the blade tip along a constant $r\theta$ line. The slot, located at $S_m = 46.6$ percent, was sealed with adhesive tape. With a needle, the tape could be punctured at any point, allowing nine measurement points over the width of the blade tip. The pneumatic data was measured using a Scanivalve pressure switch fitted to the center-line of the rotor. The effect of the centripetal acceleration on the air in the pressure lines was accounted for in the data reduction.

Static Pressure Measurements at the Rotor Casing. The static pressure at the casing was measured at 21 locations between 9.2 and 100 percent of meridional blade length. The pressure tappings were located at a constant $r\theta$ value. The logging of the static pressure data was triggered by a once per revolution trigger pulse. The time-mean, steady-state pressure level was obtained using a Scanivalve pressure switch. The unsteady pressure variation was measured with a Kulite XCS062 pressure transducer (frequency response of 125 kHz) in the same tappings. Between 18 and 23 measurements were taken over the width of the blade. The fluctuating pressure (AC coupled) was subsequently added to the steady pressure for each pressure tapping and ensemble-averaged over 50 passages.

Hot-Wire Traverses Into the Tip Gap. A single-axis hot-wire was employed in the gap region to examine the flow field between the blade tip and the casing. The hot-wire was mounted upon a two-axis traverse gear, which allowed the sensor to turn around its own axis and to move into the gap in the spanwise direction. Because the measurements are taken in the absolute frame, the advantage of this method is that reverse flow regions in the relative frame can be measured. The high spatial and temporal resolution of a hot-wire anemometer and the negligible blockage of the probe make the instrument a very appropriate means of acquiring experimental data in such an environment (see also Pandya and Lakshminarayana, 1983).

The hot-wire was calibrated for angle and velocity sensitivity in a 1.2 mm slot with a rounded inlet of radius 5 mm. This procedure roughly simulated the tip gap environment in the radial inflow

turbine. The hot-wire traverse in the radial turbine consisted of 33 positions over the distance from the casing to within 0.25 mm of the blade tip. At each immersion the hot-wire was rotated around its axis to six different angular positions, covering a range from $\alpha = 90$ deg (hot-wire perpendicular to the meridional vector) to $\alpha = -60$ deg (see Fig. 3).

A measurement was triggered once per revolution and each trace was ensemble-averaged. The signal was then processed in order to deduce the flow angle and velocity magnitude. The six sensor positions formed three different pairs. In order to deduce the absolute flow angle, the two hot-wire pairs were chosen with most equal velocity readings and the angle was calculated with a linear blending function. The velocity magnitude was deduced from the hot-wire position most perpendicular to the absolute flow angle, once the flow angle was known. Errors due to calibration and signal randomness introduce an uncertainty, especially when transforming the measured absolute velocities into the relative frame. At $S_m = 21$ percent, where the absolute tip flow angle was close to 90 deg, the maximum error on the relative velocity inside the gap was ±4 percent of the local tip speed and the maximum error on the relative angle was ±10 deg. For all other measurement locations the error on the relative velocity was less than ±3 percent of the local tip speed and the error on relative angle was less than ±4 deg.

Results and Discussion

The first aim of this project was to visualize the flow over the rotor tip of the radial inflow turbine. This is presented below. The local tip flow features are then examined closely at one particular chordwise position before expanding the discussion to the whole chord.

Tip Flow Visualized. Ammonia traces over the tip of the rotor blade are shown in Fig. 4. The estimated flow angle, obtained from the flow visualisation at the blade tip surface, is shown in Fig. 5. Three different tip flow regimes are identifiable.

1 Over the first 20 percent S_m, the flow trace indicates that the tip flow is strongly inclined in the streamwise direction. The result

---

Nomenclature

Δh_0 = isentropic stagnation enthalpy change
$\dot{m}$ = mass flow rate
p = static pressure
p_0 = stagnation pressure
$p^* = p - \frac{1}{2}\rho U^2$ = reduced static pressure
t, τ = tip gap height (z axis)
v = velocity
w = blade thickness (y axis)

C_p^* = reduced static pressure coefficient
R = scraping ratio
S = blade length
S_m = meridional length
U = blade speed
Y = loss coefficient
β = relative flow angle
γ = local blade angle (camber line)

$\delta = \beta - \gamma$ = flow angle relative to the blade
ρ = density

Subscripts

1 = stator inlet
3 = rotor inlet
n = blade normal
p = rotor blade passage
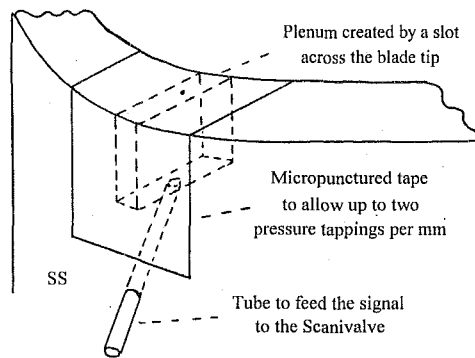
Fig. 2 High-resolution pressure measurement technique

of a more detailed study, where ammonia gas was fed into the gap from the suction side, showed that tip flow moves partly from the suction side to the pressure side in this region. The relative casing motion causes fluid to recirculate over the tip for high radii and low local blade angle. This recirculation zone in the inducer is responsible for the indistinct trace when feeding ammonia gas into the gap from the pressure side. Recently Amedick and Simon (1997) calculated the flow through a radial inflow turbine with tip clearance. For their turbine they discovered that for the first 6 percent of S_m the tip gap flow is dominated by the relative casing motion.

2   Between 20 and 60 percent of S_m, the flow direction is found to be almost perpendicular to the blade. The sharp flow trace near the blade tip surface in Fig. 4 indicates that the tip flow is driven mainly by the pressure difference over the tip.

3   Downstream of 60 percent S_m the streamlines over the tip are inclined in the streamwise direction and diverge more strongly toward the trailing edge than in the previous region. The changes in blade loading near the tip are responsible for the alteration of the flow patterns. As Huntsman and Hodson (1993) showed, the blade was designed so that the reduced static pressure, p^*, on the pressure surface at the design flow condition is uniform for the first 50 percent of the blade length (i.e., $S_m = 60$ percent) and then falls rapidly towards the rear of the blade, because the main flow is accelerated. Hence, the component of velocity parallel to the local blade angle increases. Since this component is carried into the tip gap largely unchanged (Rains, 1954), the tip flow becomes less perpendicular to the blade chord. This effect is enhanced, because the pressure difference across the blade tip is also decreasing so that the velocity normal to the blade chord is reduced. The same phenomenon was found by Heyes and Hodson (1993) in an axial blade row.

Nature of Tip Leakage Flow at Midchord. The most detailed tip investigation has been performed at 46 percent S_m. Figure

Fig. 4 Flow visualization in the tip region

6 shows the relative velocity vectors in the vicinity of the tip that were measured with the hot-wire anemometer. As the flow is driven into the gap by the pressure difference over the blade, it is turned toward the blade normal direction. The turning of the tip leakage flow is completed at a fraction of blade thickness (y/w) of 0.75. The relative angle for a given radial immersion and the streamwise momentum were found to be constant between $y/w = -0.1$ and $y/w = 0.75$. Outside this region, where steep velocity gradients occurred, a maximum error of 8 percent of the blade speed was estimated due to spatial averaging.

The thin shear layer close to the casing could not be fully resolved for this tip gap configuration. Nevertheless Fig. 6 indicates a variation in the relative angle over the height of the gap, which is caused by viscous forces near the casing. Near the gap exit (i.e., on the suction side) the flow angle relative to the blade varies from $\delta = -21$ deg near the casing to $\delta = 69$ deg at a fraction of gap height (z/t) of 0.75 (δ is positive in the direction of

Fig. 3 Hot-wire setup in the tip gap of the radial turbine
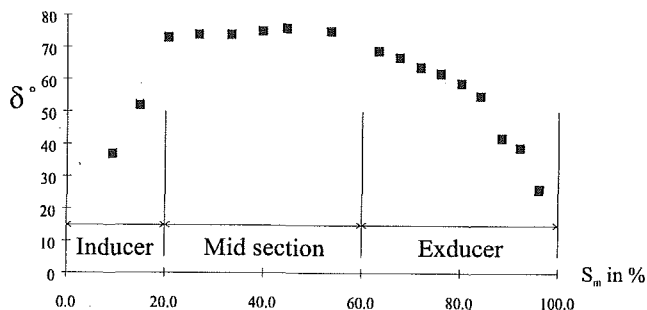
Fig. 5 Flow angle at the blade surface determined from the flow visualization experiment

Fig. 6 Relative velocity vectors at S_m = 46 percent

Fig. 8 Static pressure in the tip region at S_m = 46 percent

rotation). Given the skew of relative angle inside the gap, this latter angle agrees well with the value of $\delta = 76$ deg determined from detailed flow visualization experiments at the blade surface (see Fig. 5). The skew in relative angle has also been found by Sjolander and Cao (1995) in axial turbines.

Once the tip flow has left the tip gap at the suction side, it is opposed by flow adjacent to the casing, which is moving toward the gap exit on the suction side due to a no-slip condition at the casing. This flow (subsequently called "scraping" flow) turns the tip leakage jet sharply into the main flow direction (see Fig. 6) or toward the hub (as observed in flow visualization not presented here) and the two opposing fluids create a lift-off line. This lift-off line is associated with the formation of the scraping vortex, described by Huntsman and Hodson (1994) and Amedick and Simon (1997).

Figure 7 shows the tangential velocity components for the same location as Fig. 6. It is observed in Fig. 7 that the tip leakage flow undergoes two accelerations. The first occurs at tip gap entry and is well documented by previous research in axial turbines (e.g., Bindon, 1987). The new feature observed in the present work is a second but weaker acceleration of the tip leakage flow toward the gap exit. This acceleration is linked with the fact that the tip leakage flow at gap exit is opposed by the scraping flow. This has two effects.

1   A small part of the scraping fluid moves into the gap from the suction side and is dragged through the entire tip gap. The consequence is an area reduction for the tip gap flow and a substantial reduction of tip leakage flow in parts of the radial turbine.

2   The part of scraping fluid, which is not transported into the gap, is blocked by the leakage jet at the gap exit and "scraped" off the blade. The scraped fluid and the tip leakage jet form a dividing
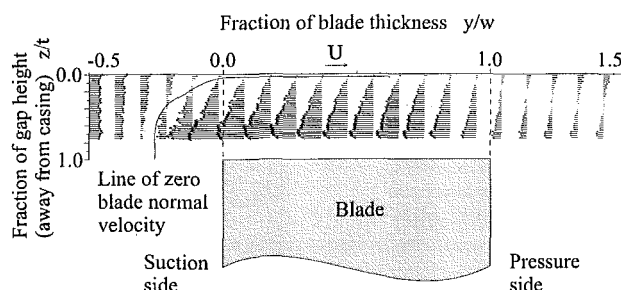
Fig. 7 Blade normal velocity vectors at S_m = 46 percent
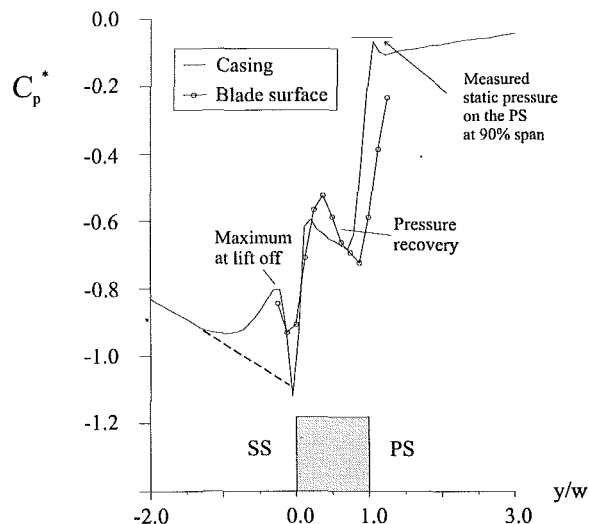
stream surface at -0.25 y/w, which is indicated by a line of zero blade normal velocity in the blade normal view of Fig. 7. As a result of this dividing stream surface, a static pressure rise is expected.

Static pressure measurements in the tip region confirm the observations made by the hot-wire measurements. All static pressure data are nondimensionalized by the blade dynamic head at rotor inlet and are presented in the form of the reduced pressure coefficient

$$Cp^*_{static} = \frac{p - p_{03rel} - \frac{1}{2}\rho(U^2 - U_3^2)}{\frac{1}{2}\rho U_3^2} \tag{1}$$

The relative stagnation pressure at rotor inlet, p_{03rel}, was calculated from the measured inlet stagnation pressure, p_{01}, and the mass-averaged loss of stagnation pressure at the exit from the stator blades ($Y_{stator} = 0.021$). Using the rotational form of Bernoulli's equation, Eq. (1) becomes

$$Cp^*_{static} = \frac{p^* - (p_{03} - \rho U_3 V_{\Theta 3})}{\frac{1}{2}\rho U_3^2} \tag{2}$$

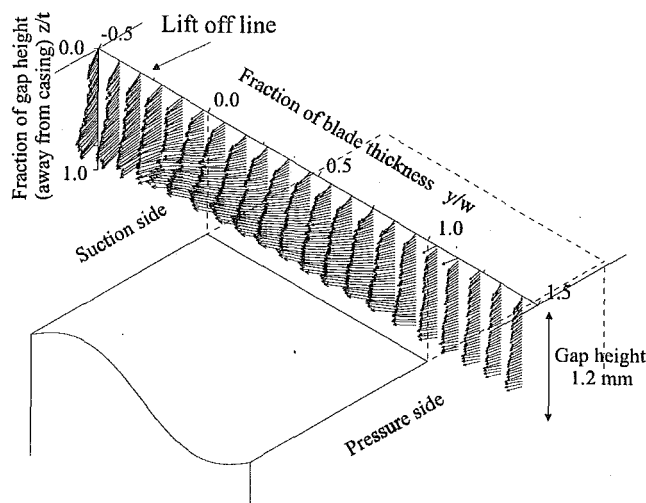Figure 8 presents the static pressure data obtained at 46 percent S_m. The pressure coefficient at the blade tip shows that the first acceleration into the gap is completed at $y/w = 0.85$ (i.e., one gap height from the pressure side corner). After the vena contracta, the pressure recovers due to mixing inside the gap. The effect of this acceleration on the pressure at the casing occurs further into the gap and is smaller in magnitude because of streamline curvature. The pressure minimum at the casing is located at $y/w = 0.7$. The same behavior has been reported by Bindon (1987) in an axial turbine cascade. The different level of pressure recovery between casing and blade surface may be due to streamline curvature of the opposite sense after the vena contracta. The effect of spatial averaging of the Kulite probe was calculated to be of no more than 0.025 C^*_p.

Heyes and Hodson (1993) suggest that complete mixing inside the gap of an axial turbine occurs for a gap width larger than six times the gap height ($\tau/w = \frac{1}{6}$). A contraction coefficient of 0.81 is calculated from the pressure at the blade surface if complete mixing occurs in the gap of the present radial turbine ($\tau/w = 0.15$ at 46 percent S_m). This is equivalent to a discharge coefficient of 0.97 and is in accordance with the predicted discharge coefficient ($C_D = 0.96$) for the given pressure side corner radius (Heyes and Hodson, 1993). In this context it is important to note that pressure side corner radii in real life turbines are often larger than those

Fig. 9 Loading distribution for different spanwise positions

Fig. 10 A relative measure of the effect of scraping

used in tip clearance research. A discharge coefficient close to one is very likely in such environments. Hence, it is questionable whether a tip gap mass flow model for radial turbines should be based on discharge coefficients.

The second pressure drop after the vena contracta corresponds to the second acceleration near the gap exit, discovered in Fig. 7. Flow visualization showed that there is little streamline divergence in the blade-to-blade plane over the tip at $S_m = 46$ percent. An incompressible Bernoulli calculation can be applied to a blade normal section of the tip gap flow field as displayed in Fig. 7. The increase in maximum velocity that represents the acceleration after the vena contracta $(0.0 < y/w < 0.3)$ corresponds to a ΔC_p^* of 0.35. Hence the simple Bernoulli calculation confirms that the second pressure drop in Fig. 8 ($y/w < 0.3$) is an inviscid phenomenon. As observed previously the acceleration is due to a mean reduction in tip leakage flow area.

In Fig. 8, a local pressure maximum can be observed near the suction side at $y/w = -0.25$. The local maximum confirms the expected rise in static pressure due to the dividing stream surface observed in Fig. 7. The extrapolation (dashed line) also suggests that this local pressure maximum does not influence the driving pressure difference for the tip leakage flow.

The pressure driven tip clearance flow at 46 percent S_m interacts strongly with the scraping fluid near the casing. The dragged fluid reduces the flow area in the tip gap and its opposition to the leakage jet is responsible for a second acceleration near the tip gap exit. It will be seen in the following paragraph that the behavior of gap flow in the midsection is in a transition regime between the behavior of leakage flow in the inducer and the exducer.

Tip Clearance Flow Over the Whole Chord. Figure 9 shows the loading distribution for different spanwise positions. The pressure at 90 percent span was obtained from data measured by Huntsman and Hodson (1993). The pressure at the ca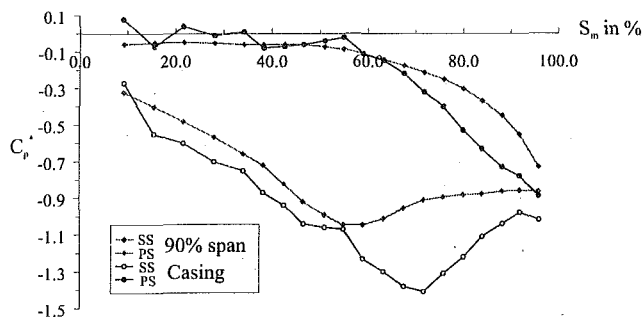sing was obtained from 20 different static pressure traces, one of which is shown in Fig. 8. The minimum pressure was taken from the ensembled data and was averaged over five blade passages.

If there was zero tip clearance, then the scraping fluid would stagnate on the blade suction surface and travel off at right angles as scraped fluid. By solving the Bernoulli equation, Rains (1954) computed the pressure difference between far upstream and the suction side corner with zero clearance. This "scraping" dynamic head amounts to $\frac{1}{2}\rho U^2 \cos^2 \gamma$, where γ is the angle between the camber line at the tip and the meridional direction (see Fig. 3). With a clearance larger than zero, the driving pressure difference over the tip ($\Delta p_{tipflow}$) is opposed by the scraping dynamic head. In order to quantify the effect of scraping on the tip clearance flow, the authors prefer, however, to think in terms of momentum. A "scraping" ratio R can be defined as the undisturbed tip gap flow momentum divided by the scraping momentum (see Fig. 10). Since the streamwise momentum over the tip is largely conserved, the driving pressure difference ($\Delta p_{tipflow}$) was calculated between p^* at 90 percent span on the pressure side and p^* at the casing near the suction side gap exit (Rains, 1954).
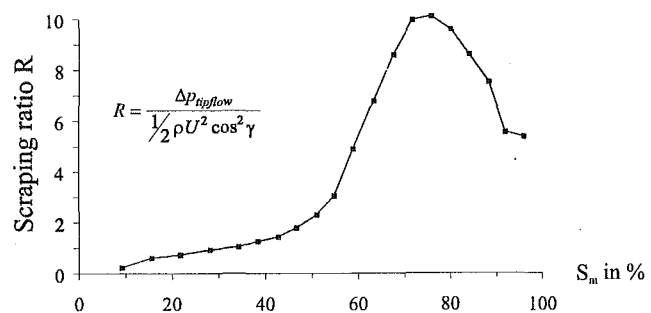
The strength of this scraping ratio R is believed to be responsible for the amount of scraping fluid dragged through the gap. A scraping ratio less than one between the leading edge and 30 percent S_m indicates a strong effect of scraping in the inducer of the present radial turbine and much dragged fluid is to be expected in this region. A scraping ratio much larger than one between 60 percent S_m and the trailing edge indicates a small effect of scraping in the exducer.

Figure 11 displays blade normal velocity vectors over the tip gap for a position near the inducer and in the exducer. At $S_m = 21$ percent dragged fluid occupies the upper half of the gap height. The large amount of dragged fluid in the gap is believed to be a result of a scraping ratio smaller than one ($R = 0.73$). The tip leakage flow in the inducer seems to be clearly dominated by the scraping effect.

At $S_m = 63$ and $S_m = 88$ percent (not presented here) the effect of scraping is so much reduced that it could not be measured by the hot-wire traverse any more. The small quantity of dragged fluid in the gap near the exducer is a consequence of the high scraping ratio observed in Fig. 10. This suggests that the tip leakage flow in the exducer of a radial turbine resembles the tip flow behavior in axial turbines, where the tip gap flow is dominated by pressure differences rather than by the scraping effect (Yaras and Sjolander, 1992a).

Figure 12 shows the reduced static pressure coefficient at the casing for the same two chordwise positions. The pressure at 21
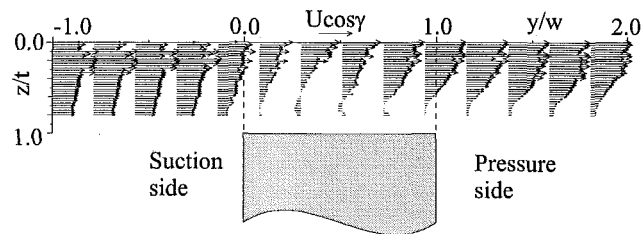
a) Blade normal velocity vectors at $S_m = 21\%$
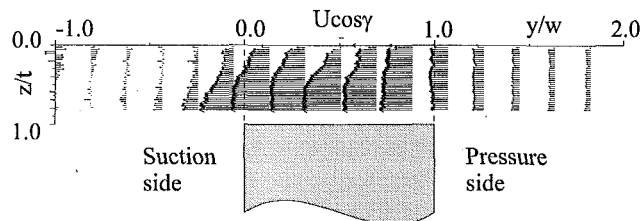
b) Blade normal velocity vectors at $S_m = 63\%$

Fig. 11 Velocity vectors near inducer and exducer
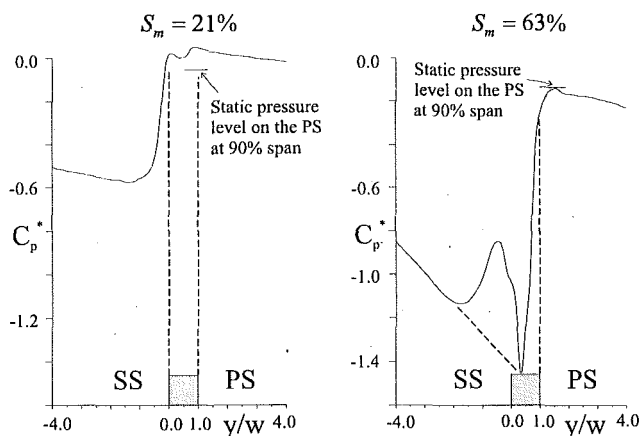
Fig. 12 Comparison of C_p^* between inducer and exducer

Fig. 13 Mass flow rate per unit chord at S_m = 46 percent

percent S_m is approximately constant inside the gap and drops only on the suction side between $y/w = 0.0$ and $y/w = -1.0$. The pressure data indicated that no local pressure maximum can be observed on the suction side between the leading edge and 42 percent S_m. Tip leakage flow in this region is so weak that most of the scraping fluid makes its way through the gap, as was shown by Fig. 11(a). The pressure "drop" is therefore due to the inertia associated with the scraping fluid. Figure 11(a) shows how the scraping fluid decelerates before entering the gap from the suction side. This deceleration outside the gap near the suction side is believed to account for the pressure difference observed in Fig. 12(a).

At $S_m = 63$ percent the tip leakage jet is much stronger because the scraping ratio R has increased. The pressure drop between the pressure side and $y/w = 0.35$ in Fig. 12(b) indicates the acceleration of flow into the tip gap. The effect of the vena contracta on the casing pressure is further retarded (compare Fig. 8), which may indicate stronger curvature of the streamlines at gap inlet. The pressure then recovers and rises toward the local pressure maximum, as the tip gap flow near the casing is slowed down due to the opposing scraping fluid (see Fig. 11(b)). The extent of the pressure maximum, which indicates the lift-off line, has increased dramatically and is now about a third of the overall pressure difference at the casing. The maximum has also moved away from the suction side, compared to 46 percent S_m. As the effect of scraping does not impinge on the suction side corner anymore, no area reduction for the tip leakage flow toward the gap exit was observed at this location. This is also confirmed in Fig. 12(b), where no decrease in C_p^* at gap exit is seen.

The extrapolation shown in Fig. 12(b) suggests again that the local pressure maximum seems not to influence the driving suction side pressure. A simple model used to calculate the tip gap mass flow rate can therefore be based on the reduced static pressure difference between 90 percent span on the pressure side and the casing on the suction side.

Tip Gap Mass Flow Rate in a Radial Inflow Turbine. The mass flow rate over the blade tip was calculated along a constant $r\theta$ value from the hot-wire measurements at four different chordwise positions. Assuming zero velocity at the blade tip surface, the blade normal velocity in the relative frame was integrated over the height of the gap. The resulting mass flow rate per unit chord at 46 percent S_m is presented in Fig. 13 as an example. It needs to be remembered that the tip flow is being turned over the first quarter of the gap. In the region where the tip flow was more or less two dimensional ($0 < y/w < 0.75$), the mass flow rate is almost constant and satisfies the requirement of the conservation of mass. In this region an average value was calculated. This value is reported in Fig. 14 for each measured chordwise position. The average mass flow rate at 46 percent S_m corresponds to 1.67
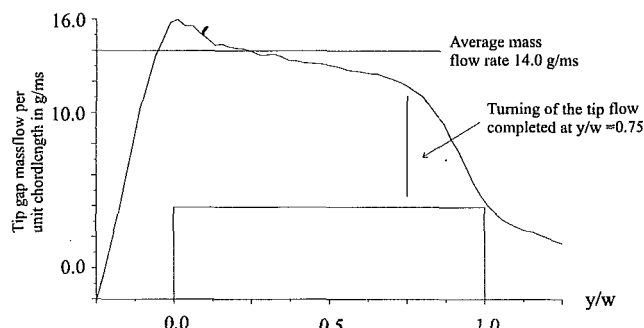
percent of the average blade passage mass flow rate per unit meridional chord.

The tip leakage mass flow model for axial turbines by Heyes and Hodson (1993) was applied to the present tip configuration, where an average discharge coefficient of 0.97 was chosen. The integrated mass flow rates in the exducer of the present radial turbine compare with those predicted by the axial turbine model, as indicated in Fig. 14. This confirms the fact that the nature of tip leakage flow in the exducer of a radial turbine is similar to an axial turbine. But Fig. 14 also shows that the same model overpredicts the amount of tip gap mass flow rate in the midsection by a factor of two and is even worse in the inducer. This is due to the effect of scraping as discussed above. It becomes apparent that a specific tip leakage mass flow model for radial turbines is needed.

The most important observation that can be drawn from Fig. 14 is that more mass flow passes through the tip gap near the exducer than near the inducer. This is partly due to the loading distribution (see Fig. 9) but is also due to the effect of scraping. If high tip gap loss arises where there is high tip gap mass flow rate, this explains why radial clearance has a much larger effect on radial turbine stage efficiency than axial clearance.

Tip Gap Loss in a Radial Inflow Turbine. Figure 15 indicates the normal kinetic energy at gap exit, calculated from the hot-wire measurements and defined as:
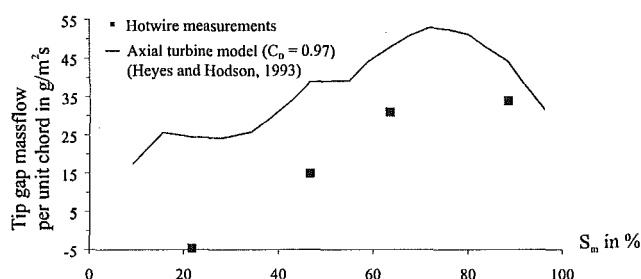
Fig. 14 Tip gap mass flow rate along the meridional chord
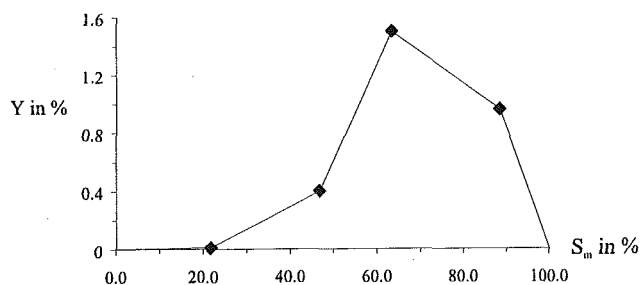
Fig. 15 Tip gap loss coefficient for four different meridional positions

$$Y = \frac{S_{\text{tip}} \cdot \int_0^\tau 0.5\rho v_n v_n^2 dz}{\dot{m}_p \cdot \Delta h_0} \qquad (3)$$

The loss coefficient Y represents the loss of efficiency that would occur, assuming that the kinetic energy transported by the normal gap velocity is ultimately lost (Yaras and Sjolander, 1992b). The kinetic energy of the scraping fluid was not taken into account. Figure 15 confirms that tip leakage loss in the exducer is more significant than in the inducer. In a radial turbine with a similar blade loading, Futral and Holeski (1970) measured a 1.6 percent drop in stage efficiency for 1 percent increase in rotor exit clearance, but only a 0.15 percent drop in stage efficiency for 1 percent increase in clearance at the rotor inlet. The integrated loss coefficient between 60 and 100 percent S_m (i.e., in the exducer) in Fig. 15 is $Y = 1$ percent. This corresponds to a 1.7 percent loss of stage efficiency for a 1 percent clearance height and agrees very well with Futral and Holeski's result. The integrated loss over the whole chord in Fig. 15 is 0.575 percent (for a 0.6 percent clearance height).

Conclusions

The details of tip clearance flow in radial turbines have been investigated for the first time. The nature of tip clearance flow in radial inflow turbines has been examined and understood. A detailed study at midchord was performed, which revealed that the tip clearance flow is opposed by scraping fluid in the relative frame. One part of this opposing scraping fluid was found to be dragged through the gap from the suction side to the pressure side. The remaining bulk of the scraping fluid was turned toward the hub and into the main flow direction. A dividing streamline separated the tip clearance flow and this second part of the scraping fluid. The dividing streamline causes a local pressure maximum outside the gap near the suction side, but does not affect the driving pressure difference.

The study of tip clearance flow in radial inflow turbines was extended over the whole chord. Blade speed and blade tip angle were found to play a key role for tip clearance effects in radial turbines. Tip clearance behavior in a radial turbine was divided into three different regions.

In the inducer most of the scraping fluid forces its way through the tip gap and the tip gap mass flow rate over the first half of the chord is significantly reduced. This is one reason a radial turbine suffers less from an increase in tip clearance than an axial turbine. At midchord little scraping fluid is dragged through the gap and from 60 percent S_m toward the rotor exit the "dragging" effect of scraping finally disappears and the tip clearance flow in this region is dominated by pressure only.

The tip gap mass flow and the tip leakage loss for the present radial turbine were quantified. The results confirmed that radial clearance has a bigger effect on stage efficiency than axial clearance for the standard NASA design. The underlying physics of Futral and Holeski's experimental result (1970) seem to be the effect of high relative motion and low blade angle near the rotor inlet.

References

Amedick, V., and Simon, H., 1997, "Numerical Simulation of the Flow Through the Rotor of a Radial Inflow Turbine," ASME Paper No. 97-GT-90.

Bindon, J. P., 1987, "Pressure Distributions in the Tip Clearance Region of an Unshrouded Axial Turbine as Affecting the Problem of Tip Burnout," ASME Paper No. 87-GT-230.

Futral, S. M., and Holeski, D. E., 1970, "Experimental Results of Varying the Blade-Shroud Clearance in a 6.02-inch Radial Inflow Turbine," NASA Technical Note D-5513.

Heyes, F. J. G., and Hodson, H. P., 1993, "The Measurement and Prediction of the Tip Clearance Flow in Linear Turbine Cascades," ASME JOURNAL OF TURBOMACHINERY, Vol. 115, pp. 376–382.

Huntsman, I., Hodson, H. P., and Hill, S. H., 1992, "The Design and Testing of a Radial Flow Turbine for Aerodynamic Research," ASME JOURNAL OF TURBOMACHINERY, Vol. 114, pp. 411–418.

Huntsman, I., and Hodson, H. P., 1993, "A Laminar Flow Rotor for a Radial Inflow Turbine," Paper No. AIAA-93-1796.

Huntsman, I., and Hodson, H. P., 1994, "An Experimental Assessment of the Aerodynamic Performance of a Low-Speed Radial Inflow Turbine," Paper No. AIAA-94-2932.

Pandya, A., and Lakshminarayana, B., 1983, "Investigation of the Tip Clearance Flow Inside and at the Exit of a Compressor Rotor Passage: Parts I and II," ASME Journal of Engineering for Power, Vol. 105, pp. 1–17.

Rains, D. A., 1954, "Tip Clearance Flows in Axial Flow Compressors and Pumps," Report No. 5, California Institute of Technology.

Sjolander, S. A., and Cao, D., 1995, "Measurements of the Flow in an Idealized Turbine Tip Gap," ASME JOURNAL OF TURBOMACHINERY, Vol. 117, pp. 578–584.

Yaras, M. I., and Sjolander, S. A., 1992, "Effects of Simulated Rotation on Tip Leakage in a Planar Cascade of Turbine Blades: Part I—Tip Gap Flow," ASME JOURNAL OF TURBOMACHINERY, Vol. 114, pp. 652–660.

Yaras, M. I., and Sjolander, S. A., 1992b, "Prediction of Tip-Leakage Losses in Axial Turbines," ASME JOURNAL OF TURBOMACHINERY, Vol. 114, pp. 204–210.

1998 Heat Transfer Committee Best Paper Award

J. P. Bons
Department of Aeronautics and Astronautics,
Air Force Institute of Technology,
Wright-Patterson AFB, OH 45433

J. L. Kerrebrock
Department of Aeronautics and Astronautics,
Massachusetts Institute of Technology,
Cambridge, MA 02139

Complementary Velocity and Heat Transfer Measurements in a Rotating Cooling Passage With Smooth Walls

An experimental investigation was conducted on the internal flowfield of a simulated smooth-wall turbine blade cooling passage. The square cross-sectioned passage was manufactured from quartz for optical accessibility. Velocity measurements were taken using Particle Image Velocimetry for both heated and non-heated cases. Thin film resistive heaters on all four exterior walls of the passage allowed heat to be added to the coolant flow without obstructing laser access. Under the same conditions, an infrared detector with associated optics collected wall temperature data for use in calculating local Nusselt number. The test section was operated with radial outward flow and at values of Reynolds number and Rotation number typical of a small turbine blade. The density ratio was 0.27. Velocity data for the non-heated case document the evolution of the Coriolis-induced double vortex. The vortex has the effect of disproportionately increasing the leading side boundary layer thickness. Also, the streamwise component of the Coriolis acceleration creates a considerably thinned side wall boundary layer. Additionally, these data reveal a highly unsteady, turbulent flowfield in the cooling passage. Velocity data for the heated case show a strongly distorted streamwise profile indicative of a buoyancy effect on the leading side. The Coriolis vortex is the mechanism for the accumulation of stagnant flow on the leading side of the passage. Heat transfer data show a maximum factor of two difference in the Nusselt number from trailing side to leading side. A first-order estimate of this heat transfer disparity based on the measured boundary layer edge velocity yields approximately the same factor of two. A momentum integral model was developed for data interpretation, which accounts for coriolis and buoyancy effects. Calculated streamwise profiles and secondary flows match the experimental data well. The model, the velocity data, and the heat transfer data combine to strongly suggest the presence of separated flow on the leading wall starting at about five hydraulic diameters from the channel inlet for the conditions studied.

Introduction

The hot section of a modern gas turbine engine is a challenging design environment. The turbine is required to operate with high inlet temperatures and aggressive blade loading to provide high specific power. These demands conflict directly with the limitations of engineering materials. To resolve this conflict, since the 1960s bleed air from the compressor has been used to cool turbine vanes, blades, casings, and disks. With cooling, engine designers have realized a 300–500°C increase in operating turbine inlet temperatures beyond previous limits.

To cool the rotating turbine blade in particular, cooling air flows through a network of serpentine cooling passages oriented along the span of the blade. Raised steps (or ribs) are commonly used to trip the boundary layers and augment the heat transfer from the metal walls in these internal cooling passages. Modern turbine design depends on reliable cooling schemes to achieve performance levels beyond the capabilities of blading materials alone. Even a deficiency of coolant creates aggravated thermal stresses in the highly stressed rotating blade, which can result in severe oxidation, creep, and local fatigue of the blade. Because of its

critical role, considerable effort has been expended to predict the performance of turbine internal cooling accurately. Design engineers realized early on, however, that because of the rotating turbine frame of reference, standard pipe flow correlations for heat transfer were inadequate. Rotation introduces Coriolis and buoyancy accelerations, which create secondary flow vortices and skew the mean flow profile. These flow nonuniformities result in non-homogeneous heat transfer from the different passage walls depending on their orientation (as depicted in Fig. 1).

Flow in a heated rotating passage can be characterized by the Reynolds number, Re, the Rotation number, Rot, and the Buoyancy parameter, Bo, defined as:

$$\text{Re} = \frac{\rho d u_{in}}{\mu} \quad \text{Rot} = \frac{\Omega d}{u_{in}} \quad \text{Bo} = \frac{T - T_{in}}{T}\left(\frac{\Omega d}{u_{in}}\right)^2 \frac{R_m}{d}$$

The Rotation number represents the ratio of Coriolis to inertial forces. The same ratio is sometimes expressed by its reciprocal, the Rossby number. The Buoyancy parameter represents the ratio of centrifugal to inertial forces and can also be expressed as

$$\text{Bo} = \frac{\beta(T - T_{in})\Omega^2 R_m d^3}{\nu\alpha}\left(\frac{\alpha}{\nu}\right)\left(\frac{\nu}{ud}\right)^2 = \frac{\text{Ra}_\Omega}{\text{Pr Re}^2}$$

where Ra_Ω is a rotational Rayleigh number (Morris, 1981). Ra_Ω is similar to the Rayleigh number from free convection analysis, the gravitational body force being replaced by a centrifugal body
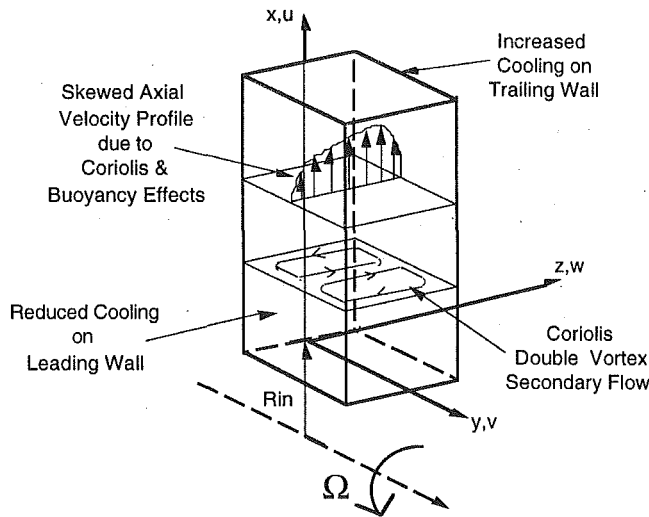
Fig. 1 Schematic of heated, rotating flow

force. Alternatively, the Buoyancy parameter can be expressed in terms of the density ratio, defined as d.r. $= (T_w - T_{in})/T_w$, and the Rotation number squared. Since the bulk of turbine cooling research reported in the literature uses this density ratio to express the effect of centrifugal buoyancy (Wagner, 1991a; Han and Zhang, 1992; Dutta et al., 1994; Tekriwal, 1996; Hsieh et al., 1997), it is used here rather than the Buoyancy parameter.

The effects of these various parameters on the cooling passage Nusselt number have been the subject of numerous experimental and computational studies. As far back as the early 1950s, papers were being published on rotating duct flows. In a rotating passage (without heat) Moore (1967) showed that the primary effect of rotation was the creation of a double-vortex secondary flow that shifts the core flow to the pressure surface for radial outflow. This creates higher skin friction and a thinner boundary layer on the pressure surface (trailing wall) and the opposite conditions on the suction surface (leading wall). With heat addition, centrifugal buoyancy is introduced into the flow, which precludes the summary use of Reynolds analogy to directly transport the effect of rotation on skin friction to heat transfer. Morris and Ayhan (1979) were first to incorporate the effect of centrifugal buoyancy in their interpretation of observed heat transfer phenomena in a rotating

circular cross-sectional cooling tube. They proposed an empirical correlation for the passage mean Nu based on Bo.

In the last decade, interest in rotating heated passage flows has intensified with the direct application being turbine blade cooling passages. Guidez (1989) published the results of experiments at Reynolds numbers higher than those previously reported, ensuring a turbulent pipe flow. He found the ratio of trailing side Nu to leading side Nu to be about two for Bo $= 0.08$, and noted that this ratio decreased with increasing Re. Following Guidez, Wagner et al. (1991a, b, 1992) methodically studied the effects of Re, Rot, d.r., flow direction, and ribs on the cooling passage heat transfer. They used the density ratio to characterize the effects of centrifugal buoyancy and found that increasing d.r. augmented Nu on both trailing and leading sides. They measured a higher ratio of trailing to leading side Nu than Guidez for similar conditions. Their Nu data are normalized by a stationary Nu correlation (Re$^{0.8}$) for pipe flow, which they found to remove Re dependency adequately in the rotating data.

At the same time, Han et al. (1994) performed experiments using a facility that can be operated in either constant wall temperature or constant wall heat flux mode (versus the Wagner and Johnson facility, which is exclusively constant wall temperature, and the Guidez facility, which is constant wall heat flux). Han et al. found even larger effects of rotation and buoyancy, the trailing to leading side Nu ratio being nearly twice the value measured by Guidez for the same Bo condition. Han et al. also observed that the thermal boundary condition influences the measured heat transfer, i.e., the constant heat flux mode having a higher Nu on both leading and trailing side than the constant wall temperature case for the same density ratio. They reasoned that because a constant heat flux produces uneven wall temperatures, the buoyancy forces are unbalanced and create better cooling everywhere as these forces destabilize the passage flow.

These and other experimental findings have succeeded in mapping out many of the parametric trends in the performance of turbine cooling passages, but because of the wide spread in the results from different facilities (Fig. 2) the cooling designer is still left without a clear understanding of the quantitative effect of rotation. This is because the underlying mechanisms causing these rotational effects on cooling are as yet unexplored. The wall heat transfer distribution is ultimately a product of the flowfield, and until recently none of the experimental work has measured the detailed velocity field inside the rotating heated passage. There are a number of researchers who have over the years made measurements in a rotating flowfield: Wagner and Velkoff (1972) with hot

Nomenclature

Bo = Buoyancy parameter $= \beta(T - T_\infty) R_m \Omega^2 d/u^2$

d = hydraulic diameter $= 4 \times$ area/perimeter

d.r. = density ratio $= (T_w - T_{in})/T_w$

k = gas thermal conductivity

l = passage length

n = power law profile exponent

Nu = Nusselt number $= qd/k_{film}(T_w - T_{film})$

Pr = Prandtl number $= \nu/\alpha$

q = surface heat flux

r or R = radial distance to axis of rotation

R_m = mean radius of test section

Ra$_\Omega$ = rotational Rayleigh number

Re = passage Reynolds number $= du_{in}/\nu$

Rot = Rotation number $= \Omega d/u$

T = local static temperature

u = x component of velocity

v = y component of velocity

v_o = velocity of wall injected boundary fluid

V = complete velocity vector

w = z component of velocity

x = radial (streamwise) direction in passage

y = axis parallel with axis of rotation

z = crossflow direction in passage

α = thermal diffusivity

β = volumetric expansion coefficient

δ = boundary layer thickness

θ = boundary layer momentum thickness

λ = wavelength of radiation

μ = viscosity

ν = kinematic viscosity

ρ = fluid density

τ_o = wall shear stress

Ω = rotational frequency

Subscripts

BS = back side passage wall

cor = Coriolis

film = average of wall and bulk

FS = front side passage wall

in = passage inlet conditions

inf = free-stream conditions

LS = leading passage wall

TS = trailing passage wall

∞ = free-stream conditions

**Trailing Wall to Leading Wall Nusselt Ratio Data
from Various Researchers Plotted vs. Buoyancy Parameter
Data for Radial Outflow, 7<x/d<9, 10000<Re<30000,
constant Temperature and constant Heat Flux Wall**

Legend:
- ⊖— Guidez '89
- ⊟ - Morris '91
- ◇ - Wagner '91
- ✕ - Barry '94
- + - Han '94
- △ - Mochizuki '94

Y-axis: Trailing Wall Nu / Leading Wall Nu

X-axis: Buoyancy Parameter

Fig. 2   Rotating heat transfer data from various researchers

Fig. 3   Schematic of internal cooling test facility

1. Vacuum Chamber / Protective Casing	11. Motor
2. Rotating Arm	12. Instrumentation Slip Ring
3. Test Section and Mirrors	13. Housing
4. Balance Weight	14. IR detector
5. Shaft	15. Imaging system
6. Power Slip Ring	16. Seals
7. Heat Exchangers	17. Optical Encoder
8. Onboard Instrumentation Box	18. Power wires
9. Inlet flow	
10. Outlet flow	

wires and more recently, Uellner and Roesner (1991), Berg et al. (1991), Tse and McGrath (1995), and Tse and Steuber (1997) with laser diagnostics. But all of these are for non-heated rotating passages and therefore omit the buoyancy effect entirely. A 1997 publication by Hsieh et al. does present velocity data using LDV in a rotating passage with heating. However, the measurements are presented only along the passage centerline and show a marginal effect of rotation up to the maximum Rot of 0.06. In fact, the limited velocity data indicate a far greater effect of the passage ribs than the rotation effect at such low Rot. Moreover, with a passage inlet radius of only one test section diameter and a nonradial passage orientation, Hsieh's experimental configuration bears little resemblance to a turbine cooling passage. So, there is as yet no comprehensive picture of the flow inside a turbine blade cooling passage, information that is critical to understanding the passage heat transfer.

On the computational front, researchers have predicted many of the experimentally measured effects of Coriolis and buoyancy. Based on Boyer (1965) and others' experimental findings that the rotating passage flow could be adequately characterized by an inviscid core region surrounded by thin wall layers, early analytical approaches employed either a perturbation method (Moore, 1967) or a momentum integral analysis (Mori and Nakayama, 1968; Ito and Nanbu, 1971). More recently, three-dimensional Navier–Stokes solvers have provided valuable flow insights including the discovery of an additional vortex pair (making four vortices in all) at high Rot (Iacovides and Launder, 1991) and the prediction of flow reversal at high Rot on the leading wall (Prakash and Zerkle, 1992). All of the heated rotating computations use the flow prediction to estimate Nu, which is then compared with experiment to assess code validity. A lack of detailed flow measurements in the heated, rotating frame has prevented direct comparison with velocity data and thus an adequate validation of the calculated flowfields.

The objective of this research is to provide the technical community with the first comprehensive measurements of velocity and heat transfer in a simulated turbine blade cooling passage. The method used to obtain the velocity measurements is particle image velocimetry (PIV). Thin film heaters on all four walls of a transparent test section provide the necessary constant heat flux wall condition, while infrared imaging of the surface provides high spatial resolution measurement of heat transfer coefficient. This allows a direct correlation of flow phenomena to heat transfer
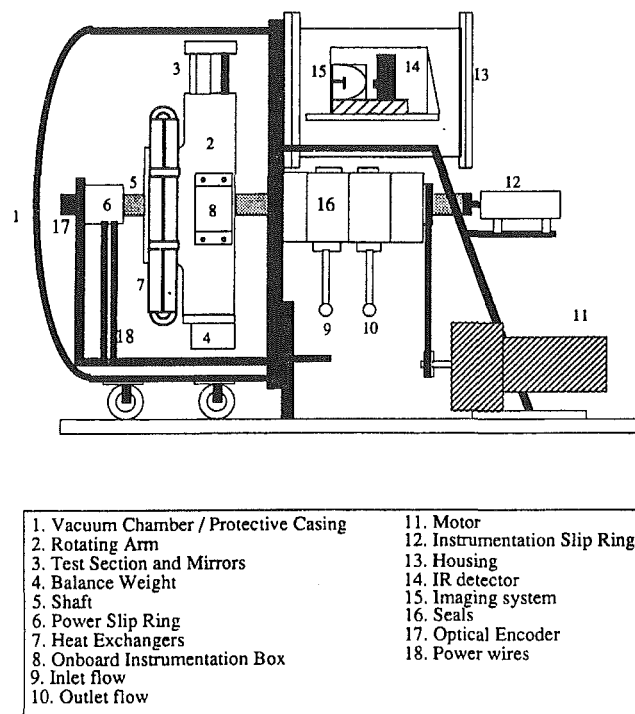
phenomena without the ambiguities of different experimental facilities. These are the specific contributions of this paper.

Experimental Method

The experimental facility used for this study is shown in Fig. 3.

Labels: Exit Instrumentation EndCap; To Infrared Detector; RTV Epoxy Seal (both ends); Quartz Test Section Installed; Downspout; Instrumentation Port; Tapered Inlet; Screen; (Mates to End of Rotating Arm)

Fig. 4   Schematic of quartz test section mounted in housing on rotating arm

Fig. 5 Schematic of infrared imaging system for wall temperature measurement

The test section is mounted at the end of a 0.4 m radius arm ($R_i/d = 40$), which spins in an evacuated chamber. Cooling air enters and exits the rotating arm and test section through seals located on the shaft. The test section ($l/d = 11.5$) is manufactured from square-bore quartz tubing and mounts to the rotating arm as shown in Fig. 4. Also indicated on Fig. 4 are the tapered test section inlet, the flow conditioning screen, and the flow thermocouple ports at inlet and exit. The test section ID is 10 mm square and the walls are ground and polished to a 1.5 mm thickness. The center 90 mm along each of the four sides is coated with a 10 mm wide swath of Indium Tin Oxide (ITO). The coating thickness is nominally 4500 Å and it is applied with electron beam sputtering to the outside of the test section. Heat fluxes up to 5 W/cm^2 and wall temperatures up to 200°C were achieved without film degradation. Cr/Ni/Au busbars (8 mm long) at either end of the ITO film provide uniform electrical contact to the ITO. The four sides are connected in a parallel circuit to allow resistive heating of the passage.

Due to a manufacturing complexity, the front side wall ITO sheet thickness is approximately 20 percent greater than the ITO thickness on the leading and trailing walls (which are roughly equivalent). This creates a lower resistance here, and a higher heat flux since more current passes through this part of the parallel resistance circuit. The back side wall's ITO thickness is conversely 20 percent less than the leading and trailing walls, causing a corresponding decrease in the heat flux here. The result is a higher heat load on the front internal wall by nearly 30 percent after accounting for temperature smearing through the test section walls. The effect of this heating imbalance is discussed in the results section.

The ITO film and quartz substrate provide 80 percent transmission at the visible wavelength of the laser used. Since the quartz is opaque in the IR spectrum, the capability of the IR scanning temperature measurement system was not compromised with the use of a transparent test section. The infrared detector is mounted on a two-axis traverse system with focusing optics (Fig. 3). The spatial resolution of the detector and optics is 1 mm^2. Two flat mirrors located at 90 deg to each other behind the test section provide optical access to all four sides of the rotating passage (Fig.

5). The horizontal traverse is used to move the focal point from one side to another and the vertical traverse allows measurement along the axis (x direction) of the passage.

To acquire a signal, the sensor and optics are moved to a desired location and remain fixed while the heated test section is rotated in front of them. When the test section passes into the focal point of the optics, the radiation emitted from the heated surface is focused onto the sensor. The sensor produces a voltage signal proportional to the level of incident radiation. Using the Stefan–Boltzmann Law, $q_{rad} \propto T^4$, the temperature of this spot on the surface can be deduced. The AC coupled sensor has a response time on the order of microseconds, which means that an entire row of data can be collected during a single pass of the test section. This data then represents the temperatures in a 1 mm wide strip on one side of the test section, at a given x location.
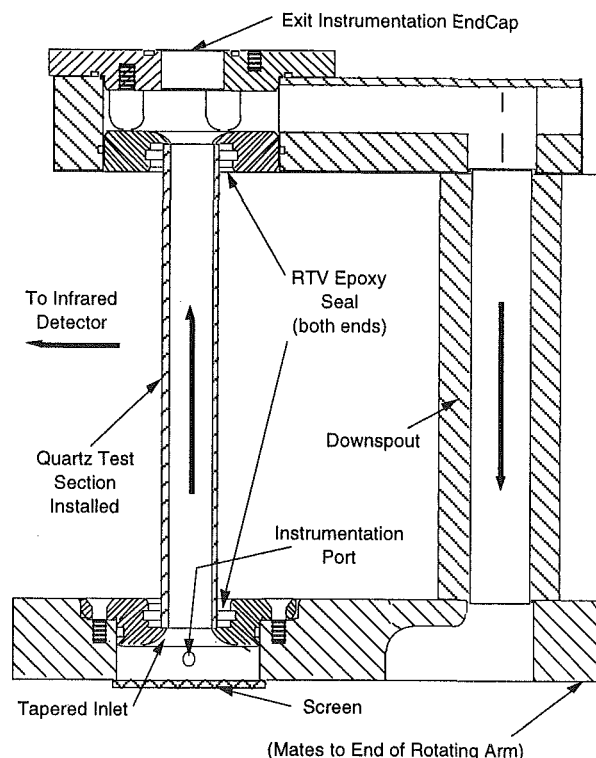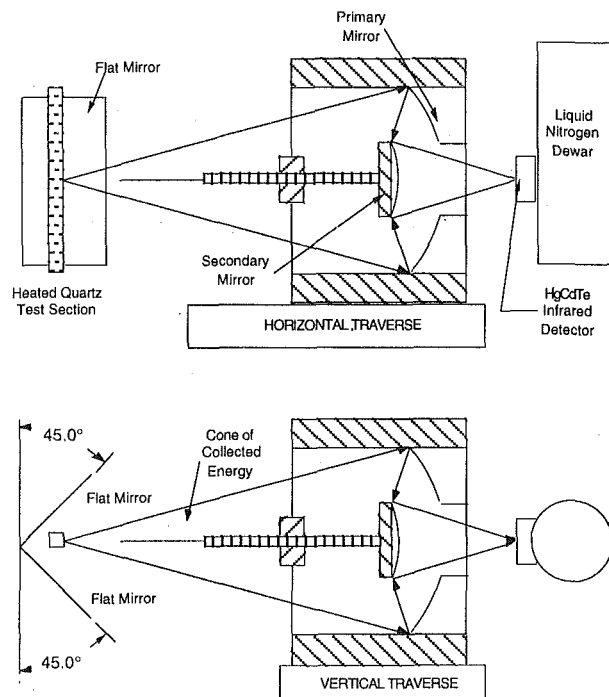
Thermocouples are used to measure coolant inlet and exit temperatures. Using the measured exterior wall temperature and ITO film heat flux, the interior wall temperature and heat flux are computed with a three-dimensional conduction algorithm. This algorithm accounts for variations in the thermal conductivity of quartz with temperature and is reported by Bons (1997). Nu is then calculated with an absolute uncertainty of 9 percent.

The Nd:YAG laser used emits two sequential 200 mJ pulses with a nominal pulse width of 10 ns ($\lambda = 532$ nm). Pulse separations of 25–35 μs were used in this research. Figure 6 is a schematic of the optical path. The spherical focusing lens and the final mirror are mounted on an optical traverse so the sheet can be moved from side to side in the test section passage ($0 < y/d < 1$). Approximately 16 cm beyond the final mirror and just before the laser entry port is a cylindrical lens, which expands the beam in only one direction to produce a planar sheet normal to the axis of rotation. The sheet thickness at the test section was measured to be 0.4 ± 0.1 mm with a height of 4 cm. Gonesh #2 incense was used to seed the flow [particle diameters ≈ 0.4 μm (Bryanston-Cross and Epstein, 1990)] and images were captured using a CCD
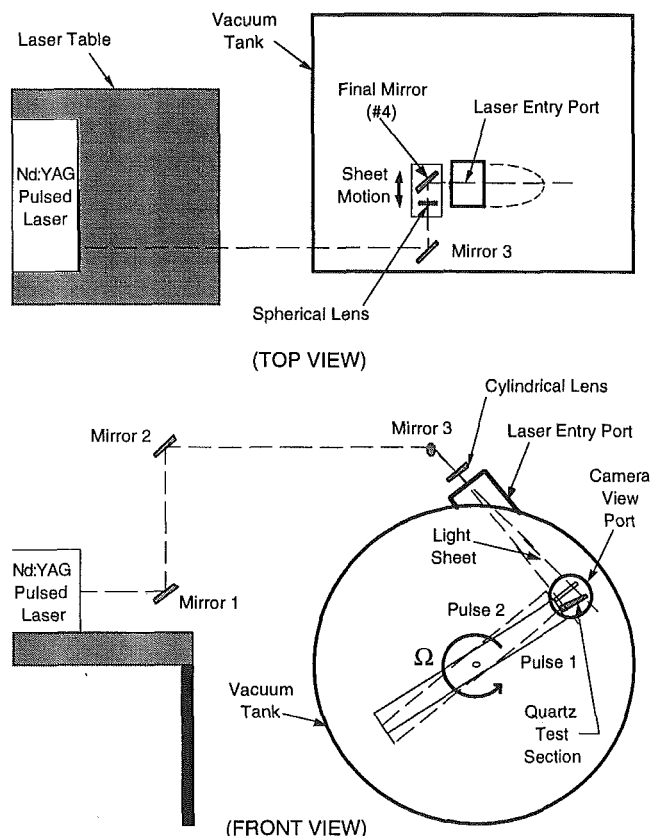

Fig. 6 Schematic of laser and optical layout

camera located at the camera view window indicated in Fig. 6. The image acquisition system is synchronized so that the laser fires and the camera forms an image only when the rotating test section is located in the camera's field of view.

Particle Image Velocimetry (PIV) relies on sequential bursts of light to provide two frozen images of particles in a flowfield. Particles are paired with their double (or correlations are performed) to yield the net motion in the two dimensions of the light sheet. An accurate knowledge of the pulse time separation then provides two components of velocity. Because the camera is stationary relative to the test section, the second test section image is displaced by an angle $\Omega \Delta t$ about the axis of rotation. To remove this angular displacement from the image, an alignment cross made from 13 μm wire is inserted into the test section prior to testing. The camera then acquires a double-image of the rotating alignment cross. The pixel distance between the two cross images, the cross' radial position from the axis of rotation, and the $\Omega \Delta t$ for the cross image are sufficient to compute the center of rotation coordinates in "pixel space." Subsequent PIV images can then be "derotated" an angle $\Omega \Delta t$ about this pixel center of rotation provided the camera is not moved from its alignment position. The principle is similar to the bias-velocity added to images in some PIV applications to remove directional ambiguity (Jefferies, 1996). With this angular displacement removed from the image, the flow velocity relative to the rotating test section is determined. The uncertainty in the velocity vectors presented here was calculated to be 6 percent. The derotation contributes an additional 5 percent of bias error to all PIV images processed with the same pixel center measurement. A more detailed description of the experimental facility and data acquisition process can be found in Bons (1997).

Analytical Model

A momentum integral model of the rotating, heated passage flow was developed to aid in the interpretation of the velocity data. The model assumes that the passage flow can be dissected into independent shear flows on each of the four passage walls and a central inviscid "core" region. The entry length for turbulent pipe flow is 10 to 15 diameters, so the flow in this turbine cooling passage (with $l/d < 15$ and a short tapered inlet orifice) is modeled as developing turbulent flow. This methodology has been used with success by Mori and Nakayama (1968), Ito and Nanbu (1971), and more recently by Chew (1993) in analyzing rotating internal flows.

With this premise of developing turbulent flow, the boundary layers on each of the four contiguous passage walls grow independently with distance from the inlet. When the passage is not rotating, the only mutual influence they have is to jointly close-off the "core" flow region, thus accelerating the fluid in the center of the passage. The boundary layer growth is calculated using the momentum integral equation (Kays and Crawford, 1980):

$$\frac{\tau_o}{\rho_o u_\infty^2} + \frac{\rho_o v_o}{\rho_\infty u_\infty} = \frac{d\theta}{dx} + \theta \left[\left(2 + \frac{\delta_d}{\theta} \right) \frac{1}{u_\infty} \frac{du_\infty}{dx} \right]$$

For turbulent flow, a power law shear stress relation is assumed.

$$u^+ = 8.75(y^+)^{1/n}$$

Substituting this into the momentum integral equation and integrating from $x = 0$ to a point $x > 0$ in the flow passage, with the initial condition that $\theta (x = 0) = 0$, produces an expression for $\theta(x)$:

$$\theta(x) = f(u_\infty, n, \nu) \left\{ \int_0^x u_\infty^{g(n)} dx \right\}^{(n+1)/(n+3)}$$

The functions f and g are lengthy algebraic expressions resulting from the integration and can be found from Bons (1997). Assuming constant inlet velocity and temperature profiles, the boundary
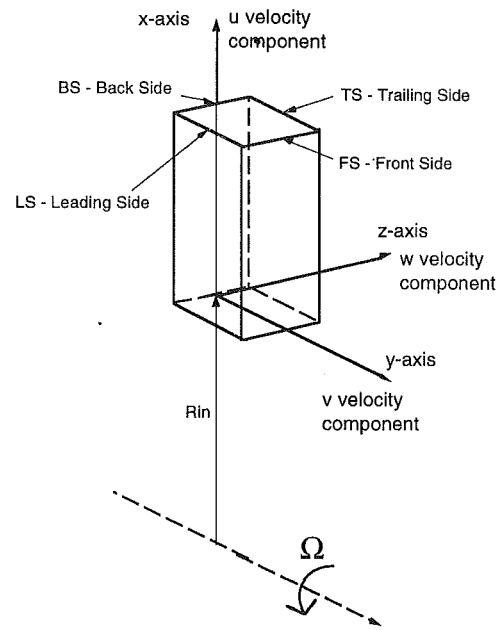
Fig. 7 Schematic of test section axis and velocity components

layer thickness can be calculated at any point downstream. The effect of the boundary layer growth on the core flow is assessed by applying conservation of mass to the passage cross section. The core flow velocity rises as the blockage due to the wall layers increases down the passage.

With this as the basic flow model, the multiple effects of rotation are assessed using the full Navier–Stokes equations for steady, incompressible flow evaluated in a coordinate system fixed to the passage, as shown in Fig. 7:

$$(\overset{*}{u} \cdot \overset{*}{\nabla})\overset{*}{u} + \frac{\partial \overline{(u_i' u_j')}}{\partial x_j} = \nu \nabla^2 \overset{*}{u} - \frac{\nabla p}{\rho} - 2\overset{*}{\Omega} \times \overset{*}{u}$$
$$+ \beta(T - T_\infty)(\overset{*}{\Omega} \times \overset{*}{\Omega} \times \overset{*}{R})$$

where $\overset{*}{u} = u\hat{\imath} + v\hat{\jmath} + w\hat{k}$, $\overset{*}{R} = (R_{in} + x)\hat{\imath} + y\hat{\jmath} + z\hat{k}$, and $\Omega = \Omega\hat{\jmath}$.

Here the Boussinesq (1930) approximation has been applied, so the density variation is shown only in the buoyancy source term.

The $-2\overset{*}{\Omega} \times \overset{*}{u}$ term is the Coriolis acceleration, which accounts for the use of a noninertial reference frame attached to the rotating passage. This Coriolis acceleration term has a $+2\Omega u$ contribution to the z-momentum equation, which generates a pressure gradient in the crossflow direction (Moore, 1967):

$$\frac{dp}{dz} = 2\Omega u_\infty \rho_\infty$$

Substituting this pressure gradient into the z-momentum equation, and solving for dw/dx (ignoring all other terms but the $+2\Omega u$ Coriolis term) yields an expression for Δw_{cor} (the added Coriolis-induced flow component for a Δx step down the passage):

$$\Delta w_{cor} \cong 2\Omega \left[\frac{u\rho}{u_\infty \rho_\infty} - 1 \right] \Delta x$$

In the side wall boundary layers, the conditions $u\rho < u_\infty \rho_\infty$ and thus $\Delta w_{cor} < 0$ create the well-documented Coriolis double vortex associated with pipe flow rotating in the orthogonal mode. The model generates the complete vortex by forcing w_{cor} to satisfy the crossflow conservation of mass ($\int w dy \cong 0$) and the no-slip condition at the sidewalls ($w (y = 0 \ \& \ d) = 0$).

One result of this vortex is the convective transport of high-

momentum core fluid into the trailing wall boundary layer. This transport energizes the boundary layer here, thus reducing its thickness. Likewise, momentum deficit (low-momentum trailing wall boundary layer fluid) is convected from the trailing wall to the side wall, and from there to the leading wall. The leading wall boundary layer then becomes the repository for the momentum deficit convected from the other walls. To account for these effects, the magnitude of convected momentum deficit is assessed at each step, and the boundary layer thickness of each passage wall is then adjusted up or down depending on the sign of the convection (up for the leading wall and down for the trailing wall).

The Coriolis acceleration also contributes a $-2\Omega w$ term in the x-momentum equation, which is incorporated into the model by assessing the associated increment of streamwise acceleration Δu_{cor}.

$$\Delta u_{\text{cor}} \cong -2\Omega \frac{w\rho}{u_\infty \rho_\infty} \Delta x$$

From this relation, it is evident that in the region near the side wall (where $w < 0$), this component results in an acceleration, whereas in the core region (where $w > 0$) there is a corresponding deceleration. This effect is not linear with rotational frequency, since $w \propto \Omega$ it follows that $\Delta u_{\text{cor}} \propto \Omega^2$.

The buoyancy acceleration term contributes a $-\Omega^2 z\beta(T - T_\infty)$ term in the z-momentum equation, which produces a positive acceleration on fluid near the leading wall ($T > T_\infty$ in the boundary layer and $z < 0$ for the leading wall). Likewise for the trailing wall (where $z > 0$), this acceleration (now of negative sign) accelerates hot trailing wall fluid toward the passage center. This buoyancy-induced center-seeking flow is modeled as mass injection from the wall into the boundary layer with normal velocity, v_o. Substituting this into the momentum integral equation, the net effect is to thicken both the trailing and leading wall boundary layers for d.r. > 0. This in turn creates a greater core acceleration.

The buoyancy acceleration term also contributes a $-\Omega^2(R_{in} + x)\beta(T - T_\infty)$ term in the x-momentum equation, which actually opposes the mean flow direction. Hot boundary layer fluid near the walls is accelerated in toward the axis of rotation while colder core fluid is accelerated away from the axis of rotation. The model incorporates this buoyant flow by allowing a region of separated flow to form near the leading wall. The separated region's spatial extent matches the mass defect of the buoyant flow and essentially pushes the turbulent boundary layer away from the physical wall to a point inside the passage. The other three walls are subjected to strong secondary flows and are considerably thinner, so the buoyancy associated with each of them is either convected to the leading wall or mixed into the respective boundary layer thickness. Experimentally measured wall temperature data and surface heat flux values are used to initiate the model. Comparisons with the measured flowfield are shown in the next section.

Results and Discussion

The experimental data are presented in two parts: first the PIV fluid velocity measurements and second the passage wall Nusselt measurements. For the PIV images, the orientation of the light sheet allows access to a plane normal to the axis of rotation (x–z plane, see Fig. 7). Since the strongest velocity gradients are expected in the y and z (nonradial) directions, the vector field from each PIV image is first averaged along the x direction (yielding $u(z)$ and $w(z)$ for each image). Due to observed randomness in the vectors, four to six images at each location are combined to produce ensemble-averaged $u(z)$ and $w(z)$ distributions at a given x and y position. The light sheet and camera are then translated in the y and x directions to obtain ensemble-averaged $u(z)$ and $w(z)$ distributions at various positions in the flow. $u(z)$ and $w(z)$ at the same x but various y positions can be "stacked up" to provide a quasi-three-dimensional look at the flowfield (assuming the mean flow is steady). Then $u(y)$ and $w(y)$ distributions can be generated
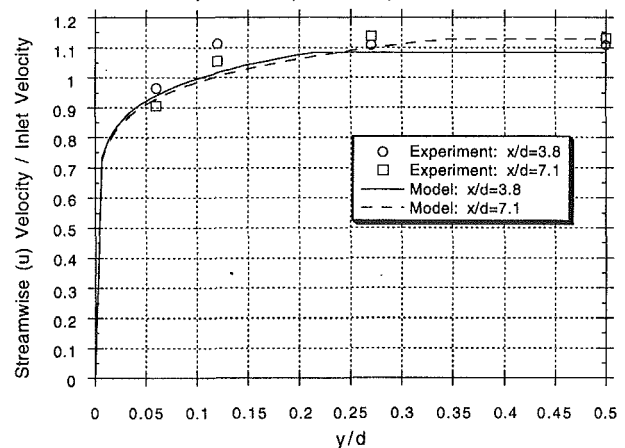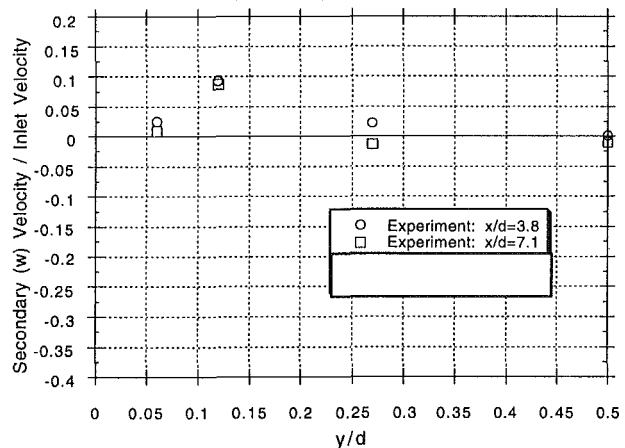
Fig. 8 Streamwise $u(y)$ and secondary $w(y)$ velocity profiles with Rot = 0.0 and d.r. = 0.0

at this same x location by interpolating between images in the y direction.

Stationary Velocity Measurements. Figure 8 shows $u(y)$ and $w(y)$ data for Re = 10,000 and Rot = 0 at two x/d locations. The model results are also indicated on the figure. Both the features of boundary layer development and core acceleration are evident in the $u(y)$ data. The $w(y)$ data show no significant transverse component when the passage is not rotating, and the model (not shown) predicts none.

Rotating Velocity Measurements. Data taken at the same Reynolds number and x/d positions, but with Rot = 0.13, are shown in Fig. 9. From the $w(y)$ data, it is clear that a secondary vortex flow is present. The strength and spatial extent of this vortex grow noticeably with x/d. The peak negative w velocity has increased by a maximum factor of 3 with a doubling of distance from the passage inlet ($x/d = 3.8$ versus 7.1). Also, the crossover point to positive w occurs near $y/d = 0.13$ at the downstream position versus 0.07 for the upstream position. This is the effect of the Coriolis acceleration component in the z-momentum equation. The model calculations also show this vortex growth. The most notable feature in the $u(y)$ data is the thinner boundary layer compared to the nonrotating case. The axial velocity is essentially flat from $y/d = 0.05$ to midpassage with only a modest rise beyond $y/d = 0.2$. In addition, the core acceleration with x/d that was evident in the stationary case is negligible here. The mechanism responsible for this result is the streamwise (x-momentum)

Data vs. Model: Streamwise Velocity Profiles on Side Wall
Re=10000, Rot=0.13, d.r.=0.0, x/d=3.8 & 7.1

Data vs. Model: Streamwise Velocity Profiles on Side Wall
Effect of Streamwise Coriolis Component in Model
Re=8100, Rot=0.2, d.r.=0,0, x/d=7.9

Data vs. Model: Secondary Velocity Profiles on Side Wall
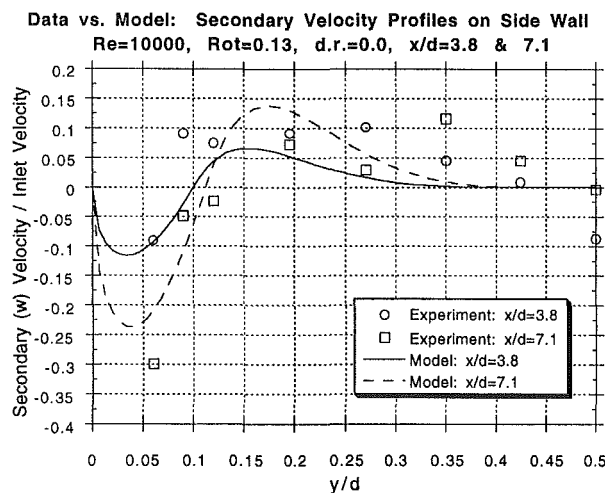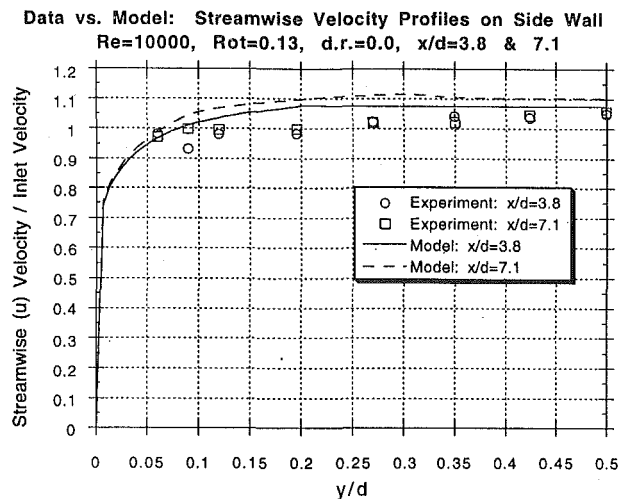Re=10000, Rot=0.13, d.r.=0.0, x/d=3.8 & 7.1

Data vs. Model: Secondary Velocity Profiles on Side Wall
Effect of Streamwise Coriolis Component in Model
Re=8100, Rot=0.2, d.r.=0,0, x/d=7.9

Fig. 9   Streamwise $u(y)$ and secondary $w(y)$ velocity profiles with Rot = 0.13 and d.r. = 0.0

Fig. 10   Streamwise $u(y)$ and secondary $w(y)$ velocity profiles with Rot = 0.2 and d.r. = 0.0; effect of streamwise component of Coriolis acceleration in model

component of the Coriolis acceleration. This acceleration produces additional streamwise momentum in the near wall region where $w < 0$ and depresses the velocity in the core region.

More striking evidence of this effect is seen in a similar data set for Rot = 0.2 (Fig. 10). Here the model calculations are plotted with and without the streamwise Coriolis effect (both incorporate the z-momentum component). The $u(y)$ data now show a dramatic rise approaching the wall rather than the flat profile witnessed for Rot = 0.13. Since u_{cor} is proportional to Ω^2 rather than simply Ω, a 60 percent rise in rotational frequency (from Rot = 0.13 to 0.2) actually produces a rise in u_{cor} by a factor of 2.4. This also creates a depression of the core velocity relative to no rotation. The $w(y)$ data in Fig. 10 show that the vortex has also been squeezed closer to the wall, and the corresponding crossflow velocities have nearly doubled. As further evidence of the streamwise Coriolis effect, the model calculation with Coriolis incorporated is more in line with the experimental results.

Figure 11 shows the $u(z)$ calculation versus the experimental data for the same case with larger Rot = 0.2. The boundary layer disparity between the trailing and leading walls is apparent. The vortex motion has thinned the trailing wall boundary layer and thickened the leading wall boundary layer. By incorporating this convection of boundary layer fluid into the model, the calculation matches the experimental data almost exactly. Other researchers have noted these same flow features to varying degrees. Berg et al. (1991) measured the velocity field in a long l/d rotating pipe (Re = 40,000 and Rot = 0.04) with laser 2-focus and found a rise of 10
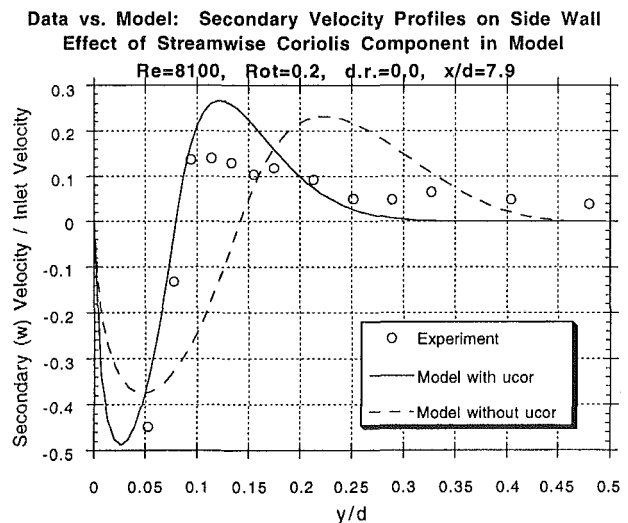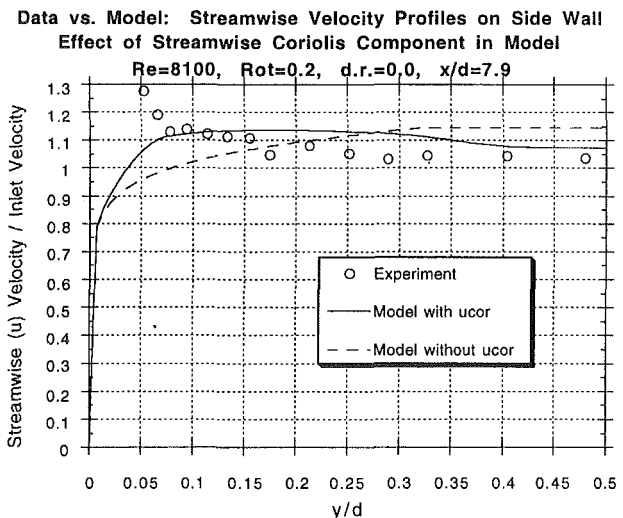
percent in the streamwise velocity from passage centerline to sidewall and a trailing-to-leading wall edge velocity ratio of 1.15. Tse and McGrath's (1995) LDV data show secondary velocity magnitudes up to 65 percent of the streamwise velocity at $x/d = 7$ for Re = 25,000 and Rot = 0.24. The streamwise velocity rise toward the side walls is also evident in their data.

Finally, typical velocity vector fields from the centerline ($y/d = 0.58$) and near-wall ($y/d = 0.93$) rotating data are shown in Fig. 12 for the Rot = 0.2 case. The near-wall vectors show the strong motion in the direction of rotation versus the centerline vectors, which are leaning in the opposite direction. The $y/d = 0.93$ vectors also show evidence of the steep dw/dy gradient captured by the finite laser sheet thickness (0.4 mm). Vectors with $w/u_{in} = -0.5$ lie side by side with $w/u_{in} = 0.0$ vectors in this two-dimensional representation of a three-dimensional flowfield.

Heated, Rotating Velocity Measurements.   Figure 13 shows the effect of heat addition to the rotating flowfield. Plotted are $u(z)$ distributions from three cases: Rot = 0.0 and d.r. = 0.0, Rot = 0.2 and d.r. = 0.0, and Rot = 0.2 and d.r. = 0.27 along with the model calculations. With heat addition, the trailing-to-leading wall disparity in streamwise velocity exceeds a maximum ratio of 2. This dwarfs the same measure from the non-heated data, shown in Fig. 11 (and again in this figure) to be only 1.1. Since Rot is identical in the two data sets, the distorted streamwise velocity profile for the heated case is clearly the result of hot, buoyant fluid collecting
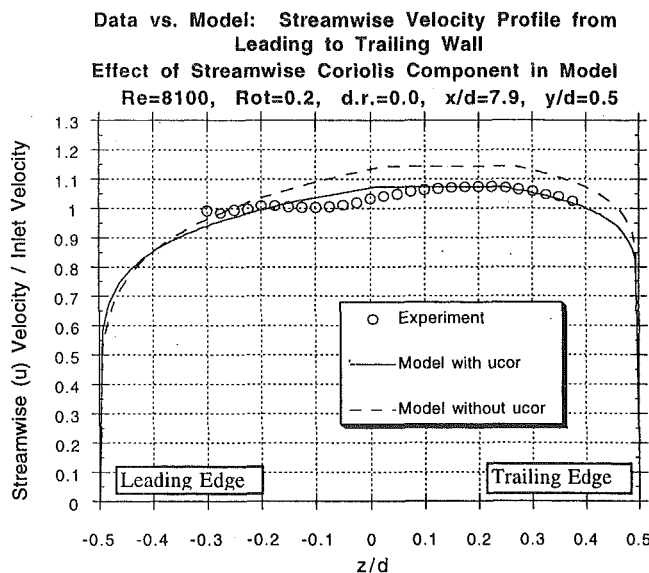
Fig. 11 Data versus model prediction of streamwise $u(z)$ velocity profiles with Rot = 0.2 and d.r. = 0.0; effect of streamwise component of Coriolis acceleration in model

on the leading wall. The fact that the model calculation for the d.r. > 0 case employs a separated leading wall profile and appears to match the trend in the data strongly suggests stagnant or reverse flow near the leading wall for these conditions. Unfortunately, it is difficult to image the near-wall region on the leading face of the test section optically due to surface reflections, but isolated vectors from a few selected PIV images do indicate the presence of stagnant or reversed flow. Figure 14 shows actual vector fields for the d.r. $= 0.27$ case where the $u(z)$ gradient and sites of stagnant flow along the leading wall are evident. The Coriolis vortex evident in the $w(y)$ data of Fig. 13 is responsible for the disproportionate effect of buoyancy on the leading wall. The hot wall fluid from the trailing and side walls all collects on the leading wall due to the convective action of the swirling vortex.

Since there are no other heated rotating velocity data to compare these new data with, the results of several computational studies that give evidence of similar flow features are discussed for comparison. Dutta et al. (1994) computed a heated, rotating flowfield for Wagner and Johnson's configuration at Re $= 25,000$, Rot $= 0.24$, and d.r. $= 0.13$ at $x/d = 9$. The code results predict a streamwise velocity of $0.7u_{in}$ at $z/d = -.35$ and $1.2u_{in}$ at $z/d = +0.35$. Also, vectors near the side walls have secondary velocity magnitudes near $0.15u_{in}$ and an estimated vortex eye position of $y/d = 0.1$. For the same conditions, but a lower Rot $= 0.12$, Tekriwal (1996, 1994) predicted nearly a factor of two in streamwise velocity from trailing side to leading side and shows cross-stream velocities near $0.2u_{in}$ with a vortex eye position of $y/d = 0.15$. At a higher Rot $= 0.48$, Tekriwal predicted reverse flow over a region extending to $\Delta z/d = 0.15$ from the leading wall. Prakash and Zerkle (1992) also predicted reverse flow for this same high Rot case. Finally, Bonhoff et al. (1997) predicted reverse flow and a peak streamwise velocity of $1.8u_{in}$ near the trailing wall for Rot $= 0.24$, Re $= 25,000$, and d.r. $= 0.15$. Although the three codes all predicted similar results (reverse flow and core velocity skewed to trailing wall), the published data are for three very different passage locations: $x/d = 8$ for Tekriwal, $x/d = 2$ for Prakash and Zerkle, and $x/d = 14$ for Bonhoff et al. The data presented here are at an $x/d = 8$, a lower Re $= 10,000$, a moderate Rot $= 0.2$, and a factor of two higher d.r. $= 0.27$ from these predictions. While a CFD prediction reproducing these exact flow conditions is not yet available, this comparison shows that the measured behavior is in the range of that previously predicted.

The Coriolis effect on the streamwise velocity is also present in
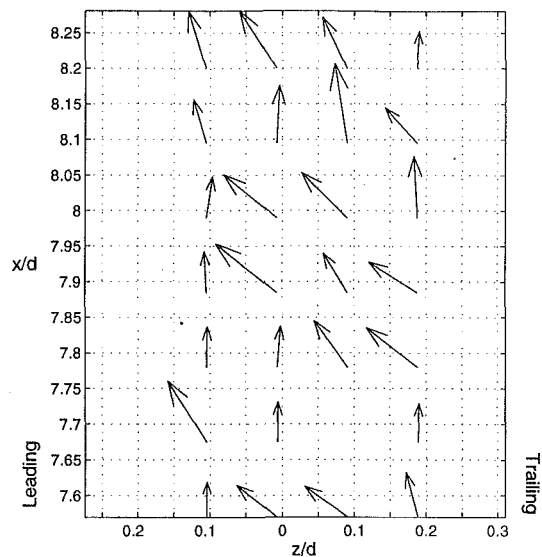
Velocity Vectors at y/d=0.93, mean $u/u_{in} = 1.21$, mean $w/u_{in} = -0.57$
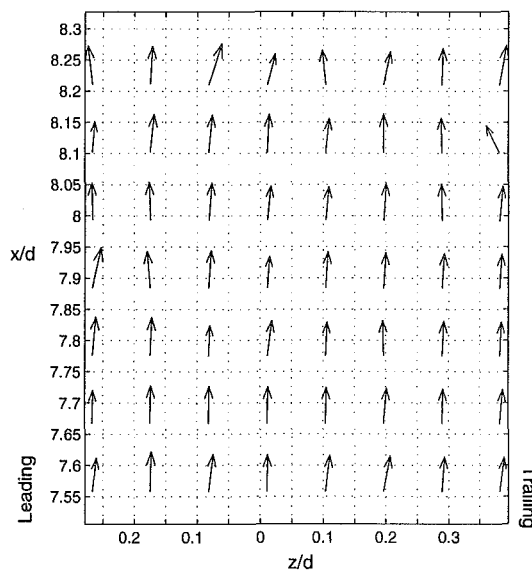
Velocity Vectors at y/d=0.58, mean $u/u_{in} = 1.04$, mean $w/u_{in} = +0.06$

Fig. 12 Sample PIV vector $x-z$ plots for Re = 8100, Rot = 0.2, and d.r. = 0.0 at $x/d = 7.9$

the heated PIV data, although now it competes directly with the buoyancy force on the side walls. Figure 15 shows $u(z)$ profiles at various y stations. The region of highest velocity is $0.1 < z/d < 0.3$ and $y/d = 0.1$ (near the back side wall). The region of lowest velocity is $-.3 < z/d < -0.1$ and $y/d = 0.86$ (near the front side wall). This unexpected side-to-side asymmetry is due to the heating imbalance mentioned earlier in the experimental facility section. Due to a manufacturing error, the front side wall has a higher heat flux than the back side wall. Because of this, buoyancy has a stronger effect on the front side wall than the back side wall, and streamwise velocities along this wall ($y/d = 1$) are lower. Upon closer inspection of the near-wall secondary velocities (w) in Fig. 13, the peak negative velocity on the front side wall ($y/d = 1$) is 20 percent higher than on the back side wall ($y/d = 0$). Also, the region of positive w velocity extends farther from the front wall than from the back side wall. Since the boundary layer to core fluid density ratio also influences w_{cor}, the stronger vortex on the front side wall is evidence of the heat load disparity between the two side walls. This combination of stronger vortex and greater

Data vs. Model: Streamwise Velocity Profiles from Leading to Trailing Wall near Passage Centerline (y/d=0.5) Re=8100, Rot=0.2 & 0.0, d.r.=0.27 & 0.0, x/d=7.9

Data vs. Model: Secondary Velocity Profiles Re=8200, Rot=0.2, d.r.=0.27, x/d=7.9
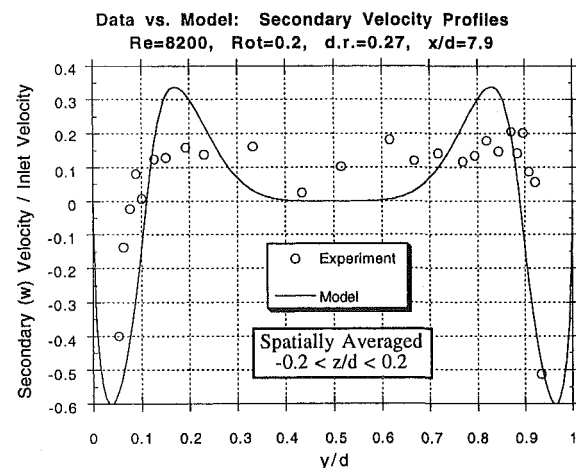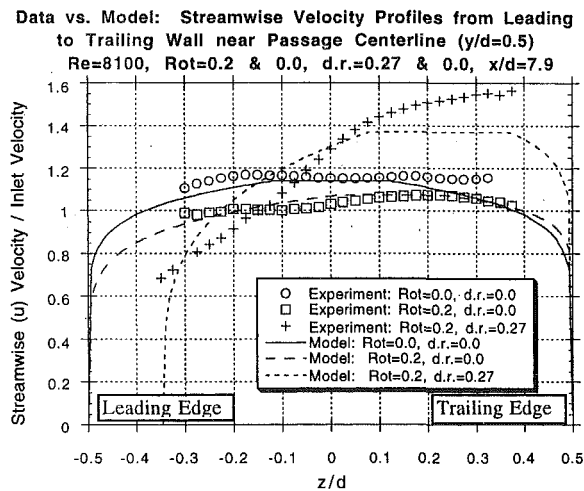
Fig. 13 Streamwise $u(y)$ and secondary $w(y)$ velocity profiles with Rot = 0.2 and d.r. = 0.27

Velocity Vectors at y/d=0.85, mean u/u_{in} = 1.06, mean w/u_{in} = +0.24
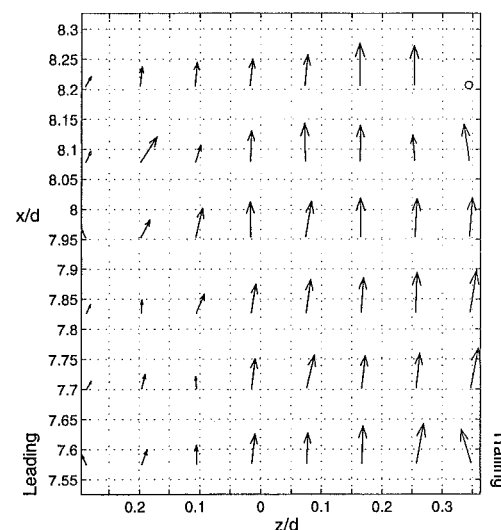
Velocity Vectors at y/d=0.79, mean u/u_{in} = 1.20, mean w/u_{in} = +0.12

Fig. 14 Sample PIV vector x–z plots for Re = 8200, Rot = 0.2, and d.r. = 0.27 at x/d = 7.9

buoyancy sharply reduce the heat transfer at the front side edge of the leading wall, as will be seen shortly.

Before presenting the heat transfer data, it is instructive to attempt a heat transfer prediction based on the velocity data alone. Comparing the leading and trailing walls, and ignoring for the moment that the data suggest separation on the leading face due to buoyancy, we could estimate the Nusselt number for each side based solely on their associated boundary layer edge velocity. From Fig. 13, this ratio appears to be approximately 2.2 (trailing wall-to-leading wall respectively). Following the analytical Dittus–Boelter (1930) correlation between Re and Nu, we would expect

$$\frac{Nu_{TS}}{Nu_{LS}} \propto \left\{ \frac{Re_{TS}}{Re_{LS}} \right\}^{0.8} = \left\{ \frac{u_{\infty TS}}{u_{\infty LS}} \right\}^{0.8} \cong 2.2^{0.8} = 1.88$$

As will be shown subsequently, this is within 6 percent of the experimentally measured Nu ratio at this x/d.

Heat Transfer Measurements. The plots of Nu shown here are normalized by the Dittus–Boelter correlation for Nu in a stationary tube:

$$Nu_{\infty} = 0.023 \; Pr^{0.4} \; Re^{0.8}$$

Data are presented for 0.02 < Rot < 0.29 all at Re $\cong$ 8200 and d.r. $\cong$ 0.27.

Figure 16 shows the Nusselt ratio contours on the inside walls of the test section for the same conditions used in the heated PIV study just presented. The four walls are displayed in succession from left to right: front side wall (y/d = 1), leading wall (z/d = −0.5), back side wall (y/d = 0), and trailing wall (z/d = +0.5) (see Fig. 7). A low-Nu spot is evident on the leading wall at x/d = 8 and a corresponding high-Nu region is located on the trailing wall at the same x/d. The Nu on the other sides appears to vary monotonically between the leading and trailing wall peak values. Upon closer inspection, the low-Nu region on the leading wall is skewed to the front side wall rather than the back side wall and the lateral Nu gradient on the front side wall appears steeper than that on the back side wall. This is evidence of the disparity in surface heat flux between the two walls. The increased heat addition on the front wall produces more buoyant hot fluid, which collects on the leading wall creating the skewed Nu map. Also, the vortex is stronger along this wall, causing a steeper Nu gradient than on the back wall. If a symmetric heat flux wall condition had been achieved, the authors would expect the flow and Nu measurements to exhibit greater symmetry about the passage centerline (y/d = 0.5).

The magnitude of these two effects is more clearly evaluated with Fig. 17, which shows the side mean Nu as a function of x. As expected $Nu_{TS} > Nu_{LS}$ by nearly a factor of 2 at x/d = 8. This nearly matches the edge velocity prediction made earlier. While Nu_{TS} climbs nearly linearly from inlet to exit, Nu_{LS} is flat until

Data: **Streamwise Velocity Profiles at various y/d**
Re=8200, Rot=0.2, d.r.=0.27, x/d=7.9
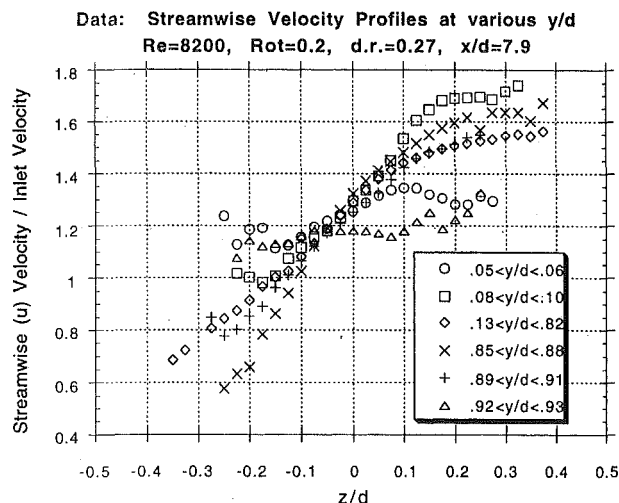
Fig. 15 Streamwise $u(z)$ velocity profile data for Re = 8200, Rot = 0.2, and d.r. = 0.27 at 6 y/d locations and x/d = 7.9

Mean Nusselt Data for 4 Passage Walls
Re=8222, Rot=0.191, d.r.=0.27, & Bo=0.448

Fig. 17 Mean side Nu(x)/Nu$_\infty$ for all four walls; Re = 8222, Rot = 0.191, and d.r. = 0.27

$x/d = 5$ and then drops to a low at $x/d = 8$. As the velocity data indicated, the buoyancy effect is considerable at $x/d = 8$, creating a huge disparity between the flowfield on the leading wall versus the trailing wall. If a region of separated flow on the leading wall is the flow feature causing this low Nu at $x/d = 8$, it is logical to pick a separation point based on the Nu data alone at approximately $x/d = 5$ (since this is where Nu$_{LS}$ begins to drop). Extrapolating further, there may be a flow reattachment at $x/d = 9$, as Nu$_{LS}$ begins to rise here. $x/d = 9$ is also near the passage exit ($l/d = 11.5$), so this rise may be due to a recirculating flow from the exit plenum.

The comparison of the front and back wall Nu ratios is more complex. On the average, Nu$_{FS}$ is 15 percent greater than Nu$_{BS}$. The greater heat load added on the front side appears to have the primary effect of strengthening the vortex here, thus creating an increased convective heat transfer and higher Nu. There are also noticeable oscillations in the Nu data. Nu$_{FS}$ initially rises with Nu$_{TS}$ but drops down coincident with the drop off in Nu$_{LS}$ at $x/d = 5$. Then, there is a reprieve from $x/d = 6$ to 8 where Nu$_{FS}$ rises and Nu$_{BS}$ drops. Finally, Nu$_{FS}$ drops to the exit and Nu$_{BS}$ overtakes Nu$_{FS}$.

To get some idea as to what may cause these apparent oscillations, Fig. 18 shows plots of Nu(y) at various x locations on the leading wall. Clearly the Nu$_{LS}$ profile flattens around $x/d = 8$, while before and after this point Nu$_{LS}$ is lower near the front side edge. One possible explanation is the collection of a strong buoyancy-generated separation bubble near the front-side/leading wall corner due to the heating imbalance. As the bubble grows with x/d, it slowly migrates laterally until it fills the whole passage width (creating the flat Nu$_{LS}$ profile near $x/d = 8$). At this point, no further migration is possible and buoyant fluid again collects disproportionately on the front side/leading wall edge. The result is

Front Side

Max Nu = 1.873 at x

Min Nu = 1.097 at o

Leading Side

Max Nu = 1.332 at x

Min Nu = 0.902 at o

Back Side

Max Nu = 1.853 at x

Min Nu = 0.91 at o

Trailing Side

Max Nu = 1.977 at x

Min Nu = 1.353 at o

Fig. 16 0.05 Nu/Nu$_\infty$ contours on inside of passage for Re = 8222, Rot = 0.191, and d.r. = 0.27

Mean Nusselt Data at 4 x/d Positions on the Leading Side
Note Change in Gradient from Front to Back Side Wall
Re=8222, Rot=0.191, d.r.=0.27, & Bo=0.448

Fig. 18 Nu(y)/Nu$_\infty$ along leading wall at four x/d stations; Re = 8222, Rot = 0.191, and d.r. = 0.27

Trailing Side to Leading Side Nusselt Ratio Data at 4 Rotations
Re=8200, d.r.=0.27, & Rot=0.288, 0.191, 0.096, and 0.019

Fig. 19 Mean side trailing-to-leading wall Nu ratio for four Rot: 0.288, 0.191, 0.096, and 0.019

a reduced Nu here after $x/d = 8$. Han and Zhang (1992) found that when a wall-to-wall heating imbalance (uneven wall temperatures) was imposed on a rotating coolant passage, Nu was higher on all of the passage walls compared with the constant wall temperature case (at the same density ratio). They postulated that the buoyancy imbalance destabilizes the core flow, creating a lateral motion that could give rise to Nu variations like those seen here. Another explanation could be the presence of a characteristic "Helmholtz-like" fluid instability due to the buoyant rotating flow: the bulk flow moving side-to-side in the passage alternating between the front and back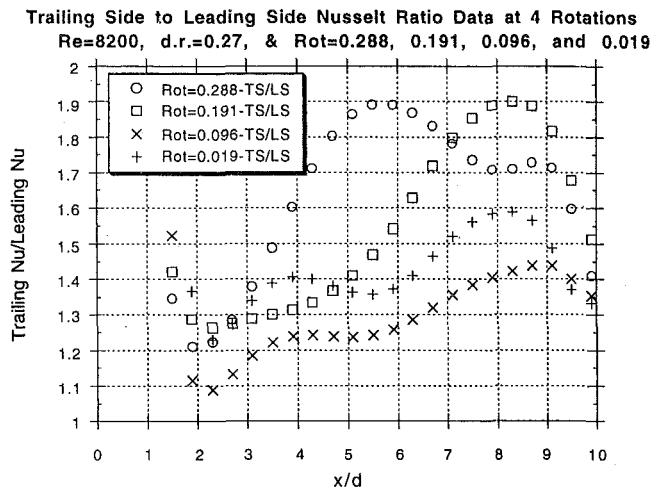 side walls. Either of these would account for the Nu oscillations in Fig. 17, but more data are needed to confirm their validity.

Figures 19 and 20 show the effect of rotation number on the ratio Nu_{TS}/Nu_{LS} and the average value $Nu_{avg} = (Nu_{LS} + Nu_{TS})/2$. Though PIV data were taken only for Rot = 0.2, trends in the Nu data with Rot can be interpreted by extrapolating from the available velocity data. If as speculated, separation caused the rise in Nu_{TS}/Nu_{LS} at $x/d = 5$ for Rot = 0.2, perhaps at the highest rotation, flow separation on the leading wall begins at $x/d = 2$ (where Nu_{TS}/Nu_{LS} rises dramatically in Fig. 19). Then beyond $x/d = 5$, the separated region may have collapsed, causing flow to move back toward the leading wall and decreasing Nu_{TS}/Nu_{LS}. From both figures, it is clear that the passage mean Nu and the trailing-to-leading wall Nu disparity grow with Rot.

Average of Trailing and Leading Nusselt Data at 4 Rotations
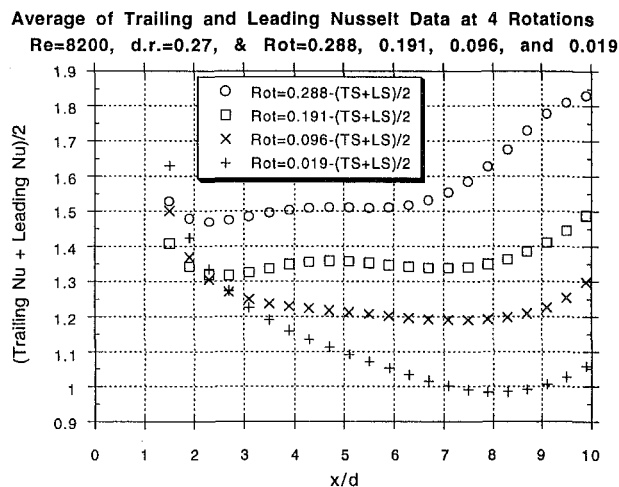**Re=8200, d.r.=0.27, & Rot=0.288, 0.191, 0.096, and 0.019**

Fig. 20 Mean side trailing plus leading wall Nu ratio average for four Rot: 0.288, 0.191, 0.096, and 0.019

Data taken by Barry (1994) on the same facility show a nearly identical trend for Nu_{TS}/Nu_{LS}, although the Barry data are at Re = 25,000. The ratio rises to approximately 2 by $x/d = 8$ and drops off toward the exit. Guidez (1989) also measured a Nu_{TS}/Nu_{LS} ratio of 2 at $x/d = 7.4$ and Re = 24,000, Rot = 0.2, and d.r. = 0.36. Wagner et al. (1991a, b) show a Nu_{TS}/Nu_{LS} ratio of nearly 3.5 for Re = 25,000, Rot = 0.2, and d.r. = 0.22. Both the Guidez and Wagner et al. data show Nu_{TS} rising to a maximum at $x/d = 8$ and Nu_{LS} dropping from inlet to $x/d = 6$ (followed by a rise thereafter).

Conclusions

An experimental investigation was conducted on the internal flowfield of a simulated turbine blade cooling passage. Velocity measurements were taken using Particle Image Velocimetry for both heated and non-heated cases. Under the same conditions, an infrared detector collected wall temperature data for use in calculating local Nusselt number. The test section was operated with radial outward flow and at values of Reynolds number, Rotation number, and density ratio typical of applications. The conclusions of the study are as follows:

1 This work contains the first reported global velocity measurements in a heated, rotating test section. This successfully demonstrates the application of PIV to a rotating flowfield. In addition, high resolution heat transfer measurements taken with the same test section operating at the same conditions allow the direct correlation of flow phenomena with heat transfer phenomena.

2 The Coriolis vortex has two significant effects on the flowfield. It transports hot, low-momentum wall fluid from the trailing wall to the side wall and finally to the leading wall of the square passage. Second, it creates a rise in streamwise velocity in the region near the side wall where the secondary flow is in the direction of rotation. The first of these two effects has the greatest impact on cooling. The accumulation of hot, low-momentum coolant near the leading wall effectively deters heat removal there.

3 The effect of buoyancy is also considerable, reducing streamwise velocities by a factor of two in regions where high temperature coolant is concentrated (near the leading wall).

4 A factor of two difference in Nu from trailing to leading wall arises due to the combination of these buoyancy and Coriolis effects. Without the Coriolis vortex, the buoyancy effect would be evenly distributed to all four walls. Without the buoyancy effect, the Coriolis vortex would only create a 10 percent shift in streamwise velocity toward the trailing wall (versus 120 percent with buoyancy). Since the wall Nu appears to correlate directly with this edge velocity, a Nu prediction based solely on the Coriolis effect would have a factor of two error. This underscores the need for full simulation of both effects simultaneously.

5 A momentum integral model has proven to be a useful tool in flow interpretation. With several refinements incorporated from the experimental data, the model calculations are accurate to within 20 percent of the observed flow features. This lends validity to the underlying model assumption of an inviscid core flow surrounded by wall shear layers. Modeling the Coriolis vortex as a momentum deficit transport mechanism that primarily exchanges hot, low-momentum boundary layer fluid between adjacent walls was found to be a successful strategy. Modeling the buoyancy effect as a separated region of stagnant flow on the leading wall also matches the experimental observation well.

Acknowledgments

sponsorship from the US Department of Energy and Solar Turbines, Inc.

References

Barry, P., 1994, "Rotational Effects on Turbine Blade Cooling," Master's Thesis, Department of Aeronautics and Astronautics, Massachusetts Institute of Technology, Cambridge, MA.

Berg, H., Hennecke, D., Elfert, M., and Hein, O., 1991, "The Effect of Rotation on Local Coolant Side Flow and Heat Transfer in Turbine Blades," ISABE 91-7016, published by AIAA, pp. 170–183.

Bonhoff, B., Tomm, U., Johnson, B., and Jennions, I., 1997, "Heat Transfer Predictions for Rotating U-Shaped Coolant Channels With Skewed Ribs and With Smooth Walls," ASME Paper No. 97-GT-162.

Bons, J., 1997, "Complementary Velocity and Heat Transfer Measurements in a Rotating Turbine Cooling Passage," PhD Thesis, Department of Aeronautics and Astronautics, Massachusetts Institute of Technology, Cambridge, MA.

Boussinesq, X. X., 1930, *Theorie Analytique de la Chaleur,* Vol. 2, Gathiers-Villars, Paris.

Boyer, D. L., 1965, "Flow Through a Rapidly Rotating Rectangular Channel," PhD Thesis, The Johns Hopkins University.

Bryanston-Cross, P., and Epstein, A., 1990, "The Application of Sub-micron Particle Visualisation for PIV at Transonic and Supersonic Speeds," *Prog. Aerospace Sci.,* Vol. 27, pp. 237–265.

Chew, J., 1993, "A Momentum-Integral Solution of Flow in a Rotating Circular Duct," *Int. J. Heat Fluid Flow,* Vol. 14, No. 3, pp. 240–245.

Dittus, F. W., and Boelter, L. M. K., 1930, University of California Publications, Vol. 2, p. 443.

Dutta, S., Andrews, M., and Han, J. C., 1994, "Numerical Prediction of Turbulent Heat Transfer in a Rotating Square Duct With Variable Rotational Buoyancy Effects," presented at the 6th AIAA/ASME Thermophysics and Heat Transfer Conference, Colorado Springs, CO, June 20–23.

Guidez, J., 1989, "Study of the Convective Heat Transfer in a Rotating Coolant Channel," ASME JOURNAL OF TURBOMACHINERY, Vol. 111, pp. 43–50.

Han, J., and Zhang, Y., 1992, "Effect of Uneven Wall Temperature on Local Heat Transfer in a Rotating Square Channel With Smooth Walls and Radial Outward Flow," ASME *Journal of Heat Transfer,* Vol. 114, pp. 850–858.

Han, J., Zhang, Y., and Lee, C., 1994, "Influence of Surface Heating Condition on Local Heat Transfer in a Rotating Square Channel With Smooth Walls and Radial Outward Flow," ASME JOURNAL OF TURBOMACHINERY, Vol. 116, pp. 149–158.

Hsieh, S., Chiang, M., and Chen, P., 1997, "Velocity Measurements and Local Heat Transfer in a Rotating Ribbed Two-Pass Square Channel With Uneven Wall Heat Flux," ASME Paper No. 97-GT-160.

Iacovides, H., and Launder, B., 1991, "Parametric and Numerical Study of Fully Developed Flow and Heat Transfer in Rotating Rectangular Ducts," ASME JOURNAL OF TURBOMACHINERY, Vol. 113, pp. 331–338.

Ito, H., and Nanbu, K., 1971, "Flow in Rotating Straight Pipes of Circular Cross Sections," ASME *Journal of Basic Engineering,* pp. 383–394.

Jefferies, R. W., 1996, "Interactions of a Quasi-Two-Dimensional Vortex With a Stationary and Oscillating Leading-Edge," PhD Thesis, Department of Mechanical Engineering, Lehigh University, PA.

Kays, W., and Crawford, M., 1980, *Convective Heat and Mass Transfer,* McGraw-Hill, New York.

Mochizuki, S., Takamura, J., Yamawaki, S., and Yang, Wen-Jei, 1994, "Heat Transfer in Serpentine Flow Passages with Rotation," ASME JOURNAL OF TURBOMACHINERY, Vol. 116, pp. 133–140.

Moore, J., 1967, "Effects of Coriolis on Turbulent Flow in Rotating Rectangular Channels," Gas Turbine Lab Report #89, Massachusetts Institute of Technology, Cambridge, MA.

Mori, Y., and Nakayama, W., 1968, "Convective Heat Transfer in Rotating Radial Circular Pipes (1st Report, Laminar Region)," *International Journal of Heat and Mass Transfer,* Vol. 11, pp. 1027–1040.

Morris, W., and Ayhan, T., 1979, "Observations on the Influence of Rotation on Heat Transfer in the Coolant Channels of Gas Turbine Rotor Blades," *Proc. Inst. Mech. Engrs.,* Vol. 193, pp. 303–311.

Morris, W., 1981, *Heat Transfer and Fluid Flow in Rotating Coolant Channels,* Research Studies Press.

Morris, W., and Ghavami-Nasr, G., 1991, "Heat Transfer Measurements in Rectangular Channels With Orthogonal Mode Rotation," ASME JOURNAL OF TURBOMACHINERY, Vol. 113, pp. 339–345.

Prakash, C., and Zerkle, R., 1992, "Prediction of Turbulent Flow and Heat Transfer in a Radially Rotating Square Duct," ASME JOURNAL OF TURBOMACHINERY, Vol. 114, pp. 835–846.

Tekriwal, P., 1996, "Effect of Aspect Ratio on the Buoyancy Driven Reverse Flow Near the Leading Wall of Rotating Cooling Passages," ASME Paper No. 96-GT-173.

Tekriwal, P., 1994, "Heat Transfer Predictions in Rotating Radial Smooth Channel: Comparative Study of k-e Models With Wall Function and Low-Re Model," ASME Paper No. 94-GT-196.

Tse, D., and McGrath, D., 1995, "A Combined Experimental/Computational Study of Flow in Turbine Blade Passage: Part I—Experimental Study," ASME Paper No. 95-GT-355.

Tse, D., and Steuber, G., 1997, "Flow in a Rotating Square Serpentine Coolant Passage With Skewed Trips," ASME Paper No. 97-GT-529.

Uellner, S., and Roesner, K., 1991, "LSV Applied to the Flow in a Rotating Channel," *Laser Anemometry: Advances and Applications—1991,* Vol. 2, ASME, pp. 541–546.

Wagner, J., Johnson, B., and Hajek, T., 1991a, "Heat Transfer in Rotating Passages With Smooth Walls and Radial Outward Flow," ASME JOURNAL OF TURBOMACHINERY, Vol. 113, pp. 42–51.

Wagner, J., Johnson, B., and Kopper, F., 1991b, "Heat Transfer in Rotating Serpentine Passages With Smooth Walls," ASME JOURNAL OF TURBOMACHINERY, Vol. 113, pp. 321–330.

Wagner, J., Johnson, B., Graziani, R., and Yeh, F., 1992, "Heat Transfer in Rotating Serpentine Passages With Trips Normal to the Flow," ASME JOURNAL OF TURBOMACHINERY, Vol. 114, pp. 847–856.

Wagner, R., and Velkoff, H., 1972, "Measurements of Secondary Flows in a Rotating Duct," ASME *Journal of Engineering for Power,* pp. 261–270.

B. L. Venable

R. A. Delaney

Allison Engine Company,
Indianapolis, IN 46206

J. A. Busby

R. L. Davis

D. J. Dorney

United Technologies Research Center,
East Hartford, CT 06108

M. G. Dunn

C. W. Haldeman

R. S. Abhari

The Ohio State University,
Columbus, OH 43235

Influence of Vane–Blade Spacing on Transonic Turbine Stage Aerodynamics: Part I—Time-Averaged Data and Analysis

A comprehensive study has been performed to determine the influence of vane-blade spacing on transonic turbine stage aerodynamics. In Part I of this paper, an investigation of the effect of turbine vane–blade interaction on the time-mean airfoil surface pressures and overall stage performance parameters is presented. Experimental data for an instrumented turbine stage are compared to two- and three-dimensional results from four different time-accurate Navier–Stokes solvers. Unsteady pressure data were taken for three vane–blade row spacings in a short-duration shock tunnel using surface-mounted, high-response pressure sensors located along the midspan of the airfoils. Results indicate that while the magnitude of the surface pressure unsteadiness on the vane and blade changes significantly with spacing, the time-mean pressures and performance numbers are not greatly affected.

Introduction

A well-developed ability to predict turbine stage unsteadiness is essential in addressing noise, efficiency, and endurance issues in future high-performance turbines. High-cycle fatigue, a problem of great interest in advanced turbines, might be quantitatively assessed as part of turbomachinery design by investigating unsteady vane–blade interactions in the design cycle. The dramatic increase in the speed and power of computational resources and the efficiency of the advanced computational algorithms in use today are making this a reality. Both two- and three-dimensional codes capable of predicting the turbine vane-blade aerodynamic interaction are now available. This interaction results from three sources: potential effects, shock interactions, and viscous effects. Many papers have been written discussing these sources of unsteadiness and their effects on turbine stage aerodynamics. Giles (1988a) demonstrated that the shocks emanating from the vane trailing edge have a significant effect on the blade lift. Ashworth et al. (1985) and Rao et al. (1994) have also conducted studies on transonic turbine unsteady aerodynamics. Dring et al. (1981) studied the effect of vane–blade spacing on performance in a low-speed turbine stage. More recently, Kelecy et al. (1995) conducted a numerical study of the effect of vane–blade spacing on transonic turbine stage performance and found little correlation between the stage adiabatic efficiency and spacing.

In this two-part paper, an experimental/computational investigation of the influence of vane–blade axial spacing on transonic turbine stage unsteady aerodynamics is presented. Both two- and three-dimensional solutions and performance numbers from four

different Navier–Stokes solvers were gathered for a common turbine rig geometry. Designed to provide unsteady pressure and heat transfer data, this high-pressure turbine rig allows for the adjustment of the spacing between the vane and blade rows. Time-mean and phase-resolved solutions have been compared to experimental data gathered during tests on this turbine in a shock tunnel facility. Three axial spacings corresponding to 20, 40, and 60 percent of the vane axial chord have been investigated. Part I of this paper presents performance numbers and comparisons between the time-mean solutions and data for each of the three axial spacings. Comparisons are also made between the maximum and minimum calculated and measured surface pressures along the vane and blade surfaces. An analysis of the phase-resolved solutions from the four codes and data is presented in Part II (Busby et al., 1999).

A secondary objective of this two-part paper is the comparison of results produced by four different state-of-the-art computer codes written specifically to solve the unsteady turbomachinery problem. Each of the codes uses a different solution algorithm and grid system. This exercise provides an assessment of the predictive capability provided by the current generation of codes dedicated to turbomachinery stage solutions.

Computational Approach

Computational results were obtained for this paper using four different computer codes. They are hereafter referred to as Procedures 1–4. The solution algorithms and grid systems varied greatly. In all cases the grid spacing at the wall was such that the turbulence model did not require wall functions. Below is a short description of each code.

Procedure 1. The time-dependent, Reynolds-averaged Navier–Stokes equations are solved with an implicit dual time-step approach coupled with a Lax–Wendroff/multiple-grid procedure (Davis et al., 1996; Ni, 1981; Ni and Bogoian, 1989; Ni and Sharma, 1990; Taka-
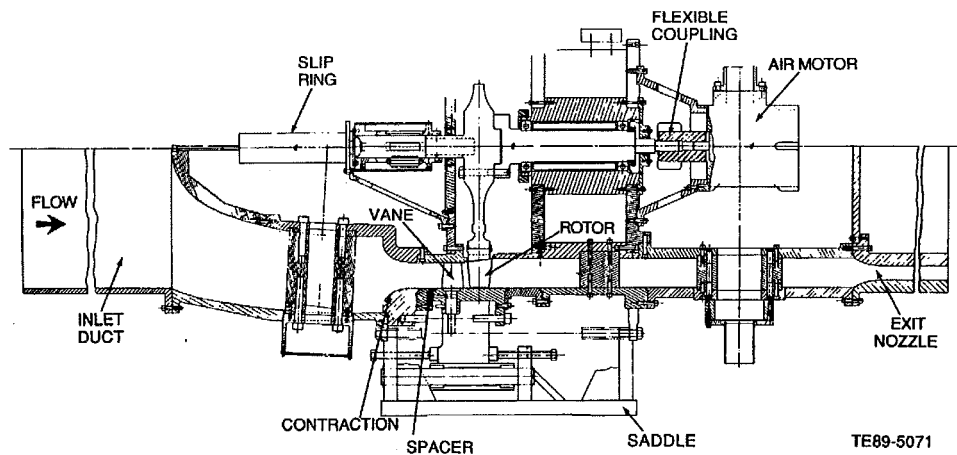
Fig. 1 Housing for turbine rig

hashi and Ni, 1991). The scheme uses central differences for the spatial derivatives with second- and fourth-order smoothing for stability. The algorithm is second-order accurate in time and space. The Baldwin–Lomax (1978) turbulence model is used to compute the turbulent viscosity.

No-slip and constant temperature wall conditions are used on all solid boundaries. Giles' (1990) two-dimensional, steady, nonreflecting, free-stream boundary conditions are used at the upstream and downstream free-stream boundaries. At the inter-blade-row boundaries where the computational grid sectors move relative to each other, the pseudo-time-rate change of the primary variables are interpolated from the adjacent blade row and added to the time-rate changes computed from the Lax–Wendroff treatment.

An **H**-grid topology is used for both the vane and blade passages. The solution domain was chosen to maintain the same spatial periodicity as the experiment. The two-dimensional simulations were performed using three radial planes with the first and third planes representing the boundary surfaces of the stream tube. The three-dimensional solutions included the tip clearance of the blade.

Procedure 2. The two-dimensional Vane–Blade Interaction code provides fully interactive solutions of turbine stage flows by solving the Reynolds-averaged Navier–Stokes equations using an explicit, five-stage Runge–Kutta algorithm similar to that presented by Swanson and Turkel (1985). The system is solved on a blade-to-blade surface of revolution. The scheme uses central differences to approximate the spatial derivatives and a dissipation scheme developed by Jameson et al. (1981) based on second- and fourth-order terms. Second-order accuracy is achieved in both space and time. Implicit residual smoothing is employed to increase the stability limit of the numerical method by accelerating the propagation of information throughout the grid system. Turbulent viscosity is modeled with the Baldwin–Lomax (1978) algebraic turbulence model. The airfoil surface boundary layers are assumed to be fully turbulent in these calculations.

A composite grid system comprised of **O**-grids around the airfoils overset on background **H**-grids is used to model the solution domain. The Chimera approach of Benek et al. (1985) is employed to transfer information between the overset grids. At the inlet and exit boundaries, nonreflecting boundary conditions are used to minimize spurious reflections. Phase-lagged periodic boundary conditions (Lewis et al., 1989) are employed to treat the periodic boundaries in the airfoil passages. The phase-lagged boundary conditions allow solutions to be obtained for stage geometries with arbitrary airfoil counts while including just one vane and one blade in the solution domain. Communication between the two **H**-grids in the interrow region as the blade rotates past the vane is provided through interpolation between the two

grids of phase-lagged boundary information. Details of the code development and validation have been presented by Rao and Delaney (1990) and Rao et al. (1994).

Procedure 3. The numerical procedure used to model this flow is a two-dimensional, Reynolds-averaged, unsteady multi-blade row code, UNSFLO, developed by Giles (1988b). This is a coupled viscous/inviscid code in which the thin shear layer Navier–Stokes equations are solved on a body-fitted boundary layer grid using an implicit algorithm, while the Euler equations are solved on an outer inviscid grid using an explicit algorithm. The interface between the two regions is handled in a conservative manner. Quasi-three-dimensional effects are included through the specification of a stream-tube thickness in the third dimension (axial velocity density ratio). Here, the Euler equations are solved using a generalization of Ni's Lax–Wendroff algorithm (Ni, 1981). Full second-order accuracy is achieved. The inviscid grid consists of an **H**-type structured grid around the vanes and the rotor blades. The viscous grid is an **O**-type mesh about each blade for which an ADI (alternating-direction-implicit) method with Roe's flux-difference splitting gives third-order upwinding for the residual operator and first-order upwinding for the implicit operator. The Baldwin–Lomax (1978) algebraic turbulence model is used in the viscous part of the solution with the location of the boundary layer transition specified. For the calculations presented herein, transition was assumed at the leading edge. For unsteady blade–vane interaction calculations, the code utilizes an innovative space–time coordinate transformation, "time-tilting" (Giles, 1988b), to permit arbitrary blade-vane pitch ratios while incurring little penalty in computation time. More details on this code and its verification may be found in Giles and Haimes (1993) and Abhari et al. (1992).

Procedure 4. This technique is based on an extension of an approach developed by Rai (1987). The flow field is divided into two basic types of zone. **O**-grids are used to resolve the flow field near the airfoils. These **O**-grids are overlaid on outer **H**-grids, which are used to resolve the flow field in the passages between airfoils. The **H**-grids are allowed to slip relative to one another to simulate the relative motion between blades and vanes. In the numerical simulations, the numbers of vanes and blades in the solution domain were chosen to maintain the same spatial periodicity as the experiment. The thin-layer or full Navier–Stokes equations, cast in the strong conservation form, are solved on both the **O**- and **H**-type grids. A fully implicit, finite-difference method is used to advance the solution of the governing equations in time. A Newton–Raphson subiteration scheme is used to reduce the linearization and factorization errors at each time step. The convective terms are evaluated using a third-order accurate upwind-biased Roe scheme, while the viscous terms are evaluated using

Table 1 Turbine stage geometry

Parameter	Vane	Blade
Number of airfoils	30	45
Chord, in. (mm)	2.66 (67.6)	1.87 (47.5)
Spacing, in. (mm)	2.03 (51.6)	1.34 (34.0)
Chord/spacing	1.32	1.39
Mean radius, in. (mm)	9.73 (247.1)	9.70 (246.4)
Aspect ratio	0.72	1.10
L.E. radius, in. (mm)	0.18 (4.6)	0.09 (2.3)
T.E. radius, in. (mm)	0.03 (0.8)	0.03 (0.8)
Hub/tip radius ratio	0.82	0.81
Tip radius, in. (mm)	10.64 (270.3)	10.64 (270.3)
T.E. blockage (%)	9.44	8.94

Fig. 2 Photograph of instrumented vane

second-order accurate central differences. The algorithm is second-order temporally accurate. The Baldwin–Lomax (1978) turbulence model is used to compute the turbulent viscosity. In steady-state simulations, the flow variables are flux-averaged at the interface between adjacent blade rows. Nonreflecting boundary conditions are then used to transfer information across the blade row interface. Further details on the numerical analysis can be found in Dorney and Davis (1992).

Experimental Apparatus

Experimental data were gathered in a short-duration shock tunnel facility capable of accommodating the weight flow and geometric requirements of large turbines. Components of the facility include a reflected shock tunnel, primary nozzle, dump tank, and control room. The helium/air-driven shock tube is 18.5 in. (0.46 m) inner diameter with a 40 ft (12.2 m) long driver section and a 60 ft (18.3 m) long driven section. The dump tank is 9 ft (2.75 m) in diameter and 34 ft (10.4 m) long. This facility is capable of test times on the order of 35 to 40 ms. The test gas in these experiments was air.

Located in the expanding portion of the flow at the upstream end of the dump tank, the turbine model housing consists of an inlet duct, an exit nozzle to govern the flow through the turbine rig, and an air motor to drive the turbine rotor. A diagram of the turbine rig housing is shown in Fig. 1. The flow enters the inlet duct at a Mach number of 0.05 and is expanded through the flow contraction to match the required vane inlet conditions. By moving the spacer and saddle, the spacing between the vane and blade can be easily changed. The pressure ratio over the stage is fixed by the nozzle located at the end of a constant area duct downstream of the rotor.

Geometric and aerodynamic data for the turbine rig are shown in Tables 1 and 2, respectively. This turbine rig can be configured with either a subsonic or transonic vane by changing the vane setting angle; however, the transonic configuration was used for this work. Both the vane and blade were instrumented at midspan with flush-mounted Kulite pressure transducers. A photograph of an instrumented vane is shown in Fig. 2. The transducers have an active area of 0.025 in. (6.25×10^{-4} m) by 0.025 in. (6.25×10^{-4} m) and a thickness of 0.013 in. (3.25×10^{-4} m). The natural frequency of these transducers is approximately 400 kHz with a
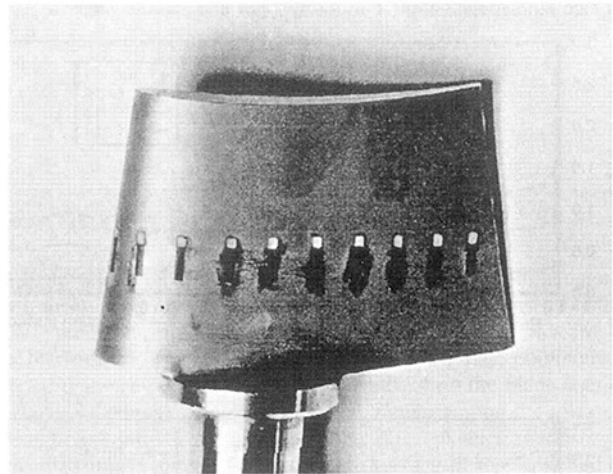
frequency of response as installed in excess of 100 kHz. Locations of the transducers installed on the vane and blade can be seen in Fig. 3. Because of the small size of the blade, it was necessary to install the blade transducers on two different blades to prevent a disturbance of the flow path. The two blades were chosen based on the circumferential periodicity of the geometry, i.e., the two instrumented blades are always oriented in an identical manner relative to the upstream vanes. Further details of the facility and turbine rig can be found in Dunn et al. (1990).

All Kulite pressure sensors are calibrated throughout the entire data system on a daily basis. Pressure transducers were grouped according to their stability over this calibration process. Seventy percent of the sensors calibrated to within ±0.1 psia (±0.690 kPa) peak-peak variation over the experimental data range: 8 to 45 psia (55 to 310 kPa). Another 23 percent were within ±0.2 psia (±1.379 kPa). The final 7 percent were within ±0.7 psia (±4.800 kPa). The uncertainty of the reduced data is greatly improved due to the fact that reported measurements are averaged over many data points, and the cumulative effect is a reduction in uncertainty of the average well below these values. However, as a very conservative number, the data can be assumed to lie within ±0.2 psia (±1.379 kPa), which is a standard deviation of ±0.067 psia (±0.460 kPa).

Tests were conducted by first pressurizing the driver tube and evacuating the driven tube and dump tank. At this time the turbine rotor was spun up to its test speed by the air motor. The diaphragms separating the driver and driven tubes were then ruptured. As the incident shock reflected off of the end of the driven tube, a fast-acting valve opened to allow the high-pressure and temperature air to flow through the model housing and turbine rig into the dump tank. Surface pressure data were taken for the three vane–blade spacings previously mentioned. The experimental pressure

Table 2 Turbine stage operating conditions

Parameter	20% Sp.	40% Sp.	60% Sp.
Speed (RPM)	11,841	11,793	11,755
p_{t1}, psia (kPa)	42.5(274.5)	45.1(313.2)	39.5(274.5)
p_4, psia (kPa)	9.5(65.9)	10.4(72.4)	9.4(65.2)
T_{t1}, R (K)	1098(610)	1177(654)	1183(657)
T_{wall}, R (K)	506(281)	499(277)	499(277)
$\dot{m}$, kg/sec	10.6	10.6	10.6

Fig. 3 Transducer locations on rig vane and blade

Vane

Blade

Fig. 4 Variation of y+ with grid, Procedure 1

sion of the data and two-dimensional midspan solutions. A comparison is then made between two-dimensional and three-dimensional predictions. Finally, both two- and three-dimensional performance calculations are presented.

Grid Refinement Study. Grid refinement studies were conducted by all participants in an effort to determine the grid size and wall spacing necessary to achieve grid-independent solutions. All solutions presented in this section are steady solutions.

Many grids of varying sizes were used in the study. Space limitations prohibit a complete listing; therefore, the focus here is on the wall spacing at the determined best grid size based on shock location and wake diffusion. The objective was to select grids that would provide grid-independent heat transfer solutions as well as surface pressure solutions. For this reason, the selected grids for Procedures 1, 2, and 4 provide $y+$ values at or below 1.0 over the vane and blade surfaces.

Figures 4 and 5 show $y+$ values and static surface pressures, p_s, nondimensionalized by the stage inlet total pressure, p_{t1}, respectively, for the grids used in the Procedure 1 grid refinement study. The corresponding grid dimensions per passage and nondimensional wall spacings are shown in Table 3. Although there are no differences in the pressure solutions for all four grids, grid 3 was chosen as the solution grid because it provided $y+$ values consistently below 1.0 along the entire vane and blade surfaces. Similar plots are shown for Procedure 2 in Figs. 6 and 7 with the corresponding grid dimensions and nondimensional wall spacings shown in Table 4. Surface pressures are again nearly constant with wall spacing. Grid 3 was chosen because of $y+$ values at or below

data are compared to computational results in the following section.

Results

Results are presented for all four codes and compared to experimental measurements. Grid refinement studies for the two-dimensional calculations are first presented, followed by a discus-

Vane

Blade

Fig. 5 Variation of pressure with grid, Procedure 1

Vane

Blade

Fig. 6 Variation of y+ with grid, Procedure 2

Fig. 7 Variation of pressure with grid, Procedure 2

1.0 for the majority of the vane and blade surfaces. A 208×75 H-grid was used for both the vane and blade in the Procedure 2 simulations.

Grid sizes used in the Procedure 3 calculations are 80×60, 143×19, 80×40, and 123×19 for the vane H-grid, vane O-grid, blade H-grid, and blade O-grid, respectively. A series of solutions were run using a variety of grid dimensions ranging up to approximately double these, and it was determined no additional resolution of the stage pressure field was gained.
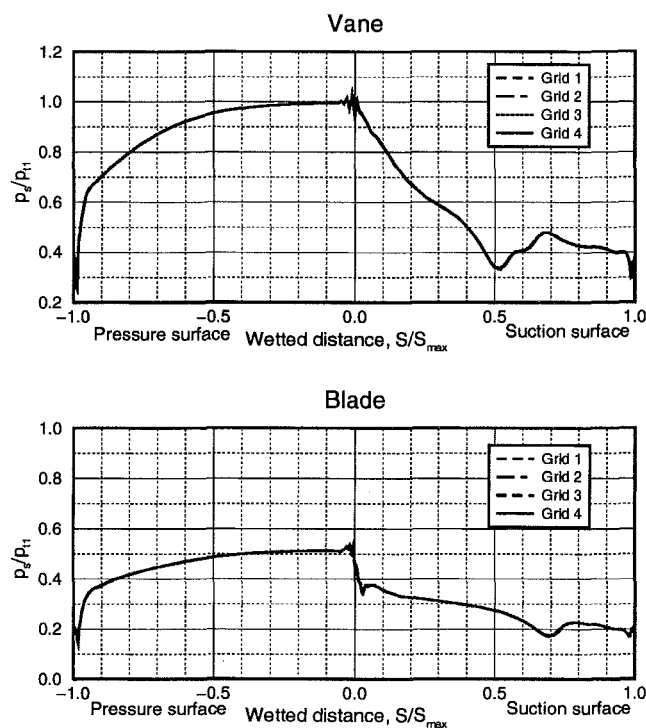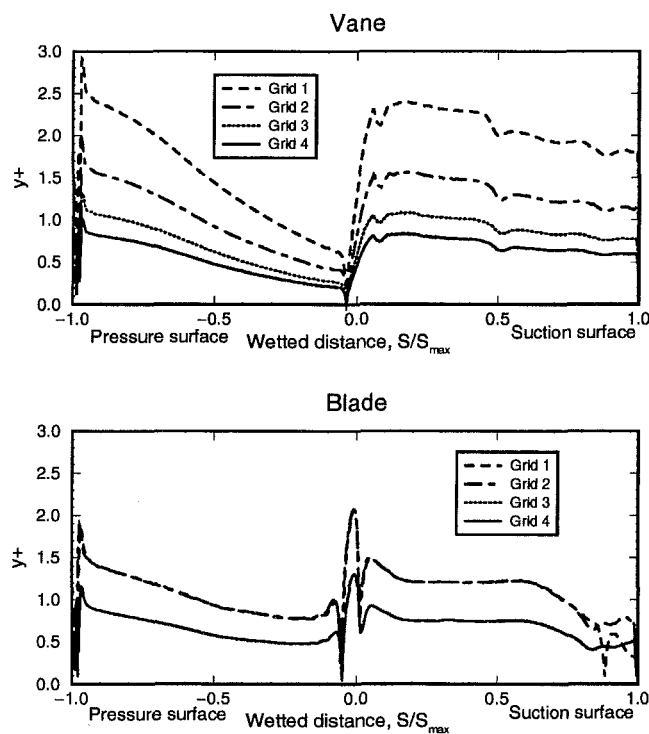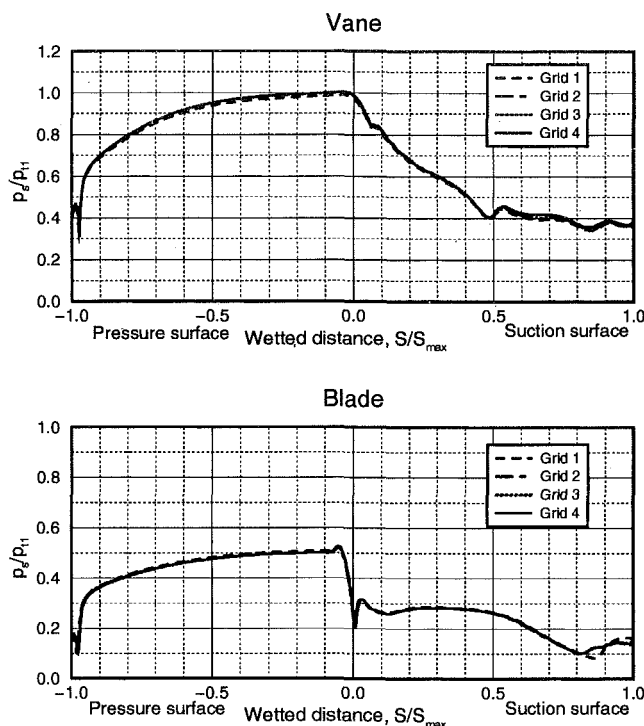
The Procedure 4 grid refinement study consisted of three primary steps. Initially, a wake convection simulation with no airfoils was performed to determine the H-grid density necessary to prevent wake diffusion. The necessary O-grid spacing and density at the wall to provide $y+$ values of less than 1.0 and 25 points in the boundary layer were then determined with a series of cascade simulations. Finally, the number of normals to the airfoil surface in the O-grid was chosen such that the shock location in the cascade was grid independent. The vane passages were discretized using 251×51 computational grid points in each O-grid and 120×45 grid points in each H-grid. Blade passages were discretized with 251×51 grid points in each O-grid and 111×45 grid points in each H-grid.

Due to the large CPU requirements for the three-dimensional code, it was not practical to do a complete grid refinement study for the three-dimensional solutions. The two-dimensional grid refinement study was used to guide the selection of the three-dimensional grid dimensions. Grid dimensions per passage for the three-dimensional solutions produced by Procedure 1 are shown in Table 5.

Table 4   Grid refinement study for Procedure 2

Grid	Vane O-grid	Blade O-grid
1	$321 \times 51, \Delta y_w = 0.00005$	$321 \times 51, \Delta y_w = 0.00005$
2	$381 \times 55, \Delta y_w = 0.00003$	$381 \times 51, \Delta y_w = 0.00005$
3	$381 \times 55, \Delta y_w = 0.00002$	$381 \times 51, \Delta y_w = 0.00003$
4	$381 \times 55, \Delta y_w = 0.00001$	$381 \times 51, \Delta y_w = 0.00003$

Table 5   Grid dimensions for Procedure 1 three-dimensional calculations

Grid	Size
Vane H	$129 \times 65 \times 57$
Blade H	$129 \times 65 \times 57$
Blade Tip	$93 \times 25 \times 9$

Time-Averaged Data.   Figures 8–10 contain two-dimensional time-mean solutions and data for the three axial spacings. Note that at 40 percent spacing, four experimental data points are missing on the blade due to transducer failure. The missing data points are at wetted distance percents of 0, 22, 48, and 74 on the blade suction surface. In general, good agreement is shown among the different predictions for all three spacings. Some discrepancies are observed near the throat location on the suction surface of the vane and on the uncovered portion of the suction surface of the blade. The former is related to differences in the geometric treatment of the airfoil trailing edge by the different grid systems, while the latter is due to differences in the stage exit boundary conditions. The predictions generally match the data well, with the exception of the vane suction surface and the blade suction surface near the trailing edge. Along the suction surface of the vane all of the codes predict a weaker expansion than the data suggests. The cause of this is unknown at this time; however, one possible explanation involves the stream tube thicknesses used in the two-dimensional calculations. Each of the two-dimensional codes models three-dimensional effects by solving the governing equations on a stream surface of revolution. Stream tube thicknesses used in the two-dimensional calculations were 0.1000, 0.0944, 0.0997, and 0.1027 for the vane leading edge, vane trailing edge, blade leading edge, and blade trailing edge, respectively. The variation was assumed to be linear across the airfoils. It can be shown that by varying the stream tube contraction along the vane, a solution that closely matches the data can be obtained. In light of the fact that the three-dimensional solutions, presented later, also show this behavior over the vane suction surface, this does not seem to be the
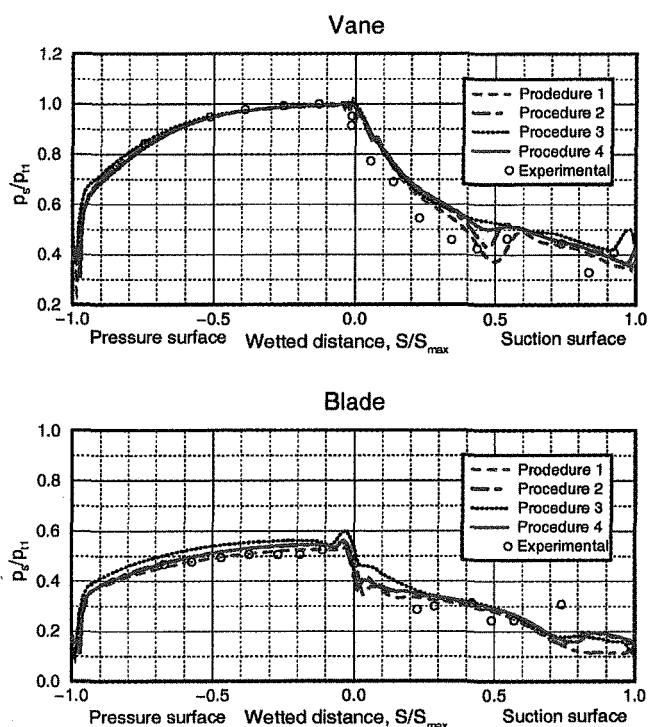

Fig. 8   Time-mean pressure, 20 percent spacing

Fig. 9 Time-mean pressure, 40 percent spacing

Fig. 11 Effect of spacing on measured mean pressure

likely cause. Other possible explanations include an error in the data or an error in the airfoil geometry, either electronic or physical. At this time, however, there is no reason to suspect either of these items, as checks have been performed in each of these areas.

Another significant difference between the predictions and data is near the trailing edge of the blade on the suction surface. At all three spacings, the last data point is missed by a large margin. This is most likely due to a difference in the back pressures between the

Fig. 10 Time-mean pressure, 60 percent spacing

solution operating conditions and the test conditions. A trailing edge shock impinging on the suction surface of the blade causes the measured pressure to rise at approximately 75 percent wetted distance. The lower back pressure used in the solutions causes this shock to be inclined at a lower angle relative to the suction surface, thus striking the blade at a point closer to the trailing edge.

The influence of spacing on the measured time-mean pressure is shown in Fig. 11. It is evident from these plots that the spacing has negligible effect on the time-averaged surface pressures of the turbine stage. This is especially significant for the blade where, as will be seen in the next section, the entire airfoil surface is enveloped in unsteadiness.
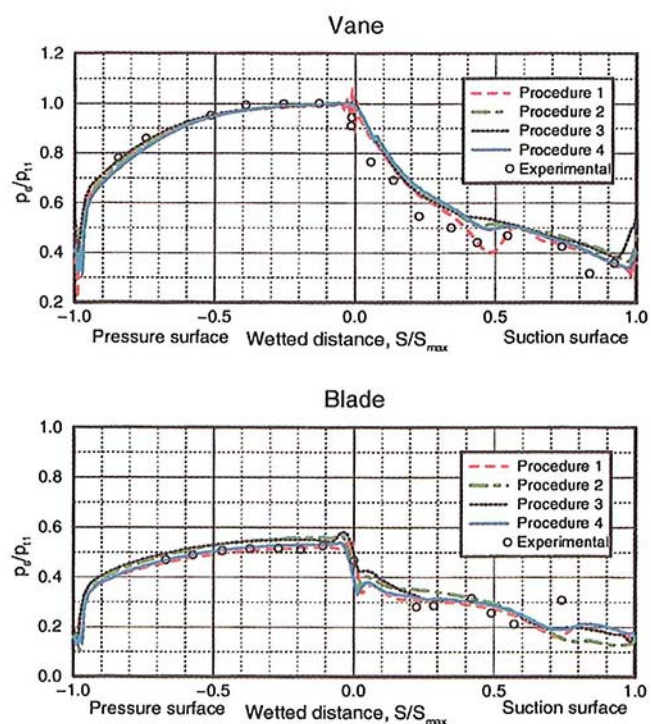
Surface Pressure Envelopes. Surface pressure envelopes for the three spacings are contained in Figs. 12–14, where two-dimensional solutions are compared to experimental data. The surface pressure envelope indicates the difference between the maximum and minimum pressure at a point during the course of one passing period. A passing period for a given row is the time for an airfoil in that row to pass one airfoil of the opposite row. All of the codes provide similar predictions of the magnitude of the surface pressure unsteadiness. The lack of unsteadiness upstream of the throat on the vane suction surface is an indication of choked conditions on the vane row. In general, Procedure 2 predicts a larger unsteady envelope than the others. Once again, the solutions match the data well at all spacings, with the exception of the two locations discussed previously. The trend is that the codes over-predict the unsteady magnitudes. This is especially apparent on the vane.

The influence of spacing on the measured pressure envelopes is demonstrated in Fig. 15. As the spacing decreases, the magnitude of the unsteadiness increases. This is due to a reduced distance available for dissipation of the shocks and wake present in the interrow region. The dependence of the unsteadiness on spacing is most apparent on the suction surfaces of the vane and blade. An increase in the magnitude of the unsteadiness by a factor of approximately two is realized by decreasing the vane–blade row spacing from 60 to 20 percent vane axial chord. In Fig. 15 at a location near the blade leading edge, it appears as though the
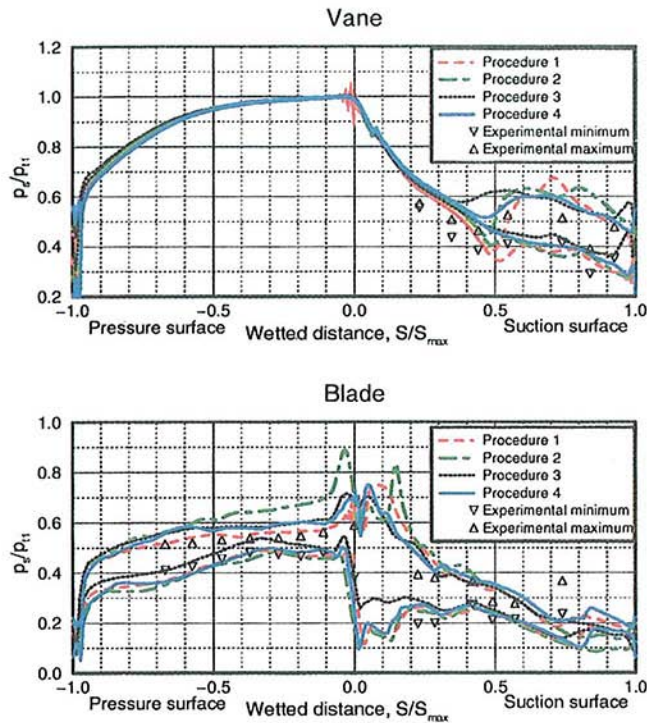
Fig. 12 Pressure envelope, 20 percent spacing
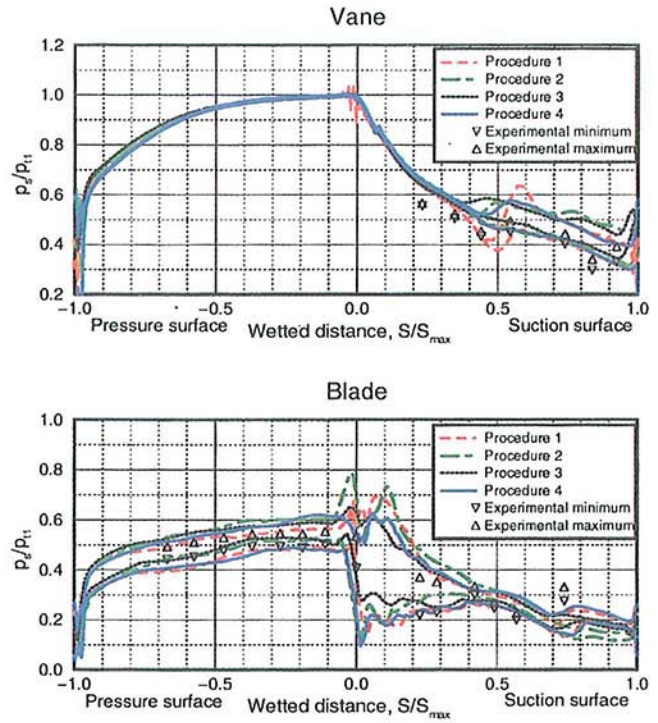
Fig. 14 Pressure envelope, 60 percent spacing

unsteadiness of the 40 percent spacing case is of lower magnitude than the 60 percent spacing case. This is deceiving because of the absence of a leading edge data point for the 40 percent case.

Two-Dimensional Versus Three-Dimensional

Figures 16–18 show comparisons between two- and three-dimensional time-mean midspan solutions provided by Procedure 1. There is good agreement between the two- and three-dimensional solutions in all cases. The three-dimensional solutions match the data better than the two-dimensional solutions at a location on the blade suction surface between $S/S_{max} = 0.15$ and $S/S_{max} = 0.4$. Note that the three-dimensional solutions also over-predict the time-mean surface pressures on the first half of the vane suction surface. Comparisons between two- and three-dimensional pressure envelopes are presented in Figs. 19–21. The two- and
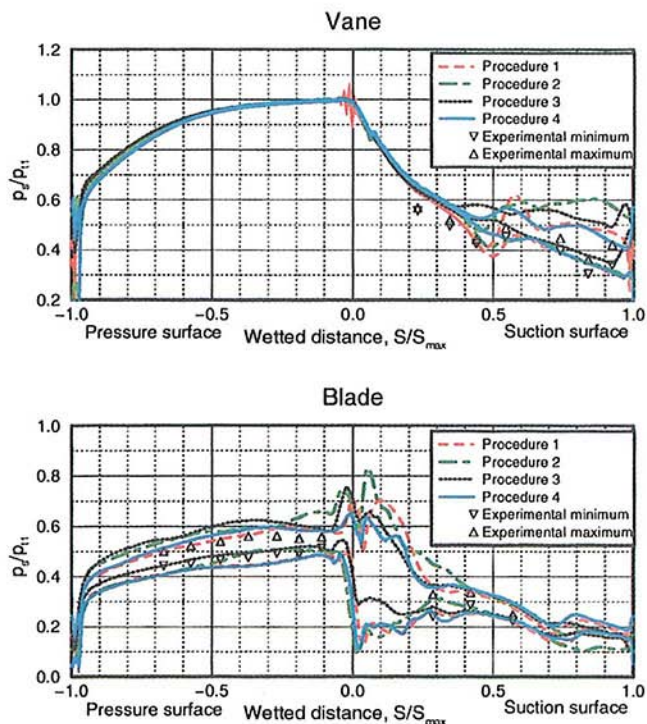
Fig. 13 Pressure envelope, 40 percent spacing
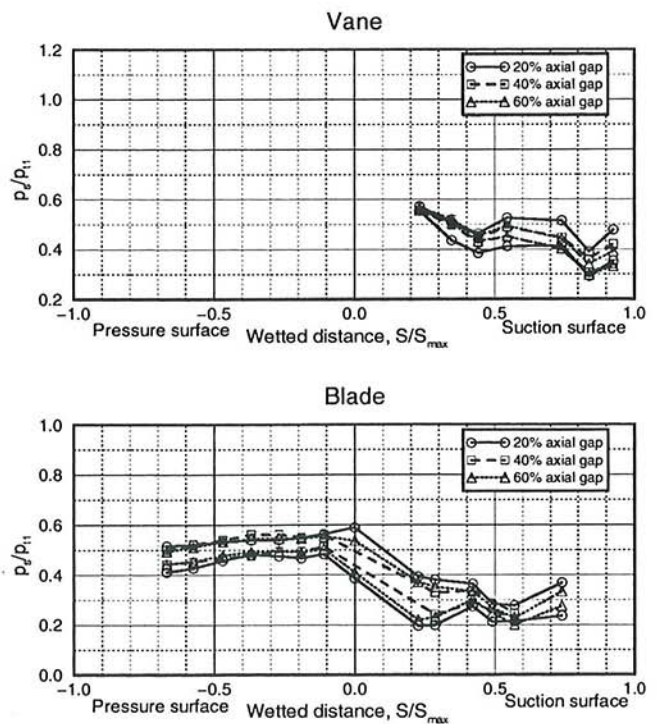
Fig. 15 Effect of spacing on measured pressure envelope
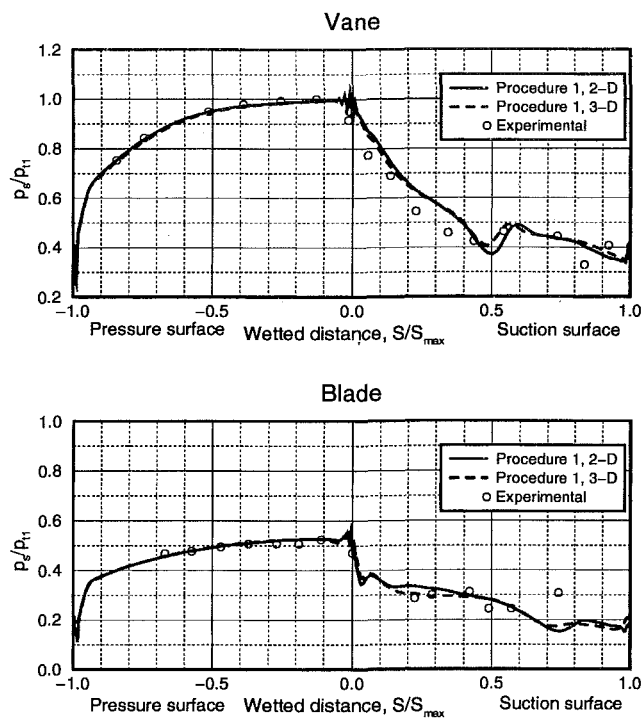
Fig. 16   Time-mean pressure, 20 percent spacing, three-dimensional
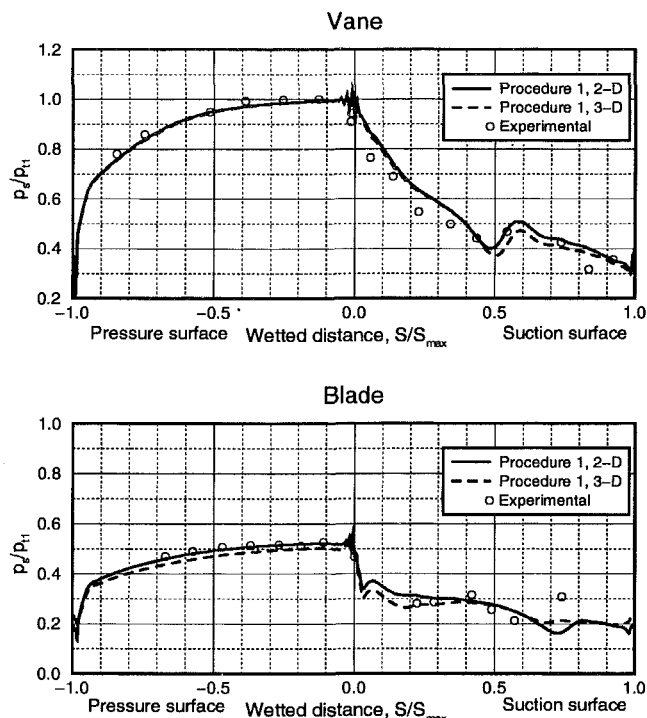
Fig. 18   Time-mean pressure, 60 percent spacing, three-dimensional

three-dimensional solutions match closely on both the vane and blade.

Performance Summary.   All of the calculations presented in previous sections were run again with adiabatic wall conditions for the performance predictions. Adiabatic efficiencies were calculated for both the two-dimensional and three-dimensional solutions using the following formula:

$$\eta_{ad} = \frac{T_{t,1} - T_{t,4}}{T_{t,1}\left[1 - \left(\dfrac{p_{t,4}}{p_{t,1}}\right)^{(\gamma - 1/\gamma)}\right]} \tag{1}$$

where T is the temperature, p is the pressure, γ is the ratio of specific heats, the subscript t denotes a total quantity, and the subscripts 1 and 4 refer to the stage inlet and exit stations, respec-
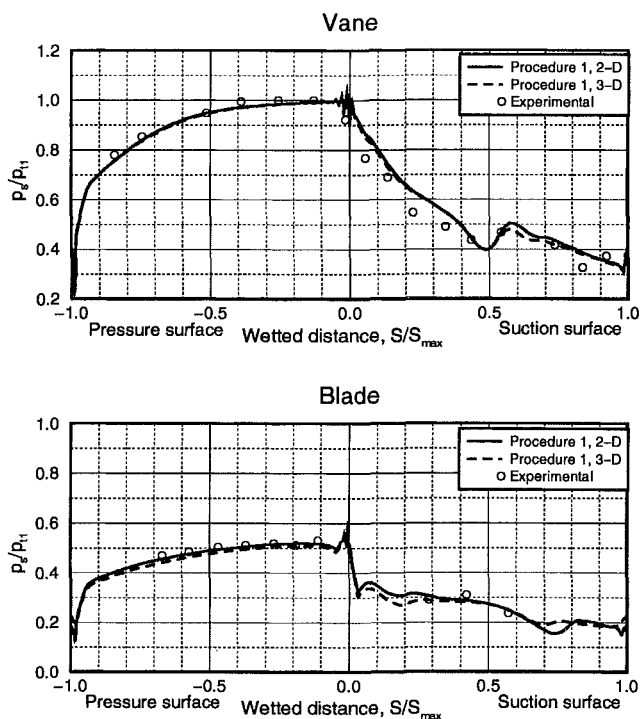
Fig. 17   Time-mean pressure, 40 percent spacing, three-dimensional
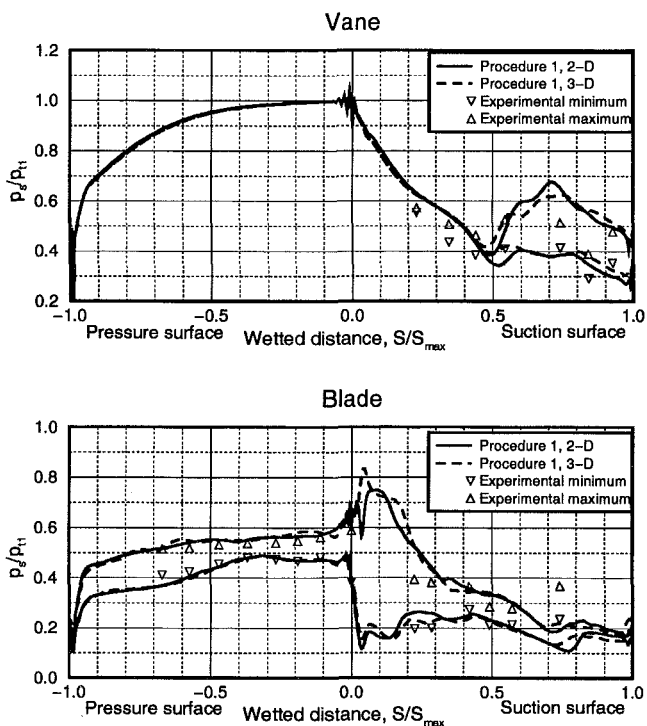
Fig. 19   Pressure envelope, 20 percent spacing, three-dimensional

Vane

Blade
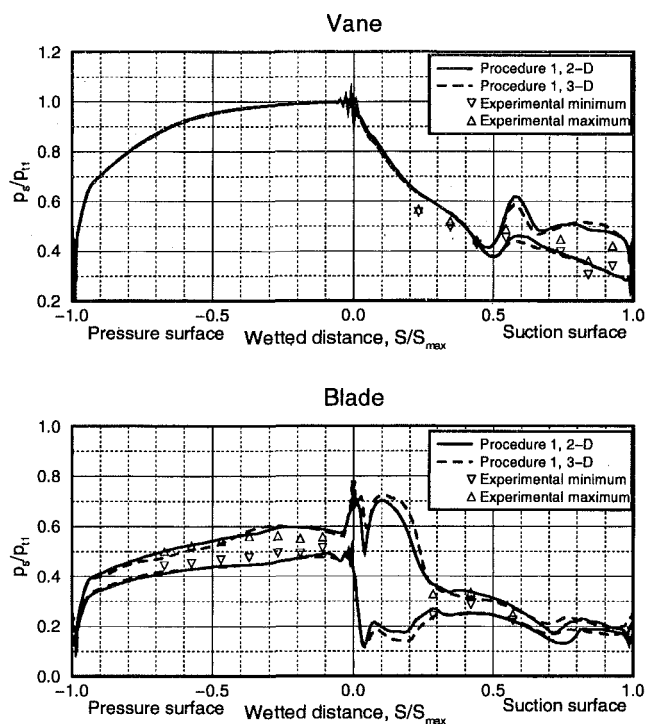
Fig. 20 Pressure envelope, 40 percent spacing, three-dimensional

tively. Values used in the efficiency calculations were mass averaged at each time step and then averaged in time.

Table 6 contains adiabatic efficiencies for the two-dimensional calculations at all three spacings. Each of the procedures predicts a slightly different efficiency level. In the absence of experimentally measured efficiencies to validate these calculations, it is difficult to say just how well each procedure predicts the absolute efficiency value; however, it is the efficiency trend with spacing

Vane

Blade

Fig. 21 Pressure envelope, 60 percent spacing, three-dimensional

Table 6 Calculated two-dimensional stage adiabatic efficiencies (percent)

	Proc. 1	Proc. 2	Proc. 3	Proc. 4
20%	92.4	93.3	89.6	92.0
40%	92.7	93.1	89.7	92.0
60%	92.7	93.1	90.0	92.6

for each procedure that is of most interest here. Reasonable confidence exists, based on previous work by Kelecy et al. (1995), in the ability to predict efficiency trends. The general trend here is that the efficiencies increase slightly as the axial spacing increases.

One might expect an increase in efficiency as the spacing increases since, as has been shown, the amplitude of the unsteadiness decreases, indicating a lessening of the severity of shock and wake interactions. Results indicate there is a decrease in the stage total pressure drop as the spacing increases, as shown in Table 7. A detailed discussion of the vane and blade performance along with an examination of the driving mechanisms is presented by Busby et al. (1999). The rate at which the pressure drop changes with unit change in spacing appears to increase as the spacing decreases. This trend is not reflected in the efficiencies. It should be noted that the change in operating conditions between each of the three spacings could also be partly responsible for the performance trends observed here. However, previous work by Kelecy et al. (1995) in which solutions for the three spacings were calculated at identical operating conditions showed similar trends.

Calculated steady, three-dimensional stage adiabatic efficiencies shown in Table 8 from the Procedure 1 three-dimensional code exhibit the same trend as the Procedure 1 two-dimensional efficiencies. The three-dimensional efficiencies are approximately 6 percent less than the two-dimensional efficiencies due to end wall losses. Based on the two-dimensional numbers presented here, the vane-blade spacing has very little influence on the stage adiabatic efficiency. However, the 0.8 percent efficiency decrease between the 60 and 20 percent spacing three-dimensional solutions could be significant.

Summary

A combined computational/experimental study of the effect of vane-blade row spacing on transonic turbine stage time-mean aerodynamics has been presented. Comparisons between computational solutions and experimental data indicate that vane-blade spacing in transonic turbines has little effect on the time-mean surface pressures of the stage. There is, however, a large change in the magnitude of the unsteadiness with changes in the spacing. With an increase in the gap from 20 to 60 percent of the vane axial chord, the surface pressure unsteady magnitude decreases by as much as a factor of two. In general, the adiabatic total pressure drop increases as the spacing decreases, with the rate at which the
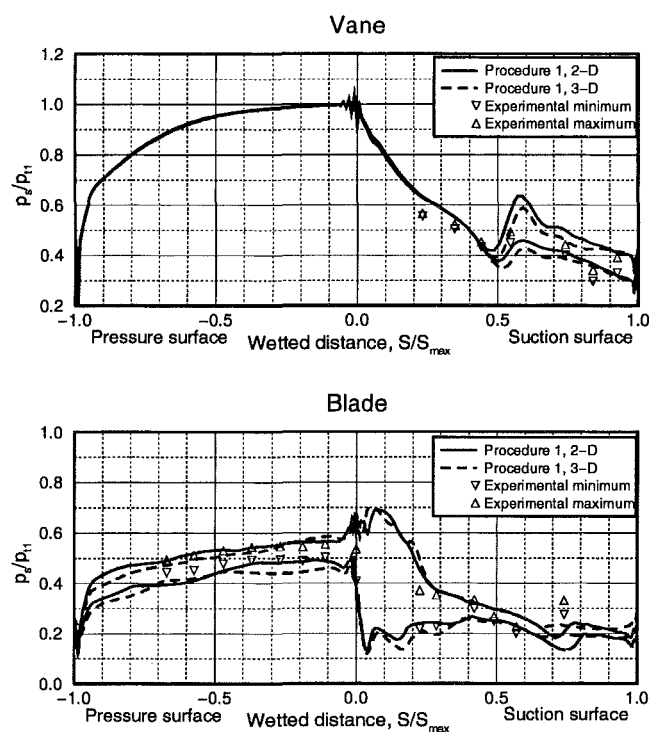
Table 7 Calculated two-dimensional stage total pressure ratio

	Proc. 1	Proc. 2	Proc. 3	Proc. 4
20%	0.287	0.280	0.297	0.298
40%	0.299	0.290	0.297	0.301
60%	0.304	0.290	0.296	0.307

Table 8 Procedure 1 calculated three-dimensional, steady stage adiabatic efficiencies

Spacing	Efficiency (%)
20%	86.5
40%	87.4
60%	87.3

drop changes with unit change in spacing greater as the spacing decreases. There is no definite corresponding trend in the adiabatic efficiencies. The adiabatic efficiencies do, however, tend to increase slightly with an increase in axial spacing.

It is apparent that all of the codes used in this work produce comparable results. As the individual methods, algorithms, and grid systems were compared, it was clear that each code has its advantages and disadvantages. It was also clear that quality solutions were produced by each of the codes.

Acknowledgments

References

Abhari, R. S., Guenette, G. R., Epstein, A. H., and Giles, M. B., 1992, "Comparison of Time-Resolved Turbine Rotor Blade Heat Transfer Measurements and Numerical Calculations," ASME JOURNAL OF TURBOMACHINERY, Vol. 114, pp. 818–827.

Ashworth, D. A., LaGraff, J. E., Schultz, D. L., and Grindrod, K. J., 1985, "Unsteady Aerodynamic and Heat Transfer Processes in a Transonic Turbine Stage," ASME *Journal of Engineering for Gas Turbines and Power*, Vol. 107, pp. 1022–1030.

Baldwin, B. S., and Lomax, H., 1978, "Thin Layer Approximation and Algebraic Model for Separated Turbulent Flow," AIAA Paper No. 78-257.

Benek, J. A., Buning, P. G., and Steger, J. L., 1985, "A 3-D Chimera Grid Embedding Technique," AIAA Paper No. 85-1523.

Busby, J. A., Davis, R. L., Dorney, D. J., Dunn, M. G., Haldeman, C. W., Abhari, R. S., Venable, B. L., and Delaney, R. A., 1999, "Influence of Vane–Blade Spacing on Transonic Turbine Stage Aerodynamics: Part II—Time-Resolved Data and Analysis," ASME JOURNAL OF TURBOMACHINERY, Vol. 121, this issue, pp. 673–682.

Davis, R. L., Shang, T., Buteau, J., and Ni, R. H., 1996, "Prediction of 3-D Unsteady Flow in Multi-stage Turbomachinery Using an Implicit Dual Time-Step Approach," AIAA Paper No. 96-2565.

Dorney, D. J., and Davis, R. L., 1992, "Navier–Stokes Analysis of Turbine Blade Heat Transfer and Performance," ASME JOURNAL OF TURBOMACHINERY, Vol. 114, pp. 795–806.

Dring, R. P., Joslyn, H. D., Hardin, L. W., and Wagner, J. H., 1981, "Research on Rotor–Stator Aerodynamic Interaction and Rotor Negative Incidence Stall," Air Force Wright Aeronautical Labs TR-81-2114.

Dunn, M., Bennett, W., Delaney, R., and Rao, K., 1990, "Investigation of Flow Through a Transonic Turbine Stage: Part II—Data/Prediction Comparison for Time-Averaged and Phase-Resolved Pressure Data," AIAA Paper No. 90-2409.

Giles, M. B., 1988a, "Stator/Rotor Interaction in a Transonic Turbine," AIAA Paper No. 88-3093.

Giles, M. B., 1988b, "UNSFLO: A Numerical Method for Unsteady Inviscid Flow in Turbomachinery," MIT Gas Turbine Laboratory Report No. 195.

Giles, M., 1990, "Nonreflecting Boundary Conditions for Euler Equation Calculations," *AIAA Journal*, Vol. 28, No. 12, pp. 2050–2058.

Giles, M. B., and Haimes, R., 1993, "Validation of a Numerical Method for Unsteady Flow Calculations," ASME JOURNAL OF TURBOMACHINERY, Vol. 115, pp. 110–117.

Jameson, A., Schmidt, W., and Turkel, E., 1981, "Numerical Solutions of the Euler Equations by Finite Volume Methods Using Runge–Kutta Time-Stepping Schemes," AIAA Paper No. 81-1259.

Kelecy, F. J., Griffin, J. W., and Delaney, R. A., 1995, "The Effect of Vane–Blade Spacing on Transonic Turbine Stage Performance," AGARD Symposium on "Loss Mechanisms and Unsteady Flows in Turbomachines," Derby, UK.

Lewis, J. P., Delaney, R. A., and Hall, E. J., 1989, "Numerical Prediction of Turbine Vane-Blade Aerodynamic Interaction," ASME JOURNAL OF TURBOMACHINERY, Vol. 111, pp. 387–393.

Ni, R. H., 1981, "A Multiple Grid Scheme for Solving the Euler Equations," *AIAA Journal*, Vol. 20, No. 11, pp. 1565–1571.

Ni, R. H., and Bogoian, J. C., 1989, "Predictions of 3-D Multi-Stage Turbine Flow Fields Using a Multiple-Grid Euler Solver," AIAA Paper No. 89-0203.

Ni, R. H., and Sharma, O. P., 1990, "Using 3-D Euler Flow Simulations to Assess Effects of Periodic Unsteady Flow Through Turbines," AIAA Paper No. 90-2357.

Rai, M. M., 1987, "Navier–Stokes Simulations of Rotor/Stator Interactions Using Patched and Overlaid Grids," AIAA *Journal of Propulsion and Power*, Vol. 3, No. 5, pp. 387–396.

Rao, K. V., and Delaney, R. A., 1990, "Investigation of Unsteady Flow Through Transonic Turbine Stage. Part I: Analysis," AIAA Paper No. 90-2408.

Rao, K. V., Delaney, R. A., and Dunn, M. G., 1994, "Vane–Blade Interaction in a Transonic Turbine Part I—Aerodynamics," AIAA *Journal of Propulsion and Power*, Vol. 10, No. 3, pp. 305–311.

Swanson, R. C., and Turkel, E., 1985, "A Multistage Time-Stepping Scheme for the Navier–Stokes Equations," AIAA Paper No. 85-0035.

Takahashi, R., and Ni, R. H., 1991, "Unsteady Hot Streak Simulation Through 1-1/2 Stage Turbine," AIAA Paper No. 91-3382.

J. A. Busby

R. L. Davis

D. J. Dorney

United Technologies Research Center,
East Hartford, CT 06108

M. G. Dunn

C. W. Haldeman

R. S. Abhari

Gas Turbine Lab,
The Ohio State University,
Columbus, OH 43235

B. L. Venable

R. A. Delaney

Allison Engine Company,
Indianapolis, IN 46206

Influence of Vane–Blade Spacing on Transonic Turbine Stage Aerodynamics: Part II—Time-Resolved Data and Analysis

This paper presents results of a combined experimental/computational investigation into the effects of vane–blade spacing on the unsteady aerodynamics of a transonic turbine stage. Time-resolved data were taken in a shock-tunnel facility in which the flow was generated with a short-duration source of heated and pressurized air. This data is compared with the results obtained from four unsteady Navier–Stokes solvers. The time-resolved flow for three axial spacings is examined. For each vane–blade spacing, the inlet conditions were nearly identical and the vane exit flow was transonic. Surface-mounted high-response pressure transducers at midspan were used to obtain the pressure measurements. The computed two-dimensional unsteady airfoil surface pressure predictions are compared with the Kulite pressure transducer measurements. The unsteady and axial spacing effects on loading and performance are examined. In general the numerical solutions compared very favorably with each other and with the experimental data. The overall predicted stage losses and efficiencies did not vary much with vane/blade axial spacing. The computations indicated that any increases in the blade relative total pressure loss were offset by a decrease in vane loss as the axial spacing was decreased. The decrease in predicted vane total pressure loss with decreased axial spacing was primarily due to a reduction in the wake mixing losses. The increase in predicted blade relative total pressure loss with a decrease in axial spacing was found to be mainly due to increased vane wake/blade interaction.

Introduction

The drive to reduce weight and cost of both military and commercial gas turbine engines has led to a reduction in the number of stages used in the compressor and turbine components. In addition, the axial extent of the compressor and turbine has also been reduced, which in turn has led to smaller axial spacing between blade rows. As a result of the overall downsizing of these components, airfoil loading has increased, secondary flows have become more influential, and shocks that arise from transonic passage flows have increased aerodynamic losses. In addition, the unsteady interaction between adjacent blade rows has become a critical factor in reducing aerodynamic performance, stability, and durability.

In an attempt to overcome some of the performance degradation issues due to downsizing of the turbine, research in the area of transonic flows in axial flow turbine passages has increased in the past several years. Many experimental and numerical studies have been performed for linear transonic turbine cascades to understand the aerodynamic loss mechanisms, including the trailing edge shock structure (Nix et al., 1997), base pressure (Doughty et al., 1992), boundary layer transition (Wesner et al., 1997), and vortex shedding (Arnone and Pacciani, 1996). Recently, similar investigations have been performed for multi-blade-row transonic turbines to understand the unsteady flow effects of hot streaks (Saxer

and Giles, 1994; Dorney and Sondak, 1996), heat transfer (Guenette et al., 1989), and shock/blade interaction (Rao and Delaney, 1990; Dunn et al., 1990) on aerodynamic performance. Only a few studies (Jennions and Adamczyk, 1997; Rangwalla, 1994; Abhari et al., 1992) have been conducted, however, to expose the unsteady, transonic flow physics responsible for performance degradation as the axial spacing between turbine blade rows is reduced.

The investigation described in this paper is focused on highlighting the unsteady flow effects responsible for changes in the unsteady loads and losses as the axial gap between vane and blade is reduced. A series of experiments along with numerical predictions have been used to illustrate the unsteady flow phenomena in this transonic turbine stage and to demonstrate the current capability in predicting these flows. A companion paper (Venable et al., 1999) discusses the effects of vane/blade axial gap on the time-averaged aerodynamics of this turbine stage.

Experimental Setup

A high-pressure transonic turbine stage (30 vanes/45 blades) was evaluated both experimentally and computationally in this program. The measurements were performed using a large shock-tunnel facility that was constructed to accommodate very large weight-flow machines. The turbine stage was installed in the shock-tunnel facility and detailed time-average and phase-resolved surface pressure measurements were obtained at the midspan of both the vane and the blade. The axial gap between the vane and the blade was set at 20, 40, and 60 percent of the vane axial chord to measure the change in aerodynamic interaction and to determine the unsteady flow effects responsible for the change. The pressure

Table 1   Stage operating conditions

	20% Gap	40% Gap	60% Gap
Rotor (rpm)	11,841	11,793	11,755
P_T Inlet (kPa)	295.0	313.2	274.5
P_S Exit (kPa)	65.9	72.4	65.2
T_T Inlet (K)	609.9	654.0	657.2
T_S Wall (K)	295.2	291.2	291.2
Massflow (kg/sec)	10.55	10.55	10.55

Table 3   Two-dimensional grid densities

Procedure	1	2	3	4
Vane O-	n/a	381x55	143x19	251x51
Vane H-	137x57	208x75	80x60	120x45
Blade O-	n/a	381x51	123x19	251x51
Blade H-	137x57	208x75	80x40	111x45

ratio, mass flow, and blade rotational speed, given in Table 1, were essentially held fixed for the three axial gap positions. These conditions resulted in both the vane and blade passages operating in transonic flow. The time-averaged measurements and computations, along with details of the geometry and flow conditions are presented in Part I of this paper (Venable et al., 1999).

The unsteady pressure data reported in this paper were obtained using miniature Kulite pressure transducers. The transducers were flush mounted on the surface and had an active area of 6.25×10^{-4} m (0.025 in.) by 6.25×10^{-4} m (0.025 in.) and a thickness of 3.25×10^{-4} m (0.0139 in.). A thin layer of silastic material was placed over the transducers to provide a thermal barrier. The natural frequency of these transducers is approximately 400 kHz, while the blade passing frequency is approximately 5.9 kHz. The frequency response of the transducers, as installed, is in excess of 100 kHz. For many of the transducers, the data were sampled simultaneously at 100 kHz and 250 kHz using two different data recording systems. An example of the influence of sampling frequency will be shown in a later section.

All Kulite pressure transducers are calibrated throughout the entire data system on a daily basis. Pressure transducers were grouped according to their stability over this calibration process. Approximately 70 percent of the sensors calibrated to within ± 0.6895 kPa (± 0.1 psia) peak-peak variation over the experimental data range: 55 to 310 kPa (8–45 psia). Another 23 percent were within ± 1.379 kPa (± 0.2 psia). The final 7 percent were within ± 4.8 kPa (± 0.7 psia). The uncertainty of the reduced data is greatly improved due to the fact that reported measurements are averaged over many data points, and the cumulative effect is a reduction in the uncertainty of the average well below these values. However, as a very conservative number, the data can be assumed to lie within the ± 1.379 kPa (± 0.2 psia), which is a standard deviation of ± 0.46 kPa (± 0.067 psia).

The vanes and blades were also instrumented with thin-film heat-flux gages so that time-resolved heat flux could be measured. These devices have extremely high frequency response and thus provide an excellent test for the codes. However, this paper will be devoted to a discussion of the pressure data and the heat-flux data will be presented at a later date.

Computational Methods

Unsteady vane/blade flow predictions were performed using four different computational approaches. The algorithms used for the computational analysis are described in Part I of this paper

(Venable et al., 1999) and are listed in Table 2. A brief review of the numerical and physical models used in these procedures, specifically for unsteady flows, will be presented here.

The computational procedures chosen for this investigation utilize a wide variety of numerical algorithms, as listed in Table 2. All of the approaches are time-accurate and are capable of computing multi-blade-row turbomachinery problems. In addition, all of the procedures used the Baldwin–Lomax model to compute the turbulent viscosity in the flow.

Other than the numerical algorithms, each approach uses a unique combination of boundary condition treatments to handle the relative movement between the vanes/blades and the circumferential periodicity between vane/blade passages. For the interface between the vane and blade passages, Procedures 1, 2, and 4 use a "sliding grid" technique, in which the residuals of the adjacent passages are interpolated and exchanged to allow proper communications between blade rows. Procedure 3 uses a "grid clicking" technique that maintains a point-match between blade rows, thus avoiding an interpolation. Procedures 1 and 4 account for vane/blade airfoil counts by executing the lowest even integral number of passages that closely approximates (or matches) the actual vane/blade airfoil count rates. In the current investigation, this was performed by solving two vane and three blade passages with circumferential periodicity being assumed across these passages. Procedures 2 and 3 solve only one passage for each blade row and use a phase-lagged periodic (Lewis et al., 1989) and "time-tilting" boundary conditions (Giles, 1988), respectively, to account for circumferential periodicity.

Two-dimensional, unsteady predictions of the midspan section of the turbine stage were performed with all four of the computational procedures. Three-dimensional endwall blockage effects were accounted for in the two-dimensional calculations through the use of streamtube cross-sectional area changes. These areas vary linearly across each blade row from the blade leading edge to the blade trailing edge. The streamtube area ratios for the vane and blades of the current investigation were obtained from a through-flow analysis for the 40 percent spacing and are listed in Part I of this paper (Venable et al., 1999).

As discussed in Part I (Venable et al., 1999), a grid refinement study was performed by each of the computational groups. The final grid distributions for the two-dimensional analyses are shown in Table 3. The number of iterations per cycle (where one cycle is the time for one blade to pass two vanes) for each computational group varied due to the differing algorithms used. Each group also performed a time-resolution study, and the resulting iteration count is shown in Table 4.

Table 2   Computational methods

Procedure	Investigators	Approach	Grid Topology	Temporal Accuracy	Spatial Accuracy
1	Busby and Davis	Implicit, Dual Time-Step (Davis, et al. (1996)) with Explicit, Multiple-Grid (Ni (1981))	H-Grid	Second Order	Second Order
2	Venable and Delaney	Explicit, Runge-Kutta (Rao (1992))	Overlaid O-Grid Around Airfoils H-Grid Through Passage	Second Order	Second Order
3	Abhari	Implicit, ADI in O-Grid, Explicit, Multiple-Grid in H-Grid (Giles (1988))	O-Grid Around Airfoils H-Grid Through Passage	Second Order	Second Order
4	Dorney and Davis	Implicit, ADI (Dorney and Davis (1992); Rai (1987))	Overlaid O-Grid Around Airfoils H-Grid Through Passage	Second Order	Third Order

Table 4 Unsteady convergence criteria

Procedure	Iter/Cycle	Global Cycles to Loss Convergence
1	300	6
2	50,000	15
3	5000	10
4	25,000	15

Results and Discussion

Unsteady pressure measurements were taken at numerous positions on the suction and pressure surfaces of both the blades and vanes at a sampling frequency of 100 kHz. This allows temporal resolution of the unsteady wave propagation through the stage.

Due to space restrictions, only five chordwise positions on each airfoil will be presented here. Spatial resolution of the vane–blade interaction was achieved by phase locking the data to a shaft encoder, which generates 500 pulses/revolution. These phase-locked data generate 16.667 samples/vane passage. The unsteady pressure data were ensemble-averaged to provide average values at 50 independent positions in a vane passage. The geometry of the turbine creates a geometric global cycle every three rotor blades (i.e., there are 30 vanes and 45 blades).

The unsteady pressure data were ensemble-averaged to obtain the time-averaged surface pressure data. These time-averaged data along with the minimum/maximum pressure envelopes and the corresponding predictions from the procedures listed in Table 2 are presented by Venable et al. (1999) in Part I of this paper. The effect of vane/blade axial spacing on the time-averaged behavior
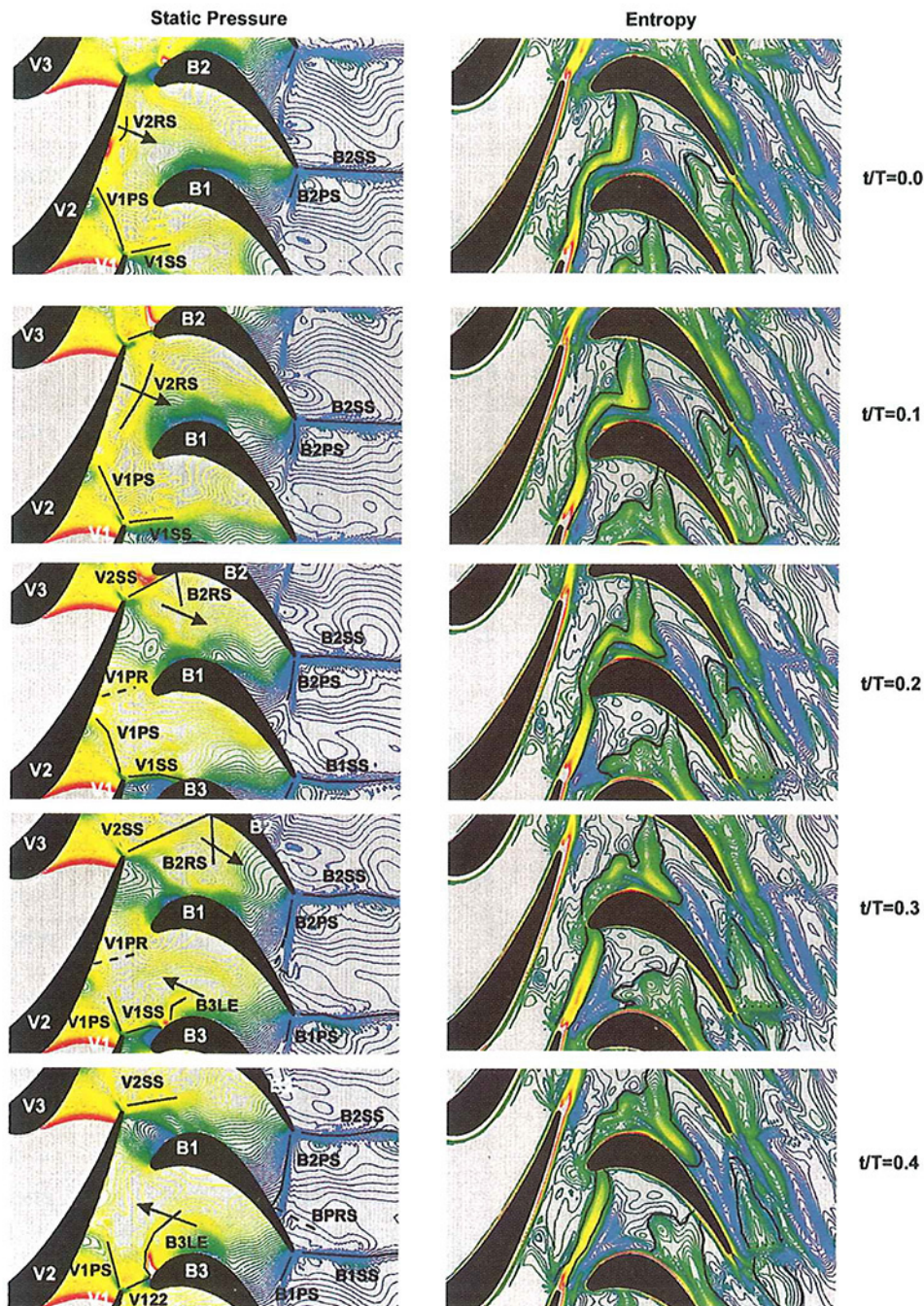
Fig. 1 Predicted instantaneous contours of static pressure and entropy (Procedure 1)

of the transonic turbine stage is also discussed in Part I. A detailed examination of the unsteady measurements and predictions for the three vane/blade axial gaps is presented below.

In general, the computational results compare favorably with each other and the measurements. Discrepancies exist between the computed and measured frequency content that will be addressed later in the paper.

Physical Mechanisms. To aid in the understanding of the complex shock system that develops for all three axial spacings, color contour plots of the predicted static pressure and entropy from Procedure 1 for one *vane-passing period* (i.e., the time for one blade to pass one vane) are shown in Fig. 1 for the 20 percent axial gap case. The time-resolved pressures on the vane and blade for various chordwise locations for one *global cycle* (i.e., two vane-passing periods) are shown in Figs. 2–4. The time scale is plotted as t/T, where T is the time for one vane-passing period. Therefore, $2T$ represents one complete global cycle.

The basic shock and wake interactions have been determined from the predictions to be essentially the same for each spacing, with some of the interactions getting weaker or propagating at slightly different speeds as the spacing increases. Therefore, the shock and wake interactions for the 20 percent spacing will be examined in detail and the results for the 40 and 60 percent spacings will be presented in Appendices A and B, respectively.

In Fig. 1, the blade is rotating in the upward direction. For the following analysis, the lowest vane will be referred to as V1 (only the trailing edge is visible) and the middle vane will be V2. The lowest blade at time $t/T = 0.0$ will be referred to as B1. B2 will be the blade above B1 and B3 will be the blade below B1. The data shown in Figs. 2–4 correspond with the instantaneous pressures experienced by V2 and B1 in Fig. 1. Figures 2–4 show the
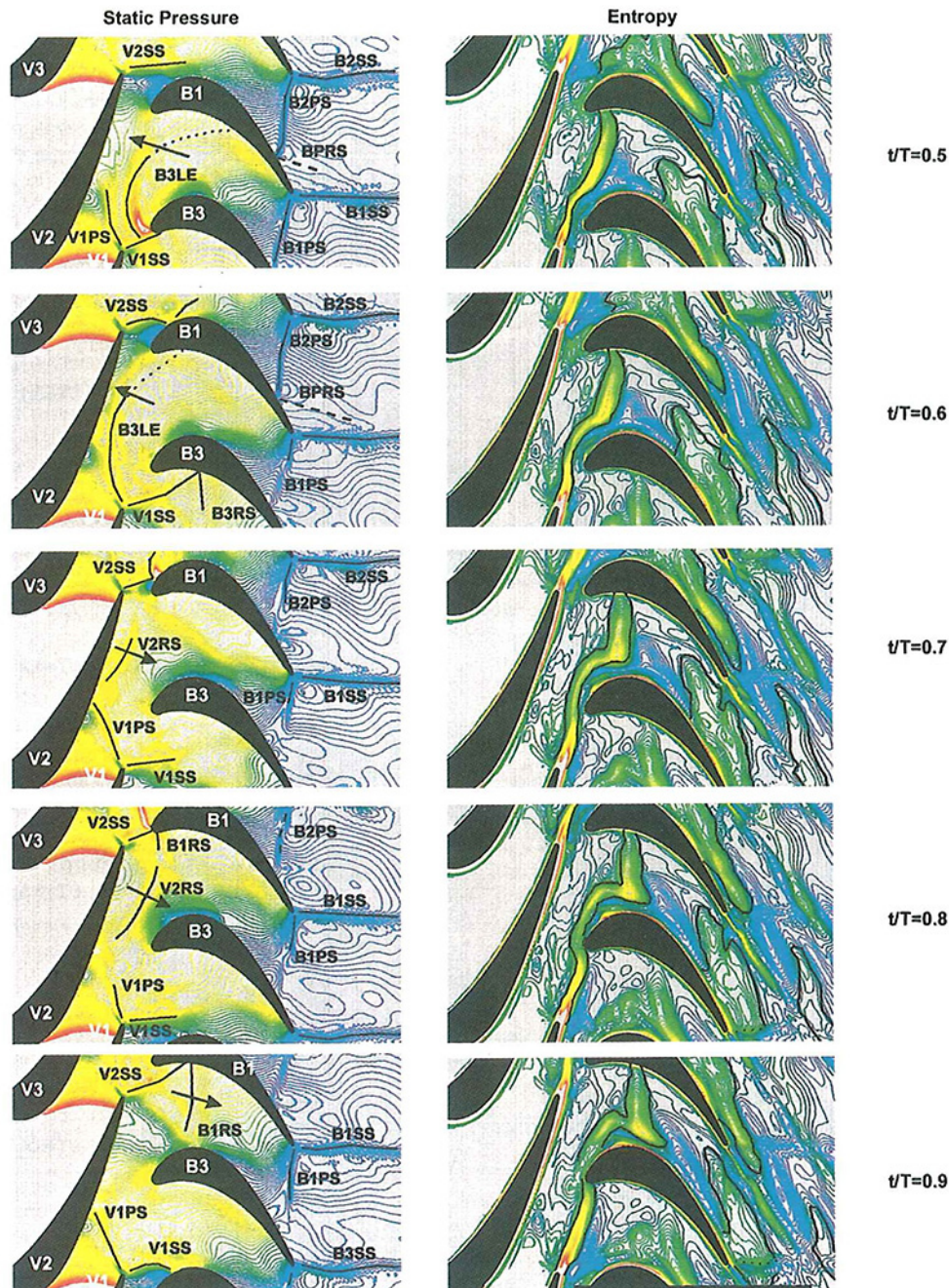
Fig. 1 (cont.) Predicted instantaneous contours of static pressure and entropy (Procedure 1)
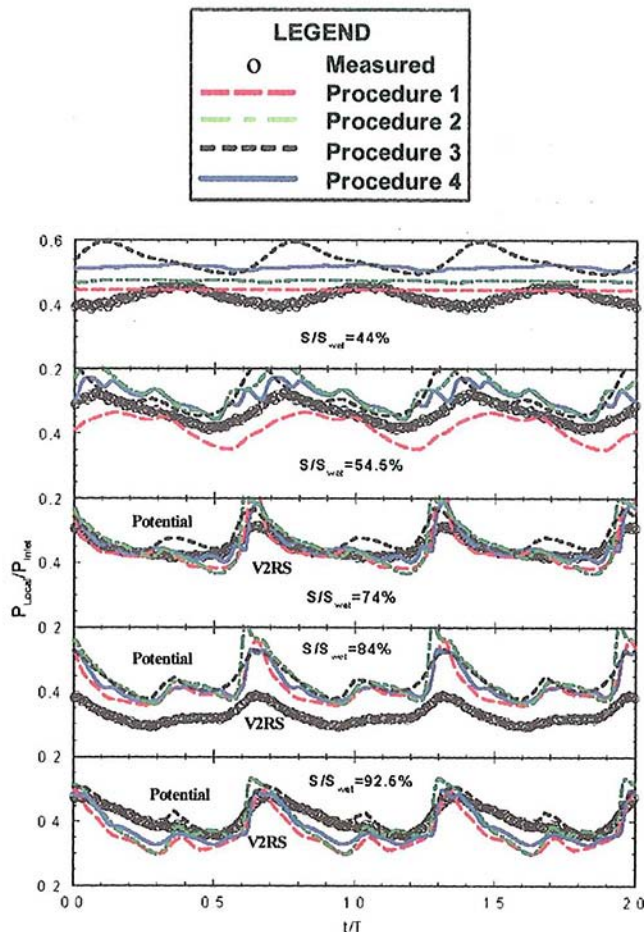
Fig. 2 Time-resolved pressures on the suction side of V2 at 20 percent axial gap

Fig. 3 Time-resolved pressures on the suction side of B1 at 20 percent axial gap

V1PS shock and both propagate upstream toward the suction side of V2. Between $t/T = 0.6$ and 0.7, the two shocks "slap" against the suction side of V2. This interaction is evident in both the measurements and the computations shown in Fig. 2 for $S/S_{\rm wet} > 60$ percent. The pressure at 54.5 percent chord on the suction side of the vane decreases just before the interaction with the B3LE shock (see Fig. 2). Notice that Figs. 1 and 2 indicate that this shock system slaps up against V2 at times $t/T = 0.0$, ~0.6 and ~1.3, which corresponds with every blade-passing period. The increase

pressure at five chordwise locations on the vane and both sides of the blade. $S_{\rm wet}$ is the wetted surface distance from the midspan leading edge of the vane or blade. The wake interactions with the blade are also noted in Figs. 3 and 4.

Two shocks emanate from the trailing edge near wake of each vane: one from the suction side and one from the pressure side. These shocks will be designated as V1PS, V1SS, V2PS, and V2SS for the V1 pressure side and suction side and V2 pressure side and suction side shocks, respectively. At $t/T = 0.0$, the V1SS shock impacts the pressure side of B1 around 60 percent wetted distance. As time increases, the blade rotates upward and the V1SS shock moves toward the trailing edge of B1. At approximately $t/T = 0.2$, B3 cuts into the V1SS shock. This shock reflects (B3LE) toward the pressure side of B1. The entropy contours in Fig. 1 at time $t/T = 0.4$ indicate that the B3LE shock encounters the V1 wake, which results in a bending of the B3LE shock.

As time increases beyond $t/T = 0.4$, the B3LE shock impacts the pressure side of B1 and moves toward the leading edge. This interaction is evident in Figs. 1 and 4 between $t/T = 0.4$ and $t/T = 0.6$. The increase in both the computed and measured pressures at $S/S_{\rm wet} = 67$ and 47 percent near $t/T = 0.5$ indicates the start of this interaction. As time increases, the computations show the shock interaction moving forward on the pressure side of B1. The computations show evidence of the B3LE shock interaction with B1 at all chordwise locations, but the measurements show the shock merging with the V1 wake interaction. The computations indicate that these two phenomena are independent, while the measurements show separate entities only at 47 and 67 percent chord.

Between $t/T = 0.5$ and 0.6, the B3LE shock coalesces with the

Fig. 4 Time-resolved pressures on the pressure side of B1 at 20 percent axial gap

a.) $S/S_{wetted} \sim 18.0\%$

○ 100 kHz
■ 250 kHz

b.) $S/S_{wetted} \sim 22.5\%$

○ 100 kHz
■ 250 kHz

Fig. 5 Influence of sampling frequency on time-resolved pressure on the suction side of B1

in pressure on the suction side of the vane prior to the shock interaction (around $t/T = 0.4$), is due to potential effects from the blade.

After the B3LE shock system slaps against V2, it reflects back toward the blades. This reflected shock/pressure wave is marked as V2RS in Fig. 1. At $t/T \sim 0.1$, V2RS combines with the reflection of the V1PS shock off of the vane and also the reflection of the V2SS shock off of the pressure side of the leading edge of B2 (B2RS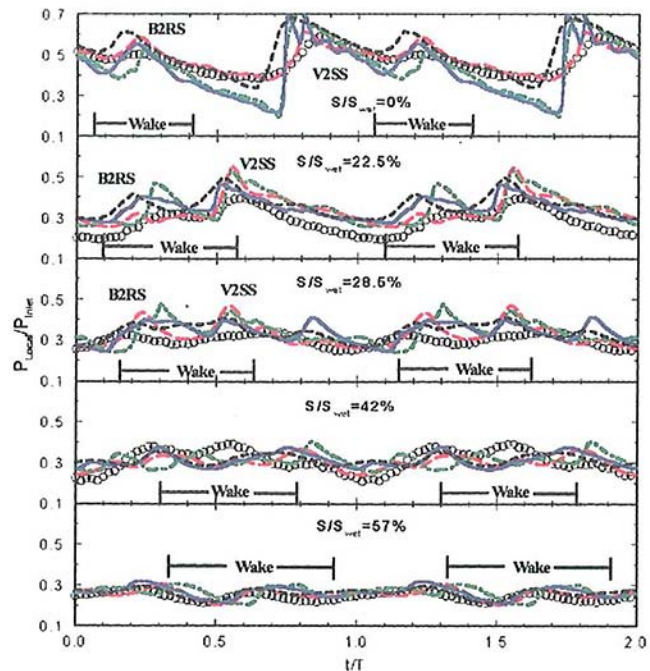). The combination of these shocks increases the strength of the V2RS shock. The V2RS shock impacts the leading edge of B1 at approximately $t/T = 0.2$. At this same time, the V1 wake also impacts the leading edge of B1. The increase in pressure at the leading edge of the suction side of the blade (see Fig. 3) is due to these shock/wake interactions. The interaction between B1 and the B2RS shock is evident in Figs. 1 and 3 between $t/T = 0.2$ and 0.3 at 22.5 percent chord. The wake interaction with the suction side can be seen at 28.5, 42, and 57 percent chord between $t/T = 0.2$ and 0.8.

Between $t/T = 0.5$ and 0.6, the V2SS shock comes into contact with the suction side of B1. This interaction is evident in Fig. 3 at 28.5 and 22.5 percent chord. The shock interaction moves forward as the blade sweeps past the vane, and can be seen impacting the leading edge at approximately $t/T = 0.8$.

The increase in pressure between $t/T = 0.0$ and 0.3 on the pressure side of the blade is due to the V1SS shock and the reflection of the V1PS shock off of the vane (V1PR). The increase in pressure occurs simultaneously at all chordwise locations (see Fig. 4).

Three-dimensional computations were performed for each axial spacing using Procedure 1. Due to space limitations, only a brief summary of the results will be presented here. The three-dimensional time-mean computations had slightly better agreement with the measurements on the suction side of both the vane and blade than did the two-dimensional computations (see Venable et al., 1999). The two-dimensional and three-dimensional time-resolved pressures for the 20 percent spacing case were nearly identical. As the spacing increases, the overall trends remain the same, but a slight change in phase occurs.

Temporal Resolution. The comparisons between the computations and measurements presented in Figs. 3 and 4 suggest that, at some locations on the blade, there is a difference in the frequency content of the time-resolved pressures. In the absence of significantly more data, it is difficult to determine whether the measurements are missing some of the frequency content or whether the frequency content in the computations is an artifact of the numerical procedure. However, it is possible to extract a little more information from the measurements. It was mentioned earlier that the measurements were generally obtained by sampling the transducers at a frequency of 100 kHz using a 40 kHz anti-aliasing filter. Further, selected·transducers were sampled using an independent data system at a frequency of 250 kHz with no anti-aliasing filter in-line. By comparison, the predictions used between 300 to 50,000 time steps (sampling rate of 885 kHz to 147,500 kHz) to compute the global cycle.

A comparison of the time-resolved surface pressure at two locations on the blade suction surface (18 and 22.5 percent wetted distance) for the 100 kHz and 250 kHz sampling frequencies is given in Fig. 5 (unfortunately, the high sampling frequency data system did not contain any of the pressure surface transducers). Figure 6 presents the FFT of the data at 22.5 percent wetted distance. The inset graph in Fig. 6 contains the data for frequencies greater than 25 kHz, with a refined scale on the ordinate. At these locations on the blade, there is very little difference between the frequency content of the two sampling frequencies for either location.

To illustrate the effects of the high-frequency phenomena seen in the computed unsteady surface pressures, the solutions were filtered, to eliminate the higher frequencies, by Fourier decomposing the solutions and then reconstructing the solutions using only frequencies less than six times the vane passing frequency or 35.4 kHz (i.e., using only the first three harmonics). The comparison between the 20 percent axial spacing experimental data for the pressure side of the blade and these temporally filtered predictions is shown in Fig. 7. In addition, a solution was computed using Procedure 1 with only 45 time steps (i.e., sampling frequency of 133 kHz) over the global cycle, in essence, using the numerics to filter the solution. This solution is also shown in Fig. 7. Comparison between Figs. 4 and 7 shows that better agreement exists between the temporally filtered predictions and the experimental data than with the unfiltered solutions. Figure 7 also shows that the Procedure 1 solution, with the reduced number of time steps over the cycle, has a similar effect of temporally filtering the solution. This approach is not recommended in general, however, since the dispersion error related to such large time steps could lead to numerical inaccuracy and instability. The results shown in Fig. 7 demonstrate that it is important, when comparing numerical predictions and unsteady experimental data, that both are at comparable levels of temporal resolution.

Effect of Spacing on Performance. To evaluate the performance in the absence of experimental data, the predicted time-

Fig. 6 Comparison of frequency content for suction surface of the blade at 22.5 percent wetted distance
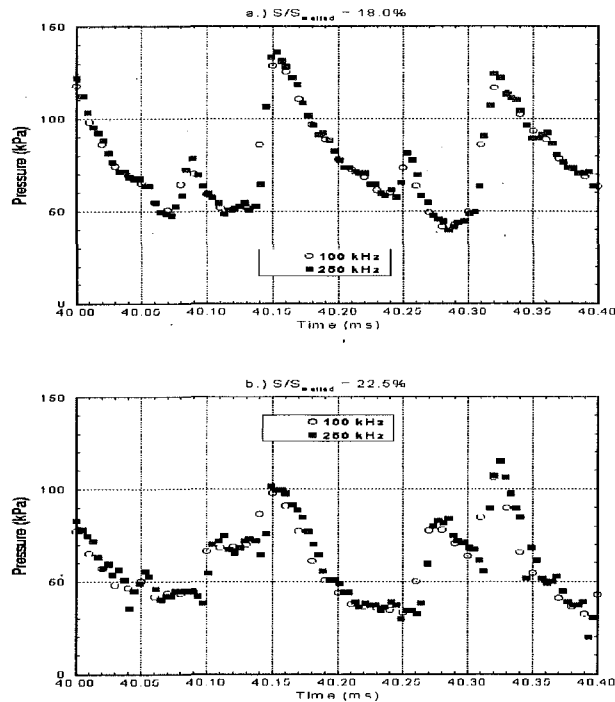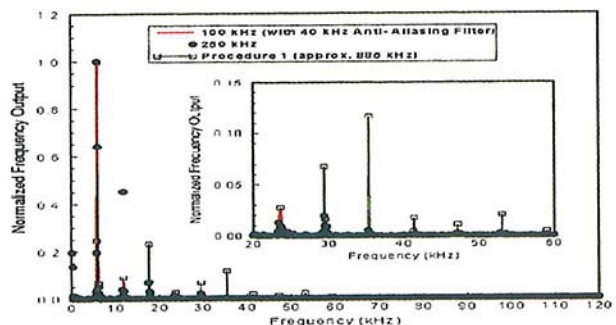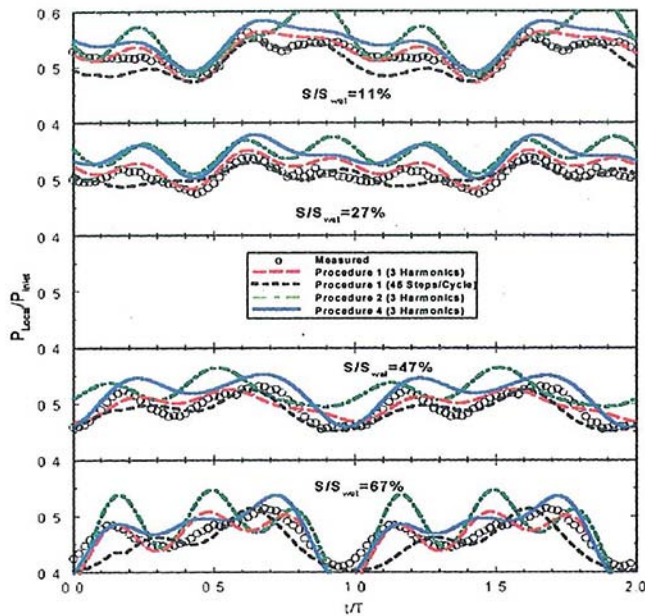
Fig. 7 Time-resolved pressures on pressure side of B1 at 20 percent axial gap and temporally filtered predictions

Fig. 9 Predicted entropy at the exit of passage V1 to V2 at midspan (Procedure 1)

averaged relative midspan total pressure losses and instantaneous pitchwise-averaged entropy (relative to the vane inlet entropy) of a given vane and blade passage are examined to understand the effects of axial spacing on the aerodynamic performance of this turbine stage. The predicted trends in efficiency resulting from the four numerical procedures have been found to be reliable for a wide variety of configurations. Venable et al. (1999) showed that the predicted, time-averaged efficiency across the stage did not vary much as a function of the vane/blade axial spacing. Figure 8 shows the predicted two-dimensional time-averaged midspan relative total pressure losses of the vane and blade resulting from Procedure 1. The time-averaged inlet and exit relative total pressures of each blade row were used to compute the total pressure loss coefficient, $(P_{Tinlet} - P_{Texit})/P_{Tinlet}$. The computational exit boundary for the vane and the inlet to the blade were located midway between the vane and blade. The exit boundary of the blade was located one axial chord downstream of the blade trailing edge. Figure 8 shows that the predicted blade relative total pressure loss increases as the vane/blade axial spacing decreases. This figure also shows that the vane relative loss has the opposite trend with axial spacing. As a result of these opposing effects, the predicted overall adiabatic stage efficiency (Venable et al., 1999) across the turbine stage varies only a small amount with vane/blade axial spacing. All of the procedures predict this same trend

Fig. 8 Predicted mean relative total pressure loss at midspan for the vane and blade (Procedure 1)

in the vane and blade relative total pressure loss as a function of vane/blade axial spacing.

Figure 9 shows the time variation of the predicted pitchwise-averaged entropy at the vane exit for the three axial spacings. All of the results used for the following discussion were obtained using Procedure 1. The other procedures showed similar trends and for clarity will not be shown. Figure 9 shows that the minimum entropy change (i.e., lowest entropy change) across the vane (V1–V2) passage for the 20 percent axial spacing occurs at approximately $t/T = 0.1$ and 0.8. At these times, the V2RS shock is reflecting off the V2 vane and there is a very strong shock interaction between the V2SS shock and the leading edge of B2 ($t/T = 0.1$) or B1 ($t/T = 0.8$). Also, the reflection of the V1SS shock off of the leading edge of B2 ($t/T = 0.1$) and B1 ($t/T = 0.8$) is sweeping upstream and crossing the V1–V2 boundary. The upstream propagating *unsteady* shock motion relative to the flow results in increases in the predicted *absolute* total pressure and total temperature across the shock, and hence a decrease in the entropy. Examination of the contours in Fig. 1 also shows that during the time interval $t/T = 0.1$–0.3, the B2 blade leading edge is aligned circumferentially with the V2 vane trailing edge. At this position, the blade leading edge interacts with the vane trailing edge pressure field and "thins" the V2 vane wake. At this same time, the B1 blade also interacts with and narrows the wake of V1. The local valley in the 20 percent spacing instantaneous entropy for the vane at $t/T = 0.4$ coincides with a similar interaction between the B3 blade leading edge and the V1 vane trailing edge. However, in this interval, the wake of the V1 vane has already been "cut" by the B1 blade and the wake/blade interaction is lower. The maximum instantaneous entropy for this spacing, located at $t/T = 0.6$, corresponds to a time where the wake interaction with the blade leading edge is at a minimum and there is little shock interaction between the leading edge of the blade and the trailing edge of the vane. Examination of the pressure contours at this time interval shows that there are no pressure waves (other than the ever-present V1PS shock) interacting with the vane.

As the spacing increases, the time-averaged entropy through the vane also increases. The increase in the average entropy is driven by an increase in the *minimum* entropy as opposed to an increase in the maximum entropy. Recall that the minimum entropy is driven by the shock and wake interactions. As the spacing is increased, this interaction is reduced resulting in an increase in the minimum entropy.

The time variation of the predicted pitchwise average entropy at the blade exit (B1–B2) for the three axial gaps is shown in Fig. 10. For the 20 percent spacing, the minimum entropy occurs at approximately $t/T = 0.3$–0.4. The flow visualization indicates that the minimum occurs when the vane wakes cut through the B1 suction-side, trailing-edge shock (B1SS) as well as the reflection of the B2 pressure-side, trailing-edge shock (B2PS) off the suction side of B1 (BPRS). Thus, the blade shock entropy at the exit is minimized. Also at this time, none of the vane wakes are exiting

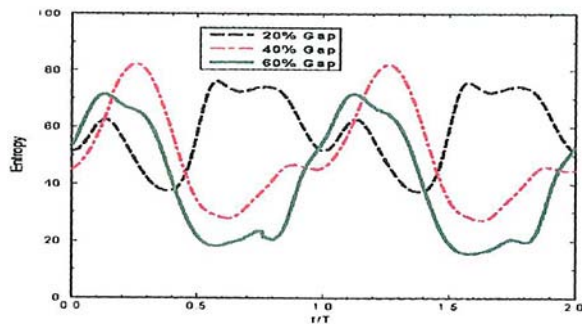**Fig. 10 Predicted entropy at the exit of passage B1 to B3 at midspan (Procedure 1)**

the stage. The entropy begins to increase (at $t/T \sim 0.5$) as B2PS strengthens because the vane wake is no longer passing through B2PS. Also at this time, the vane and blade wakes are exiting the stage. The entropy decreases slightly at $t/T = 0.7$ as the next vane wake encounters B2PS and even more at $t/T = 0.8$ as the vane wake starts to cut through B1SS. The increase in entropy at $t/T = 0.1$ may be due to the blade wake. As the vane wake interacts with the blade shock system, it decreases the interaction between blade wake and blade shock system. Thus, the blade wake does not get diffused by the B1SS shock and the increased entropy associated with the blade wake exits the stage.

Examination of instantaneous contours of entropy for the three axial gap configurations (40 and 60 percent are not shown) indicates that as the axial gap increases, the manner in which the vane wakes traverse the blade passage changes significantly. At 20 percent spacing, the vane wakes migrate toward the suction side of the blade. As the spacing increases, the wakes tend to cling to the pressure side of the blade for a longer period of time (see Appendices A and B), thus creating a less concentrated and elongated wake structure. As a result, the vane wakes interact with the B1PS and its reflection (BPRS) for a longer period of time and weaken the blade shocks considerably. This results in a reduction of the time-averaged entropy. The minimum entropy occurs when (a) the vane wake is interfering with the B2PS shock, reflected shock (BPRS), and the B1SS shock simultaneously and (b) the blade wake is not passing through the exit boundary. The maximum losses occur when the vane wake and blade wake exit the stage at the same time.

Conclusions

A experimental/computational investigation of the unsteady flow effects on the surface pressure and aerodynamic performance of a transonic turbine stage as a function of vane/blade axial spacing is presented. The results from four different Navier–Stokes numerical procedures were compared with each other as well as with the experimental data. In general the numerical solutions compared very favorably with each other and with the experimental data. The numerical solutions appear to exhibit higher frequencies and levels of unsteadiness than the experimental data at select locations on the blade. The overall predicted stage losses and efficiencies did not vary much with vane/blade axial spacing. Examination of the details of the predicted performance showed that any increases in the blade relative total pressure loss were offset by a decrease in vane loss as the axial spacing was decreased. The decrease in predicted vane loss with decreased axial spacing was due to stronger vane–blade interactions and a reduction in the wake mixing losses. The increase in predicted blade relative total pressure loss with a decrease in axial spacing was found to be mainly due to increased vane wake/blade interaction.

References

Arnone, A., and Pacciani, R., 1996, "Numerical Investigation on Wake Shedding in a Turbine Rotor Blade," *Proc. 15th International Conference on Numerical Methods in Fluid Dynamics,* June 24–28, Monterey, CA.

Abhari, R. S., Guenette, G. R., Epstein, A. H., and Giles, M. B., 1992, "Comparison of Time-Resolved Turbine Rotor Blade Heat Transfer Measurements and Numerical Calculations," ASME JOURNAL OF TURBOMACHINERY, Vol. 114, pp. 818–827.

Baldwin, B. S., and Lomax, H., 1978, "Thin Layer Approximation and Algebraic Model for Separated Turbulent Flows," AIAA Paper No. 78-257.

Davis, R. L., Shang, T., Buteau, J., and Ni, R.-H., 1996, "Prediction of 3-D Unsteady Flow in Multi-Stage Turbomachinery Using an Implicit Dual Time-Step Approach," AIAA Paper No. 96-2565.

Dorney, D. J., and Sondak, D. L., 1996, "Study of Hot Streak Phenomena in Subsonic and Transonic Flows," *International Journal of Turbo and Jet-Engines,* Vol. 13, pp. 131–141.

Dorney, D. J., and Davis, R. L., 1992, "Navier–Stokes Analysis of Turbine Blade Heat Transfer and Performance," ASME JOURNAL OF TURBOMACHINERY, Vol. 114, pp. 795–806.

Doughty, R. L., Moses, H. L., and Gregory, B. A., 1992, "The Effect of Blade Solidity on the Aerodynamic Loss of a Transonic Turbine Cascade," AIAA Paper No. 92-0393.

Dunn, M. G., Bennet, W., Delaney, R., and Rao, K., 1990, "Investigation of Unsteady Flow Through a Transonic Turbine Stage: Part II—Data/Prediction Comparison for Time-Averaged and Phase Resolved Pressure Data," AIAA Paper No. 90-2409.

Giles, M. B., 1988, "UNSFLO: A Numerical Method for Unsteady Inviscid Flow in Turbomachinery," MIT Gas Turbine Laboratory Report No. 195.

Giles, M. B., and Haimes, R., 1993, "Validation of a Numerical Method for Unsteady Flow Calculations," ASME JOURNAL OF TURBOMACHINERY, Vol. 115, pp. 110–117.

Guenette, G. R., Epstein, A. H., Giles, M. B., Haimes, R., and Norton, R. J. G., 1989, "Fully Scaled Transonic Turbine Rotor Heat Transfer Measurements," ASME JOURNAL OF TURBOMACHINERY, Vol. 111, pp. 1–7.

Jennions, I. K., and Adamczyk, J. J., 1997, "Evaluation of the Interaction Losses in a Transonic Turbine HP Rotor/LP Vane Configuration," ASME JOURNAL OF TURBOMACHINERY, Vol. 119, pp. 68–76.

Lewis, J. P., Delaney, R. A., and Hall, E. J., 1989, "Numerical Predictions of Turbine Vane-Blade Aerodynamic Interaction," ASME JOURNAL OF TURBOMACHINERY, Vol. 111, pp. 387–393.

Ni, R.-H., 1981, "A Multiple Grid Scheme for Solving the Euler Equations," *AIAA Journal,* Vol. 20, No. 11, pp. 1565–1571.

Nix, A. C., Reid, T., Peabody, H., Ng, W. F., Diller, T. E., and Schetz, J. A., 1997, "Effects of Shock Wave Passing on Turbine Blade Heat Transfer in a Transonic Cascade," AIAA Paper No. 97-0160.

Rai, M. M., 1987, "Navier–Stokes Simulations of Rotor/Stator Interactions Using Patched and Overlaid Grids," *AIAA Journal of Propulsion and Power,* Vol. 3, No. 5, pp. 387–396.

Rao, K., and Delaney, R., 1990, "Investigation of Unsteady Flow Through Transonic Turbine Stage, Part I: Analysis," AIAA Paper No. 90-2408.

Rao, K., Delaney, R., and Dunn, M., 1992, "Vane–Blade Interaction in a Transonic Turbine: Part I—Aerodynamics," AIAA Paper No. 92-3323.

Rangwalla, A. A., 1994, "Unsteady Navier–Stokes Computations for Advanced Transonic Turbine Design," AIAA Paper No. 94-2835.

Rangwalla, A. A., Madavan, N. K., and Johnson, P. D., 1992, "Application of an Unsteady Navier–Stokes Solver to Transonic Turbine Design," *AIAA Journal of Propulsion and Power,* Vol. 8, pp. 1079–1086.

Saxer, A. P., and Giles, M. B., 1994, "Predictions of three-dimensional Steady and Unsteady Inviscid Transonic Stator/Rotor Interaction With Inlet Radial Temperature Nonuniformity," ASME JOURNAL OF TURBOMACHINERY, Vol. 116, pp. 347–357.

Sieverding, C. H., Stanislas, M., and Snoech, J., 1979, "The Base Pressure Problem in Transonic Cascade," ASME Paper No. 79-GT-120.

Venable, B. L., Delaney, R. A., Dunn, M. G., Haldeman, C. W., Abhari, R. S., Busby, J. A., Davis, R. L., and Dorney, D. J., 1999, "Influence of Vane-Blade Spacing on Transonic Turbine Stage Aerodynamics: Part I—Time-Averaged Data and Analysis," ASME JOURNAL OF TURBOMACHINERY, Vol. 121, this issue, pp. 663–672.

Wesner, A., Schetz, J., Holmberg, D., and Malik, M., 1997, "Transition Predictions and Experiments in a Turbine Cascade," AIAA Paper No. 97-3011.

APPENDIX A

Unsteady Surface Pressures for 40 Percent Axial Spacing

The unsteady pressures on the vane and blade for 40 percent axial gap are shown in Figs. A1–A3. On the suction side of the blade, the transducers at the leading edge and 22.5 percent chord failed, so the measured data for these locations are not shown.

Again, the computations show higher harmonics than the measured data and phasing differences between computational approaches become more evident. Also, both the measured data and computations show reduced amplitudes of pressure for all locations.

The dominant features from the 20 percent spacing case are also evident in the 40 percent spacing case. The interaction between the B3LE shock and the vane can be seen at $t/T = 0.1$, 0.65, and 1.4 (see Fig. A1). Contour plots, similar to Fig. 1, were used to determine the interaction times between the vane wake and blade surface. These time intervals are annotated on Figs. A2 and A3. The wake interaction that was evident on the suction side of the blade for the 20 percent spacing is significantly reduced as the spacing increases (see Fig. A2), but tends to be the dominant feature on the pressure side of the blade (see Fig. A3). The computations show the wake and B3LE shock interaction as merging together, similar to the measurements. The dominant feature on the suction side of the blade is still the interaction with the V2SS shock.

Fig. A2 Time-resolved pressures on the suction side of the blade at 40 percent axial gap

LEGEND

O	Measured
— — —	Procedure 1
— ·· — ··	Procedure 2
– – – –	Procedure 3
——————	Procedure 4
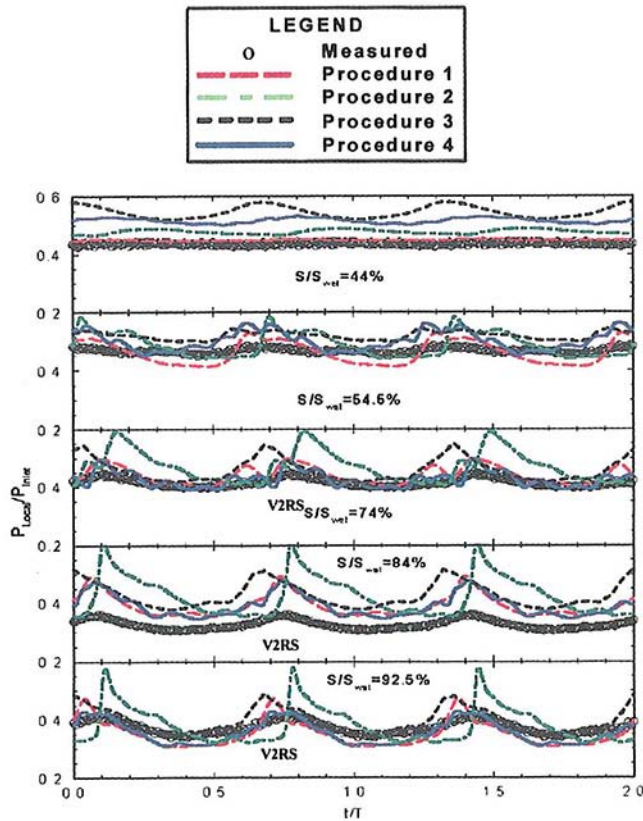
Fig. A1 Time-resolved pressures on the suction side of the vane at 40 percent axial gap
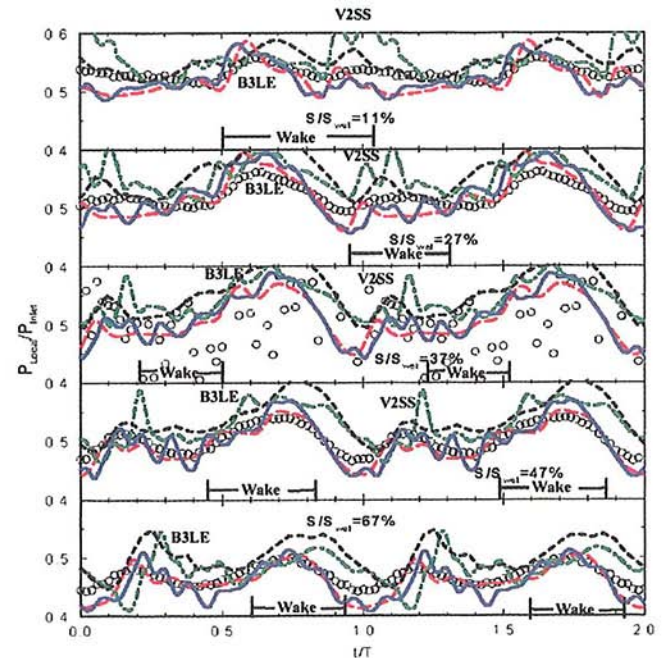
Fig. A3 Time-resolved pressures on the pressure side of the blade at 40 percent axial gap

APPENDIX B

Unsteady Surface Pressures for 60 Percent Axial Spacing

The unsteady pressures for the 60 percent axial spacing are shown in Fig. B1–B3. As with the 40 percent spacing, the same features are evident in the pressure histories. On the vane, the lower amplitude pressures spikes indicate that the impact of the B3LE shock is weak compared to the 20 and 40 percent flows. The computations also contain higher frequencies than were seen for the 20 and 40 percent spacing cases. The dominant interaction on the suction side of the blade is still with the V2SS shock.

Fig. B2 Time-resolved pressures on the suction side of the blade at 60 percent axial gap

LEGEND
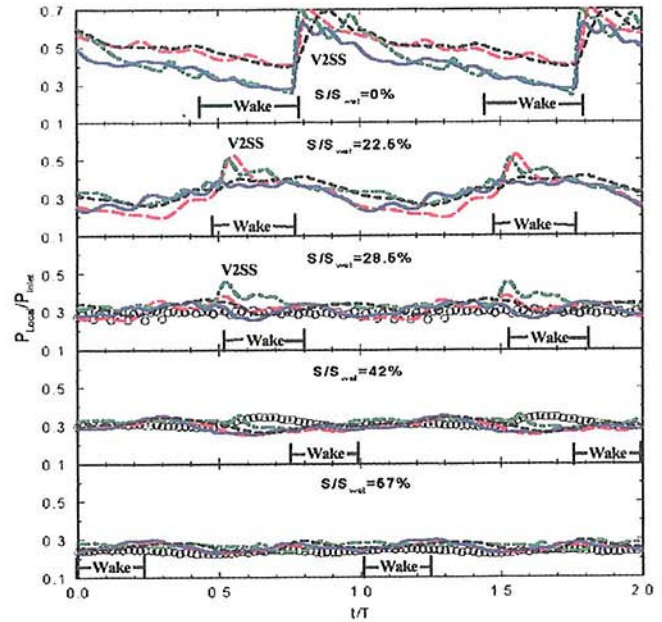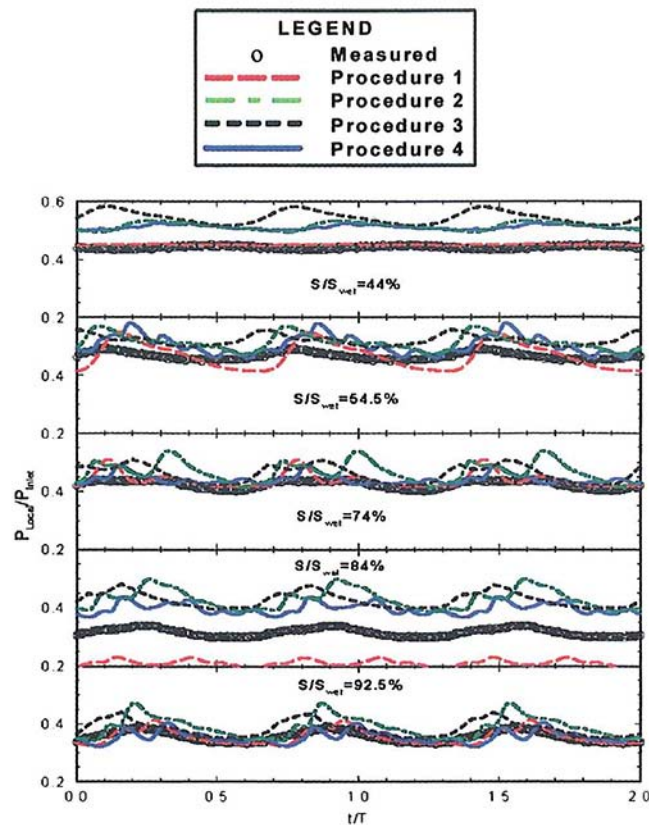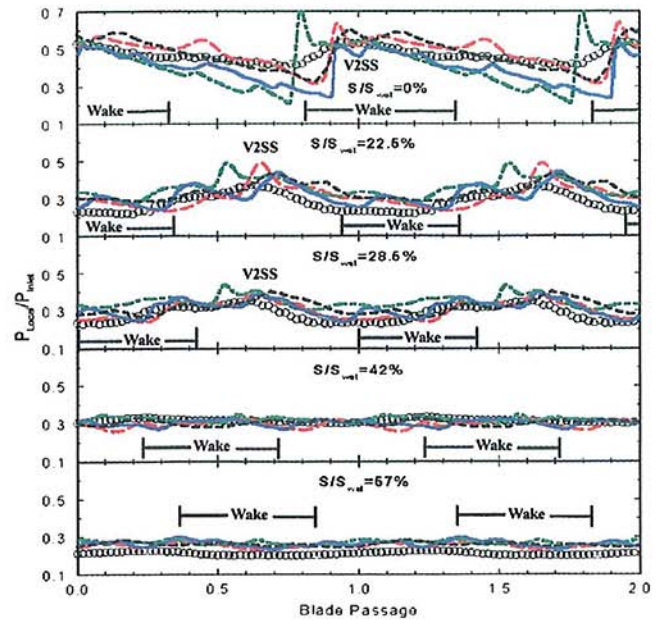| o	Measured
	Procedure 1
	Procedure 2
	Procedure 3
	Procedure 4

Fig. B1 Time-resolved pressures on the suction side of the vane at 60 percent axial gap
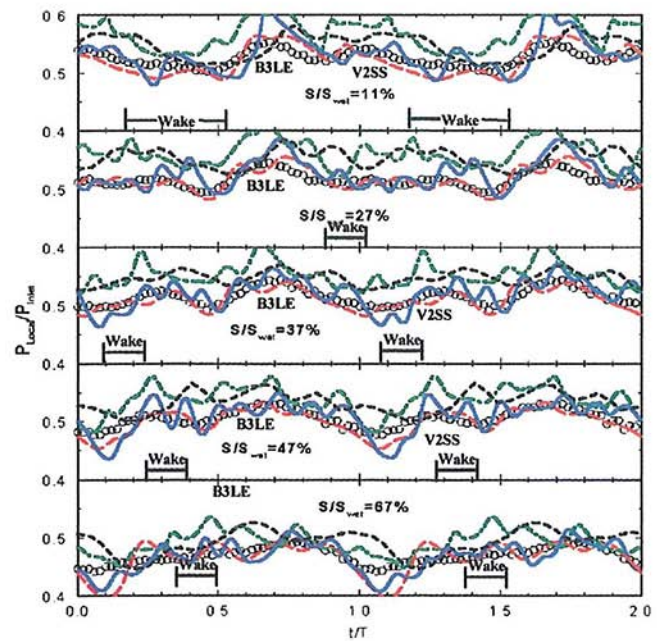

Fig. B3 Time-resolved pressures on the pressure side of the blade at 60 percent axial gap

Effects of Tip Clearance and Casing Recess on Heat Transfer and Stage Efficiency in Axial Turbines

A. A. Ameri
AYT Corporation,
Brook Park, OH 44142

E. Steinthorsson
Institute for Computational Mechanics in
Propulsion (ICOMP),
NASA Lewis Research Center,
Cleveland, OH 44135

D. L. Rigby
NYMA, Inc.,
NASA Lewis Group,
Cleveland, OH 44135

Calculations were performed to assess the effect of the tip leakage flow on the rate of heat transfer to blade, blade tip, and casing. The effect on exit angle and efficiency was also examined. Passage geometries with and without casing recess were considered. The geometry and the flow conditions of the GE-E³ first-stage turbine, which represents a modern gas turbine blade, were used for the analysis. Clearance heights of 0, 1, 1.5, and 3 percent of the passage height were considered. For the two largest clearance heights considered, different recess depths were studied. There was an increase in the thermal load on all the heat transfer surfaces considered due to enlargement of the clearance gap. Introduction of recessed casing resulted in a drop in the rate of heat transfer on the pressure side, but the picture on the suction side was found to be more complex for the smaller tip clearance height considered. For the larger tip clearance height, the effect of casing recess was an orderly reduction in the suction side heat transfer as the casing recess height was increased. There was a marked reduction of heat load and peak values on the blade tip upon introduction of casing recess; however, only a small reduction was observed on the casing itself. It was reconfirmed that there is a linear relationship between the efficiency and the tip gap height. It was also observed that the recess casing has a small effect on the efficiency but can have a moderating effect on the flow underturning at smaller tip clearances.

Introduction

The tip clearance is responsible for a significant portion of losses in turbines. Much attention is being paid to reduction in losses due to the tip clearance flows, since other sources of loss are not as amenable to manipulation as the tip clearance losses. Blade tips are also susceptible to burnouts and oxidation due to the large thermal loading on and near the blade tips. Losses and heat load in the tip region increase as the tip gap widens. This increase in losses and the increased heat load is particularly deleterious to the operation of engines under certain periods of operation, such as during take off when the clearance gap is wider. The tip clearance also widens as the engine gets older.

Tip and casing treatments are used to improve the efficiency and reduce the tip heat transfer. Among the various treatments used for the blade tip are the use of squealer-type blades, the most widely used among them being the double squealer tip, which is simply a recess in the blade tip. Ameri et al. (1998) simulated the flow and heat transfer due to tip recess and showed that the effect on efficiency was insignificant and also the heat transfer issues were not ameliorated by the tip recess. An experimental study performed by Kaiser and Bindon (1997) showed that for their $1\frac{1}{2}$ stage turbine, the recessed tip had a negative effect on the efficiency. Neither the numerical conclusions of Ameri et al. nor those of Kaiser and Bindon were in agreement with the popular belief that the tip recess increases the efficiency by reducing the tip clearance flow.

Another method employed to reduce the tip clearance losses is the use of the casing recess. In this work, in addition to the examination of the effect of the clearance height, we examine the

effect of casing recess on the tip and casing heat transfer and its influence on efficiency. There is some experimental work available in the open literature, namely that of Haas and Kofsky (1979), which addresses the effect of the casing recess on the efficiency for a small turbine. Their experiments show that the maximum efficiency is achieved using a casing recess at level with the tip of the blade. There is also one numerical study (Briley et al., 1991) of turbine blade flow that does include tip clearance and casing recess; however, their effects are not separated.

The task of calculation of the heat transfer and particularly efficiency in terms of absolute magnitudes is a formidable one, especially for complex flow passages such as the flow passage at hand. A comparative study is, however, possible if special care is taken to retain as much similarity between the grid distribution for the cases considered as possible.

In the section to follow, we will give a brief description of the numerical method used in the simulations. Next the flow field near the tip and the recess will be discussed and salient features pointed out. Then we will present the heat transfer results, which include the blade surface near the tip, the tip, and casing heat transfer. Next we will present the results of the calculations of the exit angle. Finally, we will present the results of the calculations of efficiency for a range of gap heights and casing recesses and close by presenting a summary and the conclusions.

Computational Method

The simulations in this study were performed using a multiblock computer code called TRAF3D.MB (Steinthorsson et al., 1993). This code is a general purpose flow solver designed for simulations of flows in complicated geometries. The TRAF3D.MB code solves the full compressible Reynolds-averaged, Navier–Stokes equations using a multistage Runge–Kutta-based multigrid method. It uses the finite volume method to discretize the equations. The code uses central differencing together with artificial dissipation to discretize the convective terms. The overall accuracy of the code
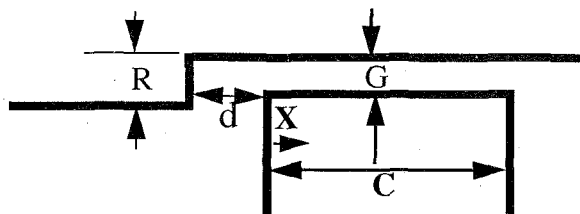
Fig. 1 Sketch of the geometry near the tip, showing nomenclature

Table 1 Summary of cases

G	d	R/G
0	---	0. (no casing recess)
1.	---	0.(no casing recess)
1.5	---	0.(no casing recess)
1.5	15%	0.5, 1. (level), 1.5
1.5	25%	0.5, 1. (level), 1.5
3	---	0.(no casing recess)
3	25%	1/3, 2/3, 1. (level)

is second order. The present version of the code (Rigby et al., 1996, 1997a; Ameri et al., 1998) employs the $k-\omega$ turbulence model developed by Wilcox (1994a, b) with subsequent modifications by Menter (1993). The model integrates to the walls and no wall functions are used. For heat transfer a constant value of 0.9 for turbulent Prandtl number, Pr_t, is used. A constant value of $Pr = 0.72$ is used. Viscosity is a function of temperature through a 0.7 power law (Schlichting, 1979) and Cp is taken to be a constant.

Geometry and the Grid

Figure 1 shows a sketch of the problem and the definitions of some of the variables used in the study. As tabulated in Table 1, four gap clearances of $G = 0, 1, 1.5,$ and 3 percent of the passage height are used. The 0 and 1 percent cases are run without casing recess. For the two wider gaps, the recess heights are varied. For the 1.5 percent gap case there are two sets of calculations for d, namely $d = 15$ and 25 percent of the chord. For the 3 percent gap $d = 25$ percent of the chord is used.

The blade chosen for this study is a generic modern gas turbine rotor blade, the General Electric E^3 (Energy Efficient Engine) design, which is detailed in two NASA reports (Halila et al., 1982; Timko, 1982). The rotor blades have a constant axial chord length of 2.87 cm and an aspect ratio of 1.39. Figure 2(a) shows the blade geometry and the basic features of the grid. The insets (b) and (c) show the details of the grid on the tip and on the casing showing the recess geometry. The grid is generated using a commercially available computer program called GridPro™. The grid topology is quite complex and the grid for a geometry with tip clearance and casing recess consists of 310 blocks. Once the grid is generated, for reasons of computational efficiency, the blocks are merged to produce a smaller number of blocks, namely 29 blocks for runs with casing recess and 26 blocks for runs without casing recess. This was done using the Method of Weakest Descent as described by Rigby et al. (1997b) and Rigby (1996). In order to keep the grids for the many cases considered in this work as similar as possible, we have assured that the general topology is the same for all the cases considered. Therefore, after the first grid was generated, the grids for the remaining similar cases could be generated

rather quickly. The viscous grid is generated by embedding grid lines where needed. We have required that the stretching ratio not exceed 1.25 for the viscous grid away from the no-slip surfaces. The distance to the first cell center adjacent to the solid wall is specified such that the distance in wall units, (y^+) is less than unity. This is verified, and the distribution of y^+ on and near the tip will be given in the results section. One attractive feature of the generated grid is that as shown in Fig. 2(b) the viscous grid wraps around the blade instead of extending into the free stream. This feature of the grid improves the convergence of the solution. Near the edge of the blade, in the tip region (Fig. 2(b)) better refinement of the grid might be required for more accurate results, however, since we are making relative comparisons, extreme measures are avoided. In spite of the above, the total number of grid points is typically around 1.3 million. 59–65 grid points are used radially within the tip clearance. 33 grid points are used to resolve the boundary layers on the blade. This does not include the "inviscid" blade-to-blade grid, which is also quite fine. At the inlet patch, the number of grid points is 85 in the pitchwise and 97 in the spanwise direction.

Run Conditions

The run conditions are provided in Table 2. The manner in which the boundary conditions are imposed both for the flow and turbulence variables are as given in Ameri et al. (1998). However, for the sake of completeness, the inlet boundary conditions are given in Figs. 3(a) and 3(b). The swirl angle in Fig. 3(a) was specified as per measurements of Timko (1982). The inlet total temperature and pressure were specified by the use of the law of the wall through the specification of the inlet boundary layer thickness at the hub and the casing. For the turbulence quantities, an inlet turbulence intensity of 8 percent and a length scale of 1 percent of axial chord was used. These values were estimated and believed to be representative of the conditions existing at the inlet of the blade row.

Nomenclature

A = inlet area
C = axial chord
C_p = constant pressure specific heat
d = distance upstream of the leading edge expressed as percent of axial chord
G = clearance height, expressed as percent of annulus height (see Fig. 1)
h = heat transfer coefficient – wall heat flux = $(T_0 - T_w)$
k = thermal conductivity or kinetic energy of turbulence = RT_0
$\dot{m}$ = mass flow rate

N = rotation rate
Pr = Prandtl number = $(\mu Cp)/k$
R = recess depth (see Fig. 1) or gas constant for air
Re = Reynolds number
T = temperature = T_0
Tu = turbulence intensity = $(\sqrt{2k/3})/V$
V = total velocity = $\sqrt{RT_0}$
v^* = friction velocity = $(\sqrt{\tau_w})/\rho$
X = distance measured from the leading edge (see Fig. 1)
y = normal distance from wall

y^+ = dimensionless distance from a wall
　　 = $y(v^*/\nu)$
γ = specific heat ratio
μ = viscosity
τ_w = wall shear stress
ρ = density
ω = $(2\pi NC)/(\sqrt{RT_0})$

Subscripts

t = total conditions
w = wall
0 = total inlet condition
1 = base case (see Fig. 14)
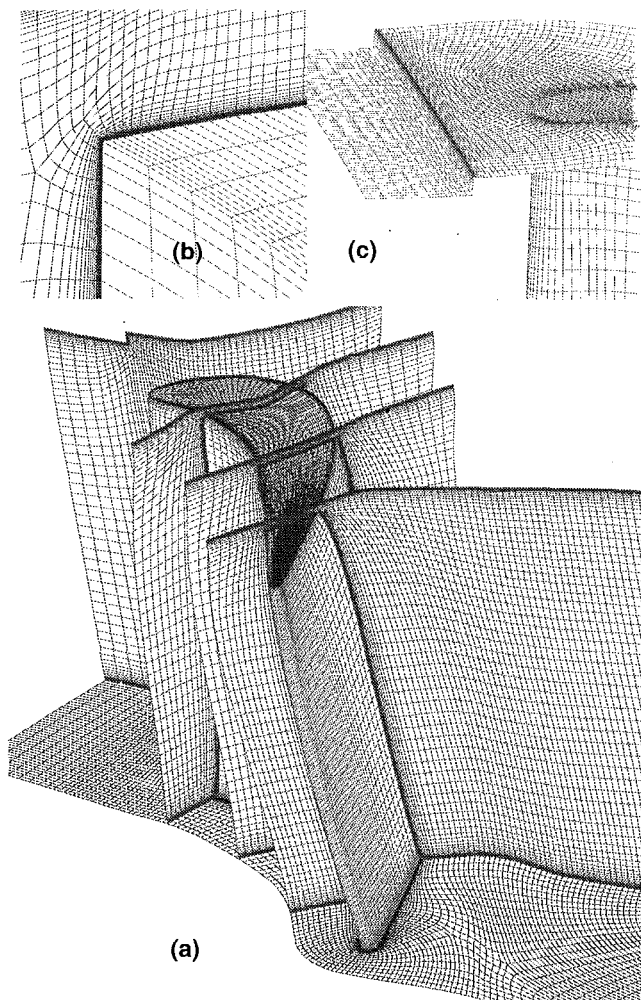
Fig. 2 *GE*, E³ first-stage rotor blade: (*a*) overall grid, (*b*) details of the tip grid near the edge, and (*c*) details of the casing grid

Fig. 3 (*a*) Inlet absolute swirl angle and (*b*) inlet total temperature and total pressure

Results and Discussion

General Remarks. All the cases presented herein have been converged to better than 0.01 percent mass flow error. The residual for all the cases dropped six to seven orders of magnitude. The heat transfer and efficiency results have been checked for convergence by comparing solutions after consecutive runs of 300 iterations. The present calculations match the experimental mass flow rate to within 0.5 percent. As described earlier, to achieve accurate resolution of heat transfer on surfaces, the grid was generated to result in dimensionless distance of the first cell center off the walls of less than unity. Figure 4 shows a typical distribution of dimensionless wall distance on and near the tip. It can be seen that the goal has been met.

Clearance gaps chosen for the study of recessed casing are relatively wide since tip clearance effects are stronger for larger

gaps, and the effects of recessed casing are expected to be more pronounced, as was shown by Haas and Kofsky (1979).

Flow Field. Figure 5 shows streamline patterns for a 1.5 percent clearance gap and those for a 3 percent clearance gap. Both cases possess a casing recess upstream. In the two figures, the edge vortex, suction side tip vortex, and a larger structure that appears to be a horseshoe vortex are present. The low-momentum fluid behind the recess also appears to be joining this larger structure in both cases. The larger tip clearance gives rise to a larger tip vortex by virtue of its larger mass flow rate through the tip. The above-mentioned structures enhance the heat transfer to the blade and will be discussed further in subsequent sections. Figure 6(*a*) shows the region behind the casing recess. The arrows in this figure and in all subsequent ones are projections of the relative velocity vectors onto the viewing area. A distinct recirculation zone (blockage) can be discerned behind the recess. Figures 6(*b*) and 6(*c*) show the flow relative to the blade at a radial location midgap of the tip clearance for the *G* = 1.5 percent without and with a casing recess upstream, respectively. The modification of the flow over the tip downstream of the recess as compared to the no-recess case is quite obvious from the two figures. In particular the larger secondary flow due to reduced fluid momentum behind the casing recess is quite apparent. The relative reduction in the magnitude of the velocity over the tip for the recessed case is also apparent from the two vector plots.

Table 2   Run conditions

Absolute press. ratio across the blade row	0.44
Reynolds number (based on inlet relative conditions) and blade chord.	200,000
Inlet Mach number (relative)	0.38
Dimensionless rotation rate, ω	0.0254
$T_{wall}/T_{total\ at\ inlet}$	0.7
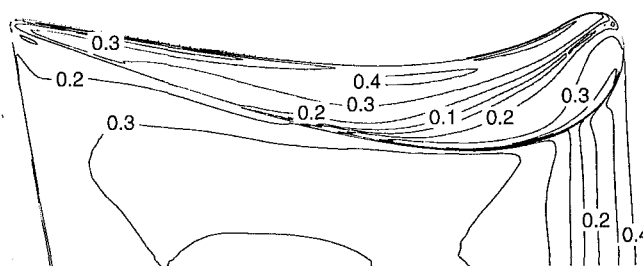
Fig. 4   Distribution of y^+ on and near the blade tip; G = 3 percent

(a)

(b)
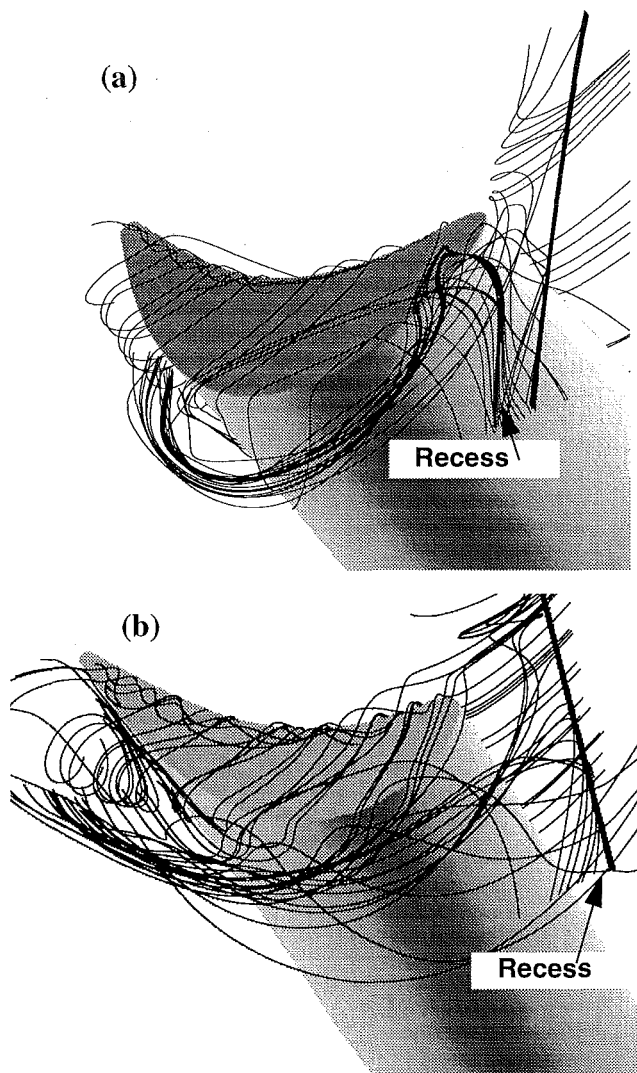
Fig. 5 Streamline patterns for (a) G = 1.5 percent, R/G = 1 at d = 15 percent and (b) G = 3 percent and R/G = 1, d = 25 percent

Further observations with regard to the flow structure will be made in connection with heat transfer in the ensuing sections.

Heat Transfer. The present computational method has been applied to a variety of turbine heat transfer problems by using an algebraic turbulence model (Ameri and Steinthorsson, 1995, 1996). The present turbulence model was tested against the heat transfer data of Metzger et al. (1989) for flow over a cavity to show suitability of the model for blade tip recess flows (Ameri et al., 1998). Very good comparison using the current method for blade surface heat transfer with experimental data was achieved by Garg and Rigby (1998). Heat transfer results for internal flows can be found from Rigby et al. (1996, 1997a).

The rate of heat transfer is presented in terms of Stanton number defined as:

$$St = \frac{h}{(\dot{m}/A)_{inlet} C_p} \qquad (1)$$

where h is the heat transfer coefficient based on the absolute inlet total temperature, C_p is the constant pressure specific heat (assumed a constant), $\dot{m}$ is the mass flow rate, and A is the inlet area. The ratio of $\dot{m}/A$ is very much a constant for the cases considered.

Blade Heat Transfer. Figure 7 shows the rate of heat transfer at the midspan. By referring to this figure and specifically the
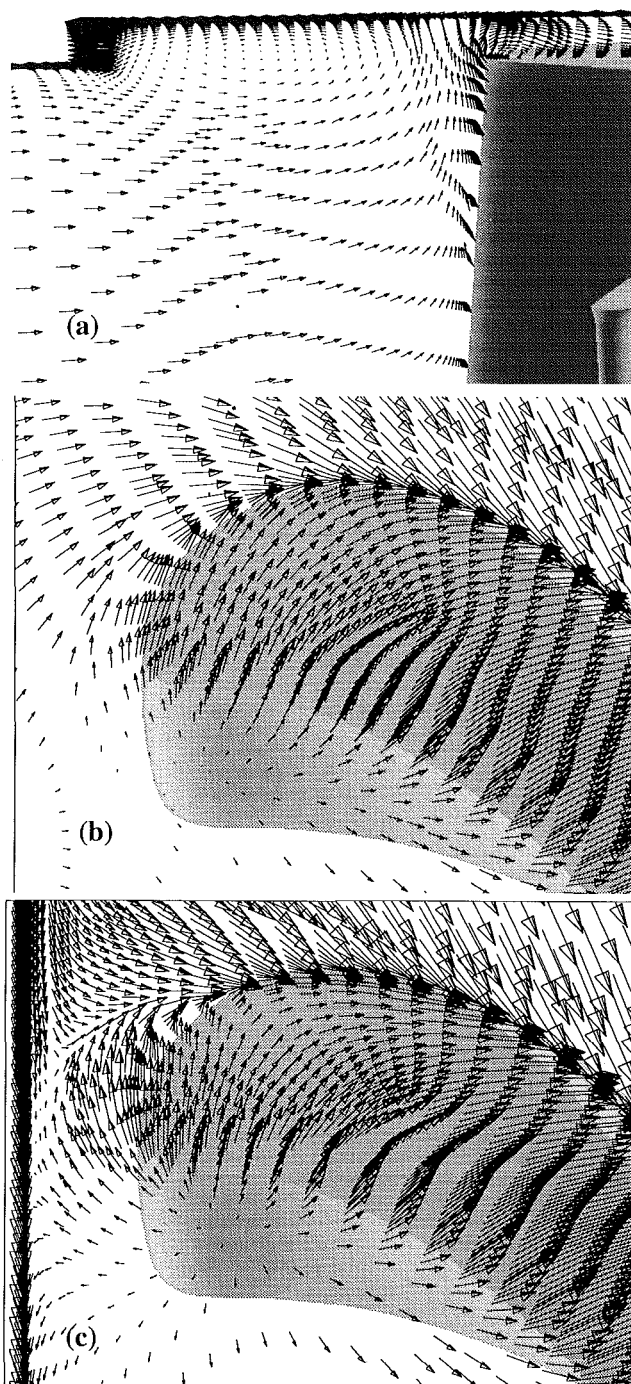
Fig. 6 Velocity vectors (a) behind the casing recess showing the recirculation zone, and radial location midgap of the tip clearance, G = 1.5 percent for, (b) no casing recess and (c) level recess at d = 0.15
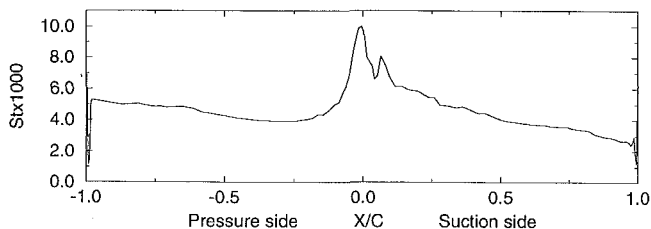
Fig. 7 Midspan blade heat transfer
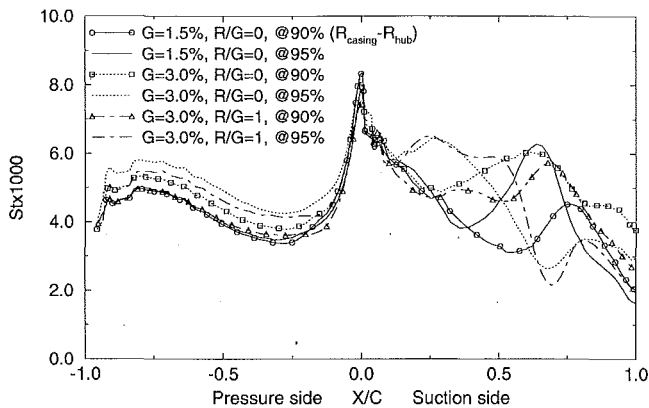
Fig. 8 Heat transfer near the tip as affected by the tip clearance height and casing recess

magnitude of the rate of heat transfer at the stagnation point, an appreciation can be gained for the magnitude of the rate of heat transfer shown elsewhere on the blade.

Figure 8 shows the blade heat transfer rate at two locations of 90 and 95 percent passage height. On the pressure side, the effect of increase in tip clearance height is to increase the blade heat transfer near the tip. Also discernible is the increase in heat transfer as the tip itself is approached due to sink effect. Introduction of a casing recess causes a drop in the pressure side heat transfer.

The heat transfer on the suction side is more complex. Figure 9 shows the suction side heat transfer contours near the tip for a number of cases. The contour plots are provided for two gap clearances of 1.5 and 3 percent and for a range of casing recess heights as needed. Figures 9(a) and 9(e) show that the effect of doubling the gap height on the suction side heat transfer is to enlarge the area on the blade influenced by the tip vortex flow, thus raising the suction side heat transfer load. The peak heat transfer for the smaller tip clearance is larger. This could be attributed to the effect of the secondary flow that runs across the passage toward the blade suction side. In Fig. 10(a) the velocity vectors at a location near the crown of the blade for the $G = 1.5$ percent, $R/G = 1$, and $d = 15$ percent are shown. The effect of the crossflow on the suction side of the blade is obvious from the figure. The "hot spots" near the tip in Figs. 9(b), 9(c), and 9(d) are attributable to this effect. The tip clearance flow on the other hand in Fig. 10(b) dominates the suction side of the blade. The 3 percent tip clearance cases all have the tip vortex dominant flows on the suction side. There is a gradual reduction of the heat loading on the suction side as the casing recess height is increased.

Tip Heat Transfer. Tip heat transfer will be presented in the form of contour plots of Stanton number accompanied by a line plot representing the average rate of heat transfer on the blade tip as a function of axial distance.

Figure 11 shows the rate of heat transfer as measured by Stanton number on the tip of the blade for three gap clearances. The line plot shows that the increasing tip clearance gap elevates the rate of heat transfer over the upstream portion of the blade but has the opposite effect on the downstream portion. Near the trailing edge, the heat transfer is mostly dominated by the size and the extent of the separation bubble.

In Fig. 12, the flow over the blade tip at three locations along the blade for the case of 3 percent tip clearance is presented. The separation of the flow upon entering in the gap is evident from that figure. The locations of flow reattachment in the planes considered have been marked with white arrows. The tip flow at the location farthest downstream on the blade shows that the hot gas from the core does not come in contact with the tip surface. Examination of the tip flow for smaller gaps (not shown to conserve space) revealed that the location on the tip where the flow does not
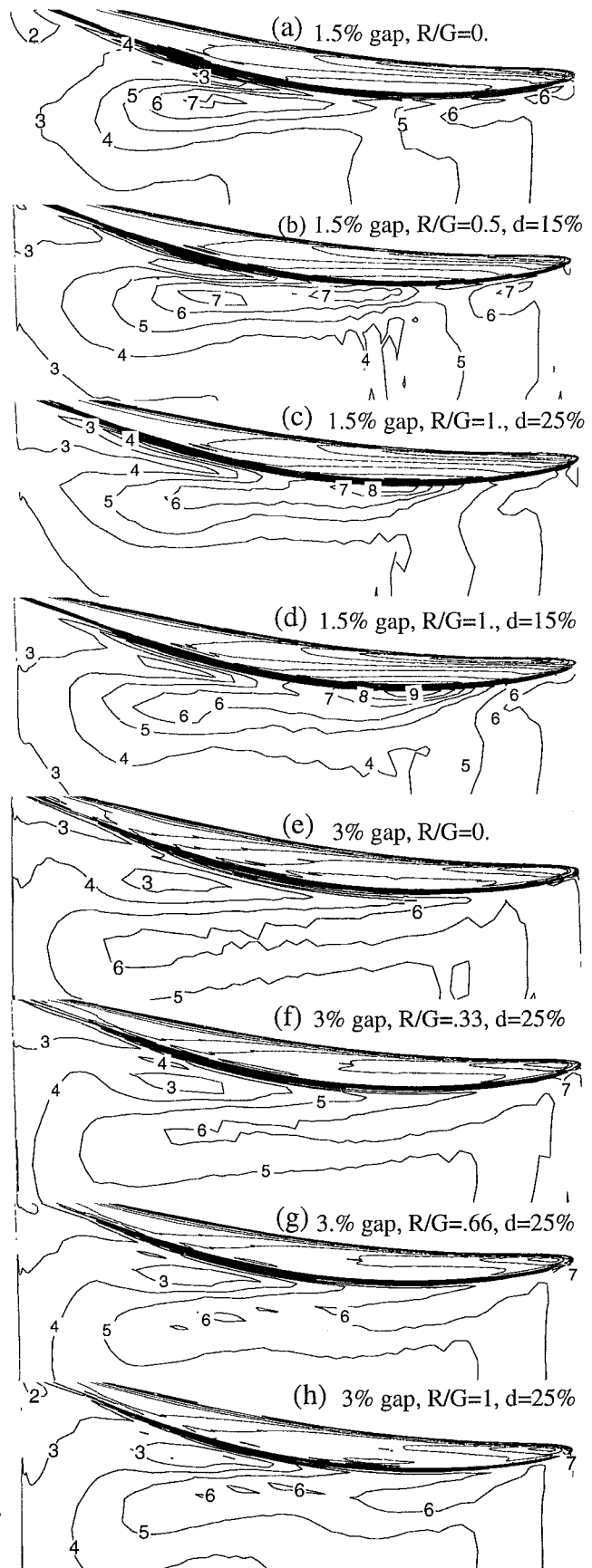
Fig. 9 Near-tip suction side heat transfer (1000× Stanton No.)

reattach moves downstream as the gap narrows. Therefore, the larger the gap size, the larger the portion of the blade where the

(a)

L.E.

(b)

T.E.
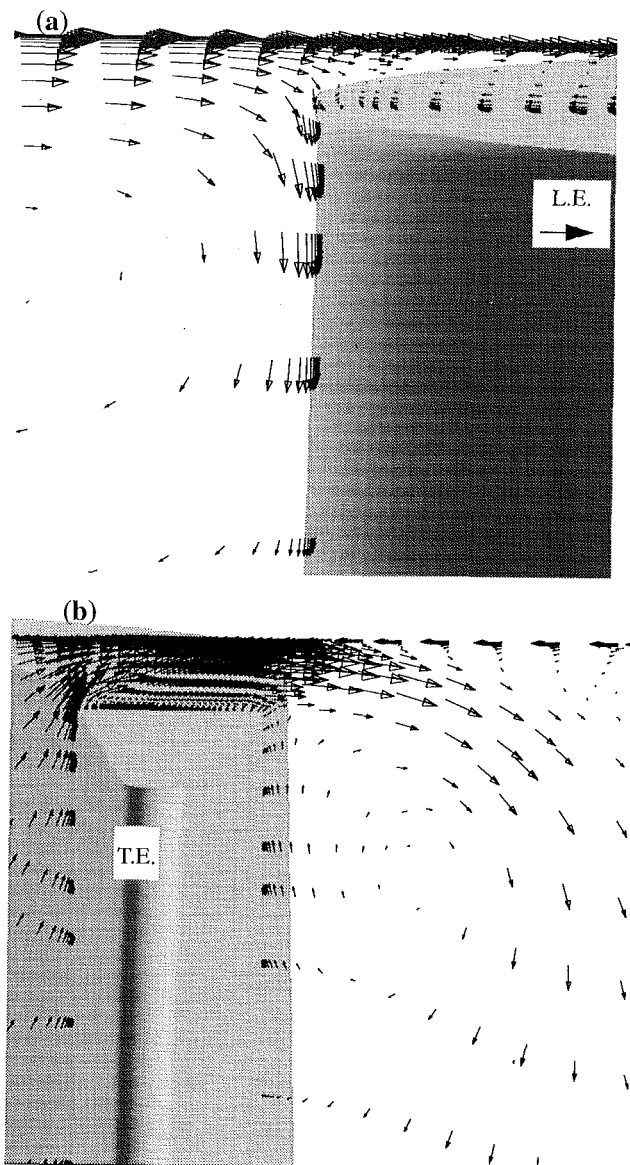
Fig. 10 Velocity vectors near the tip on the blade suction side for (a) $G = $ 1.5 percent, $R/G = 1$, and $d = 15$ percent and (b) $G = 3$ percent, $R/G = 1$

No Recess.

G=1%

(a)

G=1.5%

G=3.%

(b)

Fig. 11 (a) Contours of 1000 × Stanton number over the blade tip for three gap widths and (b) line plot of the average tip heat transfer as a function of the axial distance

flow is unattached, leading to smaller heat transfer rates in the downstream portion of the blade tip. Further discussion of the effect of the tip clearance height on the blade tip will be given at the end of this section.

To investigate the effect of casing recess on the tip heat transfer, two gap clearances of 1.5 and 3 percent were considered. Figures 13(a) and 13(b) show the effect of casing recess upstream of the blade row for $G = 1.5$ percent. A range of R/G values from 0 to 1.5 was considered. The casing recess was placed at 25 percent chord upstream. The contour plots show the local effect of the upstream recess on the blade tip heat transfer. Looking at the peak heat transfer, it can be seen that the recess on the casing reduces the peak level of heat transfer, and in general the larger the recess, the smaller the peak heat transfer. The line plot at the bottom shows the integrated average of the tip heat transfer over the blade tip. The line plots show a decreasing level of tip heat transfer as a function of casing recess depth. A different set of calculations was run for the recess placed at 15 percent chord upstream of the blade row. Figure 14 shows the results of those runs. The line plot in Fig. 14(b) clearly shows that the effect on the tip heat transfer is larger in this case ($d = 15$ percent) as compared to the case of $d = 25$ percent as one would expect intuitively.

Figure 15 shows the variation of the tip heat transfer as a function of recess depth for the larger 3 percent tip clearance. A range of recess depths is chosen, namely, R/G's of 0, 1/3, 2/3 and 1, the latter being even with the blade tip. The reduction of the tip heat transfer is again apparent from that figure; however, in this case it appears to be confined mainly to the forward portion. The reason is that for this large clearance gap the gas flows relatively unimpeded over the aft portion of the tip and is less affected by the presence of a casing recess upstream of the blade.

Figure 16 shows plots of relative total temperature, relative velocity magnitude, turbulence intensity, and kinetic energy of turbulence for the 1.5 percent clearance and no upstream recess (base case). Figures 17 and 18 show the ratios of the same quantities for $G = 1.5$, $R/G = 1$ and $G = 3$ percent, $R/G = 0$
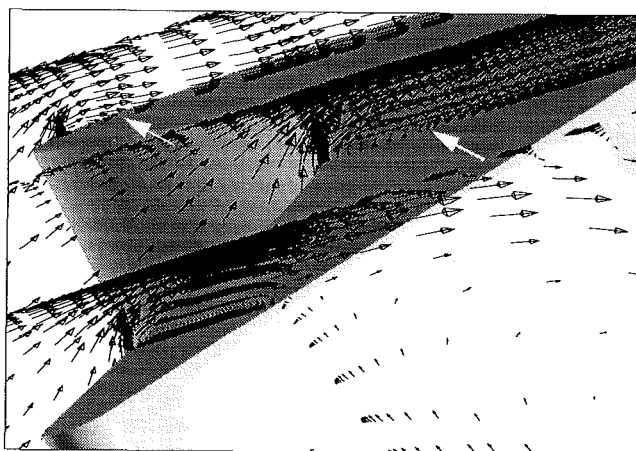
Fig. 12 Velocity vectors showing flow through the tip clearance at three locations. Observed flow reattachment is marked by the arrow.

(a)

R/G=0

R/G=0.5

R/G=1

R/G=1.5

d=25%
G=1.5%

(b)
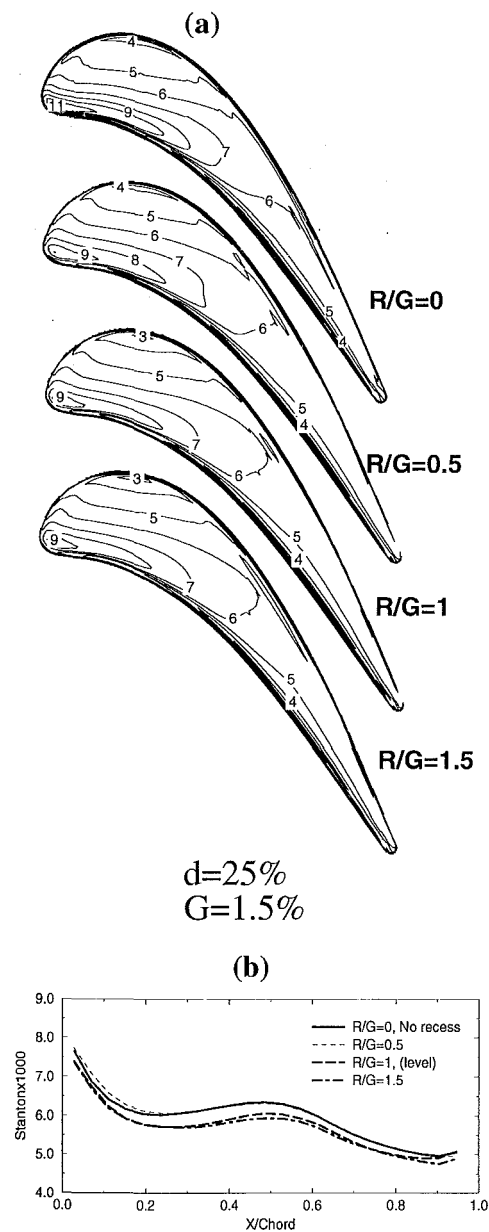
Fig. 13 (*a*) Contours of 1000 × Stanton number over the blade tip and (*b*) line plots of average tip heat transfer; *d* = 25 percent, *G* = 1.5 percent

(a)

R/G=0

R/G=0.5

R/G=1

R/G=1.5

d=15%
G=1.5%

(b)

Fig. 14 (*a*) Contours of 1000 × Stanton number over the blade tip and (*b*) line plots of average tip heat transfer; *d* = 15 percent, *G* = 1.5 percent

cases to the corresponding quantities of the base case. The purpose of those figures is to aid in determining the cause of change in tip heat transfer by the presence of a recess or by an increase in tip clearance. Referring to Figs. 16, 17, and 18, judging by the levels of turbulence intensity, it is likely that the tip flows are all fully turbulent. The drop in heat transfer for the case in Fig. 17 (corresponding to Fig. 14, $R/G = 1$) appears to be due to the reduction in the total temperature as well as the flow velocity. In fact, if one assumes a relationship of wall heat flux proportional to velocity ratio to a 0.8 power, which is commonly done for a turbulent boundary layer flow, it appears as though most of the drop in heat transfer on the tip can be accounted for by the velocity drop. The same can be said for the 3 percent clearance, where the increase in the tip heat transfer in the attached flow regions is associated with an increase in velocity.

Casing Heat Transfer. Information on the casing heat transfer can be used for cooling of the casing to alleviate "hot spots" or for the purposes of active control of tip clearance. Since the grid

rotates at the blade rotation rate, there is no unsteady effect due to rotation which is not accounted for in the calculations.

Figure 19 shows the effect of tip gap height on the circumferentially averaged casing heat transfer. The casing heat transfer, as should be expected (Epstein et al., 1985), drops by a large factor (~5) along the axial direction. It is also shown that the casing heat transfer is markedly affected by the tip clearance gap. The trend is shown to be an increase in heat transfer as the gap widens. The change in the level of heat transfer on the casing is initiated near the blade leading edge and persists past the trailing edge of the blade.

Casing heat transfer is also expected to be influenced by the presence of the recess on the casing. Figure 20 shows the effect of casing recess on the casing heat transfer. The dip on the heat transfer curve corresponds to a location just downstream of the recess where the casing is in the recirculating flow region. There is

(a)

R/G=0

R/G=0.33

R/G=0.66

R/G=1.

d=25%
G=3.0%

(b)

| R/G=0, No recess |
| R/G=0.33 |
| R/G=0.66 |
| R/G=1. (level) |

X/Chord
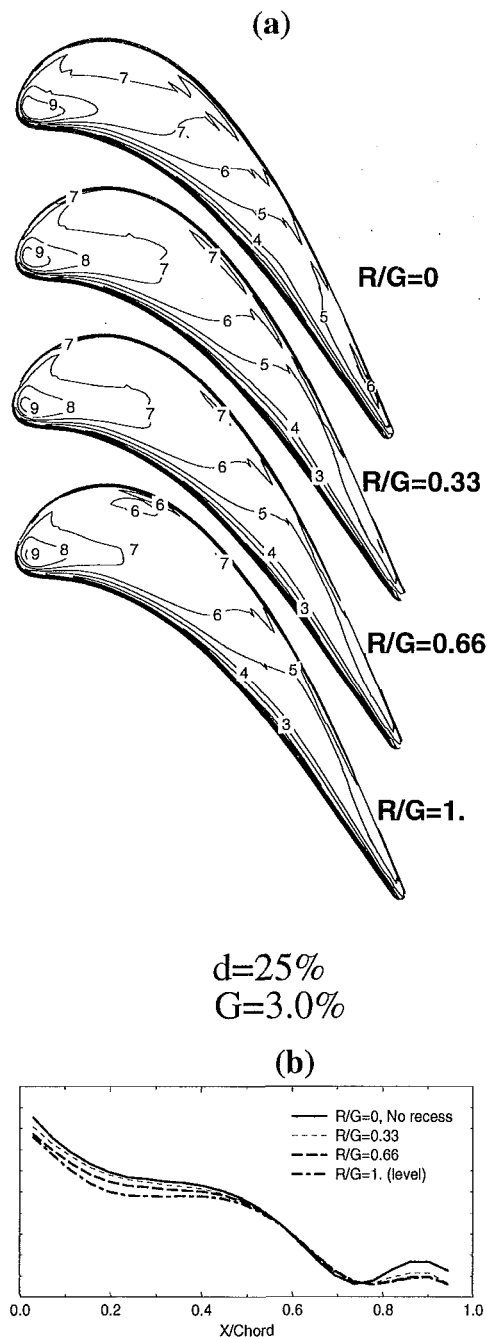
Fig. 15 (a) Contours of 1000 × Stanton number over the blade tip and (b) line plots of average tip heat transfer; d = 25 percent, G = 3.0 percent

T_{t1}

V_1

Tu_1

k_1

G=1.5%
R/G=0.

Fig. 16 Relative total temperature, velocity magnitude, turbulence intensity, and kinetic energy of turbulence at midgap, G = 1.5 percent, R/G = 0

some reduction on the rate of heat transfer on the casing due to the presence of the recess; however, it appears to be slight.

Tip Mass Flow. Figure 21(a) is a plot of mass flow rate through the tip clearance normalized by inlet mass flow rate. There is a linear relationship between the mass flow through the clearance and the tip clearance height. Figure 21(b) shows the mass flow rate through the tip gap as the upstream recess is introduced. The case of 1.5 percent tip clearance shows an increase in the mass flow rate as recess is introduced initially but shows a reduction thereafter. The mass flow rate is normalized by the tip mass flow rate without the casing recess, which is quite small for the G = 1.5 percent case, and therefore the variations in the mass flow due to the presence of the casing recess are quite small. For the 3 percent clearance, the effect of clearance height is more uniform. The

reduction in velocity in the tip region of Fig. 17 is due to blockage of the flow coming from the inlet. The fact that the mass flow rate does not change greatly suggests that the flow through the tip clearance is mainly due to the pressure difference across the blade.

Exit Angle. An important variable in the design of turbine stages is the exit angle. It is known that as the gap widens, the unguided flow through the clearance increases, and therefore it causes the flow to enter the next set of blades at an angle other than the intended design angle. Figure 22 shows the pitchwise-averaged exit angles at two axial locations for the clearance heights considered with and without casing recess. The solid lines are for cases without casing recess. All the runs having the same tip clearance height are represented with the same symbol for the purposes of easy identification. The intended design values at hub, mean, and tip are taken from Timko (1982) and are also included.

The exit angle associated with zero clearance is represented by a thick solid line without symbols. The no-clearance case is overturned near the casing (as near the hub) due to secondary flows. On the other hand, cases with tip clearance have various degrees of underturning proportional to the tip clearance height due to the
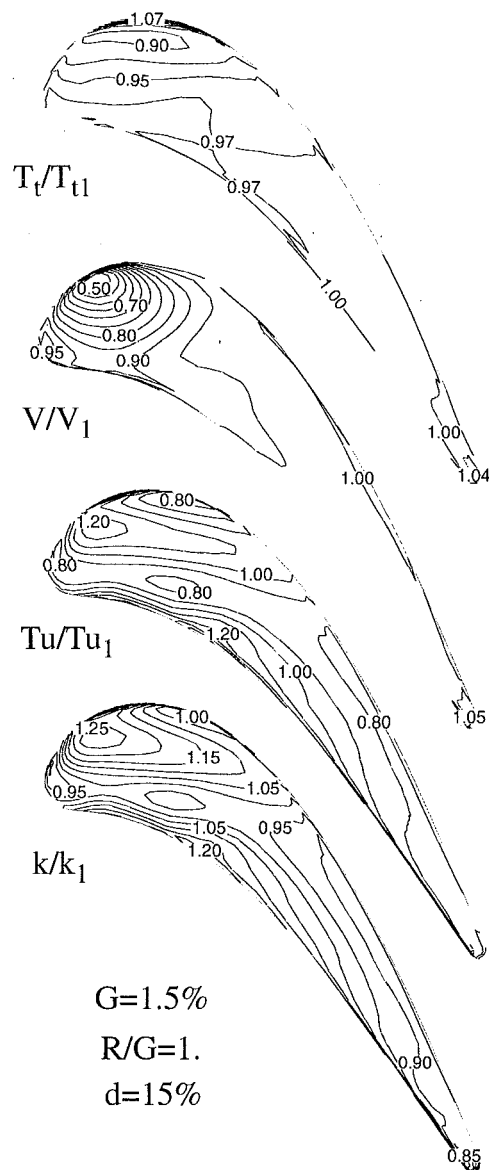
Fig. 17 Ratios of relative total temperature, velocity magnitude, turbulence intensity, and kinetic energy of turbulence at mid gap, G = 1.5 percent, R/G = 1, d = 15 percent
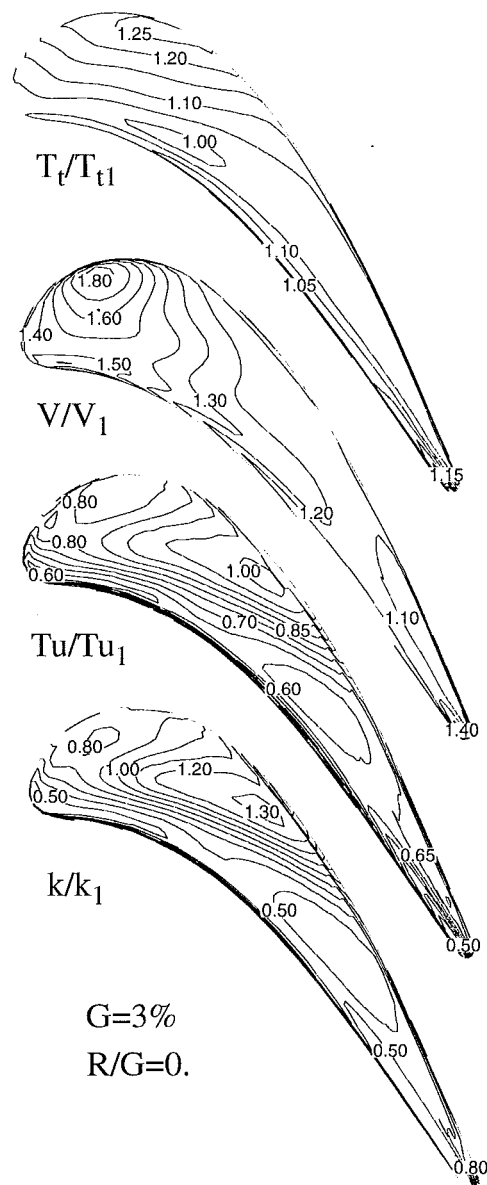
Fig. 18 Ratios of relative total temperature, velocity magnitude, turbulence intensity, and kinetic energy of turbulence at midgap, G = 3 percent, R/G = 0

suction side tip vortex. In Fig. 22(a), the no-clearance case has formed a maximum turning limit for all the other cases considered. Addition of a recess has a worsening effect for the case of large tip clearance but has an obvious moderating effect for the lower tip clearance height.

Efficiency. In a previous paper Ameri et al. (1998) presented a method to compute the adiabatic efficiency as a by-product of the heat transfer calculations. The expression used for the calculation of the adiabatic efficiency is:

$$\eta = \frac{T'_{in} - T'_{ex}}{T'_{in}\left[1 - \left(\dfrac{p'_{ex}}{p'_{in}}\right)^{(\gamma-1)/\gamma}\right]} \quad (2)$$

In this formula T' and P' signify the mass-averaged, absolute total temperature and pressure. The subscripts in and ex signify the integration location's inlet and outlet of the computational domain and γ is the specific heat ratio. Since the calculations are done with a wall boundary condition other than adiabatic, the exit total

temperature is corrected for the heat transfer. Further details can be found in Ameri et al. (1998).

For the present set of calculations, the integration planes are located at 50 percent chord upstream of the blade and 100 percent chord downstream of the blade. The exit location was selected relatively far downstream to allow for mixing to take place and therefore allow for the differences in efficiency to become apparent. Figure 23 shows the effect of the height of the tip clearance gap on the adiabatic efficiency without the presence of the casing recess. The calculations were performed for the case of no tip clearance as well as 1, 1.5, and 3 percent tip clearance cases. The solid line is a best fit to the calculations. The variation of efficiency with gap height is seen to be linear with a slope of ~1.5 point per percent gap clearance. Both the linearity and the magnitude of the slope agree with the general rule of thumb exercised by designers. The open symbols are calculated from a graphic correlation proposed by Hong and Groh (1966) as reproduced in NASA SP-290 edited by Glassman (1994). The graphic correlation expresses the efficiency as a fraction of efficiency with no clearance. The no-clearance value is obtained by extrapolation. The variation of
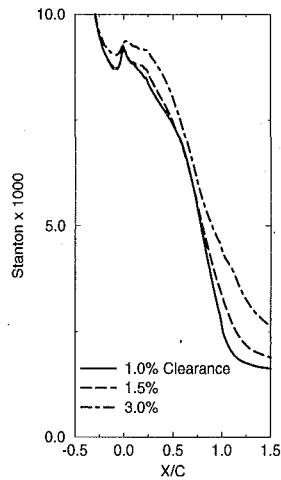
Fig. 19 Circumferentially averaged heat transfer on the casing as affected by the tip clearance height

efficiency as shown in Fig. 23 provides confidence in the results of the calculations. The efficiencies calculated suggest that the losses associated with the tip clearance are approximately 20, 30, and 45 percent of the total losses for the case of 1, 1.5, and 3 percent
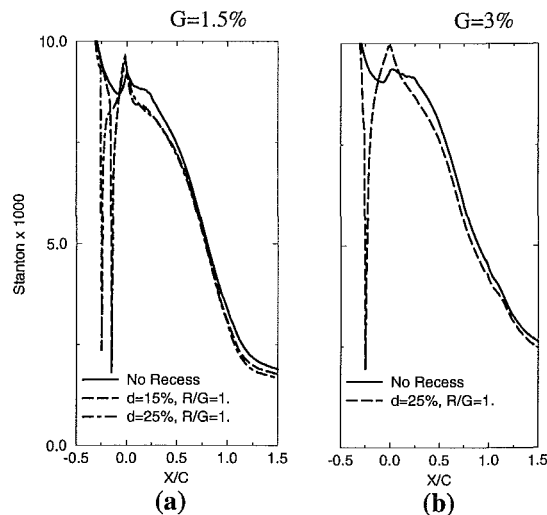
Fig. 20 Casing heat transfer as affected by the presence of the recess: (a) 1.5 and (b) 3 percent clearance
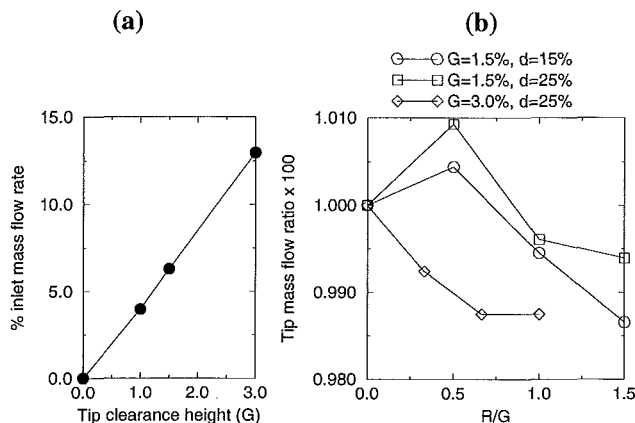
Fig. 21 (a) Tip clearance mass flow rate normalized by the inlet mass flow rate versus tip clearance height. (b) Tip clearance mass flow rate normalized by the tip mass flow rate without recess versus recess depth.
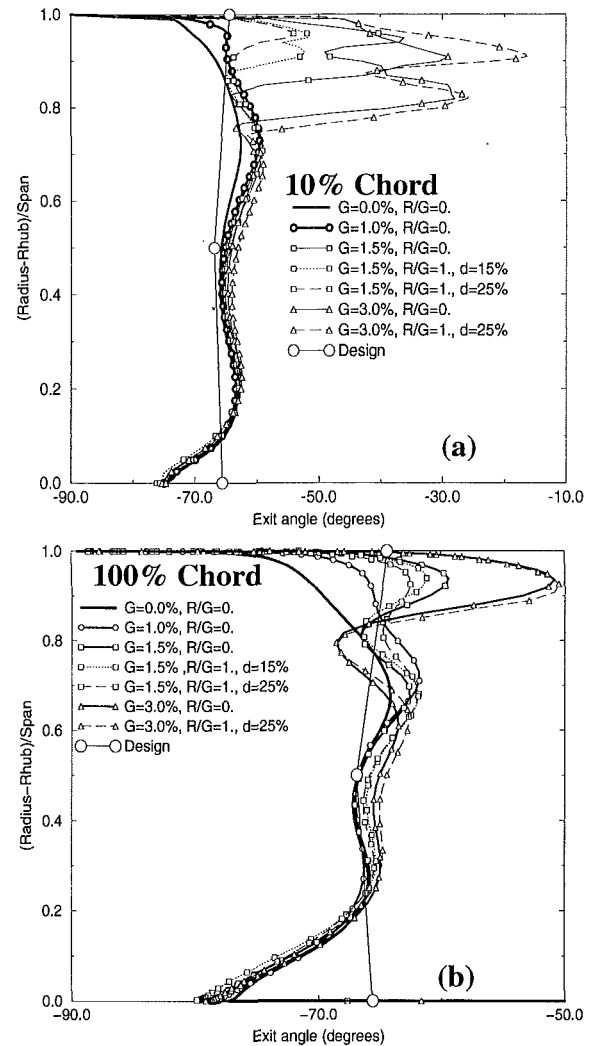
Fig. 22 Exit angle at (a) 10 percent chord and (b) 100 percent chord downstream of the blade row

clearance, respectively. This is in agreement with the work of Boyle et al. (1985) and confirms the suggestion made elsewhere that measures taken to reduce the losses due to tip leakage can have a significant effect on the total losses, especially when operating with relatively wide tip clearance.

The magnitudes of efficiency calculated here were changed slightly by the presence of the recessed casing. Table 3 shows the calculated efficiency for the 1.5 percent tip clearance cases considered. For the 1.5 percent clearance gap the magnitude of the efficiency without the recess was calculated to be 92.06 percent. For $d = 15$ percent at $R/G = 0.5$ the magnitude of the efficiency
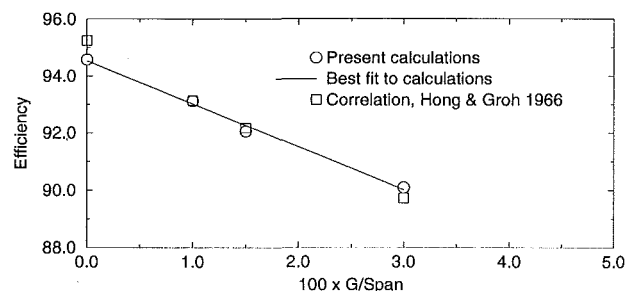
Fig. 23 Adiabatic efficiency as affected by the tip clearance height

Table 3 Efficiency, G = 1.5 percent

	R/G=0	R/G=0.5	R/G=1.	R/G=1.5
d=15%	92.06	92.24	91.85	92.16
d=25%	92.06	92.07	92.29	92.04

rose to 92.24 percent, which although it is a 0.2 percent increase, it constitutes 8 percent of the losses due to tip clearance. For $d = 25$ percent, the efficiency rose to 92.29 percent or 9.5 percent of the tip clearance losses at $R/G = 1$. For the $d = 15$ percent case the value of efficiency for $R/G = 1$ appears to be anomalous, although no reason for this drop in efficiency was found. More points might be required to capture the highs and lows of this relationship.

Table 4 contains the efficiency values for the 3 percent tip clearance cases. The efficiency reaches a maximum of 90.28 percent or an increase of 0.2 percent compared to the no-recess condition. This is an increase equivalent to recovering 4.5 percent of the losses due to the tip clearance. A trend can be inferred from the table where there is an intermediate value of casing recess height for which the efficiency reaches a peak. Further increase in the recess height leads to losses in the flow that can offset the gains otherwise attained.

Summary and Conclusions

In this paper, results are presented from three-dimensional simulations of flow and heat transfer in an unshrouded turbine rotor passage with and without casing recess. Casing recess is a configuration often found in turbine blade passages. For the purposes of the calculations, a generic modern gas turbine blade, namely that of first-stage rotor of $GE\text{-}E^3$ turbine, was selected. A multiblock grid was generated to discretize the flow field. Clearance heights of 0, 1, 1.5, and 3 percent of the passage height were considered. For the two largest clearance heights considered, different recess depths were studied.

There was an increase in the thermal load on all the heat transfer surfaces considered due to enlargement of the clearance gap.

Introduction of recessed casing resulted in a drop in the rate of heat transfer on the pressure side, but the picture on the suction side was found to be more complex for the smaller tip clearance height considered. For the larger tip clearance height the effect of casing recess was a reduction in the suction side heat transfer.

There was a marked reduction of heat load and peak values on the blade tip upon introduction of casing recess; however, only a small reduction was observed on the casing itself.

It was reconfirmed that there is a linear relationship between the efficiency and the tip gap height. It was also observed that the casing recess has a small effect on the efficiency.

It was also observed that the recessed casing can have a moderating effect on the flow underturning at smaller tip clearances.

Table 4 Efficiency, G = 3 percent

	R/G=0	R/G=1/3	R/G=2/3	R/G=1.
d=25%	90.09	90.28	90.15	90.03

Acknowledgments

References

Ameri, A. A., and Steinthorrson, E., 1995, "Prediction of Unshrouded Rotor Blade Tip Heat Transfer," ASME Paper No. 95-GT-142.

Ameri, A. A., and Steinthorrson, E., 1996, "Analysis of Gas Turbine Rotor Blade Tip and Shroud Heat Transfer," ASME Paper No. 96-GT-189.

Ameri, A. A., Steinthorsson, E., and Rigby, D. L., 1998, "Effect of Squealer Tip on Rotor Heat Transfer and Efficiency," ASME JOURNAL OF TURBOMACHINERY, Vol. 120, pp. 753–759.

Boyle, R. J., Haas, J. E., and Katsanis, T., 1985, "Comparison Between Measured Turbine Stage Performance and the Predicted Performance Using Quasi-3D Flow and Boundary Layer Analyses," *J. Propulsion Power*, Vol. 1, No. 3, pp. 242–251.

Briley, W. R., Roscoe, D. V., Gilbeling, H. J., Buggeln, R. C., and Sabnis, J. S., 1991, "Computation of Flow Past a Turbine Blade With and Without Tip Clearance," ASME Paper No. 91-GT-56.

Epstein, A. H., Guenette, G. R., Norton, R. J. G., and Cao Yuzhang, 1985, "Time Resolved Measurements of a Turbine Rotor Stationary Tip Casing Pressure and Heat Transfer Field," AIAA Paper No. 85-1220.

Garg, V. K., and Rigby, D. L., 1998, "Heat Transfer on a Film-Cooled Blade-Effect of Hole Physics," ASME Paper No. 98-GT-404.

Glassman, A. J., 1994, *Turbine Design and Application*, NASA SP-290.

Haas, J. F., and Kofsky, M. G., 1979, "Effect of Rotor Tip Clearance and Configuration on Overall Performance of a 12.77-Centimeter Tip Diameter Axial-Flow Turbine," NASA TM 79025.

Halila, E. E., Lenahan, D. T., and Thomas, T. T., 1982, "Energy Efficient Engine, High Pressure Turbine Test Hardware Detailed Design Report," NASA CR-167955.

Hong, Yong S., and Groh, F. G., 1966, "Axial Turbine Loss Analysis and Efficiency Prediction Method," Rep. D4-3220, Boeing Co., Mar. 11.

Kaiser, I., and Bindon, P. J., 1997, "The Effect of Tip Clearance on the Development of Loss Behind a Rotor and a Subsequent Nozzle," ASME Paper No. 97-GT-53.

Menter, F. R., 1993, "Zonal Two-Equation k–ω Turbulence Models for Aerodynamic Flows," Paper No. AIAA-93-2906.

Metzger, D. E., Bunker, R. S., and Chyu, M. K., 1989, "Cavity Heat Transfer on a Transverse Grooved Wall in a Narrow Channel," ASME *Journal of Heat Transfer*, Vol. 111, pp. 73–79.

Rigby, D. L., 1996, "Method of Weakest Descent for Automatic Block Merging," *Proc. 15th Int. Conf. on Num. Methods in Fluid Dynamics*, Monterey, CA, June.

Rigby, D. L., Ameri, A. A., and Steinthorsson, E., 1996, "Internal Passage Heat Transfer Prediction Using Multiblock Grids and k–ω Turbulence Model," ASME Paper No. 96-GT-188.

Rigby, D. L., Ameri, A. A., and Steinthorsson, E., 1997a, "Numerical Prediction of Heat Transfer in a Channel With Ribs and Bleed," ASME Paper No. 97-GT-431.

Rigby, D. L., Steinthorsson, E., and Coirier, W. J., 1997b, "Automatic Block Merging Using the Method of Weakest Descent," AIAA Paper No. 97-0197.

Schlichting, H., *Boundary Layer Theory*, 7th ed., McGraw-Hill, New York, pp. 312–313.

Steinthorsson, E., Liou, M. S., and Povinelli, L. A., 1993, "Development of an Explicit Multiblock/Multigrid Flow Solver for Viscous Flows in Complex Geometries," Paper No. AIAA-93-2380.

Timko, L. P., 1982, "Energy Efficient Engine High Pressure Turbine Component Test Performance Report," NASA CR-168289.

Wilcox, D. C., 1994a, *Turbulence Modeling for CFD*, DCW Industries, Inc., La Canada, CA.

Wilcox, D. C., 1994b, "Simulation of Transition With a Two-Equation Turbulence Model," *AIAA Journal*, Vol. 32, No. 2, pp. 247–255.

Mach Number Effects on Turbine Blade Transition Length Prediction

R. J. Boyle
NASA Glenn Research Center,
Cleveland, OH 44135

F. F. Simon
NASA Glenn Research Center,
Cleveland, OH 44135

The effect of a Mach number correction on a model for predicting the length of transition was investigated. The transition length decreases as the turbulent spot production rate increases. Many of the data for predicting the spot production rate come from low-speed flow experiments. Recent data and analysis showed that the spot production rate is affected by Mach number. The degree of agreement between analysis and data for turbine blade heat transfer without film cooling is strongly dependent on accurately predicting the length of transition. Consequently, turbine blade heat transfer data sets were used to validate a transition length turbulence model. A method for modifying models for the length of transition to account for Mach number effects is presented. The modification was made to two transition length models. The modified models were incorporated into the two-dimensional Navier–Stokes code, RVCQ3D.Comparisons were made between predicted and measured midspan surface heat transfer for stator and rotor turbine blades. The results showed that accounting for Mach number effects significantly improved the agreement with the experimental data.

Introduction

The accuracy of predictions for turbine blade aerodynamics and heat transfer is affected by the accuracy in predicting the region of transitioning flows. The locations on the blade where transition begins and ends can affect the aerodynamic performance. In applications where turbine blade film cooling is absent, knowledge of where transition begins and ends is important in predicting surface heat transfer. As discussed by Mayle (1991), there is an extensive amount of experimental data showing that the start and length of transition are functions of Reynolds number, turbulence intensity, and pressure gradient, in addition to any periodic disturbances that may be present.

Much of the recent theoretical analysis for the length of transition utilizes the spot production concept of Emmons (1951) for intermittency. Narasimha (1957) proposed that the intermittency follows an exponential behavior, with the exponential term being proportional to the square of the distance from the start of transition. The model proposed by Chen and Thyson (1971) accounted for variable free-stream velocity on the length of transition by an integral relationship in the exponential term. Two different approaches have been used to account for the effects of turbulence intensity and pressure gradient on the length of transition. Simon (1995), Gostelow et al. (1994), and Fraser et al. (1994) accounted for these effects by assuming that the flow conditions at transition onset were the dominant influences. Solomon et al. (1996) extended the approach of Chen and Thyson (1971) to account for free-stream flow variations on the length of transition.

Most of the experimental data used to develop correlations for the transition length were obtained at incompressible flow conditions. There is only a limited number of data that show the effect of Mach number on transition for the transonic flow regime. Dey and Narasimha (1985) proposed a variation in the spot formation rate with Mach number. Their variation showed no change in the spot formation rate until a Mach number of two, followed by a rapid decrease in the Mach two-to-four range. Recent data from Clark et al. (1994) showed that the effect of Mach number on

turbulent spot parameters was significant at substantially lower Mach numbers. Mack (1969) showed the effect of Mach number on the frequency of the Tollmein–Schlichting waves, which in turn affects the spot formation rate.

The transition spot data of Clark (1993), and the frequency results of Mack (1969) were used to derive modifications to account for the effect of Mach number on the length of transition. The modifications were incorporated into the models proposed by Simon (1995), and Solomon et al. (1996). These models were then implemented in a Navier–Stokes code. The code used, RVCQ3D, has been documented by Chima (1987) and Chima and Yokota (1988). Comparisons with experimental turbomachinery data showed that incorporating Mach number effects into the transition length model improved the agreement with experimental data. Accurate transition predictions are important whether or not surface heat transfer is present. Turbine blade heat transfer data can dramatically show transition behavior, and data are available at high free-stream Mach numbers. Therefore, turbine blade heat transfer data were chosen to illustrate the importance of including a Mach number effect on the length of transition.

The work presented herein consists of a discussion of how Mach number effects were incorporated into the transition length model. Comparisons are then shown for a variety of turbine conditions to show that incorporating a Mach number effect significantly improves the degree of agreement with the experimental data. Comparisons are made with data for both stator and rotor geometries for a range of turbulence intensities and Reynolds numbers. This is done to demonstrate that the Mach number effect is a general one, which leads to an overall improvement, and not just for a specific test case. Results are shown for two different transition length models in order to demonstrate that the results are not a function of a particular transition length model.

Description of Analysis

In the transition region the effective eddy viscosity, μ_{EFF}, is given by:

$$\mu_{EFF} = \mu_{LAM} + \gamma\mu_{TURB}$$

Different approaches have been used to determine the value of intermittency, γ. Two recent approaches to calculating the value of

Copyright © 1999 by ASME

γ are those of Simon (1995) and Solomon et al. (1996). In both methods the intermittency, γ, is a function of the pressure gradient λ. In the model of Solomon et al., the intermittency is also a function of the turbulence intensity, Tu. Simon's (1995) method utilizes an analytically developed value for the spot production rate, while the method of Solomon et al. (1996) utilizes an experimentally derived correlation for the spot production rate.

Simon's Model. In Simon's (1995) model γ is based on the intermittency path equation derived by Narasimha (1957):

$$\gamma_{Simon} = 1.0 - \exp[-n\sigma(\mathrm{Re}_S - \mathrm{Re}_{S-ST})^2]$$

The parameters in this equation are given by:

$$n\sigma = N/\mathrm{Re}_{\theta_{ST}}^3$$

Simon (1995) developed an analytic value for the nondimensional spot production rate, N:

$$N = 8.1 \times 10^{-4} \left(\frac{\Lambda \tan \alpha}{\beta} \right)^2_{ST}$$

Simon and Ashpis (1996) showed results using values for Λ, α, and β determined from the data of Gostelow et al. (1996). The dimensionless spot parameter, Λ, is the ratio of the spot area to the square of the spot half-width. Λ was determined from the zero pressure gradient data to be 2.88. α and β at the start of transition were taken as functions of pressure gradient:

$$\alpha_{ST} = 4.0 + \left(\frac{22.14}{0.79 + 2.72e^{47.63\lambda_{ST}}} \right)$$

$$\beta_{ST} = 0.71 + 1.35/\lambda_{ST}$$

Model of Solomon, Walker, and Gostelow (SWG). In the model developed by Solomon et al. (1996):

$$\gamma_{SWG} = 1.0 - \exp\left[-n \int_{s_{ST}}^{s} \frac{\sigma}{U \tan \alpha} ds \int_{s_{ST}}^{s} \tan \alpha \, ds \right]$$

In this equation n is determined by the values at the start of transition, while σ, α, and U are functions of the local conditions throughout the length of transition. The parameters in the previous equation are:

$$n = \frac{N_{ST}\nu}{\sigma_{ST}\theta_{ST}^3}$$

For favorable pressure gradients, $\lambda_{ST} > 0.0$, and

$$N_{ST} = 8.6 \times 10^{-4} \exp(-10\sqrt{\lambda_{ST}} - 0.564 \ln Tu$$

Otherwise,

$$N_{ST} = 8.6 \times 10^{-4} \exp(2.134\lambda_{ST} \ln Tu$$
$$- 59.23\lambda_{ST} - 0.564 \ln Tu)$$

The variables calculated throughout the transition length are given by:

$$\alpha = 4.0 + \left(\frac{22.14}{0.79 + 2.72e^{47.63\lambda}} \right)$$

$$\sigma = 0.03 + \left(\frac{0.37}{0.48 + 3.0e^{59.2\lambda}} \right)$$

The primary differences between the transition length model of Simon and the SWG model of Solomon et al. (1996) are that Simon's model is based exclusively on the conditions at the start of transition, and that these conditions are not a function of the local turbulence intensity.

There is no explicit Mach number effect for the correlations used in either transition length model. The measurements that provided the data for the correlations were done at low Mach numbers where the flow is incompressible. Clark et al. (1994) reported experimental data showing that the free-stream Mach number affects the spot spreading angle.

Mach Number Effects. Narasimha (1985) postulated that the transition process is likely to be the same for subsonic and supersonic flows. The effect of increasing Mach number is to decrease the longitudinal growth rate of turbulent spots. Owen and Horstman (1972) showed intermittency data at hypersonic Mach numbers that agreed with the intermittency distribution developed by Narasimha (1957) for incompressible flows. Dey and Narasimha (1985) proposed a variation in the nondimensional spot formation rate, N, with Mach number. This variation showed little change up to a Mach number of two. For $2 < M < 4$, N decreases rapidly. Recent data of Clark (1993), however, showed that there was a significant decrease in the spot spreading angle even for Mach numbers less than one. Simon (1995) utilized the method used by

---

Nomenclature

A^+ = near wall damping coefficient
C_m = ratio of compressible-to-incompressible spot production rate
c = true chord
c_x = axial chord
f = frequency
h = heat transfer coefficient
h_R = normalizing heat transfer coefficient
I = incidence angle
K = acceleration parameter
N = nondimensional spot formation rate
n = spot formation rate
Re = Reynolds number

St = Stanton number
S = surface distance
T = temperature
Tu = turbulence intensity
U = free-stream velocity
y = normal distance to surface
α = spot spreading angle
γ = intermittency
θ = momentum thickness
λ = pressure gradient parameter $= (\theta^2/\nu)dU/ds$
Λ = dimensionless spot geometry parameter
ρ = density
σ = dimensionless spot propagation parameter

Subscripts

d = leading edge diameter
GAS = molecular
LAM = laminar
M = value as a function of Mach number
P = pressure surface
S = surface distance from stagnation point; Suction surface
ST = start of transition
T = total surface distance
TURB = turbulent
IN = gas inlet
O = start of transition
0.1 = value at incompressible condition
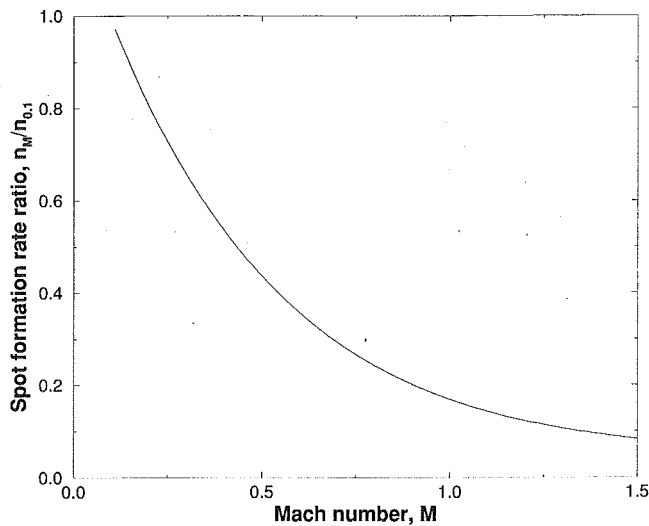2 = blade row exit
99 = percent intermittency

Fig. 1   Effect of Mach number on spot formation rate

Walker (1989) and McCormick (1968), regarding the frequency of spot formation. The turbulent spots are assumed to appear at the frequency of the Tollmein–Schlichting instability wave with the maximum amplification rate. Mack's (1969) analysis showed that the frequency of the Tollmein–Schlichting instability wave with the maximum amplification rate decreased with Mach number up to sonic conditions. Simon (1995) showed that the spot formation rate, N, and thus n, is proportional to the square of the product of the spot formation frequency, f, and the tangent of the spot spreading angle, α:

$$n \propto (f \tan \alpha)^2$$

The spot production rate at a given Mach number, N_M, can be related to the incompressible spot production rate, $N_{0.1}$, by:

$$C_m = \frac{n_M}{n_{0.1}} = \frac{N_M}{N_{0.1}} = \left(\frac{\tan \alpha_M f_M}{\tan \alpha_{0.1} f_{0.1}} \right)^2$$

The turbulent spot spreading angle data of Clark (1993) and the Tollmein–Schlichting wave frequency analysis of Mack (1969) were used to determine the effect of Mach number on the spot formation rate. Figure 1 graphically presents the relationship for the effect of Mach number on spot formation rate. The change in the spot production rate can be viewed as effectively increasing the length of transition by $\sqrt{n_M/n_{0.1}}$.

In summary, the transition length model of Simon including the effect of Mach number is:

$$\gamma_{Simon} = 1.0 - \exp[-n_{0.1}\left(\frac{n_M}{n_{0.1}}\right)\sigma(\mathrm{Re}_S - \mathrm{Re}_{S-ST})^2]$$

The SWG model corrected for Mach number effects is:

$$\gamma_{SWG} = 1.0 - \exp\left[-n_{0.1}\left(\frac{n_M}{n_{0.1}}\right)\int_{S_{ST}}^{S} \frac{\sigma}{U \tan \alpha} ds \int_{S_{ST}}^{S} \tan \alpha ds \right]$$

In each model $n_{0.1}$ is calculated based on the pressure gradient, λ, and, for the SWG model, the turbulence intensity, Tu. The start of transition was specified using Mayle's (1991) method. The momentum thickness Reynolds number at the start of transition is given by:

$$\mathrm{Re}_{\theta-ST} = 400 Tu^{-5/7}$$

The local turbulence intensity, Tu, was determined using an algebraic relationship. To determine the local turbulence from a one or two-equation turbulence model would require knowledge of the inlet length scale. For the cases examined, the inlet length scale was generally not available. The local turbulence intensity was calculated as:

$$Tu = Tu_{IN} U_{IN}/U_S$$

The local free-stream velocity, U_S, was calculated from the local pressure ratio. Mayle (1991) recommended that a lower limit of 3 percent should be used for Tu when calculating Re_θ at the start of transition.

The transition models were incorporated into a quasi-three-dimensional Navier–Stokes analysis, RVCQ3D. This code has been documented by Chima (1987) and Chima and Yokota (1988). C-type grids were generated using the method of Arnone et al. (1992). In this approach, the near-wall grid is embedded within a coarser grid obtained using the method of Sorenson (1980). For this work dense grids were used. A typical grid was 321×51. This was done to achieve high resolution within the transition region. The choice of grid parameters, such as near-wall spacing and stretching ratios, was determined using the results presented by Boyle (1991) and by Boyle and Ameri (1997). Therefore, the conclusions drawn from this work would not be affected by the size of the grids used.

The Baldwin–Lomax (1978) model was used for the turbulent eddy viscosity, μ_{TURB}. This model was used for two reasons. First, it has been shown by Ameri and Arnone (1992) and Chima (1996) that algebraic models of this type predict turbine blade surface heat transfer as accurately as two-equation models. Second, an algebraic model, rather than a two-equation model, allows a more straightforward demonstration of the effects of Mach number on the length of transition.

Because the free-stream turbulence was high for many of the cases examined, the Smith and Kuethe (1966) model was incorporated to account for the effects of free-stream turbulence on the laminar flow. The augmented laminar viscosity is:

$$\mu_{LAM} = \mu_{GAS} + (1.0 - \gamma)0.164\rho y Tu U$$

y is the normal distance from the blade, and μ_{GAS} is the molecular viscosity of the gas. Augmenting the laminar viscosity primarily affects the heat transfer in the leading edge region. The effect of the Smith and Kuethe (1966) model on the pretransition heat transfer will be discussed.

Data Comparisons

In actual turbomachines, most blade rows are subject to periodic flow field variations due to the presence of adjacent blade rows. The accuracy of prediction for the time-averaged heat transfer would be affected by the accuracy in predicting the effects of the periodic disturbances. Since the objective of this work is to illustrate the importance of Mach number effects, comparisons are made for isolated blade row test cases. In these test cases the blades were not subject to periodic disturbances. This eliminated the necessity of accurately predicting the periodic disturbance effect.

The test cases chosen were those that showed transition occurring over a significant fraction of the surface distance. The literature shows many cases where transition occurs over a very short distance near the leading edge or close to the trailing edge. These cases were not suitable test cases. Generally, moderate to high levels of turbulence intensity were required in the test cases. It is necessary to examine data from a variety of different sources, and under different conditions, in order to insure that the proposed method of accounting for Mach number effects results in improved predictive capability. Comparisons with a variety of different cases also illustrates where improvements in the models are needed. Both stator and rotor geometry test cases were examined. The stator cases chosen were from Arts et al. (1990) and Hylton et al. (1983). The rotor cases presented were those of Arts et al. (1998).

Table 1 Stator cases examined

			Suction				Pressure			
Re_2 $\times 10^{-6}$	M_2	Tu %	s_{ST}/s_T	λ_0	s_{99}/s_T	λ_{99}	s_{ST}/s_T	λ_0	s_{99}/s_T	λ_{99}
			Data - Arts et al.(1990)							
2.	0.9	6.0	0.30	0.019	0.78	-0.141	0.12	0.075	0.77	0.105
2.	1.1	6.0	0.30	0.025	0.97	-1.816	0.12	0.078	0.79	0.111
2.	1.1	4.0	0.30	0.024	0.97	-1.922	0.24	0.066	>1	97%
1.	0.8	6.0	0.36	0.053	0.77	-0.083	0.13	0.078	0.76	0.102
1.	1.1	6.0	0.57	0.025	>1	77%	0.10	0.070	0.62	0.133
			Data - Hylton et al.(1983)							
1.5	0.90	8.3	0.28	-0.005	0.58	-0.167	0.10	0.014	0.48	0.114
2.5	1.06	8.3	0.28	-0.009	0.58	0.097	0.09	-0.005	0.25	0.126

These data show rotor surface heat transfer for a range of Mach numbers, Reynolds numbers, and rotor incidence angles.

Stators. Table 1 summarizes the test conditions for each of the cases presented. The Reynolds and Mach numbers, as well as the upstream turbulence intensity, are shown for each case. Predicted values at the beginning and end of transition are also shown in the table. These predictions are for the SWG model with the Mach number effect included. The surface distance at which transition starts, s_{ST}/s_T, and the surface distance at which $\gamma = 99$ percent, s_{99}/s_T, are shown. The total surface distance, s_T, is different for the suction and pressure surfaces. The values given for λ are the predicted values at the beginning and end of transition. The predicted values for s_{99}/s_T and λ_{99} vary according to the transition length model used. The values shown in the table, therefore, are primarily useful for orientation purposes. Where the table entry is > 1 transition was not complete at the end of the vane, and the corresponding percentage number is the γ value at the trailing edge.

Data of Arts et al. (1990). Figure 2 shows a comparison of measured and predicted isentropic surface Mach numbers for this geometry. Data were given at three different exit Mach numbers, M_2, which were somewhat different from the M_2 values used for the heat transfer tests. At the lowest Mach number, the suction surface Mach number peaks midway along the surface. At the highest Mach number, the data show a peak Mach number at 80 percent of the surface distance, and the prediction shows the peak occurring somewhat later. Overall, the analysis agrees well with the data, and predicts most surface velocity gradients accurately.

Figure 3 compares heat transfer predictions with and without a Mach number correction with the experimental data. For this vane geometry, $s_S/c = 1.34$, and $s_P/c = 1.03$. The Stanton number, St, is based on the vane exit conditions. These data are for an exit Reynolds number of 2×10^6, $M_2 = 0.9$, and $Tu = 6$ percent. The
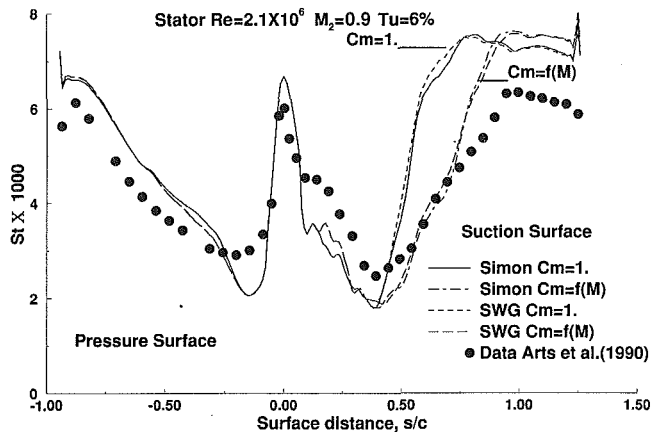
Fig. 3 Effect of Mach number correction on predicted heat transfer

predictions for the suction surface show that both Simon's model and the SWG model show improved agreement with data when the Mach number correction is used. The predicted location for the start of transition on the pressure surface was close to the leading edge. Since this was a low Mach number region, the inclusion of a Mach number effect did not change the transition length prediction. The small differences on the pressure surface are due to the differences between the Simon and SWG turbulence models. Comparing the analysis and data shows that using the ratio of local-to-inlet velocity to calculate the local turbulence intensity for the start of transition gives good agreement with the data.

Figure 4 shows comparisons for the same test conditions as in Fig. 3, but at a higher exit Mach number, M_2, of 1.1. The Mach number at the start of transition is 0.92. For both transition models, including a Mach number correction in the transition length model significantly improves the agreement for the suction surface. Along the aft portion of the suction surface, the analysis overpredicts the heat transfer. The implication of the results in this figure is that even though the Mach number correction substantially affects the length of transition, the effect may be underestimated. Mayle (1991), in a discussion of Sharma's (1987) results, indicated that the intermittency used in the energy equation could be lower than that used in the momentum equations. If this approach had been taken in the analysis, the apparent transition length would be longer.

Figure 5 shows comparisons for a reduced upstream turbulence intensity of 4 percent. The comparisons illustrate the importance of correctly predicting the start of transition. Because of the lower upstream turbulence intensity, the predicted turbulence intensity at
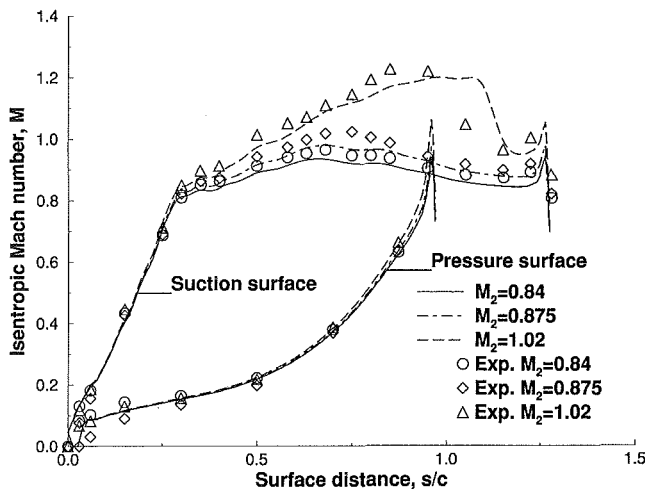

Fig. 2 Isentropic surface Mach number; data of Arts et al. (1990)

Fig. 4 Effect of Mach number correction on predicted heat transfer

Journal of Turbomachinery

Fig. 5 Effect of model assumptions on predicted heat transfer

Fig. 6 Effect of model assumptions on predicted heat transfer

the start of transition was very low. Mayle (1991) recommended that a minimum intensity of 3 percent be used in calculating the start of transition. This value produced a very early transition. Comparisons with the data show that specifying a turbulence intensity of 1.5 percent produced an early suction surface transition, while an intensity of 1 percent gave a transition after the experimental results.

Figure 5 also illustrates the effect of a variable near-wall damping coefficient, A^+, on predicted heat transfer. The variation of A^+ with pressure gradient used is the same as that used by Crawford and Kays (1976) in the STAN5 boundary layer analysis program. Pressure surface transition occurs near the leading edge. The strong favorable pressure gradient results in an increased value for A^+. This in turn reduces the length scale in the near-wall region, giving lower Stanton numbers. Paradoxically, a variable A^+ resulted in increased leading edge heat transfer. This unexpected behavior was caused by the manner in which the Smith and Kuethe (1996) leading edge augmentation model was incorporated into the analysis. The turbulence quantities were calculated everywhere, not just where $\gamma > 0$. The Smith and Kuethe model was applied only in the inner region. However, the distance from the wall at which the turbulence model crossed over from the inner to outer regions was affected by A^+. When A^+ was variable, the Smith and Kuethe model was applied over a greater distance from the wall than when $A^+ = 26$.

Next, comparisons are shown where the exit Reynolds number has been reduced by half. Figures 6 and 7 show results for $Tu = 6$ percent, and exit Mach numbers of 0.8 and 1.1. At this lower Reynolds num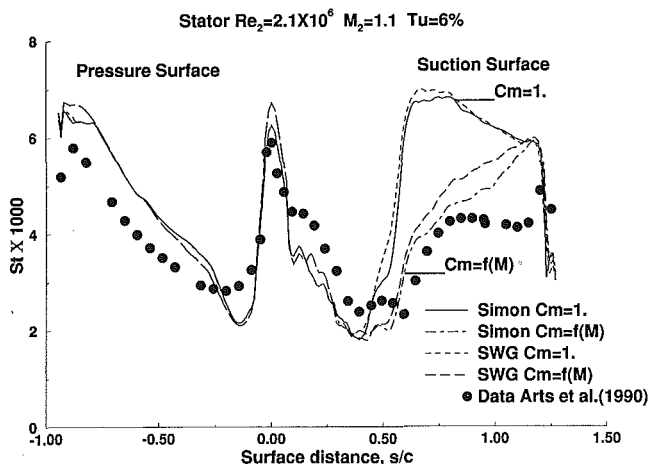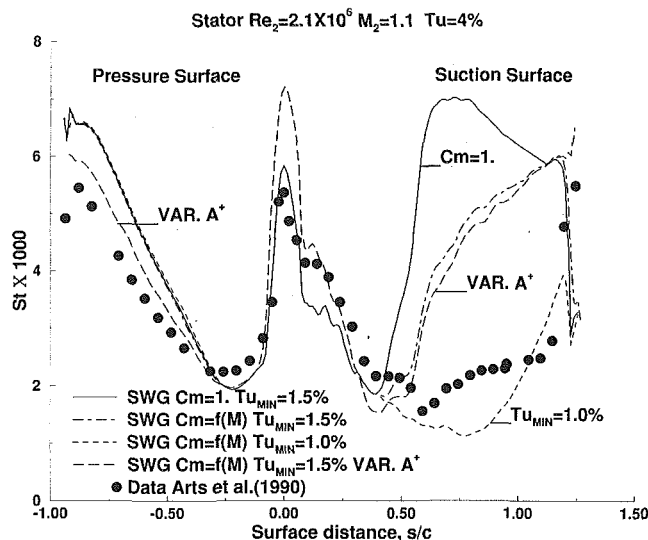ber, the degree of agreement for the pressure surface heat transfer is significantly poorer. It is felt that the primary reason for the poorer agreement on the pressure surface is that the only mechanism for relaminarization is the variation in A^+. From the data it appears that the increase in A^+ at these test conditions is insufficient. Kays and Crawford (1980) state that a boundary layer will relaminarize at K values around 1–3×10^6. Since $\lambda = K Re_\theta^2$, if the pressure gradient is high enough, and transition occurs at a low enough Re_θ, the boundary layer is likely to relaminarize. At high turbulence levels, transition begins at low Re_θ. The values of λ and Re_θ were calculated throughout the pressure surface transition region. The resulting K values were greater than the K value for relaminarization using the Kays and Crawford criteria.

On the suction surface, the choice of transition start influences the agreement with the data. The minimum turbulence intensity giving the best data agreement is the same level, 1.5 percent, as for the higher Reynolds number comparisons. However, for the lower
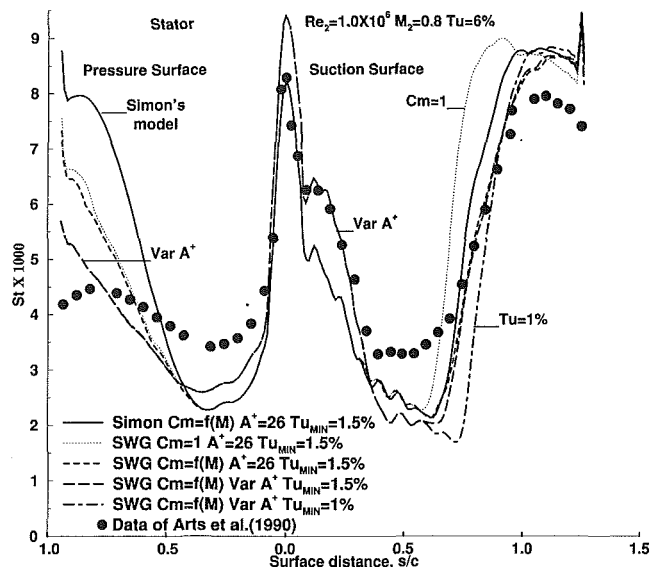
Reynolds number comparisons in the early part of transition, the analysis underpredicts the surface heat transfer.

Consistent with the results at the higher Reynolds number, the best agreement for the suction surface heat transfer occurs when the local turbulence intensity is close to 1 percent. The overall conclusion from the comparisons regarding the start of transition is that the local turbulence intensity at transition start should not be specified. Rather, it should be calculated from an appropriate model, and not have a preset lower limit.

C3X Data of Hylton et al. (1983).   The predicted and experimental isentropic surface Mach numbers for test cases 4321, ($M_2 = 0.90$), and 5521, ($M_2 = 1.06$), are shown in Fig. 8. For the lower exit Mach number, the peak suction surface Mach number is near 20 percent of the surface distance. The higher Mach number case has the peak close to 40 percent of the surface distance, after which there is rapid diffusion. From Table 1 it can be seen that transition is expected to start near 30 percent suction surface distance. If transition starts after the peak in suction surface velocity, the transition length is expected to be short because of the adverse pressure gradient. There is good agreement between the
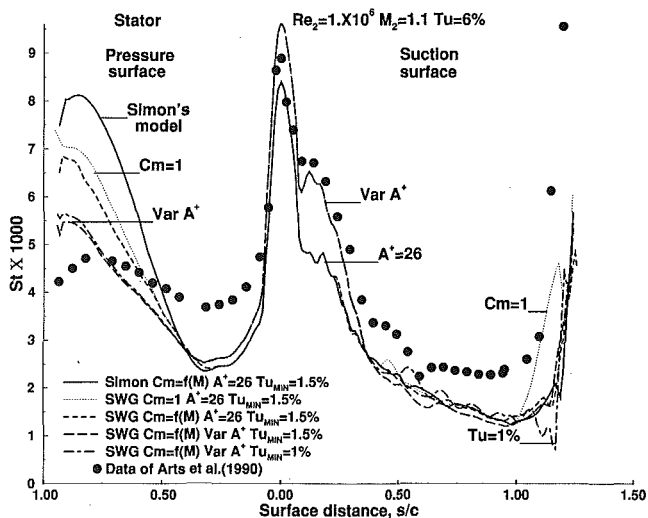
Fig. 7 Effect of model assumptions on predicted heat transfer
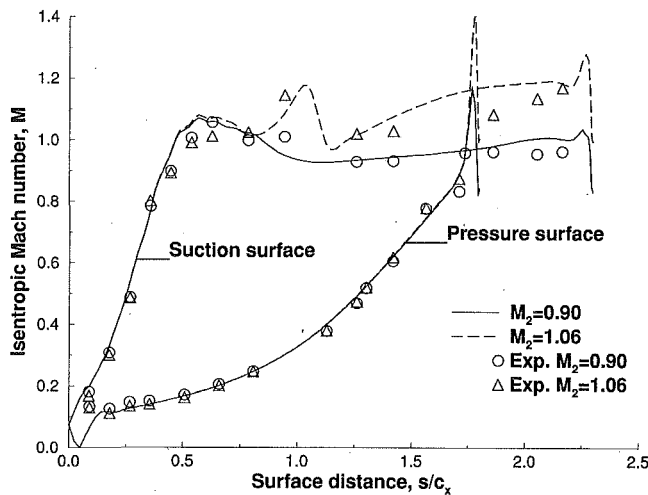
Fig. 8 Isentropic surface Mach numbers; data of Hylton et al. (1983)

Stator $Re_2=2.5X10^6$ $M_2=1.06$ Tu=8.3%

Fig. 10 Effect of model assumptions on predicted heat transfer

analysis and the data, except for the last third of the suction surface at the higher Mach number.

Figures 9 and 10 show comparisons between predicted and experimental heat transfer for cases 4321 and 5521. The actual heat transfer coefficient, h, was normalized by a reference value, h_R, of 1135 W/m²/K, as was done by Hylton et al. The cases have the same inlet Tu (8.3 percent), but differ in exit Reynolds and Mach numbers. Figure 9 shows that including a Mach number correction produced only a small change in the transition behavior. The start of transition was in an adverse pressure gradient region, and the transition length was very short. The results in Fig. 10, where transition starts in a favorable pressure gradient region, show a significant effect when the Mach number correction is applied. The suction surface data show an earlier than predicted transition start. However, changing the turbulence intensity at the start of transition from 1 to 2 percent did not improve the agreement with the data. The predicted heat transfer in the leading edge region is higher than the experimental values. Along the pressure surface incorporating A^+ as a function of pressure gradient improved the agreement with the data. Using measured surface temperatures instead of a uniform average temperature resulted in significantly better agreement with the data. However, only the rearward part of the vane was affected, and not the region where transition occurred.
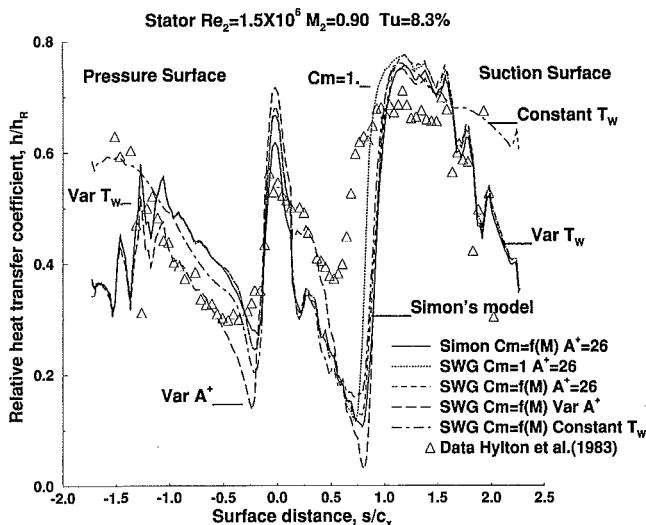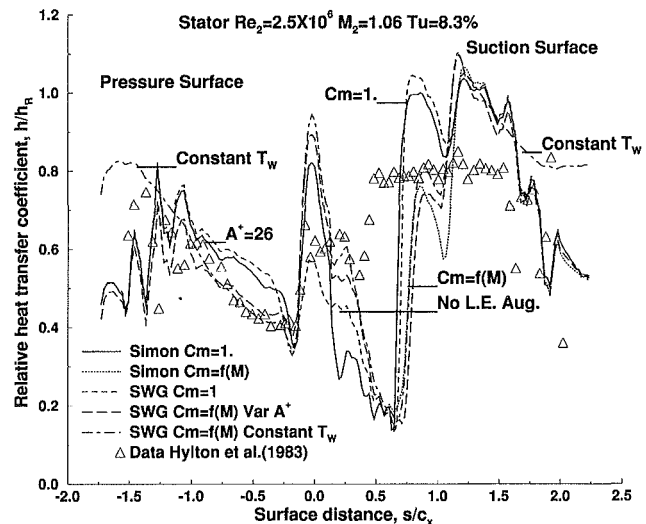
Rotors. Only data from a single source are used for comparisons for rotor surface heat transfer. The data used are those of Arts et al. (1998). These data show the variation in surface heat transfer with Reynolds number, Mach number, and perhaps most importantly, rotor incidence angle. All of the comparisons are made at an upstream Tu of 4 percent. Table 2 shows the same information as presented in Table 1, but for the rotor geometry. Figure 11 compares predicted surface isentropic Mach numbers with experimental results at different incidence angles. The primary purpose of this figure is to illustrate the degree to which incidence variations affect the surface pressures. Negative incidence, with the corresponding reduction in flow turning, gives rise to a strongly favorable pressure gradient over much of the suction surface. Away from the leading edge, the surface isentropic Mach numbers for the different incidence values converge. The analysis predicts the peak surface Mach number ahead of the experimental data, and the peak predicted value is lower than the data. When the transition region

Table 2 Rector cases examined

			Suction				Pressure			
Re_2 $\times10^{-6}$	M_2	I %	s_{ST}/s_T	λ_0	s_{99}/s_T	λ_{99}	s_{ST}/s_T	λ_0	s_{99}/s_T	λ_{99}
1.05	0.8	-5.0	0.13	0.031	0.69	0.001	0.01	-0.115	0.01	-0.382
1.05	1.1	-5.0	0.11	0.045	>1	99%	0.01	-0.261	0.01	-0.183
1.05	1.3	-5.0	0.09	0.060	>1	97%	0.01	-0.345	0.01	-0.243
1.84	1.1	-5.0	0.07	0.196	0.54	-0.034	0.01	-0.268	0.01	-0.187
1.05	1.1	-14.0	0.04	-0.025	0.89	0.015	0.01	-0.564	0.01	-0.528
1.05	1.1	5.0	0.10	-0.007	0.18	-0.182	0.01	0.010	0.03	0.200

Data - Arts et al.(1997)

Stator $Re_2=1.5X10^6$ $M_2=0.90$ Tu=8.3%

Fig. 9 Effect of model assumptions on predicted heat transfer
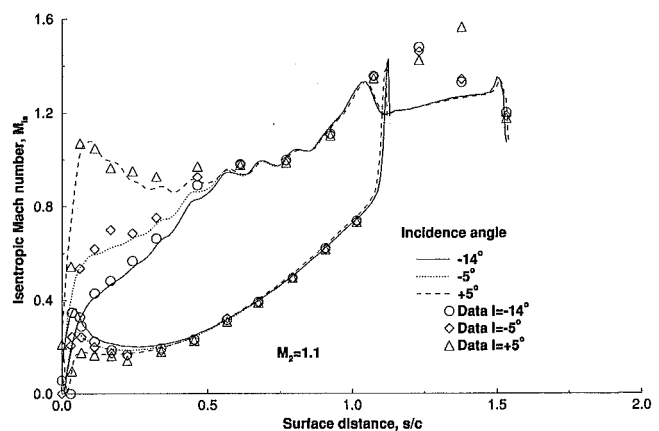
Fig. 11 Isentropic Mach number comparisons with data of Arts et al. (1997)
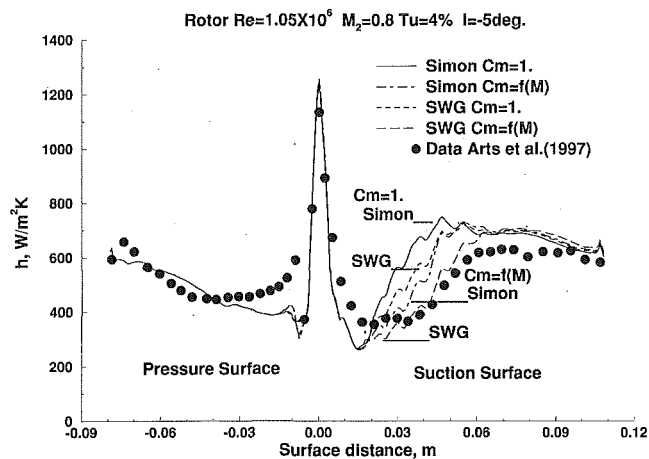
Fig. 12 Effect of Mach number correction on predicted heat transfer
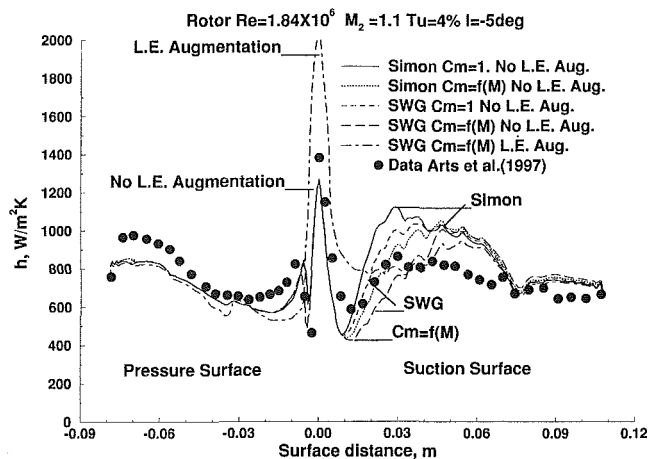
Fig. 15 Effect of model assumptions on predicted heat transfer

extends to this region, the differences in isentropic Mach numbers may affect the agreement between the analysis and experimental heat transfer.

Figures 12, 13, and 14 show the effect of an exit Mach number variation on the length of transition. The agreement between the predicted and experimental isentropic Mach numbers was closer for the subsonic exit Mach number, than for the $M_2 = 1.1$ results shown in Fig. 11. These results are for an exit Reynolds number of 1.05×10^6. Because the ratio of inlet Mach number to exit Mach

Fig. 13 Effect of model assumptions on predicted heat transfer

Fig. 14 Effect of Mach number correction on predicted heat transfer

number is much greater for a rotor than a stator, there is less variation in the free-stream Tu. Even though $Tu = 4$ percent at the inlet, the local Tu is greater than 2 percent at the start of transition. These results again show that including the effect of Mach number in the transition length modeling improves the agreement with the data. Both model predictions show better agreement with the data when a Mach number correction was used. The SWG model gives the best agreement with the data. Increasing the exit Mach number to 1.1 did not affect the degree of agreement with the data. A variable near-wall damping coefficient, A^+ did not improve the agreement for the pressure surface heat transfer.

Figure 14 shows evidence of a shock–boundary layer interaction for the highest exit Mach number. The peak isentropic Mach number was calculated to be 1.66. Even in the presence of the shock, the analysis shows good agreement with the experimental data.

Figure 15 shows the effect of an increased exit Reynolds number. Again, including a Mach number correction improved the agreement with the data for the suction surface. At this higher Reynolds number, including a leading edge augmentation resulted in heat transfer rates much higher than the experimental data. This behavior is consistent with the arguments advanced by Dullenkopf and Mayle (1992). They concluded that the coefficient in the Smith and Kuethe (1966) leading edge heat transfer model should be decreased as $Tu\sqrt{Re_d}$ increased. When $Tu\sqrt{Re_d} > 25$, the coefficient in the correlation of Smith and Kuethe (1966) should be reduced to 40 percent of its value for low values of $Tu\sqrt{Re_d}$. The data shown in Fig. 15 have $Tu\sqrt{Re_d} = 10$. A 40 to 50 percent reduction in the Smith and Kuethe model coefficient would significantly improve the agreement with the data. The pressure surface comparisons are consistent with those at the lower Reynolds number. A variable A^+ does not improve the agreement with the data.

Comparing Figs. 13, 16, and 17 shows the effect of a variation in pressure gradient caused by a variation in incidence. For a negative incidence of 14 deg, including a Mach number effect improved the agreement with the data. The higher-than-measured heat transfer midway on the suction surface implies that γ initially increased too rapidly. The positive incidence case shows transition occurring over a very short distance due to an adverse pressure gradient in this region. The positive incidence case is similar to the results shown in Fig. 9 for the C3X stator data of Hylton et al. (1983), and the degree of agreement is similar.

The prediction of the leading edge heat transfer is good for the two negative incidence cases, but the predicted values exceed the data for the positive incidence case. These results are also consistent with the conclusions of Dullenkopf and Mayle (1994) in that at high Reynolds numbers the correlation of Smith and Kuethe (1966) would overpredict the leading edge heat transfer. For the

Fig. 16 Effect of model assumptions on predicted heat transfer

same exit Reynolds number, the inlet Reynolds number increases with incidence. On the pressure surface the effect of varying A^+ with pressure gradient improved the agreement with data only for the forward region at 14 deg negative incidence. On the rear portion of the blade, assuming A^+ constant gave good agreement with the data.

Concluding Remarks

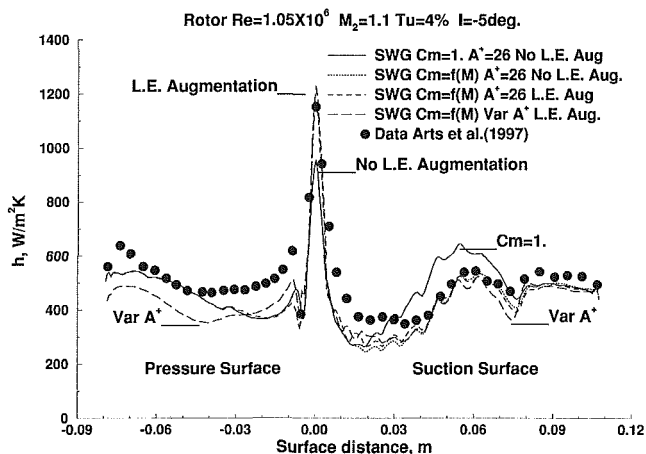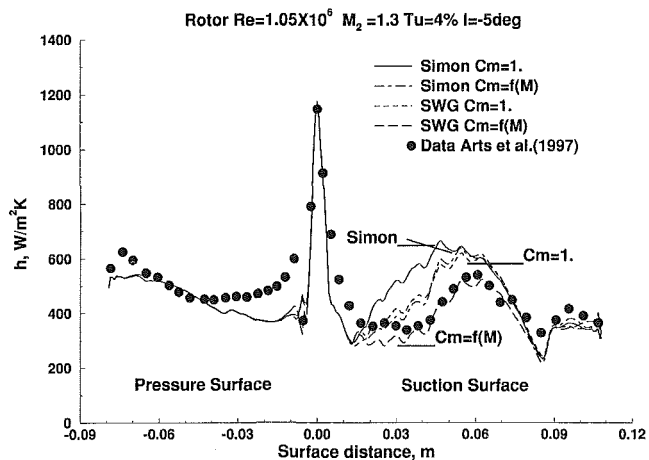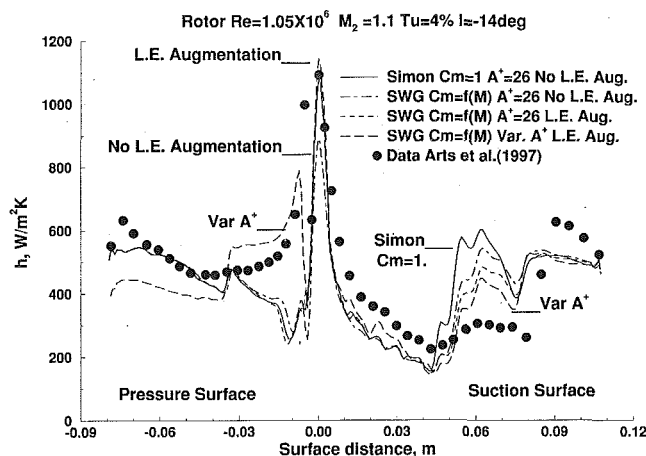The results of this work show that a Mach number effect should be incorporated in a transition model. The proposed model accounts for the effect of Mach number on both the frequency of spot formation and the turbulent spot spreading angle. The results show reasonably good agreement with the experimental data over the length of transition. Almost without exception, including the Mach number effect improved the agreement with the data for both Simon's (1995) model, and for the Solomon et al. (1996) model.

For moderate to high turbulence levels, a simple model for predicting transition onset gives reasonably good agreement with data. When the predicted level of turbulence at the start of transition is below 2 percent, best agreement with the data was achieved when $Re_{\theta\text{-}ST}$ was allowed to increase as the predicted turbulence level decreased to about 1 percent.

The analysis incorporated a model to account for the effect of free-stream turbulence on heat transfer in the laminar and transitioning regions. The model showed reasonably good agreement with the data. However, at high Reynolds numbers, the leading edge heat transfer was too high. The approach taken by Dullenkopf
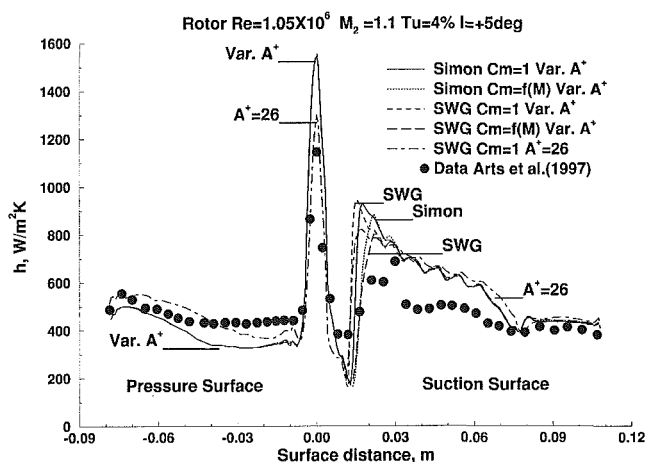
and Mayle (1994) might have led to an improved prediction. While the comparisons with data were for the entire blade surface, the primary focus of this investigation was to validate an approach to account for Mach number effects on the length of transition. The appropriateness of using a model to vary the near-wall damping coefficient, A^+ as a function of pressure gradient was not resolved. For the stator cases examined, a variable A^+ gave improved agreement. However, for the rotor cases choosing $A^+ = 26$ gave the better agreement.

References

Ameri, A. A., and Arnone, A., 1992, "Navier–Stokes Heat Transfer Predictions Using Two-Equation Turbulence Closures," AIAA Paper No. 92-3067.

Arnone, A., Liou, M.-S., and Povinelli, L. A., 1992, "Navier–Stokes Solution of Transonic Cascade Flows Using Non-Periodic C-Type Grids," AIAA *Journal of Propulsion and Power*, Vol. 8, No. 2, pp. 410–417.

Arts, T., Lambert de Rouvroit, M., and Rutherford, A.W., 1990, "Aero-Thermal Investigation of a Highly Loaded Transonic Linear Turbine Guide Vane Cascade," VKI Technical Note 174.

Arts, T., Duboue, J.-M., and Rollin, G., 1998, "Aero-Thermal Performance Measurements and Analysis of a Two-Dimensional High Turning Rotor Blade," ASME JOURNAL OF TURBOMACHINERY, Vol. 120, pp. 494–499.

Baldwin, B. S., and Lomax, H., 1978, "Thin-Layer Approximation and Algebraic Model for Separated Turbulent Flows," Paper No. AIAA-78-257.

Boyle, R. J., 1991, "Navier–Stokes Analysis of Turbine Blade Heat Transfer," ASME JOURNAL OF TURBOMACHINERY, Vol. 113, pp. 392–403.

Boyle, R. J., and Ameri, A. A., 1997, "Grid Orthogonality Effects on Predicted Turbine Midspan Heat Transfer and Performance," ASME JOURNAL OF TURBOMACHINERY, Vol. 119, pp. 31–38.

Chen, K. K., and Thyson, N. A., 1971, "Extension of Emmons' Spot Theory to Flows on Blunt Bodies," AIAA *Journal of Propulsion and Power*, Vol. 9, No. 5, pp. 821–825.

Chima, R. V., 1987, "Explicit Multigrid Algorithm for Quasi-Three-Dimensional Flows in Turbomachinery." AIAA *Journal of Propulsion and Power*, Vol. 3, No. 5, pp. 397–405.

Chima, R. V., and Yokota, J. W., 1988, "Numerical Analysis of Three-Dimensional Viscous Internal Flows," AIAA Paper No. 88-3522; NASA TM-100878.

Chima, R. V., Giel, P. W., and Boyle, R. J., 1993, "An Algebraic Turbulence Model for Three-Dimensional Viscous Flows," AAIA Paper No. 93-0083; NASA TM-105931.

Chima, R. V., 1996, "Application of the *k*–ω Turbulence Model to Quasi-Three-Dimensional Turbomachinery Flows," AIAA *Journal of Propulsion and Power*, Vol. 12, No. 6, pp. 1176–1179.

Clark, J. P., 1993, "A Study of Turbulent Spot Propagation in Turbine Representative Flows," Ph.D. Thesis, St. Catherine's College, University of Oxford.

Clark, J. P., Jones, T. V., and LaGraff, J. E., 1994, "On the Propagation of Naturally Occurring Turbulent Spots," *Journal of Engineering Mathematics*, Vol. 28, pp. 1–19.

Crawford, M. E., and Kays, W. M., 1976, "STAN5 — A Program for Numerical Computation of Two-Dimensional Internal and External Boundary Layer Flows," NASA CR-2742.

Dey, J., and Narasimha, R., 1985, "Spot Formation Rates in High Speed Flows," Report 85 FM 11, Dept. Aero. Eng., Indian Inst. Sci.

Dullenkopf, K., and Mayle, R. E., 1994, "The Effects of Incident Turbulence and Moving Wakes on Laminar Heat Transfer in Gas Turbines," ASME JOURNAL OF TURBOMACHINERY, Vol. 116, pp. 23–28.

Emmons, H. W., 1951, "The Laminar–Turbulent Transition in a Boundary Layer — Part I," *Journal of Aerospace Sciences*, Vol. 18, No. 7, pp. 490–498.

Fraser, C. J., Higazy, M. G., and Milne, J. S., 1994, "End-Stage Boundary Layer Transition Models for Engineering Calculations," *Proc. Institution of Mechanical Engineers*, Part C, Vol. 208, pp. 47–58.

Gostelow, J. P., Blunden, A. R., Walker, G. J., 1994, "Effects of Free-Stream Turbulence and Adverse Pressure Gradients on Boundary Layer Transition," ASME JOURNAL OF TURBOMACHINERY, Vol. 116, pp. 392–404.

Gostelow, J. P., Melwani, N., and Walker, G. J., 1996, "Effects of a Streamwise Pressure Gradient on Turbulent Spot Development," ASME JOURNAL OF TURBOMACHINERY, Vol. 118, pp. 737–743.

Hylton, L. D., Mihelc, M. S., Turner, E. R., Nealy, D. A., and York, R. F., 1983, "Analytical and Experimental Evaluation of the Heat Transfer Distribution Over the Surfaces of Turbine Vanes," NASA CR-168015.

Kays, W. M., and Crawford, M. E., 1980, *Convective Heat and Mass Transfer*, 2nd ed., McGraw-Hill, New York

Mack, L. M., 1969, "Boundary Layer Stability Theory," Document 900-277, Rev. A, Jet Propulsion Laboratory, Pasadena, CA.

Mayle, R. E., 1991, "The Role of Laminar–Turbulent Transition in Gas Turbine Engines," ASME JOURNAL OF TURBOMACHINERY, Vol. 113, pp. 509–537.

McCormick, M. E., 1968, "An Analysis of the Formation of Turbulent Patches in the Transition Boundary Layer," ASME *Journal of Applied Mechanics*, Vol. 35, pp. 216–219.

Narasimha, R., 1957, "On the Distribution of Intermittency in the Transition Region of a Boundary Layer," *Journal of Aerospace Sciences*, Vol. 24, No. 9, pp. 711–712.

Narasimha, R., 1985, "The Laminar–Turbulent Transition Zone in the Boundary Layer," *Journal of Aerospace Sciences*, Vol. 22, pp. 29–80.

Fig. 17 Effect of model assumptions on predicted heat transfer

Owen, F. K., and Horstman, C. C, 1972, "Hypersonic Transitional Boundary Layers," *AIAA Journal*, Vol. 8 pp. 769–775.

Sharma, O. P., 1987, "Momentum and Thermal Boundary Layer Development on Turbine Airfoil Suction Surfaces," AIAA Paper No. 87-1918.

Simon, F. F., 1995, "The Use of Transition Region Characteristics to Improve the Numerical Simulation of Heat Transfer in Bypass Transitional Flows," *International Journal of Rotating Machinery*, Vol. 2, No. 2 pp. 93–102; also NASA TM 106445.

Simon, F. F., and Ashpis, D. E., 1996, "Progress in Modeling of Laminar to Turbulent Transition on Turbine Vanes and Blades," presented at the Int. Conf. on Turbulent Heat Transfer, Mar. 10–15, San Diego, CA; also NASA TM 107180.

Smith, M. C., and Kuethe, A. M., 1966, "Effects of Turbulence on Laminar Skin Friction and Heat Transfer," *The Physics of Fluids*, Vol. 9, No. 12, pp. 2337–2344.

Solomon, W. J., Walker, G. J., and Gostelow, J. P., 1996, "Transition Length Prediction for Flows With Rapidly Changing Pressure Gradients," ASME JOURNAL OF TURBOMACHINERY, Vol. 118, pp. 744–753.

Sorenson, R. L., 1980, "A Computer Program to Generate Two-Dimensional Grids About Airfoils and Other Shapes by the Use of Poisson's Equation," NASA TM 81198.

Walker, G. J., 1989, "Transitional Flow on Axial Turbomachine Blading," *AIAA Journal*, Vol. 27, No. 5, pp. 595–602.

Measurement and Computation of Energy Separation in the Vortical Wake Flow of a Turbine Nozzle Cascade

W. E. Carscallen

T. C. Currie

Institute for Aerospace Research,
National Research Council of Canada,
Ottawa, Canada

S. I. Hogg

J. P. Gostelow

Department of Engineering,
University of Leicester,
Leicester, United Kingdom

This paper describes the observation, measurement, and computation of vortex shedding behind a cascade of turbine nozzle guide vanes that have a blunt trailing edge. At subsonic discharge speeds, periodic wake vortex shedding was observed at all times at a shedding frequency in the range 7–11 kHz. At high subsonic speeds the wake was susceptible to strong energy redistribution. The effect was greatest around an exit Mach number of 0.95 and results are presented for that condition. An unusually cold flow on the wake centerline and hot spots at the edges of the wake were measured. These were found to be a manifestation of Eckert–Weise effect energy separation in the shed vortex street. Experimental identification of these phenomena was achieved using a new stagnation temperature probe of bandwidth approaching 100 kHz. Using phase-averaging techniques, it was possible to plot contours of time-resolved entropy increase at the downstream traverse plane. Computational work has been undertaken that gives qualitative confirmation of the experimental results and provides a more detailed explanation of the fine scale structure of the vortex wake. The topology of the wake vortical structures behind blunt trailing-edged turbine blades is becoming clearer. These measurements are the first instantaneous observations of the energy separation process occurring in turbine blade wake flows. This was also the first demonstration of the use of the probe in the frequency, Mach number, and temperature ranges typical of operation behind the rotors of high-performance turbomachines such as transonic fans.

Introduction

An experimental low-aspect-ratio (0.6) highly loaded turbine stage designed for engine use in the 1980's produced anomalous temperature distributions downstream of the high-turning (76 deg) transonic nozzle guide vanes (Williamson and Moustapha, 1986). At the time the cause of these effects was not understood and a linear cascade model of the midspan section of the nozzle guide vane row was built at a scale of 4.3 times engine size. The design of the cascade and the results of a comprehensive experimental investigation of the flow field in the nozzle were reported by Carscallen and Oosthuizen (1989). Testing on this nozzle cascade also resulted in an anomalous temperature distribution. The effect was basically that in the cascade, which continuously drew in laboratory air, a significant time-averaged temperature deficit of up to 12 K was observed in the vane wakes and a stagnation temperature excess of several degrees was observed just outside the wakes. The understanding of these anomalies has been an evolving process based mainly on the results of experimental research on the linear cascade.

It was first established that, because the blading had a particularly blunt trailing edge, periodical vortex shedding was occurring into the wake over the whole discharge Mach number range between 0.3 and 1.2. At subsonic speeds this took the form of a conventional von Karman vortex street. The nature of the vortex shedding was established by submicrosecond schlieren photography and fluctuating stagnation pressure measurements (Carscallen et al., 1996). A representative schlieren photograph, corresponding to a condition close to that used for most of the testing described in this paper, is shown in Fig. 1. The flow is from left to right and the photograph demonstrates the structure of the vortex shedding, showing the interaction between the shed vortices and the acoustic waves propagating upstream from them.

There is a loss penalty associated with a thick trailing edge. This penalty is considerably larger than would result from a simple backward-facing step of similar proportions. The magnitude of the discrepancy was unexplained until fast schlieren photography came into use in cascades. When fast schlierens are taken of blunt-trailing edged turbine blades, a von Karman vortex street is observed (Lawaczek and Heinemann, 1975), often with associated sound waves propagating upstream. In addition to the loss penalty, vortex shedding may cause adverse effects, which include high-frequency sound propagation, vibrational effects, locally high heat transfer to or from the blade, and energy separation into hot and cold regions. The effect of a vortex street on close-coupled oscillating shock waves, causing strong loading fluctuations, is notoriously difficult to predict.

Possibly the strongest and least understood manifestation of periodic vortex shedding, however, is a thermo-acoustic effect, which has its maximum amplitude at high subsonic speeds. This is the Eckert–Weise effect (1943), which had been mostly studied in the context of vortex shedding from circular cylinders. A wide range of energy separation phenomena was reviewed by Eckert (1986), who concluded that energy separation was primarily caused by pressure forces acting on the fluctuating curved streamlines with only a minor contribution from viscous forces. For circular cylinders the extensive work by Kurosaka and colleagues (1987) had been followed by the work of Ng et al. (1990) who observed stagnation temperature fluctuations of 15 K rms at the relatively low Mach number of 0.4.

Upon confirmation of the periodic vortex shedding behavior of these vanes, it was hypothesized that the Eckert–Weise effect was the cause of the anomalous temperature distributions. The un-

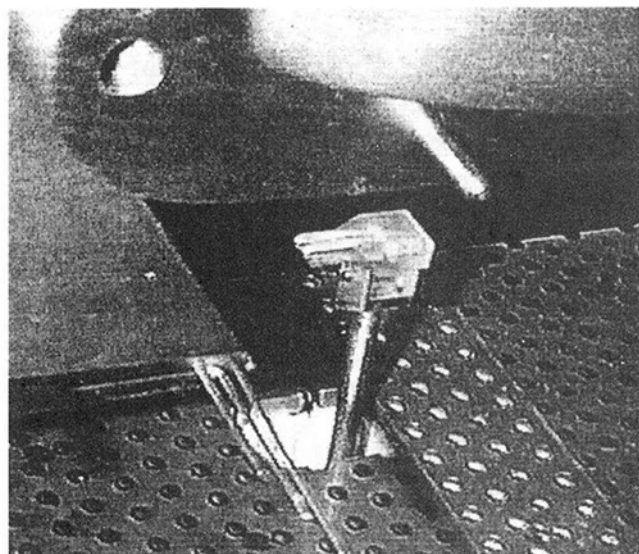Fig. 1 Schlieren visualization of vortex wake at Ma = 0.97

Fig. 2 View of the probe and the cavity in the porous tailboard

steadiness, indicated in pressure transducer data and observed with high-speed schlieren, and the depressed average values of total temperature in the wake were consistent with the kind of total temperature fluctuations observed by Kurosaka. The aim of the present work was to make direct time-resolved measurements of the temperature fluctuations in an attempt to confirm this hypothesis.

The principal difficulty was that stagnation temperature measurements were limited by the frequency response of the available instrumentation. Hitherto the fastest response device available was the aspirating probe, which has a bandwidth of the order of 20 kHz. This was clearly inadequate to resolve the vortex shedding, which has a characteristic frequency of around 10 kHz.

Meanwhile a new fast-response stagnation temperature measurement device, which was originally intended for transient test facilities, had been developed at Oxford University (Buttsworth and Jones, 1998). The new device, which has a bandwidth of the order of 100 kHz, was thought to be potentially suitable for the measurements in the vortex street. Accordingly the design work was undertaken to adapt the device for operation in the NRC continuously running tunnel. The current work marks the first application of the technique to a continuous facility.

The work described is limited to high subsonic Mach numbers for which the energy separation effect is strongest. Limited investigations have been undertaken over a wider Mach number range, including interesting vortex shedding phenomena observed at supersonic speeds, as outlined by Hogg et al. (1997).

Even under high subsonic conditions, there were issues that involved the structure of the von Karman vortex wake. The turbine blade is not a circular cylinder and the boundary layers from the two surfaces are quite unequal in thickness at the trailing edge. It was not clear what effect this would have on the wake vortices. To resolve such questions about the topology of the vortex wake, the measurements would need to be assembled into a mapping of the flow as it sweeps over the probe; suitable techniques would need to be devised to provide this information.

Test Facility and Instrumentation

Transonic turbine blade wake flows were measured in the cascade tunnel described by Carscallen et al. (1996). This continuously running in-flow cascade has six nozzle guide vanes. An adjustable perforated aluminum tailboard was used to eliminate shock wave reflection and help establish flow field periodicity. The tunnel side walls were constructed from clear lexan, permitting schlieren visualization. The nozzle guide vanes tested in this cascade have a chord of 175.3 mm (4.3 times engine size) and a solidity of 1.19. The vane aspect ratio is 0.64 with a turning angle of 76 deg and a design exit Mach number of 1.2. The vane trailing edge diameter is 6.35 mm.

Earlier measurements, using fast response pressure transducers and high-speed schlieren, had identified strong vortex shedding in the trailing edge wake flows. Time-averaged temperatures measured using a shielded thermocouple had suggested that the vortices were causing redistribution of energy across the wake.

Simultaneous time-resolved measurements of stagnation temperature and pressure were made in the wake of one blade using the device shown in Fig. 2. The downstream traverse plane was normal to the wake at 5.76 trailing edge diameters from the vane trailing edge. The device consists of three probes comprising one tube-mounted fast response transducer for measuring stagnation pressure and two 3-mm-dia fused quartz probes for measuring stagnation temperature. The fluctuating stagnation pressure was measured using a Kulite XCS-062-15A pressure transducer. The isentropic exit Mach numbers were determined by calibration from measurements of total pressure and downstream static pressure.

The stagnation temperature instrumentation is based on the fast response technique of Buttsworth and Jones (1998). It consists of two cylindrical fused quartz probes, one of which is heated prior to operation, each having a thin film platinum resistance thermometer applied to its hemispherical end. Heat flux and surface temperature

Nomenclature

c_p = specific heat at constant pressure
k = turbulence kinetic energy
Ma = isentropic exit Mach number
R = gas constant
SS = suction side
s = entropy

P = stagnation pressure
PS = pressure side
T = stagnation temperature
t = time
y = distance normal to wake
y^+ = dimensionless distance normal to wall

ϵ = turbulence dissipation
ω = rms vorticity fluctuation

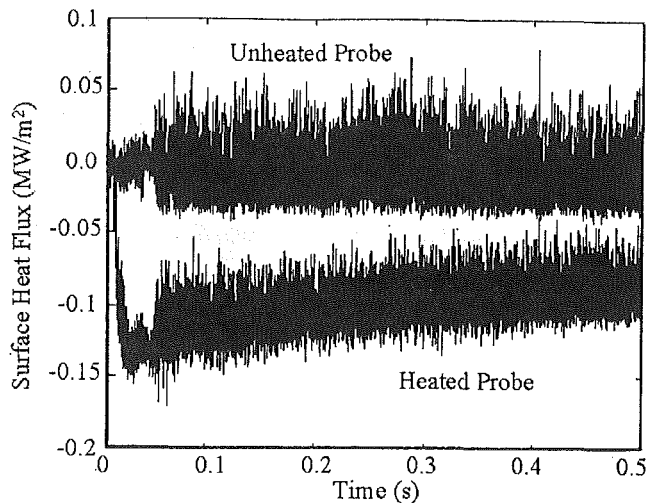**Subscripts**

1 = upstream
2 = downstream

Fig. 3 Probe transient heat flux traces

signals are recorded for both temperature probes. The heat transfer between the quartz tip of each probe and the flow is governed by the stagnation heat transfer coefficient, the surface temperature of the quartz and the local flow stagnation temperature. Running the thin film gages in constant current mode, the temperature of the quartz can be determined directly from the voltage drop across the gage. A surface heat transfer signal was also generated from the gage voltage using the heat transfer analog unit of Oldfield et al. (1982).

The bandwidth of the device used in the present measurements is limited to 87 kHz (3 dB deterioration) by the conditioning electronics that process the thin film signals. The shedding frequency is about 10 kHz, and with the measurement bandwidth of 87 kHz, faithful representation of harmonic content is quite limited. The temporal resolution is considered marginally acceptable for providing information on vortex structures.

Spatial resolution is governed by the geometry of the probes. Although the diameter of each total temperature probe is 3 mm, the sensing film is less than 1 mm long. The diameter of the Kulite transducer diaphragm is 1.57 mm, or about one quarter of the trailing edge thickness, and this limits the spatial resolution.

The heat transfer coefficient and the stagnation temperature were the unknown variables in the heat transfer process for each total temperature probe. Assuming an identical heat transfer coefficient for each probe permits the stagnation temperature to be calculated by simultaneous solution of the heat transfer equation for each probe. Corrections were applied for surface curvature and lateral conduction effects, as described by Buttsworth and Jones; their error analysis predicts a measurement accuracy of ± 3 K. As there is no stagnation enthalpy variation along the stagnation streamline, the technique is essentially Mach number independent.

The three probe heads were aligned parallel to the vane trailing edge. In this study it is assumed that the shed vortices are essentially two dimensional and that the three probes are sensing identical phases of the shed vortical structure.

The total temperature probe heads were shielded within the tailboard prior to measurements being taken. While shielded within the tailboard, an internal electric element heated one of the quartz probes, the temperature of the other probe remaining close to the stagnation temperature of the flow. Once the desired temperature difference between probes had been achieved, the device was propelled out of the tailboard and into position in the wake.

Figure 3 presents typical probe transient heat flux traces. The lower trace is for the heated probe. All signals were digitized at 250 kHz for 0.5 s after release from the tailboard. Low-pass anti-aliasing filtering was applied at 100 kHz. The traces in Fig. 3 show the initial transients as the head moves from the tailboard,

across the free-stream flow and into the measurement position within the wake. All transients have decayed within the first 0.1 s. A second fast-response pressure transducer was mounted within the trailing edge of the vane. Although this was in the base region, it was mounted off center and provided a phase reference signal for sampling the traces. Figure 4 gives a short sample of traces for the stagnation temperature and pressure and the base pressure. The stagnation temperature and pressure traces were taken close to the wake center line at Ma = 0.95. These raw data traces typically show significant variations from cycle to cycle. These variations result from turbulence and other random effects and also reflect differences in arrival times of individual vortices. It is significant that these differences between cycles are less for the base pressure than for the downstream probes. To reduce these cycle-to-cycle variations, which are present in most turbomachinery applications, a simple phase-lock averaging procedure (Gostelow, 1977) was applied.

Calibration procedures applied to the raw data resulted in the production of temperature and pressure signals in physical units. The first 37,500 readings were discarded to ensure that all remaining data had reached steady state conditions. The remaining data were analyzed in blocks of 200 readings. This permitted the phase reference to be applied and the 128 readings following this reference to be analyzed. In the rare case of a poor or ambiguous phase reference, this allowed one vortex shedding cycle of data to be discarded. It was therefore possible to obtain a satisfactorily phase-referenced record of 128 readings in all cases. For each data record this procedure was repeated 64 times, allowing an ensemble of 64 traces to be collected. The phase averaging procedure was then applied, resulting in periodic traces of stagnation pressure and stagnation temperature.

Phase-averaged records of total temperature and pressure and of base pressure were obtained at each of eleven cross-wake traverse locations. These records were then combined, using the common phase reference, and contouring procedures applied to the resulting data. The approximate wake centerline was chosen as a datum and the notation was adopted that suction side values of y are positive.
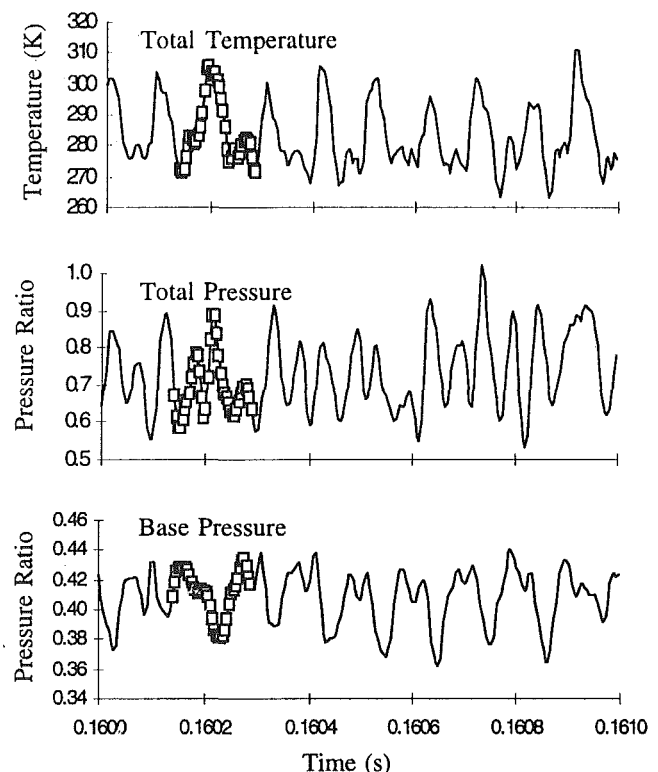

Fig. 4 Short sample of traces for stagnation temperature and pressure and base pressure
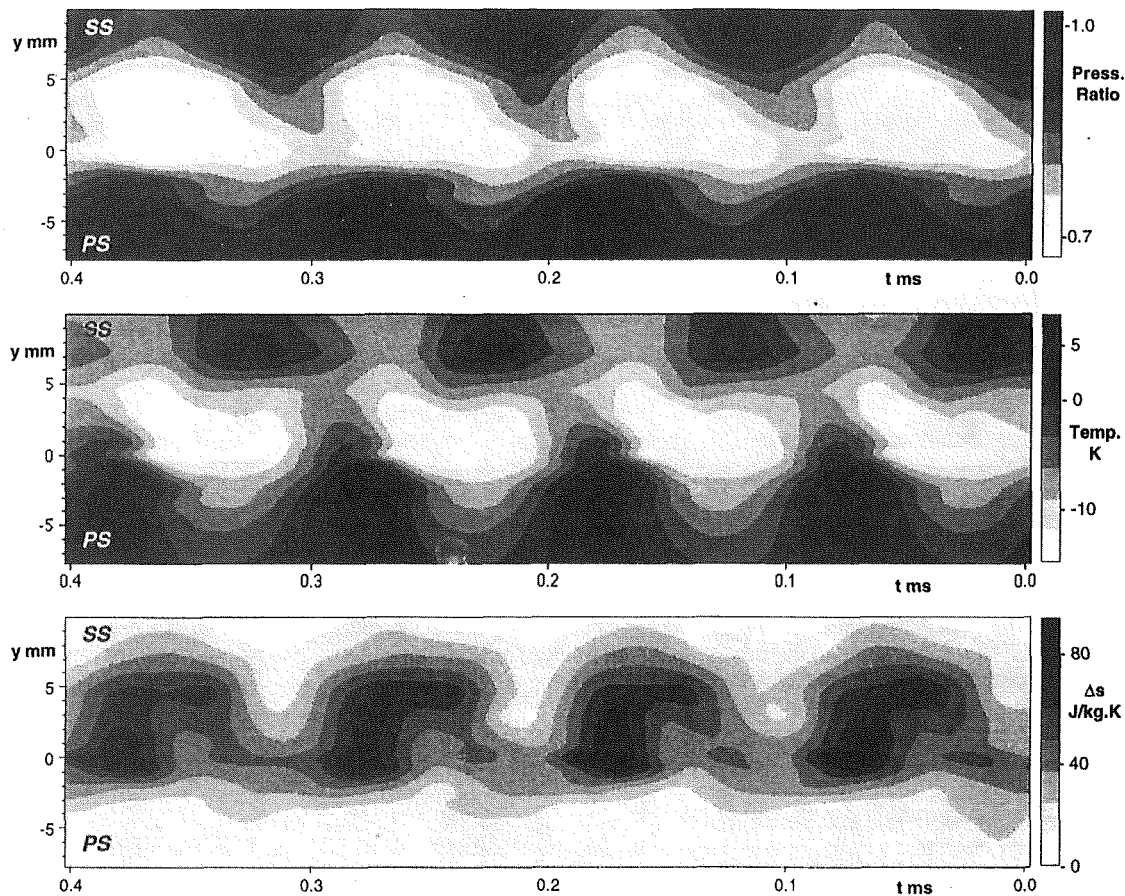
Fig. 5 Contour plots of variation of phase-averaged stagnation pressure, stagnation temperature and entropy increase with time, for Ma = 0.95

Computational Work

The unsteady implicit flow solver used has been described by Currie and Carscallen (1998). The flow solver solves the quasi-three-dimensional form of the Reynolds-averaged Navier–Stokes equations, which accounts for axial variations in stream-tube thickness (axial velocity density ratio), using an unstructured grid and a second-order accurate MUSCL implementation of Roe's flux difference splitting scheme (Roe, 1981).

The spatially-discretized Navier–Stokes equations are integrated in time using a second-order accurate, three time level implicit procedure, which uses GMRES and block ILU(0) preconditioning to solve the implicit equations at each time step. Turbulence is modeled with the zonal $k-\omega/k-\epsilon$ Shear Stress Transport formulation of Menter (1993). This formulation uses the $k-\omega$ model of Wilcox (1993) near the walls and the high-Reynolds-number form of the $k-\epsilon$ model elsewhere.

Jacobi relaxation is used to solve the implicit equations for the backward-differenced (in time) turbulence variables at each time step. The computational grid was obtained by first generating a structured O-grid, with a thickness of ~5 percent of blade chord, around the blade and then filling the remainder of the solution domain with roughly equilateral triangles. The grid was adapted to the solution by quadrisecting triangles in regions of high pressure gradient, as described by Currie and Carscallen (1998). Adaptation to boundary layers is performed by variable stretching of the O-grid away from the blade surface, maintaining the overall thickness of the structured layer constant, to obtain a y^+ of ~1 at the first nodes off of the blade surface. The simulations of vortex shedding were performed using a grid that was very highly refined in a strip straddling the vortex street downstream of the trailing edge. The cell size in this strip was ~1/50th of the trailing edge diameter. To

minimize dispersion errors, the calculations were performed using a global time step that resulted in a CFL (Courant–Friedrichs–Lewy) number of ~1 for the nodes in the strip.

Results

Contour plots are presented for 100 readings, or 0.4 ms, of phase-averaged data in Fig. 5. These have been presented in reversed time sequence to relate more closely to Lagrangian views of the vortical wake obtained from schlieren visualization and computational simulations. To obtain a realistic view of the vortex shedding process, it was necessary to apply a vortex propagation velocity to the readings. Following the recommendation of Zaman and Hussain (1981) the propagation velocity of the vortex core was applied. For the test conditions and the blading under investigation, at a free-stream Mach number of 0.95, this was found to be 178 m/s.

The pressure and temperature contours of Fig. 5 clearly represent a periodic structure with stagnation pressure dropping to less than 70 percent of the free-stream value in the vortex cores. It is not, however, immediately obvious that this corresponds to a conventional von Karman vortex street. Clarification and interpretation were required and are attempted subsequently.

The stagnation temperature contours indicate strong instantaneous temperature separation. Figure 5 indicates that stagnation temperatures in the vortex cores may be 16 K lower than free-stream values and the presence of hot spots of more than 8 K greater than the average free-stream values at the outer edge of the pressure side of the vortex wake. On the suction side this difference is just over 6 K. It should be recalled that the signals are subject to low-pass filtering at 100 kHz giving a maximum resolution of approximately ten readings per cycle and eliminating
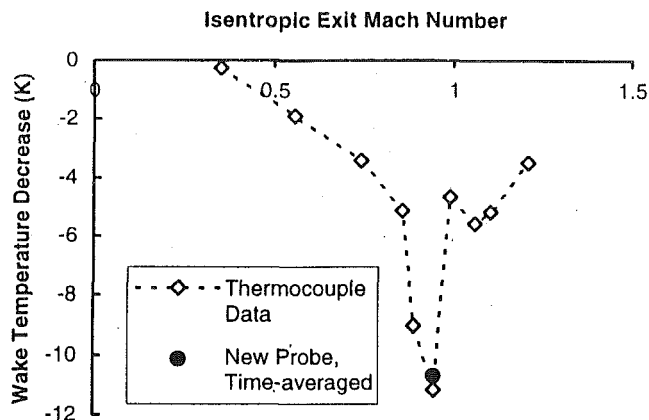
Isentropic Exit Mach Number

Fig. 6 Comparison between phase-averaged temperature measurements and previous results measured with a thermocouple wedge probe

Fig. 7 Lagrangian contours of entropy increase computed for subject cascade at Ma = 0.95

$$s_2 - s_1 = c_p \ln (T_2/T_1) - R \ln (P_2/P_1).$$

The phase-averaged stagnation pressure and temperature data may therefore be combined in the form of contours of entropy increase. This has been done in Fig. 5. The result is contours of an unfamiliar serpentine form that require elucidation. The contours represent departures from isentropic expansion or compression. Fluctuating expansions and compressions are represented by the stagnation pressure contours and the ensuing stagnation temperature fluctuations of Fig. 5. A failure of the stagnation temperature to respond to the stagnation pressure fluctuations results in an increase in entropy. The entropy increase contours are therefore sensitive spatio-temporal locators of loss and should represent the vortex street well.

What may be deduced from the contours is that although a single, distinct and conventional vortex is shed from the pressure side each shedding period, no such simple conclusion may be reached with regard to the suction side. The literature offers little other direct experimental evidence to assist in the interpretation of this behavioral difference between the vortical structures emanating from the two surfaces. Clues are nevertheless given in information such as the smoke traces of Roberts and Denton (1996). For a body having similar trailing edge aerodynamic characteristics to these blades, the vortices from the pressure surface rolled up tightly into coherent cylindrical structures; those from the suction surface were more diffuse. The salient differences between the present tests and circular cylinder wakes are:

(*i*) In these tests the suction surface trailing edge boundary layer was much thicker than that on the pressure surface, and
(*ii*) the free-stream velocity on the suction surface was higher than that on the pressure surface.

This latter topic has been addressed in fundamental work at low speed by Boldman et al. (1976), which showed the severe disruption of the symmetric vortex shedding pattern at low upper surface: lower surface velocity ratios.

Computational work using the code described in the previous section has produced the Lagrangian contour plots of entropy increase shown in Fig. 7. The experimental measurements were made in a plane 5.76 trailing edge diameters downstream of the trailing edge and this distance has been indicated by a broken line on the computational results (Figs. 7 and 8). It is instructive to observe the vortical structures just upstream and downstream of that line. These do seem to bear a close resemblance to the experimentally observed structures in the vicinity of the 0.2 ms

short-duration fluctuations from consideration. The phase-averaging procedure will also have served to eliminate or reduce short duration structures. The real instantaneous variations will therefore tend to be greater than the values given in the contour plots, as indicated in the raw total temperature data of Fig. 4.

When the unsteady temperature readings in the wake center region are averaged over time, a temperature deficiency of over 10 K is obtained. In Fig. 6 this is compared with earlier results. These were measured over a range of exit Mach numbers by wedge probe-mounted thermocouple. The agreement at the test Mach number of 0.95 is seen to be good. The earlier results (Carscallen and Oosthuizen, 1989) were obtained by traversing in a plane parallel to that of the vane trailing edges. The wake temperature difference was defined as the difference between the minimum and maximum temperatures measured. In the present tests measurements at most Mach numbers were taken only on the wake centerline. The wake temperature decrease is taken as the difference between the time-averaged measurement at the wake center and the free-stream total temperature.

The low temperatures found in the central region of the wake were not unexpected, although no direct measurements had previously been made of these behind turbine blades due to the limited bandwidth of available instrumentation. It was a surprise to find such pronounced hot spots on the edge of the wake. These had only previously been observed for shed vortices from circular cylinders in the computational work of Kurosaka and colleagues but not experimentally and certainly not in vortex shedding at high shedding frequencies of the order of 10 kHz. Upon time averaging, these hot and cold spots manifest themselves as regions of depressed stagnation temperature on the wake centerline and of increased stagnation temperature at the edge of the wake, as found in the experiments of Carscallen and Oosthuizen. The results confirm that the previous, supposedly anomalous, results were actually the result of energy separation in the vortex wake as described by Kurosaka et al. (1987).

The time-resolved stagnation temperature measurements therefore support observations of energy separation through the Eckert–Weise (1943) effect by Kurosaka and others and extend these to flows behind turbine blades at shedding frequencies of the order of 10 kHz. They also validate the use of the combined stagnation pressure and temperature device under conditions representative of transonic turbomachinery operation. It is clear, for example, that the probe has the potential to be used to give time-resolved stagnation temperature measurements in transonic fan rotor wakes and hence time-resolved efficiency measurements.

The potential of this approach for efficiency measurements is demonstrated by the use of the pressure and temperature measurements to provide contours of entropy increase. The usual relationship for the entropy increase of a perfect gas is expressed in terms of stagnation temperature and pressure ratios:
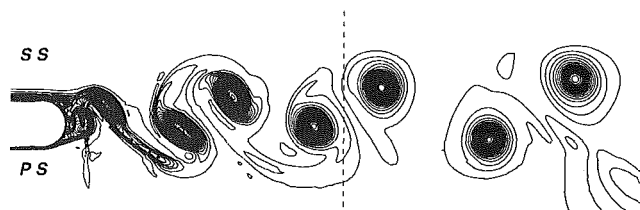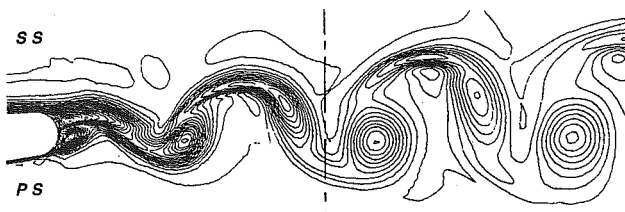

Fig. 8 Lagrangian contours of entropy increase for Ma = 0.4 computed by Arnone and Pacciani (1997)

time mark; indeed they provide an explanation of the observed structures. The only comparable computational work has been performed using an explicit code by Arnone and Pacciani (1997). This work was performed at a lower exit isentropic Mach number of 0.4 on a less highly loaded turbine nozzle cascade and the results are presented in Fig. 8.

It appears from both experimental and computational results that the vortical structures emanating from the relatively thick suction surface boundary layer, unlike those from the pressure surface, do not remain as tightly rolled cylindrical vortices but become stretched toward the centerline of the wake. The entropy increase contours associated with the suction surface shedding tend to have the appearance of bands, which are oriented relatively normal to the flow direction.

The computational results in Fig. 7 show pressure side vortices that remain tightly rolled but there appears to be some weakening of the suction side vortices. Otherwise these results seem to represent a conventional von Karman vortex street.

The results of Arnone and Pacciani also indicate tightly rolled pressure side vortices and highly strained bands of fluid connecting the pairs of vortices emanating from the suction and pressure surfaces. The vane geometries and the computational approaches are different; it would be of interest to run both codes for the precise conditions of the subject experiment.

The computational work is able to show the flow structure in much finer detail than the experimental work because the latter can only resolve one-eighth of a wavelength temporally and one-quarter of the trailing edge thickness spatially. It is thought that in most important respects the experimental vortical structures are compatible with both sets of computational work.

The raw stagnation temperature traces were investigated to see if fine scale or turbulent structures could be discerned. Little such structure was observed and it was concluded that a significant improvement in the measurement bandwidth would have been needed to observe fine-scale structure. Such an improvement in the probe and the electronics is planned.

Some experimental observations that resolve higher frequencies have been performed on the vortical structures. These are the sub-microsecond spark schlieren photographs which were taken. An example was given in Fig. 1. This photograph is compatible with the picture obtained from the computational work. In particular braids of fine-scale structure are frequently observed in the schlieren photographs. These braids extend between vortices and may be seen both in schlieren photographs such as Fig. 1 and in the computed entropy increase contours of Fig. 7. Such observations are helpful in clarifying wake vortical structures.

The new wide-bandwidth stagnation temperature probe worked well and reliably. The frequency range, high subsonic Mach number range, and temperature range were almost identical to those prevailing in many important turbomachinery applications. A typical example would be the testing of a transonic fan or compressor rotor. Furthermore, with the availability of a reliable phase reference the phase-averaging approach would lend itself well to mapping time-resolved stagnation temperature and pressure contours through periodic events such as rotor wake passing. Rotor efficiency could previously only be resolved radially; bandwidth limitations had precluded the resolution of blade-to-blade variations in efficiency. Successful demonstration of the new probe offers the possibility of implementing it for traversing in rotating machines and presenting, for the first time, localized efficiencies and loss sources in transonic fans and compressors.

Conclusions

The wake flow behind the blunt trailing edge of a turbine nozzle guide vane was found to be subjected to strong energy redistribution at high subsonic Mach numbers. Unusually cold flows on the wake centerline and hot spots at the edges of the wake were measured. These were caused by energy separation in the shed vortex street due to the Eckert–Weise effect.

Experimental identification of these phenomena was achieved using a new wide bandwidth stagnation temperature probe. This was the first demonstration of the use of the probe in the frequency, Mach number, and temperature ranges typical of operation behind the rotors of high-performance turbomachines such as transonic fans. Using phase-averaging techniques, contours of time-resolved entropy increase were plotted at the downstream traverse plane.

Computational results give qualitative confirmation of the experimental results and make it possible to provide a more detailed explanation of the fine-scale structure of the vortex wake.

Temperature redistribution and vortex shedding phenomena occur under a wide range of physical situations and geometries and have considerable importance for turbine vanes where efficiency and heat transfer considerations are paramount. In establishing the vortex shedding behavior for a particular vane configuration, this paper provides a basis for the systematic investigation of the downstream temperature redistribution.

References

Arnone, A., and Pacciani, R., 1997, "Numerical prediction of trailing edge wake shedding," ASME Paper No. 97-GT-89.

Boldman, D. R., Brinich, P. F., and Goldstein, M. E., 1976, "Vortex shedding from a blunt trailing edge with equal and unequal external mean velocities," *Journal of Fluid Mechanics,* Vol. 75, pp. 721–735.

Buttsworth, D. R., and Jones, T. V., 1998, "A fast response total temperature probe for unsteady compressible flows," ASME *Journal of Engineering for Gas Turbines and Power,* Vol. 120, pp. 694–701.

Carscallen, W. E., and Oosthuizen, P. H., 1989, "The effect of secondary flow on the redistribution of the total temperature field downstream of a stationary turbine cascade," AGARD CP-469.

Carscallen, W. E., Fleige, H. U., and Gostelow, J. P., 1996, "Transonic turbine vane wake flows," ASME Paper No. 96-GT-419.

Currie, T. C., and Carscallen, W. E., 1998, "Simulation of trailing edge vortex shedding in a transonic turbine cascade," ASME JOURNAL OF TURBOMACHINERY, Vol. 120, No. 1, pp. 10–19.

Eckert, E. R. G., and Weise, W., 1943, "Messung der Temperaturverteilung auf der Oberfläche schnell angeströmter unbeheizter Körper," *Forsch. Ing. Wesen,* Vol. 13, pp. 246–254.

Eckert, E. R. G., 1986, "Energy separation in fluid streams," *Int. Comm. Heat Mass Transfer,* Vol. 13, pp. 127–143.

Gostelow, J. P., 1977, "A new approach to the experimental study of turbomachinery flow phenomena," ASME *Journal of Engineering for Power,* Vol. 99, No. 1, pp. 97–105.

Hogg, S. I., Carscallen, W. E., Gostelow, J. P., Buttsworth, D. R., and Jones, T. V., 1997, "Wide bandwidth stagnation temperature measurements in vortical flows behind turbine vanes," ICIASF '97, Monterey, Sept.

Kurosaka, M., Gertz, J. B., Graham, J. E., Goodman, J. R., Sundaram, P., Riner, W. C., Kuroda, H., and Hankey, W. L., 1987, "Energy separation in a vortex street," *Journal of Fluid Mechanics,* Vol. 178, pp. 1–29.

Lawaczek, O., and Heinemann, H.-J., 1975, "Von Karman vortex streets in the wakes of subsonic and transonic cascades," AGARD CP-177, pp. 28.1–28.13.

Menter, F. R., 1993, "Zonal two-equation k–ω turbulence models for aerodynamic flows," AIAA Paper No. 93-2906.

Ng, W. F., Chakroun, W. M., and Kurosaka, M., 1990, "Time-resolved measurements of total temperature and pressure in the vortex street behind a cylinder," *Physics of Fluids A,* Vol. 2, No. 6, pp. 971–978.

Oldfield, M. L. G., Burd, H. J., and Doe, N. G., 1982, "Design of wide-bandwidth analogue circuits for heat transfer instrumentation in transient tunnels," *16th Symposium of International Centre for Heat and Mass Transfer,* Hemisphere Publishing, pp. 233–257.

Roberts, Q. D., and Denton, J. D., 1996, "Loss production in the wake of a simulated subsonic turbine blade," ASME Paper No. 96-GT-421.

Roe, P. L., 1981, "Approximate Riemann solvers, parameter vectors and difference schemes," *Comp. Phys.,* 43, 2 pp. 357–372.

Wilcox, D. C., 1993, "Turbulence modeling for CFD," DCW Industries, La Cañada, CA.

Williamson, R. G., and Moustapha, S. H., 1986, "Annular cascade testing of turbine nozzles at high exit Mach numbers," ASME *Journal of Fluids Engineering,* Vol. 108, pp. 313–320.

Zaman, K. B. M. Q., and Hussain, A. K. M. F., 1981, "Taylor hypothesis and large scale coherent structures," *Journal of Fluid Mechanics,* Vol. 112, pp. 379–396.

A Numerical Study of the Influence of Grid Refinement and Turbulence Modeling on the Flow Field Inside a Highly Loaded Turbine Cascade

T. Hildebrandt

NUMECA Ing.-Büro Th. Hildebrandt,
D-90530 Wendelstein, Germany

L. Fottner

Institut für Strahlantriebe,
Universität der Bundeswehr München,
D-85577 Neubiberg, Germany

A thorough numerical study was conducted to simulate the flow field inside a highly loaded linear turbine cascade. The numerical investigation was focused on the secondary flow field as well as on the prediction of the overall design goals within reasonable accuracy limits. The influence of grid resolution was investigated in order to obtain detailed information about the requirements of a grid-independent solution. Three different two-equation turbulence models were applied to two numerical grids of different resolution. Emphasis was laid on separating the influences of grid resolution and turbulence models. The Mach and Reynolds numbers as well as the level of free-stream turbulence were set to values typical of turbomachinery conditions. The computational study was carried out using a three-dimensional state-of-the-art block structured Navier–Stokes solver. The comparison of the numerical results with experiments clearly revealed the different degree of agreement between simulation and measurement. This paper describes the application of a modern flow solver to a test case that is relevant for practical turbomachinery design purposes. The agreement between the experiments and the results of the numerical study is good and in most cases well within the accuracy limits proposed by Strazisar and Denton (1995). It was found out that the main effect on the quality of the computations is the resolution of the numerical grid. The finest grid used reached over one million points halfspan, showing clearly superior results compared with a coarser, though still fine grid. The influence of different turbulence models on the numerically obtained flow field was relatively small in comparison with the grid influence.

Introduction

Today numerical schemes are capable of capturing the three-dimensional flow field inside turbomachinery cascades.

Still, considerable deficiencies in the quality of numerical flow field simulations may occur in regions that are either characterized by strong gradients in the flow behavior (e.g., shocks, boundary layers) or governed by turbulence phenomena (e.g., separations, laminar–turbulent transition). While strong flow gradients can be dealt with by using an appropriate resolution of the numerical grid—at least theoretically—turbulence still has to be modeled by more or less simplified assumptions, which hardly take into account the complexity of turbulence occurring in highly loaded turbomachinery cascades (Wunderwald, 1995). Steadily rising computational resources and continuously improved numerical algorithms also lead to higher expectations regarding the numerical results. A good agreement with respect to the entities that are easier to obtain, e.g., the midspan pressure distribution, has almost become a prerequisite of a numerical simulation. Today more emphasis is laid on the correct prediction of losses and their spanwise distribution. Although nearly all numerical simulations suffer from too high a level of predicted losses (Gregory-Smith, 1995; Denton, 1996), modern numerical schemes are generally able to predict

the qualitative loss distribution. It has been acknowledged (Strazisar and Denton, 1995) that the accurate prediction of the change between two designs and the computation of the spanwise distributions are at least as valuable as absolute accuracy. Therefore a qualitative prediction—though not the ultimate answer to the designer's needs—is an important design tool to answer the what-if questions during the design phase.

The increased level of losses in CFD simulations, which is observed in the majority of cases, can be explained by the lack of an adequate transition model. Even in turbine cascades, which usually incorporate a dominating laminar boundary layer, a physically more suitable completely laminar computation cannot be performed without inducing large separated flow regions. As a result, and taking the lack of a transition criterion into consideration, these computations have to be carried out with an entirely turbulent boundary layer, contributing to higher overall losses.

The present work has been focused on two major issues:

First, to prove the statement that a solution that is almost independent of the numerical grid can be achieved with second-order accurate numerical schemes by using on the order of 300,000 grid points for a half-span calculation of a single blade row without additional features such as tip clearance or blowing holes. For this purpose one grid with the resolution mentioned above and another with over one million points are compared.

Second, to investigate the influence of different turbulence models on the overall flow behavior as well as on more detailed flow phenomena. In accordance with the state-of-the-art in industry, only two-equation models have been used, which are generally

Table 1 Design data (T106)

Aero-/ Thermodynamics		
Isentropic outlet Mach #	$Ma_{2,th}$	0.59
Isentropic outlet Reynolds #	$Re_{2,th}$	500,000
Inlet flow angle	β_1	127.7°
Outlet flow angle	β_2	26.8°

Geometry		
Chord length	l	100 mm
Blade span	h	300 mm
Pitch ratio	t/l	0.799

Fig. 1 Linear turbine cascade T106

accessible. Efforts have been made to separate the influence of turbulence modeling from the effects of grid refinement.

Computational Method

The computational method employed here (TRACE_S) was developed by DLR Cologne (Vogel, 1997). The scheme solves the three-dimensional Reynolds-averaged Navier–Stokes equations (RANS) on general structured nonorthogonal multiblock grids. The numerical algorithm incorporated is an explicit multistage Runge–Kutta scheme with implicit residual smoothing (Jameson and Baker, 1984). Space integration is performed using a second-order accurate cell-centered finite volume central discretization with artificial dissipation. The code can be applied to both viscous and inviscid calculations. A variety of two-equation turbulence models are included, of which the standard k–ϵ model in its high- and low-Reynolds formulation (Launder and Spalding, 1974; Lam and Bremhorst, 1981) and the k–ω model (Wilcox, 1991) have been used.

The present calculations have been done using a four-step Runge–Kutta algorithm and a CFL number of 4.5.

Linear Turbine Cascade T106

The linear turbine cascade T106, which served as a test case in the present work, is based upon a typical midspan profile of an uncooled low-pressure turbine rotor. It was published as a test case in AGARD-AR-275 (Fottner, 1990) and was extensively investigated during various experimental campaigns. Measurements have been conducted concentrating on secondary flow (Weiß, 1993), side wall contouring (Duden and Fottner, 1997; Schnaus and Fottner, 1997) and blade surface boundary layer behavior (Römer, 1990). The configuration presented here features straight side walls.

Table 1 and Fig. 1 show characteristic geometric and aero-

dynamic specifications of the design data of the linear cascade T106.
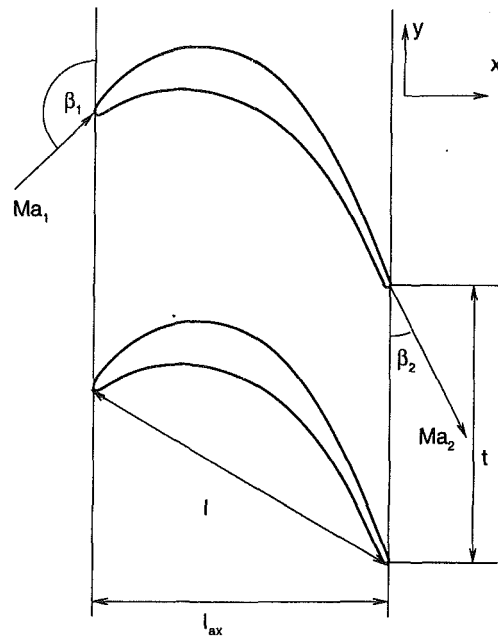
The experimental results used for comparison (Duden and Fottner, 1997) were obtained at the High Speed Cascade Wind Tunnel of the University of the German Armed Forces Munich.

Boundary Conditions. The turbine cascade examined is characterized by an entirely subsonic flow. Therefore, all but one dependent variable needs to be specified at the inlet where the experimentally determined total entities (p_t, T_t) and the flow angle are imposed (Table 2).

Since the inlet boundary layer profile is of paramount importance for the development of the secondary flow field, the measured total pressure profile $p_t(h)$ has been used instead of a power law assumption. At the outflow boundary, the static pressure, also obtained from experiments, is given. With respect to the two-equation turbulence models, the turbulence intensity level Tu_1 and the dissipation length scale L_1 are specified. While the turbulence intensity has been measured by hot-wire anemometry, the length scale has had to be obtained by correlations rather than measurements. The inflow values of the turbulent kinetic energy k and the dissipation rate ϵ are calculated directly from the quantities mentioned above. Along the solid walls an adiabatic boundary condition is set. As no mod-

Nomenclature

h = blade height, span, m
k = turbulent kinetic energy, m^{2}s^{-2}
l = chord length, m
L = turbulent length scale, m
Ma = Mach number
p = pressure, Nm^{-2}
q = dynamic head, Nm^{-2}
Re = Reynolds number
t = blade pitch, m
T = temperature, K
Tu = turbulence intensity, percent
S = strain rate, s^{-2}

v_i, v_j, v_k = velocity components, ms^{-1}
x_i, x_j, x_k = spacial components, m
y^+ = nondimensional wall distance
β = flow angle, deg
ϵ = rate of dissipation of turbulent kinetic energy, m^{2}s^{-3}
η = efficiency
μ = dynamic viscosity, kgm^{-1}s^{-1}
μ_t = eddy viscosity, kgm^{-1}s^{-1}
ρ = density, kgm^{-3}
τ_w = wall shear stress, Nm^{-2}
ω = turbulent frequency, s^{-1}

ω = loss coefficient

Subscripts

ax = axial
G = overall mass-averaged
is, th = isentropic flow conditions
MS = midspan mass-averaged
t = total
w = wall
$1, 2, \infty$ = cascade conditions: inlet, outlet, free-stream
— = time mean

Table 2 Numerical boundary conditions (T106)

Inlet	$p_{t,1,\infty}$	47540 Nm^{-2}
	$T_{t,1,\infty}$	312.9 K
	β_1	127.7°
	Tu_1	5.8%
	L_1	2 mm
Outlet	p_2	37930 Nm^{-2}

eling of the laminar–turbulent transition is available, all boundary layers are treated as completely turbulent. At the midspan plane, a symmetry boundary condition is applied.

Computational Grid. The numerical domain has been discretized by an eight-block grid topology (Fig. 2). Emphasis has been laid on a high grid quality in order to preserve as high a numerical accuracy as possible. This holds particularly for the regions which are most sensitive to numerical dissipation, e.g., the boundary layer and wake region. Therefore an O-topology has been chosen in the immediate vicinity of the blade surface to guarantee a highly orthogonal grid. Apart from the advantages of this multiblock topology, it has to be mentioned that large numbers of grid blocks necessitate more effort during the grid generation and a certain amount of computational overhead during the calculation.

In Fig. 2 every other grid point in each direction of the coarse grid (303,000 points) is displayed. The plane used for evaluation $x/l_{ax} = 1.5$ is marked. Table 3 gives an overview of the grid point distribution.

Turbulence Modeling. The time integration of the instantaneous Navier–Stokes equations leads to the fundamental closure problem of turbulence by introducing additional terms of the order $\overline{\rho v_i'' v_j''}$. Turbulence models attempt to relate the Reynolds stresses $\overline{\rho v_i'' v_j''}$ to the mean flow variables and the fluid properties.

Three different turbulence models have been applied during this numerical investigation:

Standard k–ϵ Model. The most frequently used two-equation turbulence model was first proposed by Launder and Spalding (1974). The gradient hypothesis suggested by Boussinesq (1877) is used to relate the Reynolds stresses to the mean velocity gradients

Fig. 2 S_1 view computational grid 303 k

by the turbulent viscosity. The transport equations for k and ϵ are written as:

$$\frac{\partial(\rho k)}{\partial t} + \frac{\partial(\rho v_i k)}{\partial x_i} = \frac{\partial}{\partial x_i}\left[\left(\mu + \frac{\mu_t}{\sigma_k}\right)\frac{\partial k}{\partial x_i}\right] + P_k - \rho\epsilon \quad (1)$$

$$\frac{\partial(\rho\epsilon)}{\partial t} + \frac{\partial(\rho v_i\epsilon)}{\partial x_i} = \frac{\partial}{\partial x_i}\left[\left(\mu + \frac{\mu_t}{\sigma_\epsilon}\right)\frac{\partial\epsilon}{\partial x_i}\right]$$
$$+ C_{\epsilon 1}P_k\frac{\epsilon}{k} - C_{\epsilon 2}\rho\frac{\epsilon^2}{k} \quad (2)$$

where the production term P_k is related to the strain rate S by

$$P_k = 4\mu_t S \quad (3)$$

with

$$S = \frac{1}{4}\left(\frac{\partial v_i}{\partial x_j} + \frac{\partial v_j}{\partial x_i}\right)\frac{\partial v_i}{\partial x_j}. \quad (4)$$

The eddy-viscosity relation

$$\mu_t = \rho C_\mu\frac{k^2}{\epsilon} \quad (5)$$

is used to finally close the sets of the two equations. $\sigma_k = 1.0$, $\sigma_\epsilon = 1.3$, $C_{\epsilon 1} = 1.44$, $C_{\epsilon 2} = 1.92$ and $C_\mu = 0.09$ are the standard constants of the standard k–ϵ model (Launder and Spalding, 1974).

In the vicinity of solid walls the log law representation of the boundary layer velocity profiles is used, which limits the application of the standard k–ϵ model to high-Reynolds-number flows. The model is therefore also referred to as the high-Reynolds k–ϵ model. In order to ensure high Reynolds numbers in the near-wall regions of the computational domain, the grid resolution of boundary layers should be restricted to a *minimum* nondimensional wall distance of

$$y^+ = \frac{y}{\mu_w}\sqrt{\rho_w\tau_w} \geq 30. \quad (6)$$

Considering the wide range of boundary layer profiles in turbomachinery cascades, it becomes obvious that this condition cannot always be strictly maintained.

Low-Reynolds k–ϵ Model. The above-mentioned restriction of the high-Reynolds k–ϵ model to a minimum wall distance of $y^+ \geq 30$ can be overcome by an extension suggested by Lam and Bremhorst (1981) leading to the low-Reynolds k–ϵ model. The constants $C_{\epsilon 1}$, $C_{\epsilon 2}$, and C_μ are now multiplied by the viscosity-dependent functions f_1, f_2, and f_μ

$$f_1 = 1 + (0.05/f_\mu)^3$$
$$f_2 = 1 - \exp(-\text{Re}_t^2)$$
$$f_\mu = [1 - \exp(-\text{Re}_k)]^2(1 + 20.5/\text{Re}_t) \quad (7)$$

where

$$\text{Re}_k = \frac{\rho y\sqrt{k}}{\mu} \quad \text{and} \quad \text{Re}_t = \frac{\rho k^2}{\mu\epsilon}. \quad (8)$$

Table 3 Grid resolution

	Grid points		
	total	S_1-plane	halfspan
Coarse grid	303,000	8,200	37
Fine grid	1,138,000	11,700	97

Journal of Turbomachinery

Table 4   Turbulence modeling and y^+ values

	Fine Grid	Coarse Grid
Turbulence Models	Low-Re k-ε, k-ω	Hi-Re k-ε, k-ω
y^+(Sidewall)	$\approx 0.6 \ldots 1.0$	$\approx 17 \ldots 45$
y^+(Suction Surface)	$\approx 0.1 \ldots 0.5$	$\approx 12 \ldots 28$
y^+(Pressure Surface)	$\approx 0.5 \ldots 1.3$	$\approx 20 \ldots 60$

The first grid cell should be placed inside the viscous sublayer to ensure a proper implementation of the wall boundary condition. In contrast to the high-Reynolds k-ε model, the low-Reynolds k-ε model requires a *maximum* nondimensional wall distance of

$$y^+ \leq 2. \tag{9}$$

If large regions inside the computational domain are existent where the nondimensional wall distance of the first grid cell is between $2 \leq y^+ \leq 30$, the use of neither the high-Reynolds k-ε model nor the low-Reynolds k-ε model is justified. However, these limitations sometimes have to be partially overruled by practical consideration such as computer resources and the efforts linked to a suitable grid generation.

k-ω Model.   An alternative formulation of a two-equation model has been proposed by Wilcox (1991), implementing the frequency ω of the energy-containing turbulent eddies:

$$\omega = \frac{\epsilon}{C_\mu k} = \frac{\rho k}{\mu_t} \tag{10}$$

The k-ω model can in principal be derived by substituting the ϵ-equation Eq. (2) by Eq. (10) with the introduction of a different set of constants ($\sigma_k = 2.0$, $\sigma_\epsilon = 2.0$, $C_{\epsilon 1} = 1.56$, $C_{\epsilon 2} = 1.83$, and $C_\mu = 0.09$). However, significant extensions to the k-ω model have been suggested to include the effects of rotation (Bardina et al., 1985) and compressibility (Wilcox, 1991). In the frame of the present work, the k-ω model has been used with and without wall functions according to the grid resolution.

Parameters: Grid Resolution and Turbulence Models.   The combinations of grids and turbulence models used in this numerical study are shown in Table 4. As discussed above, high- and low-Reynolds k-ε models should not be used on grids with the same resolution. In order to investigate the influence of grid resolution and turbulence models separately without sacrificing the necessary limitations of the latter, the k-ω model has been applied to both grids.

The posterior resulting y^+ values on both grids (Table 4) indicate that the use of all turbulence models on their respective grids was justified. While the low-Reynolds k-ε model was always used on a sufficiently fine grid, the high-Reynolds k-ε model encountered very limited regions of too fine a resolution. Because of the small extent of those areas (e.g., stagnation point, limited separated flow regions) these violations of Eqs. (6) and (9) can easily be accepted.

Computational Details.   All computations have been carried out on a single processor of a multiprocessor SGI Origin (R10000, 175 MHz) performing about 4.0×10^{-5} seconds per iteration per grid point. It took approximately 14 h CPU time to converge for the coarse grids (303 k) and 70 h for the fine grids (1138 k).

Each investigated parameter variation has individually been set up on a coarsened grid, which was created by skipping every other grid point in each direction. There a zero-flow initial solution has been imposed and an inviscid calculation performed. These coarse grid solutions have then been interpolated on the corresponding final grid where the viscous and turbulent calculations were carried

out. Local time stepping and implicit residual smoothing were further means to accelerate convergence.

The residual history (Fig. 3) has been evaluated by a calculation on the fine grid using the low-Reynolds k-ϵ model. The root mean square (rms) averaged density residual is displayed versus the number of iterations. Although it is obvious that convergence still has not come to an end, the computation has been stopped after 5400 iterations with respect to the CPU time spent.

A drop in the residual of nearly five orders of magnitude could be achieved, which was considered a satisfying level of convergence. No significant difference in convergence behavior could be observed between the different k-ϵ models, whereas the k-ω model shows a slightly slower convergence. Naturally, the coarse grid converged at a higher rate due to the larger possible local time steps. There, after 4000 iterations the final level of convergence at about four orders of magnitude reduction in residual was reached. Mass flow conservation has been ensured in all cases within $\pm 10^{-3}$ percent difference between inlet and outlet of the domain.

Results

Global Entities.   The first step to evaluate the results of numerical simulations is to compare the global mass-averaged parameters, loss coefficient and exit flow angle, with measurements. Averaging in the midspan plane offers the additional opportunity to separate profile and secondary losses. While the absolute level of loss in computations is usually found to be too high, the comparison between the ratio of overall and midspan losses is one possibility of revealing the correct prediction of secondary flow behavior.

Loss Coefficient.   The loss coefficient is defined

$$\omega = \frac{p_{t,1} - \overline{p_t}}{q_{2,th}} = \frac{p_{t,1} - \overline{p_t}}{p_{t,1} - p_2} \tag{11}$$

where $\overline{p_t}$ is the mass-averaged total pressure. All calculations predict the loss coefficient too high, a result of an entirely turbulent instead of a laminar–turbulent assumption. The lack of a transition model demanded either a purely turbulent or laminar calculation. A laminar calculation would certainly have been closer to reality, taking the large portions of laminar flow regions in turbine cascades into account (Weiß, 1993; Moore and Gregory-Smith, 1996). Attempts have been made to conduct laminar calculations on both grids, resulting in violent flow separations at the blade suction surface and parts of the side walls. These separations led to an unsteadily fluctuating computation, prevented a satisfactory level of convergence, and ended in even higher losses.
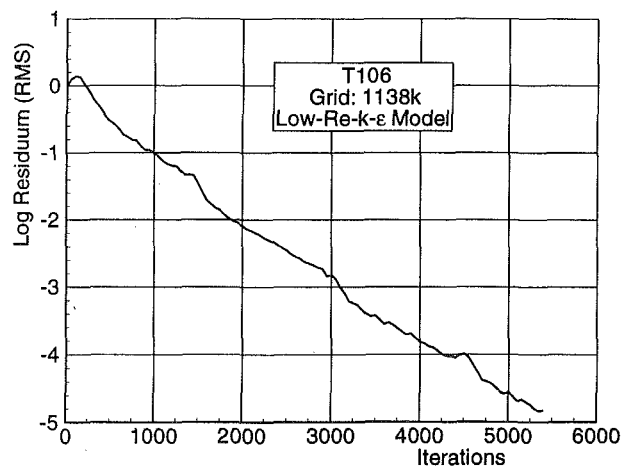

Fig. 3   Convergence history

Table 5   Mass-averaged loss coefficient at $x/l_{ax} = 1.5$

		ω_{MS}	ω_G	ω_{MS}/ω_G
	Experiment	0.021	0.035	**0.589**
303k	Hi-Re-k-ϵ	0.027	0.049	0.551
	k-ω	0.026	0.048	0.542
1,138k	Low-Re-k-ϵ	0.024	0.042	0.571
	k-ω	0.033	0.056	0.589

The differences between the high-Reynolds k–ϵ model and the k–ω model on the coarse grid are negligibly small. The increasing resolution of the boundary layer profiles and trailing edge wake in conjunction with decreasing numerical dissipation is the reason for the lower levels of losses on finer numerical grids. This obviously holds for the low-Reynolds k–ϵ model but it cannot be proved for the k–ω model. The combination of fine grid and k–ω model leads to the highest calculated loss coefficients found during the numerical study. One explanation for this odd behavior might be derived from the formulation of the k–ω model implemented in TRACE_S. Wall functions are used on coarse grids to stabilize the model numerically. On finer grids where $y^+ \leq 2.5$ these wall functions are suppressed, possibly introducing some instabilities. In spite of all these considerations the deviations between calculated and measured loss coefficients are, according to numerical experience, reasonable, ranging between 20 and 50 percent increased computational losses. However, a simple estimation shows that even a 20 percent relative difference in loss coefficient contributes to a difference of roughly 2 percent between calculated and measured isentropic efficiency, a value that undoubtedly prevents a quantitative calculation of efficiency in an industrial environment.

Still, numerical simulations can be applied usefully even in terms of loss coefficient determination as long as the absolute quantities are not taken into account, but the shape of distributions or the differences between two designs. This is proved by the ratio between midspan and overall losses ω_{MS}/ω_G (Table 5), which can be looked upon as a simple criterion of estimation as to whether the secondary flow field has been captured correctly. The deviations from the experimental loss ratio values of 0–7 percent are relatively small compared with the absolute deviations. Again the calculations on the fine grid are clearly superior to those on the coarse grid.

Exit Flow Angle. The exit flow angle has been calculated with deviations of ±0.2 deg in the midspan plane and ±0.5 deg in the overall averaged value (Table 6). This is well within the desired range of ±1.0–2.0 deg proposed by Strazisar and Denton (1995). Unlike the loss coefficient, the calculated exit flow angles do not show significant differences between the various combinations of turbulence model and grid resolution (Table 5).

Blade Surface Pressure Distribution. The static pressure distribution has been normalized by the inlet free-stream total pressure. All results are summarized in Fig. 4 for the midspan and the side wall section.

The calculated distribution along midspan almost exactly fits the measured data. No significant difference between the effects of turbulence models and grid resolution can be found. This was to be expected as viscous effects have quite a small influence on the midspan static pressure distribution as long as there are no large separation regions or laminar separation bubbles. Indeed, a very small laminar separation bubble exists in reality at ≈84 percent relative chord of the suction surface. Naturally, a laminar separation bubble cannot be captured by any turbulent calculation, which leads to a slight deviation from the experimental pressure distribution at this location.

As to the side wall static pressure distribution, the situation is quite different. Since this flow region is well inside the side wall boundary layer, it is dominated by viscous effects. Hence differences between grid resolutions and turbulence models are to be expected.

Agreement between experiment and measurement is still good at the side wall. Only in the region $0.3 < x/l_{ax} < 0.5$ the predicted static pressure is slightly too high. The differences between grids and turbulence models are still small with the exception of the k–ω model on the coarse grid, which shows the largest deviation from the measurements by predicting a local maximum in static pressure.

Pitchwise-Averaged Entities. The standard method of quantifying secondary flow effects is to display the pitchwise-averaged variables displayed versus the blade height. Compared with the global (zero-dimensional) entities the degree of averaging is lower, allowing more details of the flow to be uncovered.

Pitchwise-Averaged Loss Coefficient. The pitchwise-averaged loss coefficient ω versus the blade height obtained by mass averaging in the plane $x/l_{ax} = 1.5$ (Fig. 5) shows a marked dependence on the grid resolution. While the agreement close to the midspan plane ($h \approx 150$ mm) is within reasonable range (Table 5), the deviations are rising in the region dominated by secondary flow phenomena.

Both coarse grid solutions predict the loss peak too far away from the side wall at $h \approx 50$ mm compared with 40 mm measured. While the level of the loss peak is still in good agreement with the experiments, the area of high losses is far greater than measured. This larger area, representing the integral mass-averaged loss coefficient, obviously contributes to a high degree to the high calculated overall losses. In the immediate vicinity of the side wall ($h \approx 15$ mm) the losses are slightly underpredicted. Only minor differences between the turbulence models can be found with the k–ω model predicting local minima and maxima in the loss distribution too distant from the side wall.

The fine grid computations are in considerably better agreement with the measured data compared with the coarse grid. The loss peak at $h \approx 40$ mm has been correctly produced by the low-Reynolds k–ϵ model as well as the k–ω model. The absolute level of the loss coefficient is still too high, particularly in the case of the k–ω model. Although this model predicts the local minimum $h \approx 20$ mm at the right position and with the correct value, the close-wall region is overpredicted. On the whole, the low-Reynolds k–ϵ model leads to a more accurate prediction.

The influence of grid resolution is clearly dominating the differences between the various turbulence models.

Pitchwise-Averaged Flow Angle. Compared with the loss coefficient, the flow angle has been predicted more accurately. This has already been observed while examining the global entities and is also confirmed by its spanwise distribution. A maximum local deviation of approximately 3 deg is a very reasonable agreement.

On the coarse grid the high-Reynolds k–ϵ model and the k–ω model perform very similarly. The position of maximum underturning, like the corresponding loss peak, has been simulated too extended and too far away from the side wall. The overturning is properly positioned but is slightly overemphasized.

Table 6   Mass-averaged flow angle at $x/l_{ax} = 1.5$

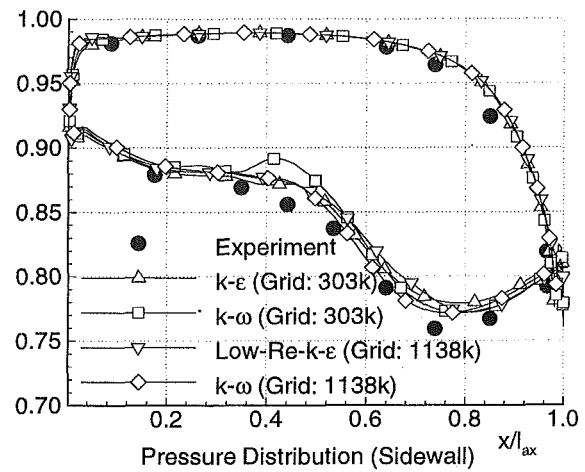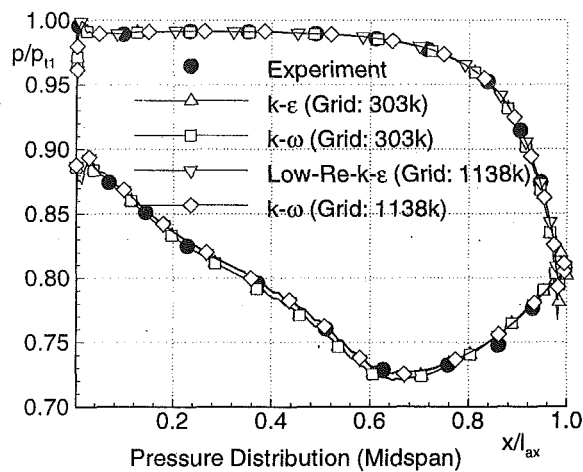|		$\beta_{2,MS}[^\circ]$	$\beta_{2,G}[^\circ]$
	Experiment	**26.8**	**27.1**
303k	Hi-Re-k-ϵ	26.9	27.6
	k-ω	27.0	27.4
1,138k	Low-Re-k-ϵ	26.6	27.0
	k-ω	26.7	27.3

Fig. 4 Blade surface pressure distribution

The fine grid calculations show an even better agreement. The spanwise flow angle distribution has been picked up qualitatively and quantitatively well. The underturning is positioned correctly ($h \approx 35$ mm) and is only slightly overpredicted. The greatest differences between experiment and computation can be found in the near-wall region where also some differences between the turbulence models are apparent. The very small local peak in flow angle in this region cannot be confirmed by the measurements due to the much coarser experimental resolution.

Again the difference between the two numerical grids is markedly greater than between the various turbulence models.

Local Loss Distribution. Local values have been obtained directly rather than by any form of averaging. Therefore, they present the most accurate method of investigating local details of the flow as no mutual compensation of any effects can occur. The local loss coefficients in the evaluated plane $x/l_{ax} = 1.5$ are shown in Figs. 6 and 7.

Looking upstream to the pressure (PS) and suction side (SS) of the trailing edge, Figs. 6 and 7 reveal the dominant flow features characteristic of high turning turbine cascades. The experiments show the

typical shape of the loss distribution with a "two-dimensional" flow region between $h = 150$ mm (midspan) and $h \approx 75$ mm. The distribution of secondary losses is characterized by three loss cores (LC1, LC2, LC3). The first loss core has its origin between the separation lines of the suction side branch of the horseshoe vortex and the passage vortex. LC2 is directly related to the passage vortex. Low-energy fluid from the side wall boundary layer is directed toward the blade suction surface by the circumferential pressure gradient. There it is rolled up and convected upspan. The passage vortex induces a counterrotating corner vortex in the corner between side wall and blade suction surface, leading to the third loss core LC3 (Duden and Fottner, 1997; Weiß, 1993). All computations are able to reproduce the loss structure mentioned above though they differ considerably in quality.

As already discussed (Table 5, Fig. 5), the overall loss level has been predicted too high.

The coarse grid computations tend to predict the sharply separated loss centers LC1 and LC2 in a too diffusive manner. In particular, the $k-\omega$ model calculation tends to amalgamate the two cores. This behavior can also be observed in CFD calcula-
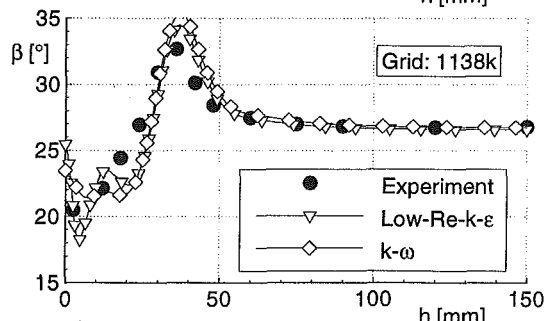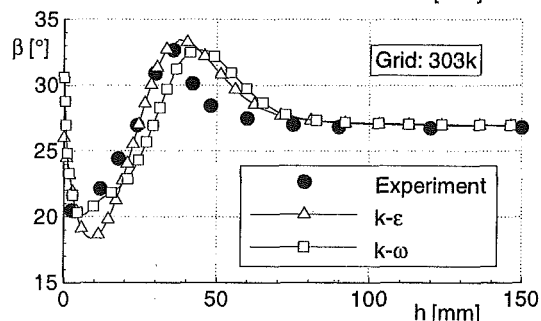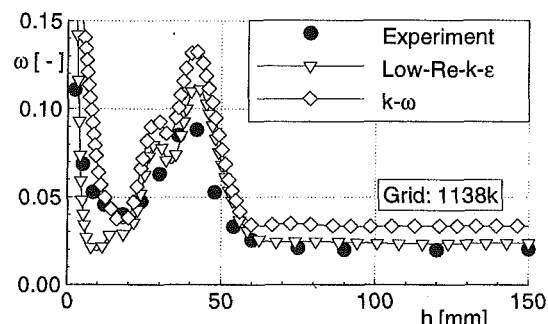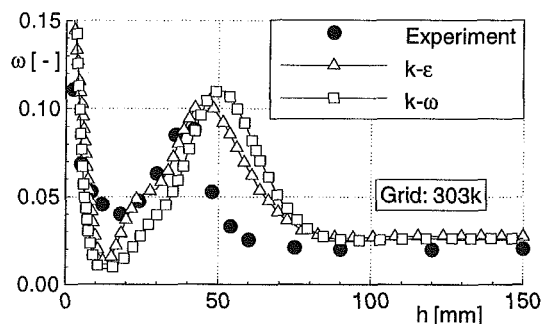

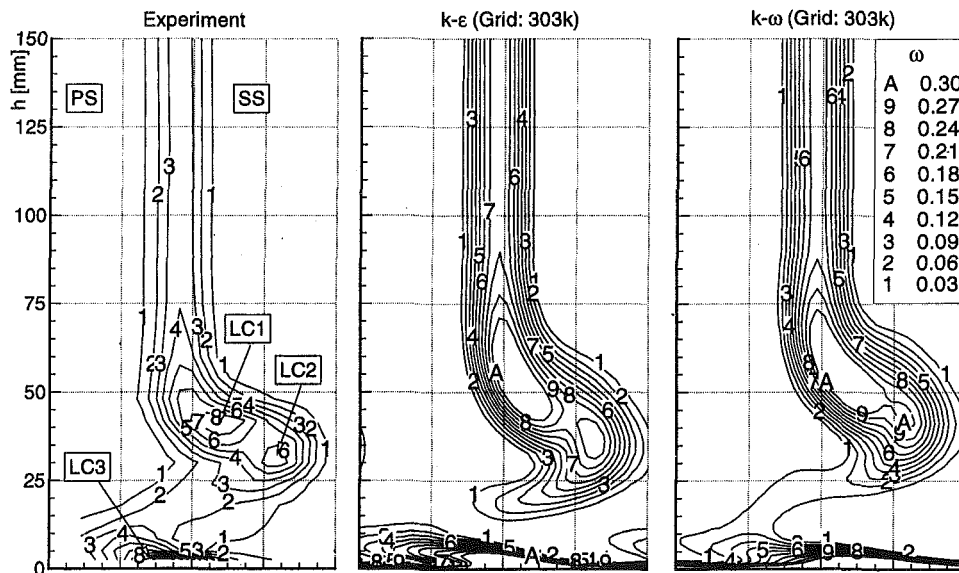**Fig. 5 Pitch-averaged loss coefficient and flow angle**

Fig. 6 Local loss coefficient ω at $x/l_{ax} = 1.5$, grid 303 k

tions of other turbine cascades with comparable grid resolutions, though featuring different turbulence models and numerical schemes (Hah and Loellbach, 1995; Hildebrandt and Fottner, 1996; Gregory-Smith, 1995). Both turbulence models used on the coarse grid predicted the location of LC1 too distant from the side wall and far too extended, which leads to a significantly smaller extension of the two-dimensional flow region. The second loss core LC2 has hardly been captured, at least not clearly. The $k-\omega$ model found LC2 too far away from the side wall and too much smeared into LC1. LC3 is reproduced fairly well by both turbulence models, although the required minimum distance of the probe from the side wall makes a detailed experimental confirmation impossible.

Even at the considered position $x/l_{ax} = 1.5$, which is located fairly downstream of the trailing edge, no extensive numerical "smearing" of the wake can be observed. The circumferential extension of the wake has been captured by all calculations. This

is considered to be mainly a result of the good quality and stream alignment of the numerical grid in the wake region. The often observed disturbance of strong flow gradients over several grid cells could largely be avoided. Only the $k-\omega$ model on the fine grid shows a slightly thickened wake.

The improvement on the fine grid is notable. The characteristic shape of the loss distribution has—compared with the coarse grid solutions—been reproduced more significantly. The loss cores LC1 and LC2 are clearly separated. Both their location and extension are almost identical to the experimental data. Again, the best results are obtained with the low-Reynolds $k-\epsilon$ model. The higher loss level of the $k-\omega$ model, which has already been observed, can be identified more closely by looking at the slightly larger circumferential extension of the wake and secondary loss region, as well as the more significant corner vortex losses (LC3). The latter may explain the differences between the low-Reynolds $k-\epsilon$ model and the $k-\omega$ model in the
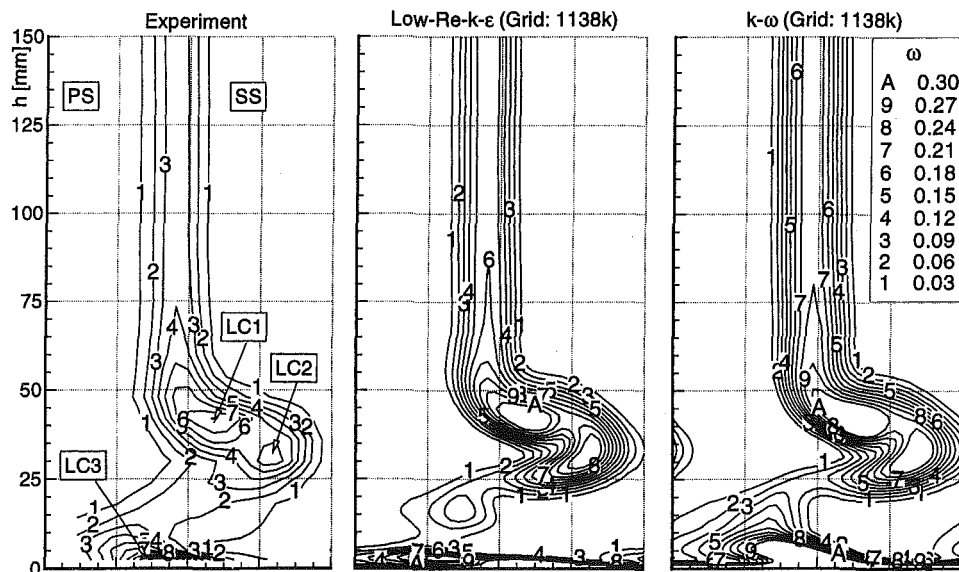

Fig. 7 Local loss coefficient ω at $x/l_{ax} = 1.5$, grid 1138 k

near-wall region already observed with the pitch-averaged loss distribution (Fig. 5).

Comparing the two computations on the different grids with the $k-\omega$ model, the influence of turbulence modeling can be separated from the effects of grid refinement, the latter being the far more dominant parameter.

Conclusion

The flow field inside the linear turbine cascade T106 has been numerically simulated using the block-structured three-dimensional Navier–Stokes solver TRACE_S. Computations have been conducted on numerical grids of different resolution using a variety of turbulence models. In order to separate the influence of grid resolution and turbulence modeling, the $k-\omega$ model has been used, which can be applied regardless of any grid resolution constraints. The following can be summarized:

- **Results:** The agreement between measurements and computations satisfies most of the accuracy requirements proposed by Strazisar and Denton (1995). It could be proved that the demanded accuracy in pressure rise (± 1–2 percent) as well as in the flow angle (± 1–2 deg) has been reached. However, the loss prediction is still far away from the goal of (± 0.5–1 percent) accuracy in the predicted isentropic efficiency. The lack of appropriate transition criteria and the instability of a purely laminar calculation demand fully turbulent calculations. Although the calculated losses are therefore predicted too high, the shape of the spanwise distributions as well as the local distributions have been predicted sufficiently accurate.

- **Computational Grid:** The chosen multiblock topology leads to a numerical grid of high quality expressed in terms of orthogonality, resolution, and smoothness. These are essential prerequisites for obtaining accurate results in regions that are dominated by viscous effects such as those considered herein. The influence of the grid refinement from an already reasonably fine 303,000 points to 1,138,000 points half-span was the most dominating parameter during this study. The often heard statement of a grid-independent solution beyond 300,000 points for testcases like this one cannot be confirmed.

- **Turbulence Modeling:** The influence of turbulence modeling was found to be considerably less significant than grid resolution. The results achieved by the $k-\epsilon$ model, in its standard as well as in its low-Reynolds formulation, differ only in details from the $k-\omega$ model. These differences mostly appear in the near wall regions. The low-Reynolds $k-\epsilon$ model performed best of all considered models. It should be remembered that typical Reynolds numbers for turbomachinery applications in conjunction with a maximum nondimensional wall distance of $y^+ \leq 2$ require numerical grid resolution on the order of 10^6 points per blade row. Therefore, the use of this model in a turbomachinery design environment may yet be limited by its large requirements of computational resources.

References

Bardina, B. S., Ferziger, J. H., and Rogallo, R. S., 1985, "Effect of Rotation on Isotropic Turbulence: Computation and Modelling," *Journal of Fluid Mech.*, Vol. 154, pp. 312–336.

Boussinesq, J., 1877, "Théorie de l'Écoulement Tourbillant," *Mém. Présenté par Divers Savants Acad. Sci. Inst. Fr.*, Vol. 23, pp. 46–50.

Denton, J. D., 1996, "Lessons from Rotor 37," Whittle Laboratory, Cambridge, UK.

Duden, A., and Fottner, L., 1997, "Influence of taper, Reynolds number, and Mach number on the secondary flow field of a highly loaded turbine cascade," *Proc. 2nd European Conference on Turbomachinery-Fluid Dynamics and Thermodynamics*, Antwerp.

Fottner, L., ed., 1990, "Test Cases for Computation of Int. Flows in Aero Engine Components," AGARD-AR-275.

Gregory-Smith, D. G., 1995, "Calculations of the Secondary Flow in a Turbine Cascade," *Computational Fluid Dynamics in Aeropropulsion*, ASME AD-Vol. 49.

Hah, C., and Loellbach, J., 1995, "Numerical Results of Linear Turbine Cascade," *Proc. ERCOFTAC Seminar and Workshop*.

Hildebrandt, T., and Fottner, L., 1996, "Durham Low Speed Turbine Cascade," *Proc. ERCOFTAC Seminar and Workshop*.

Jameson, A., and Baker, T. J., 1984, "Multigrid Solution of the Euler Equations for Aircraft Configurations," AIAA Paper No. 84-0093.

Lam, C. G., and Bremhorst, K. A., 1981, "Modified Form of the $k-\epsilon$ Model for Prediction of Wall Turbulence," ASME *Journal of Fluids Engineering*, Vol. 103, pp. 456–460.

Launder, B. E., and Spalding, D. B., 1974, "The Numerical Computation of Turbulent Flows," *Comp. Meth. Appl. Mech. Eng.*, Vol. 3, pp. 269–289.

Moore, H., and Gregory-Smith, D. G., 1996, "Transition Effects on Secondary Flows in a Turbine Cascade," ASME Paper No. 96-GT-100.

Römer, N., 1990, "Theoretische und experimentelle Untersuchungen zum Umschlagverhalten der Profilgrenzschicht an Verdichter- und Turbinengittern," Ph.D. Thesis, University of the German Armed Forces, Munich, Germany.

Schnaus, J., and Fottner, L., 1997, "Experimental and Numerical Investigations of the Influence of Endwall Inclination and Contouring on the Flow Field of a Highly Loaded Turbine Cascade," AIAA, IS 123/GE3, Chattanooga, TN.

Strazisar, A. J., and Denton, J. D., 1995, "CFD Code Assessment in Turbomachinery—A Progress Report," *IGTI Global Gas Turbine News*, pp. 12–14.

Vogel, D. T., 1997, "Numerische Untersuchung des Mischungsverhaltens von Filmkühlstrahlen in Turbinenströmungen," DLR-Report 96-35, Institut für Antriebstechnik, DLR Cologne, Germany.

Weiß, A. P., 1993, "Der Einfluß der Profilgeometrie auf die Entwicklung der Sekundärströmungen in Turbinengittern," Ph.D. Thesis, University of the German Armed Forces, Munich, Germany.

Wilcox, D. C., 1991, "Progress in Hypersonic Turbulence Modelling," AIAA Paper No. 91-1785.

Wunderwald, D., 1995, "Untersuchung der Turbulenzstrukturen in hochbelasteten Verdichter- und Turbinengittern," Ph.D. Thesis, University of the German Armed Forces, Munich, Germany.

Viscous and Inviscid Linear/Nonlinear Calculations Versus Quasi-Three-Dimensional Experimental Cascade Data for a New Aeroelastic Turbine Standard Configuration

T. H. Fransson

M. Jöcker

Chair of Heat and Power Technology,
Royal Institute of Technology,
Stockholm, Sweden

A. Bölcs

P. Ott

Laboratoire de Thermique Appliquée et de
Turbomachines,
Swiss Federal Institute of Technology,
Lausanne, Switzerland

This paper presents a new International Standard Configuration to be added to an already existing set of 10 configurations for unsteady flow through vibrating axial-flow turbomachine cascades. This 11th configuration represents a turbine blade geometry with transonic design flow conditions with a normal shock positioned at 75 percent real chord on the suction side. Out of a set of test cases covering all relevant flow regimes two cases were selected for publication: A subsonic, attached flow case, and an off-design transonic case showing a separation bubble at 30 percent real chord on the suction side. The performed tests are shown to be repeatable and suitable for code validations of numerical models predicting flutter in viscous flows. The validity of the measured data of the two public cases was examined and comparisons with other tests were conducted. Sometimes a large difference in aerodynamic damping was observed on cases with similar flow conditions. This was investigated at three transonic cases with almost identical inlet flow conditions and only small variations in outlet Mach number. It was found that the differences in the global damping are due to very local changes on the blade surface in the shock region, which obtain a large influence by the integration because of the discrete measuring points. Hence it is recommended not to look at the global damping for code validations but more precisely to the local values. These show a common tendency, which is reproducible with different numerical methods. This was demonstrated with a potential model, a linear Euler model, a nonlinear Euler model, and a Navier–Stokes solver, all applied to predict flutter of each test case with a 2D/Q3D approach. This paper demonstrates both the limitations of inviscid codes to predict flutter in viscous flow regimes, and their cost advantage in attached flow calculations. The need for viscous code development and validation is pointed out. This should justify and encourage the publication of thoroughly measured test cases with viscous effects.

Introduction

Several unsteady prediction models for flutter at attached flow conditions have appeared in the open literature (and as confidential design methods in the industry) over the last decade (see, for example, Verdon and Caspar, 1984; Whitehead and Newton, 1985; Fransson and Pandolfi, 1986; Smith, 1989; Hall et al., 1989; He, 1990; Whitehead, 1990; Sidén, 1991; Holmes and Chuang, 1991; Huff, 1991; Carstens et al., 1993; Giles and Heimes, 1993; Kahl and Klose, 1991; Gerolymos and Vallet, 1996; Groth et al., 1996; Grüber and Carstens, 1998). Several of these models show good to excellent agreement against selected test cases of mainly two-dimensional nature. However, the number of internationally accepted test cases for turbomachine blade flutter studies is largely limited to a data base established as part of the Symposium series "Unsteady Aerodynamics and Aeroelasticity in Turbomachine Cascades." This database is documented in two reports by Bölcs and Fransson (1986) and Fransson and Verdon (1991). A large need for more well-documented experimental data for code vali-

dation and for a better physical understanding of unsteady flow phenomena, and especially the propagation of disturbances, through vibrating cascades exists throughout the aeroelastic research community.

Some years ago extensive experiments on a two-dimensional section of a vibrating last-stage gas turbine blade (54 percent span) were performed in the annular test rig at the EPF-Lausanne (Bölcs et al., 1991; Bölcs and Körbächer, 1993). Many experiments have also been performed on the same geometry in the linear test facility at the EPFL (Norryd and Bölcs, 1997; Ott et al., 1998). This substantial database, especially the one from the annular test facility, has been used by a few researchers for code validation over the years (Bölcs et al., 1991; Carstens et al., 1993; Leyland et al., 1994; Grüber and Carstens, 1998). However, the blade geometry has not been available to the larger research community until presently.

Objective

The objective of the present paper is, for the first time, to make general unsteady data of the well-documented experiments, performed in an annular test facility, on a low-pressure gas turbine blade section available to the larger research community. In this process, the experimental results should be scrutinized in detail against some selected numerical models of different complexities,

with the aim to establish inconsistencies between the experiments and the models, as well as eventual differences between the various models.

Method of Attack

Out of the large quantity of experimental results available, a few test cases have been selected with the aim to illustrate the quality of the data, both as regards to the repeatability of the steady-state and unsteady results, and regards changes in unsteady behavior due to small variations in the outlet flow conditions. Such a process is of importance for any experimental results presented with the aim of comparison with theory or numerical results, and specifically for unsteady experiments, where data can only be obtained at discrete locations on a blade surface. Results from three series of subsonic, transonic, and supersonic outlet Mach numbers will be analyzed, with emphasis on the most critical conditions (transonic). Along these lines the importance of looking at the detailed unsteady pressure distribution along the blade surface is illustrated by demonstrating that the global aerodynamic damping determined from discrete pressure transducer locations in the experiments can vary significantly because of small inevitable inconsistencies in the experimental conditions.

Thereafter, numerical results from four different numerical methods are presented and compared to the experimental data.

Finally, two selected experiments are proposed as test cases for the new 11th Standard Configuration on Unsteady Flow Through Vibrating Turbomachine Cascades. They represent one subsonic case for code calibration and one transonic off-design case with high-incidence inlet flow angle and a separation bubble on the suction surface leading edge, which should be a challenge for viscous prediction model development. These cases including full geometry will be provided on the Internet together with the International Standard Configurations 1–10 (internet address: http://www.egi.kth.se/ekv/stcf).

Brief Description of Test Facility and Geometry

Several flow cases were studied in the annular non rotating cascade facility at EPF-Lausanne, which is schematically drawn in Fig. 1. The main features can be summarized as follows: Inlet and outlet conditions can be varied over a large range, where a two-settling-chamber system allows to adjust the radial flow distribution at the inlet to the blade channel. The outer diameter of the test section is 400 mm, and the blade span is 40 mm.

The test facility is supplied with air by a four-stage radial compressor with a maximum mass flow rate of 10 kg/s and a
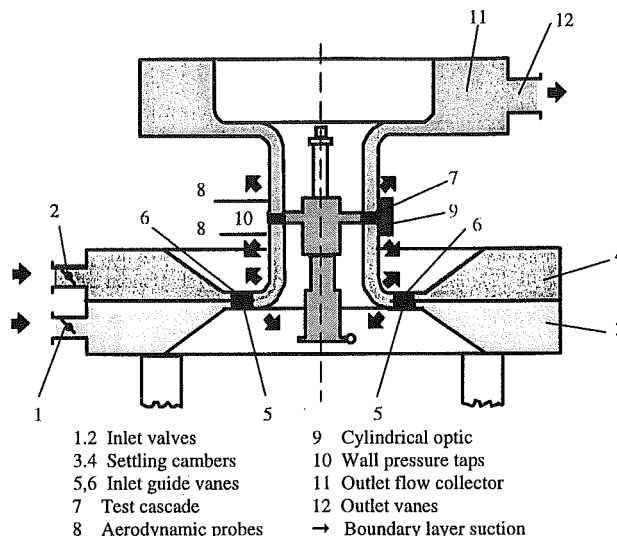

1.2 Inlet valves	9 Cylindrical optic
3.4 Settling cambers	10 Wall pressure taps
5,6 Inlet guide vanes	11 Outlet flow collector
7 Test cascade	12 Outlet vanes
8 Aerodynamic probes	→ Boundary layer suction

Fig. 1 Schematic view of the test facility at LTT/EPFL (Bölcs and Fransson, 1986)

maximum pressure ratio of 3.5. An additional compressor is used to draw off the wall boundary layers (Fig. 1).

In order to simulate unsteady flow conditions in the test cascade, all 20 blades are electromagnetically excited and controlled to vibrate in traveling wave mode. This includes the control of vibration amplitude, vibration frequency, and the interblade phase angle. The suspensions of the blades are designed to reproduce the eigenfrequency and bending direction of the first bending mode of the blade performing a solid blade motion. Also single-blade vibration data were collected to obtain the influence coefficients. More detailed information of the test facility can be found from Bölcs (1983), Bölcs and Fransson (1986), Bölcs et al. (1991), and Bölcs and Körbächer (1993).

Geometry and measuring planes of the presented configuration are illustrated in Fig. 2. Geometry data have recently been made available for all interested researchers and will be published on the internet aligned with this document.

Measurements of static and total pressures as well as the flow angles were done in the planes e1 and e2 before and behind the cascade (Fig. 2). The blade surface distributions of steady and unsteady pressures were measured with pressure taps for the steady-state and miniaturized piezo-resistive pressure transducers

--- Nomenclature ---

A_i = area elements of data points i projected into bending direction, normalized with c (sign: on $ss > 0$, on $ps < 0$)

c = chord, m

$cp = (p - p1)/(pt1 - p1)$ = steady pressure coefficient

$\tilde{c}_p(x, t) = [c \cdot \tilde{p}(x, t)]/[h \cdot (pt1 - p1)]$ = unsteady pressure coefficient

$\tilde{c}_p, \tilde{c}_{pi}$ = amplitude of unsteady pressure coefficient (first harmonic)

e = probe distance, m

f = frequency, Hz

h = bending amplitude, m

H = enthalpy, J/kg/K

IBPA, σ = interblade phase angle, deg

$k = (2 \cdot \pi \cdot f \cdot c)/(2 \cdot v_{2exp})$ = reduced frequency based on half chord and experimental outlet velocity

M = Mach number

p = pressure, Pa

$sf = (pt1 - p1)_{NOVAK}/(pt1 - p1)_{EXP}$ = scaling factor in NOVAK

v = velocity, m/s

x = chordwise coordinate, m

$XI, \Xi_h = -\Sigma_i \tilde{c}_{pi} \cdot A_i \cdot \sin \phi_i$ = aerodynamic damping due to bending >0: stable, <0: unstable

β = relative flow angle, deg

γ = stagger angle, deg

δ = bending direction, deg

$\phi, \phi_i, phi\sim$ = phase of unsteady pressure coefficient (first harmonic), deg

τ = pitch, m

Subscripts

1 = inlet
2 = outlet
i = data point
is = isentropic
t = total values
tan = tangential
$\sim$ = unsteady perturbation value (without steady part)
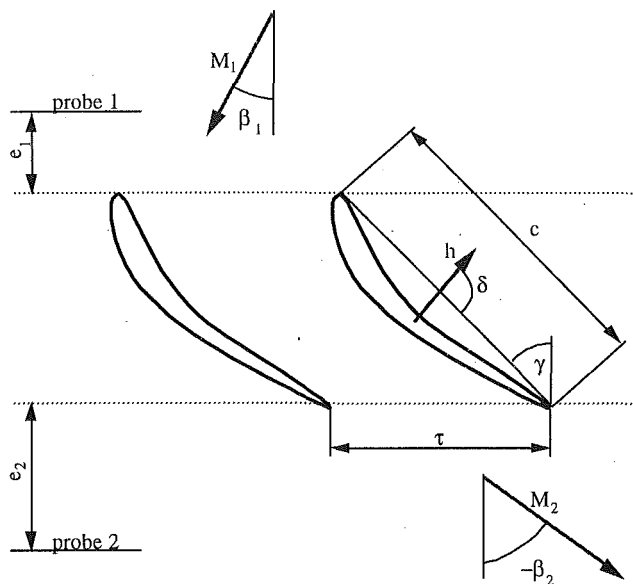
Fig. 2 STCF 11 turbine geometry at midspan (Bölcs and Körbächer, 1993)

Fig. 4 Global damping of transonic cases

for the time-dependent data measurements, all embedded at midspan on different blades. The measured flow cases on this configuration vary in incidence flow angles from 6 deg to 48 deg and in isentropic outlet Mach number from 0.64 to 1.46. The blade was designed for nominal flow conditions with an incidence angle of 16.8 deg and $M_{2is} = 1.0$.

Quality of Experimental Results

Steady Results. A review of the available steady test data shows that the obtained results are highly repeatable (Bölcs et al., 1991). Figure 3 gives an example of steady, transonic off-design data, which also demonstrates this on very sensitive flow cases. Due to small changes of the flow conditions, the position of the shock impingement was determined to vary with about 5 percent chord length for these cases. The number of measuring points on the blade surfaces is sufficient to detect the shock and the separation which occur on the suction side surface. The shown off-design cases indicate a separation bubble to be present from leading edge to 30 percent of true chord and a shock at about 75 percent of true
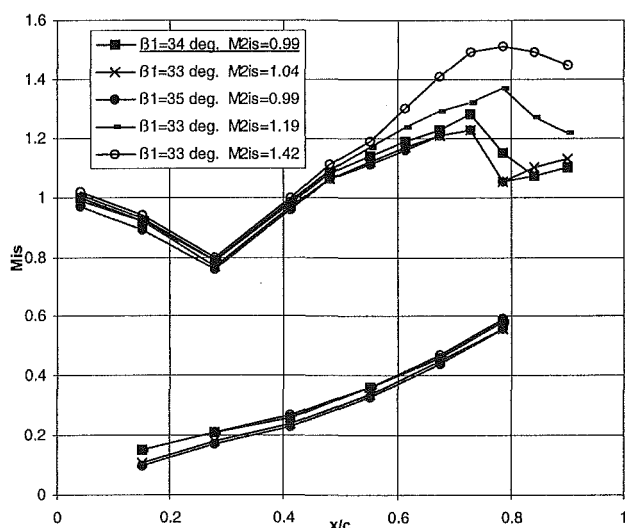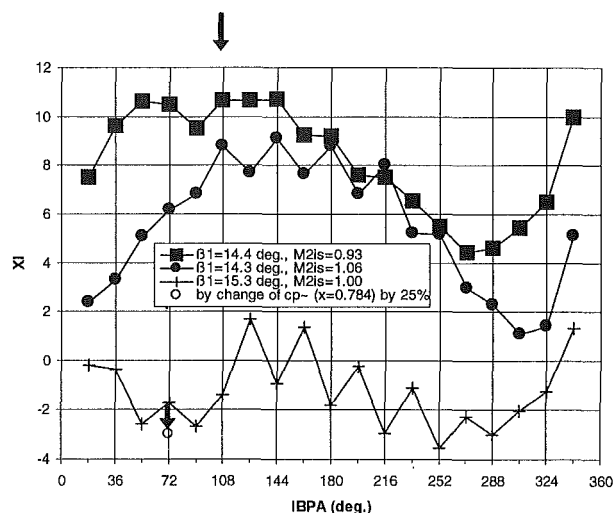

Fig. 3 Transonic off-design test cases on STCF 11

chord. A more detailed discussion on these results and their repetivity can be found in (Bölcs et al., 1991; 1993). The underlined case in Fig. 3 is made public with this document.

Reasons for the deviations between experimental data and numerical results even for subsonic attached flow (see page 7) are not known in detail. They might be found in real flow effects, which can not be captured by the applied numerical models or are lost due to the measuring technique (e.g., three-dimensional effects, side wall boundary layers, inaccuracies in measurement of pressures, estimation of flow angles, averaging of flow values over pitch and span).

Unsteady Results. The unsteady results presented here are shown to be highly repeatable (Bölcs et al., 1991), but for similar flow cases large differences of aerodynamic damping were observed.

These were strongest in the transonic flow regimes compared to subsonic or supersonic flow cases. Figure 4 plots the aerodynamic damping for three cases in the transonic flow region with similar inlet flow conditions. From such a figure it would be tempting to draw the conclusion that the experimental data are useless. However, to analyze the differences more in detail, the local values of pressure coefficients have been compared. Figures 5 and 6 show these for an interblade phase angle of 108 deg, where the differences in global aerodynamic damping were found to be large (compare Fig. 4).

It can be observed that all three cases show the same tendency in amplitude as well as in phase of the unsteady pressure response: The pressure side response shows a relatively small and constant amplitude with stabilizing phase. All cases show high but stabilizing amplitudes close to the leading edge on the suction side, whereas the response tends to be destabilizing in the shock region on the suction side with relatively high amplitudes.

It is obvious that the main differences in aerodynamic damping are caused by differences in the data from the shock region, which has the highest influence on the damping ($\propto \tilde{c}_{pi} \cdot \sin \phi_i$). These data are highly dependent on the exact position of the shock relative to the pressure transducers location. As discussed in the steady-state experimental results, the shock impingement position itself is very sensitive, especially for high incidence flow cases (Bölcs et al., 1991).

Hence, due to the limited number of pressure transducers on the pressure side (max. six transducers/channel) and on suction side (max. seven transducers/channel) the integration of the experimental data over the blade surface does not always lead to accurate results. Moreover, the obtained value is very sensitive to small changes in the flow and the following changes in shock position.
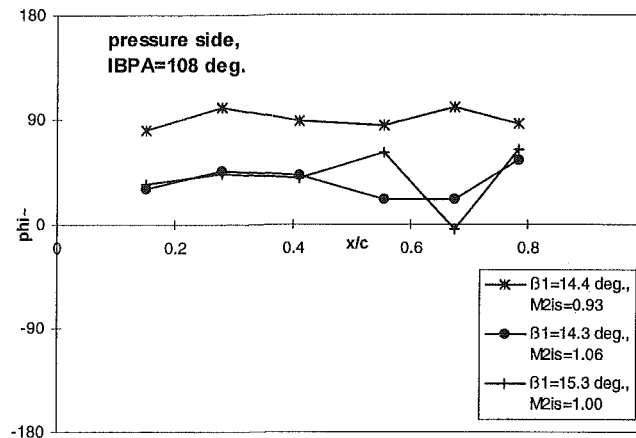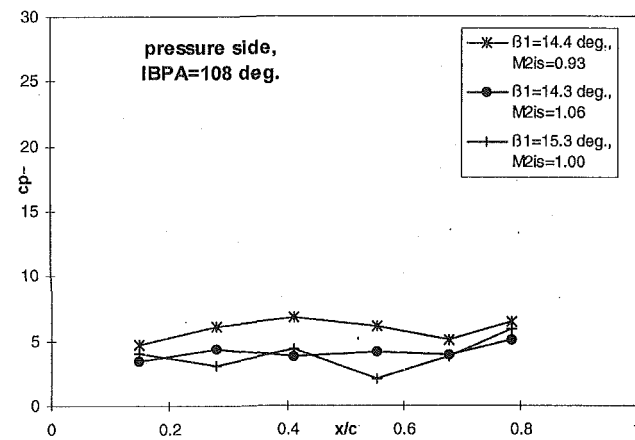
Fig. 5 Unsteady pressure (amplitude and phase of first harmonic) pressure side
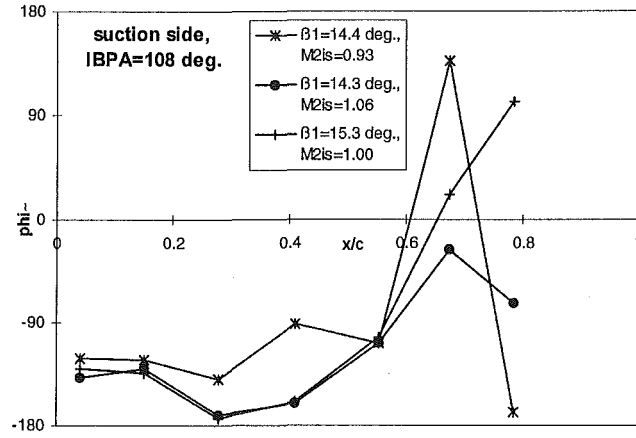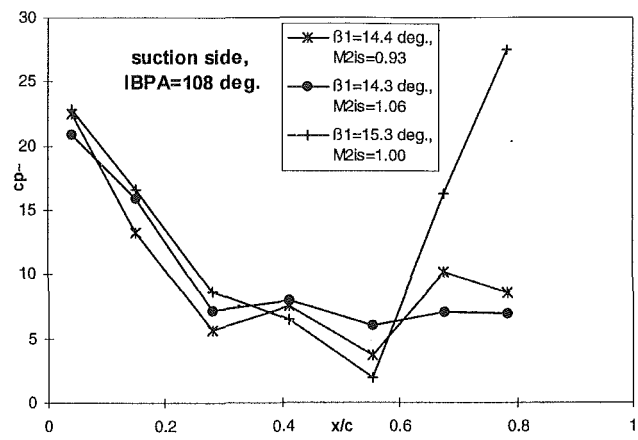

Fig. 6 Unsteady pressure (amplitude and phase of first harmonic) suction side

The following sample case study on the third case in Fig. 4 ($M_{2is} = 1.00$) demonstrates this: To change the aerodynamic damping at an IBPA of 72 deg from the original value of -1.687 to -3 (see arrow in Fig. 4), which would fit the value into a harmonic pattern, the following local change close to the shock (point $x/c = 0.78$) would be sufficient: increase of $\tilde{c}_p$ by about 25 percent (from 20.55 to 25.55). This corresponds only to a small shift in shock position, what can be judged from Fig. 6. This cannot be generalized because the single point influence depends strongly on the level of the other measurement values as well as on the phase, but it gives an impression of the data sensibility.

Hence the sensibility of the aerodynamic damping explains also the zig-zag pattern seen, when looking at the damping versus IBPA (Fig. 4): the experimental data were taken in two series, first in steps of 36 deg (36, 72, . . . deg of IBPA), then the cases in between (18, 54, . . . deg of IBPA) with a time delay of 20 minutes between neighboring IBPAs. It is reasonable to conclude that these two series had slightly different shock positions. This is confirmed by the fact that this pattern is only recognized in transonic flow cases with one subsonic exception.

From the authors' previous and present experience and from the above reasoning it is strongly suggested to compare only local values for the validation of numerical methods and evaluate integrated results only from validated codes. The local values shown here underline the quality of the data representing a good consistency even at sensible flow conditions. It also should be noticed that for all measured unsteady data accuracy is given in terms of a 95 percent confidence interval, obtained from a statistical evaluation. This information is however not presented in the diagrams.

Numerical Models

Different numerical models were applied in order to compare the experimental results with theoretical data. These cover nearly

Table 1 Calculation overview for the two selected steady-state test cases

			FINSUP	NOVAK	INST	VOLFAP
		exp. data	potential code	lin Euler	nonlin. Euler	viscous code
boundary conditions	stdy.	-	$v_{tan,1}$,	α_1, p_2	α_1, p_{t1}, p_2	α_1, p_{t1}, H_{t1}, p_2
	unst.*	-	1*	2*	3*	2*
Number of mesh nodes		-	629	2324	2500	2275 o +6075 i
timesteps	stdy.		-	-	10000	8000
	unst.		-	-	1.5E06	60000
CPU time on IBM RS 6000 / 230	stdy.			5 s	9 min	16 h	8 ¾ h
	Unst. /IBPA			9 s	40min	292 h (guess)	65 h (guess)
Subsonic case	M1	0.31	0.31	0.291	0.29	0.29
	ß1	15.2	15.2	15.2	15.2	15.2
	M2is	0.69	0.69	0.689	0.671	0.69
	k	0.2134	0.2134	0.2134	0.2134	0.2134
	h/c	0.0054	1	0.005	0.0054	0.0054
Off-Design case	M1	0.4	0.4	0.387	0.378	0.37
	ß1	34	33	33	34	33
	M2is	0.99	0.99	0.99	0.993	0.99
	k	0.1545	0.155	0.1545	0.1545	0.1545
	h/c	0.0035	1	0.005	0.0035	0.0035
Q3D option			used	not shown	-	not shown

*1 = nonreflecting, 2=1D non reflecting, 3=2D approx. non reflecting
guess = calculated from CPU time scaling factors

the whole range of 2D/Q3D aerodynamic flutter models actually used in turbomachinery research. Table 1 puts together the characteristic information of the presented calculations. The aim of the calculations was to verify the quality of the experiments and to demonstrate the applicability of the numerical methods. The influence of the unsteady boundary conditions (reflective or nonreflective) is assumed to be small due to an investigation by Krainer et al. (1998). A physical reason for this is the substantial contribution of the quasi-steady loading to the unsteady loading in high turning turbine cascades.

Q3D Potential Small Perturbation Model (FINSUP). FINSUP calculates steady and unsteady flows in cascades using a finite element method with triangular element meshes. (Whitehead and Newton, 1985; Rolls-Royce, 1989; Whitehead, 1990). The program solves the potential equations for isentropic, irrotational two-dimensional flows, where a variation of streamtube thickness is possible (Q3D). For the solutions the Newton–Raphson technique is used. For the unsteady calculations blade vibrations of small amplitudes are assumed and modeled in a single blade passage (traveling wave mode), where the blades are treated as rigid bodies. Unsteady results are obtained by a time-linearized approach. Figure 7 shows the used mesh, which resulted from a mesh influence study (Jöcker, 1994). Mesh independence of the results was not reached but the quality of results was judged to be sufficient with respect to the method.

In FINSUP, the Q3D option was used in order to obtain the correct inlet and outlet flow conditions. This did not lead to an improvement of the steady or unsteady predictions but to a decrease in static pressure on the suction surface close to leading edge (Jöcker, 1994). However, this led to the right estimation of the dynamic inlet pressure ($p_{t1} - p_1$), which is used to normalize the blade surface pressure to obtain the pressure coefficient. Another method applied in order to normalize pressures with identical factors was to introduce a scaling factor. This was done for the results obtained with the linear Euler code (NOVAK), which is described below.

Linearized Euler Model (NOVAK 2D60). NOVAK 2D60 is a time-linear solver for the 2D/Q3D Euler equations, where small periodic perturbations are assumed to disturb the mean steady flow. The blade motion is modeled in the traveling wave mode for both rigid or real mode vibrations. Unsteady results are obtained as the first harmonic pressure response on the blade surface in the frequency domain. The code needs a two-dimensional unstructured grid, where mesh adaption can be applied and the multigrid option
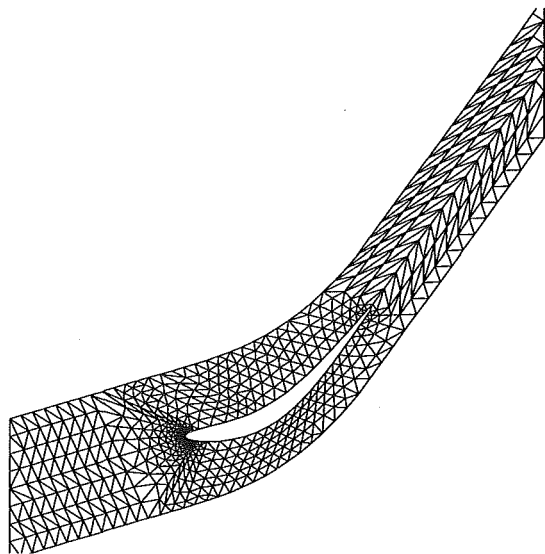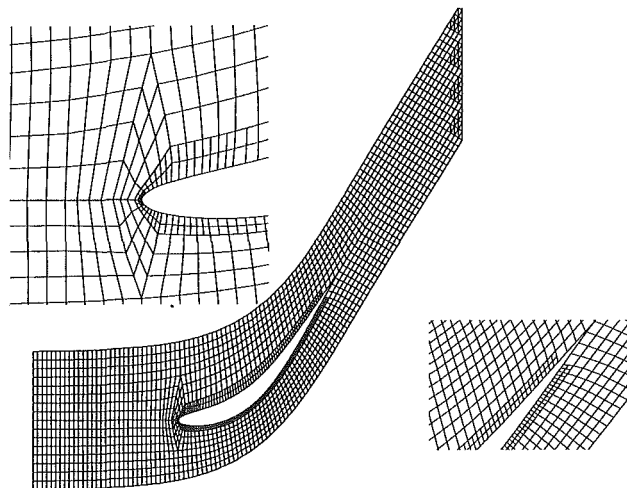

Fig. 8 Linearized Euler model structured mesh, 2324 nodes

can be chosen. The presented results are obtained on meshes optimized during a mesh study (Imfeld, 1997). Sufficient mesh independence was reached with the mesh presented in this paper. Also the influence on unsteady results were studied and a sufficient mesh independence was found. This was, however, only proved for the subsonic case. Figure 8 shows this mesh. A scaling factor sf to account for the different dynamic inlet pressures was introduced in the post processing in order to obtain comparable pressure coefficients. The Q3D method described for FINSUP was also tested to fit the dynamic inlet pressure but is not presented here.

Two-Dimensional Nonlinear Euler Model (INST). INST is an explicit solver for the steady and unsteady inviscid flow around vibrating blades in a two-dimensional cascade. It was extended to cascade flows on the basis of a nozzle flow solver (Bölcs et al., 1989).

It uses the MacCormack explicit second-order time marching scheme and the flux vector splitting method of van Leer (Anderson et al., 1987) for the space derivations. At the inlet, the flow angle is held constant, at the outlet boundary, the static pressure relative to the inlet total pressure is imposed. The main features for flutter calculations are a moving H-mesh, periodic boundary conditions and the unsteady two-dimensional approximate nonreflecting boundary conditions presented by Giles (1989). Blade motion is modeled in the traveling wave mode. All blades can be vibrated either in bending or torsional motion with fixed interblade phase angles.

For the results presented, an H-type mesh with lines locally normal to the blade surface was applied, which is shown in Fig. 9. The resolution of this mesh was judged to be sufficient for the aim of the current presentation for the subsonic case. It is believed that a local refinement of the mesh would lead to an improvement of the shock capturing (see steady results). This is planned for future work.

Q3D Nonlinear Viscous Flow Model. VOLFAP is a fully unsteady, quasi-3D viscous flow code solving the Navier–Stokes equations for a compressible fluid (Sidén, 1991). Turbulence is accounted for by a two-layer eddy viscosity model (Baldwin and Lomax, 1978). One dimensional nonreflecting boundary conditions are available in the code.

The computational mesh consists of an inner, boundary-fitted mesh (structured C-mesh) and an outer mesh of triangular elements. In the inner mesh an implicit scheme by Beam and Warming (1977) is used. The outer region is calculated with an explicit scheme using the Taylor–Galerkin Finite Element Technique. Figure 10 shows the applied mesh as well as a close up of the leading edge and trailing edge mesh regions. A mesh study was conducted by Jöcker (1994).
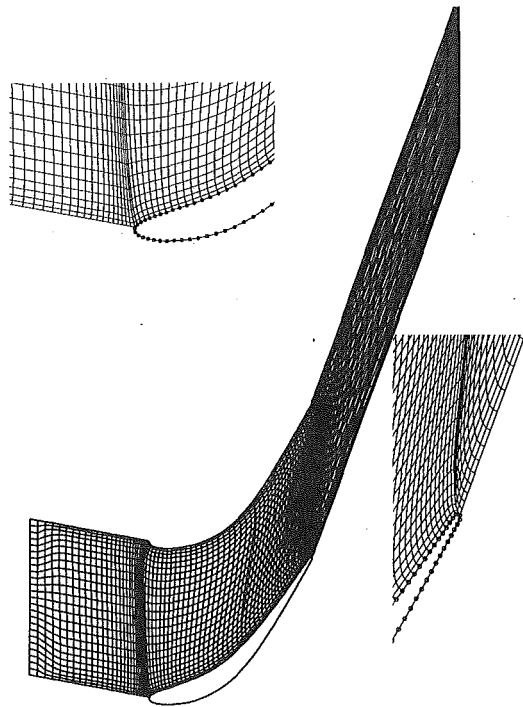

Fig. 7 Potential flow model unstructured mesh, 629 nodes

Fig. 9 Nonlinear Euler model structured mesh, 2500 nodes

Fig. 11 Surface distribution of isentropic Mach number, theory versus experiments, subsonic case

Comparison of Numerical Models and Test Cases

Steady Results. Figure 11 shows the comparison of predicted steady results for the subsonic case in terms of isentropic Mach number distribution. It demonstrates a smooth change of flow over the blade surfaces without remarkable disturbances. All calculations show the same behavior to slightly overpredict the Mach numbers in the middle of the blade on suction side compared to the experiments. This can be due to real flow effects, which cannot be described by the used prediction models. Surprisingly, the linear Euler method comes closest to the experiments.
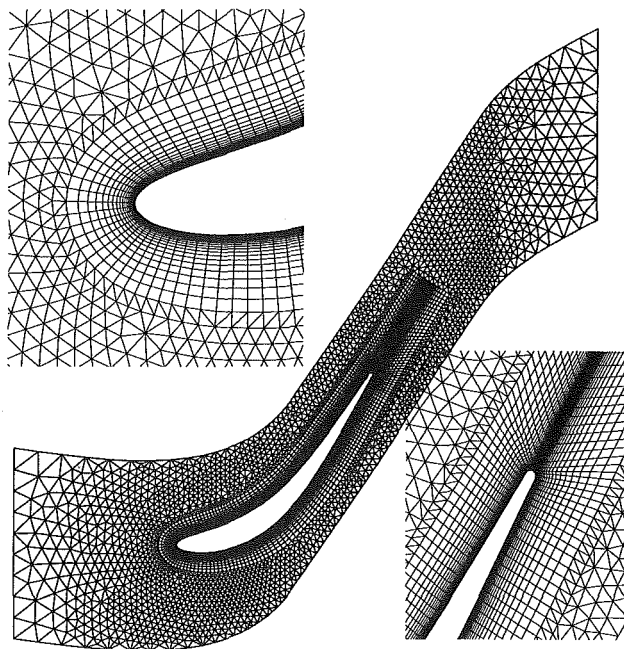
Also the off-design calculations show sufficient agreement with the experimental data, with the exception of the shock prediction (Fig. 12). The potential code does not predict a shock but rather a smooth recompression. The linear Euler code and the viscous code position the shock too far downstream, but with a better agreement of the viscous results. This was also found by Carstens et al. (1993) and Grüber and Carstens (1998). The nonlinear Euler code predicts the shock upstream of the measured position. It is assumed that with a more elaborated mesh this shock position might be predicted better. This is planned for future work.

Only the linear Euler code represents the strength of the measured shock. None of the codes can predict the measured pre-shock Mach number. This has to be seen in the context of the shock sensitivity discussed in the presentation of the experimental data: Fairly small inlet flow changes gave significantly different pre-shock conditions in the experiments. Parameter studies, which are planned for future work on the numerical inlet flow conditions, could demonstrate their influence on the predictions.

Only the viscous code can predict the separation bubble indicated by the deceleration, which occurs on ca. 15–30 percent

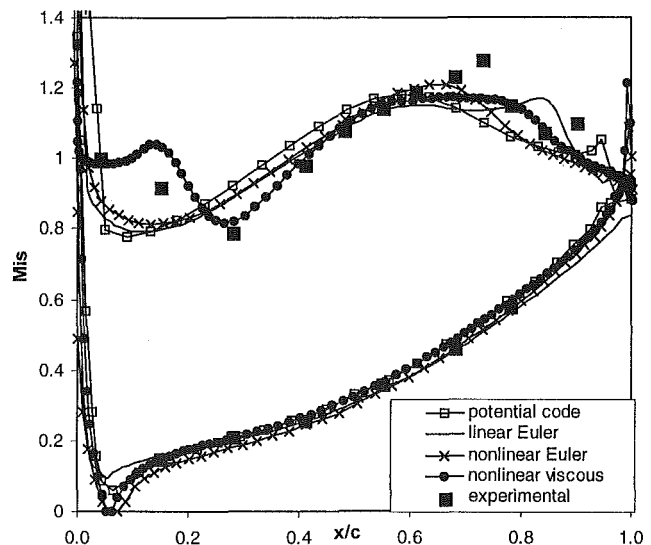Fig. 10 Viscous mesh, inner structured mesh: 27 × 225 = 6075 nodes, outer unstructured mesh: 2275 nodes

Fig. 12 Surface distribution of isentropic Mach number, theory versus experiments, off-design case
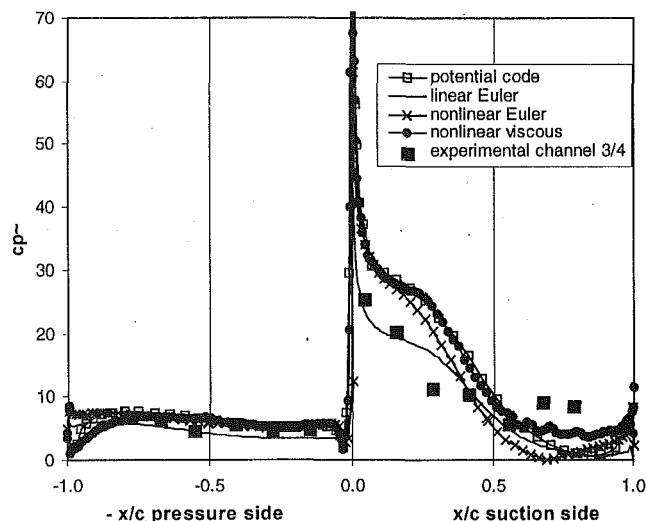
Fig. 13 Amplitude of pressure coefficient, first harmonic, subsonic case, IBPA = 180 deg
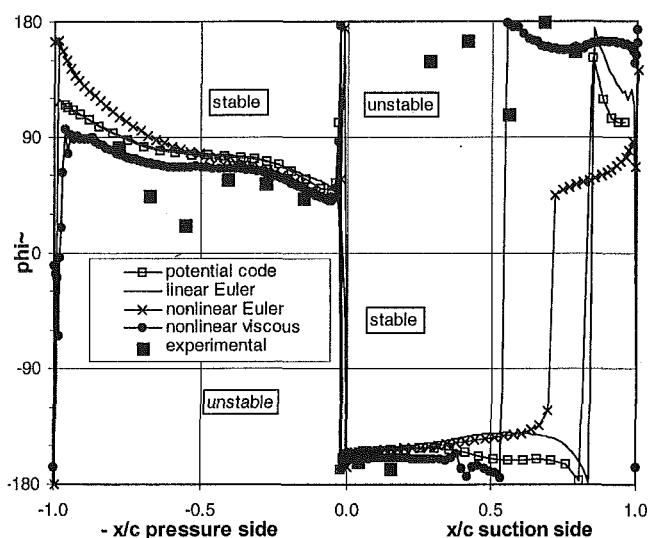

Fig. 14 Phase of pressure coefficient, first harmonic, subsonic case, IBPA = 180 deg

relative chord on suction side. This will also lead to major differences in the unsteady results, as discussed below.

Unsteady Results. For the unsteady calculations, rigid body blade vibrations in traveling wave mode were assumed. Pure bending perpendicular to chord was specified. The results presented are obtained from a Fourier transformation of the time domain solution. Only the first harmonics of the pressure responses are compared in terms of amplitude and phase. In the nonlinear results higher harmonics had nearly no influence.

Figures 13 and 14 show the pressure response for the subsonic case and Figs. 15 and 16 for the transonic off-design case. For both cases all codes predict this cascade typical stabilizing pressure response on the pressure side blade surface. Differences in the predictions are mainly in the phase. The viscous code tends to give a smaller phase angle than the other models.

Subsonic case: The amplitudes on the suction side are represented well with all codes, even though larger differences between the codes can be seen. In the phase prediction on the suction side, the inviscid results are similar, especially from the linear methods, whereas the change from stable to unstable on the blade surface is

predicted farther upstream with the viscous method. However, most of the experimental data show instability, whereas the numerical results are better represented in the stable region. Obviously this has an influence on the aerodynamic damping.

Transonic case: All codes predict a perturbation pressure due to the impinging shock on the suction side, but on different positions and of different strength. The linear Euler code and the viscous code prediction compare well to the experimental shock peak; both the other codes place it too far upstream. Also here it is assumed that a better shock capturing with an improved mesh for the nonlinear Euler calculations could give a better prediction. Still it is surprising that the peak position does not coincide with the steady shock position. The suction side calculations of the transonic case point out the necessity to use a viscous solver here, because only this code can take into account the separation bubble. Obviously its movement leads to a relatively high perturbation pressure at leading edge, with a slightly stabilizing effect for an IBPA of 180 deg.

Table 2 lists the estimated aerodynamic damping XI obtained with the different numerical methods. All damping values were integrated with the same integration scheme. The differences are as
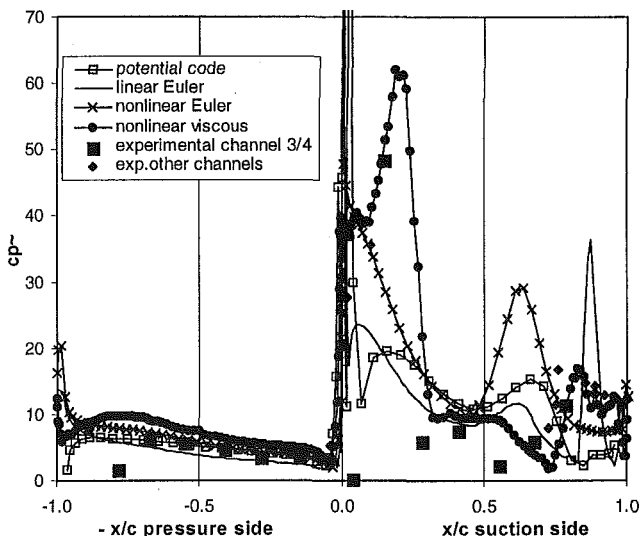

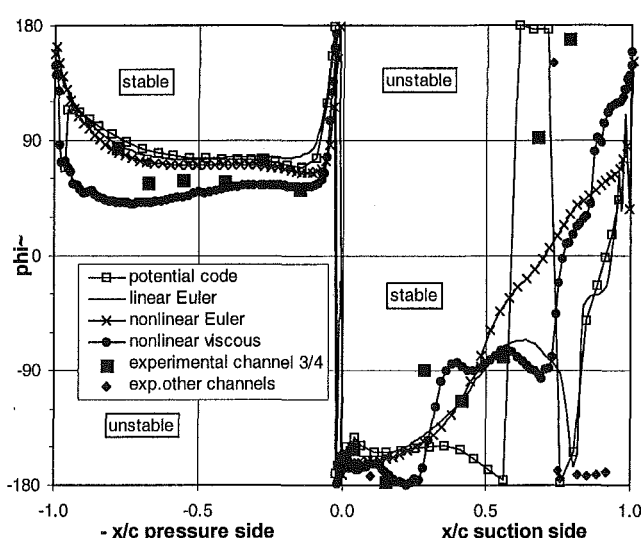**Fig. 15 Amplitude of pressure coefficient, first harmonic, off-design case, IBPA = 180 deg**

Fig. 16 Phase of pressure coefficient, first harmonic, off-design case, IBPA = 180 deg

Table 2 Predicted aerodynamic damping XI

	PREDICTED AERODYNAMIC DAMPING XI				
Case	IBPA	FINSUP	NOVAK	INST	VOLFAP
subsonic	180 deg.	10.8	9.1	9.7	8.4
transonic	180 deg.	8.4	11.7	11.0	8.9

high as 28 percent. Figures 17 and 18 show these values in comparison to the prediction by the potential code for all inter-blade phase angles. Again it can be seen that the aerodynamic damping does not point out the detailed differences in the predictions.

Conclusions

A new International Standard Configuration is presented to be added to the already existing set of 10 Standard Configurations. From the experimental data obtained at the annular test cascade at EPF-Lausanne, Switzerland, two test cases were chosen: a subsonic attached flow case and a transonic separated flow case, which are shown to be suitable for code validations. Hereby experimental effects as well as influences from evaluations have to be taken into account:

The experimental data for the subsonic case are not as sensitive to small flow variations as the off-design transonic case data. Still there are effects in the measured subsonic flow that are not covered by one of the presented 2D/Q3D methods. But all the methods used are able to predict the steady flow in a correct range and give the right tendencies of unsteady behavior. For the subsonic case the nonviscous linearized methods are sufficient and most efficient.
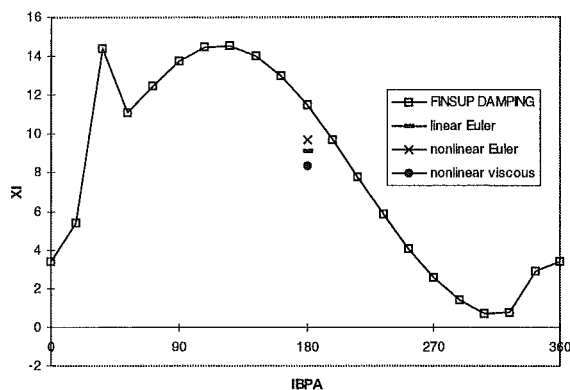
The off-design data is much more sensitive to small flow changes. The comparison of calculation results with these data must always take into account the influence of the detailed flow conditions on the preshock conditions and the shock position. The separation has a significant influence on the unsteady behavior and in order to predict stability correctly, the use of a viscous code is necessary.

The nonlinear Euler model presented here must be improved. The predictions especially for the transonic case could be improved with a better mesh, but still, looking at computing times, the results are not efficient. This is subject of future work.

It is recommended not to use integrated data like the global aerodynamic damping for code validations on such test cases, because the limited number of blade surface measurement points cannot ensure a correct evaluation.

It can be concluded that the quality of the predictions has to be improved, especially for viscous investigations. Furthermore the viscous codes must become cheaper to make them usable. That points out the need of viscous code development and the publication of well documented viscous test data. The published data on STCF 11 contribute to that.

Fig. 17 Predicted aerodynamic damping, subsonic case

Fig. 18 Predicted aerodynamic damping, transonic case

References

Anderson, W. K., Thomas, J. L., and van Leer, B., 1987, "A Comparison of Finite Volume Flow with Shock Waves," AIAA Paper No. 87-1152.

Baldwin, B., and Lomax, L., 1978, "Thin Layer Approximation and Algebraic Model for Separated Turbulent Flow," AIAA Paper No. 78-257; 197883.

Beam, R. M., and Warming, R. F., 1977, "An Implicit Factored Scheme for the Compressible Navier–Stokes Equations," *Proc. 3rd Computational Fluid Dynamics Conference,* Albuquerque, NM.

Bölcs, A., and Körbächer, H., 1993, "Periodicity and Repetivity of Unsteady Measurements of an Annular Turbine Cascade at Off-Design Flow Conditions," ASME Paper No. 93-GT-107.

Bölcs, A., Fransson, T. H., and Körbächer, H., 1991, "Time-Dependent Pressure Fluctuations on an Oscillating Turbine Cascade at Transonic Off-Design Flow Conditions," in: *Unsteady Aerodynamics, Aeroacoustics and Aeroelasticity of Turbomachines and Propellers,* H. M. Atassi, ed., Springer-Verlag, New York, pp. 547–565.

Bölcs, A., Fransson, T. H., and Platzer, M. F., 1989, "Numerical Simulation of Inviscid Transonic Flow Through Nozzels With Fluctuating Back Pressure," ASME JOURNAL OF TURBOMACHINERY, Vol. 111, pp. 169–180.

Bölcs, A., and Fransson, T. H., 1986, "Aeroelasticity in Turbomachines, Comparison of Theoretical and Experimental Cascade Results," *Communication de Laboratoire de Thermique Apliquée et de Turbomachines,* No. 1, EPF Lausanne, Switzerland.

Bölcs, A., 1983, "A Test Facility for the Investigation of Steady and Unsteady Transonic Flows in Annular Cascades," ASME Paper No. 83-GT-34.

Carstens, V., Bölcs, A., and Körbächer, H., 1993, "Comparison of Experimental and Theoretical Results for Unsteady Transonic Cascade Flow at Design and Off-Design Conditions," ASME Paper No. 93-GT-100.

Fransson, T. H., and Verdon, J. M., 1991, "Updated Report on Standard Configurations for Unsteady Flow Through Vibrating Axial-Flow Turbomachine Cascades," Report Royal Institute of Technology, Stockholm, Sweden; available on internet via http://www.egi.kth.se/ekv/stcf.

Fransson, T. H., and Verdon, J. M., 1991, "Standard Configurations for Unsteady Flow Through Vibrating Axial-Flow Turbomachine Cascades," in: *Unsteady Aerodynamics, Aeroacoustics and Aeroelasticity of Turbomachines and Propellers,* H. M. Atassi, ed., Springer-Verlag, New York, pp. 859–889.

Fransson, T. H., and Pandolfi, M., 1986, "Numerical Investigation of Unsteady Subsonic Compressible Flows Through an Oscillating Cascade," ASME Paper No. 86-GT-304.

Gerolymos, G. A., and Vallet, I., 1996, "Validation of 3D Euler Methods for

Vibrating Cascade Aerodynamics," ASME JOURNAL OF TURBOMACHINERY, Vol. 118, pp. 771–782.

Giles, M. B., 1989, "Non-reflecting Boundary Conditions for Euler Equation Calculations," AIAA Journal, Vol. 28, No. 12, pp. 2050–2058.

Giles, M., and Heimes, R., 1993, "Validation of a Numerical Method for Unsteady Flow Calculations," ASME JOURNAL OF TURBOMACHINERY, Vol. 115, pp. 110–117.

Grüber, B., and Carstens, V., 1998, "Computation of the Unsteady Transonic Flow in Harmonically Oscillating Turbine Cascades Taking Into Account Viscous Effects," ASME JOURNAL OF TURBOMACHINERY, Vol. 120, pp. 104–111.

Groth, J. P., Mårtensson, H., and Eriksson, L. E., 1996, "Validation of a 4D Finite Volume Method for Blade Flutter," ASME Paper No. 96-GT-429.

Hall, K. C., and Crawley, E. F., 1989, "Calculation of Unsteady Flows in Turbomachinery Using the Linearized Euler Equations," AIAA J., Vol. 27, pp. 778–787.

He, L., 1990, "An Euler Solution for Unsteady Flows Around Oscillating Blades," ASME JOURNAL OF TURBOMACHINERY, Vol. 112, pp. 714–722.

Holmes, D. G., and Chuang, H. A., 1991, "2D Linearized Harmonic Euler Flow Analysis for Flutter and Forced Response," in: Unsteady Aerodynamics, Aeroacoustics and Aeroelasticity of Turbomachines and Propellers, H. M. Atassi, ed., Springer-Verlag, New York, pp. 213–230.

Huff, D. L., 1991, "Unsteady Flow Field Predictions for Oscillating Cascades," in: Unsteady Aerodynamics, Aeroacoustics and Aeroelasticity of Turbomachines and Propellers, H. M. Atassi, ed., Springer-Verlag, New York, pp. 127–148.

Imfeld, L., 1997, "Numerical Determination of Unsteady Flow Through Vibrating Turbomachine-Cascades: International Standard Configurations 4 and 11 with the NOVAC2D60 Code," Diploma Thesis, KTH Stockholm.

Jöcker, M., 1994, "Validation of Unsteady Aerodynamic Prediction Models on the Turbine Configuration TCT III," Project Study, KTH Stockholm.

Kahl, G., and Klose, A., 1991, "Time Linearized Euler Calculations for Unsteady Quasi-3D Cascade Flows," in: Unsteady Aerodynamics, Aeroacoustics and Aeroelasticity of Turbomachines and Propellers, H. M. Atassi, ed., Springer-Verlag, New York, pp. 109–126.

Krainer, A., Hambraeus, T., and Fransson, T. H., 1998, "Highly Nonreflecting Boundary Conditions for Nonlinear Euler Calculations of Unsteady Turbomachinery Flows," submitted to AIAA Journal of Propulsion and Power.

Leyland, P., Ott, P., and Richter, R., 1994, "Turbine Cascade Calculations With Structured and Unstructured Meshes," presented at Second Computational Fluid Dynamics Conference, ECCOMAS, Stuttgart.

Norryd, M., and Bölcs, A., 1997, "Experimental Investigation Regarding Evolution of Unsteady Pressure in a Vibrating Turbine Cascade With Tip Gap Effects," presented at the 8th International Symposium on Unsteady Aerodynamics and Aeroelasticity of Turbomachines, Stockholm.

Ott, P., Norryd, M., and Bölcs, A., 1998, "The Influence of Tailbords on Unsteady Measurements in a Linear Cascade," ASME Paper No. 98-GT-572.

Ott, A., Bölcs, A., and Fransson, T. H., 1995, "Experimental and Numerical Study of the Time-Dependent Pressure Response of a Shock Wave Oscillating in a Nozzle," ASME JOURNAL OF TURBOMACHINERY, Vol. 117, pp. 106–114.

Rolls-Royce, 1989, "FINSUP User Guide and Reference Manual, Issue 2," Rolls-Royce Commercial Technology; Rolls Royce plc., England.

Sidén, G., 1991, "Numerical Solution of Viscous Compressible Flows Applied to Turbomachinery Blade Flutter," Ph. D. Thesis, Chalmers University of Technology, Göteborg.

Smith, T. E., 1989, "A Modal Aeroelastic Analysis Scheme for Turbomachinery Blading," NASA Report CR-187089.

Smith, S. N., 1972, "Discrete Frequency Sound Generation in Axial Flow Turbomachines," Reports and Memoranda No. 3709, Cambridge.

Verdon, J. M., and Caspar, J. K., 1984, "A Linear Aerodynamic Analysis for Unsteady Transonic Cascades," NASA-CR, 3833.

Whitehead, D. S., 1990, "A Finite Element Solution of Unsteady Two-Dimensional Flow in Cascades," International Journal of Numerical Methods in Fluids, Vol. 10.

Whitehead, D. S., and Newton, S. G., 1985, "A Finite Element Solution of Unsteady Two-Dimensional Transonic Flows in Cascades," International Journal of Numerical Methods in Fluids, Vol. 5, pp. 115–132.

APPENDIX

Table of Test Cases on STCF 11

Steady Data

case	M_1	β_1	M_{2is}	β_2	p_{t1}	p_1	p_2
	-	deg.	-	deg.	mbar	mbar	mbar
100	0.31	15.2	0.69	-66.7	1246	1164	907
200	0.4	34.0	0.99	-	2298	2063	1224

Unsteady Data

case	flow	IBPA (deg)	f (HZ)	k
101	subsonic	18	209	0.2134
102	subsonic	36	209	0.2134
103	subsonic	54	209	0.2134
104	subsonic	72	209	0.2134
105	subsonic	90	209	0.2134
106	subsonic	108	209	0.2134
107	subsonic	126	209	0.2134
108	subsonic	144	209	0.2134
109	subsonic	162	209	0.2134
110	subsonic	180	209	0.2134
111	subsonic	198	209	0.2134
112	subsonic	216	209	0.2134
113	subsonic	234	209	0.2134
114	subsonic	252	209	0.2134
115	subsonic	270	209	0.2134
116	subsonic	288	209	0.2134
117	subsonic	306	209	0.2134
118	subsonic	324	209	0.2134
119	subsonic	342	209	0.2134
201	transonic off-design	36	211.9	0.1547
202	transonic off-design	72	212.1	0.1549
203	transonic off-design	108	212.1	0.1549
204	transonic off-design	144	211.9	0.1547
205	transonic off-design	180	211.6	0.1545
206	transonic off-design	216	212.1	0.1549
207	transonic off-design	252	212.1	0.1549
208	transonic off-design	288	212.1	0.1549
209	transonic off-design	324	212.1	0.1549
210	transonic off-design	360	212.1	0.1549

A Computational Model for Short-Wavelength Stall Inception and Development in Multistage Compressors

Y. Gong

C. S. Tan

K. A. Gordon

Gas Turbine Laboratory,
Massachusetts Institute of Technology,
Cambridge, MA 02139

E. M. Greitzer[1]
United Technologies Research Center,
East Hartford, CT 06108

This paper presents a computational model for simulating axial compressor stall inception and development via disturbances with length scales on the order of several (typically about three) blade pitches. The model was designed for multistage compressors in which stall is initiated by these "short-wavelength" disturbances, also referred to as spikes. The inception process described is fundamentally nonlinear, in contrast to the essentially linear behavior seen in so-called "modal stall inception." The model was able to capture the following experimentally observed phenomena: (1) development of rotating stall via short-wavelength disturbances, (2) formation and evolution of localized short-wavelength stall cells in the first-stage of a mismatched compressor, (3) the switch from long to short-wavelength stall inception resulting from the re-staggering of the inlet guide vane, (4) the occurrence of rotating stall inception on the negatively sloped portion of the compressor characteristic. Parametric investigations indicated that: (1) short-wavelength disturbances were supported by the rotor blade row, (2) the disturbance strength was attenuated within the stators, and (3) the reduction of inter-blade row gaps can suppress the growth of short-wavelength disturbances. It is argued that each local component group (rotor plus neighboring stators) has its own instability point (i.e., conditions at which disturbances are sustained) for short-wavelength disturbances, with the instability point for the compressor set by the most unstable component group.

Introduction

Experiments performed on compressor rigs (Day, 1993; Longley et al., 1996; Silkowski, 1995; Tryfonidis et al., 1995; Weigl et al., 1996; Camp and Day, 1998) and engines (Day et al., 1999) have demonstrated that there are two routes to rotating stall in axial compressors. The first is characterized by the growth of small-amplitude, essentially two-dimensional long wavelength disturbances (on the order of the circumference), which extend axially through the compressor. These disturbances, referred to as modal stall waves, can be detected from 10 to more than 100 rotor revolutions prior to stall, and they rotate at 0.2 to 0.5 times the rotor speed (McDougall, 1988; Haynes et al., 1994; Tryfonidis et al., 1995). Two-dimensional linearized stability analyses (Moore, 1984; Moore and Greitzer, 1986; Weigl et al., 1998) give a useful description of the modal wave shape, phase speed, and growth rate for many compressors.

The second route to rotating stall is characterized by the development of three-dimensional "spike" disturbances (Day, 1993; Silkowski, 1995). These are localized to the tip region of a specific rotor in a multistage compressor and have a length scale on the order of the blade pitch. Spikes initially rotate at 0.7 to 0.8 times the rotor speed, but slow to 0.2 to 0.5 times the rotor speed as they develop into a full stall cell. The time between first detecting a spike and the final stall cell is less than five rotor revolutions, much shorter than for modal-type stall development.

Short wavelength stall inception behavior cannot be captured by current linearized stability analyses. Isolated rotor calculations performed by Hoying et al. (1999) have shown a causal link between the rotor tip leakage flow and the *formation* of the

incipient spike disturbances found in experiments, but the calculations do not provide a framework by which to examine the *development* of these localized flow events into rotating stall. Furthermore, there is currently no methodology for assessing the controlling design parameters and conditions that set the stalling behavior of a multistage compressor with short wavelength disturbances. It is the lack of such capabilities that motivated us to undertake the work presented in this paper.

The technical goal was to develop the simplest computational flow model with the capability of simulating both types of stall inception and development in a multistage axial compressor, and use the model to assess the effect of design parameters on the compressor stability to short-wavelength disturbances. To put it in another way, what we have done is to first postulate a scenario for the development of short-wavelength stall inception, work out rigorously the consequences of this scenario, subject these consequences to scrutiny using available experiments and analysis, and, based on the results, use the model to infer parametric trends for the phenomena of interest.

The paper is organized as follows: We first describe the formulation of the computational model and the procedure for using the model to simulate stall inception. Model adequacy is assessed by comparison with two- and three-dimensional linearized stability analyses and experimental data of short-wavelength stalling behavior in matched and mismatched compressors. The model is then applied to explore the design parameters and conditions that control the stalling behavior of a multistage axial compressor. The implications of these results on the two different routes to rotating stall are discussed by developing the "local component group" concept, and relating this concept to the recent short-wavelength stall arguments set forth by Hoying et al. (1999) and Camp and Day (1998).

Computational Model

To simulate short-wavelength disturbances, a model must be capable of describing the three-dimensional and nonlinear aspects

Copyright © 1999 by ASME
Transactions of the ASME

axisymmetric Euler with body force →

upstream duct | compressor | downstream duct

computational domain | plenum | throttle

Fig. 1 Illustration of the blade row model in the compression system

$$\frac{\partial}{\partial t}\begin{bmatrix}0\\rV_x\\rV_\theta\\rV_r\end{bmatrix}+\frac{\partial}{\partial x}\begin{bmatrix}rV_x\\rV_x^2+rP/\rho\\rV_xV_\theta\\rV_xV_r\end{bmatrix}+\frac{\partial}{\partial\theta}\begin{bmatrix}V_\theta\\V_\theta V_x\\V_\theta^2+P/\rho\\V_\theta V_r\end{bmatrix}$$

$$+\frac{\partial}{\partial r}\begin{bmatrix}rV_r\\rV_xV_r\\rV_\theta V_r\\rV_r^2+rP/\rho\end{bmatrix}=\begin{bmatrix}0\\0\\-V_\theta V_r\\V_\theta^2+P/\rho\end{bmatrix} \quad (1)$$

Blade Rows. The pressure rise and the turning produced by each blade row were modeled by a body force field, distributed continuously around the circumference (Fig. 1). The blade region is assumed to consist of an infinite number of blades, which restrict circumferential flow variations from redistributing. Tangential flow gradients can exist, but they do not affect the local flow dynamics in the blade row reference frame. The relative flow was therefore described by "locally axisymmetric" Euler equations with source terms depicting the body forces. In the absolute frame, these equations are given by

$$\left(\frac{\partial}{\partial t}+\Omega\frac{\partial}{\partial\theta}\right)\begin{bmatrix}0\\rV_x\\rV_\theta\\rV_r\end{bmatrix}+\frac{\partial}{\partial x}\begin{bmatrix}rV_x\\rV_x^2+rP/\rho\\rV_xV_\theta\\rV_xV_r\end{bmatrix}$$

$$+\frac{\partial}{\partial r}\begin{bmatrix}rV_r\\rV_xV_r\\rV_\theta V_r\\rV_r^2+rP/\rho\end{bmatrix}=\begin{bmatrix}0\\rF_x\\-V_\theta V_r+rF_\theta\\V_\theta^2+P/\rho+rF_r\end{bmatrix} \quad (2)$$

where

$$(F_x, F_\theta, F_r) = \mathbf{F}(\mathbf{V}(x,\theta,r),x,r). \quad (3)$$

The additional operator $\Omega\partial/\partial\theta$ in Eq. (2) arises from the transformation of the time derivative from the rotational frame to the absolute frame. The assumption of an infinite number of blades is well based for perturbations with wavelengths much longer than the blade pitch (such as modal waves). For short-wavelength disturbances, tangential redistribution within individual blade passages would be expected. The applicability of the model to simulate these disturbances will be made apparent during the model assessment.

With short-wavelength spikes there is a potential for substantial axial and radial flow redistribution within the blade row. The body force field accounts for this at every point in the blade region by responding to the local flow conditions. This contrasts with previous body force representations (Escuret and Garnier, 1994; Longley, 1997) in which the force responded only to the flow at the blade row inlet. Details of how local body force relations were generated from prescribed axisymmetric pressure rise and turning characteristics are given in the appendix.

Plenum and Throttle. Standard plenum and throttle dynamics were used to determine the pressure at the exit of the downstream duct (Greitzer, 1976). Since the plenum has little effect on

of the flow in a multistage environment. Direct use of a three-dimensional unsteady Navier–Stokes solver to compute the flow within all blade passages of a compressor is not computationally feasible, nor is it suited to our requirements. The approach taken here is to use body force distributions to represent the effects of the discrete blades on the flow field.

The body force approach is not new (Marble, 1964; Billet et al., 1988) and has been recently used by Escuret and Garnier (1994) and Longley (1997) to simulate the onset of rotating stall from long-wavelength disturbances. The work presented here constitutes the first effort, as far as the authors know, to exploit the potential for simulating three-dimensional nonlinear instability for short-wavelength disturbances in multistage compressors.

The modeled compression system consisted of an inlet duct, blade rows, inter-blade row gaps, an exit duct, and a plenum followed by a throttle (Fig. 1). The computational domain extended to the end of the downstream duct where the exit pressure was determined by the plenum and throttle dynamics. The flow was assumed to be incompressible, consistent with the low-speed compressor experiments against which the model was compared. Key elements for modeling each component are detailed in the following subsections.

Upstream Duct, Downstream Duct and Gaps. Flow in the blade-free regions was described by the unsteady three-dimensional Euler equations:

Nomenclature

F = body force per unit mass
K_t = throttle coefficient
P = static pressure
U = midspan blade speed
V = velocity
c = pseudo-speed of sound
x, θ, r = cylindrical coordinates

α = blade metal angle
β = flow angle = $\tan(\beta) = V_\theta/V_x$
δ = loss of stall margin, defined by Eq. (5)
ρ = density
ϕ = flow coefficient = V_x/U
Ψ_{ts} = total-to-static pressure rise = $(P_{exit} - P_{t,inlet})/\rho U^2$

Ψ_{tt} = total-to-total pressure rise = $(P_{t,exit} - P_{t,inlet})/\rho U^2$
Ω = rotating frequency of the blade rows

Subscripts

t = stagnation property
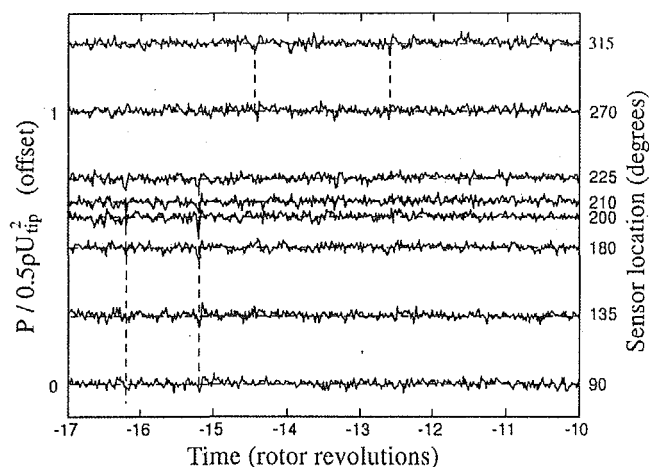x, θ, r = axial, circumferential, radial component

Fig. 2 Experimental evidence of tip-spikes prior to the development of stall at time = 0. The pressure traces, from sensors at different circumferential positions, are shifted relative to first trace so that disturbances traveling at 71 percent of rotor speed line up vertically. Guide lines identify propagating spikes (Park, 1994).

Fig. 3 Axial body force impulse used to generate spike-shaped disturbances

the development of short-wavelength disturbances, its volume was set to zero for the calculations reported, so the exit pressure was determined by the throttle relation

$$P_{\text{exit}} - P_{\text{ambient}} = K_t \phi^2 \tag{4}$$

where P_{exit} is the pressure at the exit of the downstream duct.

Numerical Method. To allow for a standard time-marching method, a pseudo-compressibility term, $(\partial/\partial t + \Omega \partial/\partial \theta) r P/c^2 \rho$, was added to the mass conservation equation. It was found that the phase speeds and growth rates of disturbances were not sensitive to c when c is sufficiently large $(c > 10\phi)$. Spatial discretization of the governing equations was based on the finite volume method of Jameson et al. (1981). Since these were low-speed calculations, only fourth-order numerical smoothing was used. The temporal discretization used the four-stage Runge–Kutta scheme with a uniform time step to ensure a time-accurate solution.

Implementation of the Model for Compressor Instability Simulations

This section addresses three issues concerning the use of the model to investigate compressor instability behavior: (1) appropriate initial flow disturbances used for initiating rotating stall, (2) the method for determining the stall point, and (3) the procedure for differentiating between the two stall inception routes.

Two types of initial flow disturbance were used in the calculations. Long-wavelength perturbations of small amplitude (less than 1 percent of the mean flow coefficient) were used to find the modal (linear) stability point. All other calculations used large-amplitude spikes of small circumferential extent that were localized at the tip region of a rotor blade row. These spikes were based on the experimental observations by Park (1994) that such disturbances can appear in a rotor prior to the development of rotating stall (Fig. 2).

The spike disturbances were generated by prescribing an impulse to the rotor axial body force lasting for 0.1 rotor revolutions and traveling at the rotor speed. A disturbance was initiated at a random position about the circumference once every few rotor revolutions. The shape of the impulse (Fig. 3) was approximately 10 deg wide, corresponding to about one blade passage in a 54-blade rotor. The magnitude of the force was equivalent to that effecting zero pressure rise in the outer 30 percent span of a blade passage, which was observed to precede stall in the simulations calculated by Hoying et al. (1999) and Vo (1999).
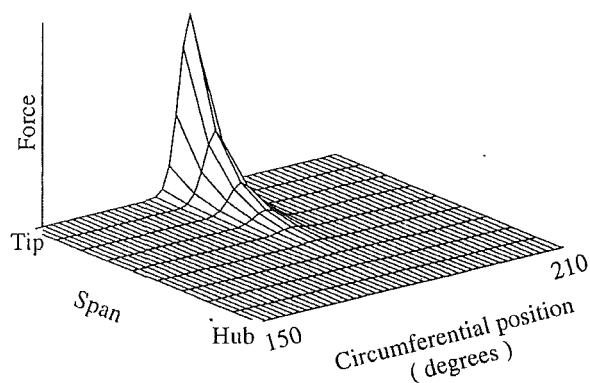
To determine the compressor stall point, the disturbances were first imposed on a steady flow at a fixed throttle coefficient known to produce a stable flow field. This procedure was repeated for lower throttle conditions until the disturbances no longer decayed, but rather grew into a full stall cell. A single simulation with a continuously closing throttle was avoided because any numerically acceptable closing rate would still be much faster than that used in experiments.

Once the stall point was determined, velocity traces were used to determine the route by which the stall cell formed. Long-wavelength inception was characterized by decay of the spike disturbance followed by growth of a long wavelength stall cell. Figure 4 shows an example of flow coefficient traces leading to stall via this route. It is noted that this is not identical to modal stall behavior due to the large amplitude of the initial disturbance. For short wavelength stall inception (Fig. 5) the spike disturbance shape remained coherent and led directly to stall without decay.

Model Assessment

The adequacy of the model and the above-described methodology were assessed by demonstrating that the model reproduced: (1) modal stall behavior as predicted by linearized stability calculations, and (2) experimentally observed short-wavelength instability phenomena. The short-wavelength stall assessments address the question of whether a model based on the assumption of an infinite number of blades can be employed to describe flow events with a length scale of only two to three blade passages.

Three multistage experiments involving short-wavelength disturbances were used for the latter assessment. The first showed a
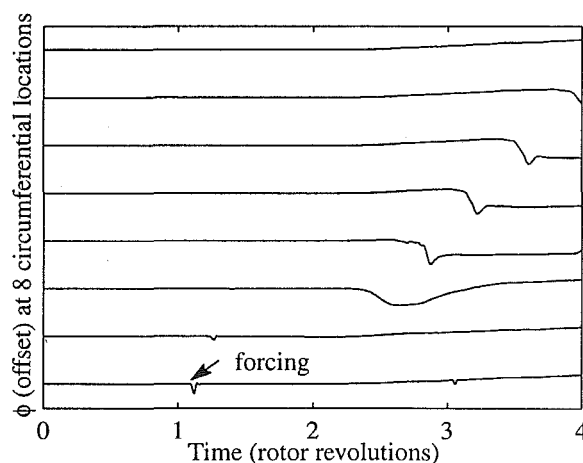

Fig. 4 Computed flow coefficient traces for a compressor stalling via long-wavelength route
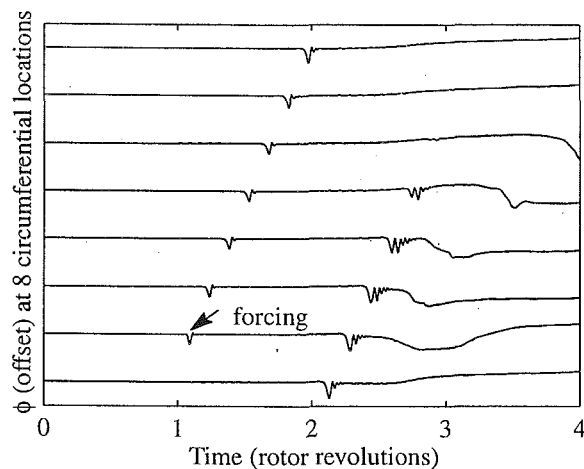
Fig. 5 Computed flow coefficient traces at the tip of the first rotor inlet for a compressor stalling via short-wavelength route

spike disturbance developing into full-scale rotating stall in a matched compressor. The second showed the localization of three-dimensional stall cells in the first stage of a mismatched compressor. The third showed a change from long-wavelength to short-wavelength stall inception routes as the incidence on the first rotor was increased; thereafter, short-wavelength stall inception occurred at a constant rotor tip incidence.

All calculations used 9 radial and 256 circumferential cells. Short-wavelength events occupying two to three blade pitches in the experiments were adequately resolved over 10 to 14 cells in the tangential direction.

Comparisons With Linear Theories. The computational model was first compared separately against two-dimensional and three-dimensional linearized theories for representative compressor geometries. The figures of merit were the growth rate and phase speed of an imposed sinusoidal perturbation with a wavelength equal to the circumference. The two-dimensional case used the parameters similar to a four-stage core compressor. The three-dimensional validation used the geometry of a single-stage fan with a hub-to-tip ratio of 0.43. Computed growth rates and phase speeds are compared in Table 1 with results of two-dimensional (Moore and Greitzer, 1986) and three-dimensional linearized models.

The excellent quantitative agreement between the computational model and the linearized analyses demonstrate that the present method can accurately capture modal instability inception and development. The more important aspect is the additional ability to reproduce short wavelength events, which we proceed to demonstrate next.

Simulation of Short-Wavelength Stall Inception. Measurements of short-wavelength disturbances growing into fully developed rotating stall in a low-speed compressor (Silkowski, 1995) were used as an experimental assessment of the computational model. The compressor (run at the General Electric Aerodynamics Research Laboratory) had a hub-to-tip ratio of 0.85, and consisted

Table 1 Comparison between modal growth rates and phase speeds for the present computational model and linearized analyses

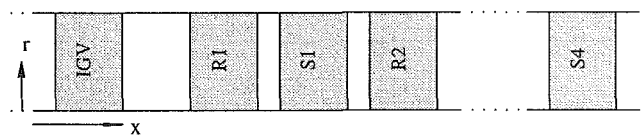|	growth rate	phase speed / rotor speed
Computational model	-0.26	0.27
2D linear model	-0.26	0.27
Computational model	-0.11	0.10
3D linear model	-0.10	0.10

Fig. 6 A scale schematic of the GE compressor represented by nine blade rows and eight gaps

of an inlet guide vane (IGV) followed by four identical stages. A schematic that shows the scale of the blades and interblade axial gaps is given in Fig. 6. Details of the compressor geometry can be found from Wisler (1981).

The pressure rise characteristics used for every rotor and stage in the model are shown in Fig. 7. The rotor characteristic were higher at the tip than the hub to satisfy radial equilibrium at the rotor exit with a nearly uniform axial velocity profile, which was observed in the experiment. The unstalled portions (to the right of the peaks) were taken directly from the experiment. The criteria for selecting the characteristic shapes to the left of the peak, as well as information on their effect on short wavelength stall phenomena, are provided by Gong (1998). The point to be emphasized is that the qualitative stalling behavior is not strongly dependent on the precise curve shapes, other than the requirement that a trough exist in the rotor characteristic at a positive flow coefficient.

This compressor stalled via short-wavelength disturbances, as shown by the axial velocity traces around the circumference (Fig. 8). The computational model qualitatively reproduced this behavior, as shown by the flow coefficient traces in Fig. 5, which are plotted to the same time scale. The same feature of a spike-shaped disturbance growing in amplitude prior to the formation of a fully developed stall cell is shown. Table 2 quantitatively summarizes the key figures of merit used for the assessment. Specifically, the rotating speed of the spike and the time taken for the spike to transition to the final stall cell were in good agreement.
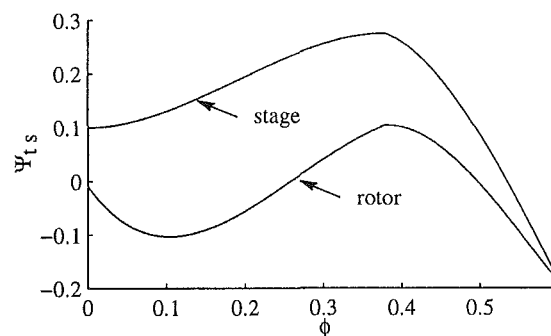

Fig. 7 The modeled axisymmetric pressure rise characteristic for each stage of the GE matched compressor
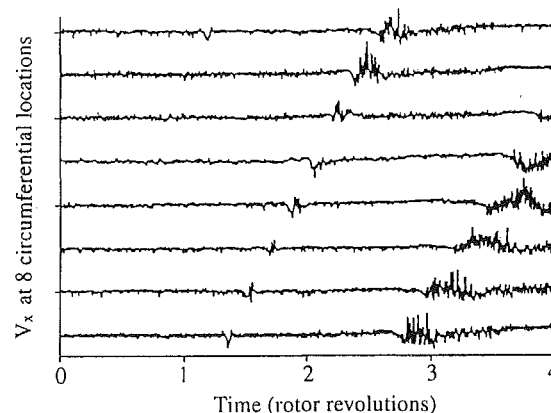

Fig. 8 Measured axial velocity traces at the tip of the first rotor inlet during stall inception (Silkowski, 1995)

	Measurement	Computation
Stall Inception Route	Spike	Spike
Rotating Speed of Spike	70-73%	83%
Rotating Speed of Final Stall Cell	45%	20%
Transition Time (rotor revolutions)	about 3	about 3

The computed results show the time sequence for short-wavelength stall inception events. The three-dimensional spike grows in amplitude until it triggers the formation of an incipient long-wavelength disturbance, which then grows into the final essentially two-dimensional stall cell. During this process the short-wavelength disturbances travel ahead of the stall cell, due to their faster rotational speed, and eventually decay in the region of higher local mass flow.

Stall in a Mismatched Compressor. Another assessment of the model's ability to describe short-wavelength stall behavior was performed for a mismatched compressor (Silkowski, 1995). By re-staggering the second through fourth rotors of the GE compressor rig so that their stage characteristics peaked at a lower flow coefficient (shown by the solid lines in Fig. 9), one or more fully developed short-wavelength stall cells could be localized in the first stage. Note that stall (defined as when asymmetric flow disturbances were no longer suppressed) occurred at the same flow coefficient as for the matched configuration. The short-length-scale cells were prevented from growing into a long-wavelength stall cell because of the stabilizing influence of the rear stages. The compressor characteristic behaved "progressively" in that the pressure rise increased and decreased smoothly without hysteresis as the overall mass flow was changed, as shown by the solid circles in Fig. 9. The number of localized cells increased from one to twelve as the flow rate decreased, until finally at a sufficiently low flow, a long-wavelength full-scale rotating stall cell developed that extended through the entire compressor.

The computations carried out qualitatively demonstrated the progressive characteristic behavior as shown by the open circles in Fig. 9. Spike disturbances were periodically forced every rotor

Fig. 10 Computed velocity trace showing a localized stall cell

revolution, but only a limited number would grow into fully developed part-span stall cells, each of equal size. As the throttle was closed, the maximum number of disturbances that would develop into stall cells increased, as indicated on the figure. Disturbances imposed in excess of the maximum amount existed only as transients and decayed within one rotor revolution. The computed width of the localized stall cells compared well with the experiment, as indicated by the velocity traces in Figs. 10 and 11. The overall assessment criteria for the mismatched configuration are summarized in Table 3.

The roles of the rotor and stator in short-wavelength stall can be understood better by examining the detailed structure of a localized cell. Figure 12 shows the computed axial velocity contours in a small segment of the first-stage annulus where the cell is localized in the tip region. The flow deficit grows stronger through the rotor and diminishes in the stator, indicating that spikes are supported by the rotor and that the stator has a stabilizing influence.

Switch Between Stall Routes and Unique Incidence for Spikes. Experiments performed by Camp and Day (1998) demonstrated that the route leading to stall could switch from long to short wavelength as the incidence on the first rotor was altered by changes in IGV stagger angle. They also showed that the incidence at the rotor tip is constant for all cases where stall occurred via spikes. Capturing this set of observations with the computational method gives another test of the model's ability to predict short *and* long-wavelength stall events accurately.
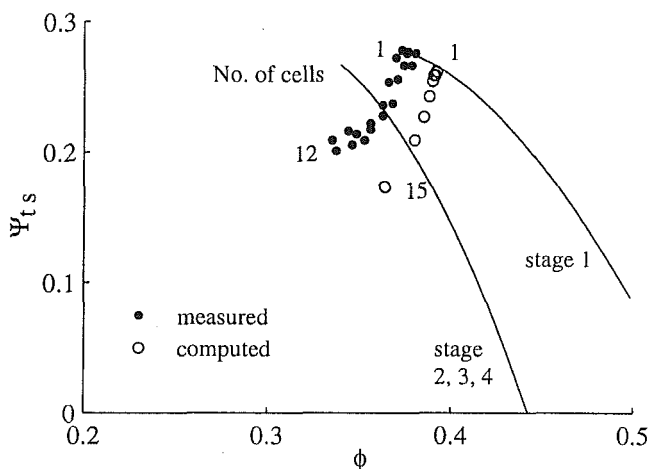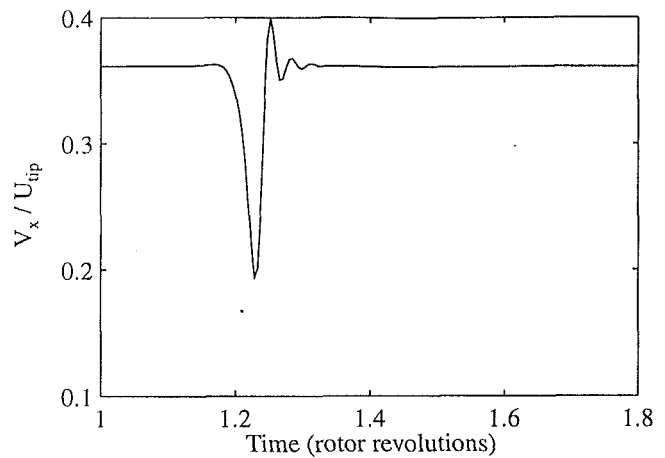

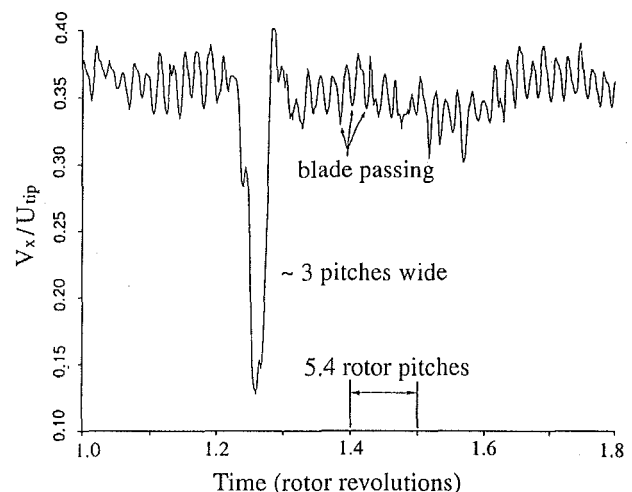Fig. 9 Measured and computed stage characteristics for the GE mismatched compressor. Circles denote the progressive stall, which deviates from the axisymmetric characteristic (solid line).

Fig. 11 Measured velocity trace showing a localized stall cell (Silkowski, 1995)

	Measurement	Computation
location	first stage rotor tip	first stage rotor tip
width of spike	2-3 pitches (out of 54)	1/20 annulus (2.7 pitches)
rotating speed	70-73%	83%
progressive stall	yes	yes
no. of stall cells	1 to 12	1 to 15

The simulations were made using the matched GE compressor as the baseline configuration. The amplitude of force impulses was kept constant for all simulations. IGV stagger angle variations were chiefly reflected in the modified first stage pressure rise characteristics. Figure 13 shows these characteristics as well as the stall points, the corresponding incidences at the tip of the first rotor, and the types of stall inception route. The trends are very similar to the observations made by Camp and Day (Fig. 14), in particular the condition of constant rotor incidence value for all cases of short-wavelength stall inception.

In summary, the model reproduced both short-wavelength and long-wavelength stalling trends from previously accepted analytical results and experimental measurements, implying that the body force model gives a good description of both modal and spike-initiated stalling events. The computational method will now be applied to determine the parameters that control multistage compressor instability behavior.

Parametric Study

To identify the conditions that set the stall point of short-wavelength disturbances in a multistage compressor, two aspects of the stall inception were examined: the types of initial flow disturbance, and the geometry of the compressor. The initial disturbances used were both small-amplitude modal perturbations and large amplitude spike-shaped impulses localized to either the tip or hub of the first rotor. The amplitude of the tip-spikes and the rotor in which they appeared were also varied. Finally, the gap lengths between particular blade rows were varied to isolate the effects of different segments of the compressor.

The baseline configuration for all simulations was the GE four-

Fig. 13 First-stage characteristics with the stall point and inception type computed for different IGV staggers

stage compressor described above in the matched configuration. In this section changes to the stall point (δ) are referenced to the computed modal stall point, which was at the peak of the pressure rise characteristic.

$$\delta = \frac{\phi_{stall} - \phi_{modal\ stall}}{\phi_{modal\ stall}} \quad (5)$$

A positive δ indicates that stall occurs at an operating point to the right of the peak, i.e., on the negatively sloped part of the overall characteristic.

Type of Initial Disturbances. Stall point and type of stall inception were determined using three types of disturbance to the body force in the first rotor: (1) small amplitude, long wavelength; (2) large amplitude, spike-shaped at the tip; (3) large amplitude, spike-shaped at the hub. The shape and amplitude of these disturbances were the same as those described in the section on "Implementation of the Model."

The results are shown in Fig. 15, which shows the stall inception route and change in stall point for the three disturbance types. Only the tip-spike disturbances led to short wavelength stall inception and the largest loss in stall margin.

Disturbance Amplitude. The effect of the disturbance size on the stalling behavior is shown in Fig. 16. The amplitude has been
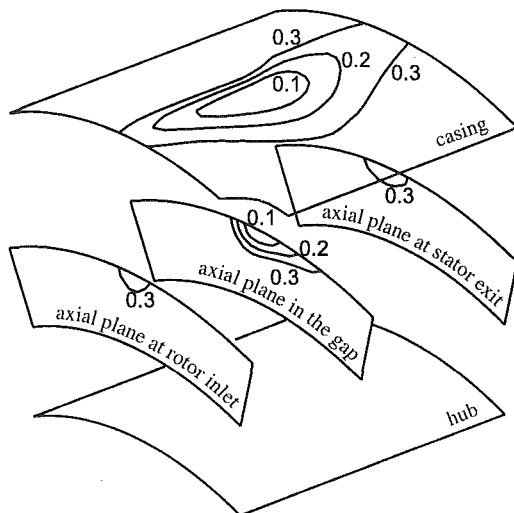

Fig. 12 Computed flow coefficient contours of a localized stall cell in the first stage of the GE mismatched configuration. A tangential extent equal to six blade pitches is shown.
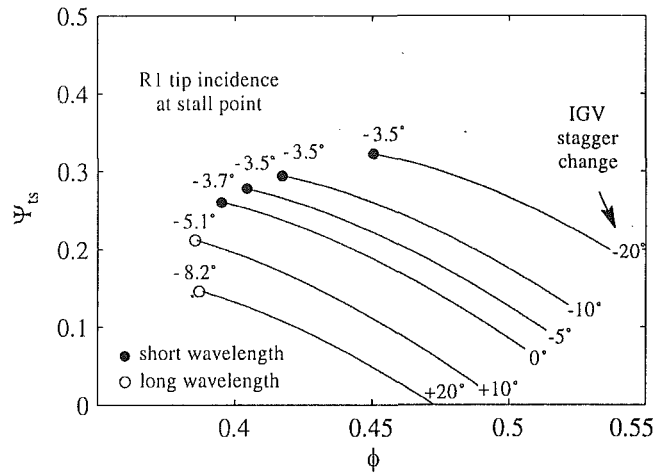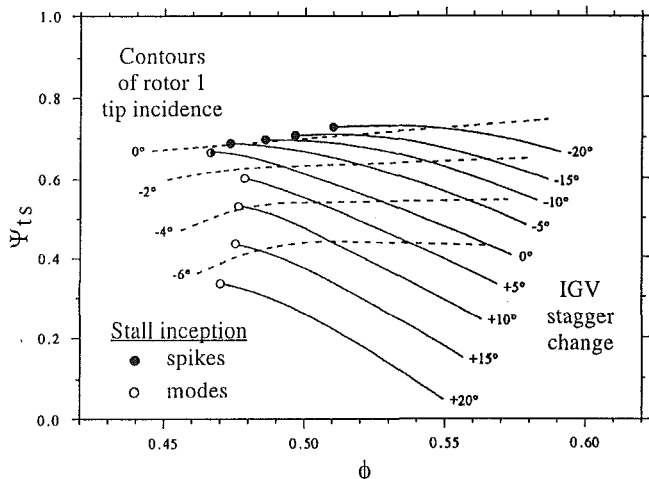

Fig. 14 First-stage characteristics with the stall point and inception type indicated for different IGV staggers. Measured by Camp and Day (1998).
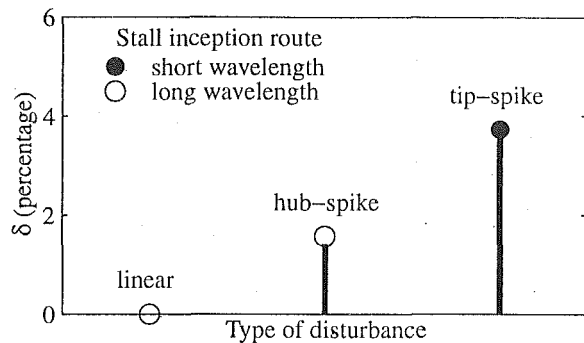
Fig. 15 Changes in stall point and inception type for different types of initial disturbances
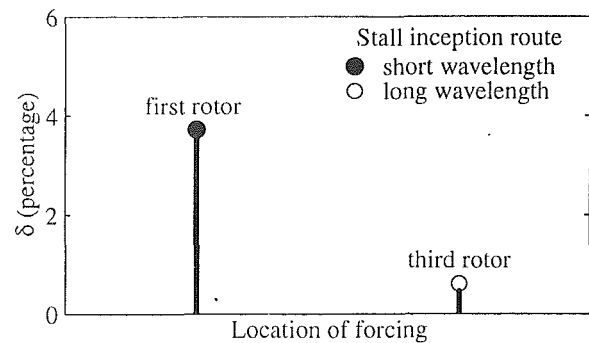

Fig. 17 Changes in stall point and inception type with location of initial spike

normalized by the baseline spike amplitude. The figure shows the following points:

1 Spike disturbances needed to be larger than a threshold amplitude to cause a short-wavelength-type inception. Below this amplitude, modal stall inception occurred.
2 The stall margin decreased as the disturbance amplitude increased. Spike inception always occurred on the negatively sloped part of the pressure rise characteristic.
3 There was an upper limit in the loss of stable flow range due to short wavelength disturbances for this configuration. Above a critical flow coefficient (given by $\delta = 7$ percent) the compressor was stable to all spike disturbance sizes tried.

The computations show that compressor instability involving short-length-scale disturbances is inherently nonlinear, in contrast with long-wavelength stall behavior, which is essentially a linear phenomenon.

Disturbance Location. In the matched compressor experiments, the short-wavelength stall cells were always initiated in the first-stage rotor. It was of interest to use the model to examine what happens when spikes are imposed in a rotor further downstream. The stalling behavior induced by tip-spikes in the third-stage rotor is compared to the baseline in Fig. 17. Only disturbances in the first-stage rotor were found to lead to short-wavelength stall inception.

An explanation for this was offered by Camp and Day (1998) who argued that rotors other than the first tended to be slightly less loaded when off-design because drops in the axial velocity increased the deviation of downstream stators more than that of the inlet guide vane. However, in the computed flow fields, the axial velocity profiles and incidence angles at all rotor inlets were essentially the same, so the loading differences between the first

rotor and subsequent rotors were small. A different explanation for why spikes select the first rotor, at least in the present configuration, is suggested in the next section.

Gap Lengths Between Blade Rows. In the GE compressor, the first rotor was unique in that the IGV-R1 gap was three times the length of all other gaps. The effect of rotor–stator gap length on the type and location of stall inception was numerically examined by independently varying the IGV-R1, R1-S1, and S1-R2 gaps. For all studies, the tip-spike impulses were imposed in the first rotor.

The results are shown in Fig. 18, which indicates that the stall point was set only by the spacing between the first rotor and its adjacent stators. Changing the S1-R2 gap had no effect on stall. Increasing the IGV-R1 or R1-S1 gaps destabilized the compressor to short-length-scale disturbances. Bringing the IGV or first stator sufficiently close to the first rotor suppressed the development of spikes entirely, so that stall occurred via long-wavelength inception. This effect supports the notion that stators have a stabilizing influence on spikes.

Similar studies done for the mismatched GE configuration gave the same qualitative trends. It was also found that the size of the localized short-wavelength stall cells increased with increasing R1-S1 gap, but were unaffected by the S1-R2 gap length.

All computations indicated that short-length-scale stalling behavior in a particular rotor was set by the adjacent blade row components, and not by the design of the rest of the compressor. The preference for spike stall in the first-stage rotor is predominantly due to the relatively large IGV-R1 gap as compared to the gaps within the downstream stages.

Discussion

We have demonstrated that a computational model based on an infinite blade number representation of the blade rows is capable of
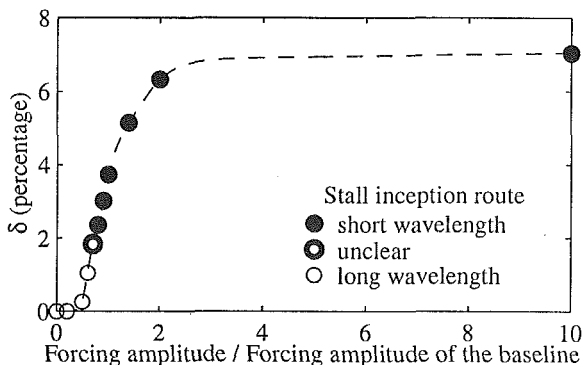

Fig. 16 Effects of initial spike forcing amplitude on stall point and inception type
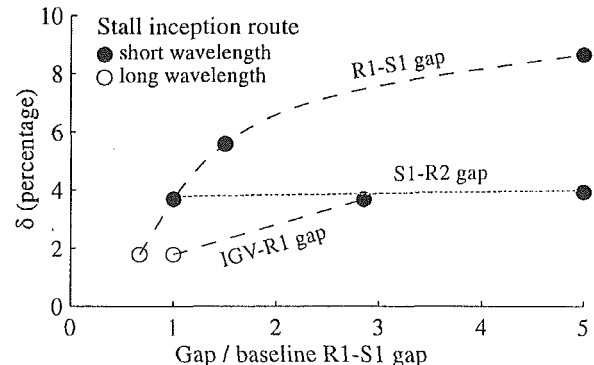

Fig. 18 Effects of IGV-R1, R1-S1, and S1-R2 gap lengths on stall point and inception type

capturing the experimentally observed characteristics of short-wavelength stall events. The significant features of this model are that it is three dimensional, nonlinear, represents each blade row individually, and uses finite amplitude spike-shaped disturbances to perturb the flow. During the model's development, it was found that short-length-scale stall behavior would not be exhibited if any one of these aspects was missing. A model with these elements is therefore the simplest one that can be used to calculate the short-wavelength stalling process. The adequacy of the model, which uses an infinite number of blade assumptions, indicates that the short-length-scale stall inceptions, observed by Camp and Day (1998), Day (1993), Day et al. (1999), Park (1994), and Silkowski (1995), can be viewed as the consequences of compression systems subjected to localized finite amplitude disturbances, and modeled without resolving the detailed flow structures within blade passages.

Up to now we have not inquired as to the physical origin of the finite amplitude tip-spike disturbances observed by Park (1994). Insight is provided by the eight-blade passage isolated rotor calculations performed by Hoying et al. (1999). Simulations at stall demonstrated that the motion of the tip vortex in and out of a rotor passage produced spike-shaped disturbances. It would seem that discrete blade passage events, such as tip vortex dynamics, are likely the sources of the short-length-scale disturbances. These need to be computed with a discrete blade model, but the infinite blade number compressor model is adequate for determining the overall effect of these disturbances on compressor stability.

Although it can be presumed that disturbances exist within the blade passages of each bladerow in a multistage compressor, the amplitude of these disturbances can be of varying magnitude. As shown in this paper, the amplitude of disturbances can affect the instability point. Recognizing where these disturbances with a threshold magnitude for initiating the instability exist, and only applying body force impulses to these stages, is an integral part of using the new model for compressor stall prediction. This aspect differs from linearized analyses, which presume that infinitesimal disturbances of all wavelengths are always present through the compressor. Further research on the physical sources of such disturbances, and the conditions for setting their amplitude, are needed to provide a rigorous basis for choosing proper disturbances.

Results from this paper indicate that the growth or decay of short-length-scale disturbances in a rotor is dependent on the characteristics of that rotor and its neighboring stators. We refer to these three blade rows as a component group. Changing the spacing of the blade rows within a component group did affect stall point, the shape of the stall cell, and stall route; however, changing the distance between the component group with spike forcing and the other blade rows had no effect. Further evidence comes from the GE assessment calculations, which showed the first stage stalled via spikes at the same flow coefficient whether the downstream stages were mismatched or not. To find the stall point of a compressor with spike disturbances, it is thus only necessary to model each individual component group containing the spikes.

The model developed here may be used to determine specific short-wavelength stall criteria, which would be valuable for compressor design. The observation by Camp and Day (1998) that the rotor incidence at stall is constant for different blade loadings is augmented by our result that this incidence angle depends on the gaps within the component group. Further calculations may determine the link between blade spacing and the critical rotor incidence, and thus develop explicit rules for the prediction of short-length-scale stall in general component group designs.

Summary and Conclusions

A three-dimensional computational model was developed for simulating the development of both long and short-wavelength compressor instabilities. Individual blade rows were represented by a body force formulated in terms of the blade's pressure rise and turning characteristics. The ability of the model to capture observed behavior was assessed against experimental measurements and analytical results. The model has been used in a set of simulations to explore the parametric trend of the instability behavior of a four-stage low speed compressor.

The following conclusions were deduced from the simulations:

1 The necessary ingredients of the model are a three-dimensional, nonlinear, row-by-row representation of compressor response to finite amplitude disturbances. The short-length-scale stalling process cannot be described if any one of these is missing.

2 Localized disturbances of sufficient amplitude (large enough to effect zero pressure rise in the tip) are required to initiate the short-wavelength route to rotating stall.

3 The computations show instability occurring on the negatively sloped part of the overall compressor characteristic, in agreement with experimental measurements. This is in direct contrast to the predictions of the modal type of analyses, in which the instability will occur at the peak of the characteristic.

4 The growth or decay of small-length-scale disturbances in a rotor is determined by the design characteristics of the isolated component group consisting of the rotor and its adjoining stators.

5 The point at which stall occurs (i.e., propagating asymmetrical disturbances do not decay) via the short-wavelength route is set by the most unstable component group where large amplitude spike disturbances are present.

6 Closing the rotor–stator gaps within the most unstable component group suppresses the growth of short-wavelength disturbances, thereby improving compressor stability.

References

Billet, G., Huard, J., Chevalier, P., and Laval, P., 1988, "Experimental and Numerical Study of the Response of an Axial Compressor to Distorted Inlet Flow," ASME Journal of Fluids Engineering, Vol. 110, pp. 355–360.

Camp, T. R., and Day, I. J., 1998, "A Study of Spike and Modal Stall Phenomena in a Low-Speed Axial Compressor," ASME JOURNAL OF TURBOMACHINERY, Vol. 120, pp. 393–401.

Day, I. J., 1993, "Stall Inception in Axial Flow Compressors," ASME JOURNAL OF TURBOMACHINERY, Vol. 115, pp. 1–9.

Day, I. J., Breuer, T., Escuret, J., Cherrett, M., and Wilson, A., 1999, "Stall Inception and the Prospects for Active Control in Four High-Speed Compressors," ASME JOURNAL OF TURBOMACHINERY, Vol. 121, pp. 18–27.

Escuret, J. F., and Garnier, V., 1994, "Numerical Simulations of Surge and Rotating Stall in Multi-Stage Axial-Flow Compressors," AIAA Paper No. 94-3202.

Gong, Y., 1998, "A Computational Model for Rotating Stall and Inlet Distortions in Multi-stage Compressors," Ph.D. Thesis, Massachusetts Institute of Technology.

Greitzer, E. M., 1976, "Surge and Rotating Stall in Axial Flow Compressors, Parts I and II," ASME Journal of Engineering for Power, Vol. 98, pp. 190–217.

Haynes, J. M., Hendricks, G. J., and Epstein, A. H., 1994, "Active Stabilization of Rotating Stall in a Three-Stage Axial Compressor," ASME JOURNAL OF TURBOMACHINERY, Vol. 116, pp. 226–239.

Hoying, D. A., Tan, C. S., Vo, H. D., and Greitzer, E. M., 1999, "Role of Blade Passage Flow Structures in Axial Compressor Rotating Stall Inception," ASME JOURNAL OF TURBOMACHINERY, Vol. 121, this issue, pp. 735–742.

Jameson, A., Schmidt, W., and Turkel, E., 1981, "Numerical Solutions of the Euler Equations by Finite Volume Methods With Runge–Kutta Time Stepping Schemes," AIAA Paper No. 81-1259.

Longley, J. P., Shin, H. W., Plumley, R. E., Silkowski, P. D., Day, I. J., Greitzer, E. M., Tan, C. S., and Wisler, D. C., 1996, "Effects of Rotating Inlet Distortion on MultiStage Compressor Stability," ASME JOURNAL OF TURBOMACHINERY, Vol. 118, pp. 181–188.

Longley, J. P., 1997, "Calculating the Flowfield Behaviour of High-Speed Multi-Stage Compressors," ASME Paper No. 97-GT-468.

Marble, F. E., 1964, "Three-Dimensional Flow in Turbomachines," Aerodynamics of Turbines and Compressors, Vol. X of High Speed Aerodynamics and Jet Propulsion, Hawthorne, W. R., ed., Princeton University Press, Princeton, NJ, pp. 83–166.

McDougall, N. M., 1988, "Stall Inception in Axial Compressors," Ph.D. Thesis, Cambridge University.

Moore, F. K., 1984, "A Theory of Rotating Stall of Multistage Axial Compressors: Parts I–III," ASME *Journal of Engineering for Gas Turbines and Power*, Vol. 106, pp. 313–336.

Moore, F. K., and Greitzer, E. M., 1986, "A Theory of Post-Stall Transients in Axial Compression Systems: Part I, II," ASME *Journal of Engineering for Gas Turbines and Power*, Vol. 108, pp. 68–76, pp. 231–239.

Park, H. G., 1994, "Unsteady Disturbance Structures in Axial Flow Compressor Stall Inception," Master's Thesis, Massachusetts Institute of Technology.

Silkowski, P. D., 1995, "Measurements of Rotor Stalling in a Matched and a Mismatched Multistage Compressor," GTL Report No. 221, Gas Turbine Laboratory, Massachusetts Institute of Technology.

Tryfonidis, M., Etchevers, O., Paduano, J. D., Hendricks, G. F., and Epstein, A. H., 1995, "Prestall Behavior of Several High-Speed Compressors," ASME JOURNAL OF TURBOMACHINERY, Vol. 117, pp. 62–80.

Vo, H. D., 1999, private communication.

Weigl, H. J., Paduano, J. D., Frechette, L. G., Epstein, A. H., and Greitzer, E. M., 1998, "Active Stabilization of Rotating Stall and Surge in a Transonic Single Stage Axial Compressor," ASME JOURNAL OF TURBOMACHINERY, Vol. 120, pp. 625–636.

Wisler, D. C., 1981, "Core Compressor Exit Stage Study, Volume IV—Data and Performance Report for the Best Stage Configuration," NASA CR-165357, NASA Lewis Research Center.

APPENDIX

Formulation of the Body Force Field

The derivation of the body force field used to represent the blade regions in the model is presented here. The forces, calculated separately for each blade row, must satisfy the following general requirements:

1 For steady-state axisymmetric flow, the blade row model must reproduce the correct overall pressure rise and turning angle.

2 The body forces must be able to locally respond to unsteady three-dimensional flow variations.

The body force distribution depends on the following three characteristics of the blade row: the total pressure rise, $\Psi_{tt}(\phi, r)$, the exit flow angle, $\beta_{exit}(\phi, r)$, and the local angle along the blade camber line, $\alpha(x, r)$.

For this particular GE compressor, it is convenient to break the body force vector into two parts, one turning the flow without work being done, the other solely producing the total pressure rise:

$$\mathbf{F} = \mathbf{F}_{\text{turning}} + \mathbf{F}_{\Psi_{tt}} \tag{6}$$

The radial component of the body force, F_r, is assumed to be zero since the blades have little radial skewness. Only the axial component of $\mathbf{F}_{\Psi_{tt}}$ contributes to the pressure rise, so

$$F_{\Psi_{tt}, \theta} = 0 \tag{7}$$

$$F_{\Psi_{tt}, x}(x, r, \theta) = f(x) \Psi_{tt}(\phi(x, r, \theta), r) \tag{8}$$

where

$$\int_{\text{leading edge}}^{\text{trailing edge}} f(x) dl = 1. \tag{9}$$

$f(x)$ is a function used to distribute the force along the streamlines (dl) through the blade region. The distribution function is forced to be small near the leading and trailing edges to reduce numerical oscillations. Equation (9) is simplified by assuming the streamlines are parallel to the axis (i.e., $dl = dx$) since all compressors used in this paper have a high hub-to-tip ratio.

$\mathbf{F}_{\text{turning}}$ is constructed so the flow turns toward the camber line angle in the relative frame of the blade row. The tangential component of the force is given by

$$F_{\theta, \text{turning}} = C V_x (r\Omega + V_x \tan(\alpha) - V_\theta). \tag{10}$$

The constant C is calibrated to produce the correct deviation angle at the design flow coefficient. $\mathbf{F}_{\text{turning}}$ is chosen normal to the local velocity $\mathbf{V}$ so that it does not affect the total pressure. Therefore,

$$F_{\text{turning}, x} = \frac{V_x}{V_\theta} F_{\text{turning}, \theta}. \tag{11}$$

D. A. Hoying

Air Force Research Laboratory,
Wright-Patterson Air Force Base,
Dayton, OH 45433

C. S. Tan

Huu Duc Vo

Gas Turbine Laboratory,
Massachusetts Institute of Technology,
Cambridge, MA 02139

E. M. Greitzer

United Technologies Research Center,
East Hartford, CT 06108

Role of Blade Passage Flow Structures in Axial Compressor Rotating Stall Inception

The influence of three-dimensional flow structures within a compressor blade passage has been examined computationally to determine their role in rotating stall inception. The computations displayed a short length-scale (or spike) type of stall inception similar to that seen in experiments; to the authors' knowledge this is the first time such a feature has been simulated. A central feature observed during the rotating stall inception was the tip clearance vortex moving forward of the blade row leading edge. Vortex kinematic arguments are used to provide a physical explanation of this motion as well as to motivate the conditions for its occurrence. The resulting criterion for this type of stall inception (the movement of the tip clearance vortex forward of the leading edge) depends upon local flow phenomena related to the tip clearance with the implication that for this and possibly other stall mechanisms the flow structure within the blade passages must be addressed to explain the stability of an axial compression system that exhibits such short length-scale disturbances.

Introduction and Background

The marked effect of axial compressor tip clearance on stable flow range is a trend that is well documented from an overall performance point of view (Smith, 1970; Koch, 1981; Cumpsty, 1989). In terms of knowledge of the basic mechanisms, however, the phenomenological links connecting tip clearance flow features to the onset of rotating stall (the event that sets the limit on the stable flow range) have by and large not been identified. In particular, on a blade passage scale, there is no accepted qualitative, let alone quantitative, description of the dynamic processes associated with transition from a situation in which the flow has blade-to-blade periodicity (including the embedded tip clearance vortex) to the strong asymmetry that characterizes rotating stall. This paper addresses the connection between tip clearance flow phenomena and rotating stall inception and illustrates the role played by the clearance vortex structure in one of the routes to compressor instability.

The work described here was motivated by the observation that two types of rotating stall inception occur in axial compressors. The first, which is characterized by waves with length scales on the order of the circumference of the compressor, and propagation speed of one-fourth to one-half of rotor rotation, has been referred to as modal stall inception. A number of investigations have been conducted of this phenomenon (e.g., Haynes et al., 1994; Tryfonidis et al., 1995), and a main conclusion is that modal development of rotating stall is associated with the growth of small amplitude sinusoidal (in the circumferential coordinate) flow disturbances. Relatively simple models that view the blade passage as a one-dimensional channel (Moore and Greitzer, 1986a, b; Haynes et al., 1994) yield good predictions of the rotational speed, growth rate, and waveform shape of such disturbances. The agreement between experiment and model implies that knowledge of the overall blade row loss (or equivalently pressure rise) and turning characteristics suffices in developing a useful analysis of the unsteady fluid dynamic features of the instability process. In this

context, the clearance flow structure (clearance vortex) is only important insofar as it affects this overall loss and turning, and it does not appear to be necessary to describe the passage flow on more than this global level to provide a physically meaningful description of instability inception.

There is, however, another, and very different, route to rotating stall, which is characterized by the appearance of disturbances with a dominant length scale much shorter than the circumference, typically on the order of several blade pitches, as well as a higher propagation speed (70 to 80 percent of rotor frequency) (Day, 1993). In contrast to modal stall inception, there is currently no mechanistic description of this phenomenon, which has been referred to as short length-scale stall inception or "spikes." Experiments show that this type of rotating stall inception possesses a radial structure (Silkowski, 1995) and that changes in the size of the tip clearance can modify the type of stall inception observed (Day, 1993).

The observations imply that a different and more detailed approach is essential to capture the development of such short length-scale stall inception. More specifically, it is necessary to include a description of the tip clearance flow structure within the individual blade passages. In this connection, in view of the pronounced effects that changes in tip clearance have on compressor stability, an important goal of this study is to clarify the link between tip clearance flow and the rotating stall onset. A specific fluid dynamic question, therefore, is what is the role of the tip clearance flow, and the tip clearance vortex, in the stall inception process. From this work it is hypothesized that the unstable motion of the tip clearance vortex forward of the compressor leading edge is a mechanism for the development of short length scale disturbances leading to compressor stall.

Methodology and Computation/Modeling Interface

Overall Approach and Focus. From the outset it is important to recognize the implications concerning this approach, which stem from the observed length scale and structure of the short length-scale disturbances. Most current approaches to describing rotating stall onset and growth employ a description in which the identities of the individual blades are lost and a particular blade row is replaced by a continuous distribution of body forces or by actuator disks, which embody a similar physical concept. Such an approximation relies on the circumferential length scale of the

---

disturbances of interest being much larger than the blade spacing. In these treatments the blade passage is viewed essentially on a control volume basis, and they cannot thus describe events occurring within the control volume. Anticipating somewhat the results to be shown, however, it can be expected that this information is needed to define the inception mechanism associated with short wave length disturbances. There is thus a requirement to describe, at an appropriate level, those aspects of blade passage flow structure relevant to rotating stall onset.

Another facet of the approach stems from the fact that current computational capabilities are insufficient to allow a full unsteady computation of rotating stall with an arbitrary level of detail. The present method, and this cannot be too strongly emphasized, was thus developed with a specific focus on the rotating stall problem. Although the development of a new computational approach is discussed, this is only a secondary counterpoint to the main theme of the paper, which is to provide insight into the physical processes of interest.

The development of an appropriate description of this problem has involved choices at a number of levels, ranging from selection of computational scheme to basic conceptual issues of what should be modeled and what should be computed directly. As an example of the latter, consider the flow through the tip clearance. A number of studies have shown that for compressors the tip leakage is very nearly a pressure-driven crossflow, that viscous effects in the tip clearance gap have little effect on the overall pattern of the leakage, and that methods that represent the tip clearance flow in a rudimentary manner appear to capture much of the basic behavior (Storer and Cumpsty, 1991; Adamczyk et al., 1993). Based on this information, it would be expected that one could decrease the computational resources required by treating the tip clearance as an inviscid region, with little or no effect on the overall objective of the study, and this was the approach taken.

Explicitly, what is sought is more nearly conceptual than numerical. We wish to obtain physical conclusions that are firmly grounded in the demonstration that the method captures the experimentally observed trends, i.e., that the overall behavior, from both steady and unsteady viewpoints, is consistent with experiment. Metrics for the calculation thus include not only steady-state behavior (rotor loss dependence having approximately the same shape as experiments) but also unsteady flow features (computed short wavelength disturbance with the same length scale, propagation speed, radial profile, and growth rate as seen in the measurements). In summary there have been a number of deliberate, and end objective driven, decisions taken about where to put the "interface" between computation and modeling to best attack this computationally intensive problem.

Specific Issues to Be Resolved. The physical features that need to be addressed are as follows: (i) There are multiple blade passages involved in a rotating stall cell and thus a potentially larger range of length scales to be captured by the numerical method than in the computation of flow in periodic blade passages (He and Ismael (1997) discussed unsteady three-dimensional Navier–Stokes simulation of 10 blade passages of NASA rotor 67.) (ii) The phenomenon is wavelike and the large range in length scales therefore implies a similar range of time scales. The wave behavior of this unsteady flow needs to be appropriately resolved. (iii) The compressor operating regime is off-design and the viscous effects that give rise to separated flow must be included. A related consideration was the division of the flow into regions of viscous and inviscid flow, as well as the amount of resolution needed for

the boundary layers. (iv) As mentioned previously, the three-dimensional flow structure associated with the tip clearance must be included.

The most challenging aspect of the problem is dealing with the range of length and time scales. A numerical integration method for dealing with this aspect of the simulation, known as a Dispersion Relation Preserving scheme, has been developed by Tam and Webb (1993). This method was created for wave propagation problems in which accurate representation of dissipative and dispersive behavior is critical. The method is a finite difference approach using an explicit time integration scheme, which possesses a factor of two improvement (in the range of wavelengths that can be propagated accurately) compared to a four-stage Runge–Kutta scheme.

To include the effects of viscosity, a k–ϵ turbulence model was incorporated with a Navier–Stokes solver to compute the flow within the compressor. Inclusion of viscous effects near the blades is clearly necessary, but away from the blades viscosity plays little role. The viscous procedure was thus only applied in the near-blade region (sized to include the boundary layers), and outside of this region Euler equations were used.

The most important aspects of the upstream and downstream flow fields in this problem are the pressure and velocity relationships. These can be well described on the basis of an inviscid flow. Put another way, the details of wake mixing in the downstream region would not be expected to have a dominant effect on the unsteady blade row behavior, and it is the latter that is critical in this problem. An Euler representation was therefore also used upstream and downstream of the blades. To reduce further the computational resources required, three-dimensional nonreflecting boundary conditions were developed, allowing shortening of the computational domain by over a factor of two.

The aspects of the code development presented here serve to illustrate how the features of the rotating stall problem have been utilized to guide the balance between modeling and detailed numerics. A detailed description of the development and validation of the code, including comparison with cascade data, is given by Hoying (1996).

Features of the Numerical Experiment

The computational investigation was based on the low-speed version of the E^3 compressor (Wisler, 1981), which had been experimentally observed to exhibit the short length-scale type of stall inception (Silkowski, 1995; Park, 1994). This compressor has a set of inlet guide vanes followed by four geometrically identical stages with a hub-to-tip radius ratio of 0.85. The rotors have a blade aspect ratio of 1.2 (compared to 1.34 for the stators) and a maximum tip Mach number of 0.2. The computed blade geometry was simplified by linearly interpolating between the tip and hub sections. The resulting airfoil had approximately 3 deg more camber between 10 and 90 percent span and approximately 2 deg lower incidence between 10 and 60 percent span. This had the effect of increasing the loading in the outer span compared to the inner portion of the blade. In the experiments cited, stall inception location was in the first-stage rotor with the strongest indications near the tip. Thus, although the actual compressor consisted of four stages, because the initial development of rotating stall was confined to the first rotor in the experiment, the single blade row geometry could be used to analyze the initial phase of the rotating stall development. The computational domain is a portion of the first rotor consisting of eight blades out of the 54 blades present.

―――――― **Nomenclature** ――――――

C_x = axial velocity
M_∞ = upstream relative incoming flow Mach number
R = gas constant

S = entropy
U = tip blade velocity
γ = specific heat ratio

ϕ = flow (axial velocity) coefficient = C_x/U
ρ = density
E^3 = energy efficient engine

The number of eight compressor blades was selected based on (two-dimensional) numerical experiments with the same geometry, which showed that eight blades were capable of also exhibiting a modal stall inception (Hoying, 1996). It is important to have the capability for exhibiting both types of stall inception so as not to prejudice the results.

With eight blades, if one wishes to preserve the three-dimensional shape of the blade, only a fraction of the circumference can be included. The maximum wave length of any nonaxisymmetric disturbance is thus limited to eight blade spacings, rather than to the full circumference. The hypothesis put forward, however, is that the short wavelength type of stall inception is a local phenomenon, so that beyond a threshold number of blades, the actual fraction of the circumference included should not be critical. With eight blades, the length of time over which periodicity is imposed will not be the same as the amount of time for a revolution of the actual rotor. To keep the distinction clear in what follows, the time it takes for the eight blades to traverse the computational domain once will be referred to as a *period* rather than a *revolution*.

The steps in the overall computational procedure involved computing the "axisymmetric" performance using a single periodic blade passage calculation with no throttle transient, followed by the multiple blade passage computation with a throttle-induced transient to allow for the presence of asymmetric flow. The single passage computation was performed to define the flow regimes of interest as well as to permit a comparison between axisymmetric and nonaxisymmetric flow fields. In the multiple blade passage calculation, no asymmetries were imposed as the small deviations arising from numerical precision errors were sufficient to induce nonaxisymmetric flow during the multiple blade computations. The details of the stalling process were then analyzed much as experimental information had been previously.

Clearances of 1.3 and 3.0 percent (of chord) corresponding to those examined experimentally were numerically simulated. In the computations, as in the experiment, the results were qualitatively similar between the small and large clearances. Only the results from the 3.0 percent case will be presented here for clarity. The blade Mach number in the computations (0.2) and in the experiments were much less than unity (~0.2) so the flow could be considered incompressible for both. Before the compressor was *throttled to stall, a steady-state solution was obtained near the peak* of the characteristic given by the single blade passage computation. The compressor mass flow was then reduced by a throttle transient from this steady solution, at a flow coefficient of 0.335, to a value of 0.300 in three periods, with conditions then held at a constant throttle setting while the rotating stall pattern developed. The large throttle change was made to avoid the long computational time required from performing multiple small throttle changes.

Figure 1 shows rotor pressure rise versus flow coefficient (based on a stream thrust average) for both the steady-state single blade configuration and the transient eight blade computation (following a single blade passage). The numbered points shown correspond to axisymmetric flow behavior at and past stall, as obtained from the single blade passage calculation. The substantial difference in the behavior near point 1, which represents the quantitatively different flow fields between the blade-to-blade periodic solution and the eight-blade calculation, is evident. Prior to stall, the difference lies in the unsteadiness in the multiblade passage calculation, where pressure fluctuations are accentuated by the axially longer flow domain (higher fluid inertia) required in the computation. Since the points on the multiblade passage speedline represent snapshots in time, they include both the high and low points of the fluctuations and are thus above and below the mean speedline from the single-blade passage calculation. The stall point, characterized by a discontinuity in the slope of the single blade passage speedline and by a temporal fluctuation in pressure rise (at approximately constant overall flow coefficient) of the multiblade passage speedline,
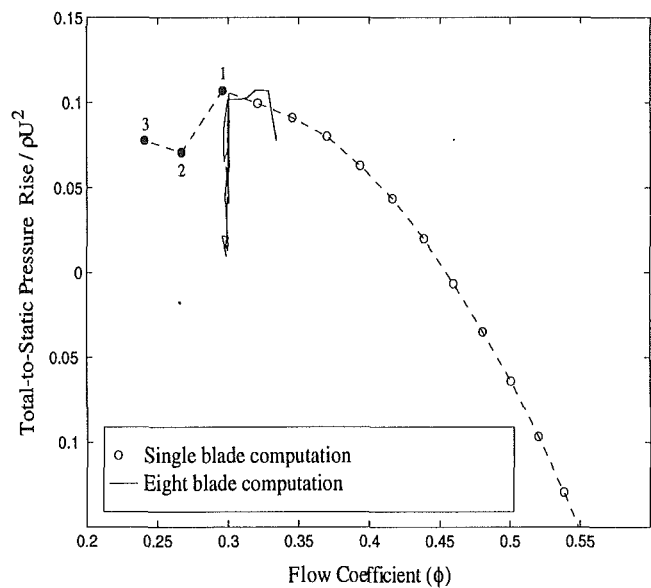

Fig. 1 Pressure rise characteristic for the E^3 rotor. Point 1 is the stall point in the single blade passage calculation. Points 2 and 3 are the corresponding results with throttle closed beyond stall. The speedline for the eight-blade calculation shows temporal fluctuations in pressure rise at stall.

matches in both calculations. However, flow behavior at and after stall is substantially different as explained later.

Characterization of Three-Dimensional Stall Inception

In analyzing the computations, the primary focus was on characterizing the flow features that participate in the development of short length-scale stall. We can divide discussion of the results into the following steps: (*i*) demonstrate that the computed stall inception has the same physical characteristics as that observed in experiment, (*ii*) identify the flow structures that are important in defining this process, (*iii*) analyze the development of these structures to provide a physical description of the inception of rotating stall.

Direct indication of the evolution of the rotating stall disturbance can be seen from the velocity distribution ahead of the compressor. Figure 2 shows traces of axial velocity parameter ($C_x/U = \phi$) versus time, in units of rotor *periods*, at eight evenly spaced circumferential locations across the eight blades, at 10 percent radial immersion from the outer case, $\frac{1}{4}$ chord ahead of the rotor. An offset has been added to all of the traces except the bottom one to allow them to be viewed together. The traces show the rapid growth of a large-amplitude short wavelength disturbance in the time interval from time = −5.34 periods to time = 0 and the two straight lines indicate the disturbance propagation speed. Points A, B, C, and D represents four time samples during the growth of the disturbance. The corresponding flow fields are plotted and discussed later in Figs. 7–10. The shape and development of these disturbances in the inlet axial velocity are qualitatively the same as the disturbances measured by Day (1993).

Two important features of this evolving flow field are illustrated in Fig. 3, which shows entropy contours on the leading edge plane of the compressor, at time = −4.1; the scale goes from −0.15 to 2.24, with entropy nondimensionalized by $\frac{1}{2} \gamma M_\infty^2 R$. Thus, an entropy increase of one unit corresponds to a loss of one relative (to the rotor) dynamic head. First is the presence of flow spilling forward of the rotor blade locally, evidenced by the high entropy (maximum $\Delta S = 2.39$) fluid in the blade passage at the leading edge. Second is that the reversed flow region is confined to the tip of the compressor.

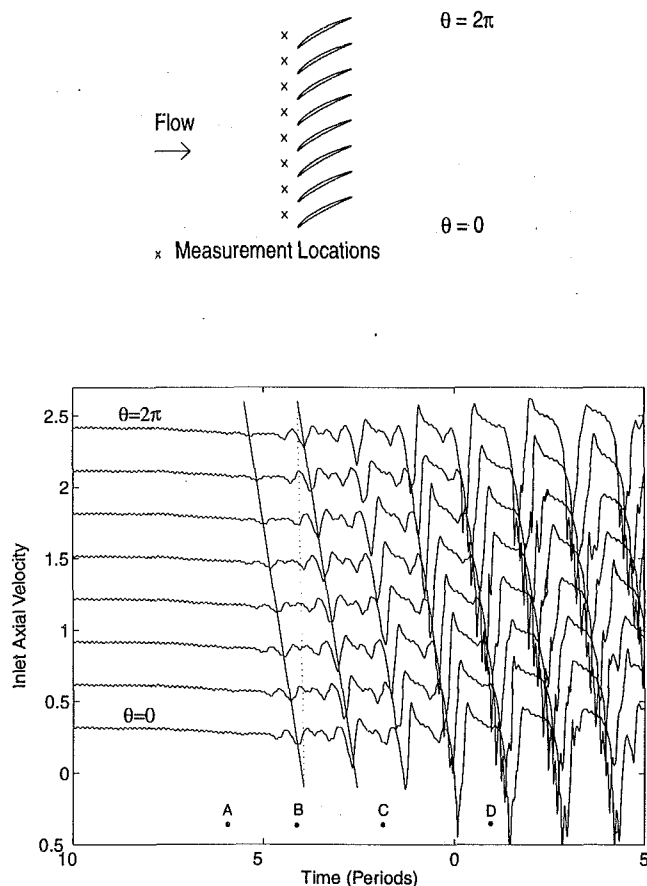The defining characteristics of the short wavelength distur-

Fig. 2 Traces of the inlet axial velocity at 10 percent radial immersion from the outer case for the E^3 rotor during a transient to stall. Points A, B, C, and D represent four different times in the stall development process.

bances are small circumferential extent, high rate of rotation, high growth rate, and localization near the tip (Day, 1993; Silkowski, 1995). The position of the disturbance at the tip of the blades has already been demonstrated in Fig. 3. To compare the size and shape of the disturbance, the upstream velocity near the tip is shown in Figs. 4 and 5 for the computations and for the experiment
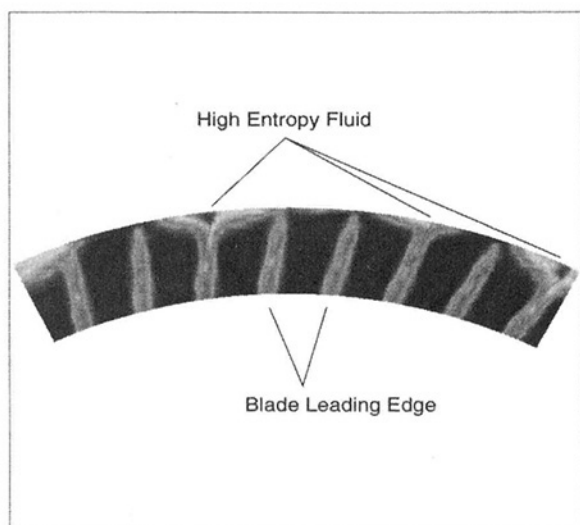

Fig. 3 Entropy contour at the leading edge of the E^3 compressor (time = −4.1, S = −0.15 to 2.24)
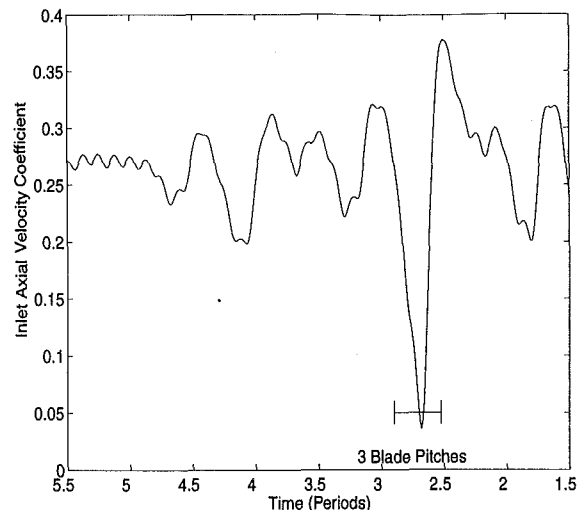

Fig. 4 Trace of the inlet axial velocity from computations for the E^3 rotor at 10 percent immersion during transient to stall (origin of time scale arbitrary)

(Silkowski, 1995), respectively. The figures show local axial velocity coefficient versus time. Both the numerical and the computational results show a disturbance approximately three blade pitches wide, although the numerical results indicate several subsidiary disturbances rather than a single spike. Other experiments, however, have shown the development of more than one short length-scale stall cell (Day, 1993), and this difference in the number of stall cells is therefore not considered a key item in the comparisons. The shapes of the disturbances shown in Figs. 4 and 5 are similar, and the computed rotational speed of the disturbance (70 percent of rotor speed) also matches the experimental result. One point that should be mentioned is that because the numerical computation does not represent the full compression system used in the experimental investigation, comparison must be done for times when the stalling disturbance is relatively small in axial
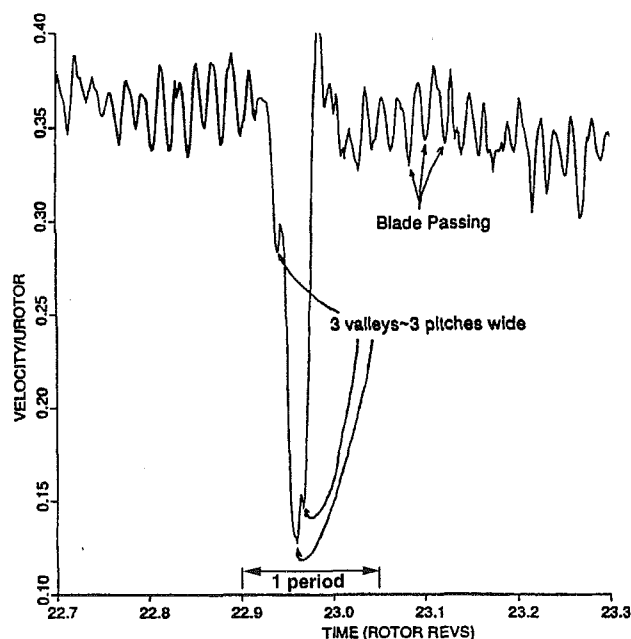

Fig. 5 Trace of the inlet axial velocity stall disturbance for the E^3 compressor tested by Silkowski (1995) at 20 percent immersion. (Origin of time scale is arbitrary. Total time scale is four periods, the same as that of Fig. 4.)
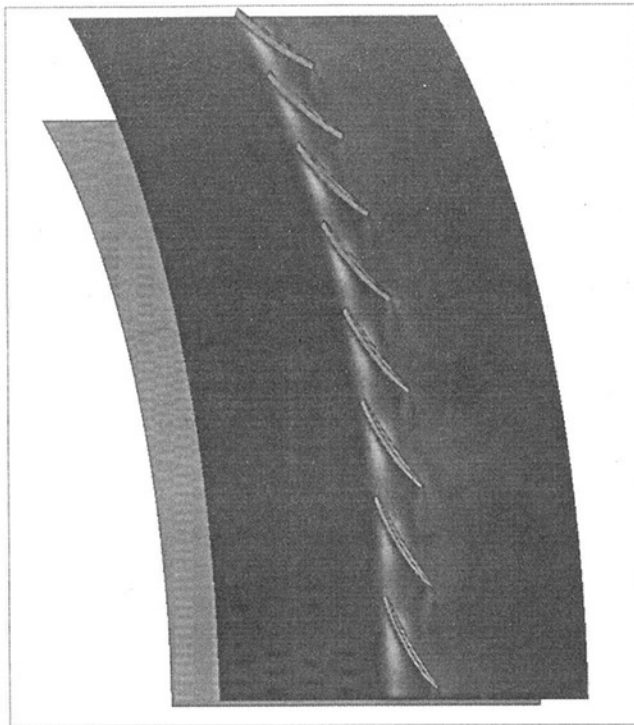
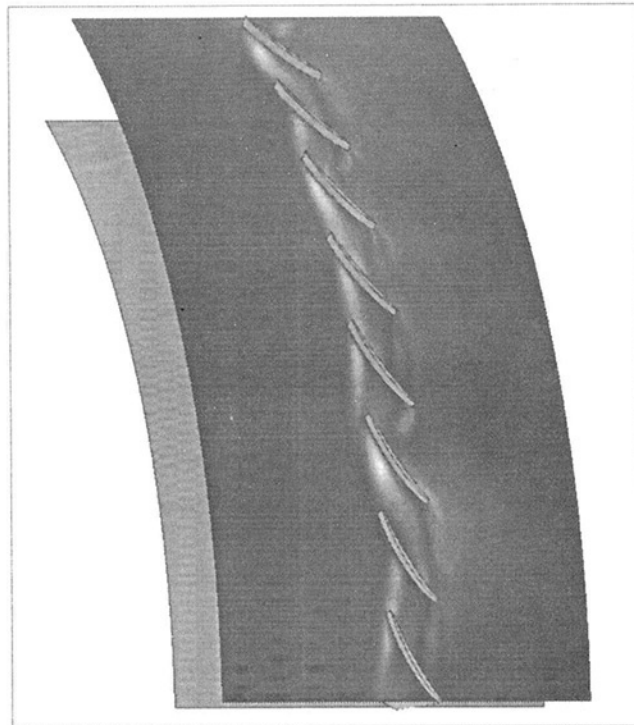Fig. 6 Vorticity contour at 8 percent immersion of the E^3 compressor (time = −5.9, point A in Fig. 2)

Fig. 7 Vorticity contour at 8 percent immersion of the E^3 compressor with (time = −4.1, point B in Fig. 2)

extent. As the disturbance extent grows, the effect of other blade rows on the disturbance in the rotor will become stronger.

We can also compare the early growth rate of the disturbance. The data of Silkowski (1995) show that the axial velocity disturbance takes roughly one rotor revolution to grow from small amplitude to the value shown in the computed results of Fig. 4. In the computation, the corresponding growth takes roughly four periods, which corresponds to 0.6 rotor revolutions, which is on the order of but smaller than the experimental value. On the basis of disturbance shape, radial location, propagation speed, and growth rate, the computations do reproduce the key features of the *initial stages* of the stall inception development observed in experiments. We emphasize that this isolated rotor calculation would not reflect the development of the instability in the multistage environment in the long-time limit.

Description of Short Length-Scale Stalling Process

Using the results, we can now examine the stalling process in more depth. We observed that the motion of the tip clearance vortex was a prominent feature during the development of the stall inception process. It was found that at the operating condition where asymmetry began to develop, the tip clearance vortex trajectory was located at the leading edge cascade plane, i.e., was perpendicular to the axial direction. Movement of the tip leakage vortex to the leading edge plane at the limiting flow coefficient has also been observed in single blade passage calculations of Weingold (1998), and more recently by Van Zante (1999). As rotating stall developed, the vortex moved upstream of the compressor and approximately formed the forward boundary of the reversed flow region of the stall cell.

To view the vortex motion during the development of rotating stall, a sequence of contour plots of the vorticity magnitude at the 92 percent span radial station are presented in Figs. 6–9. (This radial station was used because it gave a clear view of the process.) The different figures correspond to the different times during the stall development process indicated by A, B, C, and D in Fig. 2. Just before stall (Fig. 6), the tip clearance vortex stretches from

the leading edge of each rotor blade to the leading edge of its nearest neighbor. Figure 7 shows the state 1.8 periods later when nonaxisymmetric flow has begun to develop. At this point, as can be seen from the corresponding view in Fig. 3 at the same time, the flow in the lower $\frac{3}{4}$ span of the compressor shows no reversal, even
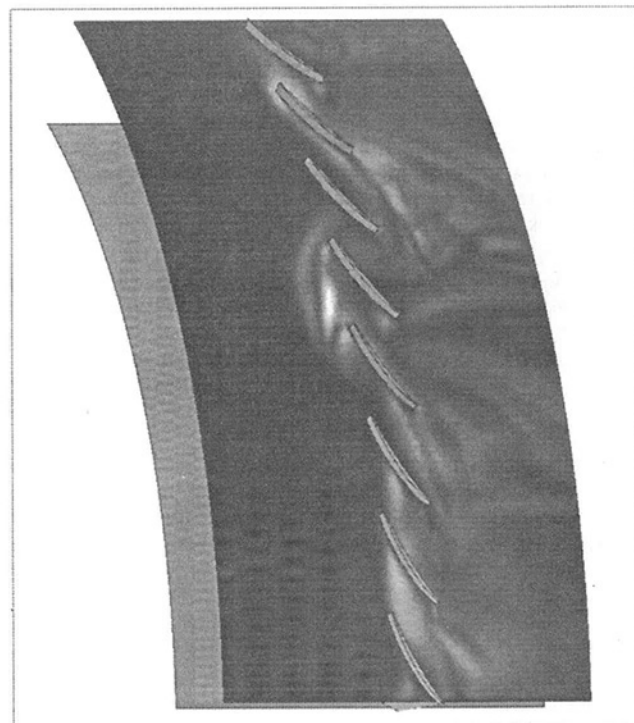

Fig. 8 Vorticity contour at 8 percent immersion of the E^3 compressor (time = −1.9, point C in Fig. 2)
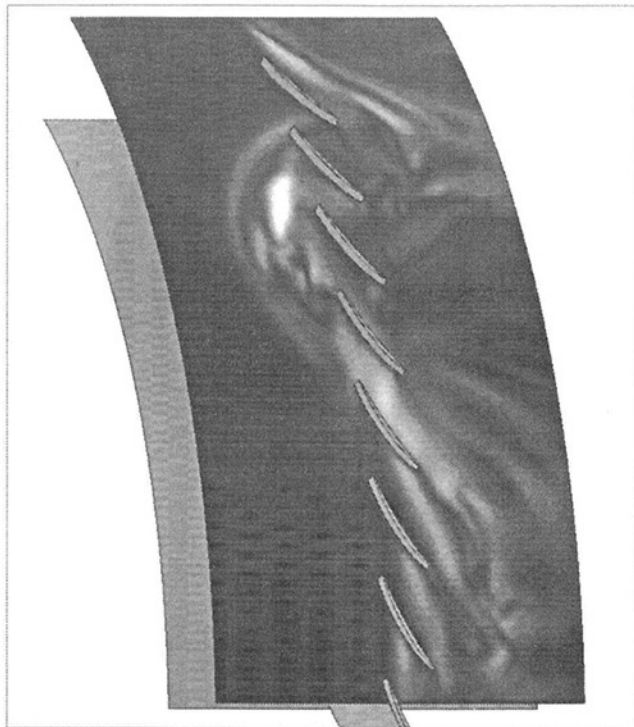
Fig. 9 Vorticity contour at 8 percent immersion of the E^3 compressor (time = 1.0, point D in Fig. 2)

Fig. 10 Tip vortex circulation and trailing edge blockage associated with tip leakage vortex for the E^3 rotor during stall development. An increase in tip vortex circulation corresponds to a movement of the tip vortex trajectory forward of the blade row and vice versa.

though there is reversed flow near the tip. Two to three short length-scale incipient stall disturbances can be seen developing, as evidenced by the presence of the tip clearance vortex forward of the leading edge of the compressor. At a later time (time = −1.9), one of these disturbances becomes dominant, as shown in Fig. 8, where the clearance vortex is evident at the leading edge of this disturbance. In Fig. 9 the dominant disturbance has propagated farther upstream and its width has increased. Later than this, the flow situation is qualitatively similar to Fig. 8, but the stall cell grows both axially and circumferentially. Although these pictures are from a single immersion location, corresponding features were evident throughout the outer 10–15 percent of the span.

The focus has so far been on the motion of tip vortex trajectory. We can also examine quantitatively the two other characteristics of the tip vortex, circulation and blockage, and how they relate to the motion of the tip vortex trajectory during the stall inception process. Blockage can be viewed as the reduction in effective flow area associated with the velocity defect introduced by the low-momentum tip leakage flow forming the vortex (Khalid, 1995). As the throttle is closed toward stall, blockage increases and it is this increase that has been previously linked to rotating stall onset. The connection between tip vortex circulation and stall onset, however, may be more fundamental and it is thus useful to examine the tip vortex circulation and the blockage versus time for a blade passage, shown in Fig. 10.

As the nonaxisymmetric flow begins to develop, the circulation of the tip clearance vortex begins an oscillatory motion of increasing amplitude. (Because the data in this plot follow a single blade, the disturbance moves past the blade. If the observer moved with the disturbance it would appear to grow, but not oscillate.) The motion of the vortex is such that when the vortex circulation increases above the pre-stall level, the vortex is forward of the blade row, and when the circulation is less, the vortex is behind the blade row leading edge. The blockage, which has been found to be associated with the vortex core fluid (Adamczyk et al., 1993; Khalid, 1995), at the rotor trailing edge also undergoes a corresponding oscillation. The blockage variation tracks the vortex circulation (and motion), but the blockage lags the vortex strength
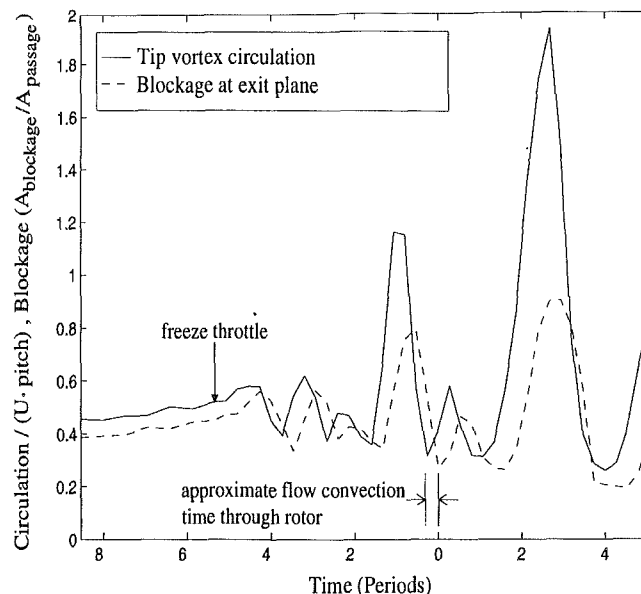
by approximately two blade passing times (0.26 period). This indicates that blockage and tip vortex circulation are linked, although the mechanism responsible for the dynamic behavior of the tip vortex has not yet been resolved.

Role of the Tip Clearance Vortex in Short Length-Scale Stall

Insight into the mechanism of short wavelength stall development can be obtained by considering the behavior of the vortex trajectory. Figure 11 shows the stable trajectories at four different flow coefficients from high flow ($\phi = 0.38$) to near stall ($\phi = 0.32$). At the higher flow coefficients the vortex trajectory lies further back in the blade passage. As the flow coefficient is

Fig. 11 Trajectories of the tip clearance vortex for the E^3 rotor for different flow coefficients

Fig. 12 Velocity induced by image vortex (meridional view)

ROTATION

Fig. 14 Development of localized disturbance

reduced, the clearance vortex trajectory becomes closer to perpendicular to the axial direction.

The behavior of the vortex equilibrium position can be interpreted from vortex kinematics, as illustrated in Fig. 12, which sh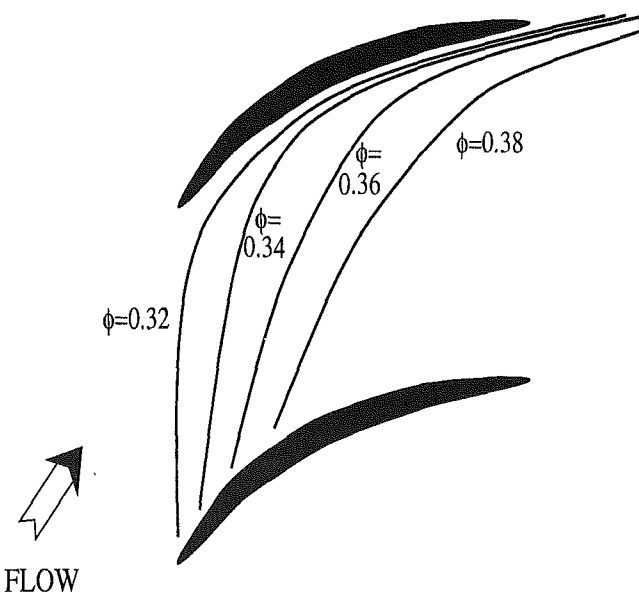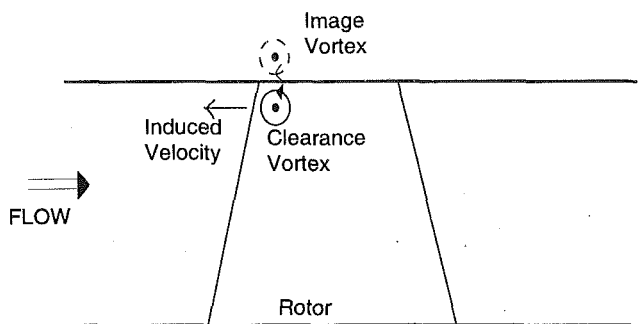ows a side view of the vortex in the blade passage along with its image across the casing wall. Because the distance of the vortex from the wall is much less than the span of the vortex along the passage, the local "self-induced" velocity can be approximated from the local orientation of the vortex, and the velocity field associated with the vortex-boundary configuration can be represented by the vortex and its image. As indicated, the induced velocity of the vortex pair is in the upstream direction.

For a given clearance vortex circulation and mean flow, there will, in general, be an angle for the vortex trajectory at which this self-induced velocity is balanced by the component of the mean flow normal to the vortex. At operating conditions near design, the trajectory will be in an equilibrium position like that shown in Fig. 13(a). Consider a displacement of the vortex from this position. If the vortex moves forward, the mean flow vector becomes more closely aligned with the perpendicular to the vortex, resulting in an increased value of velocity component normal to the vortex. The result is that the vortex tends to be returned to the original position. From these considerations, the position is stable.

As the compressor is throttled toward stall, computational results show that the strength of the clearance vortex increases and the mean flow velocity decreases. As the flow coefficient decreases (Fig. 13(b)), the equilibrium vortex trajectory swings closer to
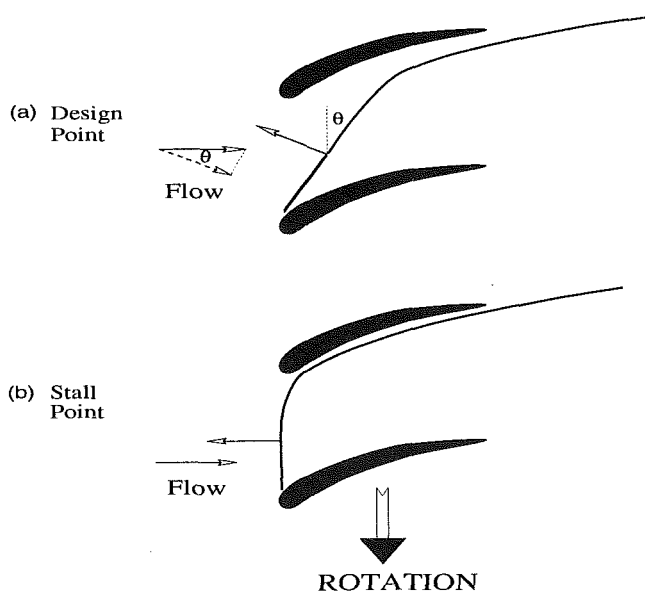
perpendicular to the axial direction. A stable equilibrium cannot exist when the vortex trajectory becomes perpendicular to axial because the ability of the flow to respond to perturbations through an increased normal component of the axial velocity is lost; if a small perturbation occurs, there is no corrective action associated with the mean flow component normal to the vortex which will restore equilibrium. (For the case studied here, this point was reached at the peak of the pressure rise characteristic.) The vortex will thus tend to propagate forward of the rotor passage and as noted, the computations show the subsequent growth in displacement out of the blade passage.

Although this description by itself does not explain why the flow breaks down into a nonaxisymmetric short length-scale stall cell, further considerations of the vortex motion are helpful in addressing this aspect. Vortex lines cannot end in the fluid so that when the vortex begins to propagate forward of the compressor, it must do so by bowing forward. The portion of the vortex in the center of the bowed region will remain perpendicular to the flow direction, but the rest of the vortex will be turned away from the main flow direction and will have a locally reduced self-induced upstream velocity. The shape of the upstream propagating vortex will alter as indicated qualitatively in Fig. 14, promoting the development of the type of localized disturbance with characteristic length of a blade spacing shown in experiments (Day, 1993).

It can be noted that a description of the entire multiblade row compression system was not required to demonstrate this unstable flow situation, although the process does not take place in isolation, and at some point the influence of the remainder of the compression system will be felt. The events described are originally local to the tip region of one blade row, and thus not significantly affected by the rest of the compression system during the initial development. The single blade row results should thus apply to the initial development of a short length-scale stall in multiblade row compressors. For compressors operating near the peak of their characteristic, such disturbances have the potential to induce rotating stall to occur in the entire compressor, as described by Gong et al. (1998).

Transient Performance With Blade-to-Blade Periodicity

We have so far been focusing on the behavior of the tip vortex in a multiblade passage environment. It is of interest to assess the behavior in a single (periodic) blade passage situation and determine the connection between a periodic solution and stall onset. Single blade passage computations show that once the tip clearance vortex reached the critical position at the leading edge of the blade row at a point on the compressor characteristic represented by point 1 in Fig. 1, it would remain there if the throttle were held fixed. If the throttle were closed past this point (points 2 and 3 in Fig. 1), the pressure rise drops and the tip vortex settles into a new

Fig. 13 Trajectory and induced velocity for the tip clearance vortex at different loading conditions: (a) design point; (b) stall point
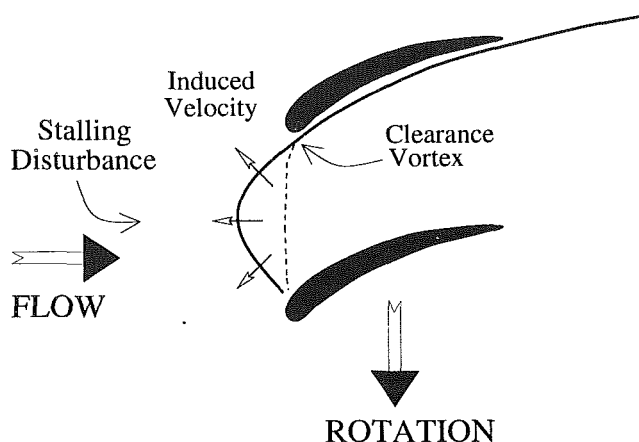
stable position[2] slightly ahead of the blade row with a bowed shape similar to Fig. 14. This is different from the multiblade passage calculation which shows growing fluctuations in pressure rise at the stall point. This behavior is associated with the dynamic motion of the tip vortex alluded to previously. Thus, the single blade calculation can simulate the behavior of the tip vortex up to the point of instability. Beyond this point, the single blade computation cannot simulate the dynamic behavior of the tip vortex because of the inherent assumption that each blade passage is decoupled from the other blade passages.

Two important observations can be derived from the single-blade calculation within its range of validity. First, the throttle point at which the clearance vortex reaches the leading edge plane closely matches the stall point of the multi-blade calculations (see Fig. 1). Second, the negative slope at stall based on the single blade speedline is consistent with past observations of short length-scale stall. (An accurate evaluation of the slope cannot be made from the multi-blade unsteady computation due to pre-stall oscillations in pressure rise created by the throttle transient.) These observations of the tip vortex position suggest that single blade computations may be useful for predicting the stall point for compressors exhibiting short length-scale rotating stall inception.

Summary and Conclusions

Computational experiments have been carried out for an isolated rotor spanning eight out of 54 blades to simulate the short length-scale rotating stall inceptions, which have been found to have fundamentally different behavior from long length-scale modal stall.

For the case shown, the short length-scale inception process is linked to the behavior of the blade passage flow field structure, specifically the tip clearance vortex. This is in contrast to the modal stalling case where a description of the flow structures within the blade passages is not required for a useful description of rotating stall inception and development.

Based on the simulations, a local stall inception criterion for the short length-scale phenomena, namely tip vortex trajectory perpendicular to the axial direction, has been identified for axial compressors. This suggests that for tip-critical compressors (as is the case here) single blade passage calculations, rather than computations of the entire annulus, may be able to predict the conditions at which a short length-scale disturbance can occur.

The origin of this stalling process has also been described in terms of the kinematics of the tip clearance vortex. Stall inception is a result of the motion of the tip clearance vortex moving out (upstream) of the blade passage; this occurs when the vortex trajectory is aligned with the blade leading edge plane, which was shown to be an unstable condition. The time evolution of the rotor exit blockage is a consequence of this motion.

Although only a single case is presented here, due to the kinematic arguments given, a similar breakdown in the axisymmetric flow field is expected in any compressor that experiences a spilling forward of the tip clearance vortex. This argument does not preclude the possibility of other modes of instability that also rely on structures within the blade passage, evidence of which has been given by Seitz and Cumpsty (1999).

While the present set of calculations is for an isolated rotor that

is known to exhibit short length-scale stall, there is a need to examine the instability behavior (including modal stall inception) of the compressor rotor in a multi-blade row environment.

References

Adamczyk, J. J., Celestina, M. L., and Greitzer, E. M., 1993, "The Role of Tip Clearance in High-Speed Fan Stall," ASME JOURNAL OF TURBOMACHINERY, Vol. 115, pp. 28–38.

Camp, T. R., 1995, "Aspects of the Off-Design Performance of Axial Flow Compressors," PhD Thesis, University of Cambridge.

Cumpsty, N. A., 1989, Compressor Aerodynamics, Longman Scientific & Technical, Essex, England.

Day, I. J., 1993, "Stall Inception in Axial Flow Compressors," ASME JOURNAL OF TURBOMACHINERY, Vol. 115, pp. 1–9.

Gong, Y., Tan, C. S., Gordon, K., and Greitzer, E. M., 1998, "A Computational Model for Short Wave-Length Stall Inception and Development in Multi-Stage Compressor," Submitted for TurboExpo98, Stockholm, Sweden.

Haynes, J. M., Hendricks, G. J., and Epstein, A. H., 1994, "Active Stabilization of Rotating Stall in a Three-Stage Axial Compressor," ASME JOURNAL OF TURBOMACHINERY, Vol. 116, pp. 226–239.

He, L., and Ismail, J. O., 1997, "Computations of Blade Row Stall Inception in Transonic Flows," Proc. ISABE 1997, Paper No. 97-7100, pp. 697–707.

Hoying, D. A., 1996, "Blade Passage Flow Structure Effects on Axial Compressor Rotating Stall Inception," PhD Thesis, Massachusetts Institute of Technology.

Khalid, S. A., 1995, "The Effects of Tip Clearance on Axial Compressor Pressure Rise," PhD Thesis, Massachusetts Institute of Technology.

Koch, C. C., 1981, "Stalling Pressure Rise Capability of Axial Flow Compressor Stages," ASME Journal of Engineering for Power, Vol. 103, pp. 645–656.

Moore, F. K., and Greitzer, E. M., 1986a, "A Theory of Post-Stall Transients in Axial Compression Systems: Part I—Development of Equations," ASME Journal of Engineering for Gas Turbines and Power, Vol. 108, pp. 68–76.

Moore, F. K., and Greitzer, E. M., 1986b, "A Theory of Post-Stall Transients in Axial Compression Systems: Part II—Application," ASME Journal of Engineering for Gas Turbines and Power, Vol. 108, pp. 231–239.

Park, H. G., 1994, "Unsteady Disturbance Structures in Axial Flow Compressor Stall Inception," Master's Thesis, Massachusetts Institute of Technology.

Seitz, P., and Cumpsty, N. A., 1999, Private Communication.

Silkowski, P. D., 1995, "Measurements of Rotor Stalling in a Matched and a Mismatched Multistage Compressor," GTL Report No. 221, Gas Turbine Laboratory, Massachusetts Institute of Technology.

Smith, L. H., Jr., 1970, "Casing Boundary Layers in Multistage Axial-Flow Compressors," Flow Research on Blading, L. S. Dzung, ed., Elsevier Pub. Co., Amsterdam.

Storer, J. A., and Cumpsty, N. A., 1991, "Tip Leakage Flows in Axial Compressors," ASME JOURNAL OF TURBOMACHINERY, Vol. 113, pp. 252–259.

Tam, C. K. W., and Webb, J. C., 1993, "Dispersion-Relation-Preserving Finite Difference Schemes for Computational Acoustics," Journal of Computational Physics, Vol. 107, pp. 262–281.

Tryfonidis, M., Etchevers, O., Paduano, J. D., Hendricks, G. F., and Epstein, A. H., 1995, "Pre-Stall Behavior of Several High-Speed Compressors," ASME JOURNAL OF TURBOMACHINERY, Vol. 117, pp. 62–80.

Van Zante, D., et al., 1999, "Recommendations for Achieving Accurate Simulation of Tip Clearance Flows in Transonic Compressor Rotors," ASME Paper No. 99-GT-390.

Weingold, H., 1998, Private Communication.

Wisler, D. C., 1981, "Core Compressor Exit Stage Study, Volume IV—Data and Performance Report for the Best Stage Configuration," NASA CR-165357, NASA Lewis Research Center.

---

[2] In contrast to the usual pressure exit boundary condition, this computational procedure incorporates a throttle as the exit boundary condition so that a stable solution can be obtained past the stall point.

Investigation of Pre-stall Mode and Pip Inception in High-Speed Compressors Through the Use of Correlation Integral

Michelle M. Bright

NASA Lewis Research Center,
Cleveland, OH 44135
email: mbright@lerc.nasa.gov

Helen K. Qammar

Leizhen Wang

University of Akron,
Akron, OH 44325

Five high-speed compressor configurations are used to identify pre-stall pressure signal activity under clean and distorted inlet conditions, and under steady injection and controlled injection conditions. Through the use of a nonlinear statistic called correlation integral, variations in the compressor dynamics are identified from the pre-stall pressure activity far before variations (modal or pip) are observed visually in the wall static pressure measurements. The correlation integral not only discerns changing dynamics of these compressors prior to stall, but is now used to measure the strength of the tip flow field for these five high-speed compressors. Results show that correlation integral value changes dramatically when the stall inception is modal; and it changes less severely when the stall inception is through pip disturbances. This algorithm can therefore distinguish from the pre-stall pressure traces when a machine is more likely to stall due to pips versus modes. When used in this manner, the correlation integral thus provides a measure of tip flow strength. The algorithm requires no predisposition about the expected behavior of the data in order to detect changing dynamics in the compressor; thus, no pre-filtering is necessary. However, by band-pass filtering the data, one can monitor changing dynamics in the tip flow field for various frequency regimes. An outcome of this is to associate changes in correlation integral value directly with frequency specific events occurring in the compressor, i.e., blade length scale events versus long length scale acoustic events. The correlation integral provides a potential advantage over linear spectral techniques because a single sensor is used for detection and analysis of the instabilities.

Introduction

In recent years the focus of compressor stall research has centered around identifying a physical process that induces rotating stall in compressors. With recent advances in the on-line identification of stall, and with successful strategies in place to extend the operating range to lower mass flow rates, active stall control in a research compressor environment is a reality. With this advent of active stall control methods, a reliable pre-stall indicator is becoming a necessity for future applications in compressors.

The existing methods to identify stall precursive events are often categorized based on the detection of long length scale (modal) or short length scale (pip) disturbances. In a paper by Tryfonidis et al. (1995), the emphasis is to study a long length scale phenomenon that leads to rotating stall. Other investigations by Day (1993), Park (1994), Camp and Day (1998), and Schulze et al. (1997) reflect the detection of short length scale (pip) activity in several high-speed compressors. In a recent report by Weigl et al. (1998) on the active stabilization of high-speed compressors, several pre-stall data sets showed modal activity, then a controller was used to suppress the modal waves, and subsequent pip activity instigated the controller to become unstable.[1] With this in mind, it would be advantageous to develop analysis and prediction techniques that detect both short and long length scale disturbances that lead to rotating stall.

Bright et al. (1997) presented a nonlinear methodology for the

detection of pre-stall behavior in a limited set of high-speed compressors. This methodology, called the correlation integral method, is based on nonlinear dynamics and chaos theory. This pre-stall detector identified in experimental data the underlying nonlinear dynamics of the fluid flow prior to the stall event. The correlation integral value was shown to change dramatically hundreds of rotor revolutions prior to the stall event in several test cases. It was also presented that the traveling wave energy algorithm (see Tryfonidis et al.), when applied to the same data, did not detect changing pre-stall behavior until after the correlation integral value changed. From this prior paper it was inferred that something inherently nonlinear was occurring in the pressure data prior to stall inception that the correlation integral perceived; and that this nonlinearity eventually triggered an occurrence of modal stall onset. Figures 1(a) and 1(b) are taken from this previous paper (Bright et al., 1997) to compare directly the application of the traveling wave energy method and the application of the correlation integral method to the same prestall pressure data. Figure 1(a) shows the traveling wave energy begin to grow around 200 rotor revolutions before stall. This method used all eight pressure sensors spaced 45 deg apart for calculation of this traveling wave energy. Figure 1(b) shows the sharp decline of the Correlation Integral value at approximately 600 rotor revolutions prior to stall as determined by a single pressure sensor.

This example is given to illustrate that correlation integral is changing in value well before spectral techniques change. Also, it is detecting some dynamic difference in the flow field prior to stall that is significant, yet undetectable by other methods.

In the present paper, we will attempt to broaden the discussion of this nonlinear methodology through a study of experimental results from a variety of compressor configurations. We will identify in these compressors the short length scale or long length scale phenomenon present prior to rotating stall through visual inspec-

---

[1] Through discussions with Ivor Day, this short length scale activity in the data was observed in the controlled data sets.
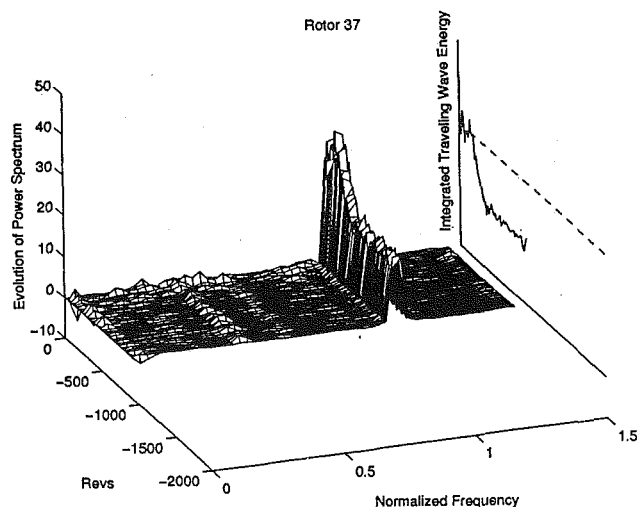
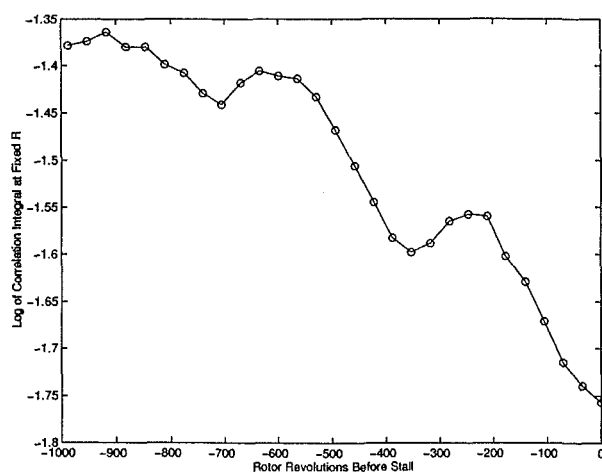**Fig. 1(a) Traveling wave energy results for rotor 37**

Fig. 1(b) Correlation integral results for rotor 37

tion of the pressure traces. With these data we will then use the correlation integral to clearly show from a single pressure trace the onset of instabilities leading to stall. We will also attempt to show in the correlation integral results some differences in the reaction of the correlation integral value during modal stall onset versus pip stall onset. The experimental results will include examples from single-stage transonic compressors with clean and distorted inlet flow, and with steady and controlled air injection.

Background

Several researchers have identified short length scale or pip disturbances in their compressor data [most notably, Day (1993)]. A robust method for detection of these pip instabilities during the onset of rotating stall, however, has not been presented. There has been a great number of investigations into the fluid physical stalling mechanisms in compressors (McDougall et al., 1990; Hoying, 1995; Paduano et al., 1993; Longley, 1997), especially with distortion present. In a recent paper by Camp and Day (1998), a measure of critical incidence of the blade tip is performed. Based on experimental measurements, a simple stall inception model is given to explain the formation of spikes and modes. It was stated in this paper that both pips and modes can occur in the same compressor, sometimes even simultaneously. Also, it was stated that in a single-stage compressor, the occurrence of modes or spikes was influenced by changing the radial distribution of rotor incidence. When the critical incidence of the rotor is exceeded, the rotor stalls.

An alternative technique is described below to monitor changing flow field conditions and to measure the strength of the tip flow field during the onset of rotating stall. This measure is sensitive to changes in long and short length scale disturbances and provides some insight into the inception of pips and modes.

Background on Correlation Integral Analysis

To begin to understand the type of physical phenomena initiating the creation of modes and pips, it is necessary to have a metric sensitive to both spatial and temporal dynamic changes. Recently, we presented a possible metric, namely the correlation integral (Bright et al., 1997) whose value showed a marked decline prior to stall in a limited set of high-speed compressor data. The correlation integral (CI) is commonly applied to highly nonlinear systems and relies on an M-dimensional reconstructed pseudo-attractor from a single sensor using time delays. The CI is defined by:

$$\text{CI}(N, R) = \frac{2}{N(N - 1)} \sum_{i=1}^{N} \sum_{j=i+1}^{N} H(R - \|y(t_i) - y(t_j)\|)$$

where y represents the M-dimensional reconstructed time series, N is the number of data points used in the reconstruction, H is the Heaviside step function, and $\|\ \ \|$ is the L_∞ norm (see Grassberger for a full discussion of this algorithm). What is essential about this algorithm is the interpoint distances $|y(t_i) - y(t_j)|$ between all pairs of points in the signal and the reference distance R. The $\text{CI}(N, R)$ includes in its calculation an auto-correlation length, which eliminates consideration of any points too close in time to one another. The correlation integral can be viewed as a measure of the average density at some scale R of the data (Lerner, 1996). Another view is that the CI is the fraction of interpoint distances within a reference distance R. As the nature of the oscillations in the data change, the inter-point distances and the corresponding CI will change dramatically.

The correlation integral was computed for all data sets presented in this paper using an embedding dimension, M, of 10 and a reconstruction delay of one; thus the dimension of the pseudo-attractor is quite high. In the earlier paper we chose a smaller value of M and a larger reconstruction delay. However, papers recently published by Kugiumtzis (1996) and Wu (1995) discuss the validity of selecting a high embedding dimension in order to reproduce the underlying dynamics of a system accurately. The use of a larger M value accentuates the decline in *total amplitude* of the CI value and does not affect *where in time* the CI value begins to decline. For this reason it is hard to compare results from our earlier paper since a small M value was used. A larger M value significantly improves the CI method for our present application since changing dynamics of the flow field are further enhanced. However, as M is increased above a value of 10, nothing more is gained, and no further "enhancement" is seen in the CI curves. Note only that the *same M* value is used for every test case.

For all the cases presented, the CI was determined for a 5000 point window of data. The window was updated every 1000 points, and the data was sampled at 3 kHz. The endpoint for the last data window was carefully chosen so that it does not include any in-stall behavior.

The key to understanding CI values is the manner in which the pseudo-attractor (or phase plane representation of the signal) changes shape and density with the onset of modes and/or pips. Consider a window of pressure data that is 5000 points long, where the amplitudes of the oscillations in the data are very similar. These regular oscillations force the trajectories of the pseudo-attractor to visit the same region repeatedly. In other words, if the data oscillate with very little variations in amplitude, then the trajectories reside on the outside "skin" of an M-dimensional sphere. This pseudo-attractor will have very high density and most of the distances between pairs of points will be both very small and narrowly distributed. This in turn means that the fraction of dis-
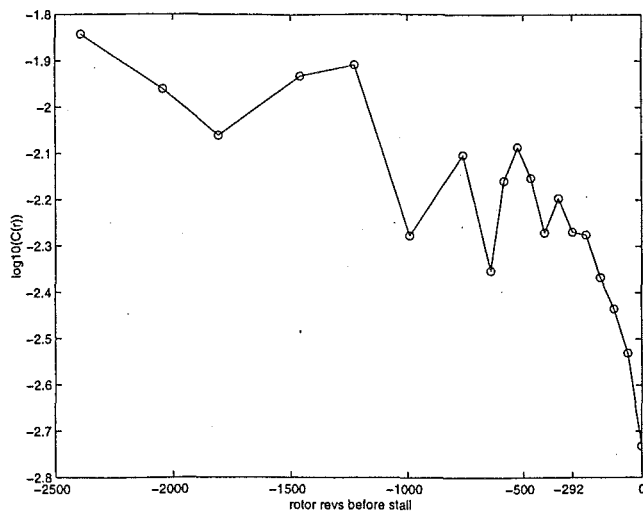
Fig. 2 CI value for data filtered at 500 Hz

tances between pairs of points will be both very small and narrowly distributed. This in turn means that the fraction of distances less than some specified R is large and results in a relatively large CI value. If the amplitudes of the oscillations are significantly different in the next data window, such as during the inception of pips or modes, then the pseudo-attractor will have a broader distribution of distances. In this case, one could visualize the trajectories now entering the "inside and outside" of the sphere, thus creating longer distances between some pairs, and a lower CI value. When comparing the pressure traces with the CI results, it is important to keep in mind that sections of a time trace with relatively small amplitude range contribute small interpoint distances and increase the CI value. Sections of a time trace with relatively large amplitude range contribute large interpoint distances and decrease the CI value.

A specific example of this concept is presented for data obtained in NASA's high-speed single-stage compressor facility. A description of the compressor and experimental procedure for this example can be found in Bright et al. (1997). The data were taken while the compressor was transitioned into stall through slow closure of the throttle. The data were originally sampled at 20 kHz and anti-aliased filtered at 10 kHz. For this example the data are then low-pass filtered at 500 Hz, generating a signal void of high-frequency variations. A pseudo-attractor is reconstructed using 5000 data point windows and the CI computed. Figure 2 shows the CI value for a fixed R as the compressor is ramped into stall. Well before the stall event, the CI maintains a high value until approximately 292 rotor revolutions before stall when it begins a rapid decline.

We now want to look further at what is occurring in the data window just prior to this decline at -292 revolutions versus what is occurring in the data window at stall (0 revolutions). Figure 3(a) depicts the distribution of all the interpoint distances in the pseudo-attractor for the data window ending at 292 revolutions before stall. Figure 3(b) is the distribution for the data window ending at stall (0 revolutions). Note that there are over 12 million interpoint distances calculated for a 5000-point pseudo-attractor. These histograms portray all the possible combinations of interpoint distances between pairs of points for 5000 samples of data. The correlation integral at a fixed R represents the ratio of the area under this curve from $R = 0$ to the fixed value of R, versus the entire area under the histogram.

In the first histogram in Fig. 3(a), the compressor operation is stable (albeit nearer to stall and not near choke) and the distances are concentrated around $R = 2.5$. This means that there are very few large interpoint distances. In the window just before stall, the histogram from Fig. 3(b) shows that increasing amplitudes caused

by developing modal instabilities have created a wider distribution of distances, which are now centered around $R = 5$. Many large interpoint distances are also present, some as high as $R = 35$. These results show, most importantly, that the CI curve yields evidence of dynamic changes that are occurring well before stall, which are not observed in the pressure traces or from a spectral analysis.

From these observations we can further characterize the growth of interpoint distances before stall and perhaps tie these observations to a physical phenomenon in the compressor. The CI method is next used on band pass filtered data sets. The previous data are now low pass filtered at 100 Hz instead of 500 Hz. Figure 4 shows the CI curve for the filtered 100 Hz data. A marked decrease in the CI curve is not evident until 140 rotor revs before stall, coincident with the observation of modes in the pressure traces.

This result is markedly different from the 500 Hz data set. This means that dynamics occurring between 100 Hz and 500 Hz contribute to the induction of stall 500 rotor revolutions before stall (see Fig. 2). However, very low-frequency dynamics, less than 100 Hz, do not contribute to the inception of stall until 140 revolutions before stall. We also have similar evidence that when this same data set is band-passed filtered at very high frequencies, between 4000 and 7000 Hz, (commensurate with blade passage frequencies), the CI value also drops around 100 revolutions
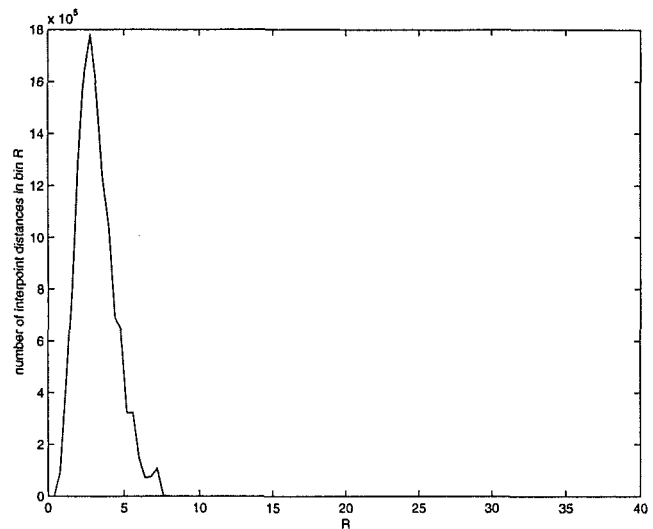

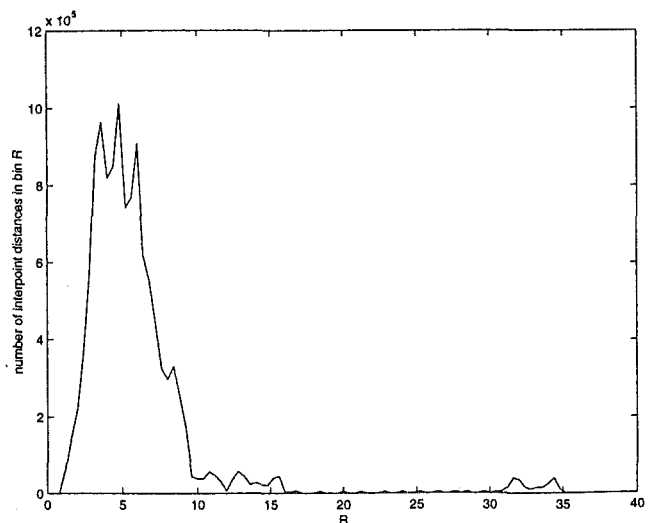Fig. 3(a)   Distribution of interpoint distances at -292 revs

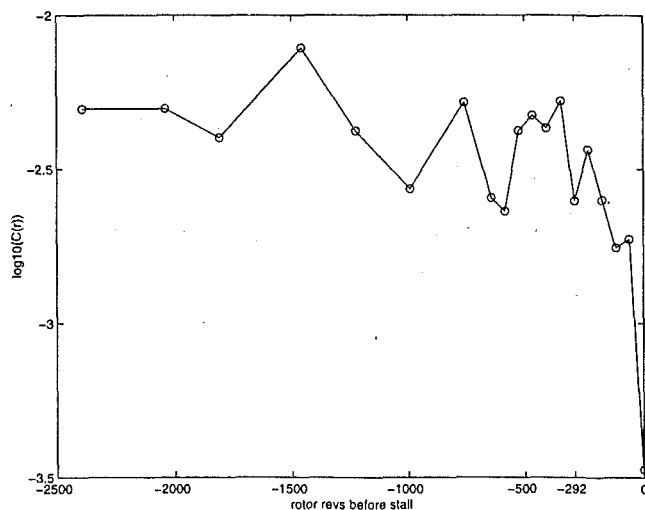Fig. 3(b)   Distribution of interpoint distances at 0 revs

Fig. 4 CI curve for 100 Hz data

before stall. This drop in CI value at high frequencies also occurs at the same time as the appearance of modes in the data (see Wang, 1998, and Li, 1997). This would point to the occurrence of both blade passage frequency events in addition to low-frequency events (below 100 Hz) that occur simultaneously before rotating stall. However, there are events in the 100 Hz to 500 Hz range that are growing and inducing these disturbances before stall. It is this range of frequency events that we will investigate further in our five test cases.

The remaining sections of this paper now describe the experiments performed on the high-speed compressors, their compressor operating conditions, and their pre-stall behavior in terms of modal or pip instabilities as seen in the pressure traces. We will also give Correlation Integral results for all the data sets. An explanation for the changes in the CI curves based on the pressure signals is also given. Finally, we conclude with a general discussion of the applicability of the CI method to future research on stall inception processes.

Experimental Setup and Data Acquisition

Experimental data were recorded from several compressors in a series of experiments that were performed between 1994 and 1997. All the data sets were collected for various configurations of the high-speed single-stage compressor rig at NASA Lewis, running either stage 35 or stage 37. Configurations of the NASA stage 35 and 37 compressor included clean inlet conditions, radial distortion, circumferential distortion, steady air injection, and controlled injected air upstream of the rotor. All the examples shown were transitioned into stall using a slow throttling maneuver. To identify modal and pip behavior specifically using the correlation integral, we will study just five test cases closely from the single-stage compressor rig. Case 1 is the stage operating with clean inlet conditions. Case 2 is the stage with 120 deg circumferential inlet distortion. Case 3 is the stage with radial inlet distortion. Case 4 is the stage with radial inlet distortion and steady air injection from 12 high-pressure air jets located circumferentially around the annulus at the inlet. Finally, case 5 is the stage with a clean casing and with controlled unsteady air injection from the actuators located at the inlet.

In all test cases, data were acquired using 5 psi range a/c coupled pressure transducers at eight equally resolved locations around the annulus. Although for the analysis using the nonlinear correlation integral method only one sensor is needed, all eight transducers are recorded for comparison with other Fourier spectral techniques. The data were recorded at 3 kHz sampling rate. All of the five test cases shown were taken from the NASA Lewis Research Center

Single-Stage Axial Compressor Test Facility, which is fully described by Weigl (1998). The NASA Stage 35 test compressor was originally designed as an inlet stage of an eight-stage 20:1 pressure ratio core compressor (Reid and Moore, 1978; Moore and Reid, 1980). The stage has a total pressure ratio of 1.82, a mass flow of 20.2 kg/s, a rotor tip speed of 455 m/s, and a rotation frequency of 286 Hz at design speed.

Stall Transients in Pressure Data

Pressure data for case 1 are presented in Fig. 5 for the stage running with a clean inlet. This is considered our baseline case and as shown the compressor stalls due to modal instabilities visible in the pressure traces before stall. At 40 revolutions before stall there appear to be spikes on top of the modes just before stall. This indicates that our high-speed stage under normal stalling conditions is considered a "modal" machine, since modal instabilities dominate the pre-stall behavior with some added pip instabilities present just before stall.

Figure 6 reveals results from case 2 when the baseline machine is configured with total pressure circumferential inlet distortion. The distortion was introduced with a magnitude of one dynamic head and a 120 deg extent and covered the full blade span. The fine mesh distortion screen was located approximately 10 chord lengths upstream of the rotor. In this case there appear to be pips occurring about 35 rotor revolutions before stall, which travel around the circumference twice but do not grow in amplitude. These pips then seem to run into the peak of a mode forming at 33 revolutions and disappear, and the machine again stalls due primarily to modal instabilities. (This experiment is more fully described by Spakovszky et al., 1999b).

Test case 3, however, indicates a distinctly different mechanism, which induces stall when radial inlet distortion is present. A fine mesh screen was placed 10 chord lengths upstream of the rotor, which covered 38 percent of the blade span in the tip region to create the distortion (see Spakovskzy et al., 1999a). The stalling mechanism in this case seems to be inherently pip like instabilities, not modal, as is evidenced in the pressure traces shown in Fig. 7 at 40 rotor revolutions before stall. There appear to be pip disturbances that rotate around the circumference of the compressor but do not grow in amplitude until five revolutions before stall. Modal instabilities do not appear in these traces at all.

Figure 8 shows the results from test case 4, where the same radial distortion configuration is in place; however, there is a constant level of steady injected air supplied from 12 injectors
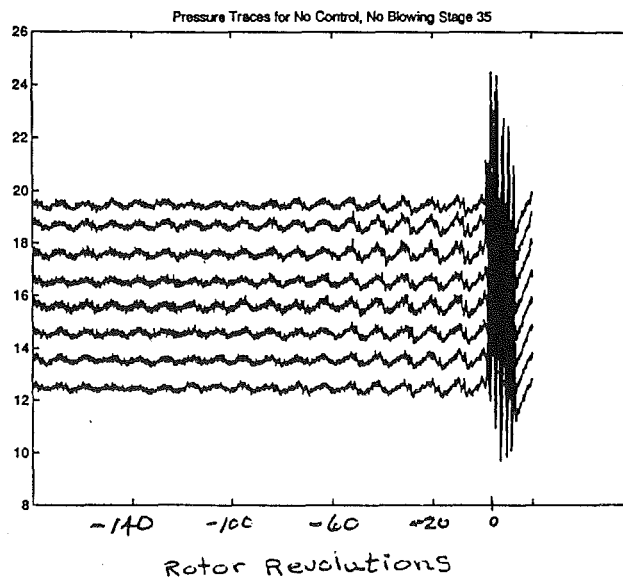

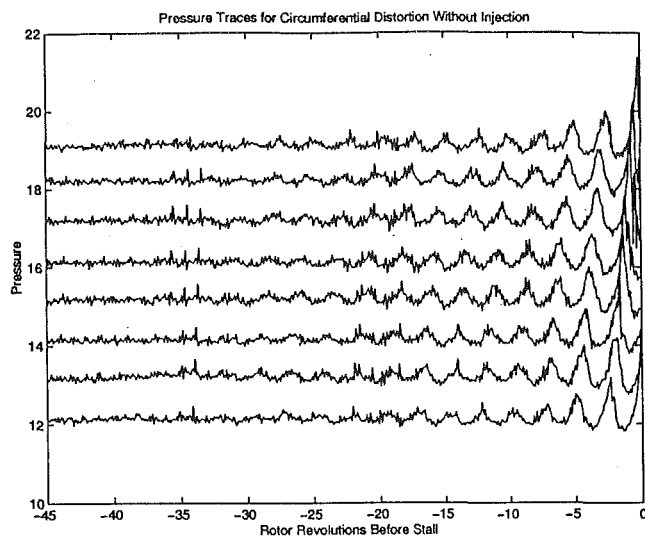Fig. 5 Pressure traces for clean inlet case

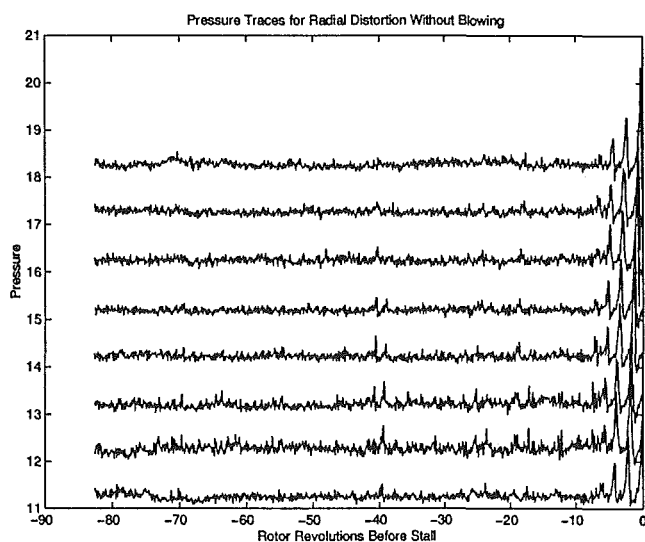Fig. 6 Pressure traces for circumferential distortion

Fig. 9 Pressure traces for controlled air injection

Fig. 7 Pressure traces for radial distortion
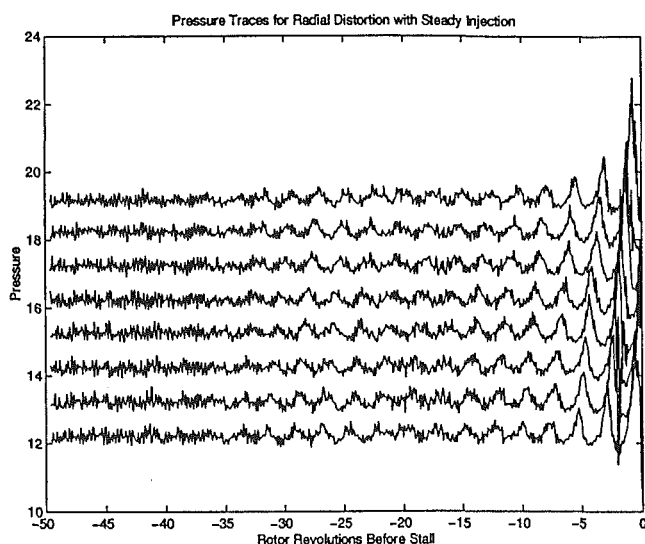
Fig. 8 Pressure traces for radial distortion with injection

located upstream of the rotor. Now the pressure traces indicate modal instabilities appearing before stall at 35 rotor revolutions, whereas the no-blowing configuration showed pips.

Finally, test case 5 reveals the clean inlet stage subjected to controlled air blowing to create a damping pattern of the pre-stall modal waves. Although the modal instabilities are damped due to the controlled injected air, it now appears that at 50 rotor revolutions before stall, pip-like disturbances travel around the circumference, collide with the peak of a forming modal wave, and induce modal waves with spikes on top that grow unstable into stall. This is shown in Fig. 9.

If we examine the compressor speed lines for all these test cases shown in Fig. 10, we see a trend in the shape of these curves as we approach stall. For the baseline case, the circumferential distortion case, and the radial distortion case with steady injected, all machines appear to stall at or beyond the peak of the compressor characteristic. The two cases that stall at the peak of the curve seem to exhibit modes with pips. The radial case with injection stalls beyond the peak of the characteristic. For the radial distortion case without injection, which showed only pip behavior, the machine stalls short of its peak. These observations would be similar to those of Camp and Day (1998) and their model of critical incidence of the rotor. Additionally, this would point to a higher tip criticality or high tip flow loading on the radially distorted stage. As discussed in the next section, the measure of this tip flow loading is an important aspect of the correlation integral algorithm.

Fig. 10 Compressor characteristics for stage 35

Fig. 11   CI curve for baseline case

Fig. 13   CI curve for radial distortion

Application of Correlation Integral to Test Cases

The CI curves were computed for these five test cases in order to gain additional insight into the pre-stall dynamic events occurring in the compressor. Figure 11 shows the CI curve at a fixed R computed from a single sensor upstream of the st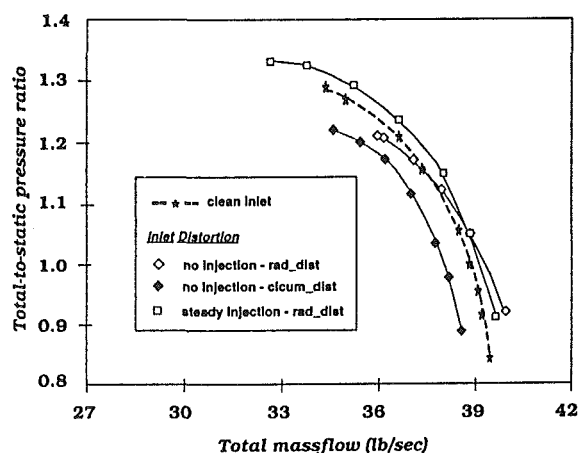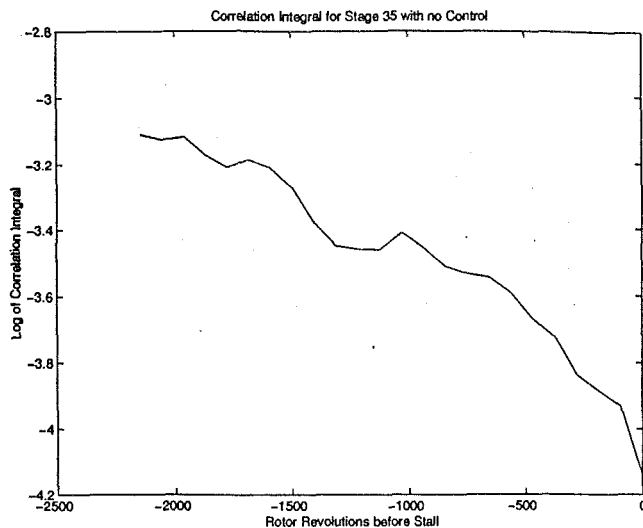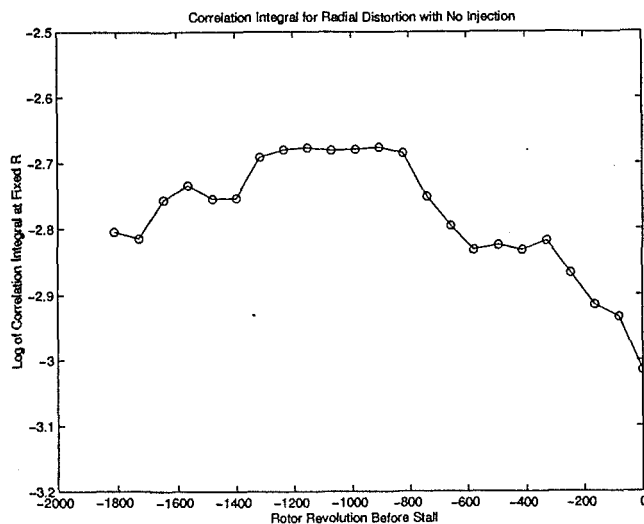age. The compressor configuration is the baseline experiment with a clean casing and no blowing or active control present. From the pressure traces, we noted that modal instabilities are visible prior to stall. In the CI curve we notice a gradual but continual decline in its value from 2000 revolutions all the way to stall. The decline in the correlation integral value is due to the *inception* of modal instabilities far before these modal disturbances appear in the pressure traces. The cumulative drop in CI value from the first inception of these modes to the stall point is about 1.0 order of magnitude since CI value is on a log 10 scale. We will look at the significance of this value for each test case.

Figure 12 shows the CI curve for case 2 when circumferential distortion is applied to the stage. At about 1500 revolutions the CI curve declines sharply with continual declines until stall. Inspection of the pressure traces revealed that incipient modal instabilities are seen prior to stall. The sharp decline in CI values for this case are again responding to the *inception* of modes in the pressure

traces before modal behavior is actually seen in the pressure traces. Additionally, in the pressure traces there appear to be spikes or pips forming, which travel around the circumference and run into (or perhaps create) a modal disturbance. The cumulative change in CI value for this case is about 0.8 orders of magnitude from first inception to stall.

Radial distortion without blowing (case 3) does not show the obvious growth of modal instabilities, but short length scale pips are found close to stall. The CI curve shown in Fig. 13 is relatively flat for this case, with only a modest decrease in its value starting at 800 rotor revs prior to stall. The total CI amplitude change is only on the order of 0.25 as the machine enters stall. This small cumulative change in CI value may be indicative that only short length scale or pip instabilities are necessary to drive the compressor into stall. From the compressor characteristic this is the only case that appears to reach a critical blade incidence at stall, which is an indicator of pip disturbances due to high tip blade loading.

A sharp decline in the CI curve from Fig. 14, however, is due to the initiation of modes in the case of radial distortion with air injection at the blade tip (test case 4). This case features a growing oscillation with the approach of stall as seen from the pressure traces in Fig. 8. At 1000 revolutions, the CI value gradually declines and at 150 rotor revs before stall, the CI curve steeply
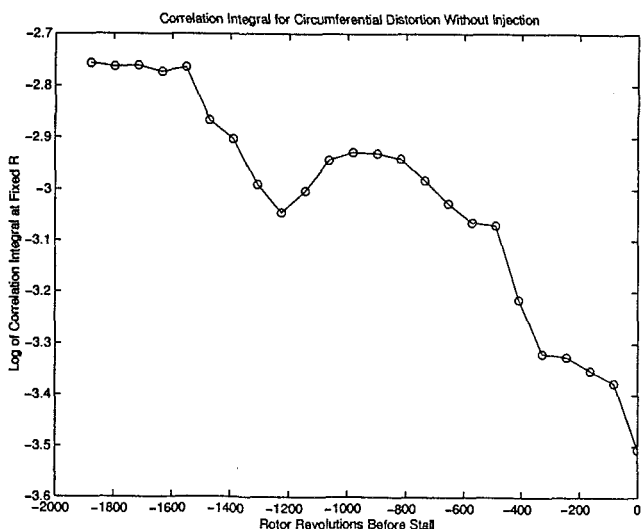

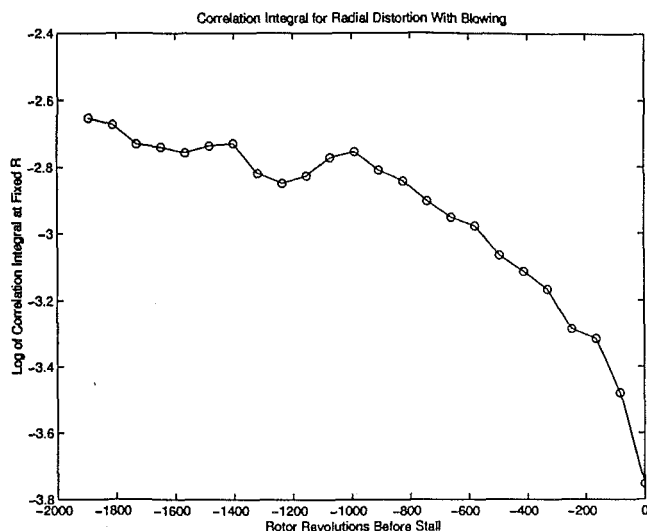Fig. 12   CI curve for circumferential distortion

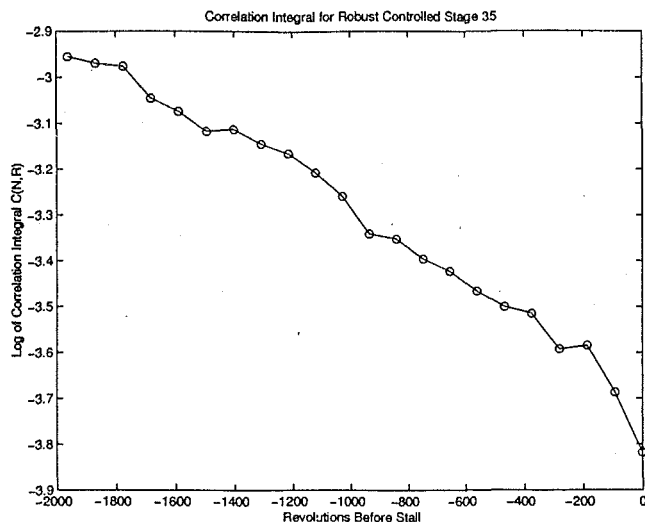Fig. 14   Radial distortion with steady injected air

Fig. 15 CI curve for controlled air injection

declines. In this case, the drop in the CI curve appears to result from long length scale modes, with pips appearing on top of the modes in the last few revolutions before stall. The cumulative change in CI value is again 1.0 order of magnitude.

This compressor stage was also operated with active stall control through unsteady air injection. The controlled injection damped out the first two harmonic modes and the surge mode as determined by the traveling wave energy method. (See Weigl et al., 1998, for a more complete discussion of this experiment). Inspection of the pressure traces from Fig. 9 shows that the modal activity is suppressed until the last 50 rotor revs, where pips seem to travel around the circumference and excite modal activity before stall. The CI plot in Fig. 15 shows a continuous decrease in amplitude in CI until the advent of stall. In this case the compressor is operating beyond its normal stalling condition for the entire data set due to the active controller continually suppressing modes through injection. Since the CI value indicates a continuous change in the dynamics, it is likely that the CI is responding to the continuously alternating actuation from the unsteady fluid of the controlled air jets in addition to the growth of incipient stall. This example also shows that a combination of modes and pips is taking place just before stall; however, the growth of modal activity appears to be the overriding activity. This example does serve as additional evidence that the CI method is sensitive to changing dynamics, whether the source is strictly from steady (distortion screen) or unsteady (controlled air jets) sources. The cumulative change in CI value for this case is on the order of 1.0.

Discussion

A comparison of these cases reveals some striking differences. For all but the radial distortion test case the compressor stalled through strongly modal events. Only in the radial distortion case was no real modal activity seen before stall. In the CI plots, the overall magnitude of change for these modal cases was on the order of 1.0. For the radial distortion case (pip case), however, the magnitude of CI value varied less than 0.25 orders of magnitude as the stage was transitioned into stall. The CI value in all these cases appears to monitor increased dynamics in the endwall region, and as such, CI is a measure of the strength of the tip flow field.

The dramatic difference in CI amplitude change between pip and modal instabilities is consistent with the concept of "critical incidence" based on the endwall fluid dynamics as suggested by Camp and Day (1998). In the case of radial distortion with no injection, the endwall loading is very high, the blade tip reaches its critical incidence and the compressor stalls through a pip instability before it can reach its peak pressure rise (see Fig. 10). For this

case the CI magnitude change is small. Only short length scale or pip instabilities are necessary to drive the compressor into stall. Modes are not given an opportunity to grow and destabilize the system. For the remaining cases the endwall loading is not as high, the blade tip does not reach critical incidence before the compressor achieves its peak pressure rise, and stall occurs primarily through modal instabilities. For these cases the CI magnitude change is large. Modes now have enough time to grow and dominate the flow field, even if pips are present. (Pips and modes are present in the cases where the compressor characteristic just reaches its peak, but the critical incidence is not reached.) If both disturbances are present, the CI value will have a cumulative effect, with the largest contribution of amplitude change due to modal disturbances. Hence a combination of *different frequency events* may work in *concert* to change the dynamic behavior measured by the CI value prior to stall.

The results shown in Figs. 2–4 show that filtering the data sets at different frequency bands in combination with this CI method can provide insight into the frequency and/or type of instability inducing stall. The histogram presentation of the correlation integral shows that a combination of low frequency (less than rotating stall frequency) and high frequency (blade passage frequency) events contribute to the induction of stall. The most significant result occurred in the data set, which included frequencies from 100 to 500 Hz. With the *exclusion* of frequency bands from this range, the prediction of stall became less robust with a shorter warning time. Therefore, something is occurring in the tip flow field in this frequency range that is detected by the correlation integral 1000 or more revolutions before stall. Blade passage frequency events (pips) and rotating stall frequency events (modes) seem to occur simultaneously, and much closer to stall. A benefit of band pass filtering the data is to associate sharp declines in the correlation integral with certain frequency bands. Since a drop in CI value is a cumulative effect of dynamic events, observing specific frequency bands of pre-stall data may help indicate exactly which events are inducing the stall. By pinpointing the frequency bands of events inducing stall, one can specifically eliminate these frequencies through active stall control.

Conclusions

The correlation integral is an effective measure of changes in pre-stall behavior in high speed compressors. This metric is sensitive to the initiation of either pips or modes or a combination of these disturbances. We have shown there is a connection between correlation integral values and changes in either short length scale or long length scale events in the compressor dynamics. The correlation integral can be used as a basis for comparing varied dynamics in distorted in-flow, steady injection, and controlled injection test cases and has been shown to detect changes in the fluid tip flow hundreds of revolutions prior to stall in all cases.

A primary result of this investigation is related to the amount that the CI value changes before stall. During modal stall, the CI value dropped 1.0 order of magnitude from steady operation to the stall point. During pip stall, the CI value dropped only 0.2 orders of magnitude from steady operation into stall. From these results the correlation integral method is indicative of the tip flow strength or criticality of the tip flow. With this in mind, CI value may help determine which control strategy is most effective in stabilizing the compressor. If the CI value changes very slightly before stall, pips are controlling the instability, and steady blowing may be an effective means to strengthen the tip flow and clear the pip behavior out of the tip region. If the CI value changes a large amount before stall, the most effective control strategy may be controlled injection to damp the modal instabilities from growing.

Correlation integral has the potential to determine what types of dynamics to look for in the data, especially if the data are band pass filtered. This may help indicate the frequency range that contains the most destabilizing disturbances.

Due to the computational complexity of correlation integral, this

algorithm is best suited for post-processed data analysis. For on-line experiments, however, an analogous algorithm for correlation integral called *structure function* (see Provenzale) can be used for real-time application. This technique can also be used to detect modal stall precursors, but is especially suited for predicting pip formation.

An added benefit of correlation integral, as well as structure function, is that they require only a single sensor to accumulate the data. This is advantageous in terms of both robustness and weight.

Finally, the correlation integral may be most useful in explaining pre-stall dynamics when those dynamics are not easily categorized by either pips or modes; as in many of the cases presented here. Perhaps with this insight we may better pursue active stall detection and control techniques for compression systems.

Acknowledgments

References

Bright, M. M., Qammar, H. K., Weigl, H. J., and Paduano, J. D., 1997, "Stall Precursor Identification in High-Speed Compressor Stages Using Chaotic Time Series Analysis Methods," ASME JOURNAL OF TURBOMACHINERY, Vol. 119, p. 491.

Camp, T. R., and Day, I. J., 1998, "A Study of Spike and Modal Stall Phenomena in a Low-Speed Axial Compressor," ASME JOURNAL OF TURBOMACHINERY, Vol. 120, pp. 393–401.

Day, I. J., 1993, "Stall Inception in Axial Flow Compressors," ASME JOURNAL OF TURBOMACHINERY, Vol. 115, pp. 1–9.

Grassberger, P., and Procaccia, I., "Measuring the Strangeness of Strange Attractors," *Physica D*, Vol. 9, 1983, p. 189.

Hoying, D. A., 1995, "Stall Inception in a Multistage High Speed Axial Compressor," *Journal of Propulsion and Power*, Vol. 11, No. 5, Sept.

Kugiumtzis, D., 1996, "State Space Reconstruction Parameters in the Analysis of Chaotic Time Series—the Role of the Time Window Length," *Physica D*, Vol. 95, p. 13.

Lerner, D. E., 1996, "Monitoring Changing Dynamics With Correlation Integral: Case Study of an Epileptic Seizure," *Physica D*, Vol. 97, p. 563.

Li, C., 1997, MS Thesis, Department of Chemical Engineering, University of Akron, Aug.

Longley, J. P., 1997, "Calculating the Flowfield Behaviour of High-Speed Multi-Stage Compressors," ASME Paper No. 97-GT-468.

McDougall, N. M., Cumpsty, N. A., and Hynes, T. P., 1990, "Stall Inception in Axial Compressors," ASME JOURNAL OF TURBOMACHINERY, Vol. 112, pp. 116–125.

Moore, D., and Reid, L., 1980, "Performance of Single-Stage Axial-Flow Transonic Compressor With Rotor and Stator Aspect Ratios of 1.19 and 1.26, Respectively, and With Design Pressure Ratio of 2.05," NASA Technical Paper 1659, Apr.

Paduano, J. D., Epstein, A. H., Valavani, L., Longley, J. P., Greitzer, E. M., and Guenette, G. R., 1993, "Active Control of Rotating Stall in a Low-Speed Axial Compressor," JOURNAL OF TURBOMACHINERY, Vol. 115, pp. 48–56.

Park, Han G., "Unsteady Disturbance Structures in Axial Flow Compressor Stall Inception," Masters Thesis, MIT, May 1994.

Provenzale, A., Smith, L. A., Vio, R., and Murante, G., "Distinguishing between Low-Dimensional Dynamics and Randomness in Measured Time Series," *Physica D*, Vol. 58, (1992) p. 31.

Reid, L., and Moore, D., 1978, "Design and Overall Performance of Four Highly Loaded, High-Speed Inlet Stages for an Advanced High-Pressure-Ratio Core Compressor," NASA Technical Paper 1337.

Schulze, R., and Hennecke, D. K., "Design of an Active Stall Avoidance System for a Subsonic Axial Compressor," presented at the RTO AVT Symposium in Toulouse, France, 11–15 May 1998 and published in RTO MP-8.

Spakovzsky, Z., Weigl, H., Paduano, J., Suder, K., and Bright, M., 1999a, "Rotating Stall Control in a High-Speed Stage With Inlet Distortion: Part I," ASME JOURNAL OF TURBOMACHINERY, Vol. 121, pp. 510–516.

Spakovzsky, Z., VanSchalkwyk, C., Paduano, J., Suder, K., and Bright, M., 1999b, "Rotating Stall Control in a High-Speed Stage With Inlet Distortion: Part II," ASME JOURNAL OF TURBOMACHINERY, Vol. 121, pp. 517–524.

Tryfonidis, M., Etchevers, O., Paduano, J. D., Epstein, A. H., and Hendricks, G. J., 1995, "Pre-Stall Behavior of Several High-Speed Compressors," ASME JOURNAL OF TURBOMACHINERY, Vol. 117, p. 62.

Wang, L., 1998, MS Thesis, Department of Chemical Engineering, University of Akron.

Weigl, H. J., Paduano, J. D., Frechette, L. G., Epstein, A. H., Greitzer, E. M., Bright, M. M., and Strazisar, A. J., 1998, "Active Stabilization of Rotating Stall and Surge in a Transonic Single Stage Axial Compressor," ASME JOURNAL OF TURBOMACHINERY, Vol. 120, pp. 625–636.

Wu, Z.-B., 1995, "Remark on Metric Analysis of Reconstructed Dynamics From Chaotic Time Series," *Physica D*, Vol. 85, p. 485.

Tip-Clearance and Secondary Flows in a Transonic Compressor Rotor

G. A. Gerolymos

I. Vallet

LEMFI, URA CNRS 1504,
Bâtiment 511,
Université Pierre-et-Marie-Curie,
91405 Orsay, Paris, France

The purpose of this paper is to investigate tip-clearance and secondary flows numerically in a transonic compressor rotor. The computational method used is based on the numerical integration of the Favre-Reynolds-averaged three-dimensional compressible Navier–Stokes equations, using the Launder–Sharma near-wall k–ε turbulence closure. In order to describe the flowfield through the tip and its interaction with the main flow accurately, a fine O-grid is used to discretize the tip-clearance gap. A patched O-grid is used to discretize locally the mixing-layer region created between the jetlike flow through the gap and the main flow. An H–O–H grid is used for the computation of the main flow. In order to substantiate the validity of the results, comparisons with experimental measurements are presented for the NASA_37 rotor near peak efficiency using three grids (of 10⁶, 2 × 10⁶, and 3 × 10⁶ points, with 21, 31, and 41 radial stations within the gap, respectively). The Launder–Sharma k–ε model underestimates the hub corner stall present in this configuration. The computational results are then used to analyze the interblade-passage secondary flows, the flow within the tip-clearance gap, and the mixing downstream of the rotor. The computational results indicate the presence of an important leakage-interaction region where the leakage-vortex after crossing the passage shock-wave mixes with the pressure-side secondary flows. A second trailing-edge tip vortex is also clearly visible.

Introduction

Leakage flow through the tip-clearance gap of axial-flow compressors, and its interaction with the passage secondary flow, have great influence both upon performance (Denton, 1993; Storer and Cumpsty, 1994) and upon stability (Adamczyk et al., 1993). Many computational methods try to avoid detailed computation of the tip-clearance gap, either using simplified models (Storer and Cumpsty, 1994; Puterbaugh and Brendel, 1997) for computing the leakage massflow (Denton, 1993; Adamczyk et al., 1993; Arnone, 1994) or modifying the blade-tip geometry to a sharp edge, and thus joining together the grid points on either side of the blade (e.g., Hah, 1986; Dawes, 1987; Jennions and Turner, 1993; Turner and Jennions, 1993; Copenhaver et al., 1993; Hah et al., 1997). These methods aim to model the influence of the leakage flow on the mainstream, assuming that leakage massflow is the only important parameter.

A few modern studies are interested in the numerical computation of the flow through the gap, as part of the solution (Rai, 1989a, b; Liu and Bozzola, 1993; Kunz et al., 1993; Basson and Lakshminarayana, 1995; Copenhaver et al., 1996, 1997; Hah and Loellbach, 1999; Ameri and Steinthorsson, 1995, 1996; Ameri et al., 1998). With the exception of Ameri et al. (1995, 1996, 1998), these studies use very few points within the tip-clearance gap (Table 1). As a consequence the fine details of the flow over the tip are not captured.

It is often argued that very coarse resolution of the tip-clearance gap is sufficient to give the overall effects of leakage and in particular its influence on flow structure. The satisfactory prediction of tip-clearance effects on flow structure and component performance are advanced as evidence that this is true (Denton, 1993; Adamczyk et al., 1993; Suder and Celestina, 1996; Puterbaugh and Brendel, 1997). Ameri et al. (1995, 1996, 1998) used

fine O-grids to predict the tip-clearance flow of a turbine rotor. The advantage of this approach is that the fine flow details within the gap are captured correctly. The purpose of this paper is to investigate the tip-clearance flow in a transonic compressor rotor, using fine grids within the gap. The flow is modeled using the Favre-Reynolds-averaged Navier–Stokes equations with near-wall low-turbulence-Reynolds-number $k–\epsilon$ turbulence closure (Gerolymos and Vallet, 1996; Gerolymos et al., 1998). This turbulence closure, although far from perfect, is state of the art, and, when correctly implemented, gives adequate quantitative results. The well-known test case of the NASA_37 rotor was chosen for this exercise (Davis et al., 1993; Strazisar, 1994). Recently the team responsible for the experimental investigation of NASA_37 rotor raised some doubts about the validity of the experimental data near the hub (Shabbir et al., 1997), but it is believed that experimental data are quite accurate near the tip. Computations are run on three progressively finer grids in order to assess the grid influence on solution. After validating the method against experimental measurements, the tip-clearance flow is studied.

Flow Model and Computational Method

The flow is modeled using the Favre-Reynolds-averaged Navier–Stokes equations with the Launder–Sharma near-wall low-turbulence-Reynolds-number $k–\epsilon$ closure. The model is well known and the particular implementation is described in detail by Gerolymos and Vallet (1996). The particular form of the mean-flow energy equation is derived by Gerolymos and Vallet (1997). The method has been extended to axial turbomachinery applications by Gerolymos et al. (1998). The $k–\epsilon$ closure used was chosen, not only because it is as good (or as bad) as various other two-equation closures, but also because it has the decisive advantage that the near-wall low-turbulence-Reynolds-number terms depend only on the turbulence-Reynolds-number Re_T. The resulting equations are therefore field equations completely independent of the distance from the wall n, and the normal to the wall $\vec{e}_n$, which greatly simplifies the numerical implementation in complex geometries (Gerolymos, 1990). It is noted that the tensor-invariant

form of the model satisfies Galilean invariance in the rotating frame-of-reference (Speziale, 1989).

Another advantage may be found in the fact that models that base their damping terms on the nondimensional distance from the wall $n^+ = n u_\tau \check{\nu}_w^{-1}$ (where u_τ is the friction velocity and $\check{\nu}_w$ the kinematic viscosity at the wall) are not well-adapted to the computation of unsteady flows (Fan et al., 1993).

Concerning transition, it is a well-established fact that all existing models are inadequate. Nonetheless, the model used was developed to predict transition and relaminarization (Jones and Launder, 1972; Launder and Sharma, 1974), and is one of the less unsatisfactory models (Savill, 1994). The resulting method is therefore always run with the turbulence model on, and depending on flow conditions may return a laminar solution. This is not the case with many other k–ϵ models, including the model of Chien (1982), which does not perform satisfactorily in transitional flows (Savill, 1994). The major deficiency of the turbulence model used is that it underestimates boundary-layer separation effects (Gerolymos, 1990), and this should be kept in mind when examining the computational results.

The mean-flow and turbulence-transport equations are written in the (x, y, z) Cartesian rotating (relative) coordinate system, and are discretized in space, on a structured grid, using a third-order upwind-biased MUSCL scheme with Van Leer flux-vector-splitting and Van Albada limiters, and the resulting semidiscrete scheme is integrated in time using a first-order implicit procedure. The mean-flow and turbulence-transport equations are integrated simultaneously. Source terms (centrifugal, Coriolis, and k–ϵ) are treated explicitly. The local-time-step is based on a combined convective (Courant) and viscous (von Neumann) criterion (MacCormack, 1982). For steady turbomachinery computations, CFL = 20 local-time steps, give good convergence and ensure stability in all the cases studied. Further details on the computational method are given by Vallet (1995), Tsanga (1997), and Gerolymos et al. (1998).

Comparison With Measurements

In order to validate the computational method, a systematic comparison with experimental data for NASA_37 rotor (Fig. 1) was undertaken. This configuration has been computed by numerous authors (Denton, 1996).

Most of these computations used simplified models for the tip clearance, and a mixing-length turbulence model. Suder and Celestina (1996) studied the interaction of the leakage flow with the main stream, both experimentally and computationally, using the Navier–Stokes solver described by Adamczyk et al. (1990), with a mixing-length closure, and a simplified model for the flow within the tip-clearance. Hah and Loellbach (1999) presented computations for this configuration using the near-wall k–ϵ closure of Chien (1982). These authors descretized the tip-clearance gap using ten radial stations and ten points tangentially across the blade (Table 1).

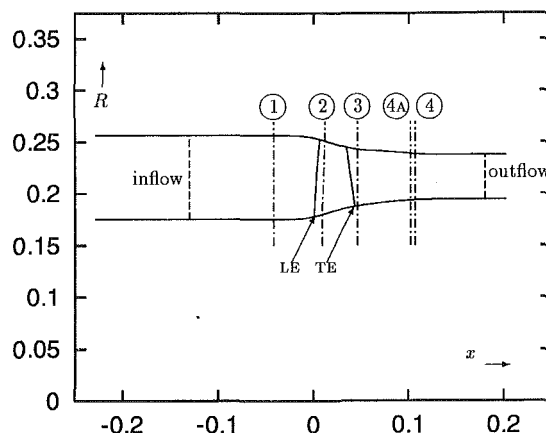The grid used in the present work consists of five domains (Fig.

Fig. 1 Meridional view of NASA_37 rotor and measurement stations

2). The space outside the tip-clearance gap is discretized using an H–O–H grid, consisting of three domains: the upstream UH-grid, the O-grid around the blade, which is generated biharmonically (Gerolymos and Tsanga, 1999), and the downstream DH-grid. The tip-clearance gap is discretized using an O-grid (TC-grid), also generated biharmonically (Gerolymos and Tsanga, 1999). The TC-grid is stretched both near the casing and at the blade tip, in order to describe correctly the boundary layers. To the authors' knowledge this is rarely the case in published studies. A jetlike structure emanates from the tip-clearance gap on the suction-side of the blade and mixes with the main flow. This creates a mixing-layer, which persists far away from the blade. One possibility to compute this part of the flowfield accurately is to stretch the blade O-grid in the same way. This would require a radially refined grid, even at regions away from the blade where this is not necessary. It was therefore prefered to use the OZ-grid (Fig. 2) patched within the O-grid of the blade. This grid is stretched both at the casing and at the blade tip, thus accurately describing the mixing of the leakage flow with the passage flow. The blade O-grid is thus stretched only near the casing and the hub, independently of the tip-clearance gap. This has the additional advantage of being able to change the grid locally, only at the neighbourhood of the blade if computations with different tip-clearance sizes are run. All stretchings of the grid near the solid walls are geometric. Details of the grid-generation procedure are given by Gerolymos and Tsanga (1999). The computational method structure and the boundary conditions between domains are described by Gerolymos et al. (1998).

Computations were run on three different grids (Table 2). By today's turbomachinery CFD standards even the coarsest grid_B is a rather fine grid (Denton, 1996; Hah and Loellbach, 1999). It has 65 radial surfaces in the flowpath, and 21 radial stations in the tip-clearance gap (note that the radial distributions in the flowpath O-grid and in the tip-gap TC-grid are independent). A very important parameter of grid quality is n_w^+ (n^+ of the first node away from the wall), which to give grid-independent results at transonic flow conditions (Vallet, 1995) must be $< \frac{1}{2}$ (note that this must be verified after the computations). For grid_B this condition is satisfied on the blade surfaces, but not on the casing and the hub where $n_w^+ \sim \frac{3}{2}$. This is also the case on the blade tip. To improve this situation, grid_C has 101 radial surfaces in the flowpath, and 31 radial stations in the tip-clearance gap. The resulting grid has $n_w^+ \sim 1$ on the casing and the hub, and is satisfactory on the blade tip. The final grid_D has 161 radial surfaces in the flowpath, and satisfies $n_w^+ < \frac{1}{2}$ everywhere. Within the tip gap it has 41 points less stretched than the 31 points of grid_C. Note that the three grids have almost identical blade-to-blade grids and differ mainly in the radial refinement.

Computed and measured performance for the NASA_37 rotor (Fig. 3) were evaluated from the computational results between

Table 1 Computational grids used within the tip-clearance gap

	grid-type	blading-type	radial[*]	across[†]
Rai (1989a, 1989b)	O	turbine rotor	5	21
Liu and Bozzola (1993)	H	turbine cascade[‡]	8	7
Kunz et al. (1993)	H	compressor cascade[‡]	11	17
Basson and Lakshminarayana (1995)	H	turbine cascade[‡]	15	21
Copenhaver et al. (1996)	H	compressor rotor	10	10
Copenhaver et al. (1997)	H	compressor rotor	6	7
Hah and Loellbach (1999)	H	compressor rotor	10	10
Ameri and Steinthorsson (1995, 1996)	O	turbine rotor	20–40	33
Ameri et al (1998)	O	turbine rotor	20–40	115
present; grid_B	O	compressor rotor	21	21
present; grid_C	O	compressor rotor	31	33
present; grid_D	O	compressor rotor	41	33

[*] points radially from the blade-tip to the shroud
[†] points tangentially across the blade
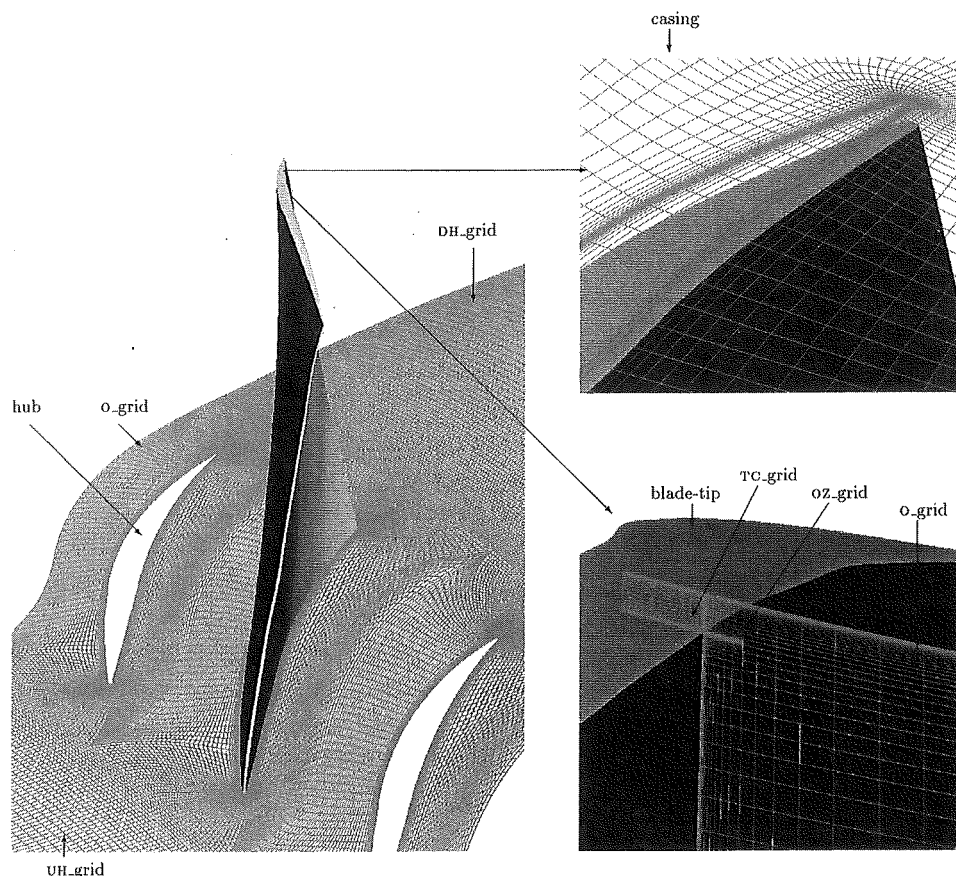[‡] linear non-rotating cascade

Fig. 2 Computational grid for NASA_37 rotor (grid_D)

stations 1 and 4 (Fig. 1) following exactly the averaging proce-
dures used in the experiment (Davis et al., 1993). Note however
that, in disagreement with Denton (1996), mass-averaging over all
grid points does not significantly change the efficiency η_{is}. All the
computations were run until full convergence of massflow $\dot{m}$,
total-to-total pressure-ratio π_{T-T} and loss. In all the cases residuals
were reduced by three orders of magnitude. Turbulence intensity at
inflow was $T_u = 3$ percent. Computations overestimate π_{T-T} and
underestimate η_{is}. Note that grid_D computes slightly higher mass-
flow than grid_B and grid_C. Detailed comparisons are presented
for point A, corresponding to 98 percent of choke massflow $\dot{m}_{CH}$.
In order to correct for the differences in operating diagram be-
tween computation and experiment, the corresponding computed
point is taken at the same value of $\dot{m}\pi_{T-T}^{-1}$ (Fig. 3), corresponding
to roughly the same work done by the rotor. The resulting mass-
flow difference is within measurement accuracy of ± 0.14 kg s^{-1}
(Strazisar, 1994).

Comparison of computed and measured pitchwise-averaged
quantities (Davis et al., 1993) at stations 1, 3, and 4 (Fig. 4) show
satisfactory agreement except concerning the p_{tM} deficit near the
hub at station 4. Hah and Loellbach (1999) attribute this deficit to
important corner stall, which could have been underestimated by
the present k–ϵ model. Shabbir et al. (1997) argue that this is due
to massflow leakage emanating from a small gap between the
stationary and rotating parts of the hub flowpath upstream of the

rotor. Although it is not certain whether this was the case in the
experiment, it might explain why all computational results fail to
reproduce this deficit in p_{tM} (Denton, 1996). The present authors
believe that the deficiency of the computations is presumably a
combination of these two effects. Note also that the finest grid
gives the fullest total pressure distribution at the hub. The differ-
ence in computed and measured flow-angle is due to the difference
in massflow (Hah and Loellbach, 1999).

Results obtained using the three grids are in quite good agree-
ment, except at the tip. Refining the radial grid resolution and the
tip-clearance grid reduces the total temperature values near the tip,
improving the prediction with respect to measurements. This is a
significant result because it shows that the model used for the
tip-clearance flow has an impact on work and efficiency.

Detailed comparisons of computed relative Mach number $\check{M}_{w x \theta,ad}$
(Fig. 5) and absolute flow-angle $\check{\alpha}_{x\theta}$ (Fig. 6) show state-of-the-art
agreement with measurements. Note that plotted quantities were
calculated using only the x and θ components of velocity, and
assuming rothalpy conservation, as was done for the experimental
values (Davis et al., 1993; Strazisar, 1994). Although the wake
depth is overestimated as in all published results (Denton, 1996),
the prediction of the flow at 20 percent axial-chord χ_x is quite
satisfactory, giving the correct $\check{M}_w$ level behind the shock. The
experimental shock-wave seems more smeared at 95 percent span
than the computed one, which might be due to both unsteady
effects in the experimental flow and to a slightly underestimated
clearance gap in the computations, where the nominal clearance
$\delta_{TC} = 0.356$ mm (Strazisar, 1994) was used. Comparison between
the three grids used shows that these results are indeed grid
independent, contrary to what happens above 95 percent span.

A better understanding of the radial penetration of the tip-
clearance flow is given by considering relative Mach-number

Table 2   Summary of computational grids

	UH*	o†	DH*	TC†	oz†	points‡	n_w^+
grid_B	49×41× 65	201×45× 65	81×61× 65	201×11×21	201×21×31	1 149 421	< 1.5
grid_C	49×41×101	201×53×101	81×61×101	201×17×31	201×21×41	1 955 587	< 1.0
grid_D	49×41×161	201×53×161	81×61×161	201×17×41	201×21×61	3 067 042	< 0.5

* axial×tangential×radial
† around the blade×away from blade×radial
‡ without o-grid points overlapped by the oz-grid
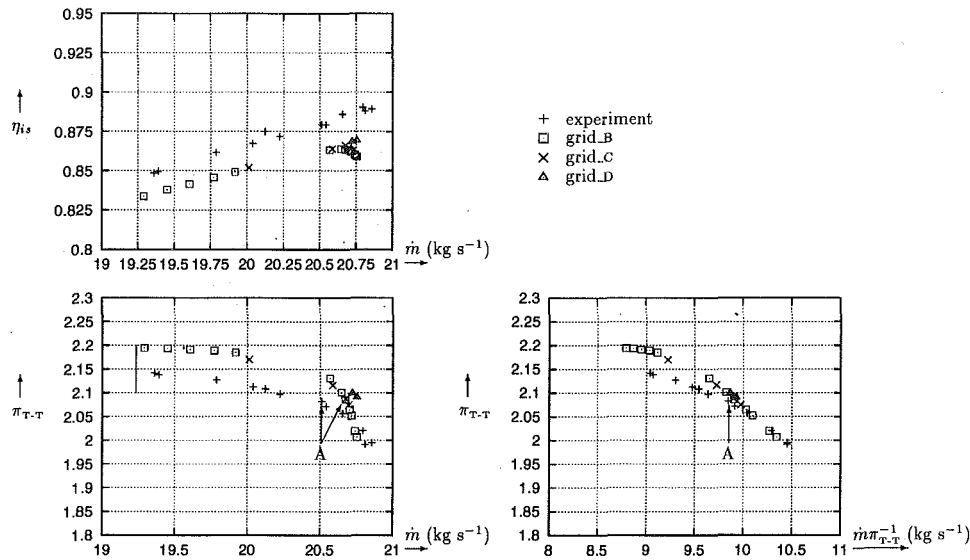
Fig. 3 Computed and measured operating map for NASA_37 rotor (point A: $\dot{m}\pi_{\mathrm{T\text{-}T}}^{-1}$ = 9.85 kg s^{-1})

contours $\breve{M}_w$ at 95 percent span, 98 percent span, and 99 percent span (Fig. 7). The tip vortex is clearly seen at 98 percent span and 99 percent span, while the low speed clearance interaction region is visible also at 95 percent span.

In conclusion, the method gives satisfactory results over the upper 70 percent of the span. The discrepancy near the hub does not seem to influence the flow at the tip, which is the main theme of the present work.

Tip-Clearance and Secondary Flows

A quite good representation of leakage flow and its interaction with interblade-passage flow is obtained through entropy contours (Copenhaver et al., 1996). Levels of entropy

$$\breve{s} - s_{\mathrm{ISA}} = c_p \ln \frac{\breve{T}_t}{288.15} - R_g \ln \frac{\breve{p}_t}{101325} \qquad (1)$$
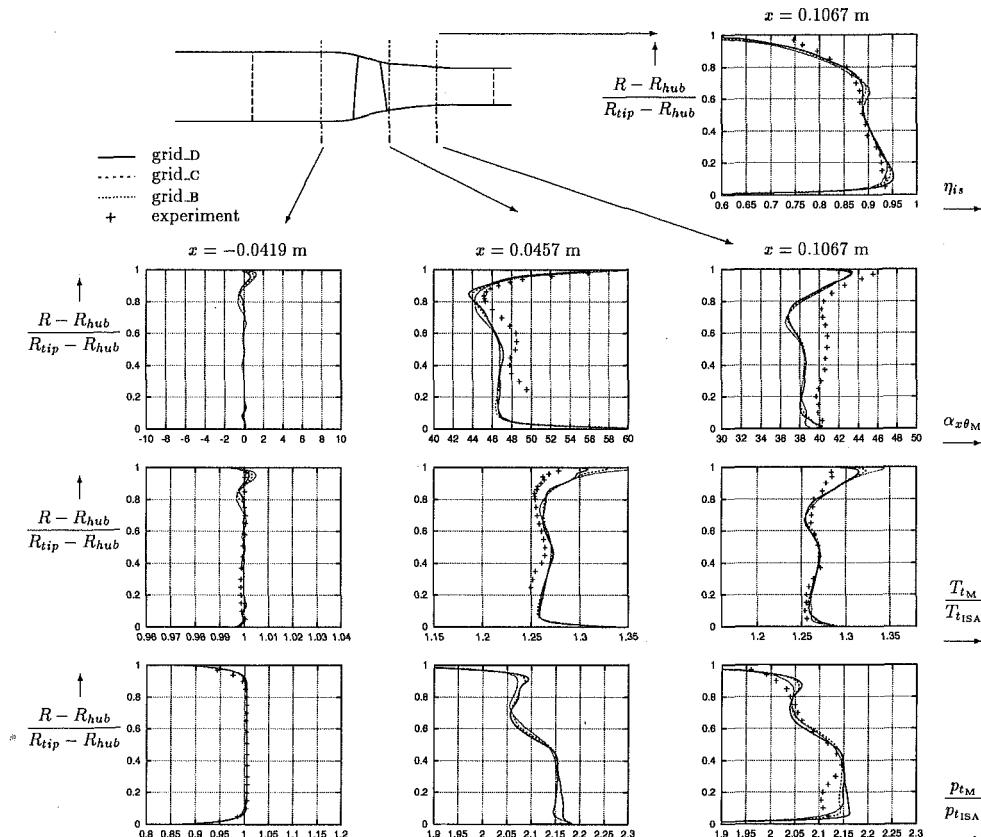
Fig. 4 Computed and measured radial distributions of pitchwise-averaged flow-angle $\alpha_{x\theta\mathrm{M}}$, total-pressure $p_{t\mathrm{M}}$, and total-temperature $T_{t\mathrm{M}}$, for NASA_37 rotor ($\dot{m}\pi_{\mathrm{T\text{-}T}}^{-1}$ = 9.85 kg s^{-1}; T_u = 3%; δ_{TC} = 0.356 mm)

$$\check{M}_{W_{x\theta,ad}} = \sqrt{\frac{\check{V}_x^2 + \check{W}_\theta^2}{(\gamma-1)[h_{t_{ISA}} - \frac{1}{2}(\check{V}_x^2 + \check{V}_\theta^2) + \Omega R \check{V}_\theta]}}$$
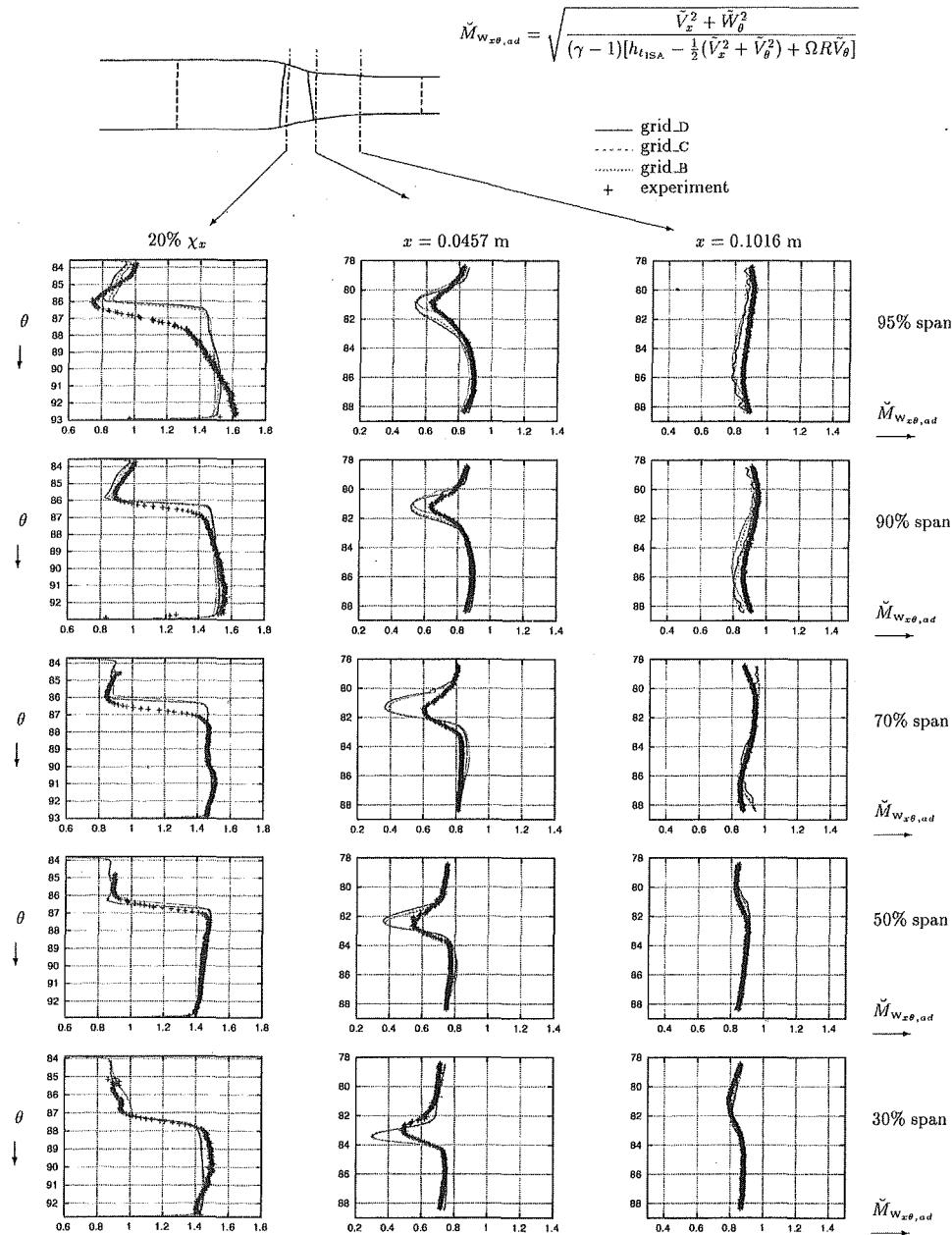
Fig. 5 Comparison of computed and measured pitchwise distributions of $\check{M}_{Wx\theta,ad}$ for NASA_37 rotor ($\dot{m}\pi_{\text{T-T}}^{-1} =$ 9.85 kg s^{-1}; T_u = 3 percent; δ_{TC} = 0.356 mm)

where $\check{s}$ is the entropy, s_{ISA} the entropy at standard conditions (which are the inflow conditions for the present case), c_p the specific heat capacity at constant pressure, R_g the gas constant, $\check{T}_t$ the total temperature, and $\check{p}_t$ the total pressure, are presented (Fig. 8) at various axial ($x =$ const) locations (Table 3). The flow that leaks over the blade in the leading-edge (LE) neighborhood (plane B) mixes with the passage flow and creates a high-entropy region that is convected toward the middle of the passage (plane C) until it reaches the shock-wave (plane D). Note that the shock-wave (SW) is clearly seen as an entropy jump (Fig. 8). Then this high-entropy region traverses the shock-wave (plane F) and reaches the pressure-side (PS) of the next blade (plane G). At this point two regions of high entropy, one emanating from the tip-clearance gap and extending to midpassage (concentrated near the casing), and another from midpassage to the pressure-side (with greater spanwise penetration) exist (Fig. 8).

These high-entropy structures can be identified with secondary flows (Fig. 8). The projection on the axial planes of the relative velocity $\vec{W}$ variation around its pitchwise mass-averaged value $\vec{W}_M$

$$\vec{W}_{s_{R\theta}} = (\check{W}_R - W_{R_M})\vec{e}_R + (\check{W}_\theta - W_{\theta_M})\vec{e}_\theta \tag{2}$$

is plotted at planes B, D, and G (Fig. 8). At plane B the leakage vortex emanates from the gap. At plane D this vortex has reached the shock-wave, which is identified in the $\vec{W}_{s_{R\theta}}$ plots as a region of important radial flow migration. At plane G a large secondary flow structure is observed, extending from the shock-wave to the pressure-side, corresponding to the second high entropy region (Fig. 8). At plane I (Fig. 8) the high-entropy region is more diffuse, with lower maxima as compared to upstream planes. This is mainly due to mixing by the secondary flows.

An alternative sensor to entropy is turbulence kinetic energy k, that surprisingly has not yet been exploited by authors that solve an equation for k (Hah, 1986; Copenhaver et al., 1993; Jennions and Turner, 1993; Turner and Jennions, 1993; Suder and Celestina, 1996;

$$\breve{\alpha}_{x\theta}: \quad \left[\cos \breve{\alpha}_{x\theta} = \frac{\tilde{V}_x}{\sqrt{\tilde{V}_x^2 + \tilde{V}_\theta^2}} \quad , \quad \sin \breve{\alpha}_{x\theta} = \frac{\tilde{V}_\theta}{\sqrt{\tilde{V}_x^2 + \tilde{V}_\theta^2}} \right]$$
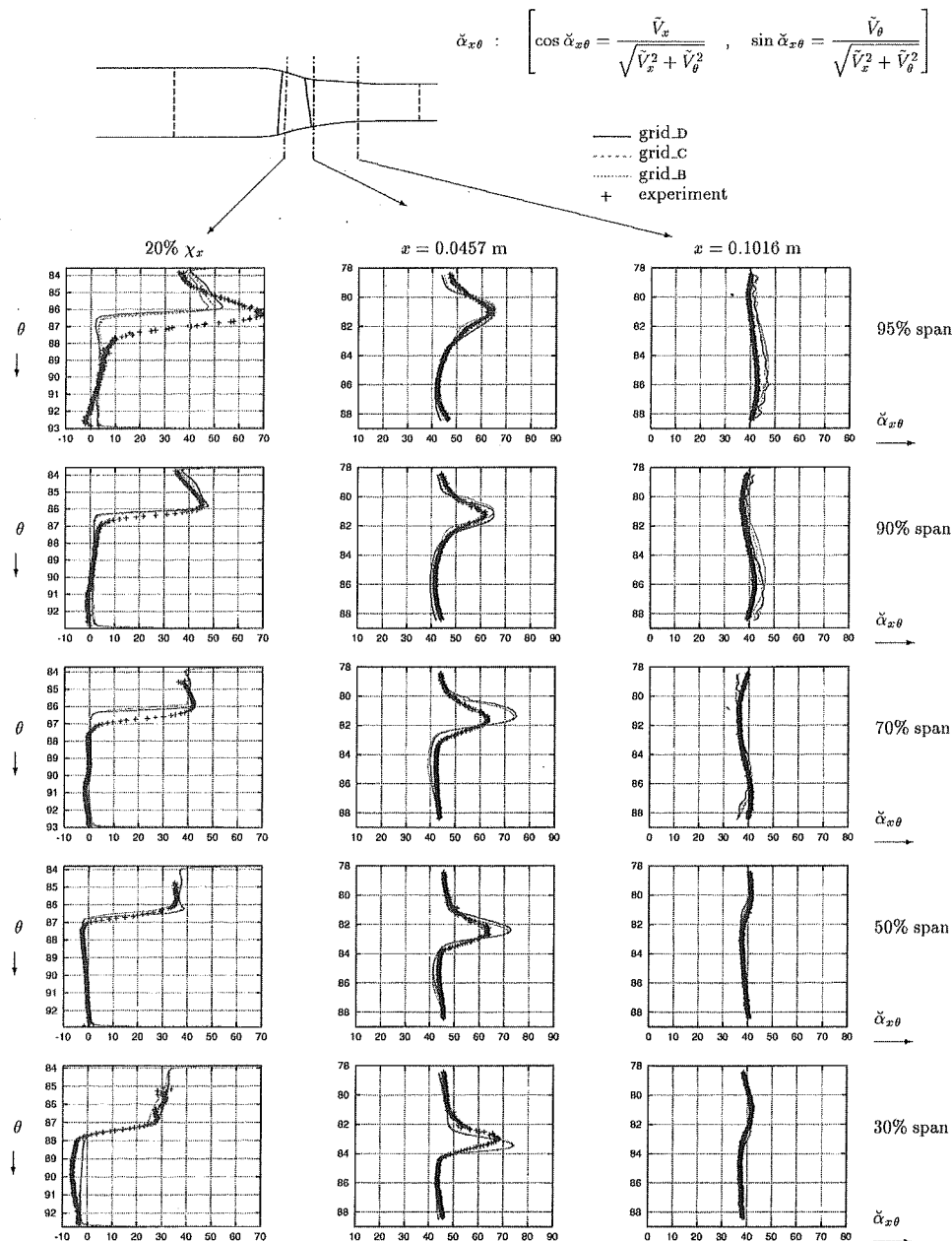
—— grid_D
······· grid_C
·········· grid_B
+ experiment

Fig. 6 Comparison of computed and measured pitchwise distributions of $\breve{\alpha}_{x\theta}$ for NASA_37 rotor ($\dot{m}\pi_{T\text{-}T}^{-1}$ = 9.85 kg s^{-1}; T_u = 3 percent; δ_{TC} = 0.356 mm)

Copenhaver et al., 1996, 1997; Shabbir et al., 1997). Examination of k-levels at various axial planes (Fig. 9) shows that the same information is contained in k as in $\breve{s}$. The close-up of k-levels near the blade tip shows how k is produced by the mixing of leakage flow emanating from the tip-clearance gap. Note that at plane I, near the trailing-edge (TE) air comes over the tip from the green region of k, with almost unchanged turbulence kinetic energy until it leaks on the suction-side and mixes with the passage flow. The high values of k (Fig. 9) and $\breve{s}$ (Fig. 8) near the suction-side trailing-edge are indicative of boundary-layer separation.

Plots of $\breve{M}_w$ in the blade-tip region (Fig. 10) indicate that for most of the blade chordwise length (planes A–H) flow acceleration from the pressure-side over the tip is supersonic through a Prandtl–Meyer expansion fan. The $\breve{M}_w$ contours clearly indicate the mixing layer formed by the leakage flow emanating over the suction-side blade-tip. At plane G the leakage flow terminates in a low $\breve{M}_w$ region, corresponding to the leakage-interaction region (Fig. 10). The relative velocity vectors over the blade-tip at planes A (near

the leading-edge) and J (near the trailing-edge) indicate the presence of a highly three-dimensional vortical structure as the flow is accelerated over the tip on the pressure-side (Fig. 10).

The use of a fine grid in the tip-clearance-gap (grid_D has 41 radial surfaces, and a total of 140,097 points within the gap) makes it possible to resolve the boundary layers on the blade-tip and on the casing, and to plot velocity profiles inside the tip-clearance-gap (Fig. 11). In the relative frame of reference the blade-tip is fixed ($\tilde{W} = 0$) and the casing rotates at $\tilde{W}_\theta = -\Omega R$ (in the present case $\Omega > 0$ so that the relative velocity of the casing is in the negative θ direction). Radial profiles of the three components of the relative flow velocity, $\tilde{W}_x$, $\tilde{W}_R$, $\tilde{W}_\theta$ are plotted for various positions from the pressure-side (0 percent thickness) to the suction-side (100 percent thickness), at three axial planes A, G, and J (Fig. 11).

At plane A the flow is largely tangential (Fig. 11), with a turbulent Couette flow profile (Schlichting, 1979), between the entraining casing and the fixed tip. At the pressure-side edge, near the tip, there are high radial velocities, as the flow is radially
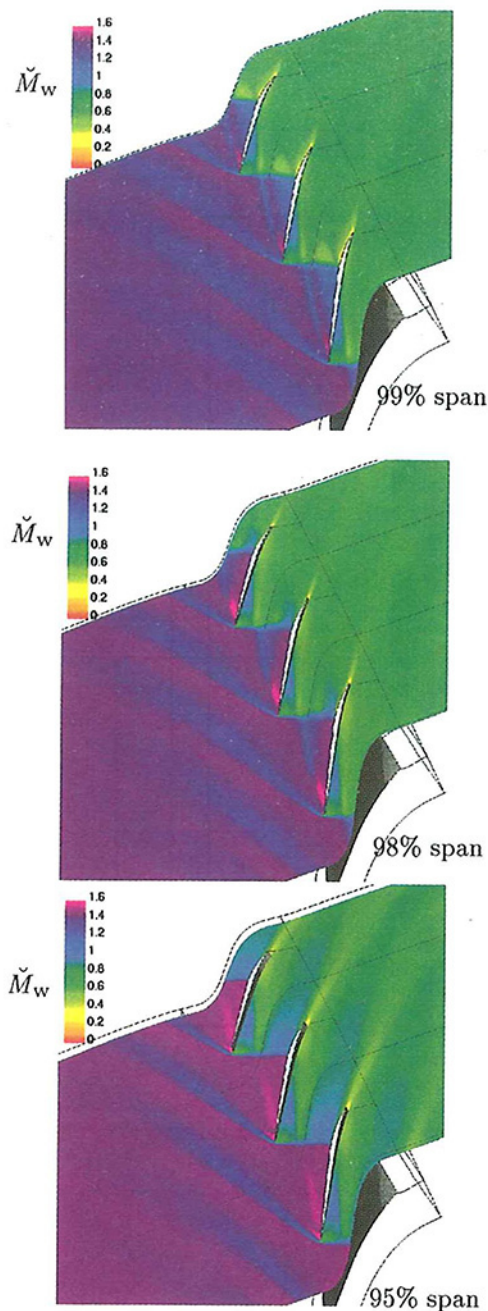
Fig. 7 Computed $\check{M}_w$ at various spanwise stations near the blade-tip for NASA_37 rotor ($\dot{m}\pi_{T \cdot T}^{-1} = 9.85$ kg s^{-1}; $T_u = 3$ percent; $\delta_{TC} = 0.356$ mm)

accelerated over the tip. Inside the gap, at station A radial velocities are negligible, while axial velocities change sign from negative near the tip at the pressure-side to positive further inside the gap. The blade-tip boundary-layer thickens substantially inside the gap. The vortical flow structure observed at plane A (Fig. 10) is associated with the variations of $\tilde{W}_x$ and $\tilde{W}_R$. At plane G, near mid-chord, the $\tilde{W}_\theta$ flow structure is again a Couette-flow with pressure-gradient, while there are important variations of $\tilde{W}_x$ (Fig. 11). Note that these planes are $x = $ const planes, while the flow across the tip makes an angle of about -110 to -120 deg in the $x-\theta$ plane with the x direction. Again the important variation of $\tilde{W}_x$ across the gap near the tip is associated with the three-dimensional flow structure. At plane J the $\tilde{W}_\theta$ and $\tilde{W}_x$ profiles indicate that the tip boundary-layer undergoes three-dimensional separation and reattachment (Fig. 11).

Leakage Flow Structure

Several authors (Adamczyk et al., 1993; Suder and Celestina, 1996; Copenhaver et al., 1996; Puterbaugh and Brendel, 1997) have studied the structure of leakage flow in transonic compressors, and attributed the growth of the vortex and the creation of the high-entropy, low-speed region to the interaction of the vortex with the shock-wave. The interaction of the streamwise vorticity with the shock-wave creates an axial velocity deficit in the vortex core (Smart and Kalkhoran, 1997). However, examination of the flow structure (Fig. 8) raises the question whether this effect is not simply an addition to the well-known subsonic compressor leakage-interaction region. In this case Lakshminarayana et al. (1995) have suggested that the interaction of the leakage vortex with the passage secondary flows creates a region of low velocity and high entropy, which they called leakage-interaction region. In the present transonic flow, from the leading-edge to plane D, the shock-wave is seen to separate the leakage-flow from the passage secondary flow occurring in the region between the shock-wave and the pressure-side (Fig. 8). When the leakage flow crosses the shock-wave, it interacts with the passage secondary flow, creating the leakage-interaction region. It is plausible to assume that there is a direct analogy between the subsonic and transonic case, and that the shock-wave acts as a barrier between the pressure-side secondary flows and the leakage flow. When this barrier is crossed, the leakage-interaction region is created in much the same way as in the subsonic flow case (Lakshminarayana et al., 1995), with the additional effect of vortex growth and axial velocity deficit due to the interaction with the shockwave.

In order to understand the leakage flow structure better, streamlines near the blade tip are plotted (Fig. 12). Examination of the relative flow streamlines coming from upstream and going into the passage at 95 percent span (green streamlines) and at 98 percent span (red streamlines) shows clearly the secondary flows near the pressure-side in the leading-edge neighborhood. Because of the three-dimensional structure of the casing boundary layer (and the relative motion between the casing and the blades) the incoming flow direction differs greatly between 95 percent span and 98 percent span. At 95 percent span, as the flow goes into the passage it is deflected by the blades (green streamlines). At 98 percent span, the streamlines near the pressure-side of the blade go straight (and slightly upward) into the clearance gap, feeding the leakage flow of the next channel for the first half of the blade (red streamlines). This fluid crosses the gap and reappears on the suction-side of the next blade creating the leakage vortex in the leading-edge neighborhood (blue streamlines near the LE). It is noticeable that this vortex continues in much the same direction as the incoming flow feeding the gap (blue streamlines forming the vortex are almost parallel to the incoming red streamlines). The vortex is formed both from leakage fluid and from fluid entrained from the suction-side boundary-layer near the tip. The vortex moves forward in this direction (Fig. 12) until it meets the pressure-side flow, that has been deflected by the blades. At this point the vortex mixes rapidly with the pressure-side flow, turns sharply in its direction, and grows substantially. This is the leakage-interaction-region (Lakshminarayana et al., 1995) corresponding to low velocity and high loss. It is important to note how the vortex turns sharply to follow the direction of the blades. This sharp turning of the vortex trajectory is not due to the shock-wave, which is almost normal to the flow for the present configuration. It occurs after the vortex has crossed the shock-wave. It is noted that the vortex trajectory calculated by Suder and Celestina (1996) for the same configuration is quite the same as the one computed in the present work (although these authors credited the shock-wave/vortex interaction theory with explaining the important radial penetration of the vortex). In the present computations we did not remark any noticeable modification of the vortex size or direction when it interacts with the shock-wave.

Examination of the flow after the sharp turning of the vortex near the pressure-side shows that for the second half of the blade,
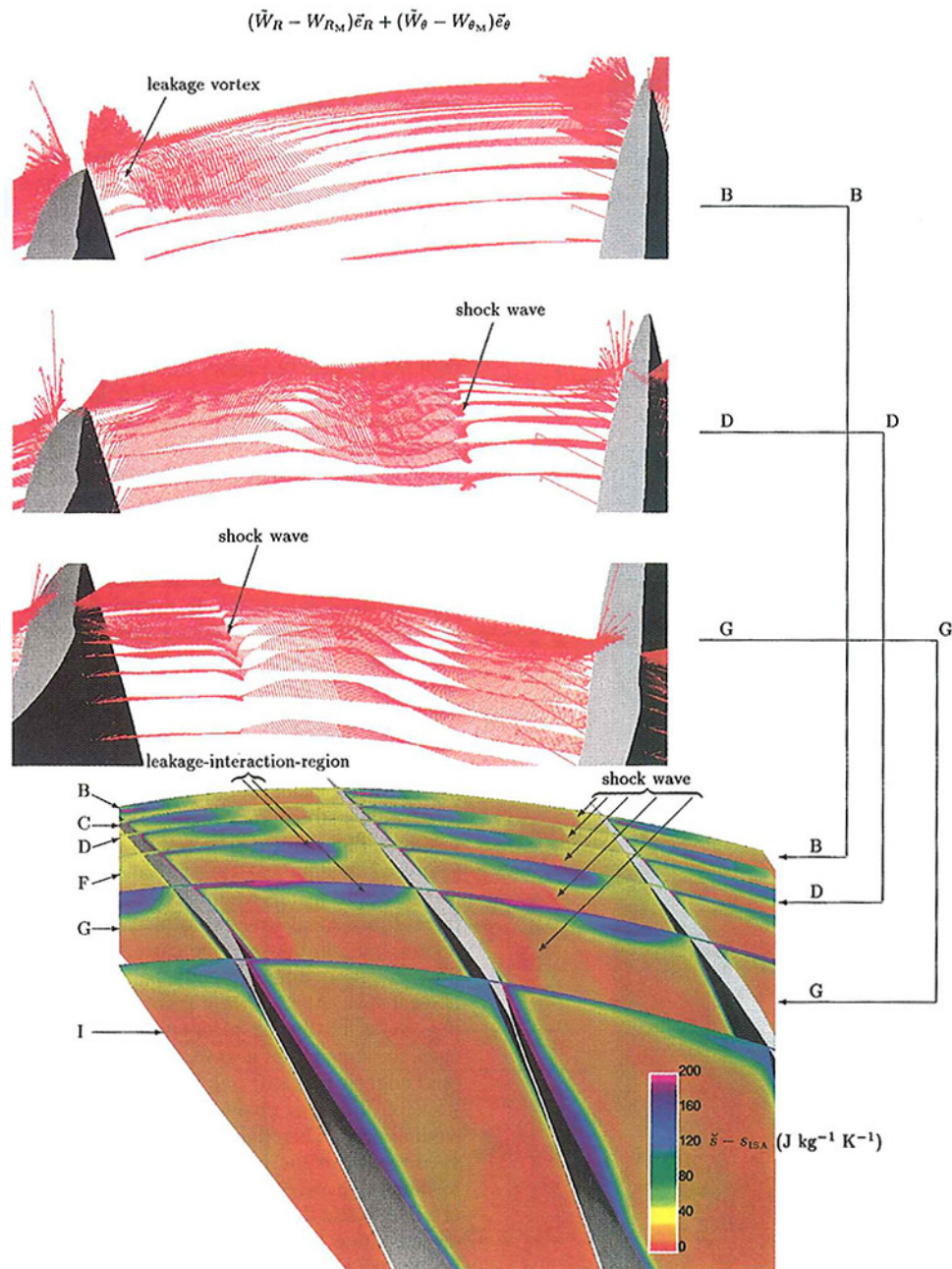
$$(\bar{W}_R - W_{R_M})\vec{e}_R + (\bar{W}_\theta - W_{\theta_M})\vec{e}_\theta$$

Fig. 8 Entropy levels and secondary flows in the interblade passage of NASA_37 rotor ($\dot{m}\pi_{T\cdot T}^{-1} = 9.85$ kg s^{-1}; $T_u = 3$ percent; $\delta_{TC} = 0.356$ mm; grid_D)

it is the leakage vortex of the previous blade that feeds the leakage flow through the gap (blue streamlines going into the gap). The flow leaking out of the gap on the suction-side near the trailing-edge is almost parallel to the leakage vortex direction near the pressure-side (after the leakage vortex has turned). This flow, together with the suction-side boundary-layer that it entrains near the blade-tip, forms a second trailing-edge tip-vortex, clearly seen in the plots (Fig. 12). Note that Suder and Celestina (1996) observed such a second vortex in their calculations of the NASA_37 rotor at 60 percent design speed, but did not report its presence also at design speed. In our case however, this second TE-tip-vortex is formed both by leakage fluid and by fluid moving radially upward in the suction-side boundary-layer.

The leakage flow structure between these two vortices is important because it presumably explains the presence in the entropy contours (Fig. 8) of a high-entropy region concentrated near the tip, between midpassage and the suction-side of the blades (plane G). In this region the leakage flow and the suction-side boundary-layer fluid it entrains move almost tangentially toward the neighboring blade (Fig. 12). The high-entropy fluid of the suction boundary-layer mixes with the flow leaking from the gap to form a high entropy region (Fig. 8). The streamlines, although this is not seen in the plot, have at this station (plane G) a marked tendancy to move radially upward, thus concentrating the high-entropy fluid near the casing (Fig. 8). This movement might be enhanced by the interaction between the shock-wave and the fluid near the casing. Note, however, that the casing is moving in the relative frame of reference, in the same direction as the leakage flow, and as a consequence this is neither a classical shock-wave/boundary-layer interaction on a fixed wall, neither a shock-wave/vortex interac-

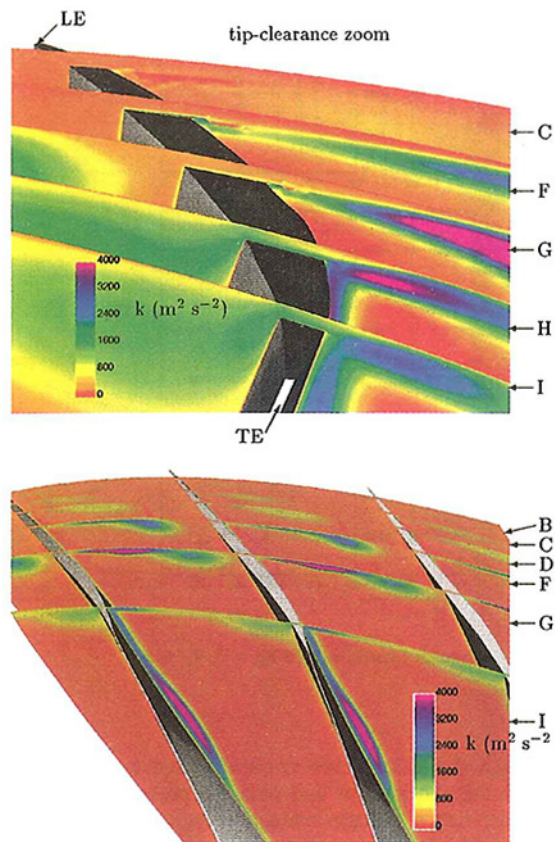**Table 3   Axial planes location**

plane	A	B	C	D	E	F	G	H	I	J	K	L
x (m)	0.007	0.008	0.010	0.012	0.013	0.015	0.020	0.025	0.030	0.033	0.040	0.042

Fig. 9 Turbulence kinetic energy in the interblade passage of NASA_37 rotor ($\dot{m}\pi_{T.T}^{-1} = 9.85$ kg s^{-1}; $T_u = 3$ percent; $\delta_{TC} = 0.356$ mm; grid_D)

tion. It is believed that this second high-entropy region has not an important effect on the general leakage flow structure.

Downstream Flow Mixing

The rake measurements used for comparison with computations for the NASA_37 rotor were obtained at station 4, located more than two axial chords downstream of the trailing-edge. This renders the test case more difficult, since the complex mixing downstream of the rotor directly influences the comparison. This is a flow relaxing after having sustained the pressure gradients within the rotor, precisely the type of flow where the k–ϵ model is at its worse (Gerolymos, 1990; Gerolymos and Vallet, 1996, 1997). At plane L, which is situated just before the trailing-edge near the hub, and just after the trailing-edge for the upper 60 percent span, plots of $\check{M}_w$ and k (Fig. 13) indicate both the downstream evolution of the tip-clearance flow and the important boundary-layer separation on the suction-side between 40 and 80 percent span. On the contrary, the present computations underestimate the corner stall computed by Hah and Loellbach (1999) near the hub suction-side trailing-edge. This is presumably a deficiency of the Launder–Sharma (1974) k–ϵ model, which seems to underestimate flow separation compared to the Chien (1982) model used by Hah and Loellbach (1999).

There is important mixing of the flow downstream toward station 4 (Fig. 14). Spanwise mixing of the blades' wakes and the tip-clearance flow form a large secondary flow region that fills the upper 30–40 percent of the flowpath. The flow mixing is complicated by the important acceleration near the hub due to the flowpath convergence (Fig. 1).

Conclusions

A three-dimensional compressible Navier–Stokes solver with near-wall low-turbulence-Reynolds-number closure was used to study the flow with tip-clearance in a transonic compressor rotor (NASA_37). Comparison of computational results with measurements is state of the art, with the discrepancy in the p_{tM} distribution near the hub that is observed in most computations of this test case. This discrepancy is attributed to underestimation of hub corner stall by the turbulence model, and perhaps leakage problems in the experimental setup. Comparison of computations and measurements near the tip is satisfactory. Results using three different grids of 10^6, 2×10^6, and 3×10^6 points, with accurate resolution of the flow within the tip-clearance-gap, demonstrate that the results are grid independent everywhere, with the exception of the T_{tM} distribution near the tip, where grid refinement substantially improves the agreement between computations and measurements.

Investigation of the flowfield inside the interblade-passage, near the tip, leads to suggesting an alternative scenario to the leakage
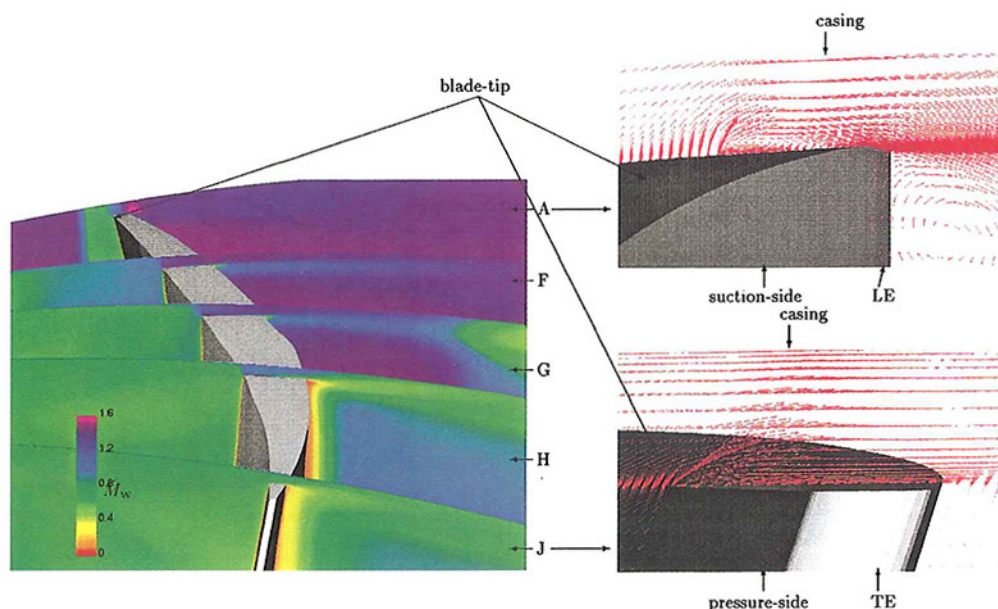

Fig. 10 Relative Mach number levels and clearance-gap relative flow in the tip-region of NASA_37 rotor ($\dot{m}\pi_{T.T}^{-1} = 9.85$ kg s^{-1}; $T_u = 3$ percent; $\delta_{TC} = 0.356$ mm; grid_D)

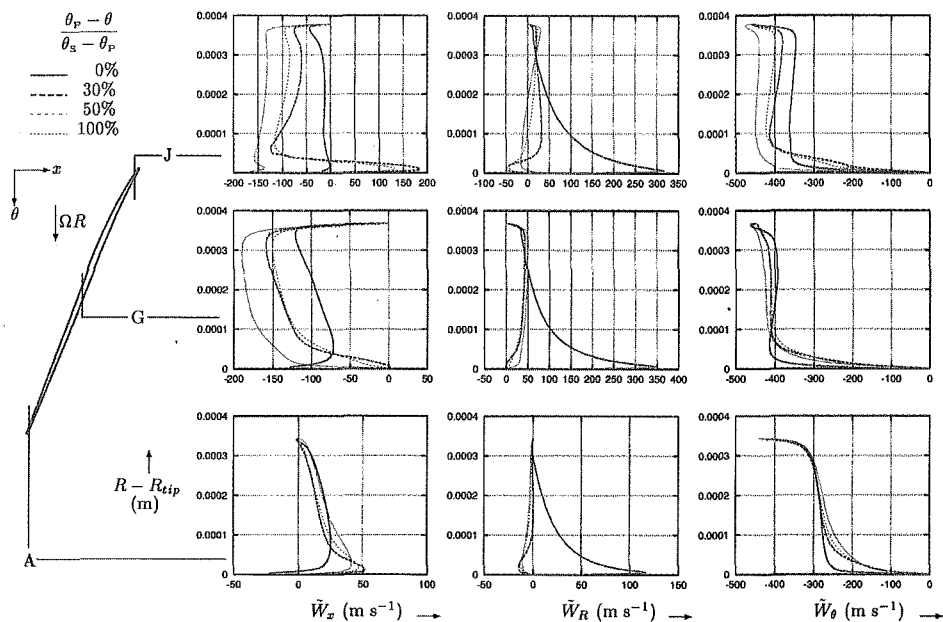Fig. 11 Relative velocities inside the tip-clearance gap for NASA_37 rotor ($\dot{m}\pi_{\mathrm{T\cdot T}}^{-1} = 9.85$ kg s^{-1}; $T_u = 3$ percent; $\delta_{\mathrm{TC}} = 0.356$ mm; grid_D)

flow interaction with the passage shock-wave. It is believed that in the fore part of the blade the shock-wave surface separates the leakage flow from the secondary flows between the shock-wave and the pressure-side of the blade. When, as the flow progresses downstream, the leakage flow crosses the shock-wave, it interacts both with the shock-wave and with the pressure-side secondary flows generating a leakage-interaction region of low speed, high entropy, and high turbulence, in a way analogous to the subsonic

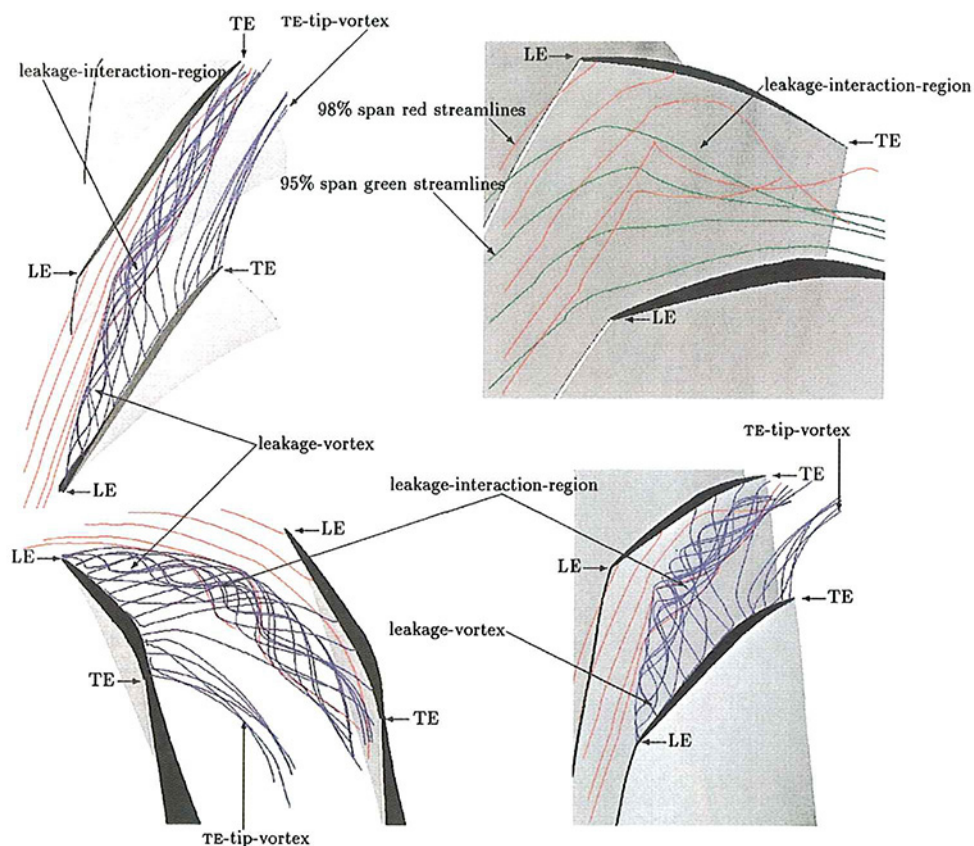Fig. 12 Computed relative flow streamlines near the blade-tip for NASA_37 rotor (blue streamlines coming from the tip-clearance gap and the suction-side near-tip boundary-layer; red streamlines coming from upstream at 98 percent span; green streamlines coming from upstream at 95 percent span; $\dot{m}\pi_{\mathrm{T\cdot T}}^{-1} = 9.85$ kg s^{-1}; $T_u = 3$ percent; $\delta_{\mathrm{TC}} = 0.356$ mm; grid_D)
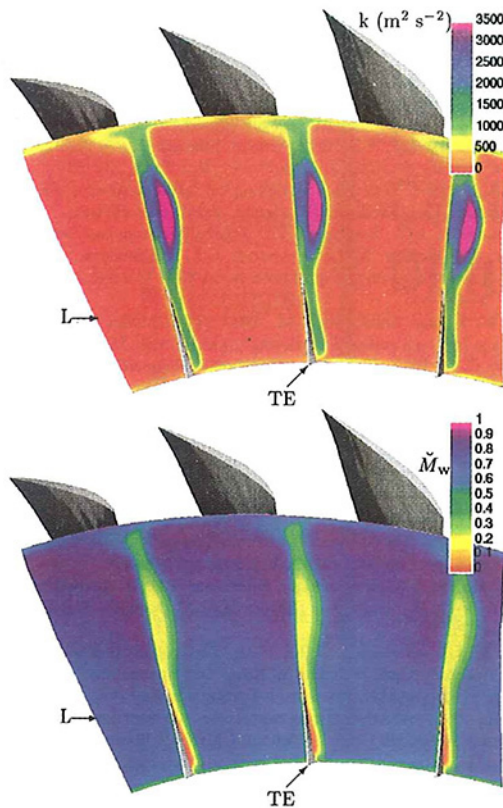
Fig. 13 Flow structure near the trailing-edge of NASA_37 rotor ($\dot{m}\pi_{\text{T-T}}^{-1} = 9.85$ kg s^{-1}; $T_u = 3$ percent; $\delta_{\text{TC}} = 0.356$ mm; grid_D)

case described by Lakshminarayana et al. (1995). Further research is needed to investigate the relative importance of shock-wave/vortex interaction and vortex/pressure-side-flow interaction in the generation of tip-clearance losses.
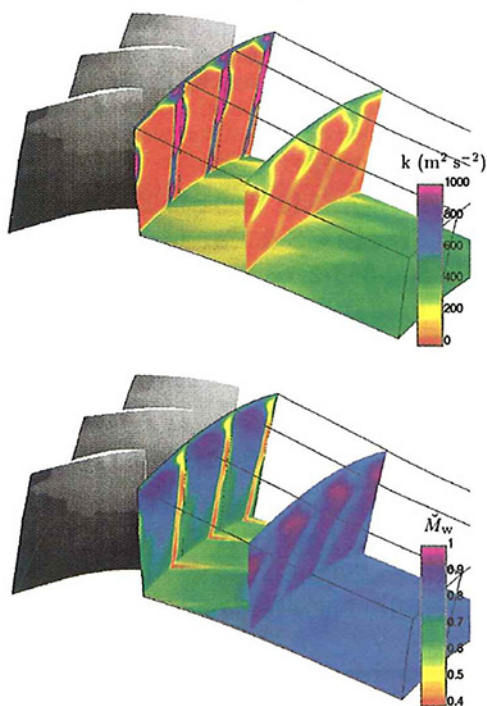

Fig. 14 Flow structure ($\check{M}_w$ and k) downstream of the trailing-edge of NASA_37 rotor ($\dot{m}\pi_{\text{T-T}}^{-1} = 9.85$ kg s^{-1}; $T_u = 3$ percent; $\delta_{\text{TC}} = 0.356$ mm; grid_D)

Detailed velocity profiles inside the tip-clearance-gap are obtained (to the authors' knowledge for the first time in a transonic compressor) with sufficient resolution of blade-tip and casing boundary-layers. The flow is a Couette-type flow, between the tip and the casing. Flow acceleration over the blade-tip is associated with a three-dimensional vortical structure, while important tip boundary-layer thickening occurs within the gap. Both these effects are associated with flow blockage inside the tip-clearance gap. It is believed that such computations will improve understanding of the flow inside the gap, and as consequence will help in the development of simple models to compute leakage massflow and losses.

For the particular test case studied (NASA_37 rotor) rake measurements were taken far downstream of the trailing-edge. The region of important flow mixing between the blades' trailing-edge and the measurement station is particularly difficult to compute using classical turbulence models, which invariably fail to correctly reproduce turbulent flow relaxation after separation. This may also partially explain why this test case is so difficult to predict accurately.

Acknowledgments

References

Adamczyk, J. J., Celestina, M. L., Beach, T. A., and Barnett, M., 1990, "Simulation of 3-D Viscous Flow Within a Multistage Turbine," ASME JOURNAL OF TURBOMACHINERY, Vol. 112, pp. 370–376.

Adamczyk, J. J., Celestina, M. L., and Greitzer, E. M., 1993, "The Role of Tip Clearance in High-Speed Fan Stall," ASME JOURNAL OF TURBOMACHINERY, Vol. 115, pp. 28–39.

Ameri, A. A., and Steinthorsson, E., 1995, "Prediction of Unshrouded Rotor Blade Tip Heat Transfer," ASME Paper No. 95-GT-142.

Ameri, A. A., and Steinthorsson, E., 1996, "Analysis of Gas Turbine Rotor Blade Tip and Shroud Heat Transfer," ASME Paper No. 96-GT-189.

Ameri, A. A., Steinthorsson, E., and Rigby, D. L., 1998, "Effect of Squealer Tip on Rotor Heat Transfer and Efficiency," ASME JOURNAL OF TURBOMACHINERY, Vol. 120, pp. 753–759.

Arnone, A., 1994, "Viscous Analysis of 3-D Rotor Flow Using a Multigrid Method," ASME JOURNAL OF TURBOMACHINERY, Vol. 116, pp. 435–445.

Basson, A., and Lakshminarayana, B., 1995, "Numerical Simulation of Tip Clearance Effects in Turbomachinery," ASME JOURNAL OF TURBOMACHINERY, Vol. 117, pp. 348–359.

Chien, K. Y., 1982, "Predictions of Channel and Boundary-Layer Flows With a Low-Reynolds Number Turbulence Model," AIAA J., Vol. 20, pp. 33–38.

Copenhaver, W. W., Hah, C., and Puterbaugh, S. L., 1993, "3-D Flow Phenomena in a Transonic, High-Throughflow, Axial-Flow Compressor Stage," ASME JOURNAL OF TURBOMACHINERY, Vol. 115, pp. 240–248.

Copenhaver, W. W., Mayhew, E. R., Hah, C., and Wadia, A. R., 1996, "The Effect of Tip Clearance on a Swept Transonic Compressor Rotor," ASME JOURNAL OF TURBOMACHINERY, Vol. 118, pp. 230–239.

Copenhaver, W. W., Puterbaugh, S. L., and Hah, C., 1997, "Unsteady Flow and Shock Motion in a Transonic Compressor Rotor," J. Prop. Power, Vol. 13, pp. 17–23.

Davis, R. L., Delaney, R. A., Denton, J. D., Giles, M. B., Strazisar, A. J., and Wisler, D. C., 1993, "CFD Code Assessment in Turbomachinery—Author's Information Package," ASME Turbomachinery Committee.

Dawes, W. N., 1987, "A Numerical Analysis of the 3-D Viscous Flow in a Transonic Compressor Rotor and Comparison With Experiment," ASME JOURNAL OF TURBOMACHINERY, Vol. 109, pp. 83–90.

Denton, J. D., 1993, "Loss Mechanisms in Turbomachines," ASME JOURNAL OF TURBOMACHINERY, Vol. 115, pp. 621–656.

Denton, J. D., 1996, "Lessons Learned from Rotor 37," presented at the 3rd International Symposium on Experimental and Computational Aerothermodynamics of Internal Flows (ISAIF), Beijing, China, Sept. 1–6.

Fan, S., Lakshminarayana, B., and Barnett, M., 1993, "Low-Reynolds-Number k–ϵ Model for Unsteady Turbulent Boundary-Layer Flows," AIAA J., Vol. 31, pp. 1774–1784.

Gerolymos, G. A., 1990, "Implicit Multiple-Grid Computation of the Compressible Navier–Stokes Equations Using k–ϵ Turbulence Closure," AIAA J., Vol. 28, pp. 1707–1717.

Gerolymos, G. A., and Vallet, I., 1996, "Implicit Computation of the 3-D Com-

pressible Navier–Stokes Equations Using k–ϵ Turbulence Closure," *AIAA J.*, Vol. 34, pp. 1320–1321.

Gerolymos, G. A., and Vallet, I., 1997, "Near-Wall Reynolds-Stress 3-D Transonic Flows Computation," *AIAA J.*, Vol. 35, pp. 228–236.

Gerolymos, G. A., Tsanga, G., and Vallet, I., 1998, "Near-Wall k–ϵ Computation of 3-D Transonic Turbomachinery Flows With Tip-Clearance," *AIAA J.*, Vol. 36, pp. 1769–1777.

Gerolymos, G. A., and Tsanga, G., 1999, "Automatic Biharmonic 3-D Grid Generation for Multistage Axial Turbomachinery With Tip-Clearance," *J. Prop. Power*, Vol. 15, pp. 476–479.

Hah, C., 1986, "A Numerical Modeling of Endwall and Tip-Clearance Flow of an Isolated Compressor Rotor," ASME *Journal of Engineering for Gas Turbines and Power*, Vol. 108, pp. 15–21.

Hah, C., Puterbaugh, S. L., and Copenhaver, W. W., 1997, "Unsteady Aerodynamic Flow Phenomena in a Transonic Compressor Stage," *J. Prop. Power*, Vol. 13, pp. 329–333.

Hah, C., and Loellbach, J., 1999, "Development of Hub Corner Stall and Its Influence on the Performance of Axial Compressor Blade Rows," ASME JOURNAL OF TURBOMACHINERY, Vol. 121, pp. 67–77.

Jennions, I. K., and Turner, M. G., 1993, "3-D Navier–Stokes Computations of Transonic Fan Flow using an Explicit Flow Solver and an Implicit k–ϵ Turbulence Model," ASME JOURNAL OF TURBOMACHINERY, Vol. 115, pp. 261–272.

Jones, W. P., and Launder, B. E., 1972, "The Prediction of Laminarization With a 2-Equation Model of Turbulence," *Int. J. Heat Mass Transf.*, Vol. 15, pp. 301–314.

Kunz, R. F., Lakshminarayana, B., and Basson, A. H., 1993, "Investigation of Tip-Clearance Phenomena in an Axial Compressor Cascade Using Euler and Navier–Stokes Procedures," ASME JOURNAL OF TURBOMACHINERY, Vol. 115, pp. 453–467.

Lakshminarayana, B., Zaccaria, M., and Marathe, B., 1995, "The Structure of Tip Clearance Flow in Axial Flow Compressors," ASME JOURNAL OF TURBOMACHINERY, Vol. 117, pp. 336–347.

Launder, B. E., and Sharma, B. I., 1974, "Application of the Energy Dissipation Model of Turbulence to the Calculation of Flows Near a Spinning Disk," *Lett. Heat Mass Transf.*, Vol. 1, pp. 131–138.

Liu, J. S., and Bozzola, R., 1993, "3-D Navier–Stokes Analysis of Tip Clearance Flow in Linear Turbine Cascades," *AIAA J.*, Vol. 31, pp. 2068–2074.

MacCormack, R. W., 1982, "A Numerical Method for Solving the Equations of Compressible Viscous Flow," *AIAA J.*, Vol. 20, pp. 1275–1281.

Puterbaugh, S. L., and Brendel, M., 1997, "Tip Clearance Flow-Shock Interaction in a Transonic Compressor Rotor," *J. Prop. Power*, Vol. 13, pp. 24–30.

Rai, M. M., 1989a, "3-D Navier–Stokes Simulations of Turbine Rotor–Stator Interaction: Part I—Methodology," *J. Prop. Power*, Vol. 5, pp. 305–311.

Rai, M. M., 1989b, "3-D Navier–Stokes Simulations of Turbine Rotor–Stator Interaction: Part II—Results," *J. Prop. Power*, Vol. 5, pp. 312–319.

Savill, A. M., 1994, "Transition Modelling for Turbomachinery," ERCOFTAC 3-D Turbomachinery Flow Prediction Workshop, Val d'Isère, France.

Schlichting, H., 1979, *Boundary-Layer Theory*, McGraw-Hill, New York, p. 590.

Shabbir, A., Celestina, M. L., Adamczyk, J. J., and Strazisar, A. J., 1997, "The Effect of Hub Leakage on 2 High Speed Axial Flow Compressor Rotors," ASME Paper No. 97-GT-346.

Smart, M. K., and Kalkhoran, I. M., 1997, "Flow Model for Predicting Normal Shock-Wave Induced Vortex Breakdown," *AIAA J.*, Vol. 35, pp. 1589–1596.

Speziale, C. G., 1989, "Turbulence Modeling in Noninertial Frames of Reference," *Theor. Comp. Fluid Dyn.*, Vol. 1, pp. 3–19.

Storer, J. A., and Cumpsty, N. A., 1994, "An Approximate Analysis and Prediction Method for Tip Clearance Loss in Axial Compressors," ASME JOURNAL OF TURBOMACHINERY, Vol. 116, pp. 648–656.

Strazisar, A. J., 1994, "Data Report and Data Diskette for NASA Transonic Compressor Rotor 37," NASA Lewis Research Center.

Suder, K. L., and Celestina, M. L., 1996, "Experimental and Computational Investigation of the Tip Clearance Flow in a Transonic Axial Compressor Rotor," ASME JOURNAL OF TURBOMACHINERY, Vol. 118, pp. 218–229.

Tsanga, G., 1997, "Aérodynamique Numérique 3-D des Turbomachines Axiales Multiétages avec Fermeture k–ϵ Bas-Reynolds," Doctorat, Université Pierre-et-Marie-Curie, Paris.

Turner, M. G., and Jennions, I. K., 1993, "An Investigation of Turbulence Modeling in Transonic Fans Including a Novel Implementation of an Implicit k–ϵ Turbulence Model," ASME JOURNAL OF TURBOMACHINERY, Vol. 115, pp. 249–260.

Vallet, I., 1995, "Aérodynamique Numérique 3-D Instationnaire avec Fermeture Bas-Reynolds au Second Ordre," Doctorat, Université Pierre-et-Marie-Curie, Paris.

Experimental Investigation of Unsteady Flow Phenomena in a Centrifugal Compressor Vaned Diffuser of Variable Geometry

F. Justen[1]

K. U. Ziegler

H. E. Gallus

Rheinisch-Westfälische Technische
Hochschule Aachen,
Institut für Strahlantriebe und
Turboarbeitsmaschinen,
D-52056 Aachen, Germany

The behavior of vaned radial diffusers is generally considered to be due to the flow phenomena in the vaneless and the semi-vaned space in the diffuser inlet region. Even considering unsteady aspects, the adjacent diffuser channel is regarded as less important. The flat wedge vaned diffuser of the centrifugal compressor stage investigated allows an independent continuous adjustment of the diffuser vane angle and the radial gap between impeller outlet and diffuser vane inlet, so that information about the importance of these geometric parameters can be obtained. The time-dependent pressure distribution on the diffuser front wall and on the suction and pressure surfaces of the diffuser vanes reveal that in the semi-vaned space mainly the region near the vane suction side is influenced by the unsteady impeller-diffuser interaction. Downstream in the diffuser channel the unsteadiness does not decay. Here, pressure fluctuations are appearing that are distinctly higher than the pressure fluctuations in the vaneless space. An estimation of the influence of the unsteadiness on the operating performance of the centrifugal compressor stage is made by measurements at choke and surge limit for different diffuser geometries.

Introduction

In the last years the development of centrifugal compressor stages has reached a standard that requires, for further optimization, a better understanding of the unsteady flow aspects, especially if vaned diffusers are considered. Unsteady flow phenomena have significant influence on the loading, the efficiency, the pressure ratio, and the noise emission of centrifugal compressor stages. Modern impellers reach absolute discharge Mach numbers between 0.9 and 1.3, so that at least transonic diffuser inlet conditions are expected. Owing to the highly distorted impeller discharge flow, the flow field in the diffuser inlet region is determined by strong velocity and flow angle fluctuations, as well in circumferential as in axial direction (Eckardt, 1975; Krain, 1980; Krain et al., 1995). With increasing radius in the vaneless space, the flow mixes out comparatively fast in circumferential direction due to intensive exchange of momentum between jet and wake flow, whereas the nonuniformity in axial direction remains longer (e.g., Haß and Rautenberg, 1977).

Early after the introduction of the "jet-wake" model by Dean and Senoo (1960), numerous experimental as well as theoretical approaches to model the impeller discharge flow were published (e.g., Johnston and Dean, 1966; Eckardt, 1973; Senoo and Ishida, 1975). Progress of unsteady measurement techniques allows for a longer time a quite precise prediction of the flow patterns in centrifugal compressor stages with vaneless diffusers (Japikse, 1987). Comparable results for vaned diffusers could not be achieved as yet, because the region between impeller exit and diffuser inlet is determined by phenomena that are difficult to model theoretically and to obtain experimentally:

• Unsteady flow characteristic: Starting from a simplified model, Dean and Senoo (1960) developed a method describing the mixing process approximately. In the rotating frame of reference the flow

is regarded as steady and two dimensional. The blade pitch is divided into two zones with different, but in each case constant velocities and equal flow angles. As a consequence of the nonuniformity of the relative flow, the absolute flow must be unsteady.

• Impeller–diffuser interaction: The diffuser receives the inhomogeneous impeller discharge flow as an unsteady inlet flow, while the presence of the diffuser vanes means an unsteady disturbance for the impeller. Unsteady impeller–diffuser interactions were investigated early by Krain (1981), Fisher and Inoue (1981), and Arndt et al. (1990). However, coincident results do not exist yet.

• Increase of boundary layer thickness and shock boundary layer interaction: The development of boundary layers in the viscous flow in the vaneless and semi-vaned space is determined substantially by the pressure gradient in flow direction. The boundary layer is turbulent, three-dimensional, and involved in secondary flow effects.

The flow phenomena mentioned above are not independent from each other concerning their development and extent. An enlargement of the radial gap, for instance, leads to a reduction of impeller–diffuser interaction and to a more uniform diffuser inlet flow, but also to an increased growth of boundary layer thickness.

The transfer of experimental results to different types of centrifugal compressors in order to derive a generally valid design method for vaned diffusers is very problematic. Impeller, diffuser, and other compressor components cannot be regarded as isolated parts. On the contrary, losses and operating performance of the stage are determined by the interaction of all components; i.e., empirical methods derived from component studies only have a limited universal validity to describe the real flow characteristics in the stage.

Further problems arise, attempting to predict the operating performance close to the limits of the compressor characteristics. Especially stages with vaned diffusers and transonic flow conditions have a limited operating range. As the point with maximum efficiency is usually located close to surge limit, it is necessary to expand the range of control up to the limits of the particular characteristic in order to enable an efficient operation. Several publications are concerned with the causal mechanisms triggering
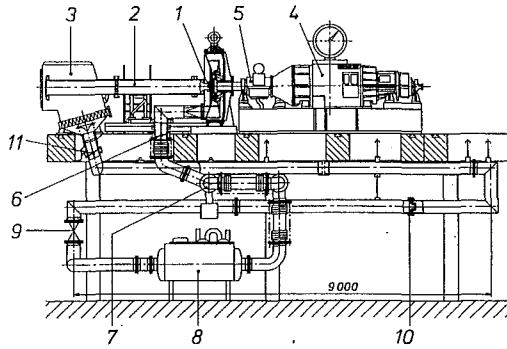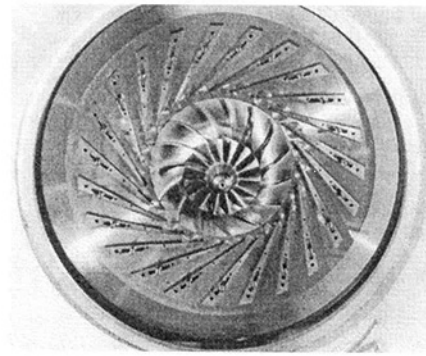
Fig. 1 Centrifugal compressor test bed

Fig. 2 Stage with dismounted front wall

the instability of a centrifugal compressor. For instance, Elder and Gill (1985) state different diffuser variables influencing the location of the stability limit, e.g., the number of impeller and diffuser blades, the pressure recovery in the semi-vaned space or the sensitiveness of the diffuser vanes to incidence.

Experimental Facility

The experimental investigations were carried out on a centrifugal compressor stage with a vaned diffuser of variable geometry. A detailed description of the development, the technical realization, and the measurement of compressor maps is given by Rothstein (1993).

Test Bed. The compressor stage is run in a closed loop using air and allowing a variation of the pressure level (Fig. 1). The components of the test bed are: compressor stage (1), suction pipe with honeycomb (2), settling chamber with air filter (3), throttle arrangement (6, 7, 9, 11), heat exchanger (8), flow nozzle in conformity with DIN 1952 (10), 500 kW d.c. motor with continuous speed control (4), gearbox with speed increasing ratio of 25 (5).

Centrifugal Compressor Stage. The stage consists of an unshrouded impeller with 15 backswept blades (38 deg backsweep from radial) and a diffuser with 23 wedge vanes. The design of suction pipe and inlet contour and omission of inlet guide vanes ensure axial flow at impeller inlet. Figure 2 shows a view of the

stage, with the diffuser front wall dismounted. The aerodynamic design of the wedge vaned diffuser is based on the characteristic parameters for flat diffusers (Runstadler et al., 1975). The construction of the diffuser allows an independent continuous adjustment of the diffuser vane angle, indicated by the vane suction side angle α_{4SS}, and the radial gap between impeller outlet and diffuser vane inlet, indicated by the radius ratio r_4/r_2 (Figs. 3 and 4). The most important data of the stage for nominal speed and diffuser reference geometry are collected in Table 1.

Test Program. The following detailed measurements were carried out to estimate the influence of radial gap and diffuser vane angle on unsteady flow phenomena in the vaned radial diffuser:

- unsteady pressure measurements on the diffuser front wall
- unsteady pressure measurements on suction and pressure surface of the diffuser vanes at midspan
- unsteady pressure measurements at the stability limit
- unsteady schlieren observations in the diffuser inlet region.

For four different diffuser geometries (Table 2) the measurements were carried out at three different speeds in each case ($n_{red}/n_{red,0}$ = 60, 70, 80 percent), and at each speed in three different operating points (choke limit, middle region of characteristic, close to surge limit). The investigations at the stability limit are an exception. They were carried out for two different radial gaps (r_4/r_2 = 1.10 and 1.06) both combined with the same

---

Nomenclature

$AR = h_6/h_5$ = area ratio (Kline et al., 1959)

$AS = b_5/h_5$ = aspect ratio (Kline et al., 1959)

F = fluctuation (Eq. (1))

L = length of diffuser channel (Fig. 3)

$LWR = L/h_5$ = length–width ratio (Kline et al., 1959)

b = constant meridional diffuser height

c = absolute velocity

f = frequency of pressure fluctuation

f_0 = blade passing frequency

h = diffuser width (Fig. 3)

$\dot{m}$ = mass flow

n = shaft speed

p = pressure

r = radius

s = arc length

t = time, impeller blade pitch

x/l = dimensionless channel coordinate (Fig. 6)

α_{4SS} = diffuser vane suction side angle (Fig. 3) (from positive circumferential direction)

η_{ts} = total isentropic efficiency

2Θ = diffuser channel divergence angle (Fig. 3)

π = pressure ratio

Subscripts

$I, II, III,$
$\quad IV, V$ = operating points close to surge limit (I = relatively far, V = very close to surge limit)

0 = nominal speed

1 = impeller inlet

2 = impeller exit

4 = diffuser inlet

5 = diffuser throat

6 = diffuser exit

N = reference geometry

PS = pressure side

SS = suction side

max = period maximum value of time dependent signal

min = period minimum value of time dependent signal

red = corrected to ISA inlet conditions (p = 1.013 bar, T = 288.15 K)

t = total

Superscripts

$^-$ = time-averaged value

$^\sim$ = time-dependent portion of the signal (e.g., $\tilde{p}(t) = p(t) - \bar{p}$)
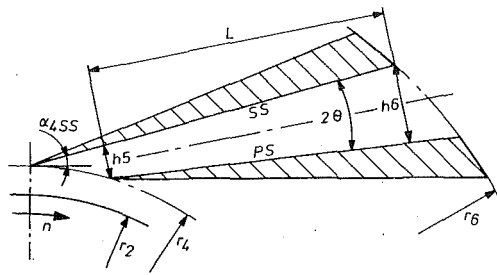
Fig. 3 Adjustable geometry parameters α_{4SS} and r_4/r_2

Fig. 5 Compressor maps for the investigated diffuser geometries

vane angle (α_{4SS} = 16.5 deg). The compressor maps of the investigated diffuser geometries are shown in Fig. 5.

Measurement Techniques. The experimental investigation of high loaded centrifugal compressors makes high demands on the used measurement technique. The achievable stage pressure ratios cause a corresponding thermal loading of all components in direct or indirect contact with the fluid. Probes positioned directly after impeller exit are exposed to an extreme dynamic loading due to the highly unsteady flow. In addition, owing to the very sensible transonic flow in the mostly narrow flow channels, the use of probes even of smallest dimensions is restricted or impossible. Although laser measurement techniques are most suitable under these conditions, their utilization is not efficient for first basic studies due to the large expenditure of installation.

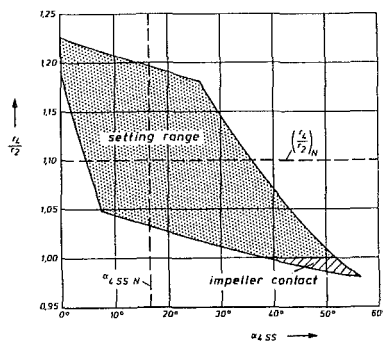For measuring the endwall pressure distribution, there are 120

measuring points available on the diffuser front wall (Fig. 6). To acquire the vane pressure distribution, 21 measuring positions on each side of the vane at midspan and one additional on the vane leading edge are used (Fig. 6). Because of the good rotational symmetry (Rothstein, 1993) the measuring points can be distributed on three measuring vanes used simultaneously. With the adjustment mechanisms shown in Fig. 7 the measuring vanes can be adapted to different diffuser geometries. The periodic pressure fluctuations are measured with semiconductor pressure transducers of the type Kulite XCS-093 (reference pressure type). Their natural frequency is 200 kHz, and the membrane diameter is 0.96 mm. Owing to the nonreproducible zero displacement, they are used only to measure the fluctuating portion of the signal. For recording the time-dependent signals, a transient recorder with eight channels, 65,536 words memory per channel, and a maximum sampling frequency of 10 MHz is used. Because of the large measurement expenditure and the considerable amount of data the unsteady wall pressure measurements are limited to the first half of the diffuser channel. To adjust every measuring point, a Kulite is fitted in a multiple eccentric adjustment mechanism (Fig. 8).

Fig. 4 Setting range of vane angle and radial gap (Rothstein, 1993)

Table 1 Stage data for nominal speed and diffuser reference geometry

number of impeller blades	z_i	= 15
blade angle impeller exit (from positive circumferential direction)	β_2	= 128°
impeller tip radius	r_2	= 135 mm
impeller tip speed	u_2	= 498 m/s
relative tip Mach number impeller inlet	Ma_{w1}	= 0.95
absolute Mach number impeller exit	Ma_2	= 0.94
shaft speed	n_0	= 35200 1/min
number of diffuser vanes	z_d	= 23
meridional diffuser height	b	= 11 mm
radial gap	r_4/r_2	= 1.10
diffuser vane angle (from positive circumferential direction)	α_{4SS}	= 16.5°
diffuser channel divergence angle (constant for all diffuser geometries)	2Θ	= 9°

Table 2 Diffuser channel characteristic numbers for the investigated diffuser geometries

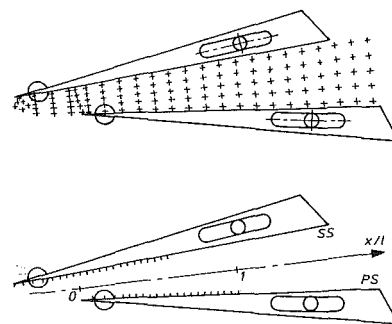| r_4/r_2	α_{4SS}	AS	AR	LWR
1.10	16.5°	0.70	2.42	9.00
1.10	14.5°	0.76	2.53	9.73
1.06	16.5°	0.73	2.48	9.42
1.06	14.5°	0.79	2.60	10.19

Fig. 6 Available measuring positions on diffuser front wall and vane surfaces
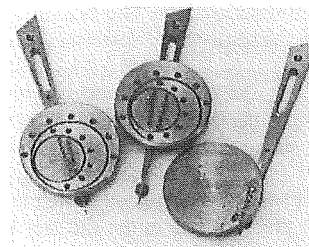
Fig. 7 Measuring vanes with adjustment mechanism

Journal of Turbomachinery

OCTOBER 1999, Vol. 121 / **765**
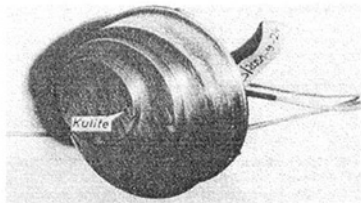
Fig. 8 Semiconductor pressure transducer with adjustment mechanism

The limitation in space and financial aspects (43 measuring points) do not allow an application of Kulites flush to the surfaces of the diffuser vanes, so that a separation of measuring point and pressure transducer is necessary. By that, the pressure signal is falsified, because amplitude damping and phase shift are occurring. A thorough investigation and calibration of the dynamic systems behavior, as described by Justen (1993), becomes necessary.

For visualization and qualitative analysis of the flow, the well-known schlieren method according to Toepler is applied. The stroboscopic exposure is realized with a high-frequency spark lamp allowing a flash duration of less than 20 ns. Through an adjustable delay circuit a spark can be triggered at different rotor positions.

Experimental Investigations

Unsteady Diffuser Flow. In the following figures showing the unsteady pressure distribution on the diffuser front wall "s" represents the coordinate in circumferential direction and "t" is the arc length of an impeller blade pitch. The specified values of the isobars are the local static pressures normalized by the pressure in the settling chamber (Fig. 1, number 3). Starting from $s/t = 0$, the figures show from left to right and from top to bottom instantaneous pressure distributions for eight equidistant circumferential impeller positions.

Figure 9 shows the unsteady pressure contours for an operating point close to surge limit at 80 percent nominal speed. At the impeller position $s/t = 0$ an impairment of the pressure rise can be recognized in the diffuser throat decaying not before the impeller has rotated to $s/t = 0.375$. At the same time the isobar $\pi = 2.17$ moves downstream, and raises the distance to the isobar $\pi = 2.12$, which hardly moves. This reveals a diminishing pressure rise shortly after the diffuser throat. The isobars in the rear part of the diffuser channel demonstrate a reverse tendency. Here, close to the pressure side at $s/t = 0$ a zone with distinctly higher pressure between two isobars of equal value can be identified, which expands up to the suction side after a rotation to $s/t = 0.125$. The pressure contours upstream of this region do not change their position at this time. From $s/t = 0.375$ on, the isobars with higher pressure level travel toward diffuser exit. Simultaneously the isobars situated before reduce their distance, and move in the direction of the throat. As a result of this, two isobars with the same pressure value occur in the diffuser channel despite divergent flow path ($\pi = 2.34$ at $s/t = 0.625$). At $s/t = 0.5$ an impairment of the pressure rise before the throat becomes visible causing a diminished pressure gradient in the semi-vaned space. At $s/t = 0.875$ the growing high pressure region close to the pressure side can clearly be identified already. The beginning enhancement of the pressure rise in the semi-vaned space can be recognized as well (compare $s/t = 0$).

As revealed by Fig. 10, a reduced diffuser vane angle does not change the basic structure of the time-dependent diffuser flow. The distinctly weaker disturbances in the diffuser throat region are remarkable. At $s/t = 0$ the high-pressure zone in the rear part of the diffuser channel already ranges over the entire flow path. The impairment of the pressure rise in the diffuser throat has traveled downstream. Here as well, the isobars with higher pressure level travel toward diffuser exit from $s/t = 0.375$ on. Likewise, the

Fig. 9 Time-dependent pressure contours ($r_4/r_2 = 1.06$, $\alpha_{4SS} = 16.5$ deg, $n_{red}/n_{red,0} = 0.8$, close to surge limit)

slight drop of the pressure gradient in the semi-vaned space between $s/t = 0.5$ and $s/t = 0.75$ can be detected.

Observing the pressure signals of the single measuring points

Fig. 10 Time-dependent pressure contours ($r_4/r_2 = 1.06$, $\alpha_{4SS} = 14.5$ deg, $n_{red}/n_{red,0} = 0.8$, close to surge limit)

Fig. 11 Pressure fluctuations on vane surfaces ($r_4/r_2 = 1.06$, $\alpha_{4SS} = 14.5$ deg, $n_{red}/n_{red,0} = 0.8$, close to surge limit)
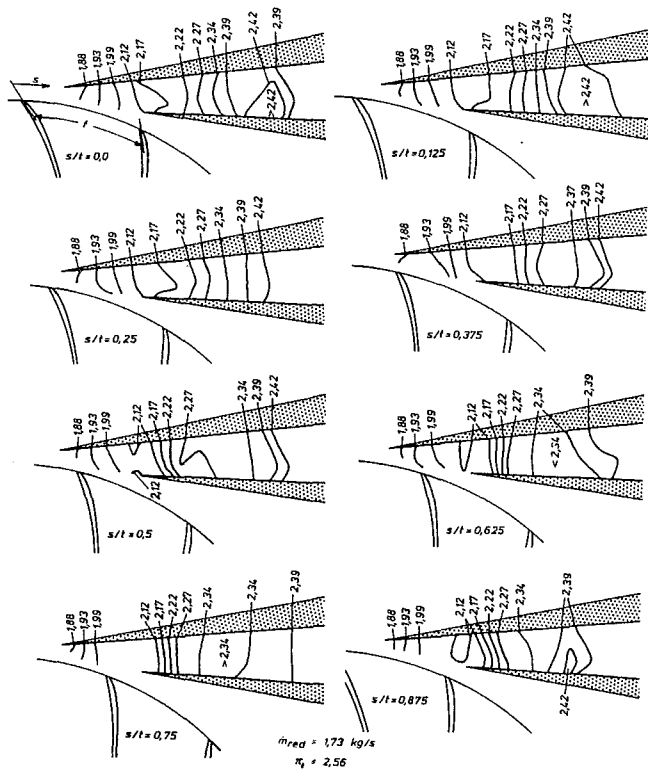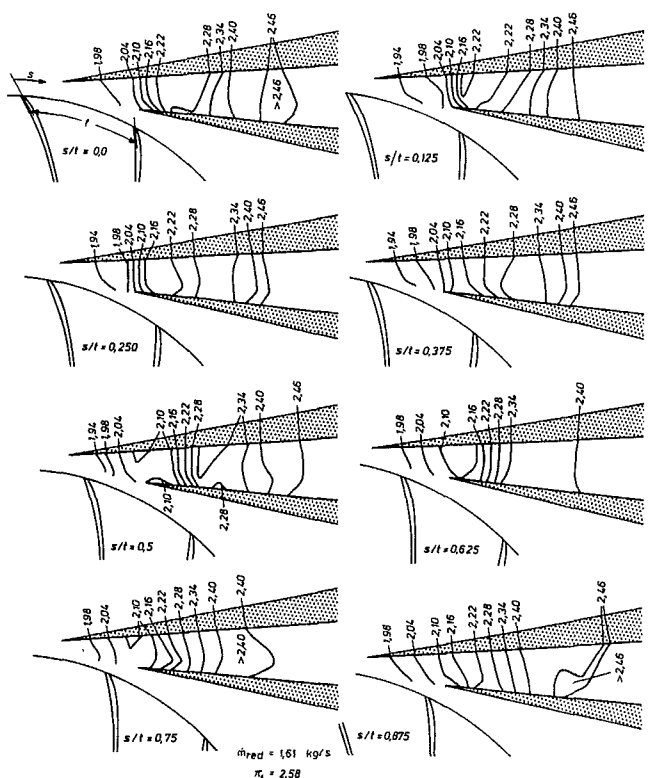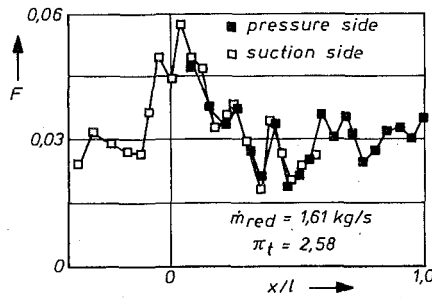

Fig. 12 Time-dependent pressure contours ($r_4/r_2 = 1.10$, $\alpha_{4SS} = 16.5$ deg, $n_{red}/n_{red,0} = 0.8$, close to surge limit)

during the passing of an impeller blade pitch, a consequence for the diffuser flow can be shown (Fig. 11, 13, and 15). By plotting the local normalized pressure fluctuations according to:

$$F(x/l) = \frac{p_{max}(x/l) - p_{min}(x/l)}{2\bar{p}(x/l)} \qquad (1)$$

versus the dimensionless channel coordinate (Fig. 6), zones of high and low pressure fluctuations can clearly be distinguished. After the diffuser throat suction and pressure side show similar trends. In operating points close to the surge limit the shape of the fluctuations within the diffuser channel is comparable to a standing wave, because the reference pressure perpendicular to the diffuser channel is constant due to the proper channel flow, and the relative maxima and minima of the fluctuations of suction and pressure side occur at the same x/l position. Interference phenomena of at least two pressure waves are the cause of the standing wave. Due to a reflection at the exit of the diffuser blading the upstream and the downstream running pressure waves are interfering. The superposition of their instantaneous values results in the total fluctuation value for each position. Hence, the unsteady effects do not decay along the diffuser channel, but maintain the fluctuation level inspite of the increasing local reference pressure.

Figure 11 shows such a diagram. Here, pressure fluctuations from measurements on suction and pressure surface of a diffuser vane at midspan are plotted versus the dimensionless channel coordinate for the same diffuser geometry and operating point as in Fig. 10. The measurements on the vane suction surface reveal pronounced relative maxima and minima in the semi-vaned space. In this region, the steep increase of the fluctuations shortly before the diffuser throat after a slight decrease is remarkable. This is due to intensified reflection phenomena and herewith to intensified impeller–diffuser interactions. In the diffuser throat the fluctuations first decrease slightly, but then increase to their maximum. Within the diffuser channel, suction side and pressure side show very similar courses. Due to their common positions of relative maxima and minima, they indicate a node–antinode structure and herewith a standing wave.

An enlargement of the radial gap leads to a decrease of unsteadiness due to the momentum exchange process, so that a distinctly reduced fluctuation level results at the diffuser vanes leading edges. As an example, Fig. 12 shows the time-dependent pressure contours for an enlarged radial gap, but otherwise comparable conditions as in Fig. 9. The smooth structure of all instantaneous pressure distributions is remarkable. If the isobar $\pi = 2.22$ was not plotted, at any time homogeneous channel flow could be assumed. The actual movement of the isobars occurs downstream. The distinct motion in this region depending on the rotor position reveals noticeable pressure fluctuations within the diffuser channel.

Besides the generally diminished level of the pressure fluctuations, the enlargement of the radial gap changes as well the course of the fluctuations along the channel centerline, especially in the semi-vaned space. For an enlarged radial gap, but otherwise comparable conditions as in Fig. 11, Fig. 13 gives an example. In the
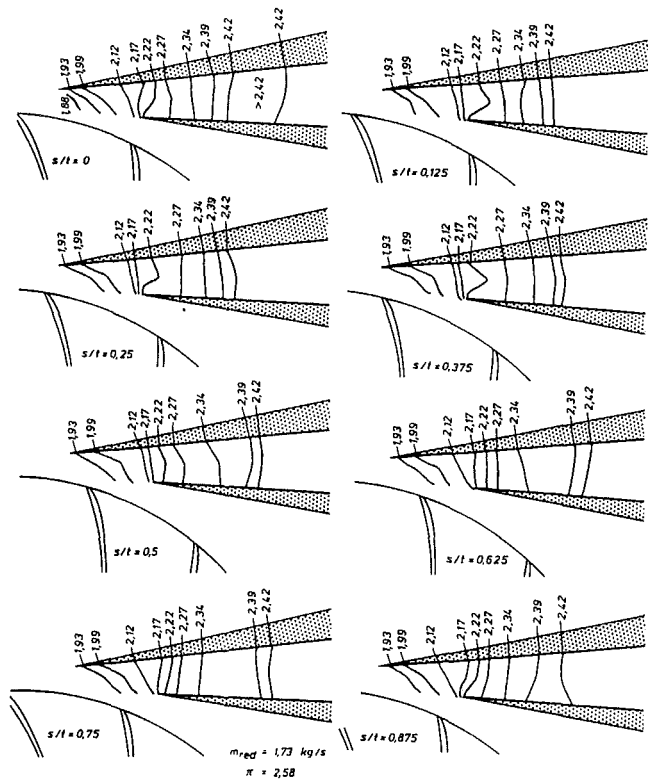
semi-vaned space the fluctuations grow nearly linearly at first. Thereby a relative maximum is reached, nearly coinciding with the relative minimum of the smaller radial gap, concerning both the position and the value. In the sequel, after a distinct drop before the throat, here as well the absolute maximum of the suction-sided fluctuations is not reached before the diffuser throat. In the adjacent diffuser channel the enlargement of the radius ratio leads to an elongation of the oscillation antinodes, so that fewer relative maxima and minima are visible in Fig. 13. A qualitative comparison of Figs. 11 and 13 reveals the common fluctuation structure at both radial gaps. In the semi-vaned space the fluctuation increases at first, drops more or less strongly before the diffuser throat, and reaches its absolute maximum after a steep rise not before the throat. The following decrease of the fluctuation passes in a comparable manner as well.

An increasing mass flow leads to a growing negative incidence of the diffuser vanes leading edges. As a result of this, a distinct pressure-sided low pressure zone in the throat region is extending. In Fig. 14 an operating point in the middle region of the 80 percent nominal speed characteristic is displayed. At $s/t = 0$ a low-
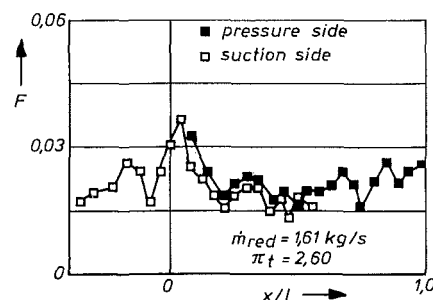

Fig. 13 Pressure fluctuations on vane surfaces ($r_4/r_2 = 1.10$, $\alpha_{4SS} = 14.5$ deg, $n_{red}/n_{red,0} = 0.8$, close to surge limit)
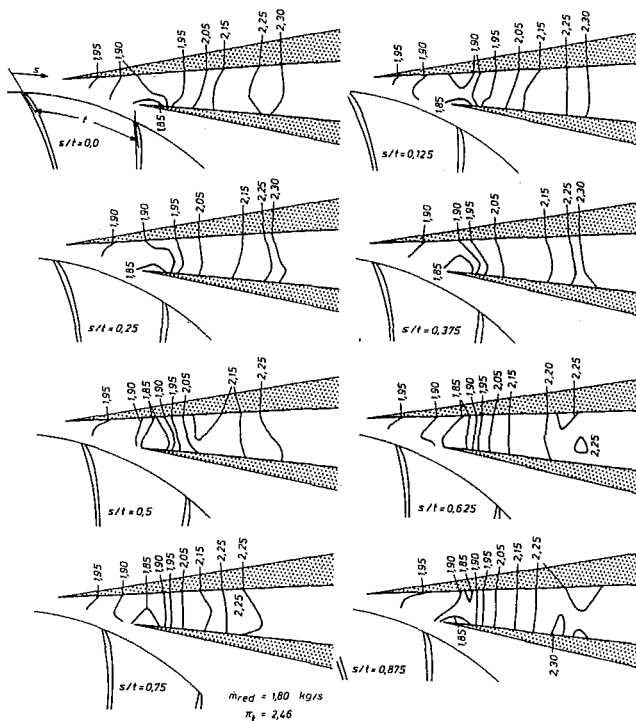
Fig. 14 Time-dependent pressure contours ($r_4/r_2 = 1.06$, $\alpha_{4SS} = 14.5$ deg, $n_{red}/n_{red,0} = 0.8$, middle region of characteristic)

Fig. 16 Pressure fluctuations on vane pressure side during one impeller-pitch period ($r_4/r_2 = 1.06$, $\alpha_{4SS} = 14.5$ deg, $n_{red}/n_{red,0} = 0.6$, close to surge limit)

pressure zone ($\pi = 1.85$) can be detected extending to the suction side in the course of a rotation through half of an impeller pitch. In this manner the flow is accelerated after passing the throat, so that the pressure rise sets in downstream. While the impeller rotates on, the low-pressure zone decreases and moves back to the pressure side. The distortion of the pressure contours in the semi-vaned space reveals the upstream effect of the described throat flow on the inlet region of the diffuser. In addition, the impairment of the pressure rise in the throat region causes small zones of higher pressure downstream in the diffuser channel.

The incidence of the diffuser vanes, caused by increased mass flow, as well influences significantly the pressure fluctuations within the diffuser channel. For the same operating point as in Fig. 14, in Fig. 15 the local fluctuations on the diffuser front wall are plotted. In general, the fluctuations have moved toward the suction side. The considerable rise of the suction-sided fluctuations in the throat region indicates an increased interaction between alternating incidence of the diffuser vanes and reflection phenomena.

A reduction of shaft speed does not change the basic structure of the results presented above (see Justen, 1993). For that reason, a figure showing these results shall be renounced here.

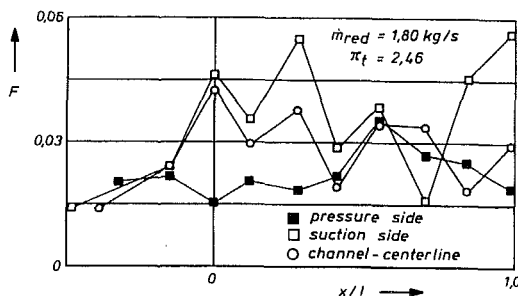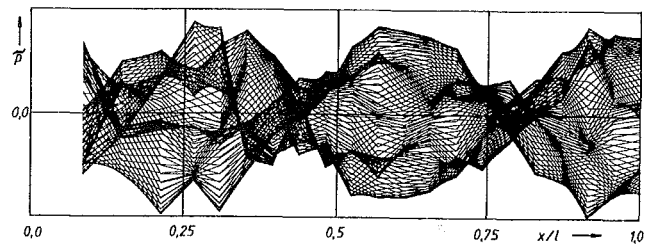In conclusion, a further preparation of the experimental data is presented in Fig. 16. The local time-dependent portions of the signal from the vane pressure side are plotted versus the dimensionless channel coordinate for several equidistant time intervals within a rotation through one impeller pitch. The resulting node–antinode structure reveals clearly a standing wave in the diffuser channel. It must be mentioned that this diagram cannot be compared with the figures above, since here only the time-dependent portions of the pressure signals are plotted without considering the increasing steady mean pressure.

Regarding Figs. 11, 13, 15, and 16, it should be noticed that the position $x/l = 1.0$ is located in the middle region of the diffuser channel and not at the end. As shown in Fig. 6 the last measuring point on the vane pressure side is found at $x/l = 1.0$.

Unsteady Investigations Close to Choke and Surge Limit

Choke Limit. Running the compressor at the choke limit, the steady schlieren photos of the diffuser flow show the shocks as bright broad stripes (Justen, 1993). In contrast to this, the use of the high-frequency spark lamp allows a detailed observation of the shock oscillation depending on impeller position. By exposing with only one flash, instantaneous shock configurations, as shown in Fig. 17, can be visualized. The two schlieren photos in the upper part of Fig. 17 represent two different rotor positions in an operating point, where the flow is still choked. The left picture reveals clearly that the strong shock is perpendicular in the middle of the channel only. At the leading edge the distinct pressure-sided low-pressure region caused by high incidence can be identified. The right photo shows that the shock has moved upstream due to a

Fig. 15 Pressure fluctuations on diffuser front wall ($r_4/r_2 = 1.06$, $\alpha_{4SS} = 14.5$ deg, $n_{red}/n_{red,0} = 0.8$, middle region of char)
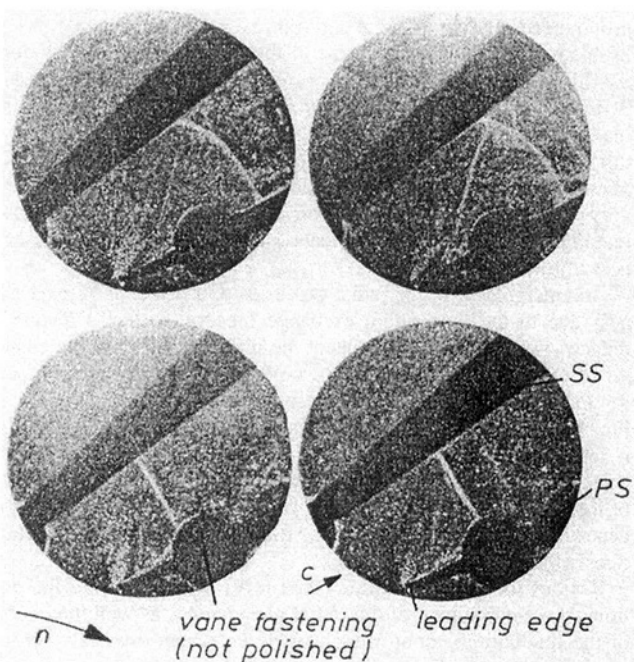

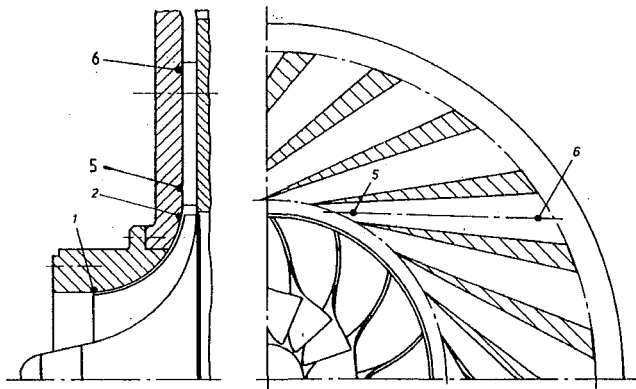Fig. 17 Stroboscopic schlieren photos at choke limit

Fig. 18 Positions of unsteady pressure transducers for measurements at surge limit

rotation of the impeller through few degrees. The stronger curvature of the strong shock at the vane suction side compared with the pressure side is obviously due to an additional shock wave attached to the vane leading edge. This shock configuration is described in detail by Bölcs and Suter (1986). The lower part of Fig. 17 shows again two stroboscopic schlieren photos at different impeller positions in an operating point slightly more throttled. The raising of the back pressure leads to a lower incidence, so that the additional shock described above does not appear any more. The strong shock has moved upstream, and now is perpendicular to the channel centerline. The operating point shown here is the real choke limit, because a further little raise of the back pressure leads to a complete unchoking of the diffuser, and herewith the compressor's range of control begins.

Surge Limit. In each case one semiconductor pressure transducer mounted flush in the diffuser front wall at impeller inlet, at impeller exit, at the diffuser throat, and at diffuser exit (numbers 1, 2, 5, and 6 in Fig. 18) allows an investigation of unsteady flow phenomena shortly before and during surge. For an estimation of the mechanical loading during surge, the axial shaft movement is recorded additionally. First, the compressor is pre-throttled with a pressure-sided slide valve (No. 7 in Fig. 1). To exclude the influence of a changed characteristic of the closed loop, always the same end position of the slide valve is adjusted. The further throttling up to the surge limit is done by a slow stepwise closing of the pressure-sided butterfly valve (No. 6 in Fig. 1). The fast-opening mechanism of this valve is connected with the transient recorder, which allows the recording of data in a certain space of time before the release of the fast-opening mechanism, depending on the chosen pre-trigger. Surge is identified by the "acoustic method," because it is accompanied by an audible sound comparable to a heavy hammer stroke on a pipe. The reason for pre-throttling with a slide valve is to keep the mechanical loading of the butterfly valve low in order to avoid the danger of jamming.

Figure 19 shows the courses of the unsteady pressure signals at 80 percent nominal speed. Before the first surge cycle impeller exit (2) and diffuser throat (5) reveal already a distinct alteration of the pressure signal, while impeller inlet (1) and diffuser exit (6) do not show any noticeable changes. The beginning of reverse flow is characterized by a slight pressure drop at diffuser exit, whereas impeller inlet and exit and diffuser throat show a steep positive pressure rise. Simultaneously, the rotor moves abruptly toward the shroud, leading to a heavy loading of the thrust bearing and involving the danger of an impeller shroud contact. During the reverse flow operation both impeller exit and diffuser throat have strong pressure oscillations decreasing to the normal level shortly before reaching the pressure minimum. The following normalization first leads to an overswing of the pressure signals in the diffuser, whereas in the impeller a stable state is reached relatively quickly. The restart of the regular flow can be identified clearly by
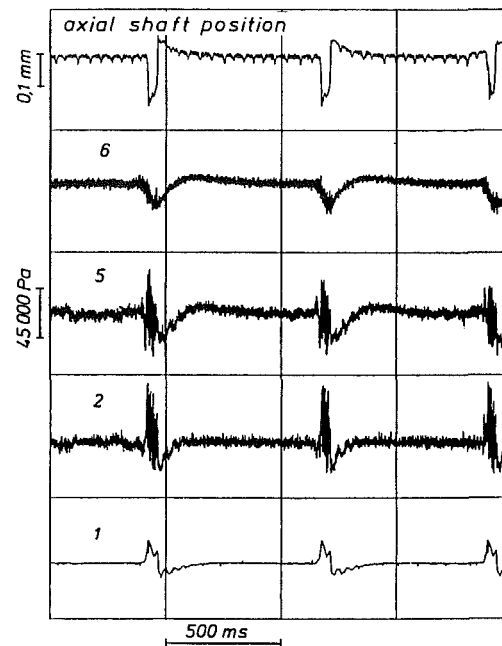
Fig. 19 Real-time signals during surge (r_4/r_2 = 1.10, α_{4SS} = 16.5 deg, $n_{red}/n_{red,0}$ = 0.8)

the backward shift of the rotor. In the time between two surge cycles, the flow can be characterized as stable.

Figure 20 shows an extended time scale. It can be seen that there is a pressure rise in the impeller accompanied by a pressure drop in the diffuser throat, before the pressure begins to decrease in the diffuser exit (not yet visible in Fig. 20). The instability of the system is obviously triggered by a local degradation of the flow in the diffuser throat, causing increased oscillation amplitudes in this region and leading to a pressure rise at impeller inlet and exit. A further signal analysis of the section with increased amplitudes does not reveal frequencies typical for rotating stall.

In Fig. 21 the frequency spectra during the approach to the stability limit are plotted. In a moderate operating point relatively far from the stability limit (number *1* in Fig. 21) impeller exit, diffuser throat, and diffuser exit show very similar spectra. Impeller and diffuser exit have a little more pronounced second harmonic. Throttling the compressor, the first harmonics in the dif-
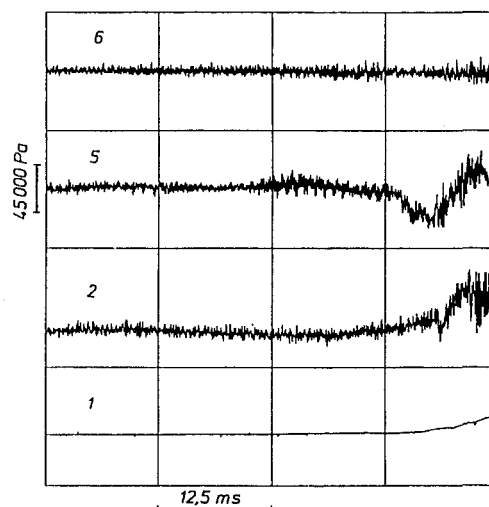

Fig. 20 Real-time signals shortly before the first surge cycle (r_4/r_2 = 1.10, α_{4SS} = 16.5 deg, $n_{red}/n_{red,0}$ = 0.8)
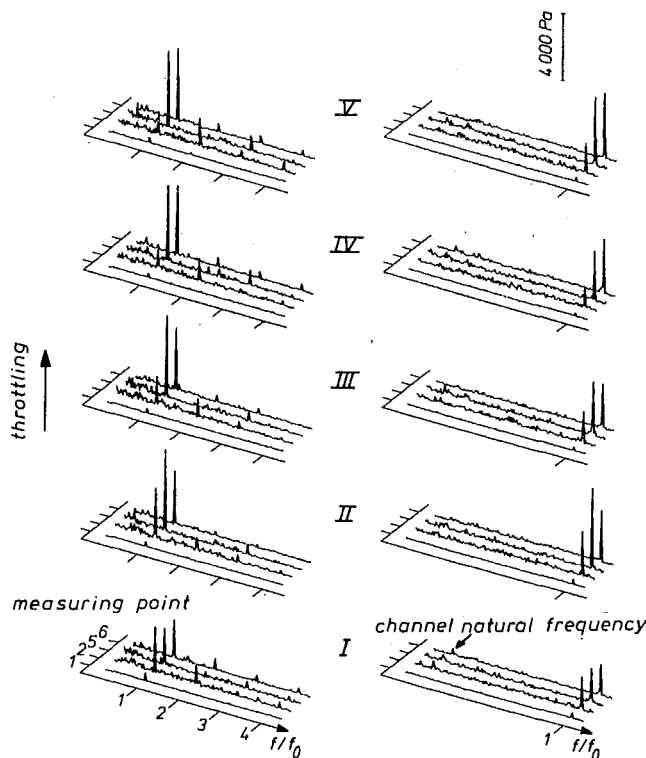
Fig. 21 Frequency spectra during approach to stability limit ($r_4/r_2 =$ 1.10, $\alpha_{4SS} = 16.5$ deg, $n_{red}/n_{red,0} = 0.8$)

fuser, at first especially in the diffuser throat, increase reaching their maximum close to the stability limit (number V in Fig. 21). (The phenomenon of the non-decaying pressure fluctuations along the diffuser channel was discussed above.) As the mass flow is reduced, the first harmonic at impeller exit decreases. This indicates a more uniform relative flow field across the blade pitch close to the shroud in highly throttled operating points, typical of backswept impellers (Rhone and Baumann, 1988). The increased amplitudes in the lower frequency range (right part of Fig. 21) occur in all operating points, and can be interpreted as the natural frequency of the diffuser channel. It is remarkable that distinct amplitudes of this frequency appear at impeller exit as well, as a result of the upstream effect of the vaned diffuser.

The influence of a smaller radial gap is described with the help of Fig. 22. Here, the impeller exit shows a distinct alteration of the pressure signal before the first surge cycle, whereas in the diffuser throat only a slightly increased amplitude can be detected. With a lower radial gap the instability now is triggered obviously by the impeller. Here as well, a further analysis of the signal does not reveal frequencies typical for rotating stall.

For two additional shaft speeds (60 and 70 percent nominal speed) the courses of the unsteady pressure signals up to the first surge cycle are given in Figs. 23 and 24. At $n_{red}/n_{red,0} = 0.6$, the impeller exit shows the first remarkable alterations, whereas at $n_{red}/n_{red,0} = 0.7$ it cannot be definitely clarified, if the diffuser throat or the impeller exit triggers the instability.

In the literature it is often reported on an inducer stall triggering the instability of the system (e.g., Jansen et al., 1980; Kosuge et al., 1982). For an analysis of this, in Fig. 25 the frequency spectra at impeller inlet during the approach to the stability limit are plotted. In all operating points the first harmonic is dominating the higher harmonics. The signal components of lower frequency in the right part of Fig. 25 do not give any hints at rotating stall. The variations of the amplitudes can be explained by stochastic events, because they vanish through an averaging of the signal and a following Fourier transformation.

The region between impeller exit and diffuser throat is sure to be

Fig. 22 Real-time signals shortly before the first surge cycle ($r_4/r_2 =$ 1.06, $\alpha_{4SS} = 16.5$ deg, $n_{red}/n_{red,0} = 0.8$)

critical in regard of the triggering of instability. In general, here the first remarkable alterations are appearing, which trigger the instability of the system due to an interactive building-up process. The radial gap determines the amplitudes of the fundamental pressure fluctuations already in the stable regime, and thus influences first of all the "sharpness" of the surge limit. As the results show likewise, the unsteady measurements do not allow direct conclusions about the position of the operating point relative to the surge limit. The first remarkable alterations do not appear before reaching the surge limit.

Conclusions

Unsteady flow phenomena in a vaned radial diffuser have been investigated with the help of unsteady pressure measurements on the diffuser front wall and on suction and pressure surface of the diffuser vanes at midspan, considering four different diffuser geometries and different operating points.

The wall pressure distributions presented allow an observation of the static pressure rise depending on impeller position, and offer vivid instantaneous views of the pressure field. It is shown that for all operating points and diffuser geometries, the unsteadiness of
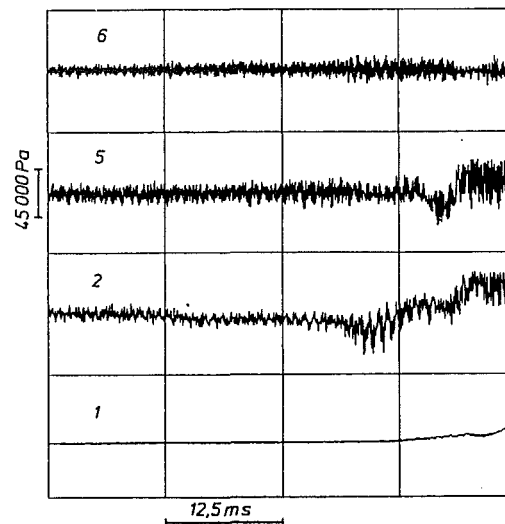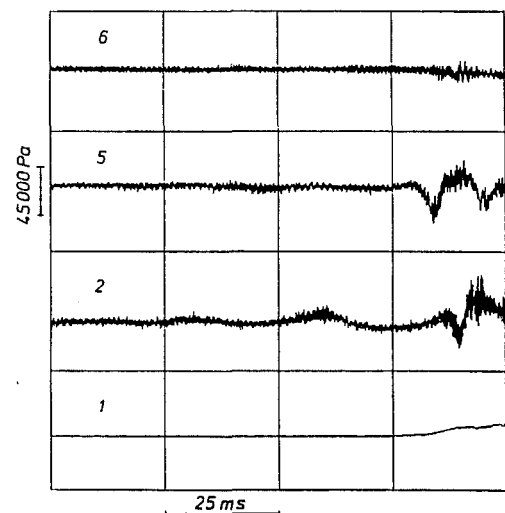

Fig. 23 Real-time signals shortly before the first surge cycle ($r_4/r_2 =$ 1.10, $\alpha_{4SS} = 16.5$ deg, $n_{red}/n_{red,0} = 0.6$)
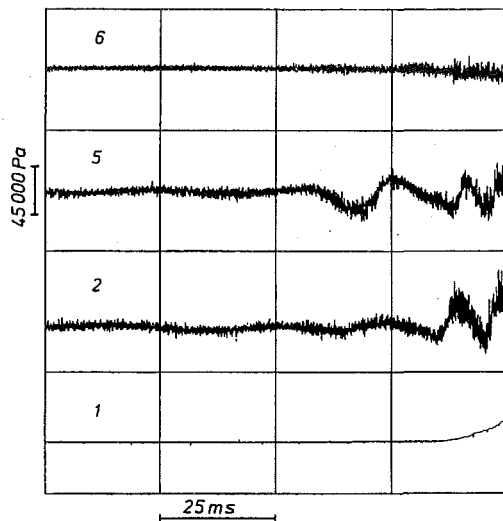
Fig. 24 Real-time signals shortly before the first surge cycle (r_4/r_2 = 1.10, α_{4SS} = 16.5 deg, $n_{red}/n_{red,0}$ = 0.7)

and the resulting separated region on the vane pressure side. Consequently, operating points close to the choke limit are determined by supersonic flow and shocks in the diffuser channel, despite subsonic diffuser inlet flow.

After overstepping the stability limit, the beginning reverse flow is characterized by a slight pressure drop at diffuser exit, whereas impeller inlet and exit and diffuser throat show a steep positive pressure rise. Simultaneously, the rotor moves abruptly toward the shroud. During the reverse flow operation both impeller exit and diffuser throat have strong pressure oscillations decreasing to the normal level shortly before reaching the pressure minimum. A preceding rotating stall or inducer stall cannot be detected. A single component of the stage, which triggers the instability of the system at all shaft speeds and diffuser geometries, cannot be identified. In addition, the unsteady measurements do not allow direct conclusions about the position of the operating point relative to the surge limit.

Acknowledgments

the impeller discharge flow influences not only the time-dependent pressure rise in the vaneless and semi-vaned space, but also the configuration in the adjacent diffuser channel to a high degree. The pressure fluctuations occurring there are caused by a periodic stimulation by the jet-wake flow. An analysis of the amplitudes of the pressure fluctuations reveals that in the semi-vaned space especially the region close to the vane suction side is influenced by unsteady impeller–diffuser interactions. Downstream in the diffuser channel the unsteadiness does not decay, even with an enlarged radial gap. Here, pressure fluctuations are appearing that can be distinctly higher than the pressure fluctuations in the vaneless space, depending on the operating point. The amplification of a pressure wave without additional energy input is possible through the interference with other pressure waves, in this case caused by reflections at the exit of the diffuser blading and at the side-walls. In operating points close to the surge limit, the shape of the local pressure fluctuations within the diffuser channel is comparable to the structure of a standing wave.

At the choke limit the diffuser throat region acts as a convergent/divergent nozzle, owing to the steep inlet flow angle
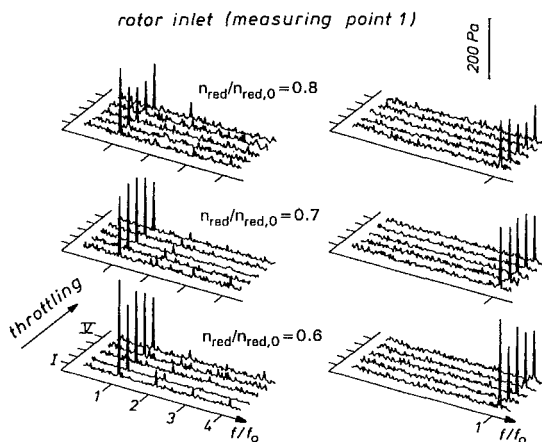

Fig. 25 Frequency spectra at impeller inlet during approach to stability limit (r_4/r_2 = 1.10, α_{4SS} = 16.5 deg)

References

Arndt, N., Acosta, A. J., Brennen, C. E., and Caughey, T. K., 1990, "Experimental Investigation of Rotor–Stator Interaction in a Centrifugal Pump With Several Vaned Diffusers," ASME JOURNAL OF TURBOMACHINERY, Vol. 112, pp. 98–108.

Bölcs, A., and Suter, P., 1986, *Transsonische Turbomaschinen*, Verlag G. Braun, Karlsruhe.

Dean, R., and Senoo, Y., 1960, "Rotating Wakes in Vaneless Diffusers," ASME *Journal of Basic Engineering*, Vol. 82.

Eckardt, D., 1973, "Untersuchung der Strahl-/Totwasserströmung hinter einem hochbelasteten Radialverdichterlaufrad," Diss. RWTH Aachen.

Eckardt, D., 1975, "Instantaneous Measurements in the Jet and Wake Discharge Flow of a Centrifugal Impeller," ASME *Journal of Engineering for Power*, Vol. 97.

Elder, R. L., and Gill, M. E., 1985, "A Discussion of the Factors Affecting Surge in Centrifugal Compressors," ASME *Journal of Engineering for Gas Turbines and Power*, Vol. 107, pp. 499–506.

Fisher, E., and Inoue, M., 1981, "A Study of Diffuser/Rotor Interaction in a Centrifugal Compressor," *Journal of Mechanical Engineers*, Vol. 23, No. 3.

Haß, U., and Rautenberg, M., 1977, "Zum Einfluß des Mischungsprozesses und der Reibung nach dem Laufrad eines hochbelasteten Radialverdichters auf den statischen und totalen Druckverlauf," Konstruktion 29.

Jansen, W., Carter, A., and Swarden, M., 1980, "Improvements in Surge Margin for Centrifugal Compressors," AGARD Conference Proceedings No. 282-19.

Japikse, D., 1987, "The Technology of Centrifugal Compressors: A Design Approach and New Goals for Research," VKI Lecture Series 1987-01.

Johnston, J., and Dean, R., 1966, "Losses in Vaneless Diffusers of Centrifugal Compressors and Pumps," ASME *Journal of Engineering for Power*, Vol. 82.

Justen, F., 1993, "Experimentelle Untersuchung instationärer Strömungsvorgänge im beschaufelten Diffusor variabler Geometrie einer hochbelasteten Radialverdichterstufe," Diss. RWTH Aachen.

Kline, S., Abbot, D., and Fox, R., 1959, "Optimum Design of Straight-Walled Diffusers," ASME *Journal of Basic Engineering*, Vol. 81.

Kosuge, H., Ito, T., and Nakanishi, K., 1982, "A Consideration Concerning Stall and Surge Limitations Within Centrifugal Compressors," ASME *Journal of Engineering for Power*, Vol. 104, No. 4.

Krain, H., 1980, "Experimental and Theoretical Investigations on the Internal Flow in a Centrifugal Compressor," AGARD Conference Proc. No. 282-1.

Krain, H., 1981, "A Study on Centrifugal Impeller and Diffuser Flow," ASME *Journal of Engineering for Power*, Vol. 103.

Krain, H., Hoffmann, B., and Pak, H., 1995, "Aerodynamics of a Centrifugal Compressor Impeller with Transonic Inlet Conditions," ASME Paper No. 95-GT-79.

Rhone, K., and Baumann, K., 1988, "Untersuchungen der Strömung am Austritt eines offenen Radialverdichterlaufrades und Vergleich mit der klassischen Jet-Wake Theorie," VDI Berichte No. 706.

Rothstein, M., 1993, "Entwicklung und experimentelle Untersuchung eines Radialverdichters mit beschaufeltem Diffusor variabler Geometrie," Diss. RWTH Aachen.

, Runstadler, P., Dolan, F., and Dean, R., 1975, "Diffuser Data Book," CREARE Technical Note 186.

Senoo, Y., and Ishida, M., 1975, "Behavior of Several Asymmetric Flow in a Vaneless Diffuser," ASME *Journal of Engineering for Power*, Vol. 97.

The Design of an Improved Endwall Film-Cooling Configuration

S. Friedrichs

BMW Rolls-Royce GmbH,
Dahlewitz, Germany

H. P. Hodson

W. N. Dawes

Whittle Laboratory,
University of Cambridge,
Cambridge, United Kingdom

The endwall film-cooling cooling configuration investigated by Friedrichs et al. (1996, 1997) had in principle sufficient cooling flow for the endwall, but in practice, the redistribution of this coolant by secondary flows left large endwall areas uncooled. This paper describes the attempt to improve upon this datum cooling configuration by redistributing the available coolant to provide a better coolant coverage on the endwall surface, while keeping the associated aerodynamic losses small. The design of the new, improved cooling configuration was based on the understanding of endwall film-cooling described by Friedrichs et al. (1996, 1997). Computational fluid dynamics were used to predict the basic flow and pressure field without coolant ejection. Using this as a basis, the above-described understanding was used to place cooling holes so that they would provide the necessary cooling coverage at minimal aerodynamic penalty. The simple analytical modeling developed by Friedrichs et al. (1997) was then used to check that the coolant consumption and the increase in aerodynamic loss lay within the limits of the design goal. The improved cooling configuration was tested experimentally in a large-scale, low-speed linear cascade. An analysis of the results shows that the redesign of the cooling configuration has been successful in achieving an improved coolant coverage with lower aerodynamic losses, while using the same amount of coolant as in the datum cooling configuration. The improved cooling configuration has reconfirmed conclusions from Friedrichs et al. (1996, 1997): First, coolant ejection downstream of the three-dimensional separation lines on the endwall does not change the secondary flow structures; second, placement of holes in regions of high static pressure helps reduce the aerodynamic penalties of platform coolant ejection; finally, taking account of secondary flow can improve the design of endwall film-cooling configurations.

Introduction

An increase in the thrust and cycle efficiency of gas turbines can be achieved through higher turbine entry temperatures. Maintaining adequate life at these temperatures requires the development of materials and efficient cooling methods. One cooling method that has gained increasing importance is endwall film-cooling, where coolant air is discharged through discrete holes in the inner and outer endwalls (platforms) of a turbine blade passage. After leaving the holes, the coolant forms a protective layer between the hot mainstream gas and the surface that is to be protected.

The flow near the endwalls, into which the coolant is being ejected, is inherently three dimensional due to the presence of secondary flow. The turning of the mainstream flow within the blade passage produces a blade-to-blade pressure gradient that generates a transverse component of flow within the endwall boundary layers. The inlet boundary layer undergoes three-dimensional separation and is entrained into vortices that are formed near the endwall. A general overview of secondary flow in turbine blade passages is given by Sieverding (1984). Harrison (1989) and Friedrichs et al. (1996, 1997) describe the secondary flow structures in the turbine cascade used in this investigation.

The ejected coolant interacts with this three-dimensional flow. Friedrichs et al. (1996, 1997) found that this interaction not only influences the distribution of the coolant, and hence the cooling effectiveness, but also influences the generation of aerodynamic loss. They concluded that it is necessary to take the three-dimensional nature of the endwall flow into account in the design

of endwall film-cooling configurations. Coolant ejection locations have to be viewed with respect to the three-dimensional separation lines on the endwall, taking account of the fact that these can be changed due to upstream endwall coolant ejection. Previous investigations of endwall film-cooling, such as the ones by Blair (1974), Takeishi et al. (1990), Granser and Schulenberg (1990), Bourguignon (1985), Bario et al. (1990), Harasgama and Burton (1992), Jabbari et al. (1996), Goldman and McLallin (1977), and Sieverding and Wilputte (1981) support these conclusions.

Datum Cooling Configuration

The datum cooling configuration as investigated by Friedrichs et al. (1996, 1997) could have provided a complete coolant coverage of the endwall in the absence of secondary flows. In practice, large uncooled areas remained (see Fig. 1).

Design Goal. In this paper we will attempt to improve upon the datum cooling configuration by redistributing coolant to provide a better coolant coverage on the endwall surface, while keeping the associated aerodynamic losses small. This goal is to be achieved by applying the basic understanding described by Friedrichs et al. (1996, 1997) and by using numerical modeling and prediction tools in the design process.

The endwall film-cooling investigation presented here and by Friedrichs et al. (1996, 1997) was performed on a large-scale, low-speed, linear turbine cascade. The cascade consists of four blades with a true chord of 278 mm, a span of 300 mm, and a pitch of 230 mm. The flow enters the cascade at an angle of 40 deg and is turned through 105 deg. With the low aspect ratio and high turning angle, the blades produce strong secondary flows. These are stronger than the ones found in high-pressure turbine nozzle guide vanes with typical turning angles of 70 to 75 deg, and therefore allow a more detailed observation of the basic interac-
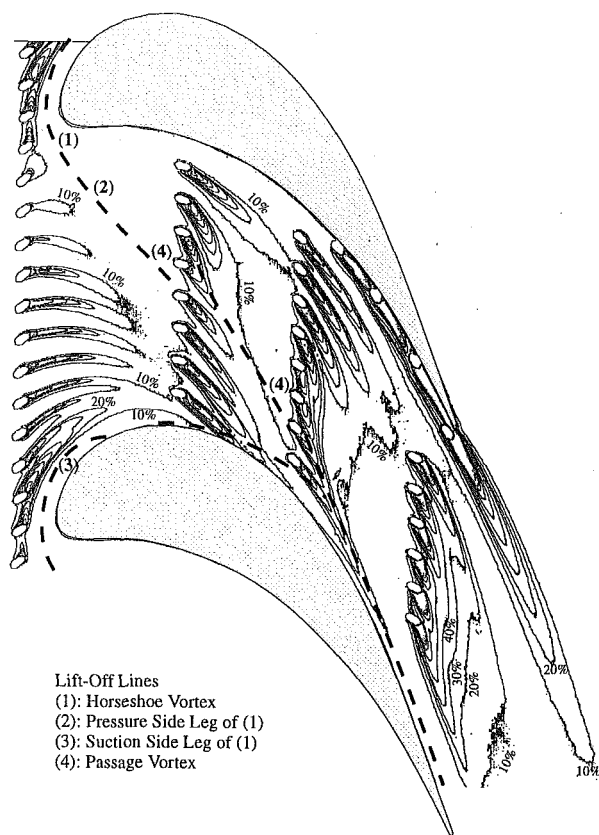
Fig. 1 Adiabatic film-cooling effectiveness on the endwall surface for the datum cooling configuration, at an inlet blowing ratio of $M_{inlet} = 1.0$ (Friedrichs et al., 1996, 1997)

Lift-Off Lines
(1): Horseshoe Vortex
(2): Pressure Side Leg of (1)
(3): Suction Side Leg of (1)
(4): Passage Vortex

cooling and radial inlet temperature profiles. Heat transfer coefficients are also low in this region, due to low velocities and reasonably two-dimensional flow.

Upstream of the three-dimensional separation lines, adequate coolant coverage at almost no aerodynamic penalty was already provided by the datum cooling configuration. If necessary, cooling performance could be increased by setting the holes in the row upstream of the leading edge at an angle to the local free stream to provide compound angle ejection. This will increase film-cooling effectiveness but will also increase aerodynamic losses due to enhanced mixing. Further improvements in cooling performance could be achieved by adding a second row of holes, staggered to the first one, or by using holes with flared exits (fan shaped holes).

Downstream of the Three-Dimensional Separation Lines. Downstream of the three-dimensional separation lines on the endwall there is a large need for cooling. Secondary flows, combined with radial inlet temperature profiles, result in hotter mainstream flow being swept down onto the endwall surfaces. Velocities are high and, together with the new, thin boundary layer formed downstream of the three-dimensional separation lines, this leads to elevated heat transfer coefficient levels.

Providing the necessary coolant coverage downstream of the three-dimensional separation lines has been shown to be more difficult, as there are interactions between the coolant ejected from the endwall and the secondary flow in the blade passage.

The improved cooling configuration aims to provide cooling to all of the endwall surface in the blade passage downstream of the three-dimensional separation lines. For this region, a uniform need for cooling is assumed. In practice there will be local variations in the need for cooling, which will have been determined by design experience and numerical predictions. As a result, there will be locally varying cooling design goals that can differ, even between hub and casing.

The design goal for the improved cooling configuration was to achieve a complete coolant coverage downstream of the three-dimensional separation lines at the same coolant consumption as that used by the holes of the datum cooling configuration located downstream of the three-dimensional separation lines. Furthermore, the aerodynamic penalty was to be less than or equal to that incurred by the "downstream" holes of the datum cooling configuration.

tions between endwall coolant ejection and the passage flow field. Details of the basic cascade without coolant ejection can be found from Harrison (1989).

In both the datum and the improved cooling configuration, coolant air is ejected from a common plenum chamber through cylindrical holes in one endwall of the cascade. In both cooling configurations, the holes have a diameter of 4 mm and eject at an angle of 30 deg to the surface. The thickness of the endwall is 12 mm, giving a length to diameter ratio of 6, typical of endwall film-cooling configurations.

The datum cooling configuration is shown in Fig. 1. Rows of holes are located at four axial positions: upstream of the leading edge, at 30, 60, and 90 percent axial chord. Four single holes are located near the blade pressure surface. All of the holes, except for the row at 90 percent axial chord and the hole at the trailing edge, eject in approximately the inviscid streamline direction. This cooling configuration might be expected to provide cooling to most of the endwall surface in the absence of secondary flow effects. In practice, Fig. 1 shows that large uncooled areas remain.

Upstream of the Three-Dimensional Separation Lines. The need for cooling upstream of the three-dimensional separation lines (lift-off lines) on the endwall is small. Inlet gas temperatures near the endwalls tend to be relatively cool as a result of combustor

Designing the Improved Cooling Configuration

The results from Friedrichs et al. (1996, 1997) have shown that in designing endwall film-cooling configurations, it is necessary to take account of the interactions between the coolant ejected from the endwall and the secondary flow in the blade passage. This requires the interactions to be understood and it requires a prediction of the strengths and locations of the secondary flow structures. In addition, a prediction of the hole exit static pressure field is required. This will allow coolant consumption to be determined and can be used to estimate the loss increase due to coolant ejection by performing a mixing calculation such as the one described by Friedrichs et al. (1997).

A structured mesh three-dimensional Navier–Stokes prediction is able to give reasonable predictions of the flow and pressure fields in the blade passage without coolant ejection. Here, BTOB3D, a three-dimensional Navier–Stokes code written by Dawes (1988), was used for such a computational simulation. It

---

Nomenclature

$M = (\rho_{coolant} \cdot V_{coolant})/(\rho_{free\text{-}stream} \cdot V_{free\text{-}stream})$
$\quad$ = local blowing ratio
M_{inlet} = inlet blowing ratio (blowing ratio of an idealized loss free coolant hole ejecting to inlet conditions)

p_{inlet} = cascade inlet static pressure
$P_{0\,inlet}$ = cascade inlet stagnation pressure

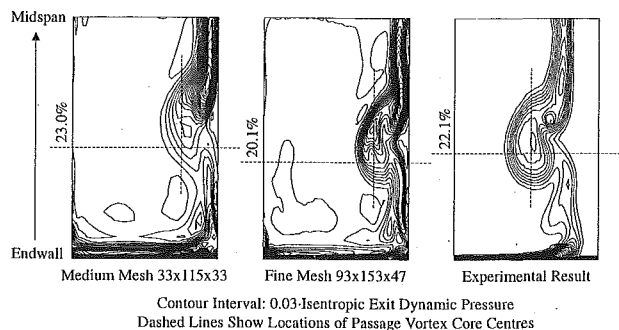$P_{0\,plenum}$ = coolant plenum stagnation pressure

Fig. 2 Comparison of predicted and measured stagnation pressure loss contours without coolant ejection at 123 percent axial chord

solves the Reynolds-averaged Navier–Stokes equations with a mixing length turbulence model on a structured grid H-Mesh. A time-marching procedure is used to advance the flow field from the initial guess to the converged solution. Local time stepping and multigrid acceleration are used to accelerate convergence to the steady state. The simulation is not time accurate, but only uses the time-stepping scheme to achieve a final steady-state solution. An adaptive artificial viscosity term is added to the governing equations to control odd-even point solution decoupling and to suppress oscillations in regions with strong pressure gradients. Details of the solution procedure and discretisation scheme are given by Dawes (1988).

Computational simulations of the cascade without film-cooling were performed using two mesh resolutions, a medium one with ~125,000 nodes (33 × 115 × 33) and a fine one with ~670,000 nodes (93 × 153 × 47).

The computational predictions were compared with measurements of the endwall static pressure field. The comparison showed good agreement for both the medium and the fine mesh resolutions, thus illustrating the expected mesh independence for these results.

A comparison of computationally and experimentally determined stagnation pressure loss contours in the traversing plane located at 23 percent axial chord downstream of the trailing edges is shown in Fig. 2. As the flow in the computational prediction was compressible, an effective stagnation pressure loss was calculated from the entropy increase across the cascade. Although the depth of the wake and the loss core are overpredicted by the computational simulation, the comparison in Fig. 2 shows very good agreement of the shape and position of the loss core that is associated with the passage vortex, thus giving confidence in the correct prediction of the strengths and locations of the secondary flow structures.

The endwall surface flow without coolant ejection, as predicted by using the medium mesh resolution, is visualised in Fig. 3 by tracing particle paths. The differences between the medium and fine mesh resolutions were small. In both cases the saddle point upstream of the leading edge, the three-dimensional separation lines on the endwall, and the endwall crossflow can clearly be seen. Comparisons with the experimental surface-flow visualization shown in Fig. 4 show that the location of the saddle point, the locations of the lift-off lines, and the endwall crossflow are predicted reasonably well.

As illustrated in Fig. 3, a prediction of the surface-flow field without coolant ejection can be used to estimate coolant trajectories from potential ejection locations. The coolant trajectories shown in Fig. 3 were drawn by hand, superimposed on a printout of the predicted endwall surface-flow field. When estimating coolant trajectories in this way, account has to be taken of the fact that the surface-flow field can change under the influence of the ejected coolant (see Friedrichs et al., 1996; 1997). For coolant ejection downstream of the three-dimensional separation lines on the endwall, the investigations of Friedrichs et al. (1996, 1997) have

Hand-Drawn Coolant Trajectory Estimates Superimposed on the Endwall Surface-Flow of a CFD Simulation Without Coolant Ejection
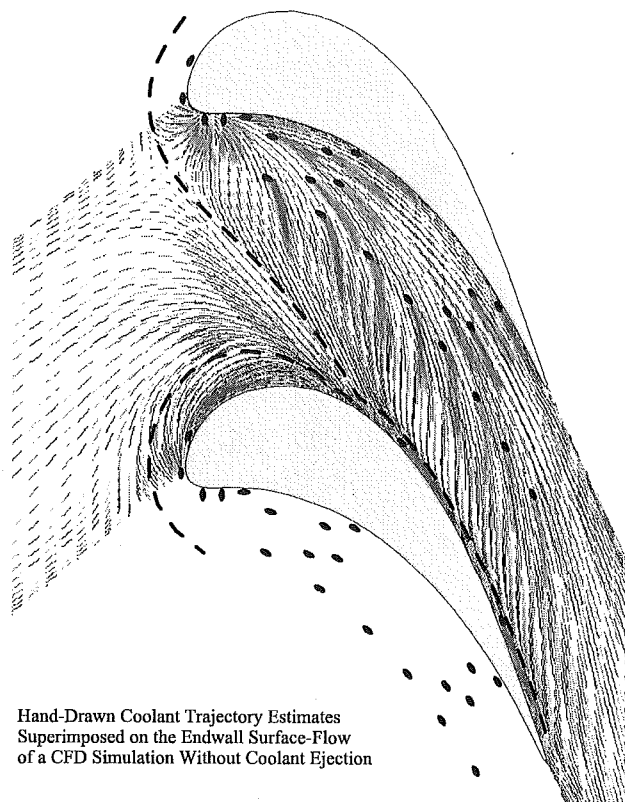
Fig. 3 Design of the improved cooling configuration by using an uncooled three-dimensional Navier–Stokes prediction of the endwall surface-flow to estimate coolant trajectories

shown that the strength of the endwall crossflow is reduced, but the locations of the three-dimensional separation lines remain unchanged.

The endwall surface-flow, as visualized in Fig. 3, can be divided into several distinct regions requiring individual cooling hole placements. A schematic of the regions used for the design of the improved cooling configuration is shown in Fig. 5.

The first region lies between the lift-off line of the leading edge horseshoe vortex and the leading edge itself. Cooling holes were
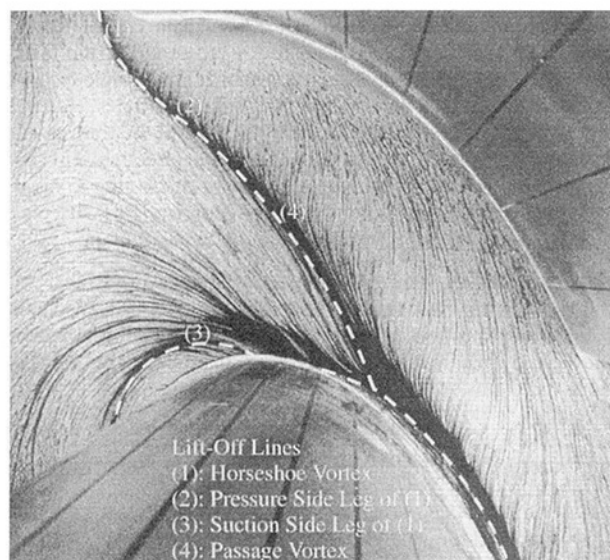
Fig. 4 Oil and dye surface-flow visualization on the endwall without coolant ejection (Friedrichs et al., 1996)
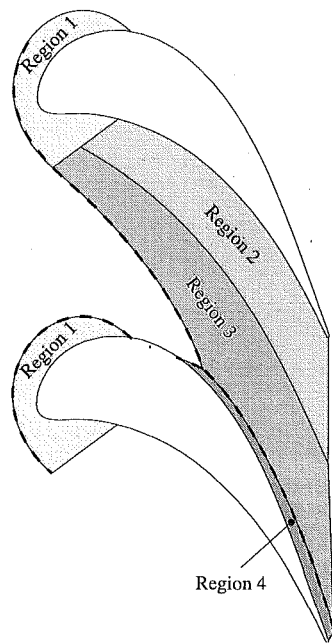
Fig. 5 Schematic of the regions of the endwall surface-flow requiring individual cooling hole placements (only downstream of the three-dimensional separation lines)

placed around the leading edge in an attempt to use the endwall surface flow to provide coolant coverage for this region.

The second region lies between the blade pressure surface and an imaginary line located halfway between the lift-off line of the main passage vortex and the blade pressure surface. The surface-flow in this region approximately follows the inviscid streamline direction, requiring a "classical" cooling hole arrangement. Two groups of holes with two staggered rows each are placed in this region to provide the necessary coolant coverage.

The third region lies between the imaginary line described above and the lift-off line of the main passage vortex. This region experiences strong endwall crossflow, with the surface-flow being turned from the inviscid streamline direction toward the blade suction surface. Several cooling holes are placed along the imaginary line that lies halfway between the lift-off line of the main passage vortex and the blade pressure surface. The strong endwall crossflow was expected to turn the ejected coolant toward the blade suction surface and so provide coolant coverage for this region. As there are no cooling holes upstream of this line, the endwall crossflow was expected to remain unchanged under the influence of coolant ejection.

The last region lies in the corner between the blade suction surface and the endwall. Two single holes are placed in this corner with the intention of feeding coolant into the corner vortex located here.

The same BTOB3D calculation that was used to predict the endwall surface-flow shown in Fig. 3 was also used to predict the endwall static pressure field. This prediction was used to determine the exit static pressures without coolant ejection for the holes of the improved cooling configuration.

In the design phase of the improved cooling configuration, coolant consumption was estimated by using the predicted hole exit static pressures without coolant ejection together with a discharge coefficient that was estimated based on the datum cooling configuration. The individual hole mass flows obtained from this estimate were used in a constant static pressure mixing calculation (as described by Friedrichs et al., 1997) to estimate the associated increase in aerodynamic loss. Both of these estimates were needed to determine whether the improved cooling configuration could be expected to meet the design goal with respect to coolant consumption and aerodynamic loss.

The final design of the improved cooling configuration is shown in Fig. 6. The coolant holes are mostly placed in regions of high static pressure in an attempt to minimize the aerodynamic penalty of coolant ejection. Appropriate hole spacings were judged based on the experience gained with the datum cooling configuration (see Fig. 1). Possible manufacturing constraints in real engine applications were not taken into account. The estimated coolant coverage, coolant consumption, and increase in aerodynamic loss promised to fulfil the design goal. Testing the improved coolant configuration confirmed the estimates; the results are given below.

Testing the Improved Cooling Configuration

The results presented in this paper and by Friedrichs et al. (1996, 1997) were produced with air being supplied to the common plenum chamber at approximately the same temperature as the free stream, resulting in a unity coolant-to-free-stream density ratio. The cascade was operating at a Reynolds number of 8.6×10^5 based on exit velocity and true chord and an exit Mach number of 0.02. Harrison (1989) measured the inlet boundary layer at a point half an axial chord upstream of the leading edge and found it to have a thickness of 18 mm, a displacement thickness of 2.6 mm, a momentum thickness of 1.9 mm, and a shape factor of 1.36. The inlet turbulence level of the free stream was 0.5 percent.

The improved cooling configuration was tested at two different coolant supply pressures. As in Friedrichs et al. (1997), the coolant supply pressure can be characterized by defining an inlet blowing ratio M_{inlet}. This is the blowing ratio that an idealized, loss free coolant hole would have when ejecting to inlet conditions. It is defined as:

$$M_{\text{inlet}} = \sqrt{\frac{P_{0_{\text{plenum}}} - p_{\text{inlet}}}{P_{0_{\text{inlet}}} - p_{\text{inlet}}}} \tag{1}$$
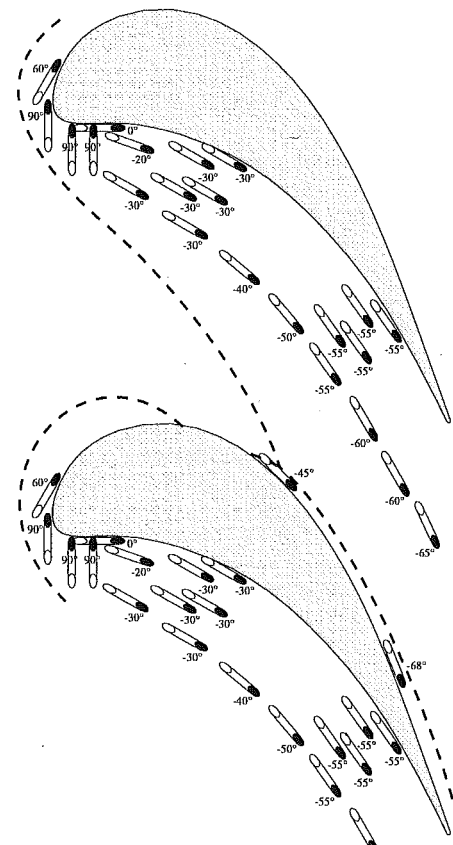

Fig. 6 Cooling hole positions and exit angles of the improved cooling configuration (black ellipses indicate hole exit locations on the blade passage side of the endwall)
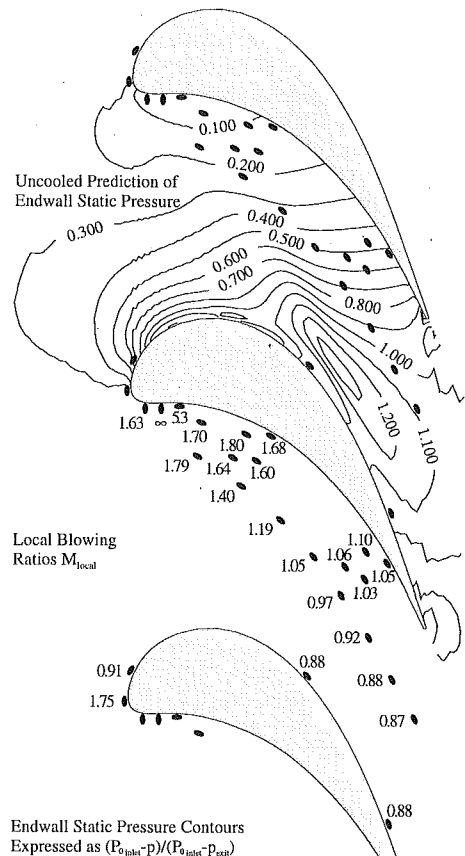
Fig. 7 Endwall static pressure contours predicted without coolant ejection and local hole blowing ratios for the improved cooling configuration at $M_{inlet} = 2.0$

Fig. 8 Oil and dye surface-flow visualization on the film-cooled endwall at an inlet blowing ratio of $M_{inlet} = 1.0$

The inlet blowing ratio M_{inlet} is different from the local blowing ratio M, which is defined individually for each hole as the coolant density–velocity product divided by the free-stream density–velocity product. Local blowing ratios M can be calculated from the total measured coolant massflow and the uncooled hole-exit static pressures, assuming a uniform discharge coefficient for all of the coolant holes.

At an inlet blowing ratio of $M_{inlet} = 1.0$, the coolant plenum pressure is equal to the inlet stagnation pressure. In this special case, all coolant holes operate with a local blowing ratio $M \approx 0.67$, a value equal to the average discharge coefficient at $M_{inlet} = 1.0$. Nonetheless, the individual hole mass flows vary with the endwall static pressure, increasing toward the cascade exit.

For all other values of M_{inlet} the local hole blowing ratios M will vary. Shown in Fig. 7 are the local blowing ratios determined for an inlet blowing ratio of $M_{inlet} = 2.0$. The local blowing ratios can be seen to vary with the endwall static pressure between $M = 0.87$ near the passage exit and $M \to \infty$ near the stagnation point. This is important, as the tendency of coolant jets to lift-off the surface increases with local blowing ratio (lift-off is usually associated with a blowing ratio greater than unity).

Coolant Consumption. The coolant consumption of the improved cooling configuration was to be approximately equal to that of the holes located downstream of the three-dimensional separation lines in the datum cooling configuration. In the datum cooling configuration, these were the holes at 90 percent axial chord, at 60 percent axial chord, in the pressure surface and endwall corner, and the four holes at 30 percent axial chord located next to the blade pressure surface.

At $M_{inlet} = 1.0$ (the design point) the coolant massflow through "downstream" holes of the datum cooling configuration was equal to 0.80 percent of the passage inlet massflow, if both endwalls had
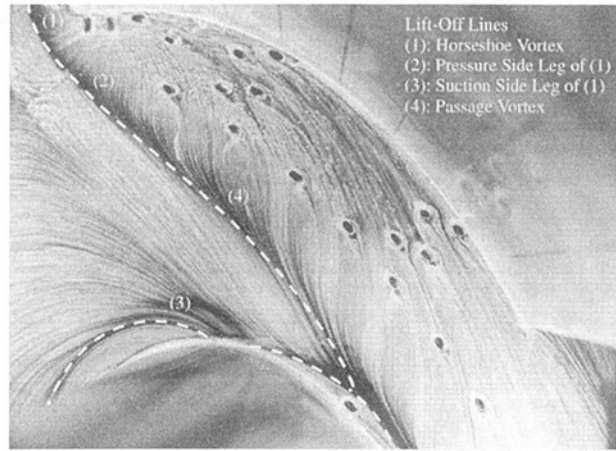
been cooled. At $M_{inlet} = 1.0$ the coolant massflow through the improved cooling configuration was measured to be 0.79 percent of the passage inlet massflow, if both endwalls had been cooled. Due to different flow characteristics, these values differ at higher inlet blowing ratios, illustrating that not only the design point has to be analyzed, but also deviations from this condition. At $M_{inlet} = 2.0$, the "downstream" holes of the datum cooling configuration consumed 1.35 percent and the holes of the improved cooling configuration consumed 1.62 percent of the passage inlet massflow, if both endwalls had been cooled.

Surface-Flow Visualization. Figures 8 and 9 show oil and dye visualizations of the endwall surface-flow under influence of coolant ejection. For ease of comparison, the lift-off lines determined from Figs. 8 and 9 are repeated in some of the following figures.

A comparison with the uncooled surface-flow shown in Fig. 4 illustrates that the three-dimensional separation lines on the endwall are not affected by the downstream ejection. Similarly, the crossflow in the region between the lift-off line of the main passage vortex and the row of holes in the middle of the blade passage (region 3) is not affected by coolant ejection. As a result, the row of holes in the middle of the blade passage can be expected to provide the intended coolant coverage.

Downstream of ejection, coolant ejection reduces the endwall crossflow and turns the endwall surface-flow toward the inviscid streamline direction. This was observed in the datum cooling
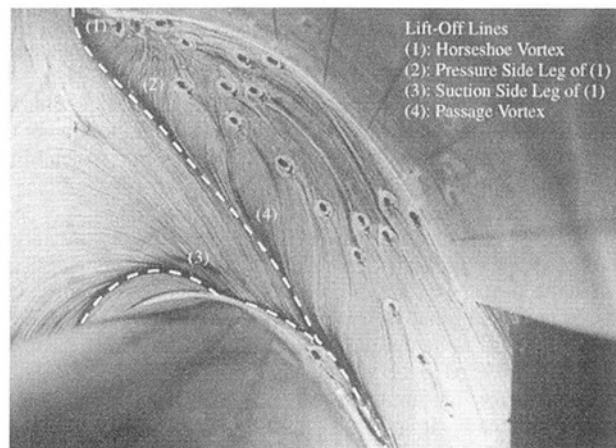

Fig. 9 Oil and dye surface-flow visualization on the film-cooled endwall at an inlet blowing ratio of $M_{inlet} = 2.0$
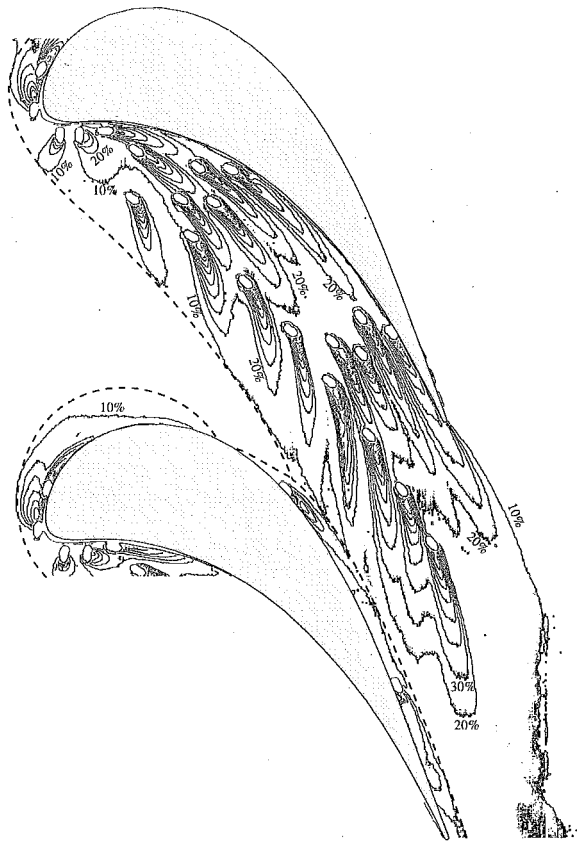
Fig. 10   Adiabatic film-cooling effectiveness on the endwall surface for the improved cooling configuration at $M_{\mathrm{inlet}} = 1.0$

configuration and can be observed in the region between the row of holes in the middle of the blade passage and the blade pressure surface (region 2). As the cooling design in this region assumes flow in approximately the inviscid streamline direction, the intended coolant coverage can be expected to be achieved.

Adiabatic Film-Cooling Effectiveness. The improved cooling configuration was intended to provide complete coolant coverage for the endwall surface downstream of the three-dimensional separation lines. To what extent this has been achieved can be seen in Figs. 10 and 11. These figures show the distributions of adiabatic film-cooling effectiveness on the endwall surface for inlet blowing ratios of $M_{\mathrm{inlet}} = 1.0$ and $M_{\mathrm{inlet}} = 2.0$, measured using the ammonia and diazo technique as described by Friedrichs et al. (1996). A comparison of the trailing edge regions of the upper and lower blades in Fig. 10 and Fig. 11 shows that only one passage was cooled. In order to reduce ammonia consumption, only the holes visible in Figs. 10 and 11 were ejecting coolant; the rest of the holes shown in Fig. 6 were closed off.

Figures 10 and 11 show that providing coolant coverage around the blade leading edge is difficult, especially in the vicinity of the stagnation point. Hole exit static pressures are high, resulting in low coolant mass flows and high local blowing ratios. As Fig. 7 illustrates, local blowing ratios in the vicinity of the stagnation point rise disproportionately with inlet blowing ratio. As a result, coolant jets in this region are likely to have lifted off the surface at $M_{\mathrm{inlet}} = 2.0$. Hole exit static pressures fall around the suction side of the blade leading edge. As a result, the area between the lift-off line of the suction side leg of the leading edge horseshoe vortex and the blade is reasonably well cooled, even at the higher inlet blowing ratio of $M_{\mathrm{inlet}} = 2.0$.

The two regions located between the lift-off line of the main passage vortex and the blade pressure surface are well cooled. Next to the blade pressure surface, the two double rows of holes

maintain a complete coolant coverage of above 10 percent adiabatic film-cooling effectiveness. The coolant trajectories from the holes in the middle of the blade passage are turned toward the blade suction surface and provide an almost complete coolant coverage of above 10 percent cooling effectiveness up to the lift-off line of the passage vortex. At the higher inlet blowing ratio the trajectories from the holes in the middle of the blade passage are not turned immediately, but follow the ejection direction in the vicinity of the holes. Nonetheless, they are eventually turned, and with the help of the endwall crossflow, the coolant is distributed to provide the necessary coolant coverage.

The blade suction surface and endwall corner is another region that is difficult to cool. Some cooling is provided from the two holes located in this region, but the levels of adiabatic film-cooling effectiveness are low and fall to under 10 percent for $M_{\mathrm{inlet}} = 1.0$. The shape of the coolant trajectories from the two holes located in this region indicates the presence of a corner vortex, which is probably responsible for the difficulties in cooling this region.

Axial variations of pitchwise averaged film-cooling effectiveness were determined for the improved configuration and the "downstream" holes of the datum cooling configuration, to enable quantitative comparisons to be made.

Unfortunately, such comparisons have to disregard any pitchwise variations in the cooling provided and the need for cooling. Similarly, an overall averaged value of film-cooling effectiveness can only be used for meaningful comparisons if a uniform need for cooling on the endwall is implicitly assumed. To take account of the local need for cooling, the endwall needs to be divided into regions that are defined by their local need for cooling. Averages for these regions can then be used for meaningful comparisons.

Here the cooling performance of the improved cooling configuration is compared to that of the datum cooling configuration. The region used for comparison is shown in Fig. 12; it is the endwall surface downstream of the three-dimensional separation lines, between the leading and trailing edge planes. When the pitchwise averages were performed for this region, the hole and blade cut-
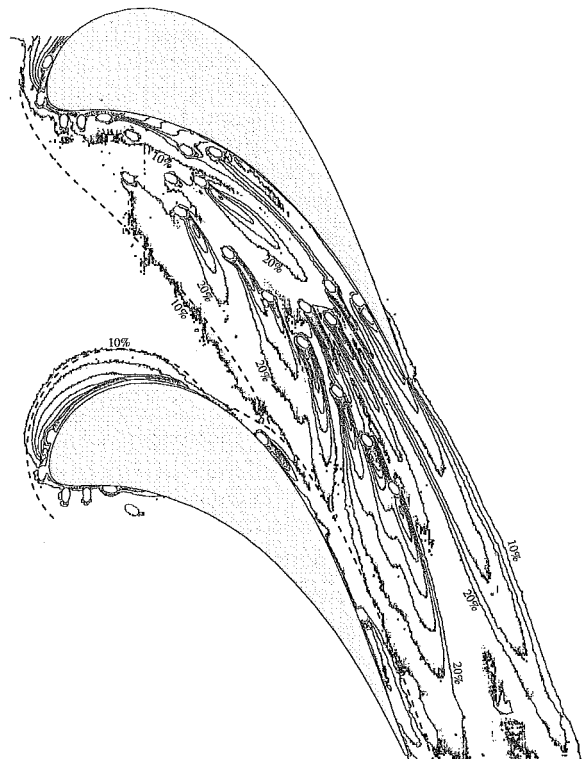

Fig. 11   Adiabatic film-cooling effectiveness on the endwall surface for the improved cooling configuration at $M_{\mathrm{inlet}} = 2.0$
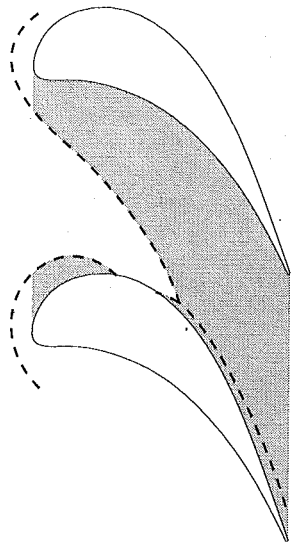
Fig. 12 Schematic of the endwall regions over which the averaging of film-cooling effectiveness was performed

outs and the endwall surface upstream of the three-dimensional separation lines were disregarded in the averaging process.

Comparisons of the axial variations of pitchwise-averaged film-cooling effectiveness for the improved configuration and the "downstream" holes of the datum cooling configuration are shown in Figs. 13 and 14. These axial variations were used to determine an overall average film-cooling effectiveness for the endwall surface downstream of the three-dimensional separation lines, between the leading and trailing edge planes.

The axial variations of the pitchwise averages reflect the fact that the improved cooling configuration no longer has the large, uncooled areas observed in the datum cooling configuration. The
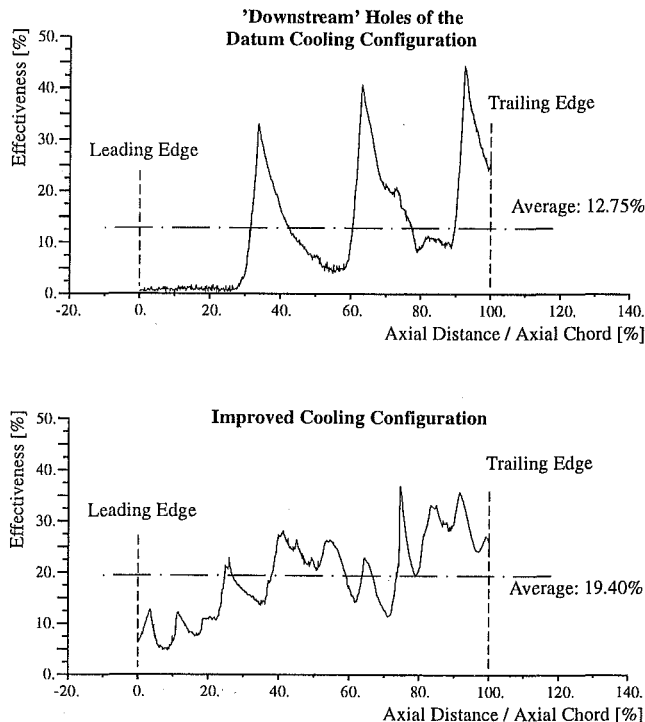

Fig. 13 Axial variation of pitchwise-averaged film-cooling effectiveness for the improved cooling configuration and the "downstream" holes of the datum configuration at M_{inlet} = 1.0
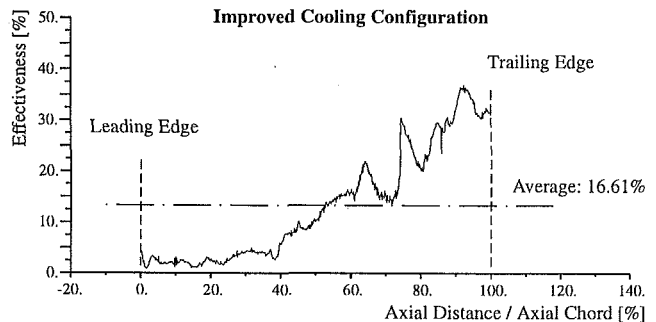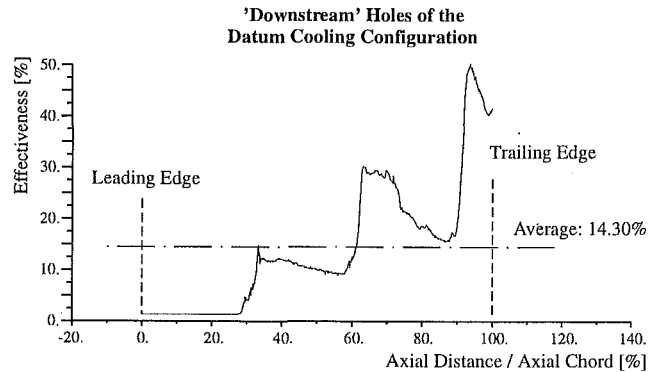

Fig. 14 Axial variation of pitchwise-averaged film-cooling effectiveness for the improved cooling configuration and the "downstream" holes of the datum configuration at M_{inlet} = 2.0

basic tendency remains: The pitchwise-averaged film-cooling effectiveness rises toward the rear of the blade passage.

At M_{inlet} = 1.0 the improved cooling configuration provides a significantly higher average cooling effectiveness (19.40 percent) than the "downstream" holes of the datum cooling configuration (12.75 percent). At M_{inlet} = 2.0 the difference between the two is smaller, but still the improved cooling configuration provides a higher average film-cooling effectiveness (16.61 versus 14.30 percent). The average cooling effectiveness of the datum cooling configuration increases with increasing inlet blowing ratio, whereas the improved cooling configuration displays a reduced average cooling effectiveness at the higher inlet blowing ratio. The axial variations of pitchwise averages show that this is due to a reduced effectiveness of the holes in the first half of the blade passage, as a result of the coolant having the tendency to lift off the surface.

To quantify cooling performance, the achieved levels of average film-cooling effectiveness have to be compared to the amount of coolant used. This has been done by dividing the cooling effectiveness by the coolant mass flow, expressed as percentage of the passage mass flow if both endwalls had been cooled, and is shown in Table 1.

A comparison of the values shown in Table 1 clearly shows the increased cooling performance of the improved cooling configuration. At the design condition of M_{inlet} = 1.0, the improved cooling configuration displays a cooling performance that is over

Table 1 Comparison of the average film-cooling effectiveness, per percent coolant mass flow, of the improved cooling configuration and the "downstream" holes of the datum configuration

Effectiveness per % Coolant Flow	Datum Configuration 'Downstream' Holes	Improved Cooling Configuration
M_{inlet} = 1.0	15.9%	24.6%
M_{inlet} = 2.0	10.6%	10.3%

Midspan / Endwall axis; panels labeled Uncooled (22.0%), $M_{inlet} = 1.0$ (22.7%), $M_{inlet} = 2.0$ (22.8%)

Contour Interval: 0.03·Isentropic Exit Dynamic Pressure
Dashed Lines Show Locations of Passage Vortex Core Centres

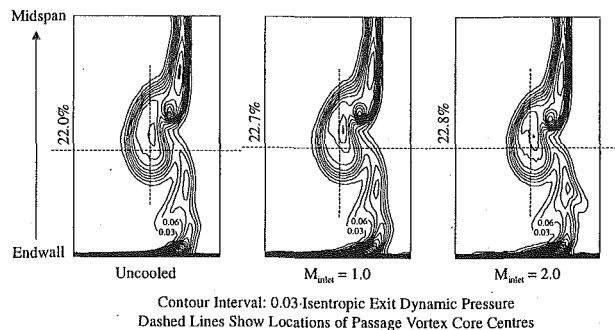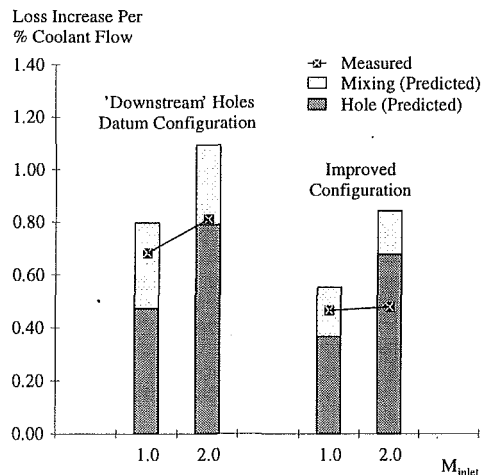**Fig. 15 Contours of stagnation pressure loss for all of the holes of the improved cooling configuration blowing simultaneously**

Fig. 16 Comparison of measured and calculated losses, per percent coolant massflow, for the two cooling configurations

50 percent higher than the "downstream" holes of the datum cooling configuration. At the higher inlet blowing ratio of 2.0, the cooling performances of the two cooling configurations are similar. Both cooling configurations are more efficient at the lower inlet blowing ratio.

The assessment of cooling performance given above was made under the assumption that the heat transfer coefficient distribution hardly changes between the two cooling configurations. Strictly speaking, one should compare heat flux levels, as they are responsible for the resulting metal temperatures. Nonetheless, adiabatic film-cooling effectiveness describes the distribution of the coolant and is considered to be the dominating parameter.

Aerodynamic Performance. The flow field downstream of the cascade was measured in an axial plane located at 23 percent axial chord downstream of the trailing edges. Measurements were performed with and without coolant ejection from the improved cooling configuration. The traversing plane for these aerodynamic measurements is the same as for the datum cooling configuration (see Friedrichs et al., 1997). It is shifted relative to the wake centerlines to capture the entire wake and loss core downstream of a blade. As this traversing plane covers fluid from two neighboring passages, both of these passages were cooled as shown in Fig. 6.

Figure 15 shows contours of stagnation pressure loss with and without coolant ejection. The uncooled measurements from Friedrichs et al. (1997) (shown in Fig. 2) were repeated to obtain a new datum, after the cascade was dismantled to install a new endwall with the improved cooling configuration. The uncooled contour plot in Fig. 15 shows only subtle differences to the uncooled contour plot in Fig. 2. The very small differences between the two illustrate excellent repeatability, even after a reassembly of the experimental setup.

A comparison of the loss contours and the spanwise positions of the passage vortex core centers with and without coolant ejection shows that coolant ejection from the improved cooling configuration has almost no effect on the secondary flow downstream of the cascade. As expected, the biggest differences can be observed in the endwall exit boundary layer which is slightly thickened due to coolant ejection.

Table 2 shows a comparison of the loss increase, per percent coolant flow, of the "downstream" holes of the datum cooling configuration and the improved cooling configuration. The improved cooling configuration displays lower loss increases, per

Table 2 Comparison of the loss increase, per percent coolant mass flow, of the "downstream" holes of the datum cooling configuration and the improved cooling configuration

Loss Increase per % Coolant Flow	Datum Configuration 'Downstream' Holes	Improved Cooling Configuration
$M_{inlet} = 1.0$	0.68%	0.44%
$M_{inlet} = 2.0$	0.81%	0.66%

percent coolant flow, at both inlet blowing ratios. The absolute loss increases, even at the higher coolant consumption of the improved cooling configuration at $M_{inlet} = 2.0$, are lower than for the "downstream" holes of the datum cooling configuration.

Figure 16 shows a comparison of the measured and predicted loss increases, per percent coolant flow, for the improved cooling configuration and the "downstream" holes of the datum cooling configuration. The predictions were performed by using the measured coolant mass flow, the predicted hole exit static pressures, and a constant static pressure mixing calculation as described by Friedrichs et al. (1997).

The measured loss increases are consistently lower than the sum of the hole and mixing losses, indicating some form of loss reduction in the blade passage. As the secondary flow structures were shown to be unchanged due to coolant ejection downstream of the three-dimensional separation lines, it has to be assumed that the difference is due to reduced loss production on the endwall surfaces and measurement and modeling uncertainties. (Uncertainty for the experimentally determined mixed-out loss coefficient is ±0.12 percent of the isentropic exit dynamic pressure.) Nonetheless, the predicted loss increases display the same trend as the measured loss increases; both indicate that the improved cooling configuration incurs less aerodynamic penalty than the "downstream" holes of the datum cooling configuration, thus fulfilling the aerodynamic part of the design goal.

Read-Across to Engine Design

The investigations described in this paper were performed in a low-speed, linear cascade. This is a simplified model of high-pressure turbine nozzle guide vanes in real engines. Many effects, such as inlet pressure and temperature profiles, inlet turbulence levels, radial pressure gradients, gaps and steps in the endwalls between neighboring vanes, transonic flow, endwall "hot spots" and coolant-to-mainstream density ratios are not modeled in the experiments. These effects will have their impact on the secondary flow structures, the endwall boundary layers, and the behavior of the coolant jets. Therefore, it is not the cooling design from Fig. 6 that should be transferred to the engine environment, but rather the basic design methodology presented in this paper.

Comparisons with engine geometries, or with other cooling configurations, should be performed relative to the secondary flow structures and the endwall surface flow. Comparisons with other operating conditions should be performed on the basis of momentum ratios. Analogous to the definition of the inlet blowing ratio M_{inlet} (Eq. (1)), an inlet momentum ratio I_{inlet} can be defined to characterize the coolant supply pressure. This would then be the

momentum ratio that an idealized loss-free coolant hole would have when ejecting to inlet conditions.

An example: For a gas turbine with an inlet Mach number of 0.15, a ratio of plenum to inlet stagnation pressure of 1.03, a ratio of specific heat capacities for the coolant of 1.36, and a ratio of specific heat capacities for the mainstream of 1.28, the inlet momentum ratio I_{inlet} is equal to 3.07. The corresponding experiments in this paper (with unity density ratio) would have had an inlet blowing ratio M_{inlet} of 1.75. For this hypothetical engine case, the design point would be at a higher inlet blowing (momentum) ratio and would perhaps require a cooling design that is more resistant to coolant jet lift-off in regions of high exit static pressure (for example through compound angle ejection or holes with shaped exits). The basic design methodology, however, would be the one presented in this paper, i.e., using an uncooled CFD prediction of the actual secondary flows, dividing the endwalls into regions, and then providing coolant to these regions dependent on the local need for cooling.

Conclusions

The redesign of the cooling configuration downstream of the three-dimensional separation lines on the endwall has been successful in achieving improved coolant coverage with lower aerodynamic losses, while using the same amount of coolant as in the datum cooling configuration.

The maximum benefits are achieved at the design point of M_{inlet} = 1.0. At the higher inlet blowing ratio of M_{inlet} = 2.0, the redesign has a coolant consumption that is higher than in the datum configuration. However, the aerodynamic penalty is reduced and an improved coolant coverage is obtained.

The design of the improved cooling configuration was based on the understanding and the numerical modeling described by Friedrichs et al. (1996, 1997). Computational fluid dynamics were used to predict the basic flow field and pressure field in the cascade without coolant ejection. Using this as a basis, the previously gained understanding was used to place cooling holes so that they would provide the necessary cooling coverage at minimal aerodynamic penalty. Simple analytical modeling was then used to check that the coolant consumption and the increase in aerodynamic loss lay within the limits of the design goal.

The improved cooling configuration exhibited interactions between the secondary flow and the ejected coolant similar to those observed by Friedrichs et al. (1996, 1997). It can be concluded that, first, coolant ejection downstream of the three-dimensional separation lines on the endwall does not change the secondary flow structures. Second, placement of holes in regions of high static pressure helps to reduce the aerodynamic penalties of platform coolant ejection. Finally, taking account of the secondary flow and the interactions between the ejected coolant and the secondary flow can improve the design of endwall film-cooling configurations.

References

Bario, F., Leboeuf, F., Onvani, A., and Seddini, A., 1990, "Aerodynamics of Cooling Jets Introduced in the Secondary Flow of a Low-Speed Turbine Cascade," ASME JOURNAL OF TURBOMACHINERY, Vol. 112, pp. 539–546.

Blair, M. F., 1974, "An Experimental Study of Heat Transfer and Film Cooling on Large-Scale Turbine Endwalls," ASME *Journal of Heat Transfer,* Vol. 96, pp. 524–529.

Bourguignon, A. E., 1985, "Etudes des Transferts Thermiques sur les Plates-Formes de Distributeur de Turbine avec et sans Film de Refroidissement," AGARD-CP-390, *Heat Transfer and Cooling in Gas Turbines.*

Dawes, W. N., 1988, "A Computer Program for the Analysis of Three Dimensional Viscous Compressible Flow in Turbomachinery Blade Rows," Whittle Laboratory, University of Cambridge.

Friedrichs, S., Hodson, H. P., and Dawes, W. N., 1996, "Distribution of Film-Cooling Effectiveness on a Turbine Endwall Measured Using the Ammonia and Diazo Technique," ASME JOURNAL OF TURBOMACHINERY, Vol. 118, pp. 613–621.

Friedrichs, S., Hodson, H. P., and Dawes, W. N., 1997, "Aerodynamic Aspects of Endwall Film-Cooling," ASME JOURNAL OF TURBOMACHINERY, Vol. 119, pp. 786–793.

Goldman, L. J., and McLallin, K. L., 1977, "Effect of Endwall Cooling on Secondary Flows in Turbine Stator Vanes," AGARD-CPP-214.

Granser, D., and Schulenberg, T., 1990, "Prediction and Measurement of Film Cooling Effectiveness for a First-Stage Turbine Vane Shroud," ASME Paper No. 90-GT-95.

Harasgama, S. P., and Burton, C. D., 1992, "Film Cooling Research on the Endwall of a Turbine Nozzle Guide Vane in a Short Duration Annular Cascade: Part 1—Experimental Technique and Results," ASME JOURNAL OF TURBOMACHINERY, Vol. 114, pp. 734–740.

Harrison, S., 1989, "The Influence of Blade Stacking on Turbine Losses," Ph.D. Thesis, University of Cambridge; see also Harrison, S., 1990, "Secondary Loss Generation in a Linear Cascade of High-Turning Turbine Blades," ASME JOURNAL OF TURBOMACHINERY, Vol. 112, pp. 618–624.

Jabbari, M. Y., Marston, K. C., Eckert, E. R. G., and Goldstein, R. J., 1996, "Film Cooling of the Gas Turbine Endwall by Discrete-Hole Injection," ASME JOURNAL OF TURBOMACHINERY, Vol. 118, No. 2.

Sieverding, C. H., 1984, "Recent Progress in the Understanding of Basic Aspects of Secondary Flows in Turbine Blade Passages," ASME *Journal of Engineering for Gas Turbines and Power,* Vol. 107, pp. 248–257.

Sieverding, C. H., and Wilputte, P., 1981, "Influence of Mach Number and Endwall Cooling on Secondary Flows in a Straight Nozzle Cascade," ASME *Journal of Engineering for Gas Turbines and Power,* Vol. 113, No. 2.

Takeishi, K., Matsuura, M., Aoki, S., and Sato, T., 1990, "An Experimental Study of Heat Transfer and Film Cooling on Low Aspect Ratio Turbine Nozzles," ASME JOURNAL OF TURBOMACHINERY, Vol. 112, pp. 488–496.

Curvature Effects on Discrete-Hole Film Cooling

M. K. Berhe[1]

S. V. Patankar

Department of Mechanical Engineering,
University of Minnesota,
Minneapolis, MN 55455

A numerical study has been conducted to investigate the effects of surface curvature on cooling effectiveness using three-dimensional film cooling geometries that included the mainflow, injection hole, and supply plenum regions. Three surfaces were considered in this study, namely, convex, concave, and flat surfaces. The fully elliptic, three-dimensional Navier–Stokes equations were solved over a body-fitted grid. The effects of streamline curvature were taken into account by using algebraic relations for the turbulent viscosity and the turbulent Prandtl number in a modified k–ε turbulence model. Computations were performed for blowing ratios of 0.5, 1.0, and 1.5 at a density ratio of 2.0. The computed and experimental cooling effectiveness results were compared. For the most part, the cooling effectiveness was predicted quite well. A comparison of the cooling performances over the three surfaces reveals that the effect of streamline curvature on cooling effectiveness is very significant. For the low blowing ratios considered, the convex surface resulted in a higher cooling effectiveness than both the flat and concave surfaces. The flow structures over the three surfaces also exhibited important differences. On the concave surface, the flow involved a stronger vorticity and greater mixing of the coolant jet with the mainstream gases. On the convex surface, the counterrotating vortices were suppressed and the coolant jet pressed to the surface by a strong cross-stream pressure gradient.

Introduction

Discrete-hole film cooling is used to protect turbine blades from the high temperature of combustion gases. In this cooling mechanism, coolant air is bled from the compressor and directed into the internal cavities of the turbine blades. This air not only circulates within these cavities, but also flows into the external blade surfaces through rows of discrete holes to form a blanket of protective cold film over these surfaces.

Over the past 30 years, discrete-hole film cooling has been the subject of many investigations. Much of this research was, however, conducted on flat-plate geometries. Although many important lessons have been obtained from these studies—such as the qualitative understanding of the effects of a number of film cooling variables—the quantitative applicability of these lessons to cooling of actual turbine blades is much less known. Turbine blades have curved surfaces that are known to introduce additional flow effects not present in flows over flat surfaces.

One of the effects of streamline curvature is to alter the magnitudes of the near-wall shear stresses. It has been found that turbulent shear stresses are damped on convex surfaces (Meroney and Bradshaw, 1975), and amplified on concave surfaces (Barlow and Johnston, 1988). It was also found that the changes in these stresses (due to curvature) are rather large. As discussed by Gibson (1978), in contrast to laminar flows where the fractional change in the shear stresses is of the same order of magnitude as δ/R, the change in the turbulent shear stresses is an order of magnitude greater. On strongly curved convex surfaces, for example, the shear stresses can be totally destroyed (So and Mellor, 1973; Gillis and Johnston, 1983). And, on concave surfaces, it is believed that the eddy structures are re-organized and new vortices created (Tani, 1962). The new vortices, known as the Taylor–Gortler vortices, are suspected to destabilize the boundary layer and greatly enhance mixing on these surfaces.

Schwarz et al. (1991) attempted to explain the effects of surface curvature in terms of two opposing forces. These are the cross-stream pressure gradients and the centrifugal forces. Cross-stream pressure gradients exist because the pressure near curved surfaces is different from that in the free stream. On convex surfaces, the near-wall pressure is lower than the free-stream pressure. The resulting pressure gradient pushes the flow toward the walls and suppresses the near-wall Reynolds stresses. On concave surfaces, the near-wall pressure is higher than the free-stream pressure. This gives rise to a pressure gradient that forces the flow away from the walls and destabilizes the boundary layer. As for the centrifugal forces, their effect is to push the flow toward the wall on concave surfaces, and away from the wall on convex surfaces. Furthermore, when the flow involves fluids of different velocities, as is the case in jet-in-crossflow, the strength of the centrifugal forces involved is also different. On a convex surface, high-speed fluids are pushed farther away from the wall than low-speed fluids. On a concave surface, high-speed fluids are drawn nearer to the wall than low-speed fluids.

The implication of this discussion is that the film cooling performances on curved surfaces differ from those on flat surfaces. On convex surfaces, the damping of the Reynolds stresses results in less mixing of the coolant jet with the mainstream gases. In the absence of deep penetration, this implies that the cooling effectiveness is higher on these surfaces. On concave surfaces, on the other hand, the more vigorous mixing of the coolant jet with the mainstream gases gives rise to a low cooling effectiveness on these surfaces.

These conclusions have been confirmed by several experimental studies. Mayle et al. (1977) conducted slot injection effectiveness studies on convex, concave, and flat surfaces for blowing rates of 0.5 to 0.9. They found that the cooling effectiveness was highest on the convex surface and lowest on the concave surface. Ito et al. (1978) conducted discrete-hole film cooling studies for blowing rates ranging from 0.2 to 2.98. They also found that, for low blowing ratio jets, the cooling effectiveness on the convex surface was higher than that on the concave surface. Furthermore, they showed that the convex, flat, and concave surfaces had comparable cooling effectiveness when $I \cos^2 \alpha$ was of the order of unity. Furuhama et al. (1983) and Kasagi et al. (1987) also experimen-

tally investigated full coverage film cooling on curved surfaces for blowing rates of 0.4 and 0.3–0.65, respectively. They also found that convex surfaces were easier to cool than flat or concave surfaces.

More recently, Schwarz (1986) studied discrete-hole film cooling over convex and concave surfaces using a variable radius of curvature. On convex surfaces, he found that the laterally averaged effectiveness initially increased with the momentum flux ratio, I, reached a maximum value near $I = 0.5$, and continuously decreased when I was further increased. On concave surfaces, on the other hand, the laterally averaged effectiveness monotonously increased when I was increased. Stone (1992) also conducted similar experiments and arrived at similar conclusions.

On the computational side, most of the three-dimensional discrete-hole film cooling studies conducted so far are limited to flat plate geometries. Examples are those of Berhe (1997), Leitner (1997), Leylek and Zerkle (1994), and Demuren et al. (1986). Recently, a few studies have also been conducted on curved surfaces specific to the leading edge of turbine blades. Examples are those of He et al. (1995), Lin et al. (1997), and Martin and Thole (1997). In these studies, the leading edge of a turbine blade was modeled in the form of a circular plate with a flat afterbody. However, these studies did not specifically investigate the effects of streamline curvature on film cooling performance. To our knowledge, no comparable computational study exists (as the present one) that investigated the effects of surface curvature on discrete-hole film cooling. The present numerical investigation was thus conducted: (1) to compute the cooling effectiveness for the three surfaces (convex, flat, and concave) and verify the findings of the above-cited experimental studies, (2) to study the differences and similarities of the flow structures over the three surfaces, and (3) to deduce the implication of these results to film cooling of the suction and pressure surfaces of actual turbine blades.
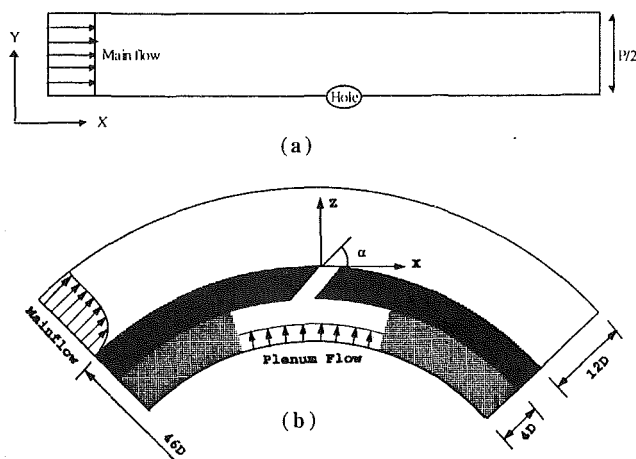

Fig. 1 The convex film cooling geometry: (a) top view, (b) front view

Test Cases Considered

As mentioned above, three types of film cooling geometries were considered in this study, namely, convex, flat, and concave geometries. Each film cooling geometry considered included the mainflow, injection hole, and supply plenum regions. Figure 1 shows the convex film cooling geometry studied. The radius of curvature of the test surface in this geometry was $46D$. The concave and flat film cooling geometries considered were the same as the convex geometry shown except that their test surfaces had radii of curvature of $-45D$ and ∞, respectively. These film cooling geometries were experimentally studied by Schwarz (1986) and Stone (1992). Hence, the results obtained from these studies will

Nomenclature

$C_1, C_2, \ldots$ = turbulence model constants
D = diameter of injection hole
DR = density ratio = ρ_j/ρ_∞
f = wall-damping function
H = plenum height
I = momentum flux ratio = $\rho_j U_j^2/\rho_\infty U_\infty^2$
k = turbulent kinetic energy
K_1, K_2 = constants in the Reynolds stress and C_μ equations
L = length of injection hole
M = blowing ratio = $\rho_j U_j/\rho_\infty U_\infty$
n = wall-normal distance
n^+ = normalized wall-normal distance = $n\sqrt{\tau_w/\rho}/\nu$
P = lateral spacing between holes (also static pressure)
P_{ij} = production rates of Reynolds stresses
P_k = production of turbulent kinetic energy
R = radius of curvature of the test surface
Ri_t = gradient Richardson number
S = curvature parameter
S_T = source term in the energy equation
t = temperature fluctuation (also time)
T = temperature

T_u = turbulence intensity level = $\sqrt{k/1.5}/U_\infty$
u = fluctuation of mean velocity
U = mean velocity
x_i, x_j = general coordinates in the i and j directions
X = horizontal distance measured from hole leading edge
Y = lateral distance measured from hole centerline plane
Z = vertical distance measured from hole leading edge
Δ = coefficient in the algebraic stress model
α = injection angle of coolant jet
β = eddy-viscosity coefficient
δ = boundary layer height
δ_{ij} = Kronecker delta
ϵ = dissipation rate of turbulent kinetic energy
γ = coefficient in mixing-length modification
ζ = wall-normal coordinate
η = local adiabatic film cooling effectiveness
η_c = centerline adiabatic film cooling effectiveness
$\bar{\eta}$ = laterally averaged film cooling effectiveness
μ = laminar viscosity
μ_t = turbulent viscosity
ν = laminar kinematic viscosity

ν_t = turbulent kinematic viscosity
ξ = streamwise coordinate
ρ = density
σ = laminar Prandtl number
σ_t = turbulent Prandtl number
τ = shear stress
ϕ = intermediate functions in Reynolds stress and heat flux equations
φ, λ = constants in the Reynolds stress equations
χ = eddy-diffusivity coefficient

Subscripts and Superscripts

aw = adiabatic wall temperature
c = at centerline plane
j = coolant jet
l = measured from the hole leading edge
t = measured from the hole trailing edge (also turbulent flow)
w = at the wall
ζ = along the wall-normal direction
ξ = along the streamwise direction
∞ = free-stream/mainstream quantity
$+$ = nondimensional symbol

Table 1 Value of flow and geometric variables

Variable	Value	Variable	value
U_∞	12 m/s	D	11.1 mm
T_∞	298 K	α	35°
DR	2.0	L/D	5.0
M	0.5, 1.0, 1.5	P/D	3.0

be used to validate the present numerical results. The flow and geomteric variables used are given in Table 1.

Calculation Procedure

Several numerical studies have shown that the presently popular two-equation turbulence models, such as the $k-\epsilon$ model, cannot model flows that have significant streamline curvature adequately. Although the $k-\epsilon$ turbulence model incorporates some effects of curvature (Luo and Lakshminarayana, 1997) and may thus be used for weakly curved flows, it is nevertheless considered inadequate for flows with mild to strong curvature. Over the years, various models have thus been proposed that incorporate the effects of surface curvature. They range from models that employ simple modifications to the length scale and/or the turbulent viscosity, to those with full Reynolds stress closures. In the following paragraphs, we will briefly review a few of these models.

Launder et al. (1977) modified the $k-\epsilon$ model by making the constant $C_{\epsilon 2}$ in the ϵ equation, Eq. (7), a function of the gradient Richardson number. This model essentially makes the length scale a function of streamline curvature, and was particularly designed for boundary layer type curved flows. Park and Chung (1989) also proposed a $k-\epsilon$-based model where both C_μ and $C_{\epsilon 2}$ are functions of streamline curvature. They applied this model to recirculating flows, such as flows over front- and backward-facing steps. A more advanced model was proposed by Gibson (1978) who, through a more rigorous analysis, derived algebraic expressions for both the Reynolds stresses and the eddy viscosity coefficient, C_μ. Leschziner and Rodi (1981) later simplified these expressions by assuming local equilibrium of turbulence. More recently, models employing full Reynolds stress closures have also been proposed as applicable for strongly curved surfaces. An example is the curvature model of Luo and Lakshminarayana (1997), which was applied for flows over a 90 deg bend.

In the present study, the shear-stress model of Leschziner and Rodi (1981) is used to close the momentum equations. For comparison purposes, the shear-stress models of Launder et al. (1977) and Park and Chung (1989) were also tested. The model of Launder et al. (1977) gave nearly identical results to that of Leschziner and Rodi (1981). However, the model of Park and Chung (1989) gave a slightly higher correction than the other two models. The simpler shear-stress model of Leschziner and Rodi (1981) was used because the streamline curvature considered in the present study is mild: $\delta/R \sim 0.03$, as opposed to $\delta/R \sim 0.2$ for moderate curvature, and $\delta/R \sim 1$ for strong curvature. Details of this shear-stress model are given shortly.

The effect of streamline curvature is not limited to the shear stresses; curvature also affects the heat fluxes. A notable work in this area is that of Gibson (1978) who studied the effect of streamline curvature on heat fluxes and formulated a heat-flux model that can be used in conjunction with the $k-\epsilon$ turbulence model. In this model, the effect of streamline curvature on heat fluxes is taken into account by making the Prandtl number a function of a curvature parameter. In the present study, this model is used to close the energy equation. Details of this model are given shortly. One of the main conclusions of Gibson (1978) was that streamline curvature does not affect the heat fluxes in the same

proportion as it affects the shear stresses: It affects the shear stresses more than the heat fluxes. We will further discuss this issue later in this paper.

Basic Equations. The governing equations for steady-state turbulent flows can be written in Cartesian tensor as follows.
Continuity:

$$\frac{\partial \rho U_j}{\partial x_i} = 0 \tag{1}$$

Momentum:

$$\frac{\partial \rho U_i U_j}{\partial x_j} = -\frac{\partial P}{\partial x_i} + \frac{\partial}{\partial x_j}\left[\mu\left(\frac{\partial U_i}{\partial x_j} + \frac{\partial U_j}{\partial x_i}\right) - \rho\overline{u_i u_j}\right] \tag{2}$$

Energy:

$$\frac{\partial \rho U_j T}{\partial x_j} = \frac{\partial}{\partial x_j}\left[\frac{\mu}{\sigma}\left(\frac{\partial T}{\partial x_j}\right) - \rho\overline{u_j t}\right] + S_T \tag{3}$$

The Reynolds stresses that appear in the momentum equation are modeled through Boussinesq's eddy viscosity concept, which assumes that the Reynolds stresses are proportional to the mean strain rates. That is,

$$-\overline{u_i u_j} = \nu_t\left(\frac{\partial U_i}{\partial x_j} + \frac{\partial U_j}{\partial x_i}\right) - \frac{2k}{3}\delta_{ij} \tag{4}$$

To close these equations, the turbulent eddy viscosity, ν_t, must first be determined. In the $k-\epsilon$ turbulence model, it is approximated by

$$\nu_t = C_\mu \frac{k^2}{\epsilon} \tag{5}$$

where the turbulent kinetic energy, k, and the dissipation rates, ϵ, are obtained by solving the following two transport equations:

$$\frac{Dk}{Dt} = \frac{\partial}{\partial x_j}\left(\frac{\nu_t}{\sigma_k}\frac{\partial k}{\partial x_j}\right) + P_k - \epsilon \tag{6}$$

$$\frac{D\epsilon}{Dt} = \frac{\partial}{\partial x_j}\left(\frac{\nu_t}{\sigma_\epsilon}\frac{\partial \epsilon}{\partial x_j}\right) + C_{\epsilon 1}\frac{\epsilon}{k}P_k - C_{\epsilon 2}\frac{\epsilon^2}{k} \tag{7}$$

P_k, the production of turbulent kinetic energy, is given by

$$P_k = \nu_t\left(\frac{\partial U_i}{\partial x_j} + \frac{\partial U_j}{\partial x_i}\right)\frac{\partial U_i}{\partial x_j} \tag{8}$$

The values of the empirical constants, σ_k, $C_{\epsilon 1}$, $C_{\epsilon 2}$, and σ_ϵ are, respectively, 1.0, 1.44, 1.92, and 1.3. The energy equation, Eq. (3), is closed using Reynolds analogy between heat and momentum transfer as follows:

$$-\overline{u_j t} = \frac{\nu_t}{\sigma_t}\frac{\partial T}{\partial x_j} \tag{9}$$

where σ_t is the turbulent Prandtl number, which is usually assumed to be approximately equal to 0.9. The problem with Eqs. (4) and (9) is that they do not adequately take the effects of surface curvature into account. Hence, new closure relations are needed so that the turbulent shear stresses and heat fluxes are functions of the streamline curvature. These relations are given in the following two subsections.

The Shear-Stress Model. As mentioned above, the shear-stress model used in the present investigation is that of Leschziner and Rodi (1981). To obtain the curvature-dependent turbulent viscosity used in this model, Leschziner and Rodi (1981) simplified the algebraic stress model of Gibson (1978) by assuming local equilibrium of turbulence and neglecting the transport terms. The

simplified algebraic equations for the Reynolds stresses are given by:

$$\frac{\overline{u_i u_j}}{k} = \frac{K_1}{\epsilon} P_{ij} - \delta_{ij} K_2 \qquad (10)$$

where

$$K_1 = \frac{1 - \varphi}{\lambda} \qquad (11)$$

$$K_2 = \frac{2}{3} \frac{(1 - \lambda - \varphi)}{\lambda} \qquad (12)$$

λ and φ are model constants equal to 1.5 and 0.6, respectively. For two-dimensional curved surfaces, P_{ij}, the production rates of the Reynolds stresses, are given by:

$$P_{\xi\xi} = -2\overline{u_\xi^2} \frac{\partial U_\xi}{\partial \xi} - 2\overline{u_\xi u_\zeta}\left(\frac{\partial U_\xi}{\partial \zeta} + \frac{U_\xi}{R_\xi} \right) \qquad (13)$$

$$P_{\zeta\zeta} = -2\overline{u_\zeta^2} \frac{\partial U_\zeta}{\partial \zeta} + 4\overline{u_\zeta u_\xi} \frac{U_\xi}{R_\xi} \qquad (14)$$

$$P_{\zeta\xi} = -2\overline{u_\zeta^2} \frac{\partial U_\xi}{\partial \zeta} + (2\overline{u_\xi^2} - \overline{u_\zeta^2}) \frac{U_\xi}{R_\xi} \qquad (15)$$

The most important stress in Eq. (10) is the shear stress $\overline{u_\xi u_\zeta}$. To isolate this stress and obtain its dependence on the rate of strain, Leschziner and Rodi (1981) further assumed that

$$\frac{\partial U_\zeta}{\partial \zeta} = \frac{\partial U_\xi}{\partial \xi} = 0 \qquad (16)$$

From Eqs. (10)–(15), the dominant shear stress then becomes

$$-\overline{u_\xi u_\zeta} = C_\mu^* \frac{k^2}{\epsilon} \left(\frac{\partial U_\xi}{\partial \zeta} - \frac{U_\xi}{R_\xi} \right) \qquad (17)$$

The turbulent viscosity coefficient, C_μ^*, is now given as a function of the gradient Richardson number, Ri_t, as,

$$C_\mu^* = \frac{-K_1 K_2}{[1 + 8K_1 Ri_t]} \qquad (18)$$

where

$$Ri_t = \frac{k^2}{\epsilon^2} S(1 + S)\left(\frac{\partial U_\xi}{\partial \zeta} \right)^2 \qquad (19)$$

$$S = \left(\frac{U_\xi}{R_\xi} \right) \Big/ \left(\frac{\partial U_\xi}{\partial \zeta} \right) \qquad (20)$$

S is the curvature parameter; it is positive for convex surfaces and negative for concave surfaces. In Eq. (18), $-K_1 K_2 = 0.13$, as compared to the "standard" value of 0.09 in the k–ϵ model. To avoid the slight inconsistency, Leschziner and Rodi (1981) suggested that this value be replaced by 0.09.

The effect of surface curvature is now evident in Eq. (18) by noting that, for convex surfaces, $Ri_t > 0$. This decreases C_μ^*, which in turn diminishes the eddy viscosity. For concave surfaces, on the other hand, $Ri_t < 0$ and, consequently, the eddy viscosity is increased.

The Heat-Flux Model. Most of the studies on streamline curvature have been conducted on modeling of the Reynolds stresses. And, so far, the attention given to the associated heat transfer problem is very little. To close the energy equation, the conventional practice has been to use the Reynolds analogy with an assumed constant Prandtl number. However, as the following analysis shows, the Prandtl number is itself a strong function of streamline curvature. In other words, in the presence of a variable

streamline curvature, we cannot assume a fixed relationship between the turbulent viscosity and the turbulent diffusivity. To obtain a more accurate prediction of heat transfer on curved surfaces, therefore, we need to have a more elaborate modeling of the heat fluxes.

In this paper, we adopt the algebraic heat-flux model of Gibson (1978) and arrive at a gradient-transfer expression. This expression links the dominant heat flux with the main temperature gradient using a Prandtl number which is a function of a curvature parameter, S. For two-dimensional thin shear layers (and assuming local equilibrium of turbulence), the algebraic expressions for the turbulent heat fluxes are (Gibson, 1978),

$$\overline{u_\xi t} = -\phi_t \frac{k}{\epsilon} \overline{u_\xi u_\zeta} \frac{\partial T}{\partial \zeta} - \phi_t' \frac{k}{\epsilon} \overline{u_\xi t} \frac{\partial U_\xi}{\partial \zeta} \qquad (21)$$

$$\overline{u_\zeta t} = -\phi_{t_1} \frac{k}{\epsilon} \overline{u_\zeta^2} \frac{\partial T}{\partial \zeta} + \phi_{t_1}' \frac{k}{\epsilon} \overline{u_\xi t} \frac{\partial U_\xi}{\partial \zeta} \qquad (22)$$

where

$$\phi_t = \frac{1}{C_{1t}} \qquad (23)$$

$$\phi_t' = \phi_t (1 - C_{2t})(1 + S) \qquad (24)$$

$$\phi_{t_1} = \frac{\phi_t}{(1 + C_{1t}' f \phi_t)} \qquad (25)$$

$$\phi_{t_1}' = 2\phi_{t_1} S(1 - C_{2t}) \qquad (26)$$

Based on heat transfer data from turbulent plane flows, Gibson and Launder (1978) determined the model constants C_{1t}, C_{2t}, and C_{1t}' to be 3.0, 0.33, and 0.5, respectively. To express the dominant heat flux, $\overline{u_\xi t}$, as a function of the cross-stream temperature gradient, $\partial T/\partial \zeta$, we need the expressions for the normal and shear stresses that appear in the Eqs. (21)–(26). Again, from Gibson (1978), these are given by:

$$\frac{\overline{u_\xi^2}}{k} = \frac{2}{3}(1 + \phi_4) + \phi_5 \frac{\overline{u_\zeta^2}}{k} + \phi_3 \frac{2S}{1 - S} \qquad (27)$$

$$\frac{\overline{u_\zeta^2}}{k} = \frac{2}{3} \frac{1 - \phi_2}{1 + 2\phi_5} - \frac{2S}{1 - S} \frac{\phi_7}{1 + 2\phi_5} \qquad (28)$$

$$-\frac{\overline{u_\xi u_\zeta}}{k} = \left(\frac{\beta}{1 - S} \frac{\overline{u_\zeta^2}}{k} \right) \qquad (29)$$

where

$$\phi_2 = (1 - C_2 + 2C_2' C_2 f)/\Delta \qquad (30)$$

$$\phi_3 = (2 - 2C_2 + 2C_2' C_2 f)/\Delta \qquad (31)$$

$$\phi_4 = (2 - 2C_2 + C_2' C_2 f)/\Delta \qquad (32)$$

$$\phi_5 = C_1' f/\Delta \qquad (33)$$

$$\phi_7 = (2 - 2C_2 + 4C_2' C_2 f)/\Delta \qquad (34)$$

$$\beta = \phi(1 - \gamma S) \qquad (35)$$

$$\phi = (1 - C_2 + 1.5C_2' C_2 f)/(\Delta + 1.5f C_1') \qquad (36)$$

$$\Delta = C_1 - 1 \qquad (37)$$

$$f = \frac{1 - \gamma S}{1 - S} \qquad (38)$$

$$\gamma = 2\frac{\overline{u_\xi^2}}{\overline{u_\zeta^2}} - 1 \qquad (39)$$

The constants C_1, C_2, C_1', and C_2' were determined from plane-flow data and are 1.8, 0.6, 0.5, and 0.3, respectively. From Eqs. (10), (15), (28), and (29), the gradient equation for the shear stress, $\overline{u_\xi u_\zeta}$, now becomes

$$\overline{u_\xi u_\zeta} = -\beta \frac{k}{\epsilon} \overline{u_\zeta^2} \frac{\partial U_\xi}{\partial \zeta} \qquad (40)$$

Similarly, from Eqs. (21) and (22) and (40), the heat flux-gradient equation can be obtained as

$$\overline{u_\zeta t} = -\chi \frac{k}{\epsilon} \overline{u_\zeta^2} \frac{\partial T}{\partial \zeta} \qquad (41)$$

where

$$\chi = \frac{\phi_{t1} - a\phi_t\phi_{t1}'}{1 + a\phi_t'\phi_{t1}'} \qquad (42)$$

$$a = \frac{k}{\overline{u_\zeta^2}(1 - S)} \qquad (43)$$

Combining Eqs. (40) and (41), the turbulent Prandtl number, σ_t, can now be expressed as

$$\sigma_t = \frac{\beta}{\chi} = \frac{\beta + a\phi_t'\phi_{t1}'}{\phi_{t1} - a\phi_t\phi_{t1}'} \qquad (44)$$

In the results and discussion section, we will see the strong variation of the turbulent Prandtl number, σ_t, with the curvature parameter, S, and how it affects the cooling effectiveness. Before we do so, however, we will briefly discuss other computational details such as the solution methodology, discretization, boundary conditions, and convergence criteria used in these computations.

Solution Methodology. The fully elliptic, three-dimensional Navier–Stokes equations were solved over a body-fitted grid using the control volume methodology described in Patankar (1980). Turbulence closure was achieved using the modified k–ϵ model described above, where the shear stresses are functions of streamline curvature as given by Eqs. (17) and (18). The energy equation was solved using the Reynolds analogy along with a curvature-dependent Prandtl number given by Eq. (44). The wall function approach described in Launder and Spalding (1974) was used. This is because the surface curvature considered in the present study is mild ($\delta/R \sim 0.03$). As discussed by Patel and Sotiropoulos (1997), except for strongly curved flows ($\delta/R \sim 1$), the assumption of local equilibrium and the law of the wall remain unaffected by curvature. This practice was found adequate, for example, in Rodi and Scheuerer (1983) for flows over moderately curved surfaces ($\delta/R \sim 0.2$).

Discretization. The computational domains were discretized into approximately 130/15/85 cells in the $X/Y/Z$ directions. The near-orthogonal grid used on/inside the surface and volume elements of these domains was generated by solving two- and three-dimensional Poisson equations, respectively. Grid stretching (or contraction) was limited to about 30 percent. n^+ values of about 50, 30, and 20 were used inside the main flow, the injection hole, and the plenum, respectively. A sample grid showing the vicinity of the injection hole is shown in Fig. 2.

To check for grid independence, grid sizes as large as 200 and 350 percent of the original number of cells were considered. The observed difference in cooling effectiveness were, however, limited to about 3 and 4 percent, respectively. The velocity profiles (discussed later in this paper) showed no discernible differences. In light of the marginal gain in accuracy and the very high cost of computation associated with the finer grids, the first grid was used in all of the computations reported in this paper. It must also be noted that, as reported in Schwarz (1986), the experimental errors themselves were around 5 percent.
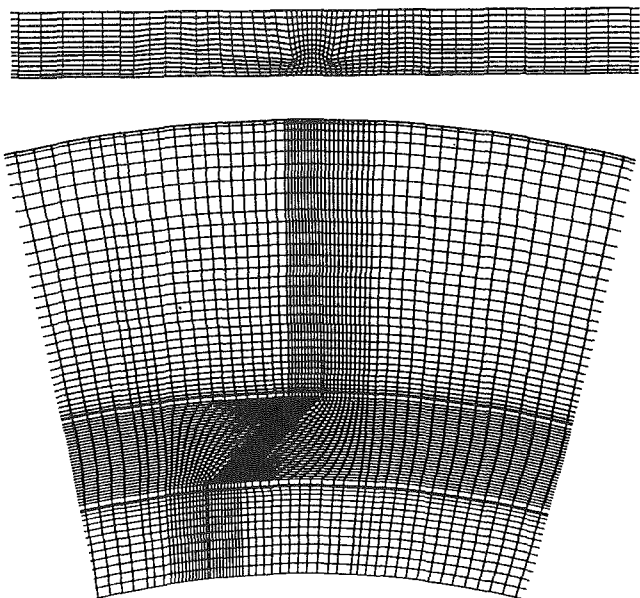

Fig. 2 A partial view of the convex grid in the vicinity of the injection hole (centerline plane)

Boundary Conditions. In the mainstream, the inlet velocity profile was prescribed to match the boundary layer height and the displacement thickness (at the point of injection) used in the experimental studies of Schwarz (1986) and Stone (1992). In these studies, the boundary layer height was $4D$ on both the convex and concave surfaces. The displacement thicknesses were $0.4D$ and $1.0D$ on the convex and concave surfaces, respectively. It must be noted that these quantities were measured in the absence of coolant injection.

The temperature and turbulence intensity levels at inlet to the mainstream were 298 K and 0.2 percent, respectively. At plenum inlet, the turbulence intensity was also 0.2 percent, and the temperature and velocity fields were calculated to satisfy the prescribed density ratio and blowing ratio, respectively. The turbulent kinetic energy and dissipation rates were calculated from Eqs. (45) and (46). Since the free-stream turbulence involved in this study was very low, however, the calculation results were found to be insensitive to these specifications. This was also found to be the case in a recent study by He et al. (1995):

$$k = 1.5 T_u^2 U_\infty^2 \qquad (45)$$

$$\epsilon = \frac{20 c_\mu^{3/4} k^{3/2}}{D} \qquad (46)$$

Symmetry conditions were imposed on the two bounding lateral planes. The top boundary in the mainstream was made a wall where the wall-normal velocity and the gradients of all other variables were zero. At the outflow boundary, a no-flux condition was imposed for all of the variables.

Initialization. As has been found by previous investigators, one of the main problems in these computations was achieving satisfactory convergence, especially when the blowing ratio is high. This is due to the coupling of the above-mentioned three regions (mainflow, injection hole, and plenum) and the strong interaction that exists between the coolant jet and the mainstream. Many test runs were therefore conducted to study the convergence behavior of these computations and to establish an initialization procedure and a set of relaxation factors that gave satisfactory convergence. In all of the tests reported in this paper, a relaxation factor of 0.6 was used for the three velocity components and the

temperature, and 0.4 was used for k, ϵ, and μ_t. Pressure was not relaxed.

For a blowing ratio of 0.5, the domain was initialized as follows. In the interior of all flow regions, k and ϵ were initialized by using Eqs. (45) and (46) and a high turbulence level of about 20 percent. In the main flow, the streamwise mean velocity and temperature were assigned their respective free-stream values. The lateral and vertical velocities were made zero. In the plenum and injection hole, uniform vertical velocities were assigned depending on the blowing ratio and the local flow area under consideration, and the temperature was assigned the specified coolant temperature.

For the higher blowing ratios, $M = 1.0$ and 1.5, the domain was initialized using a converged solution at the lower blowing ratios. In particular, the velocity field was initialized by scaling up the velocity field of the lower blowing ratio. Such a scaling of the velocity field facilitated convergence in these computations and (unlike in previous computational studies) enabled us to march in blowing ratio increments of 0.5.

Convergence Criteria. To establish convergence, both the normalized residuals and the change in cooling effectiveness were monitored. Computations were assumed converged when the normalized residuals were of the order of $1e$-4. In a typical computation at a blowing ratio of 0.5, convergence was achieved in about 350 iterations. One iteration took about 45 seconds of CPU time in a 9 processor, CRAY C90 Supercomputer used in these computations. For blowing ratios of 1.0 and 1.5, convergence was achieved in about 250 iterations, starting from a converged solution at the lower blowing ratio.

Calculation of the Adiabatic Effectiveness. The adiabatic film cooling effectiveness, η, was calculated using Eq. (47). To obtain the adiabatic wall temperature, T_{aw}, a very low conductivity ($1e$-10) was specified inside the test plate. The laterally averaged effectiveness was calculated from Eq. (48).

$$\eta = \frac{T_{aw} - T_\infty}{T_j - T_\infty} \qquad (47)$$

$$\bar{\eta} = \frac{\Sigma(\eta \cdot \Delta y)}{\Sigma(\Delta y)} \qquad (48)$$

Results and Discussion

In this section, we first show the variations of σ_t and C_μ^* on the convex and concave surfaces considered. We then compare the computed and measured cooling effectiveness distributions on these surfaces. A three-way comparison of the computed cooling effectiveness distributions for convex, flat, and concave surfaces is then presented. Finally, we discuss the computed velocity profiles in cross-stream-planes for the three surfaces.

The Variations of σ_t and C_μ^*. Figure 3 shows the variation of σ_t with the curvature parameter, S, as given by Eq. (44). On the convex surface, σ_t is lower than its nominal value of about 0.9; on the concave surface, it is higher. Assuming that μ_t is constant, larger σ_t implies that the thermal diffusivity (μ_t/σ_t) is lower, and smaller σ_t implies that the thermal diffusivity is higher. However, as Fig. 4 shows, μ_t also changes with surface curvature: on convex surfaces it is smaller, and on concave surfaces it is larger (than its flat plate values). In other words, both σ_t and μ_t change in the same direction with surface curvature. As Gibson noted (1978), this means that the turbulent heat transfer is less affected by curvature than is the shear stress.

Figure 4 shows the variations of both σ_t and C_μ^* on the convex and concave surfaces. On the convex surface, σ_t decreases from its near-wall value of about 0.9 to a low value of about 0.4 farther from the wall. On the concave surface, it increases from about 0.9 near the wall to as high as 1.5 farther from the wall. C_μ also shows similar variations; it can be as low as 0.04 on the convex surface,
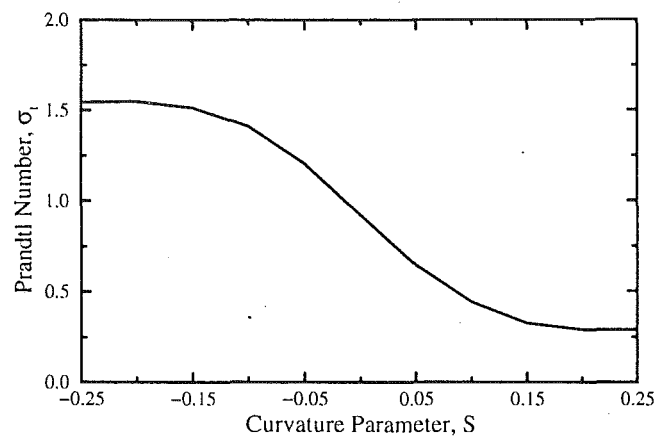

Fig. 3 The variation of the turbulent Prandtl number, σ_t, with the curvature parameter, S

or as high as 0.2 on the concave surface. Note that its nominal value is 0.09.

The Adiabatic Effectiveness. Figures 5 and 6 show the adiabatic effectiveness distributions on the convex surface for $M = 0.5$ and $M = 1.0$, respectively. In each figure, the computed values are compared against the experimental results of Schwarz (1986). It is evident that the centerline effectiveness is predicted very well. The plot shows an accurate representation of the rapid decrease of the adiabatic effectiveness in the near-field, followed by a slow decrease of effectiveness in the far-field. As for the laterally averaged effectiveness, although the far-field predictions are good, the near-field values are
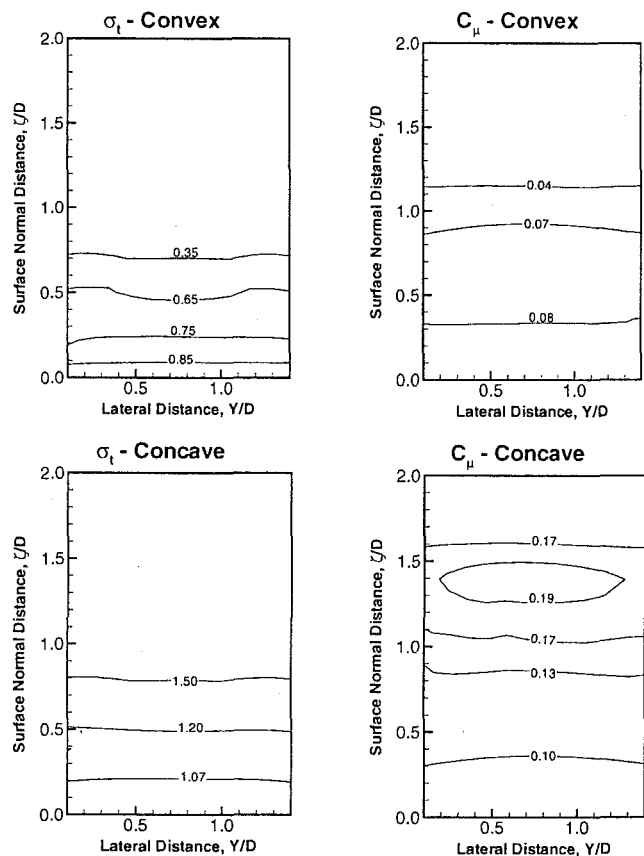

Fig. 4 The distributions of σ_t and C_μ^* on the convex and concave surfaces
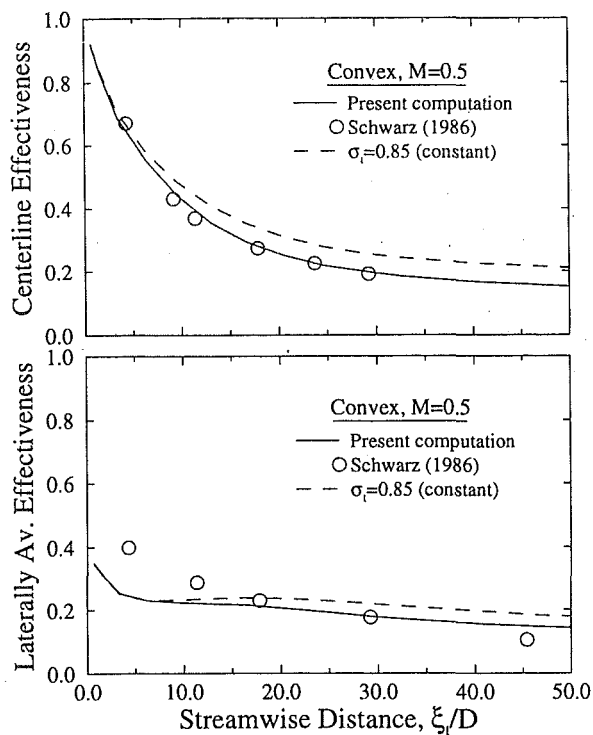
Fig. 5 Computed and experimental effectiveness distributions for the convex surface ($M = 0.5$)
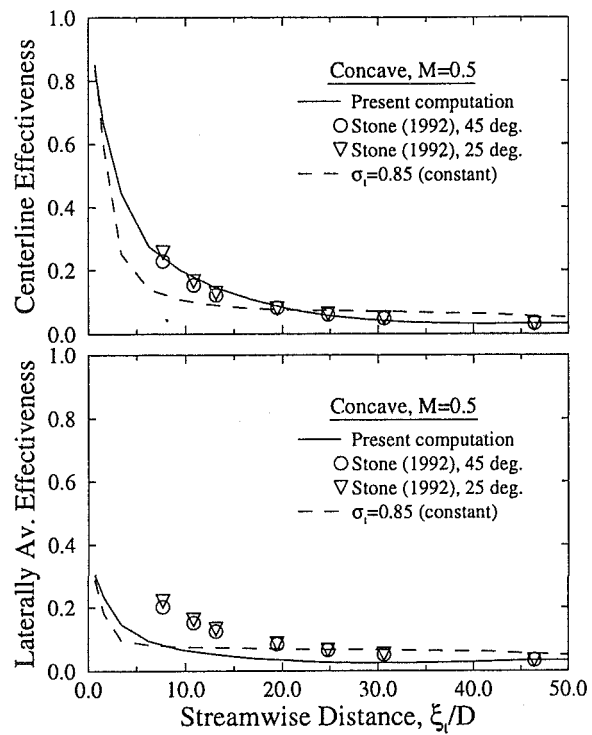

Fig. 7 Computed and experimental effectiveness distributions for the concave surface ($M = 0.5$)

underpredicted. This can be attributed to the isotropic nature of the modified $k-\epsilon$ turbulence model used in this study. Experiments by Wang et al. (1996) and preliminary investigation by the present authors have shown that, near the injection hole, the near-wall lateral diffusivities may be an order of magnitude larger than the values predicted by isotropic models. Work is

currently underway to further investigate this issue using anisotropy turbulence models.

The dashed lines in Fig. 5 show the cooling effectiveness distribution obtained using a constant Prandtl number ($\sigma_t = 0.85$). It is obvious that the adiabatic effectiveness values obtained using the new, curvature-dependent σ_t are lower than those ob-
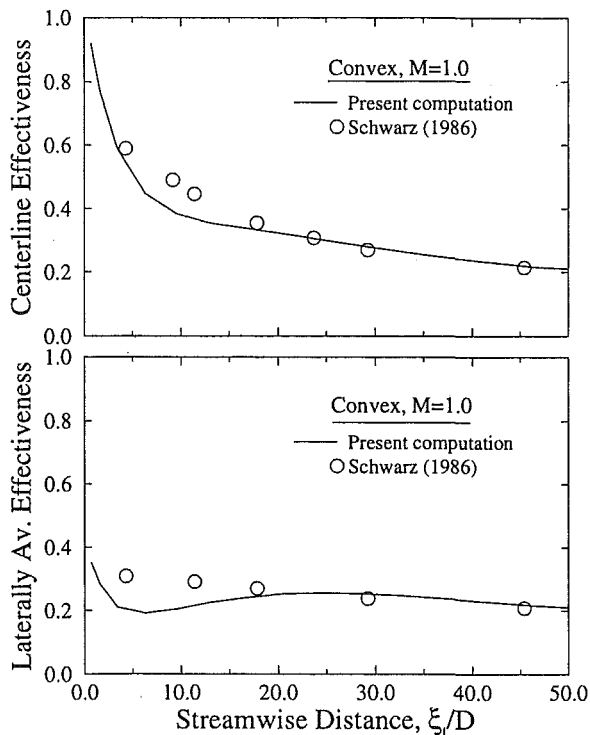

Fig. 6 Computed and experimental effectiveness distributions for the convex surface ($M = 1$)
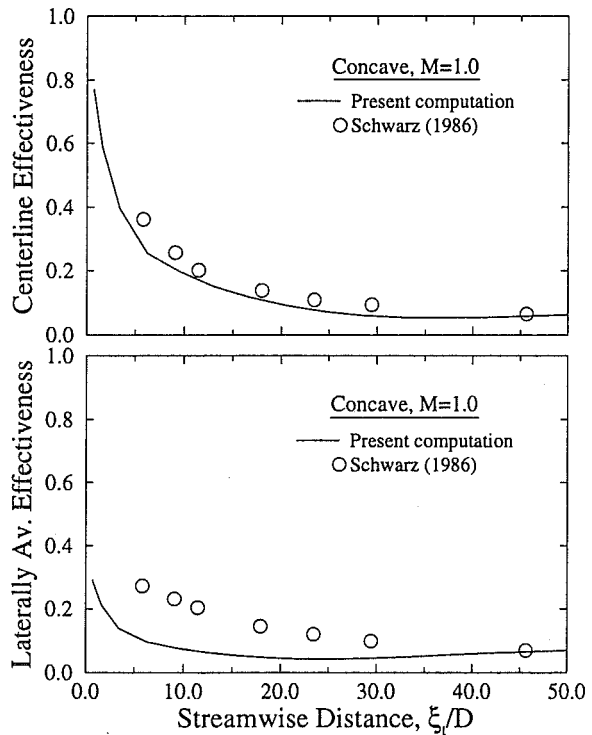

Fig. 8 Computed and experimental effectiveness distributions for the concave surface ($M = 1$)
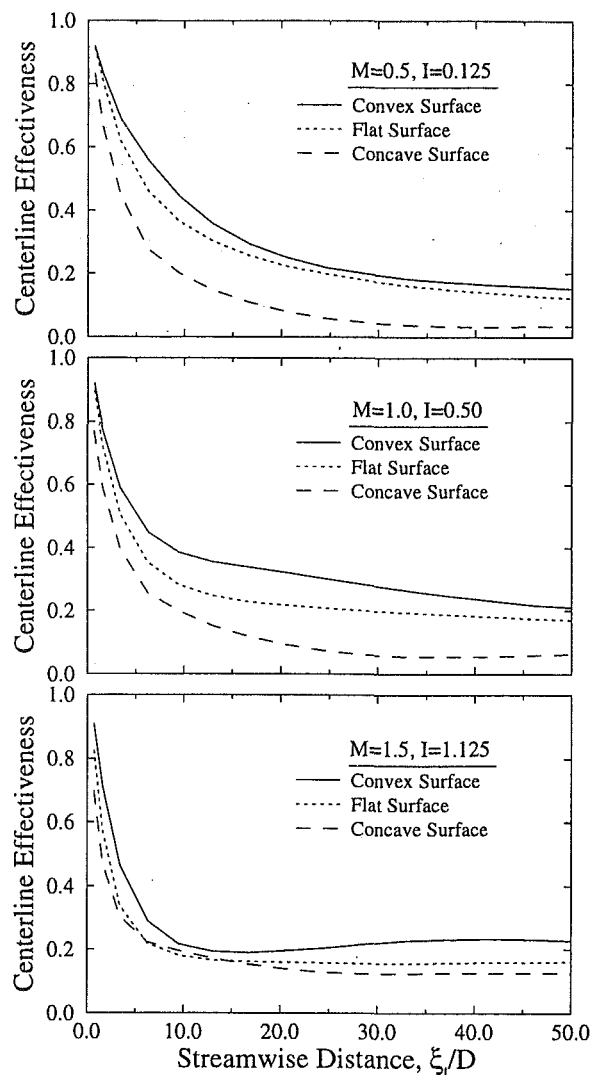
Fig. 9 Comparison of the centerline effectiveness of convex, flat, and concave surfaces
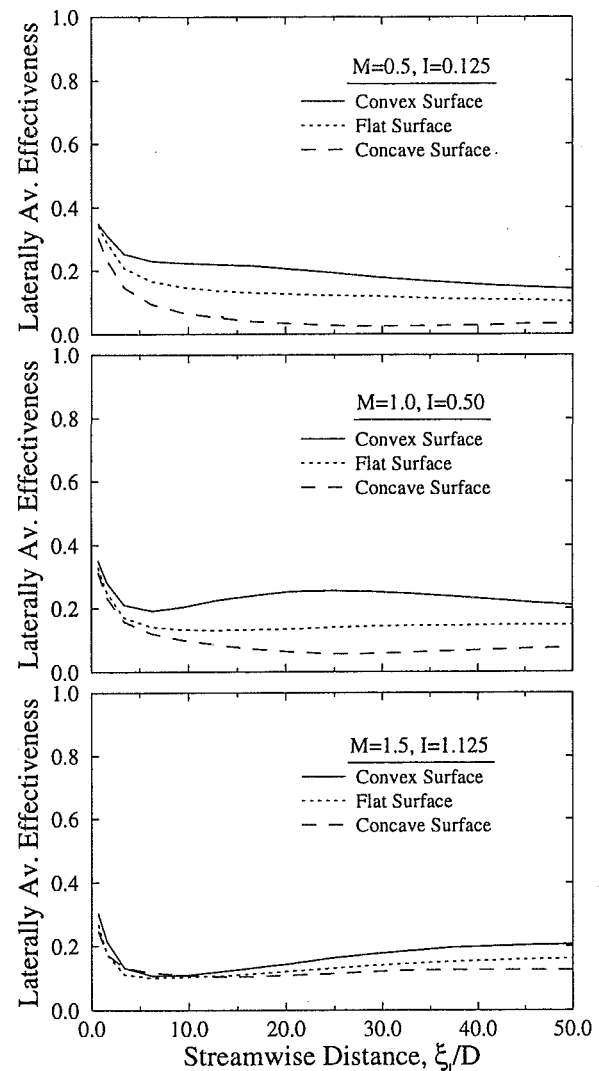

Fig. 10 Comparison of the laterally averaged effectiveness of convex, flat, and concave surfaces

tained using a constant σ_t. This is because, as shown in Figs. 3 and 4, on the convex surface, the Prandtl number is lower than its nominal value of about 0.9. This means that the thermal diffusivity is larger and, consequently, the cooling effectiveness is lower.

Figures 7 and 8 show the effectiveness distributions for the concave surface. Again, the computed and experimental values are given for both $M = 0.5$ and $M = 1.0$. The experimental values displayed in these figures are those of Stone (1992) and were obtained using injection angles of 25 and 45 deg. It must be noted that the results for these two angles are essentially the same and can thus represent the 35 deg results. Overall, the centerline effectiveness in these figures is predicted quite well. In the near-field, the laterally averaged effectiveness is again underpredicted. As we noted earlier, this is due to the isotropic nature of the modified k–ϵ turbulence model used in these computations.

Note that the effectiveness values displayed in Figs. 7 and 8 are very low. That is, at these blowing ratios, the concave surface is for the most part unprotected. The implication is that, for film cooling design purposes, both the suction and pressure surfaces of turbine blades must be dealt separately.

The dashed lines in Fig. 7 show the results for a constant Prandtl number. In the near-field, the cooling effectiveness is lower because the assumed value ($\sigma_t = 0.85$) is lower than the values shown in Fig. 4 for this surface. This implies that the thermal diffusivity is higher and, consequently, the cooling effectiveness is

lower. In the far-field, the cooling effectiveness is higher because of the diffusion of some of the coolant gases back to the surface.

Figures 9 and 10 show three-way comparisons of the distributions of cooling effectiveness for convex, flat, and concave surfaces for blowing rates of 0.5, 1.0, and 1.5. From these figures, it is evident that the effect of surface curvature is very significant. For the three blowing ratios shown, the convex surface has a higher cooling effectiveness than both the concave and flat surfaces. Furthermore, the relative cooling performances on the three surfaces depends on the blowing ratio. The difference in cooling performance between the convex and concave surfaces appears to be larger at $M = 1.0$ than at $M = 0.5$ or $M = 1.5$. At $M = 1.5$, the difference has narrowed significantly. This is consistent with the findings of Schwarz (1986), who noted that the difference between the cooling effectiveness distributions over the convex and concave surfaces initially increases with blowing ratio, reaches a maximum, and then decreases with further increase in blowing ratio. At sufficiently high blowing ratios, it is expected that the concave surface will have higher cooling effectiveness than both the convex and flat surfaces. In the next subsection, we will discuss the underlying reasons for these results using velocity plots in cross-stream planes.

The Velocity Field. Figure 11 shows contour plots of normalized streamwise mean velocity (U_ξ/U_∞) for the convex, flat, and

(a) Convex Surface

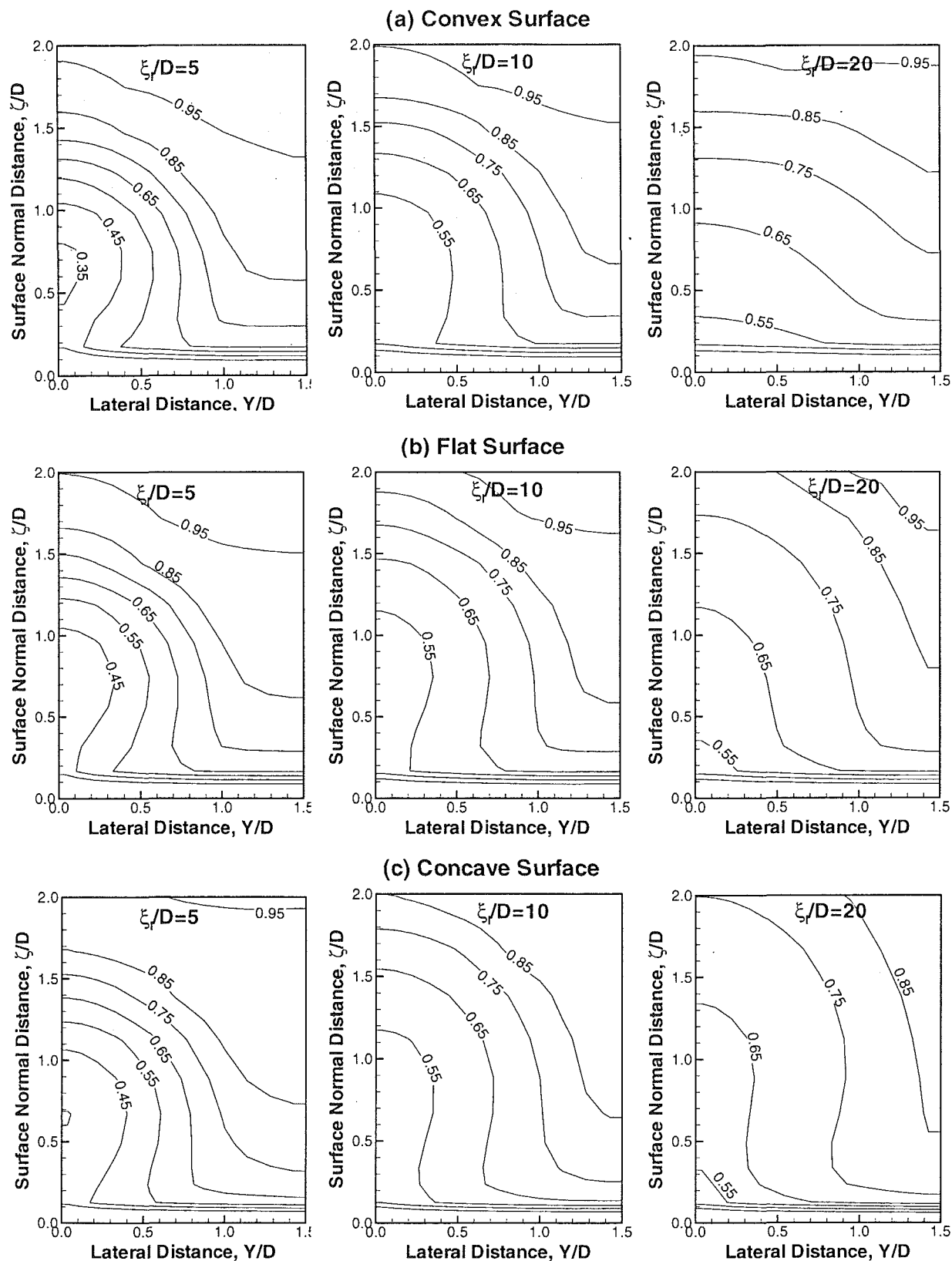## (b) Flat Surface

(c) Concave Surface

Fig. 11 U_ξ/U_∞ contours on convex, flat, and concave surfaces for three cross-stream planes ($M = 1.0$)

concave surfaces for $M = 1.0$. Three plots are shown for each surface, corresponding to cross-stream planes at $\xi/D = 5$, 10, and 20. Examination of these plots reveals that the flow structures over the three surfaces are distinctly different. First, the jet spreading characteristics into the mainstream are different. The jet spread on

the concave surface is larger than those on the convex or flat surfaces. Second, the rates of flow relaxation are different. On the convex surface, the flow has nearly returned to normal at $\xi_1/D = 20$, whereas on the concave surface, the jet is still spreading. This indicates that whereas the convex surface stabilizes the boundary
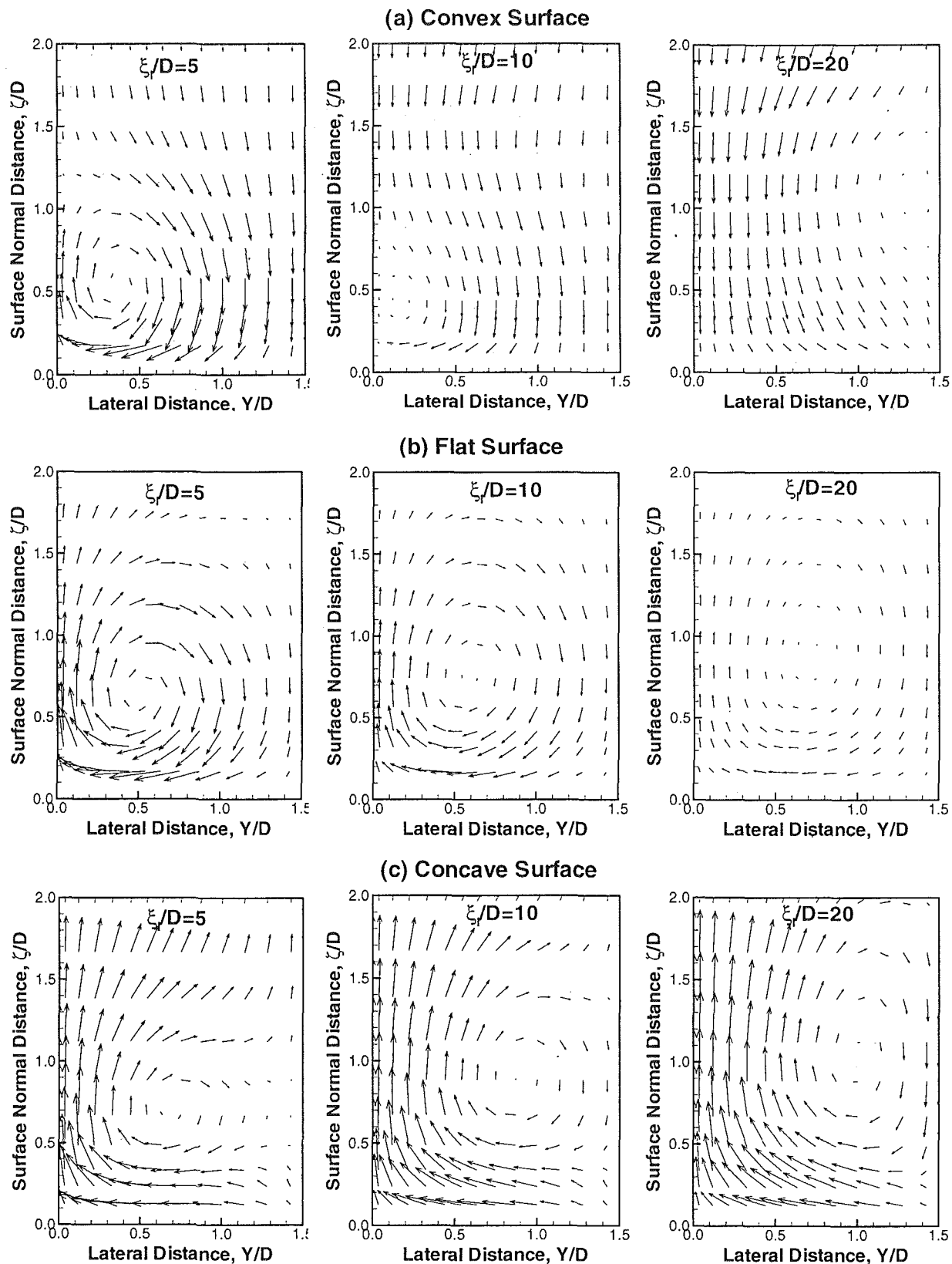
(a) Convex Surface

(b) Flat Surface

(c) Concave Surface

Fig. 12 Counterrotating vortices on convex, flat, and concave surfaces (M = 1.0, scale: 10 cm = 1 m/s)

layer, the concave surface destabilizes it. These characteristics are consistent with the observations we made earlier that convex surfaces are easier to cool than concave or flat surfaces.

Figure 12 shows the velocity vector plots for the three surfaces. Three plots are shown for each surface, corresponding to cross-stream planes at $\xi/D = 5$, 10, and 20. Again, the vortex structures over the three surfaces are different. On the flat surface, we see the usual counterrotating vortices, the strength of which decreases with the increase in streamwise distance. On the concave surface, a more vigorous vortex structure is evident. In contrast to the

flat-plate vortices, these vortices remain rather strong for a longer streamwise distance. On the convex surface, on the other hand, the vortices are quickly damped and replaced by a wall-bound flow. It must be noted that the counterrotating vortices are one of the main factors responsible for the degradation of film cooling effectiveness at high blowing ratios. The elimination of these vortices (and their replacement by a wall-bound flow) is therefore very beneficial and is responsible for making the convex surface easier to cool than the other two surfaces.

As discussed in the introduction, the above-noted differences in film cooling performance can be explained using differences in cross-stream pressure gradients and centrifugal forces. On a convex surface, the cross-stream pressure gradient tends to push the flow toward the wall. This reduces mixing and increases cooling effectiveness. On the other hand, on a concave surface, the pressure gradient tends to push the flow away from the wall. This increases mixing and lowers the cooling effectiveness. As the blowing ratio increases, however, the centrifugal force becomes stronger and plays a more dominant role. On a concave surface, it forces the coolant jet toward the wall, and on a convex surface, it pulls the coolant jet away from the wall. The result is that, on the convex surface, the cooling effectiveness decreases, and on the concave surface, it increases.

In conclusion, for the blowing ratios considered, the convex surface is easier to cool than the concave or flat surfaces. It has also been shown that, the concave surface considered, which is representative of the pressure surfaces of actual turbine blades, is essentially unprotected when $P/D = 3$. In the companion paper by Berhe and Patankar (1999), we discuss various ways by which the film cooling performance on both the pressure and suction surfaces of turbine blades can be enhanced.

Conclusions

Three-dimensional discrete-hole film cooling computations have been conducted to study the effects of surface curvature on cooling performance. Three surfaces were studied, namely, convex, concave, and flat surfaces. The film cooling geometries considered included the mainflow, injection hole, and supply plenum regions.

Streamline curvature was shown to have a very significant effect on turbulent shear stresses. On convex surfaces, the shear stresses are damped, and on concave surfaces, they are amplified. Although to a lesser degree, it was also shown that streamline curvature affects heat fluxes.

For the blowing ratios of 0.5 to 1.5 considered, the convex surface had higher cooling effectiveness than the flat surface; and the flat surface had higher cooling effectiveness than the concave surface. The difference in film cooling performance between the convex and concave surfaces was larger at $M = 1$ than at $M = 0.5$ or $M = 1.5$.

The flows over concave surfaces are characterized by strong vorticities. The resulting greater mixing of the coolant jets with the mainstream gases gives rise to a lower cooling effectiveness on these surfaces. On convex surfaces, the vortices are damped and the coolant jets pressed to the surface by cross-stream pressure gradients. This results in a greater cooling effectiveness over these surfaces.

Acknowledgments

References

Barlow, R. S., and Johnston, J. P., 1988, "Structure of a Turbulent Boundary Layer on a Concave Surface," *Journal of Fluid Mechanics,* Vol. 60, p. 43.

Berhe, M. K., 1997, "A Numerical Study of Discrete-Hole Film Cooling," Ph.D. Thesis, University of Minnesota, MN.

Berhe, M. K., and Patankar, S. V., 1999, "Investigation of Film Cooling Parameters Using Curved Discrete-Hole Models," ASME JOURNAL OF TURBOMACHINERY, Vol. 121, this issue, pp. 792–803.

Demuren, A. D., Rodi, W., and Schonung, B., 1986, "Systematic Study of the Film Cooling With a Three-Dimensional Calculation Procedure," ASME JOURNAL OF TURBOMACHINERY, Vol. 108, pp. 124–130.

Furuhama, K., Moffat, R. J., and Frota, M. N., 1983, "Heat Transfer and Turbulence Measurements of a Film-Cooled Flow Over a Convexly Curved Surface," Paper No. 83-Tokyo-IGTC-16.

Gibson, M. M., 1978, "An Algebraic Stress and Heat-Flux Model for Turbulent Shear Flow With Streamline Curvature," *International Journal of Heat and Mass Transfer,* Vol. 21, pp. 1609–1617.

Gibson, M. M., and Launder, B. E., 1978, "Ground Effects on Pressure Fluctuations in the Atmospheric Boundary Layer," *Journal of Fluid Mechanics,* Vol. 86(3), 491.

Gillis, J. C., and Johnston, J. P., 1983, "Turbulent Boundary-Layer Flow and Structure on a Convex Wall and Its Redevelopment on a Flat Wall," *Journal of Fluid Mechanics,* Vol. 135, pp. 123.

He, P., Salcudean, M., and Gartshore, I. S., 1995, "Computation of Film Cooling for the Leading Edge Region of a Turbine Blade Model," ASME Paper No. 95-GT-20.

Ito, S., Goldstein, R. J., and Eckert, E. R. G., 1978, "Film Cooling of Gas Turbine Blades," ASME *Journal of Engineering for Power,* Vol. 100, pp. 476–481.

Kasagi, S., Hirata, K., Ikeyama, M., Makino, M., and Kumada, M., 1987, "Effects of the Wall Curvature on Full-Coverage Film Cooling Effectiveness," *Heat Transfer and Fluid Flow in Rotating Machinery,* Wen-Jei Yang, ed., Washington: Hemisphere Publishing Corp.

Kohli, A., and Bogard, D. G., 1997, "Adiabatic Effectiveness, Thermal Fields, and Velocity Fields for Film Cooling With Large Angle Injection," ASME JOURNAL OF TURBOMACHINERY, Vol. 119, pp. 352–358.

Launder, B. E., and Spalding, D. B., 1974, "The Numerical Computation of Turbulent Flows," *Computer Methods in Applied Mechanics and Engineering,* Vol. 3, pp. 269–289.

Launder, B. E., Priddin, C. H., and Sharma, B. S., 1977, "The Calculation of Turbulent Boundary Layers on Spinning and Curved Surfaces," ASME *Journal of Fluids Engineering,* Vol. 99, pp. 231–239.

Leitner, A., 1997, "Prediction of Three-Dimensional Film Cooling Situations," Ph.D. Thesis, University of Minnesota, MN.

Leschziner, M. A., and Rodi, W., 1981, "Calculation of Annular and Twin Parallel Jets Using Various Discretization Schemes and Turbulence Model Variations," ASME *Journal of Fluids Engineering,* Vol. 103, pp. 352–360.

Leylek, J. H., and Zerkle, R. D., 1994, "Discrete-Jet Film Cooling: A Comparison of Computational Results With Experiments," ASME JOURNAL OF TURBOMACHINERY, Vol. 116, pp. 358–368.

Lin, Y. L., Stephens, M. A., and Shih, T. I-P., 1997, "Computation of Leading-Edge Film Cooling With Injection Through Rows of Compound-Angle Holes," ASME Paper No. 97-GT-298.

Luo, J., and Lakshminarayana, B., 1997, "Prediction of Strongly Curved Turbulent Duct Flows With Reynolds Stress Model," *AIAA Journal,* Vol. 35, No. 1, pp. 91–98.

Martin, C. A., and Thole, K. A., 1997, "Leading Edge Film-Cooling With Compound Angle Injection," ASME Paper No. 97-GT-297.

Mayle, R. E., Kopper, F. C., Blair, M. F., and Bailey, D. A., 1977, "Effects of Streamwise Curvature on Film Cooling," ASME *Journal of Engineering for Power,* Vol. 99, pp. 77–82.

Meroney, R. N., and Bradshaw, P., 1975, "Turbulent Boundary-Layer Growth Over a Longitudinally Curved Surface," *AIAA J.,* Vol. 13, No. 11, pp. 1448.

Park, S. W., and Chung, M. K., 1989, "Curvature-Dependent Two-Equation Model for Prediction of Turbulent Recirculating Flows," *AIAA Journal,* Vol. 27, No. 3, pp. 340–344.

Patankar, S. V., 1980, *Numerical Heat Transfer and Fluid Flow,* Hemisphere Publishing Corporation, New York.

Patel, V. C., and Sotiropoulos, F., 1997, "Longitudinal Curvature Effects in Turbulent Boundary Layers," *Prog. Aerospace Sci.,* Vol. 33, pp. 1–70.

Rodi, W., and Scheuerer, G., 1983, "Calculation of Curved Shear Layers With Two-Equation Turbulence Models," *Physics of Fluids,* Vol. 26, pp. 1422–1436.

Schwarz, S. G., 1986, "Film Cooling of Curved Surfaces," Ph.D. Thesis, University of Minnesota, Minneapolis, MN.

Schwarz, S. G., Goldstein, R. J., and Eckert, E. R. G., 1991, "The Influence of Curvature on Film Cooling Performance," ASME JOURNAL OF TURBOMACHINERY, Vol. 113, pp. 472–478.

So, R. M., and Mellor, G. L., 1973, "Experiment on Convex Curvature Effects in Turbulent Boundary Layers," *Journal of Fluid Mechanics,* Vol. 60(1), pp. 43–62.

Stone, L. D., 1992, "Film Cooling of Curved Surfaces at Low Injection Angles," M.S. Thesis, University of Minnesota, Minneapolis, MN.

Tani, I., 1962, "Production of Longitudinal Vortices in the Boundary Layer Along a Concave Wall," *J. Geophysical Research,* Vol. 67, pp. 3075–3080.

Wang, L., Tsang, H., Simon, T. W., and Eckert, E. R. G., 1996, "Measurement of Mean Flow and Eddy Transport Over a Film Cooling Surface," *Proc. Natl. Heat Transfer Conference,* Houston, TX.

Investigation of Discrete-Hole Film Cooling Parameters Using Curved-Plate Models

M. K. Berhe[1]

S. V. Patankar

Department of Mechanical Engineering,
111 Church Street SE,
Minneapolis, MN 55455

Computations have been conducted on curved, three-dimensional discrete-hole film cooling geometries that included the mainflow, injection hole, and supply plenum regions. Both convex and concave film cooling geometries were studied. The effects of several film cooling parameters have been investigated, including the effects of blowing ratio, injection angle, hole length, hole spacing, and hole staggering. The blowing ratio was varied from 0.5 to 1.5, the injection angle from 35 to 65 deg, the hole length from 1.75D to 6.0D, and the hole spacing from 2D to 3D. The staggered-hole arrangement considered included two rows. The computations were performed by solving the fully elliptic, three-dimensional Navier–Stokes equations over a body-fitted grid. Turbulence closure was achieved using a modified k–ε model in which algebraic relations were used for the turbulent viscosity and the turbulent Prandtl number. The results presented and discussed include plots of adiabatic effectiveness as well as plots of velocity contours and velocity vectors in cross-stream planes. The present study reveals that the blowing ratio, hole spacing, and hole staggering are among the most significant film cooling parameters. Furthermore: (1) The optimum blowing ratios for curved surfaces are higher than those for flat surfaces, (2) a reduction of hole spacing from 3D to 2D resulted in a very significant increase in adiabatic effectiveness, especially on the concave surface, (3) the increase in cooling effectiveness with decreasing hole spacing was found to be due to not only the increased coolant mass per unit area, but also the smaller jet penetration and the weaker counterrotating vortices, (4) for all practical purposes, the hole length was found to be a much less significant film cooling parameter.

Introduction

Over the years, several experimental studies have been conducted on curved-plate geometries to investigate the effects of various parameters on film cooling performance. Schwarz (1986) studied the effect of blowing ratio on cooling effectiveness and found that the optimum blowing ratio depends on the type of surface curvature involved. On convex surfaces representative of suction surfaces of turbine blades, he found that the optimum blowing ratio was of the order of 1.0. On concave surfaces, on the other hand, higher blowing rates always provided higher cooling effectiveness. Cruse et al. (1997) conducted experiments on a curved-plate geometry representative of the leading edge of turbine blades. They found that the optimum blowing ratio was of the order of 1.5. This is higher than the value obtained by Schwarz (1986), indicating that the optimum blowing ratio is higher on strongly curved surfaces.

Kruse (1985) investigated the effects of injection angle and hole spacing on cooling effectiveness of curved surfaces. He considered injection angles of 10 to 90 deg and found that the smaller injection angles performed better than the larger angles. He also found a strong effect of hole spacing on cooling effectiveness. He showed that, when the hole spacing is small, the counterrotating system of vortices of adjacent jets interact in such a way that the tendency to re-attach to the wall is intensified and the jet penetration is reduced. Recently, Stone (1992) also studied the effect of injection angle on convex and concave surfaces and found that, at low blowing rates, the effect of injection angle is insignificant. However, at high blowing rates, the smallest injection angle (15

deg) provided the best cooling performance. The larger angles he studied, 25 and 45 deg, gave nearly the same level of cooling effectiveness.

Hole staggering was also found to play the same role as reducing the hole spacing, i.e., it decreases the jet penetration and enhances the film cooling effectiveness. Ames (1998) studied the effects of hole staggering on the pressure and suction surfaces of turbine blades. He reported elevated levels of cooling effectiveness when the injection holes were staggered. The enhancement in cooling effectiveness was especially high for larger blowing ratios.

Numerical studies have also been conducted on curved surfaces. Many of these studies were, however, conducted on curved surfaces applicable to the leading edge of turbine blades. He et al. (1995) modeled the leading edge of a turbine blade using a semicircular plate with a flat afterbody and the standard k–ε turbulence model. They reported distributions of velocity, temperature, pressure, kinetic energy, and adiabatic effectiveness following two staggered rows of holes. The spanwise inclined holes they studied resulted in good film cooling coverage at low blowing ratios. However, the coverage deteriorated at high blowing ratios. Lin et al. (1997) conducted a similar study and documented the interaction of the mainstream gases with the coolant jets. Martin and Thole (1997) also studied nearly the same geometry as the preceding two studies and reported flow and effectiveness results following two staggered rows of leading edge holes. Among other things, they found that the film cooling coverage was uneven following the two rows of holes. Garg and Gaugler (1996) modeled the leading edge of an actual turbine blade using an algebraic turbulence model and an assumed velocity profile at hole exit. They reported nonuniform distribution of heat flux in both the streamwise and spanwise directions, resulting in regions of good and bad film cooling coverage.

As already mentioned, the above-cited numerical studies were conducted on curved surfaces specific to the leading edge of turbine blades, as opposed to curved surfaces applicable to the

(a)

(b)

Fig. 1 The film cooling computational geometry, (a) top view and (b) front view

lateral spacing between holes is $4D$ and the streamwise distance between rows is $5D$.

Computational Details

The computational procedure followed in this study is given in the companion paper by Berhe and Patankar (1999). In this paper, the calculation procedure is described, which involves a modified $k-\epsilon$ turbulence model where algebraic relations are used for the turbulent viscosity and the turbulent Prandtl number. Also given are details of the solution methodology, discretization, boundary conditions, initialization, and convergence criteria.

Results and Discussion

In this section, we discuss the effects of several film cooling parameters on film cooling performance, including the effects of blowing ratio, injection angle, hole length, hole spacing, and hole staggering. The results presented and discussed include plots of adiabatic effectiveness as well as plots of streamwise mean velocity contours and velocity vector for several cross-stream planes. Also given are comparisons between the present results and those of flat-plate studies and their implications to film cooling of pressure and suction surfaces of actual turbine blades.

The Effect of Blowing Ratio. As discussed in the companion paper by Berhe and Patankar (1999), the effect of blowing on film cooling effectiveness is determined by the sum total of the effects of: (1) the coolant mass injected per unit area, (2) the jet penetration into the mainstream, and (3) the strength of the counterrotating vortices. In general, higher blowing ratios produce increased coolant mass per unit area, greater jet penetration, and stronger counterrotating vortices. Although the increase in coolant mass per unit area tends to increase the cooling effectiveness, both greater jet penetration and stronger vortices decrease the cooling performance.

The effect of blowing ratio on cooling effectiveness is shown in

pressure and suction surfaces. In addition, although the surface curvatures involved in these models were very strong, the turbulence models used in these studies did not take the effects of streamline curvature into account. In the present study, we have addressed these issues and investigated the effects of several parameters using curved-plate models applicable to the suction and pressure surfaces of actual turbine blades. The main features of this study are: (1) Realistic, curved film cooling geometries have been used that included the mainflow, injection hole, and supply plenum regions, (2) the effects of streamline curvature was taken into account by using a modified $k-\epsilon$ turbulence model in which algebraic relations are used to calculate the turbulent viscosity and the turbulent Prandtl number, (3) the effects of several parameters on film cooling effectiveness have been studied, and (4) the underlying reasons for these effects have been discussed using velocity contours and velocity vectors at several cross-stream planes.

Test Cases Considered

Computations were performed for a wide variety of test cases. The blowing ratio was varied from 0.5 to 1.5, the injection angle from 35 to 65 deg, the hole spacing from $2D$ to $3D$, and the hole length from $1.75D$ to $6.0D$. The basic film cooling geometry considered in this study is shown in Fig. 1. The flow and geometric variables used are given in Table 1. The effect of hole staggering was studied by considering the geometry shown in Fig. 2 where the

---

——— **Nomenclature** ———

D = diameter of injection hole
DR = density ratio = ρ_j/ρ_∞
H = plenum height
I = momentum ratio = $\rho_j U_j^2/\rho_\infty U_\infty^2$
k = turbulent kinetic energy
L = length of injection hole
M = blowing ratio = $\rho_j U_j/\rho_\infty U_\infty$
P = hole spacing or pitch
T = temperature
Tu = turbulence intensity level = $\sqrt{k}/1.5/U_\infty$
U = gas velocity
X = horizontal distance measured from the hole leading edge at hole exit

Y = lateral distance measured from hole centerline plane
Z = vertical distance from the test surface measured from the hole leading edge
α = injection angle
ϵ = dissipation rate of turbulent kinetic energy
ζ = wall-normal coordinate
η = local adiabatic film cooling effectiveness
η_c = centerline adiabatic film cooling effectiveness
$\bar{\eta}$ = laterally averaged film cooling effectiveness

ξ = streamwise coordinate
ρ = gas density

Subscripts and Superscripts

j = coolant jet
l = measured from the hole leading edge
t = measured from the hole trailing edge (also turbulent flow)
w = at the wall
ζ = along the wall-normal direction
ξ = along the streamwise direction
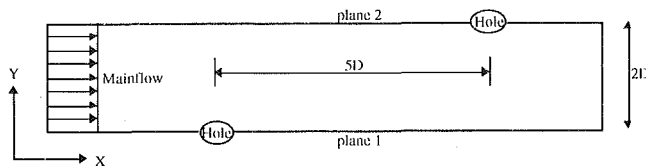∞ = free-stream quantity

---

Fig. 2 Top view of the staggered-hole arrangement considered (a partial view)

Fig. 3. This figure shows the variations of the centerline and laterally averaged effectiveness for blowing ratios of 0.5, 1.0, and 1.5. The general trend in this figure is that, in the near-field, the cooling effectiveness decreases with the increase in blowing ratio, and in the far-field, it increases with the increase in blowing ratio. The optimum blowing ratio in this figure appears to be around $M = 1.0$. This is in contrast to the optimum blowing ratio of about 0.5 established by many flat-plate studies. For comparison purposes, the variation of cooling effectiveness with blowing ratio obtained from a flat-plate model of Berhe (1997) is given in Fig. 4. In this figure, the optimum blowing ratio is around 0.5. It must be noted that the only difference between these two configurations is surface curvature.

The implication of these results is that the optimum blowing ratios on suction surfaces of turbine blades are higher than the values established by flat-plate models. Further, for strongly curved surfaces, such as the leading edges of turbine blades, the optimum blowing ratios may be even higher. In fact, in a recent study, Cruse et al. (1997) have shown that, at the leading edge, the optimum blowing ratio may be greater than 1.5. The reasons for the higher optimum blowing ratios on convex surfaces are: (1) the jet penetration is smaller, and (2) the counterrotating vortices are weaker. As discussed in the companion paper by Berhe and Patankar (1999), on convex surfaces, pressure gradients exist that force the coolant jets toward the walls. As a result, the critical blowing ratio at which jet lift-off occurs is higher and, consequently, the optimum blowing ratio is larger. In addition, as
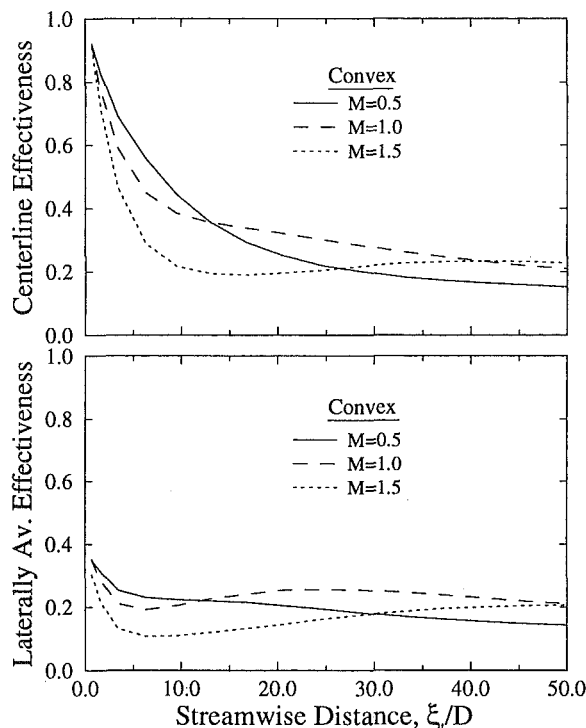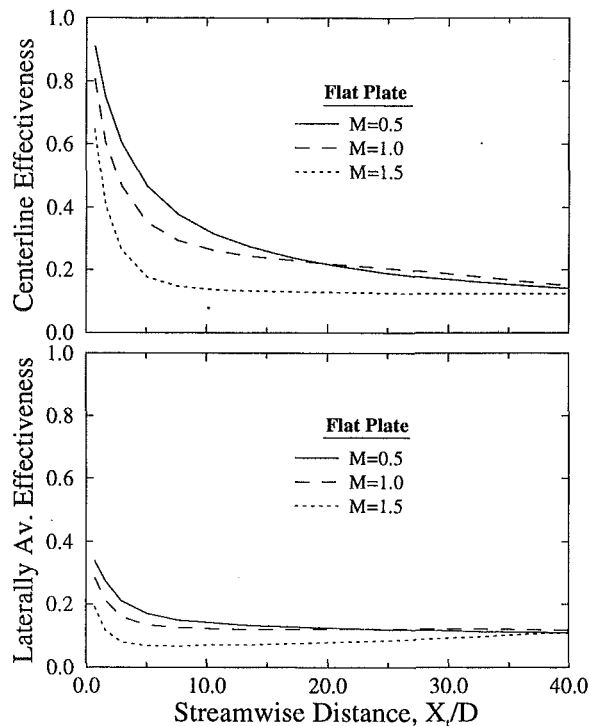

Fig. 4 The effect of blowing ratio on cooling effectiveness of flat surface ($\alpha = 35$ deg, $L/D = 4$)

discussed in the introduction, convex surfaces are known to reduce the near-wall shear stresses and suppress the negative effects of the counterrotating vortices.

Figures 5 and 6 show the effects of blowing ratio on jet penetration and counterrotating vortices on the convex surface. These figures show contours plots of U_ξ/U_∞ and velocity vector plots in cross-stream planes. Three plots are shown for each blowing ratio ($M = 0.5$ and $M = 1.5$) corresponding to streamwise locations of $5D$, $10D$, and $20D$. From Fig. 5, it is evident that, at $M = 0.5$, the jet is fully attached to the surface. However, at $M = 1.5$, the jet appears to be is first detached and then reattached farther downstream. This detachment of the coolant jet from the test surface is responsible for much of the decrease in the near-field cooling effectiveness shown in Fig. 3. Figure 6 shows the amplification of the strength of the counterrotating vortices with the increase in blowing ratio. For $M = 0.5$, the counterrotating vortices are almost fully suppressed at $\xi_1/D = 5$. However, for $M = 1.5$, the vortices are still strong even at $\xi_1/D = 10$. As we have already discussed, stronger vortices generally degrade the film cooling performance by replacing the near-wall cold air with hot, mainstream gases.

The effect of blowing ratio on cooling effectiveness of the concave surface is shown in Fig. 7. Examination of this figure reveals two main points. First, the effect of blowing ratio on cooling effectiveness of concave surfaces is not as strong as its effect on cooling effectiveness of convex surfaces. This is because, on concave surfaces, the flow is dominated by strong vortices. This results in a greater mixing of the coolant jets with mainstream gases and produces a slow increase of effectiveness with blowing ratio. The second point to be noted is that, as Schwarz (1986) observed, for much of the downstream region, the cooling effectiveness increases with the increase in blowing ratio. This result is also consistent with the findings of Ames (1997) who showed that higher blowing ratios generally produce higher cooling effectiveness on pressure surfaces of turbine blades.

The Effect of Injection Angle. The main effect of injection angle is that it changes the jet trajectory or jet penetration into the
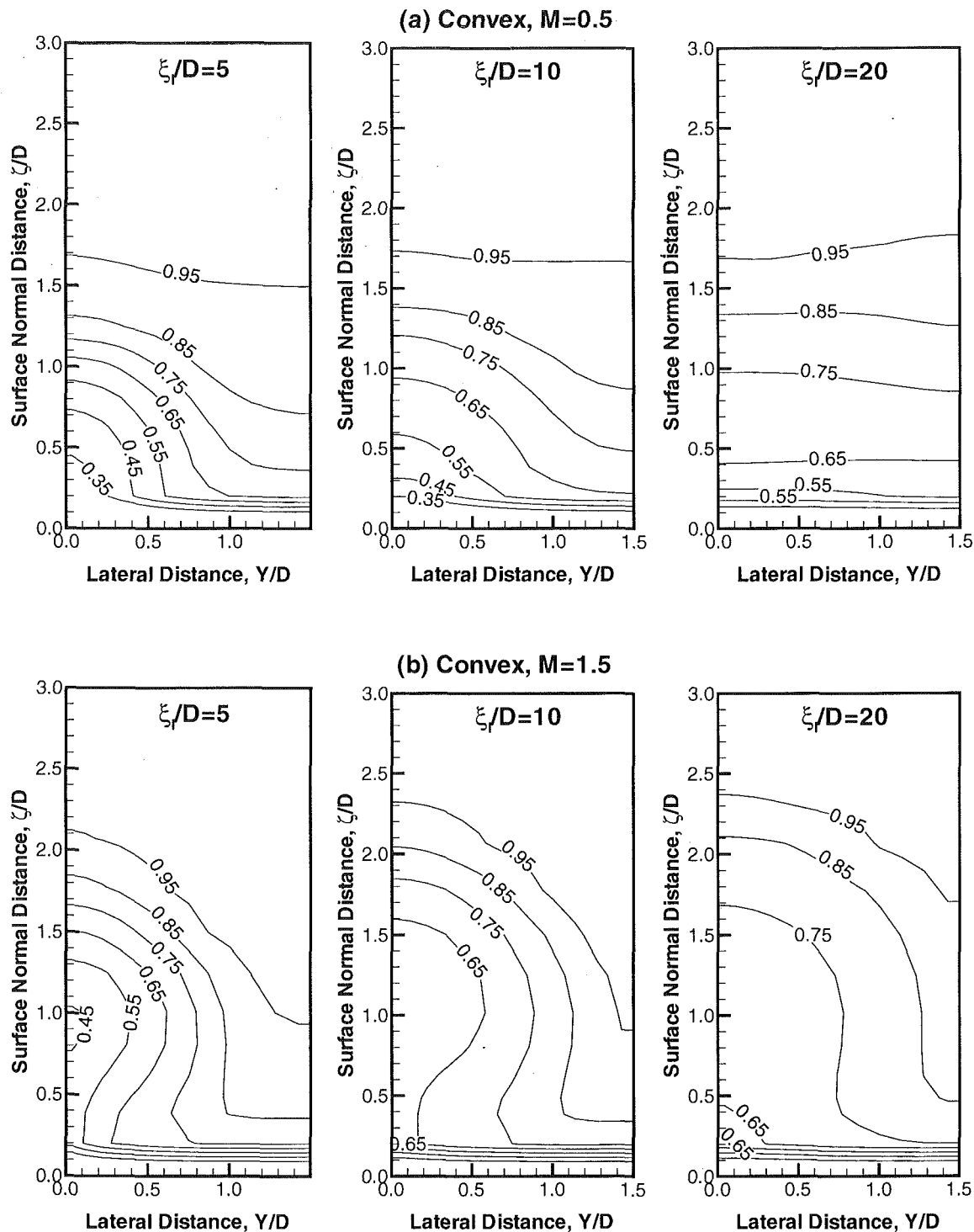

Fig. 3 The effect of blowing ratio on cooling effectiveness of a convex surface ($\alpha = 35$ deg, $L/D = 5$)

(a) Convex, M=0.5

(b) Convex, M=1.5

Fig. 5 The effect of blowing ratio on U_ξ/U_∞ contours in cross-stream planes on a convex surface

mainstream. As the injection angle increases, the vertical momentum increases. This, in turn, increases the jet penetration and lowers the cooling effectiveness. Examination of velocity vector plots in cross-stream planes reveals that, unlike the blowing ratio, the injection angle does not appear to affect the counter-rotating vortices.

Figure 8 shows the distribution of cooling effectiveness for injection angles of 35, 45, and 65 deg. It is clear that, for both $M = 0.5$ and $M = 1.0$, the smallest injection angle produced the best cooling performance. As just mentioned, this is because the larger injection angles deploy more of the coolant fluid away from the

test surface. However, it must be noted that the above-noted decrease in cooling effectiveness with increased injection angle is not as large as those reported in earlier studies using flat-plate models, such as those of Kohli and Bogard (1997), and Berhe (1997). This is because, on convex surfaces, the effect of increased jet penetration (due to larger angles) is partly compensated by cross-stream pressure gradients, which force the coolant jets back to the walls.

The effect of injection angle was also investigated on film cooling performance of concave surfaces. Computations were performed for injection angle of 35 and 65 degrees for $M = 0.5$ and
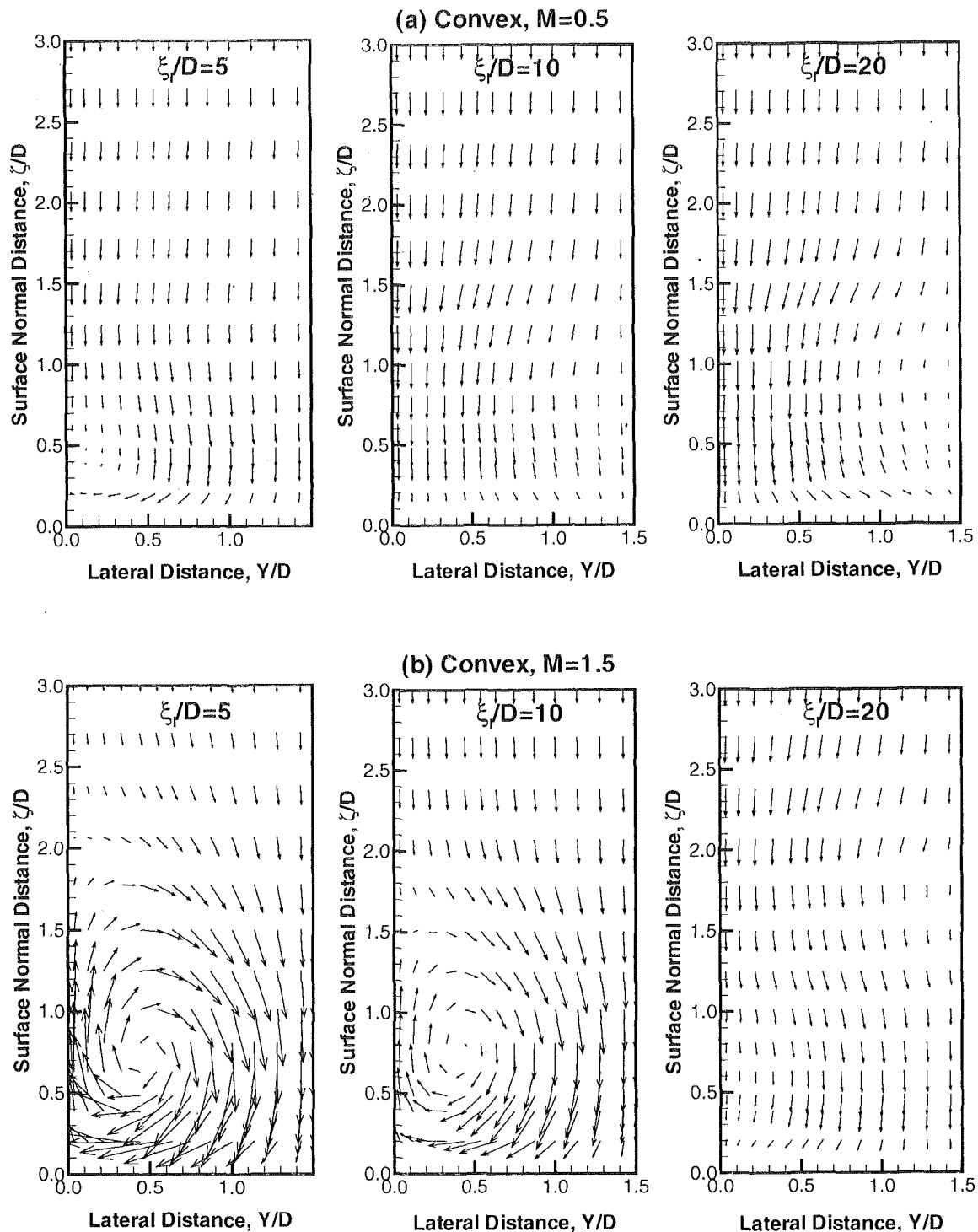
Fig. 6   The effect of blowing ratio on counterrotating vortices on a convex surface

$M = 1.0$. For both blowing ratios, the effect of injection angle on cooling effectiveness was found to be essentially insignificant. The result for $M = 1.0$ is shown in Fig. 9. The conclusion is that the effect of injection angle on cooling effectiveness of concave surfaces is much weaker than its effect on cooling effectiveness of flat surfaces. The insensitivity of the cooling effectiveness to variations in injection angle may be attributed to the stronger mixing that exists on these surfaces. As we have discussed earlier, on concave surfaces, the injected coolant mass is thoroughly mixed with the mainstream gases, so the effect of increased jet penetration due to larger injection angles is minimized. However, we have

also found that, when the hole spacing is reduced, the effect of injection angle becomes more significant. We will further discuss this issue later in this paper.

In conclusion, the present computations show that the injection angle still has a significant effect on cooling performance of convex surfaces. However, on concave surfaces, its effect is greatly reduced by the stronger vortices that exist on these surfaces.

The Effect of Hole Spacing.   To study the effect of hole spacing on film cooling performance, we considered two values of the P/D ratio, $P/D = 3$ and $P/D = 2$. Computations were
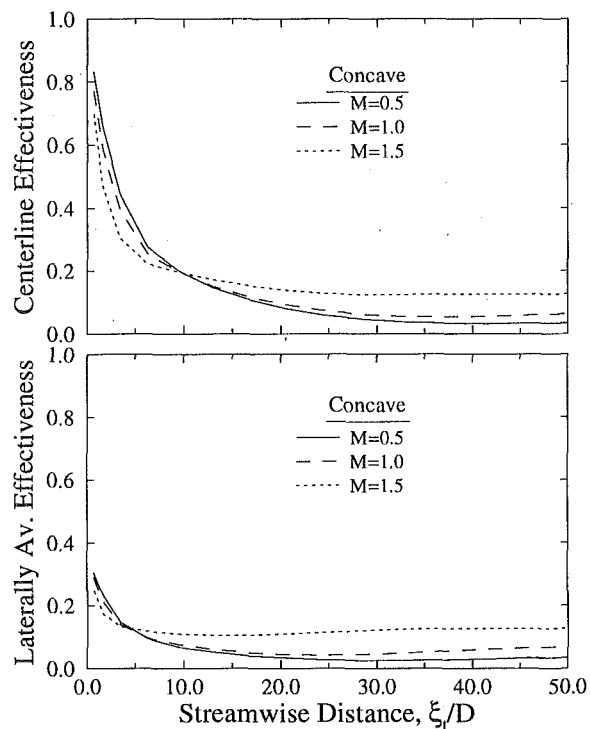
Fig. 7 The effect of blowing ratio on cooling effectiveness of a concave surface (α = 35 deg, L/D = 5)
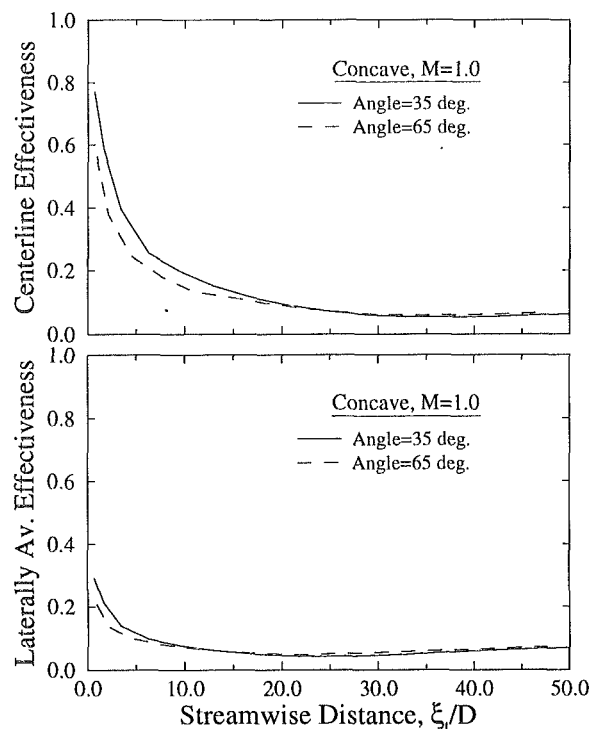

Fig. 9 The effect of injection angle on cooling effectiveness of a concave surface (M = 1.0, P/D = 3)

performed on both the convex and concave film cooling geometries. Figures 10 and 11 show the distribution of the centerline and laterally averaged effectiveness for the convex surface for M = 0.5 and M = 1.0, respectively. It is obvious that the smaller hole spacing has produced a significant increase in cooling effectiveness, especially in the laterally averaged effectiveness. Further-

more, the increase in cooling effectiveness is greater at M = 1.0 than at M = 0.5.

Figures 12 and 13 show the corresponding distribution of cooling effectiveness for the concave surface for M = 0.5 and M = 1.0, respectively. It is evident that, in this case, the small change in P/D ratio has produced a dramatic increase in the cooling effectiveness,
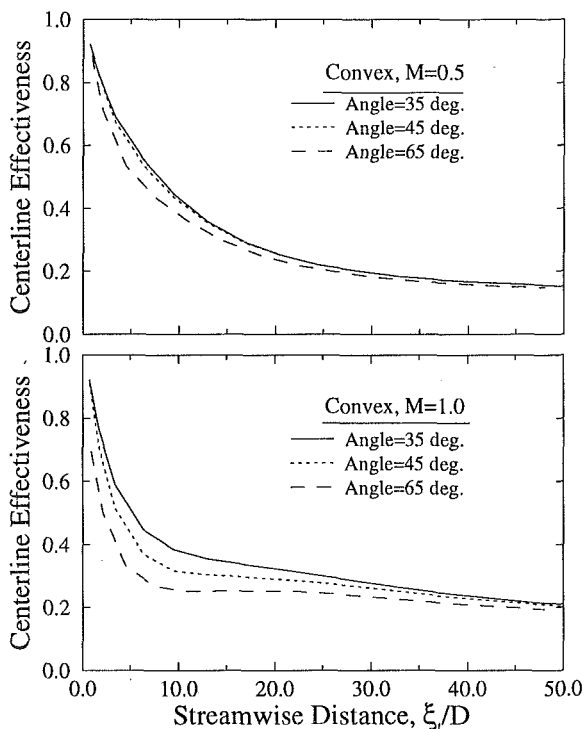

Fig. 8 The effect of injection angle on cooling effectiveness of a convex surface (L/D = 5)
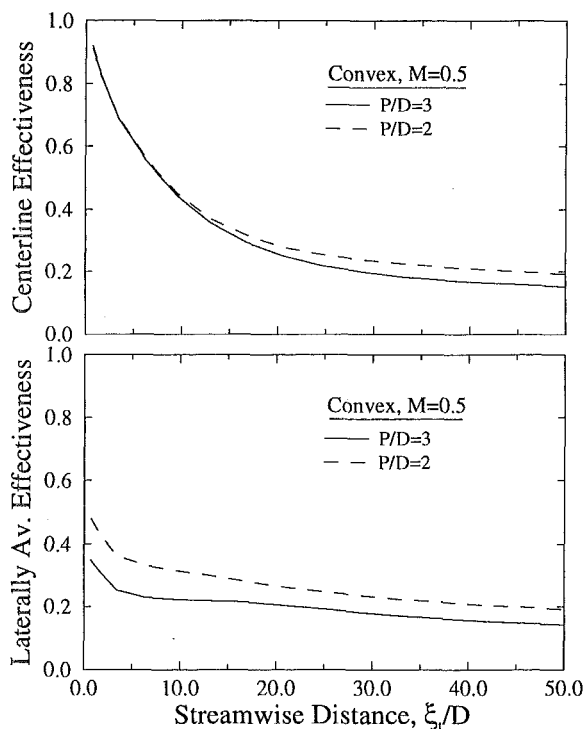

Fig. 10 The effect of hole spacing on cooling effectiveness of a convex surface (M = 0.5)
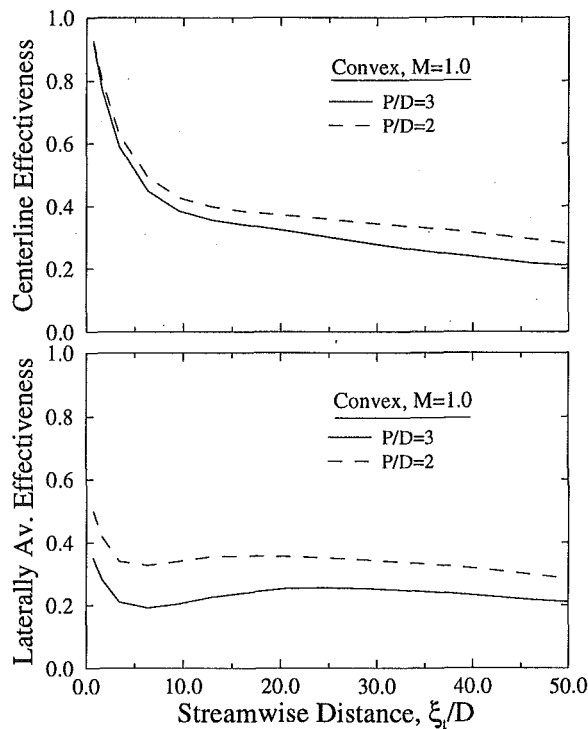
Fig. 11 The effect of hole spacing on cooling effectiveness of a convex surface ($M = 1.0$)
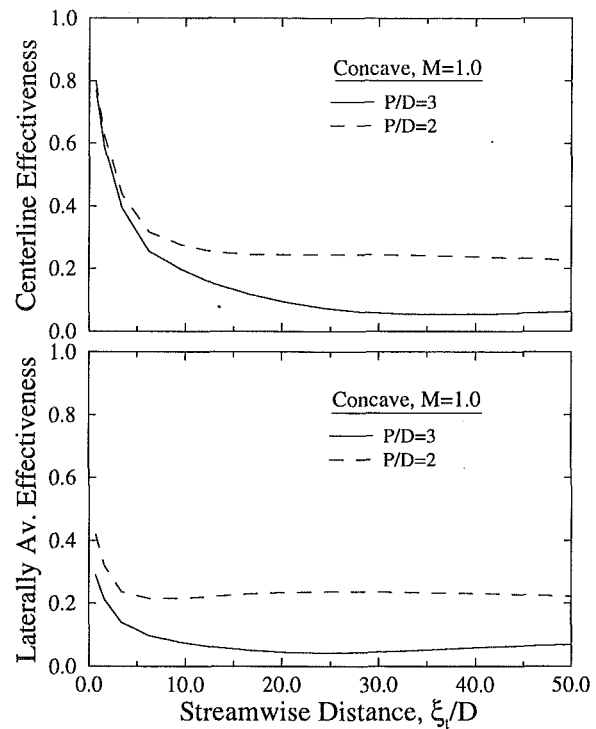

Fig. 13 The effect of hole spacing on cooling effectiveness of a concave surface ($M = 1.0$)

especially for $M = 1.0$. The concave surface, which at $P/D = 3$ is almost unprotected from the effects of the hot gases, now has a much higher cooling effectiveness. In addition, note that (1) Both the centerline and laterally averaged effectiveness appear to be comparable, and (2) for much of the region downstream of the injection hole, the cooling effectiveness is rather uniform. These are the qualities one

would want in a good discrete-hole film cooling. Hence, hole spacings smaller than the ones normally used in practical film cooling applications ($P/D \sim 3$) appear to be highly desirable and essential to protect curved surfaces adequately.

To study the underlying reasons for the higher film cooling performance at $P/D = 2$, we examined plots of the streamwise mean velocity contours and velocity vectors in cross-stream planes. We found that the higher cooling performance at $P/D = 2$ is due not only to the increased coolant mass per unit area, but also to the smaller jet penetration and weaker counterrotating vortices. Figures 14 and 15 show, respectively, plots of the streamwise mean velocity contours and velocity vectors in cross-stream planes at $\xi_1 = 5D$, $10D$, and $20D$. From Fig. 14, it is clear that, for $P/D = 2$, the jet penetration is smaller and the rate of flow relaxation higher than for $P/D = 3$. In addition, from the velocity vector plots displayed in Fig. 15, we can see that the counterrotating vortices for $P/D = 2$ are significantly weaker than those for $P/D = 3$. These results are consistent with the findings of Kruse (1985), who noted that when the hole spacing is small, the counterrotating system of vortices of adjacent jets interacts in such a way that the tendency to re-attach to the wall is intensified and the jet penetration into the mainstream is reduced.

In the subsection that discusses the effect of injection angle on cooling effectiveness, we concluded that, on concave surfaces, the effect of injection angle on cooling effectiveness is very weak. The main reason given for the insensitivity of cooling effectiveness to variations in injection angle was the existence of stronger vortices on these surfaces. Tests were, therefore, conducted to re-examine the effect of injection angle on cooling effectiveness for $P/D = 2$, since in this case the vortices are weaker. We considered two injection angles for this purpose, 35 and 65 deg. The resulting distribution of cooling effectiveness are shown in Fig. 16. As may be expected, for $P/D = 2$, the effect of injection angle on cooling effectiveness is more significant than was the case for $P/D = 3$.

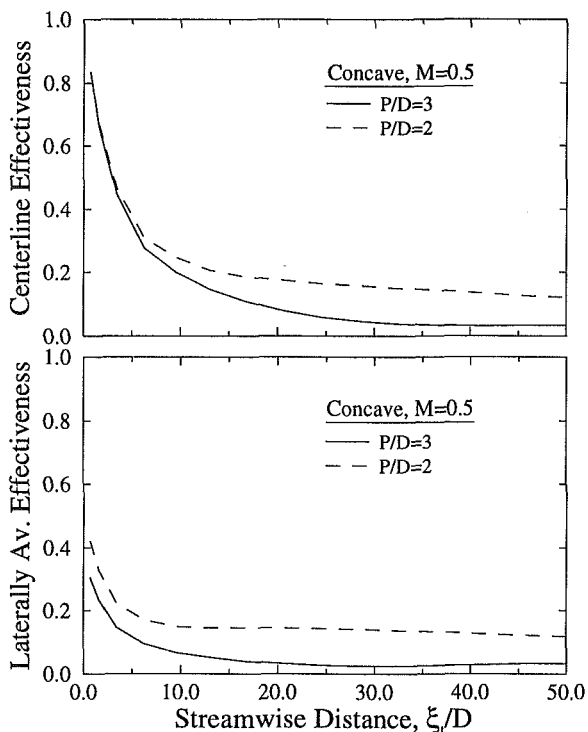**The Effect of Hole Staggering.** The advantages of a smaller hole spacing can also be realized by using a staggered-hole arrangement. For example, instead of having one row of holes where
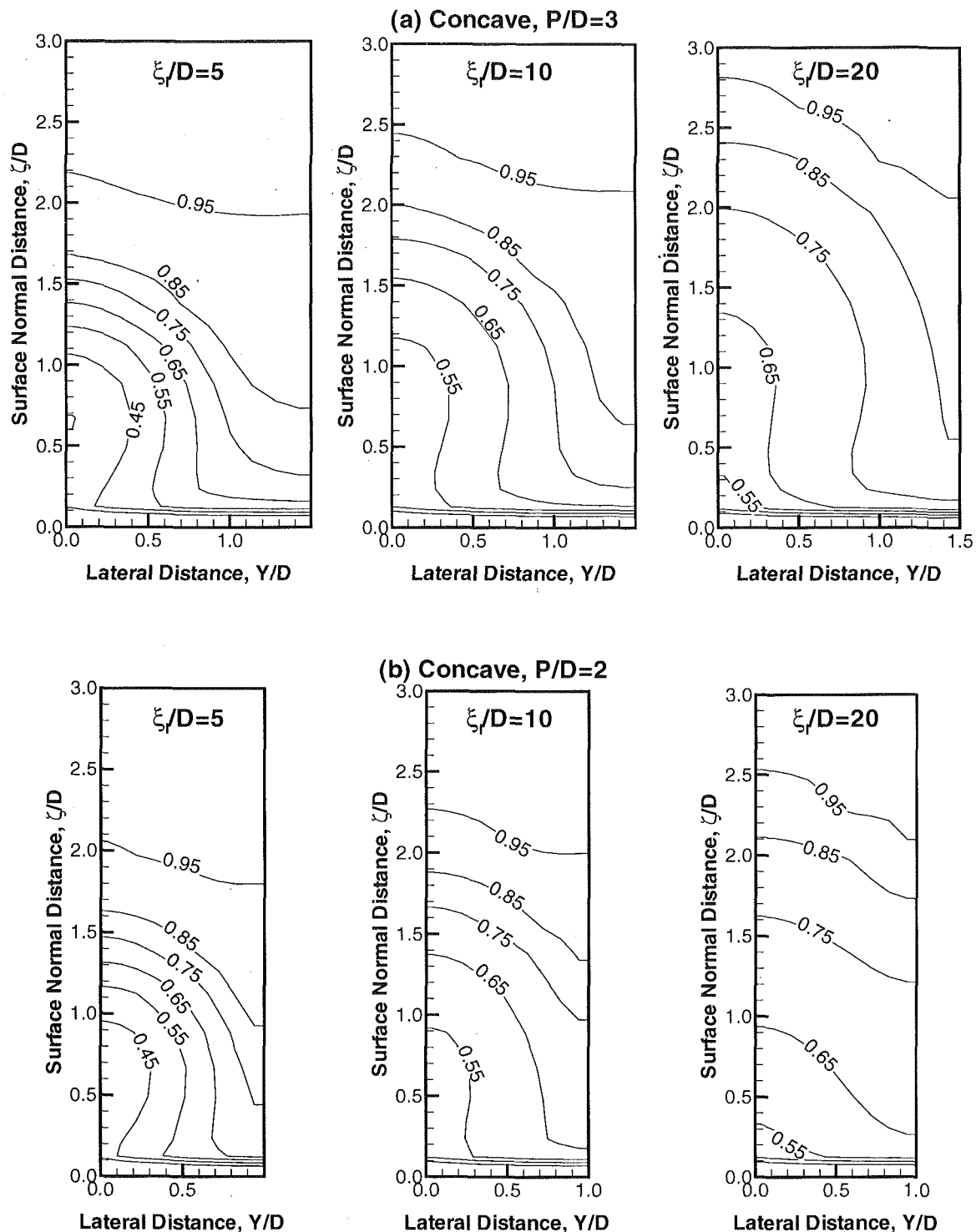

Fig. 12 The effect of hole spacing on cooling effectiveness of a concave surface ($M = 0.5$)

(a) Concave, P/D=3

(b) Concave, P/D=2

Fig. 14 The effect of hole spacing on U_ξ/U_∞ contours of a concave surface ($M = 1.0$)

the hole spacing is $2D$, we can have two rows of staggered holes where the hole spacing in each row is $4D$. To demonstrate this, we considered the film cooling layout shown in Fig. 2. This figure shows two rows of staggered holes, where the streamwise distance between rows is $5D$. Since injection is streamwise, by symmetry, only half of each hole was considered. Both convex and concave surfaces were studied with this configuration for blowing rates of 0.5 and 1.0. The other geometric parameters used in this case were the same as those used earlier, i.e., $\alpha = 35$ deg, $L/D = 5$, etc.

Figures 17 and 18 show the distribution of adiabatic effectiveness on the convex surface for $M = 0.5$ and $M = 1.0$, respec-

tively. In these figures, the results for the staggered-hole arrangement ($P/D = 4$) are compared against the results for the one-hole arrangement with $P/D = 2$. From these figures, we may note the following two main points. First, except in the region between the two rows, the laterally averaged effectivenesses for the two film cooling arrangements are nearly the same for both $M = 0.5$ and $M = 1.0$. In the region between the two rows, the cooling effectiveness for the staggered-hole arrangement is lower because there is only one hole to cover a larger area ($P/D = 4$). Second, the centerline effectiveness following the second hole (plane 2) is much larger than the centerline effectiveness following the first
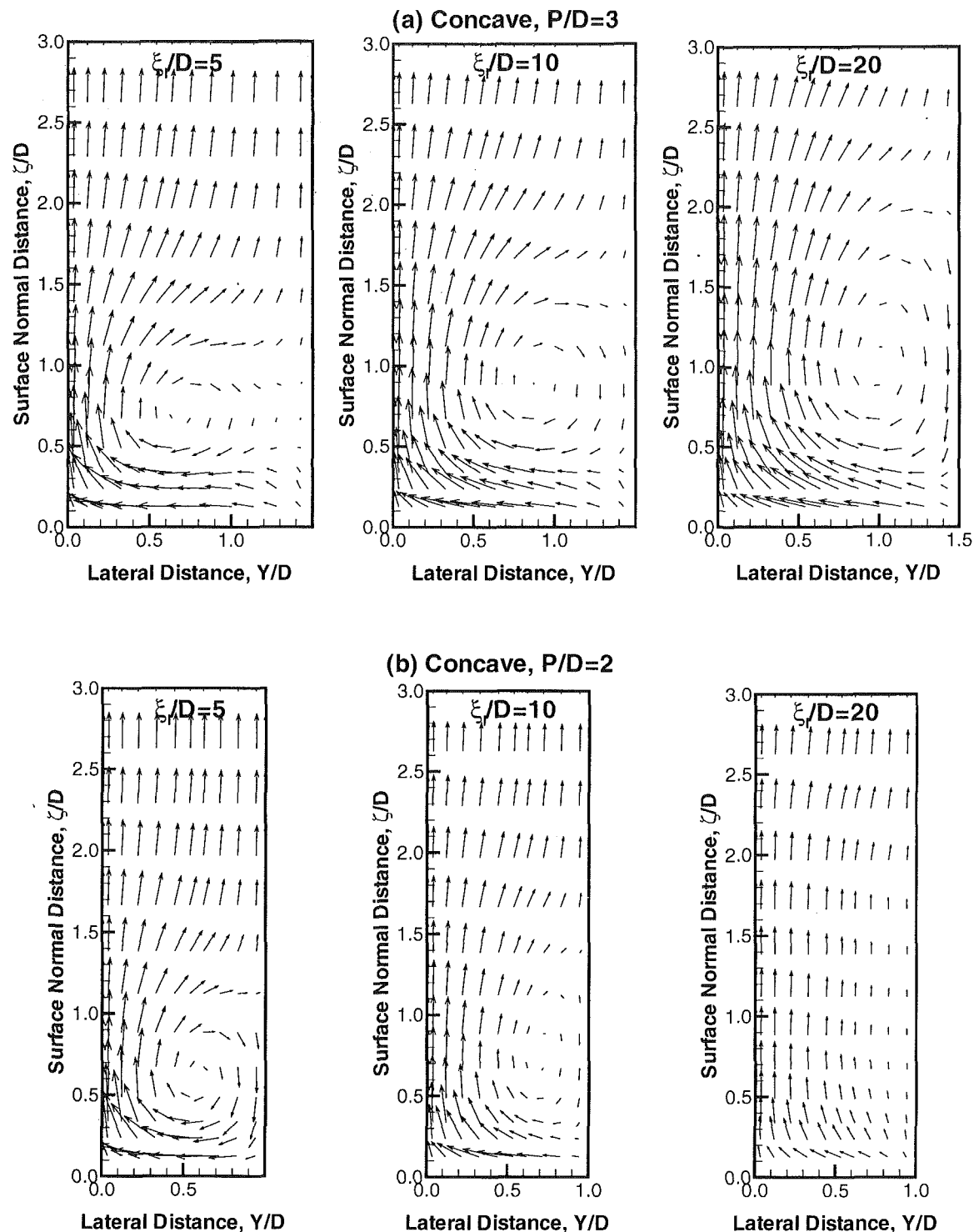
(a) Concave, P/D=3

(b) Concave, P/D=2

Fig. 15   The effect of hole spacing on counterrotating vortices of a concave surface (M = 1.0)

hole (plane 1). This is because the development of the counterrotating system of vortices following the second hole is inhibited by the vortices of the first hole. To a lesser degree, the vortices of the first hole are also affected by vortices of the second hole.

Figures 19 and 20 show the effects of hole staggering on film cooling effectiveness of the concave surface for $M = 0.5$ and $M = 1.0$, respectively. Again, the results for the one-hole arrangement are compared with the results for the staggered-hole arrangement. The results shown are very similar to those shown in Figs. 17 and 18. First, the laterally averaged effectiveness for the two film cooling arrangements are nearly the same. Second, the distribution

of the centerline effectiveness following the second hole (plane 2) is much larger than that following the first row (plane 1). This is again due to the suppression of the vortices of the second hole by the vortices of the first hole.

The effects of hole staggering on jet penetration and counterrotating vortices were studied using plots of U_ξ/U_∞ contours and velocity vectors in cross-stream planes. Figure 21 shows these plots for the concave surface for $M = 1.0$. By comparing these plots with the plots shown in Figs. 14 and 15 (at $\xi_1 = 5D$), we can see that, for the staggered-hole arrangement, the jet penetration is also smaller and the counterrotating vortices weaker. Note that the
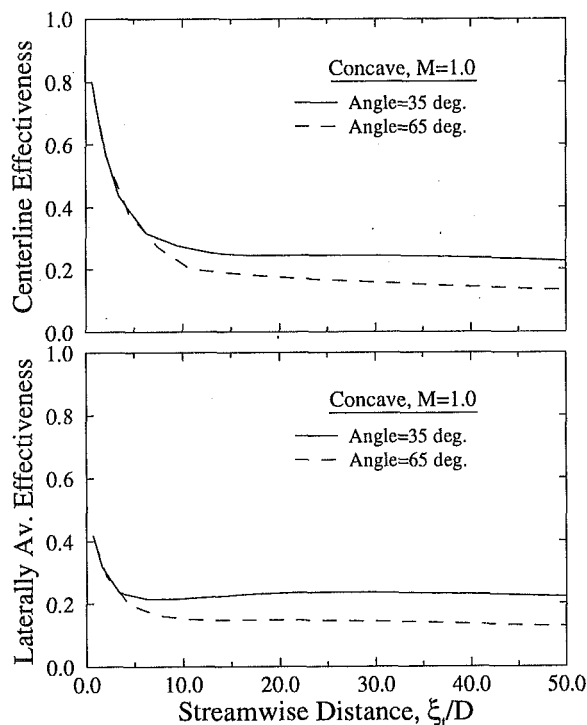
Fig. 16 The effect of injection angle on cooling effectiveness of a concave surface (*M* = 1.0, *P/D* = 2)
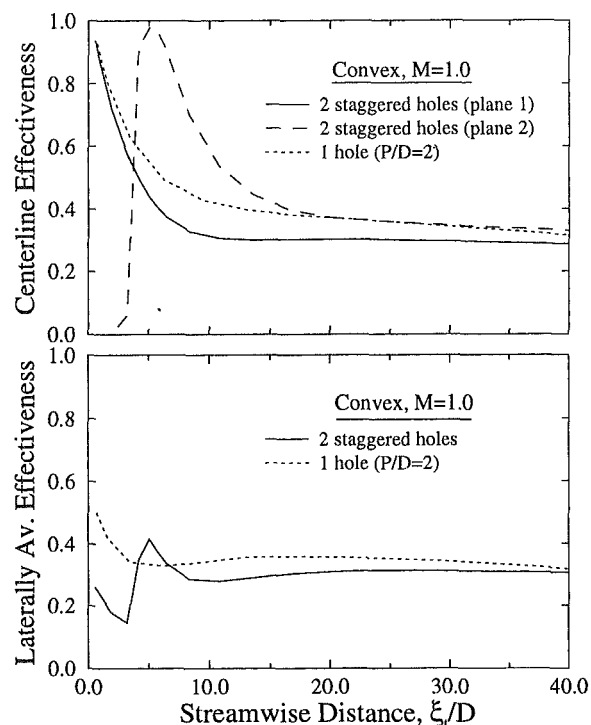
Fig. 18 The effect of hole staggering on cooling effectiveness of a convex surface (*M* = 1.0)

plots shown in Fig. 21 are for streamwise distances of $10D$, $20D$, and $40D$, following the leading edge of the first row. Hence, as far as the second row is concerned, these streamwise distances are equivalent to $5D$, $15D$, and $35D$, respectively, from the leading edge of the second hole. In conclusion, hole staggering also reduces jet penetration, weakens counterrotating vortices, and increases the film cooling effectiveness.

The Effect of Hole Length. The effect of hole length on cooling performances of convex and concave surfaces was investigated by considering L/D ratios of 1.75, 5.0, and 6.0. For the blowing ratios of 0.5, 1.0, and 1.5 examined, the computed cooling effectiveness results for the three L/D ratios were found to be essentially the same, i.e., no significant differences were observed.

Fig. 17 The effect of hole staggering on cooling effectiveness of a convex surface (*M* = 0.5)
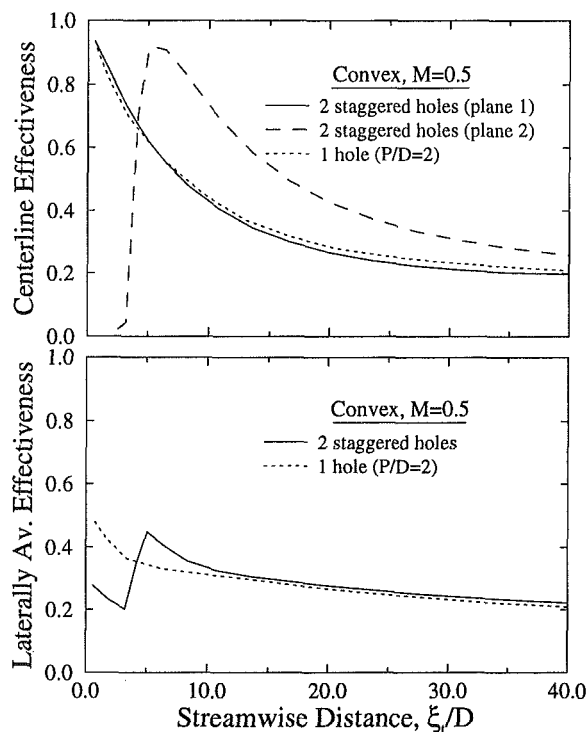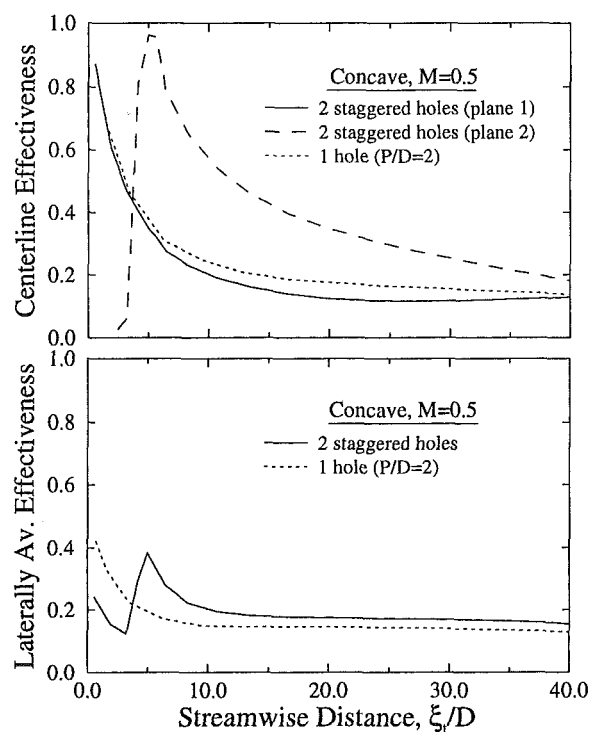

Fig. 19 The effect of hole staggering on cooling effectiveness of a concave surface (*M* = 0.5)
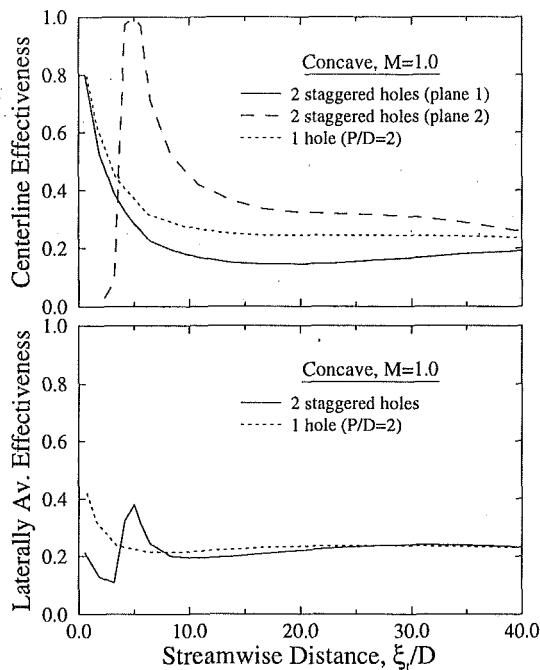
Fig. 20 The effect of hole staggering on cooling effectiveness of a concave surface ($M = 1.0$)

As discussed by Berhe (1997), on both the flat and curved surfaces, the main effect of hole length is to change the velocity and turbulence intensity profiles at hole exit. However, the effect of these changes on cooling effectiveness is small, especially on curved surfaces. This is because of the existence of pressure gradients on convex surfaces and strong vortices on concave surfaces. On convex surfaces, the pressure gradient forces the coolant jets toward the walls so that the effect of some variations in the velocity profile at hole exit is minimized. Similarly, on concave surfaces, the coolant jets are more thoroughly mixed with the mainstream gases so the effect of some variations in velocity profile at hole exit is insignificant. In conclusion, as far as surface cooling effectiveness is concerned, the hole length is not a significant film cooling parameter.

Conclusions

Three-dimensional film cooling computations have been conducted on convex and concave film cooling geometries, which included the mainflow, injection hole, and supply plenum regions. The effects of several parameters on film cooling performance have been investigated, including the effects of blowing ratio, injection angle, hole length, hole spacing, and hole staggering. The results presented and discussed include plots of adiabatic effectiveness as well as plots of velocity contours and velocity vectors at several cross-sectional planes.

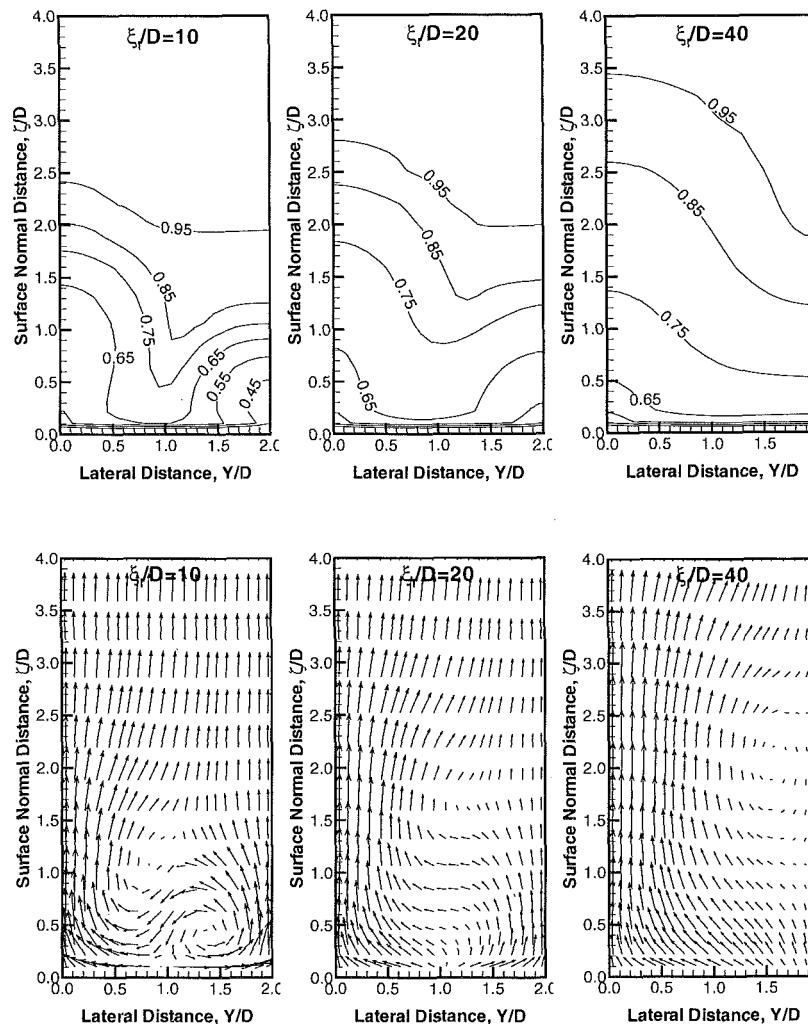The blowing ratio is one of the most significant parameters

Fig. 21 The effect of hole staggering on U_ξ/U_∞ contours and counterrotating vortices on a concave surface ($M = 1.0$)

investigated. Higher blowing ratios produce larger jet penetration and stronger counterrotating vortices. These two factors degrade the film cooling performance when the blowing ratio exceeds its optimum value. On the convex geometry studied, the optimum blowing ratio was found to be around 1.0, as contrasted to the optimum blowing ratio of about 0.5 obtained for flat-plate geometries. The optimum blowing ratio on convex surfaces is higher because the pressure gradients that exist on these surfaces force the coolant jets toward the walls. On the other hand, on the concave surface studied, larger blowing ratios generally produced higher cooling effectiveness.

The injection angle affects the cooling effectiveness mainly by affecting the jet penetration into the mainstream. On the convex surface studied, smaller injection angles produced higher cooling effectiveness than larger angles. However, on the concave surface studied, the effect of injection angle on cooling effectiveness was found to be much less significant.

Hole spacing was found to have a very significant effect on cooling effectiveness, especially on concave surfaces. By reducing the hole spacing from $3D$ to $2D$, a dramatic increase in both the centerline and laterally averaged cooling effectiveness was obtained. This increase in cooling effectiveness was found to be due to not only the increase in coolant mass per unit area, but also the decrease in jet penetration and the weakening of the counterrotating vortices.

The advantages of a smaller hole spacing can also be realized by using a staggered-hole arrangement. The staggered-hole arrangement studied produced smaller jet penetration, weaker vortices, and higher cooling effectiveness.

Except in situations where the hole length is very small, the hole length was found to have an insignificant effect on cooling effectiveness of curved surfaces. This is because, on both convex and concave surfaces, surface effects (vortices on concave surfaces and pressure gradients on convex surfaces) minimize the effects of changes in velocity and turbulence profiles at hole exit.

References

Ames, F. E., 1998, "Aspects of Vane Film Cooling With High Turbulence: Part II—Adiabatic Effectiveness," ASME JOURNAL OF TURBOMACHINERY, Vol. 120, pp. 777–784.

Berhe, M. K., 1997, "A Numerical Study of Discrete-Hole Film Cooling," Ph.D. Thesis, University of Minnesota, MN.

Berhe, M. K., and Patankar, S. V., 1999, "Curvature Effects on Discrete-Hole Film Cooling," ASME JOURNAL OF TURBOMACHINERY, Vol. 121, this issue, pp. 781–791.

Cruse, M. W., Yuki, U. M., and Bogard, D. G., 1997, "Investigation of Various Parametric Influences on Leading Edge Film Cooling," ASME Paper No. 97-GT-296.

Garg, V. K., and Gaugler, R. E., 1996, "Leading Edge Film Cooling Effects on Turbine Blade Heat Transfer," Numerical Heat Transfer, Vol. 30, Part A, pp. 165–187.

He, P., Salcudean, M., and Gartshore, I. S., 1995, "Computation of Film Cooling for the Leading Edge Region of a Turbine Blade Model," ASME Paper No. 95-GT-20.

Kohli, A., and Bogard, D. G., 1997, "Adiabatic Effectiveness, Thermal Fields, and Velocity Fields for Film Cooling With Large Angle Injection," ASME JOURNAL OF TURBOMACHINERY, Vol. 119, pp. 352–358.

Kruse, H., 1985, "Effects of Hole Geometry, Wall Curvature and Pressure Gradient on Film Cooling Downstream of a Single Row," Heat Transfer and Cooling in Gas Turbines, AGARD-CP-390.

Lin, Y. L., Stephens, M. A., and Shih, T. I.-P., 1997, "Computation of Leading-Edge Film Cooling With Injection through Rows of Compound-Angle Holes," ASME Paper No. 97-GT-298.

Martin, C. A., and Thole, K. A., 1997, "Leading Edge Film-Cooling With Compound Angle Injection," ASME Paper No. 97-GT-297.

Schwarz, S. G., 1986, "Film Cooling of Curved Surfaces," Ph.D. Thesis, University of Minnesota, MN.

Stone, L. D., 1992, "Film Cooling of Curved Surfaces at Low Injection Angles," M.S. Thesis, University of Minnesota, MN.

Heat Transfer and Flow Phenomena in a Swirl Chamber Simulating Turbine Blade Internal Cooling

C. R. Hedlund[1]
Graduate Student.

P. M. Ligrani
Professor.

Convective Heat Transfer Laboratory,
Department of Mechanical Engineering;
University of Utah,
Salt Lake City, UT 84112

H.-K. Moon
Principal Engineer.

B. Glezer
Head of Heat Transfer and Turbine Cooling.

Solar Turbines Inc.,
Turbine Cooling Design and Analysis,
San Diego, CA 92186

Heat transfer and fluid mechanics results are given for a swirl chamber whose geometry models an internal passage used to cool the leading edge of a turbine blade. The Reynolds numbers investigated, based on inlet duct characteristics, include values that are the same as in the application (18,000–19,400). The ratio of absolute air temperature between the inlet and wall of the swirl chamber ranges from 0.62 to 0.86 for the heat transfer measurements. Spatial variations of surface Nusselt numbers along swirl chamber surfaces are measured using infrared thermography in conjunction with thermocouples, energy balances, digital image processing, and in situ calibration procedures. The structure and streamwise development of arrays of Görtler vortex pairs, which develop along concave surfaces, are apparent from flow visualizations. Overall swirl chamber structure is also described from time-averaged surveys of the circumferential component of velocity, total pressure, static pressure, and the circumferential component of vorticity. Important variations of surface Nusselt numbers and time-averaged flow characteristics are present due to arrays of Görtler vortex pairs, especially near each of the two inlets, where Nusselt numbers are highest. Nusselt numbers then decrease and become more spatially uniform along the interior surface of the chamber as the flows advect away from each inlet.

Introduction

Swirl chambers are internal flow passages arranged with either spinning vanes, internal inserts, or inlets and outlets configured to produce large-scale swirling of the flow (relative to the chamber dimensions) generally about the principal chamber axis. Because of their unique flow and thermal characteristics, they are applied to a considerable variety of engineering situations. Swirl chambers are used to fractionate solid particulates suspended and transported with liquids and gases, to enhance mixing processes in combustion chambers, to increase the quality at which critical heat flux occurs in two-phase flows, and for spray-drying applications when used with an atomizer. Devices producing large-scale swirling are also employed to enhance surface heat and mass transfer levels. As such, swirl chambers are employed in heat exchangers, automobile engines, furnaces, biomedical devices, and devices used for heating and cooling of metal ingots. In the present study, heat transfer and fluid mechanics within a swirl chamber are investigated as applied to augmentation of heat transfer rates for internal turbine blade cooling, a new application recently introduced by Glezer et al. (1996, 1997). Such high-pressure blades are employed in industrial gas turbines used for power generation.

Kreith and Margolis (1959) first proposed that swirl induced in tube flows can augment surface heat transfer rates relative to unswirled flows. Khalatov and Zagumennov (1990), Glezer et al. (1996, 1998), Ligrani et al. (1997), Moon et al. (1998), Thambu et al. (1999), Hedlund et al. (1999), and others later employed tangential jets from wall slots to induce large-scale swirling in internal tube flows. Swirling flows are also induced in tubes using twisted tape inserts to augment measured surface heat transfer

rates by a number of investigators, including Date (1974) and Hong and Bergles (1976). Recent experimental investigations of fluid mechanics in swirl chambers with single-phase flow, wall injection, and no heat transfer include Kumar and Conover (1993), Dong and Lilly (1993), Bruun et al. (1993), Fitouri et al. (1995), and Chang and Dhir (1994). Rotating vanes, blades, propellers, or honeycombs are used near tube entrances by Sampers et al. (1992), Li and Tomita (1994), and Kok et al. (1993) to induce swirl in adiabatic flows. Surveys of swirl flow investigations are presented by Gambil and Bundy (1962), Bergles (1969), Razgaitis and Holman (1976), Papadopoulos et al. (1991), and Ligrani et al. (1997).

The present study extends understanding of the physical behavior of flows in swirl chambers because both heat transfer and fluid mechanics results are given for a geometry that models an internal passage used to cool the leading edge of a turbine blade. Because multiple inlets are employed at fixed locations to induce swirling, the geometry of our swirl chamber is different from the geometries used in all other existing investigations (except for Ligrani et al., 1997, and Glezer et al., 1998). Particular attention is devoted to flow and thermal behavior near the internal concave surface of the swirl chamber. Spatial variations of surface Nusselt numbers along swirl chamber surfaces are given, measured using infrared thermography in conjunction with thermocouples, energy balances, digital image processing, and *in situ* calibration procedures. The structure and streamwise development of arrays of Görtler vortex pairs, which develop along concave surfaces, are described from flow visualizations. Overall swirl chamber structure is also described from time-averaged surveys of the circumferential component of velocity, total pressure, static pressure, and the circumferential component of vorticity.

Experimental Apparatus and Procedures

Swirl Chamber for Heat Transfer Measurements. A schematic of the swirl chamber used for heat transfer measurements is
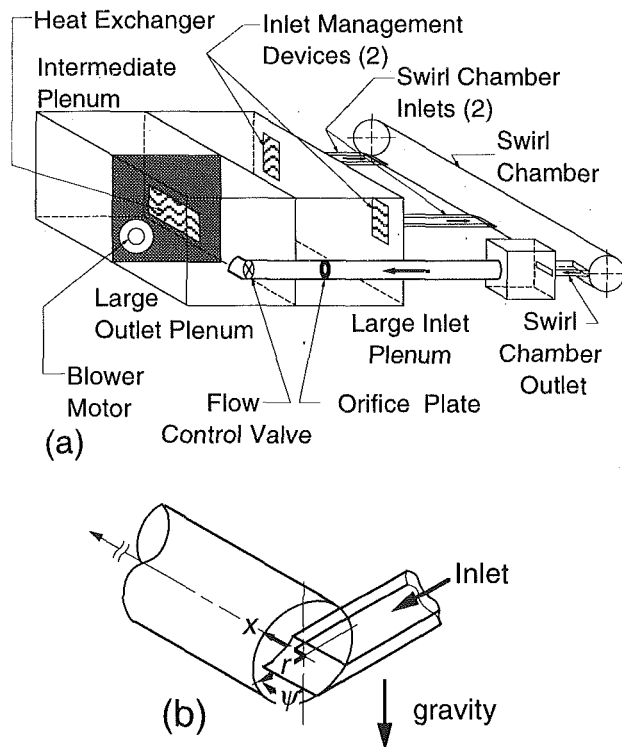

(a)

(b)

Fig. 1 Swirl chamber used for heat transfer measurements: (a) schematic drawing; (b) coordinate system

shown in Fig. 1(a). The coordinate system is shown in Fig. 1(b). The air used within the swirl chamber is circulated in a closed loop by a Dayton 5CO87-80CFM induced draft blower, which forces air through the facility, starting with a series of three large 1 m square plenums. A Bonneville crossflow heat exchanger is located between two of these plenums, and is cooled by circulating the flow rate of liquid nitrogen required to give the desired air temperature at its exit. As the air exits the heat exchanger, it enters the third plenum, from which the air passes into one of two rectangular bell mouth inlets, each followed by a honeycomb, two screens, and a two-dimensional 10 to 1 contraction ratio nozzle. Each of the two nozzles leads to a rectangular cross-sectional inlet duct 21.7 hydraulic diameters in length, connected to the principle swirl chamber cylinder so that one surface is tangent to the cylinder inner circumference. The cylinder length is 1.43 m, and its inner and

outer diameters are 0.191 m and 0.203 m, respectively. Because the ratio of the radial extent of the inlet duct to the radius of curvature of the swirl chamber is 0.160, the curvature near cylinder walls is considered to be "strong." With this arrangement, the flow has important axial and circumferential components of velocity, and the overall flow pattern through the cylinder is similar to a helix. The exit duct from the cylinder is oriented in a radial/axial plane near the end of the swirl chamber cylinder at a location along the cylinder farthest from the inlet ducts. This exit duct is then connected to a 0.305 m square plenum, which is followed by a pipe containing a valve and an orifice plate, used to regulate and measure the air flow rate, respectively. This pipe is then connected to the same large plenum adjoining the blower inlet.

All exterior and many interior surfaces of the facility are insulated with two to three layers of 2.54-cm-thick, Elastomer Products black neoprene foam insulation ($k = 0.038$ W/m K) to minimize heat losses. Calibrated copper-constantan thermocouples are located between the three layers of insulation located outside of the main cylinder of the swirl chamber to determine conduction losses. Between the first layer and the 0.635-cm-thick acrylic cylinder of the chamber are 11 custom-made Electrofilm etched-foil heaters (each encapsulated between two thin layers of capton) to provide a constant heat flux boundary condition on the concave test surface. The acrylic cylinder contains 30 copper-constantan thermocouples, and its inner surface is adjacent to the air stream. Each of these thermocouples is located 0.0508 cm just below this surface to provide measurements of local surface temperatures, after correction for thermal contact resistance and temperature drop through the 0.0508 cm thickness of acrylic. Acrylic is chosen because of its low thermal conductivity ($k = 0.16$ W/m K at 20°C) to minimize axial and circumferential conduction along the test surface, and thus minimize "smearing" of spatially varying temperature gradients along the test surface. Acrylic also works well for infrared imaging because its surface emissivity ranges from 0.60 to 0.65. The power to each foil heater is controlled and regulated by a separate variac power supply. Energy balances, performed on each heated segment of the swirl chamber cylinder, then allow determination of local magnitudes of the convective heat flux.

As the facility is prepared for measurements, frost build-up is minimized by lowering the air temperature to just below the dew point to condense all water vapor from the air within the facility. This liquid water is then drained from the facility. Air temperatures as low as −120°C are then obtained with additional cooling as the air continues to re-circulate through the closed-loop facility. The mixed-mean temperature of the air entering the swirl chamber is measured using five calibrated copper-constantan thermocouples

---

Nomenclature

D = diameter of main swirl chamber cylinder

D_H = hydraulic diameter of one swirl chamber inlet

h = heat transfer coefficient = $\dot{q}''/(T_w - T_i)$

k = thermal conductivity

L = upstream (smallest axial) location of axial/radial measurement or visualization plane, measured from $x = 0$

Nu = Nusselt number = hD/k

P_a = ambient pressure external to the swirl chamber at entrances to inlet ducts

P_s = static pressure in swirl chamber

P_t = total pressure in swirl chamber

$\dot{q}''$ = local wall heat flux

Re_D = Reynolds number based on swirl chamber main cylinder characteristics = $\bar{U}D/\nu$

Re = Reynolds number based on inlet duct characteristics = $2\bar{V}D_H/\nu$

r = radial distance measured from swirl chamber centerline

r_o = radius of the large cylinder comprising the swirl chamber

T = temperature

u_x = axial component of velocity

u_r = radial component of velocity

u_ψ = circumferential component of velocity

$\bar{U}$ = average axial velocity across swirl chamber cylinder

$\bar{V}$ = average bulk velocity at one swirl chamber inlet

x = axial distance measured from swirl chamber end face

ν = fluid kinematic viscosity

ρ = fluid density

ψ = circumferential angle measured from swirl chamber vertical plane

ω_ψ = circumferential component of vorticity

Subscripts

i = mixed-mean value at the cylinder inlet

w = local wall value

Superscripts
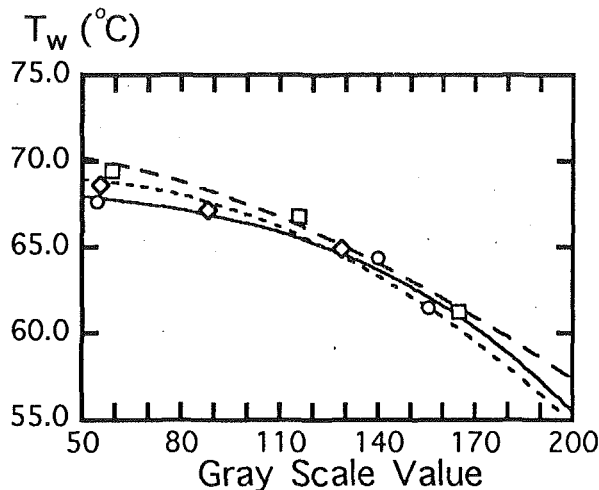
$^-$ = spatially averaged

Fig. 2 Example calibrations of the infrared imaging system for different window orientations and different camera views into the swirl chamber

spread across the cross section of each inlet duct, just downstream of each nozzle. These locations are chosen for these measurements because temperature and velocity profiles are uniform across the duct, allowing simple determination of local mixed-mean temperatures. Mixed-mean temperature at each entrance to the cylinder is then determined after accounting for conduction losses through each inlet duct. With this approach, the ratio of cylinder inlet mixed-mean temperature to local wall temperature is as low as 0.57, which is close to the value in the application. All measurements are obtained when the swirl chamber is steady state, achieved when temperatures from the 30 thermocouples (on the swirl chamber surface) vary by less than 0.1°C over a 10 minute period.

Local Nusselt Number Measurement. Spatially resolved temperature distributions along the swirl chamber concave surface are determined using infrared imaging in conjunction with thermocouples, energy balances, digital image processing, and *in situ* calibration procedures. To accomplish this, the infrared radiation emitted by the heated interior surface of the swirl chamber is captured using a VideoTherm 340 Infrared Imaging Camera, which operates at infrared wave lengths from 8 μm to 14 μm. Temperatures, measured using the 30 calibrated, copper-constantan thermocouples distributed along the swirl chamber surface adjacent to the flow, are used to perform the *in situ* calibrations simultaneously as the radiation contours from surface temperature variations are recorded.

This is accomplished as the camera views the test surface through a custom-made, cylindrical zinc–selenide window (which transmits infrared wave lengths between 6 and 17 μm). Reflection and radiation from surrounding laboratory sources are minimized using an opaque shield, which covers the camera lens and the zinc selenide window. Frost build-up on the outside of the window is eliminated using a small heated air stream from a hair dryer. The window is located on a segment of the swirl chamber, which is either rotated or relocated axially so that the camera can view different portions of the interior surface of the swirl chamber. At least two, and as many as five, thermocouple junction locations are present in any field viewed by the camera. The exact spatial locations and pixel locations of these thermocouple junctions and the coordinates of a 12.7 cm × 12.7 cm field of view are known from calibration maps obtained prior to measurements. During this procedure, the camera is focused, and rigidly mounted and oriented relative to the test surface in the same way as when radiation contours are recorded.

With these data, gray scale values at pixel locations within videotaped images from the infrared imaging camera are readily

converted to temperatures. Examples of such calibration data are shown in Fig. 2 for three different camera views of the test surface. Because such calibration data depend strongly on camera adjustment, the same brightness, contrast, and aperture camera settings are used for all three data sets. Each calibration data set shown in Fig. 2 is fit to a second- or third-order polynomial. The slight differences between the three calibration data sets result because transmissivity of the zinc selenide window and the emissivity of the swirl chamber test surface both exhibit small variations as camera angle, camera and test surface orientation, surface temperatures, or experimental conditions are changed. The *in situ* calibration approach is advantageous because it rigorously and accurately accounts for these variations.

Images from the infrared camera are recorded as 8-bit gray scale images on commercial videotape using a Panasonic AG-1960 video recorder. Images are then digitized using NIH Image v1.60 software, operated on a Power Macintosh 7500 computer. Subsequent software is used to perform coordinate transformations to correct for non-rectangular, "stretched," or distorted recorded images because of camera perspective or because camera lens orientation is not normal to the curved target surface. This software also converts each of 256 possible gray scale values to temperature at each pixel location using calibration data, and then determines values of local Nusselt numbers. Thermal conductivity in the Nusselt number is based on the average temperature of the air at the cylinder inlets. Contour plots of local surface temperature and Nusselt number (in "unrolled" planar, Cartesian coordinates) are prepared using DeltaGraph v4.0 software. Each individual image covers a 250 pixel by 250 pixel area. 42 of these images are used to produce the data presented in Fig. 9.

Swirl Chamber for Flow Measurements. A second swirl chamber is used for flow measurements and is described by Ligrani et al. (1997). Location of inlets and outlet are shown in the schematic drawing in Fig. 4. The coordinate system, shown in Fig. 1(*b*), and overall layout, shown in Fig. 1(*a*), also apply to this chamber. The main cylinder is 4.477 m long in the *x* direction, and is made of clear acrylic to allow visualization of flow phenomena inside. It also includes several doors, and numerous slots lined with foam for insertion of the five-hole pressure probe or smoke injection tubes. Outer diameter is 0.610 m, and inner diameter is 0.597 m. Overall swirl chamber size is chosen to achieve the same inlet passage Reynolds numbers as in the application, with average mean velocities low enough to visualize the flow. Prior to entering the main cylinder of the swirl chamber, air from the laboratory is managed in the same way as in the swirl chamber used for heat transfer measurements. In this facility, flow is induced by suction from a L. J. Wing Mfg. Co. A1/4A4W5 vane axial fan. All flow measurements and visualizations in this facility are made isothermally without surface heat transfer.

Flow Visualization. The smoke injection for flow visualization is used to identify vortex structures. Smoke from burning mesquite wood in a specially designed smoke generator is injected into the facility one of two ways: (*i*) into the inlet bellmouth, prior to conditioning the flow, using a cylindrical manifold with a row of small tubes, which produce an array of quiescent, laminar jets of smoke, or (*ii*) through the cylinder wall through one of the slots lined with foam. In either case, the smoke forms into a single thin layer next to the concave surface of the swirl chamber cylinder as it enters the flow. The smoke in this layer is neutrally buoyant in laboratory air, very dense, and has fairly uniform particle size distribution. As the smoke is advected downstream, the secondary flows that accompany Görtler vortex development cause the smoke to be rearranged in patterns that show the locations and distributions of the Görtler vortices. Smoke patterns are illuminated in different planes using spot lights directed through slits in black paper (used to line the exterior of the experimental apparatus) to illuminate thin, axial/radial planes (or sheets) of light. Images are recorded using a Dage-MTI CCD72 camera and control box with a Computar Inc. 12.5 mm, F1.8 lens, connected to a Panasonic

AG-1960 type 4-head, multiplex videocassette recorder. Images recorded on videotape (taken individually or in sequence) are then processed and digitized using Apple Video processing and capture software employed on a Macintosh Power PC computer. Images are then enhanced, further processed, and arranged for printing using Adobe PhotoShop software on the same computer. Additional details are provided by Ligrani et al. (1997).

Total Pressure, Static Pressure, and Mean Velocity Components. A United Sensor DC-250-24-CD five-hole pressure probe, and a five-hole pressure probe manufactured at the University of Utah, each with a conical shaped sensing head of 6.35 mm diameter, are used to obtain time-averaged surveys of total pressure, static pressure, and the three mean velocity components. Procedures for calibration and measurement are described by Ligrani et al. (1989a, b, 1997). To obtain the surveys, the probe is mounted on an automated two-dimensional traverse, and inserted into the chamber through slots lined with foam to prevent air leakage. Outputs of the five-hole probe are connected to five Validyne DP103-06 pressure transducers, which measure differential pressures up to 2.5 mm of water. Signals from each transducer are then processed using Celesco CD10D Carrier-Demodulators. Voltages from the Carrier-Demodulators are acquired using Hewlett-Packard 44422A data acquisition cards installed in a Hewlett-Packard 3497A data acquisition control unit. This control unit, the Superior Electric type M092-FD310 Mitas stepping motors on the two-dimensional traverse, a Superior Electric Modulynx Mitas type PMS085-C2AR controller, and a Superior Electric Modulynx Mitas type PMS085-D050 motor drive are controlled by a Hewlett-Packard 362 Series computer. Contour plots of measured quantities are generated using a polynomial interpolating technique (within DeltaGraph software) between data points. In each survey plane, data points are spaced either 0.51 cm or 1.27 cm apart. Ligrani et al. (1997) provide additional details.

Uncertainty Estimates

Uncertainty estimates are based on 95 percent confidence levels, and determined using procedures described by Moffat (1988). The uncertainties of total pressure and static pressure (relative to atmospheric pressure) in mm of water differential pressure are ±0.015 and ±0.008, respectively (or ±0.15 and ±0.08, respectively, in Pascals). Uncertainties for circumferential, radial, and axial velocity components are ±0.07, ±0.03, and ±0.03 m/s, respectively. Uncertainty for circumferential vorticity is about ±2.4 l/s. Reynolds number uncertainty is ±20. Uncertainty of temperatures measured with thermocouples is ±0.15°C. Spatial and temperature resolutions achieved with the infrared imaging are 0.8 mm and 0.2°C, respectively. Nusselt number uncertainty is then about ±3.5.

Experimental Results and Discussion

Flow Visualization Results. Visualized flow patterns showing the streamwise development of the near-wall flow structure through the swirl chamber for Re = 4450 are presented in Fig. 3. Results at this particular Reynolds number are presented because they illustrate many flow characteristics also observed at Reynolds numbers from 1500 to 20,000. Because the smoke is a uniform, neutrally buoyant layer about 0.5 cm thick near the concave surface just after it is injected into the swirl chamber, secondary flow events that emanate from near the concave surface are smoke-rich, and correspond to light patterns in the figures. Events that originate somewhat away from the surface are free of smoke, and thus, correspond to dark patterns in the figures. Each photographic image in Fig. 3 shows flow behavior in a radial/axial plane arranged so that the concave surface of the swirl chamber is at the bottom of each image and flow moves out of the plane of the paper (axial flow then moves from right to left). Images are given for different ψ (which identifies the circumferential position of the
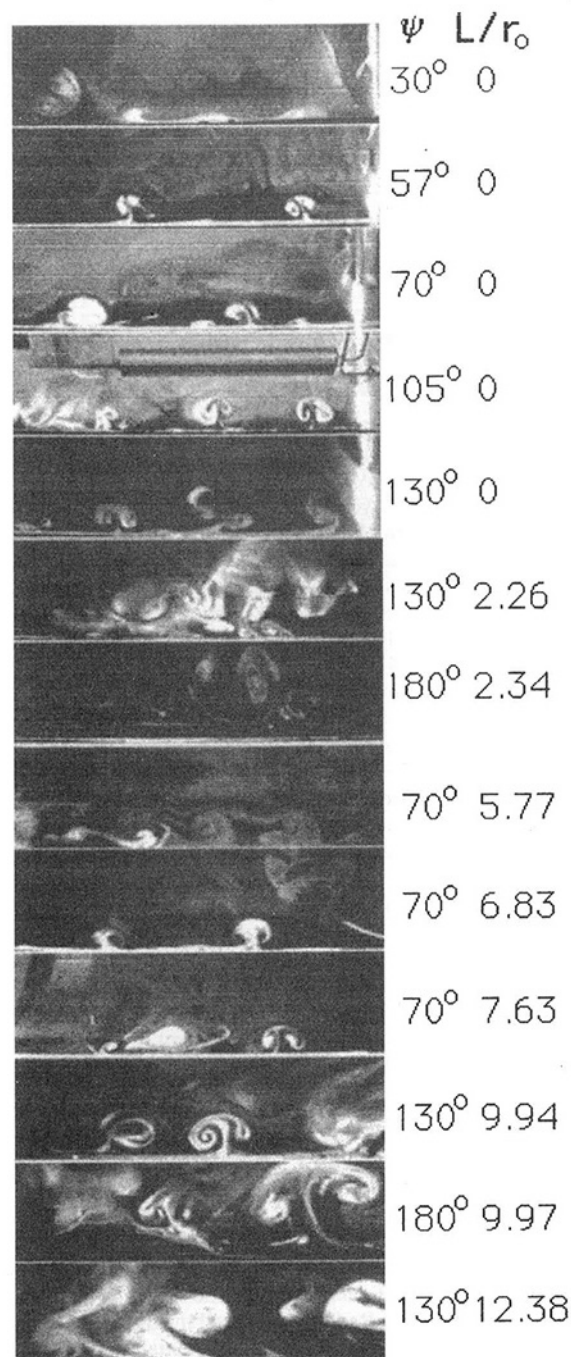

Fig. 3 Flow patterns in different visualized axial/radial planes at a constant Reynolds number Re of 4450. The ψ and L of the 13 visualized planes are identified in Fig. 4.

visualized plane) and different L (which identify the axial positions, at the smallest x values, of the right-most edges of visualization planes).

The images in Fig. 3 are presented for 13 different locations as the Reynolds number is held constant (Re = 4450). The ψ and L of the 13 locations are identified in Fig. 4, and chosen to follow the helical trajectory of the smoke as it is advected around the concave interior surface of the swirl chamber. Each image in Fig. 3 represents an instantaneous snapshot from a sequence of time-varying video images. Visualized images at almost every measurement station evidence the presence of numerous Görtler vortex pairs of different size near the concave surface of the chamber, where each vortex pair is identified by a mushroom-shaped smoke pattern. In many cases, a Görtler vortex pair is evident near the lower right-
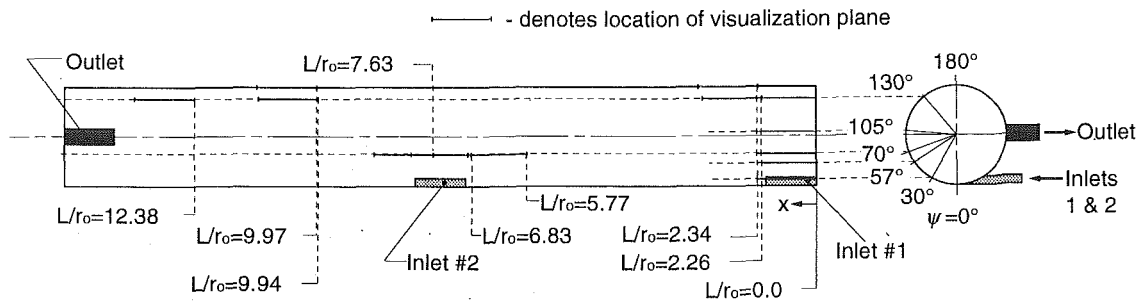
Fig. 4 Schematic of swirl chamber geometry showing locations of axial/radial visualization planes

hand corner of each photographic image for $L/r_0 = 0$, formed by the end wall at $x = 0$ m and the concave surface. This particular vortex pair seems to have a preferred axial location, due to the presence of the shear layer on the end wall. The distortion of the mushroom-shaped smoke patterns, especially at larger L values, evidences flow unsteadiness. Collections of highly distorted, highly unsteady vortex pairs of different size are also evident near the concave surface in many of the images.

The vortex pairs in Fig. 3 are initially very small for $\psi = 30$ deg and $L/r_o = 0$, $\psi = 57$ deg and $L/r_o = 0$, and $\psi = 70$ deg and $L/r_o = 0$ just downstream of the first swirl chamber inlet, which is located at x/r_o from 0 to 1. The vortex pairs then increase in size, number, and distortion with additional streamwise development until the smoke within them becomes quite diffuse at $\psi = 70$ deg and $L/r_o = 5.77$. Afterward, a new set of smaller Görtler vortex pair are evident near the concave surface at $\psi = 70$ deg and $L/r_o = 6.83$, and $\psi = 70$ deg and $L/r_o = 7.63$. These are present because of the growth of a new shear layer in the air from the second swirl chamber inlet, which is located at x/r_o from 7 to 8, as shown in Fig. 4. As the flow continues to develop downstream, the vortex pairs not only become increasingly distorted because of flow unsteadiness, but also dramatically increase in size. Much of the skewness and three dimensionality of the Görtler vortex pairs at these locations are due to the axial component of flow in the swirl chamber. Also particularly apparent at these locations is the continuous interactions and intermingling of different-sized Görtler vortex pairs with each other. As the Reynolds number increases, interactions between adjacent vortex pairs generally become more intense, chaotic, and frequent (Ligrani et al., 1997).

Variation of Swirl Number Magnitudes. According to Ogawa (1993), the swirl number is defined as the ratio of the nondimensional moment of momentum of the flow (with respect to the swirl chamber cylinder axis) to the nondimensional axial momentum of the flow. Radially averaged magnitudes of the swirl number, measured in the $\psi = 90$ deg axial/radial plane, are presented in Fig. 5 as it varies with nondimensional axial position
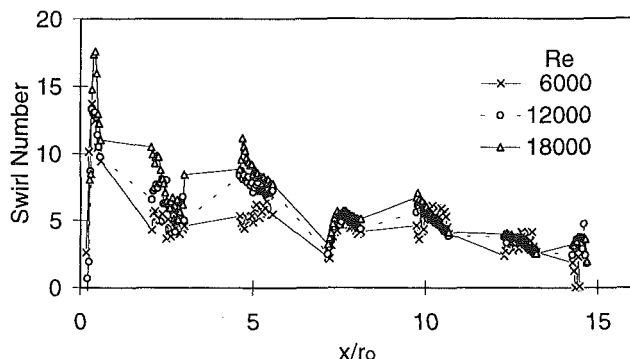
for Re of 6000, 12,000, and 18,000.

Magnitudes of the swirl number are quite high near the first inlet duct, which is located at x/r_o from 0 to 1. This is because of the proximity of this inlet to one swirl chamber end face, which restricts the axial component of the flow. As a result, axial flow momentum is relatively small in this portion of the swirl chamber, giving high swirl numbers. Assuming one-dimensional flow leaving the inlet duct and that all axial flow components are spread uniformly over the swirl chamber cross section, the ideal swirl number is 18.9 at these same axial positions. Measured swirl number can then not exceed this value, which is consistent with the results at $x/r_o = 0$–1 in Fig. 5.

Swirl number values in Fig. 5 are then lower at other swirl chamber axial locations as x/r_o increases and local axial velocities become more significant. Magnitudes seem to decrease gradually, but steadily, as x/r_o increases, and the outlet of the swirl chamber at $x/r_o = 14$–15 is approached. Swirl numbers measured near the second inlet located at $x/r_o = 7$–8 are consistent with this trend (without any local increases) because the flow turns just after it leaves this inlet, and because of fluid velocities in the axial direction at $x/r_o = 7$–8. Values as high as 6 at these locations indicate high nondimensional circumferential moment of momentum relative to nondimensional axial momentum.

Fig. 5 Variation of swirl number through the swirl chamber at different Reynolds numbers
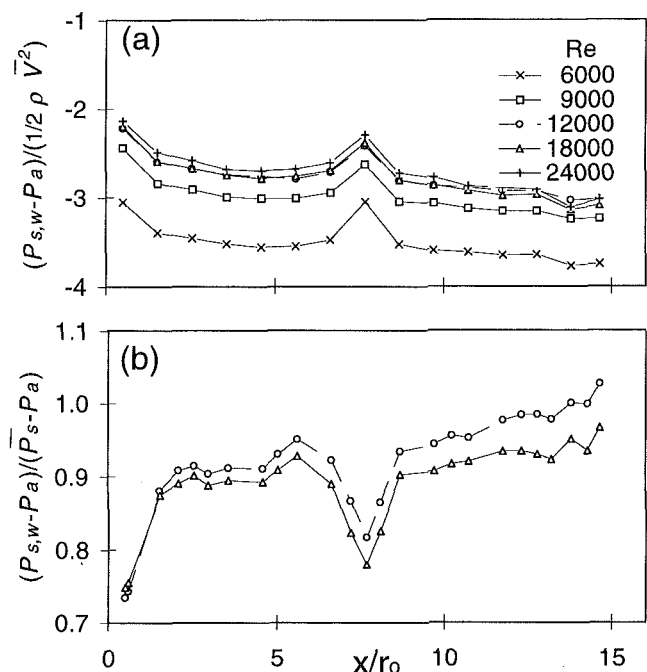
Fig. 6 Variation of static pressure through the swirl chamber at different Reynolds numbers: (a) normalized wall static pressure; (b) ratio of wall static pressure and radially averaged static pressure
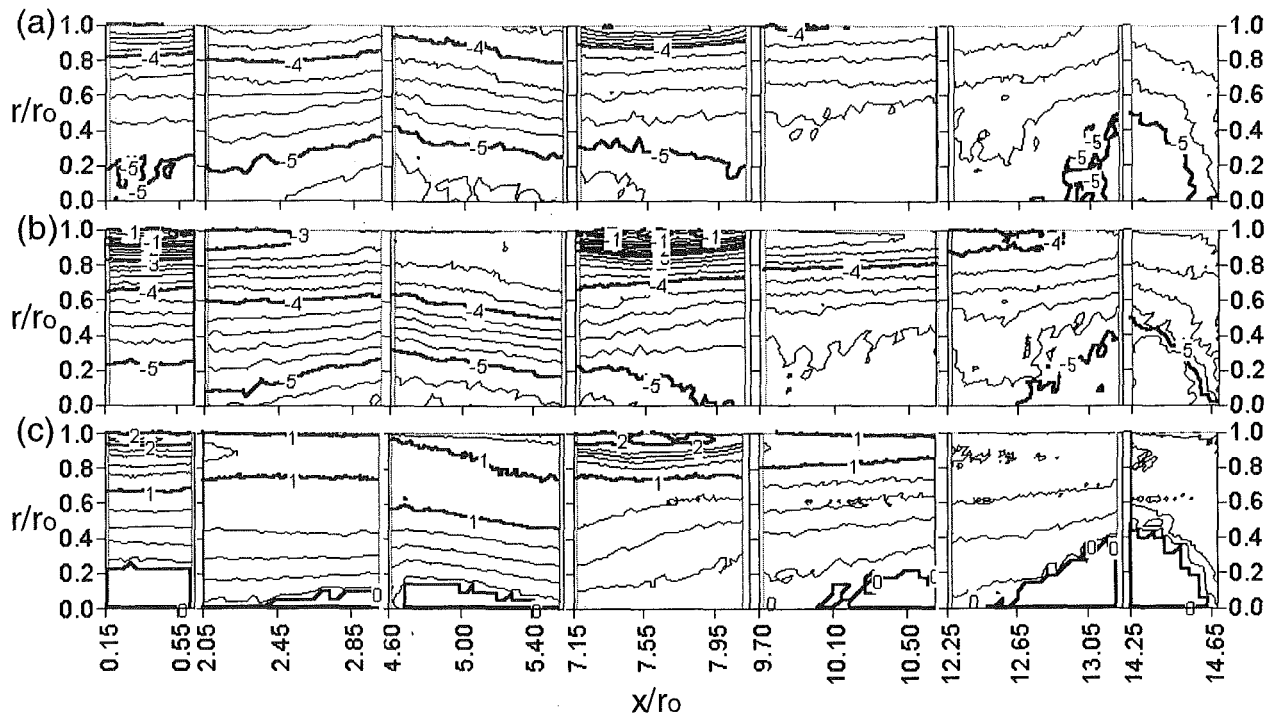
Fig. 7 Surveys along the length of the swirl chamber at Re ≈ 18,000 for the axial–radial plane located at ψ = 90 deg: (a) static pressure, P_s – P_a (Pa); (b) total pressure, P_t – P_a (Pa); (c) circumferential velocity, u_ψ (m/s)

Variation of Wall Static Pressure. Magnitudes of time-averaged surface static pressure are presented in Fig. 6(a) as dependent upon nondimensional axial position for Re of 6000, 9000, 12,000, 18,000, and 24,000. These measurements are obtained along the length of the swirl chamber at the ψ = 45 deg circumferential location. Surface static pressures are normalized by the spatially averaged kinetic energy of the inlet duct and measured relative to pressure at the entrance of the inlet ducts. The most important decreases of time-averaged static pressure occur just downstream of inlet ducts, and are believed to be mostly due to: (i) streamline curvature as flow from the tangential inlet ducts bends in the axial direction, (ii) shear between high-speed fluid from the inlet ducts and adjacent low-speed fluid in the main cylinder of the swirl chamber, and (iii) the development of small-scale secondary flows within the arrays of initially developing Görtler vortex pairs. From Fig. 6(a), it is evident that normalized wall static pressure data collapse together when the flow in the swirl chamber is fully turbulent for all three fully turbulent Reynolds numbers investigated (Re = 12,000, 18,000, and 24,000).

Ratios of time-averaged wall static pressure to time-averaged radially averaged static pressure (where the latter are measured at the ψ = 90 deg circumferential location) are presented in Fig. 6(b) as dependent upon nondimensional axial position for Re of 12,000 and 18,000. Important variations of this quantity are evident throughout the swirl chamber, with the largest changes just downstream of each inlet duct (located at x/r_o from 0 to 1 and from 7 to 8). Such data are valuable to designers of internal cooling systems because they allow the determination of spatially averaged static pressures and pressure drops from wall measured values.

Surveys of Time-Averaged Circumferential Velocity, Static Pressure, Total Pressure, and Circumferential Vorticity. Examples of time-averaged surveys of circumferential velocity, static pressure, total pressure, and circumferential vorticity are presented in Figs. 7 and 8. In these figures, r/r_o = 0 represents the cylinder axis of symmetry, and r/r_o = 1 (r = 29.85 cm) locates the concave surface. Because x/r_o increases from left to right, these plots are inverted in this direction compared to flow visualization images. Static and total pressures are both measured with respect

to the pressure at the swirl chamber inlets (at laboratory air pressure), and thus, these values are negative since the swirl chamber is operated at pressures less than the ambient value. Results at a Reynolds number of 18,000 are selected for presentation because of its match to the Reynolds number within the application.

Parts (a), (b), and (c) of Fig. 7 show surveys of static pressure, total pressure, and circumferential velocity, respectively, from one axial-radial measurement plane located along the entire length of the swirl chamber. These provide a complete picture of swirl chamber flow characteristics measured at ψ = 90 deg and Re = 18,000. The gaps between plotted ranges of x/r_o correspond to regions not surveyed because of the absence of probe access slots at these x/r_o locations in the swirl chamber main cylinder. The figures show that the total pressure and static pressure are highest at locations near the swirl chamber inlets (x/r_o = 0–1, and x/r_o =
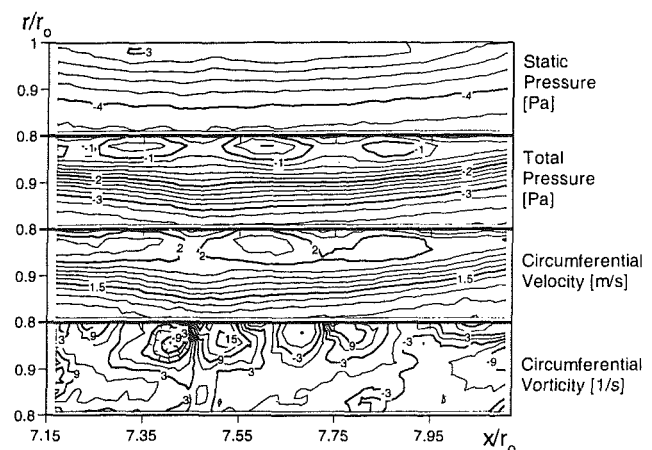

Fig. 8 Surveys of static pressure (P_s – P_a (Pa)), total pressure (P_t – P_a (Pa)), circumferential velocity, (u_ψ (m/s)), and circumferential vorticity (ω_ψ (I/s)) at ψ = 90 deg and Re = 18,000 for L/r_o = 7.15–8.15 and r/r_o = 0.8–1.0, just downstream of the second inlet
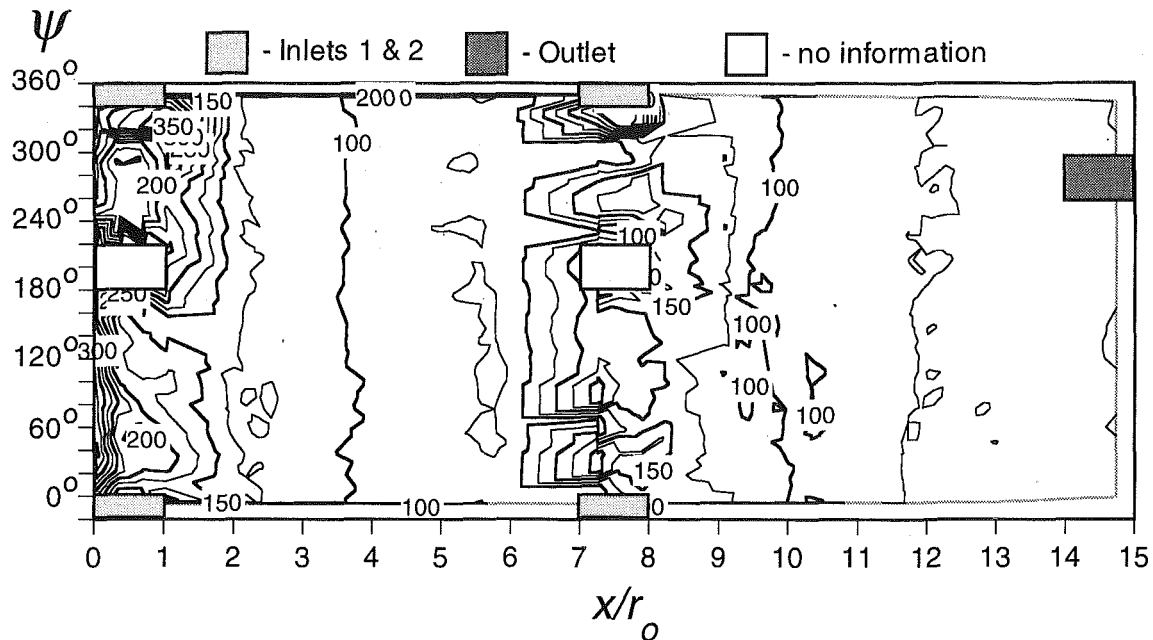
Fig. 9 Local surface Nusselt number distribution for Re = 19,400 (Re$_D$ = 7205) and T_i/T_w = 0.85 at x/r_o = 0–15 and ψ = 0–360 deg

7–8). Magnitudes of both quantities then decrease as flow moves away from these inlets, with the lowest pressure levels (or most negative $P_s - P_a$ and $P_t - P_a$) near the swirl chamber outlet at x/r_o = 14–15. Static pressure distributions measured *at the surface,* presented in Fig. 6(a), show similar qualitative trends. Static pressures also generally decrease (that is, $P_s - P_a$ becomes more negative) at each value of x/r_o as r/r_o decreases in Fig. 7(a). Total pressure distributions in Fig. 7(b) have similar qualitative trends, but with local maxima near r/r_o = 0.90–0.95 at most x/r_o locations, and higher magnitudes compared to static pressures at all locations where circumferential velocity is greater than zero. Total pressure distributions are quite convoluted due to very large gradients (just downstream of each inlet) at x/r_o = 0.15–0.65, r/r_o = 0.8–1.0, and x/r_o = 7.15–8.15, r/r_o = 0.8–1.0. Enlargements of these surveys near the second inlet are presented in Fig. 8 to provide additional information on detailed flow characteristics at that location.

Like the total pressure and static pressure, magnitudes of circumferential velocity in Fig. 7(c) generally decrease as flow moves away from each inlet, with the largest region of zero velocity at x/r_o = 12.5–15 near the swirl chamber outlet. (Inlet and outlet locations are identified on Fig. 4.) Circumferential velocity distributions at several axial locations are also similar to distributions in bounded wall jets, especially at x/r_o = 0–1 just downstream of the first inlet. Peak values are additionally evident at most all x/r_o locations near r/r_o = 0.90–0.95. Consequently, circumferential velocities generally increase at each value of x/r_o as r/r_o decreases for r/r_o > 0.90–0.95, and decrease as r/r_o decreases for r/r_o < 0.90–0.95. These two different types of behavior locate two different shear layers within the swirl chamber flow at the ψ = 90 deg circumferential position.

The results in Fig. 8 are obtained at ψ = 90 deg and Re = 18,000 at x/r_o = 7.15–8.15 and r/r_o = 0.8–1.0, just downstream of the second inlet (ψ = 0 deg, x/r_o = 7–8). As a result, measurements at these locations provide data corresponding to initial Görtler vortex pair development, and enlargement of the details of the surveys presented in Figs. 7(a), 7(b), and 7(c). Distributions of circumferential vorticity in Fig. 8 are determined from velocity components in the axial and radial directions using $\omega_\psi = \partial u_r/\partial x - \partial u_x/\partial r$.

Surveys of this quantity in Fig. 8 show regions of positive and negative time-averaged circumferential vorticity adjacent to each

other near the concave surface at r/r_o = 0.8–1.0. Each of these evidences a pair of counterrotating Görtler vortices, which are either fairly steady or have preferred positions if they vary significantly in time. In Fig. 8, pairs of vorticity concentration of opposite sign are located at x/r_o = 7.3–7.6, and x/r_o = 7.6–7.9. *Portions* of pairs of vorticity concentration are evident in Fig. 8 at x/r_o < 7.3 and x/r_o > 7.9. Deficits of total pressure and circumferential velocity are present in upwash regions (where secondary flows are directed away from the concave surface), which are located between two regions of vorticity concentration of opposite sign in each vortex pair. These are located at or near x/r_o of 7.2, 7.45, 7.75, and 8.0 in Fig. 8. Such results are important because they illustrate time-averaged Görtler vortex pair structure and further demonstrate the existence of these vortices in fully turbulent swirl chamber flows.

Local Nusselt Number Variations. Figure 9 shows the distribution of local surface Nusselt numbers at x/r_o = 0–15 for Re = 19,400 (Re$_D$ = 7205) and T_i/T_w = 0.85. These distributions are measured around the entire swirl chamber circumference (ψ = 0–360 deg) using the infrared imaging procedures described earlier. Complex Nusselt number variations are evident in the figure, especially just downstream of the inlets located at x/r_o = 0–1 and x/r_o = 7–8. Not only are Nusselt numbers highest in this region due to arrays of Görtler vortex pairs, but gradients of the Nusselt number are evident in both the x and ψ directions. Nusselt numbers then decrease and become more spatially uniform along the interior surface of the chamber as the flows advect away from each inlet. At 2 < x/r_o < 6 and at x/r_o > 9, Nusselt numbers are then quite uniform with ψ, varying mostly only in the x direction.

Figure 10 presents an enlarged portion of Fig. 9 to show the local surface Nusselt number distribution at x/r_o = 7.0–8.0 and ψ = 0–50 deg. The infrared image in Fig. 10(a) clearly shows surface variations due to Görtler vortex pairs in the form of light and dark stripes, which correspond to vortex pair trajectories along the concave surface of the chamber. This image is as recorded directly from the camera with some enhancement, but no corrections for camera angle and perspective. Surface temperature increases as image regions in Fig. 10(a) become lighter and whiter. Lower surface temperatures then coincide with higher local Nusselt numbers and higher temperatures coincide with lower local Nusselt numbers.
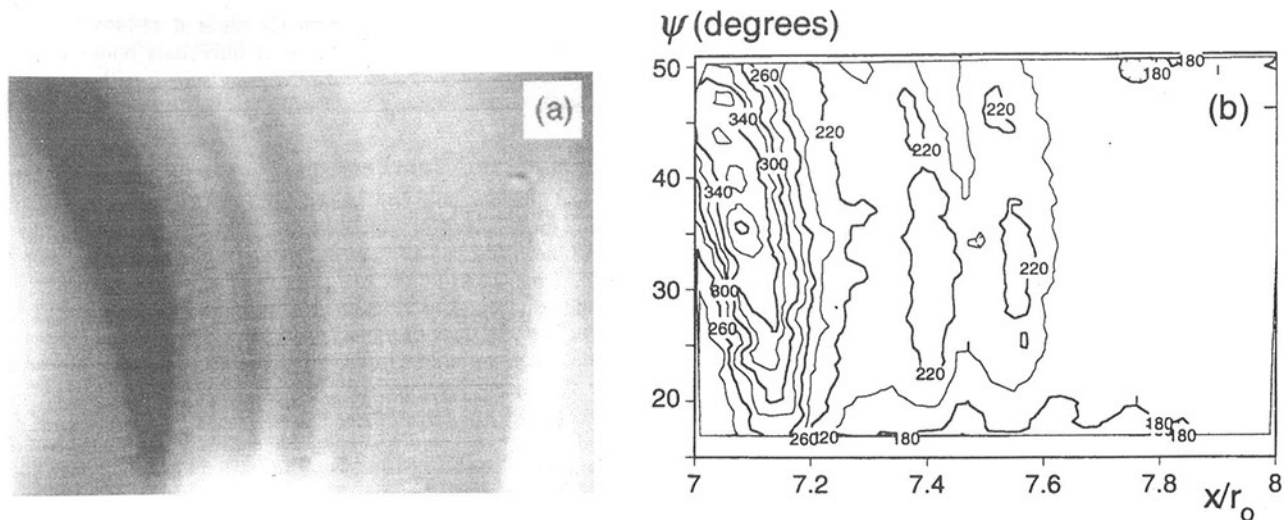
Fig. 10 Enlarged portion of Fig. 9 to show surface variations due to Görtler vortex pairs for Re = 19,400 (Re_D = 7205) and T_i/T_w = 0.85 at x/r_o = 7.0–8.0 and ψ = 0–50 deg, just downstream of the second inlet: (*a*) enhanced infrared image; (*b*) Nusselt number contours

Spatially resolved Nusselt numbers, determined from this infrared image, are shown in Fig. 10(*b*). In spite of the relatively high Reynolds number of this flow, important Nusselt number variations due to the Görtler vortex pairs are evident, where higher and lower local Nusselt numbers correspond to vortex pair downwash and upwash regions, respectively. Such variations are entirely consistent with the circumferential vorticity contours shown in the bottom portion of Fig. 8 for ψ = 90 deg. The high Nusselt number region located at x/r_o = 7.0–7.2 in Fig. 10(*b*) is due to the shear layer near the edge of the inlet jet. This shear layer contains a shear layer vortex like the ones seen the many of the visualization images presented in Fig. 3. The results in Fig. 10(*b*) additionally illustrate the excellent accuracy and spatial resolution obtained with the infrared imaging techniques employed for the study.

Spatially Averaged Nusselt Number Variations. Circumferentially averaged Nusselt number distributions, determined from the results in Fig. 9 (x/r_o = 0–15), are presented in Fig. 11(*a*) for Re = 19,400 (Re_D = 7205) and T_i/T_w = 0.85. Also included in this figure are data points determined from thermocouple measurements, made at discrete point locations. Such data, along with other thermocouple measurements, are used to determine the in situ calibrations of the infrared images. All local thermocouple data thus accurately match local infrared data at all thermocouple measurement stations. The thermocouple data are a bit lower than the infrared data in Fig. 11(*a*) because they are based on averages of 3–4 measurements (spaced 90° apart), which does not give an accurate (or complete) circumferential average. Circumferential-averages of the infrared data at particular x/r_o, on the other hand, are determined from about 1300 data points spaced uniformly around the swirl chamber circumference. In both cases, Nusselt numbers show important decreases as x/r_o increases away from cylinder inlet locations.

Circumferentially averaged Nusselt number distributions (determined entirely from thermocouple measurements) are presented in Fig. 11(*b*) for different Re, different Re_D, and different T_i/T_w, ranging from 0.62 to 0.86. Important quantitative and qualitative information is provided by these data, even though values may differ somewhat from circumferential averages based on larger numbers of data points. As for the data in Fig. 11(*a*), Nusselt numbers in Fig. 11(*b*) also show important decreases as x/r_o increases away from cylinder inlets located at x/r_o = 0–1 and x/r_o = 7–8. In addition, Nusselt numbers at particular x/r_o decrease as Re decreases, when T_i/T_w ranges from 0.62 to 0.67.

Figure 11(*b*) also shows that Nusselt numbers for Re = 17,600–19,400 change by important amounts as the T_i/T_w temperature ratio is changed. At each x/r_o value investigated, Nusselt numbers decrease significantly as the temperature ratio increases from 0.66 to 0.86. Changes are evident at all x/r_o investigated, especially near each of the two inlets. Responsible are centrifugal forces in the swirl chamber, which force cool, high-density fluid near the hot surfaces by increasing amounts as T_i/T_w decreases. This acts to

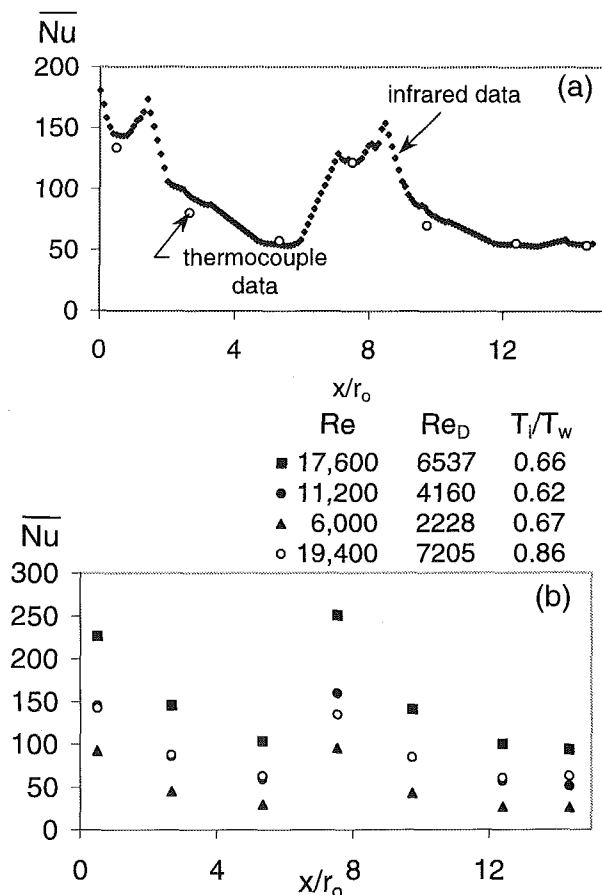| Re	Re_D	T_i/T_w
■ 17,600	6537	0.66
● 11,200	4160	0.62
▲ 6,000	2228	0.67
○ 19,400	7205	0.86

Fig. 11 Circumferentially averaged Nusselt numbers as dependent upon x/r_o: (*a*) Nusselt numbers for Re = 19,400 (Re_D = 7205) and T_i/T_w = 0.85; (*b*) Nusselt numbers for different Re and Re_D and for different T_i/T_w
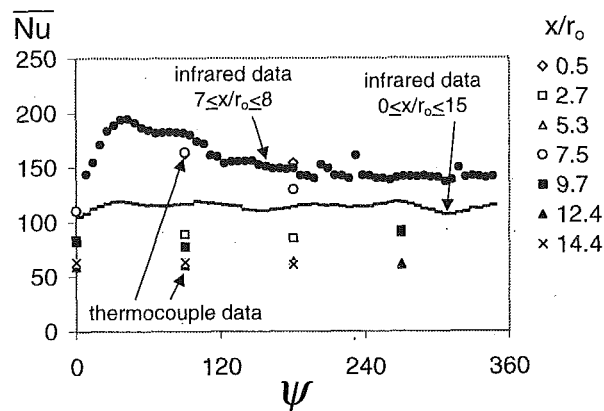
Fig. 12 Axially averaged Nusselt number variation with ψ for Re = 19,400 (Re$_D$ = 7205) and T_i/T_w = 0.85

enhance surface heat transfer coefficients, especially when the intermingling of cool dense fluid with hot, low-density fluid is supplemented by arrays of interacting Görtler vortex pairs (like the ones shown in Fig. 3).

Axially averaged Nusselt number distributions, determined from the infrared results in Fig. 9 at x/r_o = 7–8, and at x/r_o = 0–15 are presented in Fig. 12 for Re = 19,400 (Re$_D$ = 7205) and T_i/T_w = 0.85. Also included on this figure are Nusselt numbers, determined from individual thermocouple measurements at different x/r_o, for the same Re and T_i/T_w. Trends of the infrared-determined Nusselt numbers (denoted by the solid circle data) for x/r_o = 7–8 are consistent with the thermocouple-determined data for x/r_o = 7.5. These and other Nusselt number data in the figure show that the most important variations with ψ are near and just downstream of each inlet at x/r_o = 0.5, and at x/r_o = 7.5. As x/r_o increases relative to these values, Nusselt numbers then become approximately circumferentially uniform and invariant with ψ. The Nusselt number data determined from spatial averages of infrared measurements at x/r_o = 0–15 are lower than values averaged over x/r_o = 7–8 in Fig. 12.

Globally averaged (in axial and circumferential directions) Nusselt numbers (determined entirely from thermocouple measurements) are compared with data from Glezer et al. (1996) and a correlation from Moon et al. (1998) in Fig. 13. The Glezer et al. data are obtained from a swirl chamber with an inlet made of a continuous axial slot spanning the entire axial length of the chamber. In spite of this difference, the present data show trends that are largely consistent with the correlation and data from those papers. In particular, the present data point for Re = 19,400 and T_i/T_w =
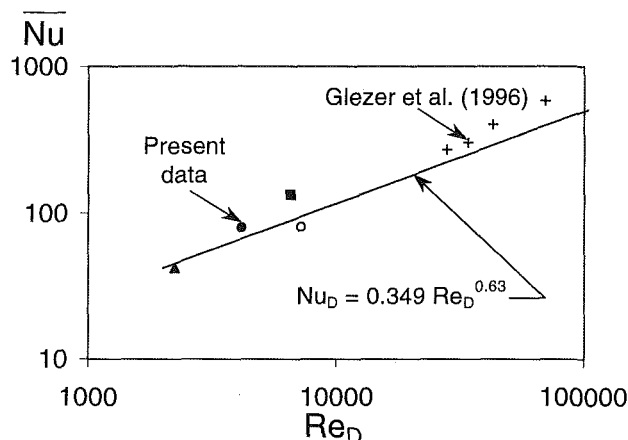
0.86 is in line with all four of the Glezer et al. (1996) data points for about the same T_i/T_w. The other three data points from the present study for T_i/T_w = 0.62–67 also line up with each other, but with a higher slope compared to the data at the higher T_i/T_w.

Summary and Conclusions

Heat transfer and flow measurements from a swirl chamber, which models a cooling passage located near the leading edge of a turbine blade, are presented for Re from 4450 to 19,400, and T_i/T_w from 0.62 to 0.86.

Spatially resolved Nusselt number distributions, measured on the concave surface of the chamber using infrared imaging, show complicated variations through the chamber, especially near and just downstream of each of the swirl chamber inlets. Nusselt numbers are highest at these locations, and Nusselt number gradients are present in both the axial and circumferential directions. The most interesting Nusselt number variations are directly due to the Görtler vortex pairs, which result in arrays of parallel high and low local Nusselt number streaks, where higher and lower values correspond to vortex pair downwash and upwash regions, respectively. Such variations are entirely consistent with surveys of time-averaged circumferential vorticity, circumferential velocity, static pressure, and total pressure. Also present near inlets are augmented Nusselt numbers produced by the shear layer near the edge of the inlet jet, which contains a shear layer vortex seen in visualization images. As the flows advect away from each inlet, Nusselt numbers decrease and become more spatially uniform along the interior surface of the chamber. Such results illustrate the excellent accuracy and spatial resolution obtained with the infrared imaging techniques employed for the study.

Spatially averaged Nusselt numbers additionally show important variations with Reynolds number Re, temperature ratio, T_i/T_w, nondimensional axial location x/r_o, and circumferential location ψ. Like local data, circumferentially averaged Nusselt number distributions show important decreases as x/r_o increases relative to cylinder inlet locations. Effects of changing the T_i/T_w temperature ratio are very strong and evident at all x/r_o investigated, especially near each of the two inlets. When T_i/T_w ranges from 0.62 to 0.67, circumferentially averaged Nusselt numbers at particular x/r_o decrease as Re decreases. Axially averaged Nusselt number distributions show the most important variations with ψ near and just downstream of each inlet. As flow moves away from these inlets, axially averaged Nusselt numbers then become approximately circumferentially uniform and invariant with ψ.

Especially important to augmentation of local and spatially averaged Nusselt numbers near each of the inlets are: (*i*) centrifugal forces, which force cool, high-density fluid near the hot surfaces by increasing amounts as T_i/T_w decreases, (*ii*) re-initiation of thin thermal boundary layers, (*iii*) small-scale secondary flows within the arrays of initially developing Görtler vortex pairs, (*iv*) continuous interactions and intermingling of different-sized Görtler vortex pairs with each other, especially at higher Reynolds numbers and at locations just downstream of inlet ducts, and (*v*) skewness and three dimensionality of Görtler vortex pairs produced by the axial component of flow in the swirl chamber.

Fig. 13 Globally averaged Nusselt number variation with Re$_D$. Symbol labels for the present data are given in Fig. 11.

References

Bergles, A. E., 1969, "Survey and Evaluation of Techniques to Augment Convective Heat and Mass Transfer," *International Journal of Heat and Mass Transfer,* Vol. 1, pp. 331–413.

Bruun, H. H., Fitouri, A., and Khan, M. K., 1993, "The Use of a Multiposition Single Yawed Hot-Wire Probe for Measurements in Swirling Flow," *Thermal Anemometry,* ASME FED-Vol. 167, pp. 57–65.

Chang, F., and Dhir, V. K., 1994, "Turbulent Flow Field in Tangentially Injected Swirl Flows in Tubes," *International Journal of Heat and Fluid Flow,* Vol. 15, No. 5, pp. 346–356.

Date, A. W., 1974, "Prediction of Fully Developed Flow in a Tube Containing a Twisted-Tape," *International Journal of Heat and Mass Transfer,* Vol. 17, pp. 845–859.

Dong, M., and Lilley, D. G., 1993, "Parameter Effects on Flow Patterns in Confined Turbulent Swirling Flows," *Computer Modelling, Cofiring and NO$_x$ Control,* ASME FACT-Vol. 17, pp. 17–21.

Fitouri, A., Khan, M. K., and Bruun, H. H., 1995, "A Multiposition Hot-Wire Technique for the Study of Swirling Flows in Vortex Chambers," *Experimental Thermal and Fluid Science,* Vol. 10, pp. 142–151.

Gambill, W. R., and Bundy, R. D., 1962, "An Evaluation of the Present Status of Swirl-Flow Heat Transfer," ASME Paper No. 62-HT-42, pp. 1–12.

Glezer, B., Moon, H.-K., and O'Connell, T., 1996, "A Novel Technique for the Internal Blade Cooling," ASME Paper No. 96-GT-181.

Glezer, B., Lin, T., and Moon, H.-K., 1997, "An Improved Turbine Cooling System," U.S. Patent No. 5603606.

Glezer, B., Moon, H.-K., Kerrebrock, J., Bons, J., and Guenette, G., 1998, "Heat Transfer in a Rotating Radial Channel With Swirling Internal Flow," ASME Paper No. 98-GT-214.

Hedlund, C. R., Ligrani, P. M., Glezer, B., and Moon, H.-K., 1999, "Heat Transfer in a Swirl Chamber at Different Temperature Ratios and Reynolds Numbers," *Int. Journal of Heat and Mass Transfer,* Vol. 42.

Hong, S. W., and Bergles, A. E., 1976, "Augmentation of Laminar Flow Heat Transfer in Tubes by Means of Twisted-Tape Inserts," ASME *Journal of Heat Transfer,* Vol. 98, pp. 251–256.

Khalatov, A. A., and Zagumennov, I. M., 1990, "Heat Transfer and Fluid Dynamics Near Flat Surfaces in Confined Swirling Flows," *Proc. Ninth International Heat Transfer Conference,* Jerusalem, Israel, pp. 329–334.

Kok, J. B. W., Rosendal, F. J. J., and Brouwers, J. J. H., 1993, "LDA-Measurements on Swirling Flows in Tubes," *SPIE Laser Anemometry Advances and Applications,* Vol. 2052, pp. 721–728.

Kreith, F., and Margolis, D., 1959, "Heat Transfer and Friction in Turbulent Vortex Flow," *Appl. Sci. Research,* Vol. 8, pp. 457–473.

Kumar, R., and Conover, T., 1993, "Flow Visualization Studies of a Swirling Flow in a Cylinder," *Experimental Thermal and Fluid Science,* Vol. 7, pp. 254–262.

Li, H., and Tomita, Y., 1994, "Characteristics of Swirling Flow in a Circular Pipe," ASME *Journal of Fluids Engineering,* Vol. 116, pp. 370–373.

Ligrani, P. M., Hedlund, C. R., Thambu, R., Babinchak, B. T., Moon, H.-K., and Glezer, B., 1997, "Flow Phenomena in Swirl Chambers," ASME Paper No. 97-GT-530.

Ligrani, P. M., Singer, B. A., and Baun, L. R., 1989a, "Miniature Five-Hole Pressure Probe for Measurement of Three Mean Velocity Components in Low Speed Flow," *Journal of Physics E—Scientific Instruments,* Vol. 22, No. 10, pp. 868–876.

Ligrani, P. M., Singer, B. A., and Baun, L. R., 1989b, "Spatial Resolution and Downwash Velocity Corrections for Multiple-Hole Pressure Probes in Complex Flows," *Experiments in Fluids,* Vol. 7, No. 6, pp. 424–426.

Moffat, R. J., 1988, "Describing the Uncertainties in Experimental Results," *Experimental Thermal and Fluid Science,* Vol. 1, No. 1, pp. 3–17.

Moon, H.-K., O'Connell, T., and Glezer, B., 1998, "Heat Transfer Enhancement in a Circular Channel Using Lengthwise Continuous Tangential Injection," *IHTC, Proc. International Heat Transfer Congress,* Seoul, South Korea.

Ogawa, A., 1993, *Vortex Flow,* CRC Press.

Papadopoulos, P., France, D. M., and Minkowycz, W. J., 1991, "Heat Transfer to Dispersed Swirl Flow of High-Pressure Water With Low Wall Super Heat," *Experimental Heat Transfer,* Vol. 4, pp. 153–169.

Razgaitis, R., and Holman, J. P., 1976, "A Survey of Heat Transfer in Confined Swirling Flows," *Future Energy Production Systems, Heat and Mass Transfer Processes,* Vol. 2, Academic Press, New York, pp. 831–866.

Sampers, W. F. J., Lamers, A. P. G. G., and Van Steenhoven, A. A., 1992, "Experimental and Numerical Analysis of a Turbulent Swirling Flow in a Tube," *ICHEME Symposium Series No. 129,* Vol. 2, pp. 765–771.

Thambu, R., Babinchak, B. T., Ligrani, P. M., Hedlund, C. R., Moon, H.-K., and Glezer, B., 1999, "Flow in a Simple Swirl Chamber With and Without Controlled Inlet Forcing," *Experiments in Fluids,* Vol. 26, pp. 347–357.

Local Measurement of Loss Using Heated Thin-Film Sensors

M. R. D. Davies

F. K. O'Donnell

PEI Technologies: Stokes
Research Institute,
Department of Mechanical & Aeronautical
Engineering,
University of Limerick,
Limerick, Ireland

A calibration equation is derived linking the nondimensional entropy generation rate per unit area with the nondimensional aerodynamic wall shear stress and free-stream pressure gradient. It is proposed that the latter quantities, which can be measured from surface sensors, be used to measure the profile entropy generation rate. It is shown that the equation is accurate for a wide range of well-defined laminar profiles. To measure the dimensional entropy generation rate per unit area requires measurement of the thickness of the boundary layer. A general profile equation is given and used to show the range of accuracy of a further simplification to the calibration. For flows with low free-stream pressure gradients, the entropy generation rate is very simply related to the wall shear stress, if both are expressed without units. An array of heated thin film sensors is calibrated for the measurement of wall shear stress, thus demonstrating the feasibility of using them to measure profile entropy generation rate.

Introduction

With turbine section efficiencies of over 90 percent (Denton 1993), the modern jet engine gas turbine is considered by many to be technically mature. However, extensive research and development continues due to the large economic benefits of even marginal increases in efficiency and performance. Improvement in turbine efficiency depends largely on the designers' ability to predict the magnitude and location of loss, where a loss mechanism may be defined as any flow feature which reduces the efficiency of the turbine.

The development of any loss prediction method requires validation by means of accurate measurements of flows at engine representative conditions. To this end, Duffy et al. (1995) calibrated an isolated heated thin-film sensor for the measurement of aerodynamic wall shear stress in laminar flow with a favorable free stream pressure gradient. This calibration was further developed and extended to turbulent flows by Davies et al. (1997).

In laminar and turbulent shear flows the wall shear stress is a measure of the surface velocity gradient, which is almost always at a maximum at this point. The local rate of entropy generation is proportional to the local velocity gradient squared; therefore this too is at a maximum at the wall. Two points follow from this: First, both the shear stress and the entropy generation rate are good measures of a code's ability to predict boundary layer loss. Second, the question arises as to whether it is possible to measure entropy generation rate across a boundary layer using a surface-mounted sensor. To do so would be highly desirable because traversing a very thin turbine boundary layer as a blade rotates under engine representative conditions would be very technically challenging, and current optical techniques do not have the spatial resolution to determine the near-wall velocity gradients under such conditions. This paper will address both of these points by first deriving a local entropy generation rate calibration and second demonstrating how this new calibration may be applied to an array of surface-mounted heated thin-film sensors.

The initial theoretical approach developed for the calibration considers the case of isothermal, incompressible laminar flow in the presence of weak and strong favorable free-stream pressure gradients. The resulting calibration equation is semi-empirical, requiring the experimental determination of a constant. It links the entropy generation rate per unit area to the wall shear stress when they are both expressed nondimensionally. To determine the dimensioned entropy requires knowledge of the boundary layer thickness. The problem of measuring the surface distribution of profile loss is thereby reduced from the requirement to know the whole field to that of knowing two parameters: the shear stress and the boundary layer thickness.

An existing aerodynamic wall shear stress calibration for isolated heated thin-film sensors is applied to an array of heated thin film sensors. The sensors used for this work have been designed and manufactured by Motoren- und Turbinen-Union (MTU), their use is comprehensively described by Schröder (1996) and they have previously been used qualitatively by Tiedemann (1997) on an aerodynamically scaled turbine stage in conjunction with a rotating anemometer, described by Davies et al. (1997).

Entropy Generation in Laminar Isothermal Flow

Following the nondimensional method of Dalton and Davies (1999), and assuming that the rate of change of boundary layer thickness is small, Curle's (1961) approximation to the near-wall boundary layer may be written as:

$$\frac{\partial^2 u^*}{\partial y^{*2}} = \frac{\partial p^*}{\partial x^*} \tag{1}$$

where: $\quad u^* = \frac{u}{u_\infty}, \quad y^* = \frac{y}{\delta}, \quad p^* = \frac{p\delta}{\mu u_\infty}, \quad x^* = \frac{x}{\delta}$

where x^* and y^* directions are curvilinear parallel and normal to the considered surface respectively. This integrates to:

$$\frac{\partial u^*}{\partial y^*} = \tau_w^* + \frac{\partial p^*}{\partial x^*} y^* \tag{2}$$

where: $\quad \tau_w^* = \frac{\tau_w \delta}{\mu u_\infty}$

Assuming that the entropy is generated principally due to the shear parallel to the surface, the rate of entropy generation per unit volume due to viscous friction in an incompressible flow without heat transfer is given by Bejan (1979) as:

$$\dot{S}''' = \frac{\mu}{T} \left(\frac{\partial u}{\partial y} \right)^2 \tag{3}$$

This is equal to the dissipation function divided by the local temperature. It may be thought of as the heat generated in the

---

boundary layer per unit volume divided by the local temperature, therefore making it similar to the standard expression for equilibrium entropy change. An expression for the turbulent contribution to the entropy generation rate can be derived from this analogy as:

$$\dot{S}''' = \frac{\tau'_{xy}}{T} \frac{\partial \bar{u}}{\partial y} \qquad (4)$$

From Eq. (3) the nondimensional entropy generation rate is:

$$\dot{S}'''* = \left(\frac{\partial u*}{\partial y*} \right)^2 \qquad (5)$$

$$\text{where:} \quad \dot{S}'''* = \frac{\dot{S}''' T \delta^2}{\mu u_\infty^2}$$

In any calibration experiment or theory the boundary layer velocity profile must be fully defined. The entropy generation rate per unit area is therefore determined from:

$$\dot{S}''* = \int_0^1 \left(\frac{\partial u*}{\partial y*} \right)^2 dy* \qquad (6)$$

$$\text{where:} \quad \dot{S}''* = \frac{\dot{S}'' T \delta}{\mu u_\infty^2}$$

This term integrated around a blade or vane profile gives the entropy generation rate per unit span length, or the profile entropy generation rate. It is the local value, however, that is of interest here as it shows where on the profile the entropy is generated.

For the measurement of entropy generation rate per unit area using surface sensors, it is not possible to integrate to the edge of the boundary layer because the assumptions of Eq. (1) only apply to the near-wall region. Thus the integration limits are taken as zero to $\Delta*$, where $\Delta*$ is the fraction of the boundary layer in the region where the velocity gradients are highest and within which most of the entropy is generated. Substituting Eq. (1) into Eq. (6) and integrating to $\Delta*$:

$$\dot{S}''* = \Delta* \left[\tau_w^{*2} + \frac{\partial p*}{\partial x*} \Delta* \left(\frac{dp*}{dx*} \frac{\Delta*}{3} + \tau_w* \right) \right] \qquad (7)$$

This equation is independent of the free-stream velocity and reduces to:

$$\frac{\dot{S}'' T \mu}{\Delta* \tau_w^2} = 1 + \frac{\Delta}{\tau_w^2} \frac{\partial p}{\partial x} \left(\frac{\Delta}{3} \frac{\partial p}{\partial x} + \tau_w \right) \qquad (8)$$
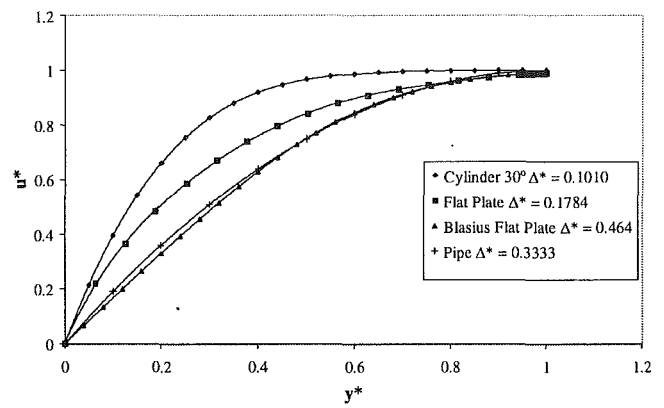

Fig. 1 Comparison of boundary layer velocity profiles

Evaluation of $\Delta*$ in Negligible Pressure Gradient Flows.

$\Delta*$ is found for a range of flow species by using well-defined boundary layer profiles to evaluate $\dot{S}''*$ from Eq. (6). Equation (7) is then solved for $\Delta*$ using the known value of τ_w^*, and $\partial p*/\partial x*$ if appropriate. Considering the case of a pressure gradient sufficiently small that the second term on the right-hand side of Eq. (1) may be neglected, Eq. (7) may be rewritten for the purpose of calibration as:

$$\Delta* = \int_0^1 \left(\frac{du*}{dy*} \right)^2 dy* \bigg/ \left(\frac{\partial u*}{\partial y*} \right)_{y*=0} \qquad (9)$$

Figure 1 shows the nondimensional velocity profile measured on a flat plate identical to that described by Duffy et al. (1995). The variation between the measured profile and the Blasius flat plate profile, also shown, is attributed to the elliptical leading edge of the plate employed in this experiment.

From Eq. (9) $\Delta*$ is found to be 0.1784 for the flat plate measurement and 0.4647 for the Blasius profile. Following the same reasoning as that used in the shear stress calibration of Davies et al. (1997), that the pressure gradient term is small in laminar pipe flow, $\Delta*$ may also be found for a circular pipe. The velocity gradient is:

$$\frac{\partial u*}{\partial r*} = 2r* \qquad (10)$$

$$\text{where:} \quad r* = \frac{r}{R} \quad \text{and} \quad u* = \frac{u}{u_0}$$

Nomenclature

C_1 = calibration constant, V²/K
C_2 = calibration constant, m
K = thermal conductivity, W/mK
L_{eff} = effective sensor length, m
Pr = Prandtl number
R_h = ohmic resistance, Ω
R = pipe radius, m
Re = Reynolds number
$\dot{S}'''$ = entropy generation rate per unit volume, W/m³K
$\dot{S}''$ = entropy generation rate per unit area, W/m²K
T = temperature, K

V = voltage, V
a = calibration constant
p = pressure, N/m²
r = pipe radial direction, m
u = x-direction velocity, m/s
W_{eff} = effective sensor width, m
x, y = surface and normal curvilinear coordinates, m
$\Delta*$ = entropy generation rate constant
δ = boundary layer thickness, m
μ = dynamic viscosity, kg/ms
ρ = density, kg/m³

τ_w = aerodynamic wall shear stress, N/m²
τ'_{xy} = turbulent apparent shear stress, N/m²

Subscripts

s = sensor
∞ = approach condition
∞_x = edge of boundary layer condition
0 = zero flow, or centerline condition
M = max sensor temperature
L = mean sensor temperature

Superscripts

$*$ = nondimensional parameter

Table 1 Comparison of values of Δ^* evaluated from various flow species

Flow Species	Δ^*	τ_w^*	$\Delta^*\tau_w^{*1.5}$
Cylinder 30°	0.1010	4.6449	1.0111
Cylinder 40°	0.1150	4.1981	0.9891
Flat Plate	0.1784	2.9310	0.8950
Blasius Flat Plate	0.4647	1.6761	1.0083
Pipe Flow	0.3333	2.000	0.9427

Therefore:

$$\dot{S}''^* = \frac{4}{3} \quad \text{and} \quad \tau_w^* = \frac{\partial u^*}{\partial r^*}\Big|_{r^*=1} = 2$$

The value of Δ^* in laminar pipe flow is then $\frac{1}{3}$.

Evaluation of Δ^* in Presence of Free-Stream Pressure Gradient. Considering flow past a circular cylinder, the velocity distribution in the boundary layer can be found from the Blasius series as shown by Schlichting (1979). Using an experimentally determined pressure gradient, the value of Δ^* is determined by iteration from Eq. (7) to be 0.101 at a cylinder angle of 30 deg and 0.115 at an angle of 40 deg. It is evident that the value of Δ^* varies between the distinctly different flow species of flat plate, circular pipe, and circular cylinder. Considering the boundary layer velocity distributions of these three flow species as shown in Fig. 1, it is clear that, as expected from the nature of the calibration Eq. (7), the value of Δ^* depends upon the fullness of the profile.

A more consistent calibration constant may be found from the product of Δ^* and the nondimensional wall shear stress raised to the power of 1.5, as shown in Table 1. A striking result follows from this:

$$\Delta^* = \tau_w^{*-1.5} \qquad (11)$$

For a very wide range of profile shapes the integration distance to evaluate the generated entropy is a very simple function of the nondimensional wall shear stress. The larger this stress, the less the fraction of the boundary layer that must be integrated over. This result implies that Eq. (7) may now be rewritten without Δ^* as:

$$\dot{S}''^* = \tau_w^{*0.5}\left[1 + \frac{\partial p^*}{\partial x^*}\tau_2^{*-2.5}\left(\frac{\tau_w^{*-2.5}}{3}\frac{\partial p^*}{\partial x^*} + 1\right)\right] \qquad (12)$$

For the case of negligible pressure gradient a second striking result follows:

$$\dot{S}''^* = \tau_w^{*0.5} \qquad (13)$$

Adding dimensions to this equation shows that for a linear profile, the entropy generation rate per unit area is equal to the work done against friction per unit area and temperature. Figure 2 shows that the error in the evaluation of the entropy generation rate using Eq. (12) is less than ±5 percent.

Evaluation of Δ^* Using a General Velocity Profile. It is of interest to know over what range of profiles the approximation of Eq. (13) is valid, because there are advantages in knowing the entropy generation rate without having to know the local pressure gradient.

The velocity profile of any boundary layer may be expressed in terms of τ_w^* and H_δ, a new boundary layer velocity profile shape factor, using Eq. (14), which is a modification of a thermal boundary layer profile given by Wallace (1996):

$$u^* = 1 - e^{y^*}(y^* - 1)^2\left(1 - \frac{y^*(1 - \tau_w^*)}{H_\delta}\right)^{-H_\delta} \qquad (14)$$
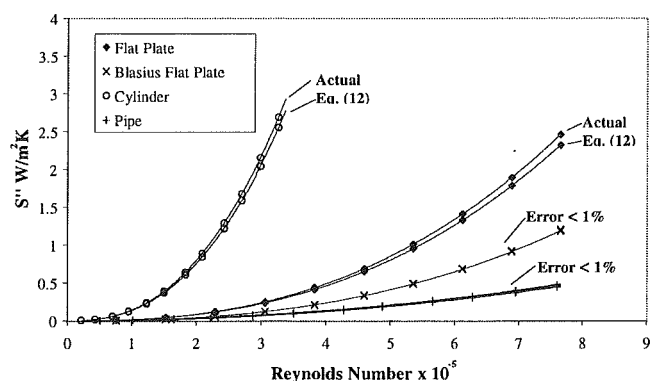

Fig. 2 Comparison of entropy generation rates for flat plate, pipe flow, and cylinder flow evaluated using Eq. (12) and exactly from the velocity profile

where $u^* = (u/u_{\infty x})$.

Plotted in accordance with Eq. (14), all profiles have values of velocity and position between 1 and 0. The wall shear stress determines the wall velocity gradient and the value of H_δ determines the fullness of the profile.

Figure 3 demonstrates that Eq. (14) can be used to curve fit the boundary layer velocity profiles of the flat plate, pipe flow, and circular cylinder already considered. Substitution of Eq. (14) into Eq. (9) allows the value of Δ^* to be found for a range of velocity profiles by varying values of τ_w^* and H_δ. Figure 4 gives an example of the range of velocity profiles for which Eq. (13) is valid for a value of H_δ equal to 2.

It is therefore possible to determine the local rate of entropy generation per unit area, for a wide range of velocity profiles using
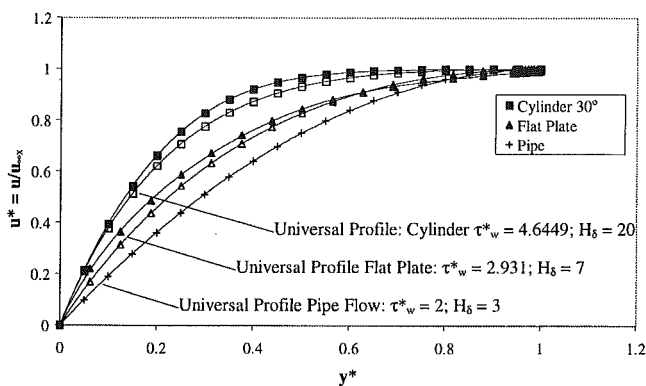

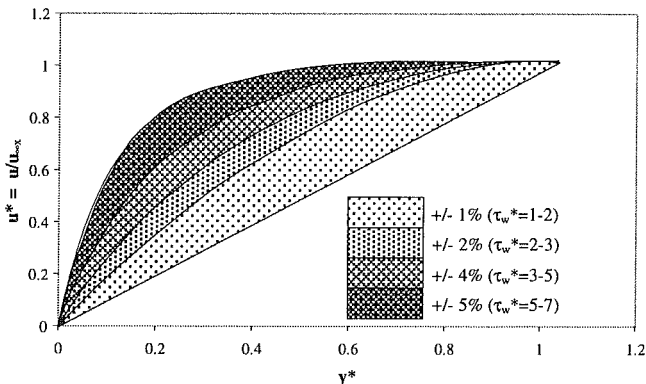Fig. 3 Velocity profile as described by Eq. (14) compared with actual velocity profiles

Fig. 4 Range of velocity profiles for which the simplified Eq. (13) is valid with H_δ = 2. Shading shows the error in using Eq. (13) in this region to predict entropy generation rate.
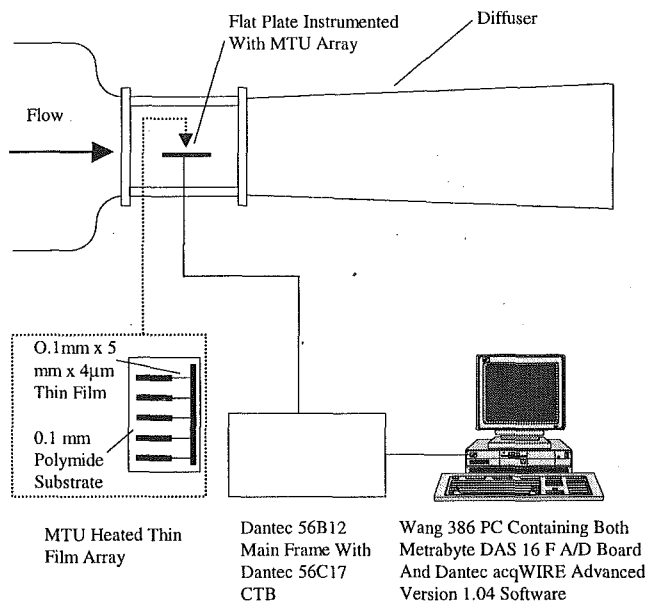
Fig. 5 Schematic diagram of heated thin film calibration experiment

Fig. 6 Determination of wall shear stress calibration constants

Eq. (13), from a direct measurement of the local nondimensional aerodynamic wall shear stress τ_w^*. For profiles outside of this region it is necessary to use the full form of the calibration equation shown in Eq. (12). In the remaining sections, the aerodynamic wall shear stress calibration of an array of heated thin films is given and their application to entropy generation rate is outlined.

Laminar Aerodynamic Wall Shear Stress Calibration

Fitzgerald et al. (1998) have shown that the Davies and Duffy (1995) aerodynamic wall shear stress calibration for heated thin-film sensors may be written in the form of Eq. (15). C_1 and C_2 are constants, which may be determined from calibration experiments:

$$\tau_w = \left(\frac{V_s^2 - V_0^2}{C_1(T_s - T_\infty)} \right)^3 + C_2\left(\frac{dp}{dx} \right) \quad (15)$$

The MTU heated thin-film array, as described by Schröder (1996), consists of pure nickel thin films $0.1 \text{ mm} \times 5.00 \text{ mm} \times 4$ μm deposited onto a 0.1 mm thick polyimide substrate at 2.5 mm intervals. The array is mounted flush with the surface and is operated in constant-temperature bridge mode, as part of a Wheatstone bridge in the feedback loop of a high gain DC amplifier, at an overheat temperature of 60 K.

Evaluation of the Aerodynamic Wall Shear Stress Calibration Constants. The calibration procedure remains the same as that outlined by Duffy et al. (1995) and Davies et al. (1997). Multipoint calibrations plotting the variation in $(V_s^2 - V_0^2)$ over a range of wall shear stress values were used to determine the constants C_1 and C_2. The first constant C_1 is associated with a negligible pressure gradient flow and is found from flat plate experimentation. The second constant C_2 is determined in the presence of a pressure gradient on a cylinder where the wall shear stress is found from analytical predictions. The calibration experiment is carried out using the apparatus outlined in Fig. 5. The calibration plot to find C_1 and C_2 is shown in Fig. 6.

Although the values of the constants C_1 and C_2 found in this investigation differ from those found by Fitzgerald et al. (1998), it is found that the value of a, the low dp/dx calibration constant given by Duffy et al. (1995) as 0.00403, is measured as 0.0409. Therefore this constant is independent of sensor dimensions, materials, and operating temperature and may be applied to any heated thin film sensor. The relationship between C_1 and a is:
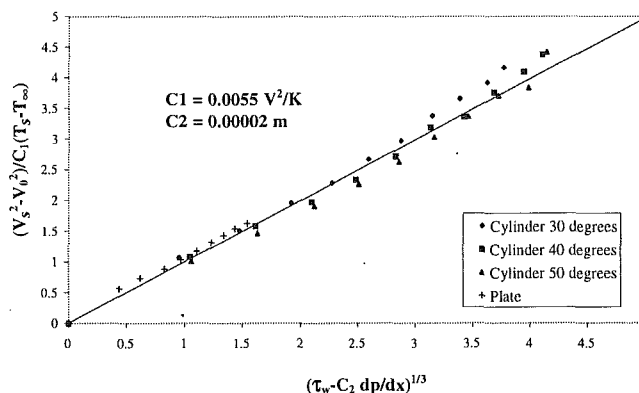
$$C_1 = \left(\frac{2\rho \ \mathrm{Pr} L_{\mathrm{eff}}^2 a}{\mu^2} \right)^{1/3} \left(\frac{(T_L - T_\infty)^{2/3}(T_M - T_\infty)^{1/3}}{(T_s - T_\infty)} \right) KR_h W_{\mathrm{eff}} \quad (16)$$

Thermal Interaction Between Heated Thin Films. As the heated thin films are operating in an array and the sensors are very sensitive to temperature, it is necessary to consider the thermal interaction between adjacent sensors operating simultaneously. From the thermal image shown in Fig. 7, which is recorded using the thermal imaging procedure described by Duffy et al. (1995), the effective thermal length is found to be 0.62 mm. As the sensor spacing is much greater than the effective thermal length of each sensor, it is assumed that there will be no conductive thermal interaction through the substrate. This also implies that there will be no convective interaction as the surface is adiabatic immediately downstream of the heated area.

Measurement of Local Entropy Generation Rate Using a Heated Thin-Film Array

Using the heated thin-film array calibrated for the measurement of local aerodynamic wall shear stress, it is now possible to determine the local entropy generation rate from either Eq. (12) or (13), using the nondimensional wall shear stress τ_w^* given by Eq. (17). The present form of the equation requires the thickness of the velocity boundary layer; therefore, in its current form this measurement technique is restricted to flows where the boundary layer thickness is determinable:

$$\tau_w^* = \left[\left(\frac{\delta}{\mu u_\infty} \right)^{1/3} \left(\frac{V_s^2 - V_0^2}{C_1(T_s - T_\infty)} \right)^3 + \frac{C_2(\mu u_\infty)^{2/3}}{\delta^{1/3}} \frac{\partial p^*}{\partial x^*} \right]^3 \quad (17)$$

The boundary layer thickness may be found by probe or optical traverses of the outer boundary layer. This is much less technically
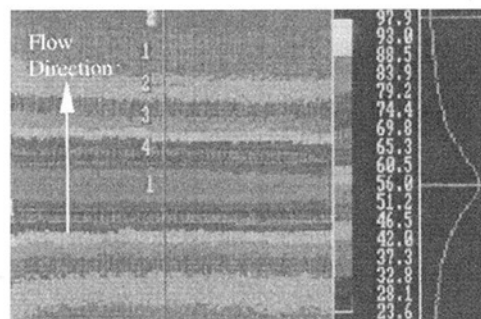

Fig. 7 Thermal image of MTU heated thin film operating at an overheat temperature of 60 K

challenging than the definition of the entire velocity boundary layer and the problem of local entropy generation rate measurement has now been reduced to a two-parameter measurement.

It is notable that for fully developed flows, the local entropy generation rate per unit area can be found from surface shear because the boundary layer thickness is known. Therefore, in its present form, the calibration may be used directly to measure the entropy generation rate in developed flow such as pipe flow or internal cooling passages of turbine blades.

Equation (4) suggests the extension of this calibration to turbulent flow and as such would allow the measurement of local entropy generation rate over the entire surface of a turbine blade. However, as shown by Fitzgerald et al. (1998) the aerodynamic wall shear stress on a blade suction surface is highest in the leading edge region where the flow is laminar. Thus the current laminar calibration is valid for the region where the entropy generation rate is possibly greatest and hence of most interest.

Conclusions

- An entropy generation rate calibration is derived for the direct measurement of local entropy generation rate in isothermal laminar flow with favorable free-stream pressure gradient.
- The entropy generation rate in a flow with negligible pressure gradient is shown to be equal to the square root of the local nondimensional aerodynamic wall shear stress.
- A new velocity boundary layer velocity profile is presented and shown to be applicable to a wide variety of flow species.
- An array of heated thin-film sensors is calibrated for the measurement of local wall shear stress and the low-pressure gradient calibration constant is found to be almost identical to that found for a different sensor at a different overheat.
- The problem of local entropy generation rate measurement is reduced form a boundary layer field measurement to a two-parameter measurement.

References

Bejan, A., 1979, "A Study of Entropy Generation in Fundamental Convective Heat Transfer," ASME *Journal of Heat Transfer,* Vol. 101, pp. 718–725.

Curle, N., 1961, "Heat Transfer Through a Constant-Property Laminar Boundary Layer," *Aero. Res. Council,* Rep. & Mem. No. 3300.

Dalton, T., and Davies, M. R. D., 1999, "Dimensional Analysis in Heat Transfer," ASME *Journal of Heat Transfer,* Vol. 121, p. 471.

Dantec Elektronic, 1988, "Instruction Manual For 56C17 CTA," Skovlunde, Denmark.

Davies, M. R. D., Byrne, C. M., and Dillon, P., 1997, "Instrumentation Systems for Continuous Flow Turbine Rotor," ASME Paper No. 97-GT-315.

Davies, M. R. D., and Duffy, J. T., 1995, "A Semi-Empirical Theory for Surface Mounted Aerodynamic Wall Shear Stress Gauges," ASME Paper No. 95-GT-193.

Davies, M. R. D., Fitzgerald, J. E., Duffy, J. T., and O'Donnell, F. K., 1997, "Measurement of Aerodynamic Wall Shear Stress With Heated Thin Film Gauges," ASME Paper No. 97-GT-211.

Denton, J. D., 1993, "Loss Mechanisms in Turbomachines," ASME JOURNAL OF TURBOMACHINERY, Vol. 115, pp. 621–656.

Duffy, J. T., 1995, "The Calibration of Surface Mounted Aerodynamic Wall Shear Stress Gauges," Ph.D. Thesis, Dept. of Mech. & Aero. Eng., University of Limerick, Ireland.

Duffy, J. T., Davies, M. R. D., and Hamilton, L., 1995, "The Calibration of a Surface Mounted Aerodynamic Wall Shear Stress Gauge in Laminar Flow With a Free-Stream Pressure Gradient," ASME Paper No. 95-GT-127.

Fitzgerald, J. E., Niven, A. J., and Davies, M. R. D., 1998, "Turbine Blade Aerodynamic Wall Shear Stress Measurements and Predictions," ASME Paper No. 98-GT-562.

Schlichting, H., 1979, *Boundary Layer Theory,* 7th ed., McGraw-Hill, New York.

Schröder, Th., 1996, "Hot Film Instrumentation of the Rotor for the DLR Transonic Turbine Test Facility," IMT Area 3 Turbine Project Contract AER2-CT92-004, Task A 3.3.

Tiedemann, M., 1997, "Stator Wake Effects on the Boundary Layer Transition of a Transonic Turbine Rotor Blade," "Eurotherm Seminar No. 55, Heat transfer in single phase flows 5," Sept. 18–19, 1997, Santorini, Greece.

Wallace, J., 1996, "Turbine Blade Boundary Layer Entropy Generation Measurement," Ph.D. Thesis, Dept. of Mech. & Aero. Eng., University of Limerick, Ireland.